Principles and theory
of protein-based pattern formation

Fridtjof Brauns

Principles and theory
of protein-based pattern formation

Fridtjof Brauns

A dissertation submitted to the Faculty of Physics

at the Ludwig–Maximilians–Universität München for the degree of
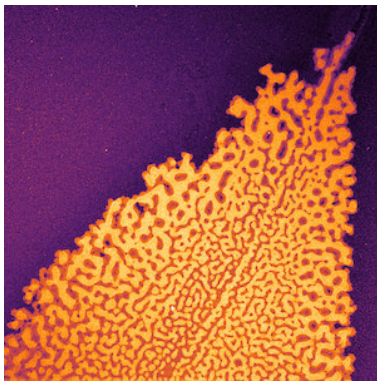
DOCTOR RERUM NATURALIUM

Munich, 14th April 2021

Zusammenfassung (Summary in German)

Die Kurve ist das göttliche Objekt.
Die Parametrisierung ist menschlich
und damit bedeutungslos.

— Detlef Dürr

Biologische Systeme führen Funktionen durch das orchestrierte Zusammenspiel vieler kleiner Komponenten ohne einen "Dirigenten" aus. Solche Selbstorganisation durchdringt das Leben auf vielen Skalen, von der subzellulären Ebene bis zu Populationen vieler Organismen und ganzen Ökosystemen. Auf der intrazellulären Ebene koordiniert und instruieren proteinbasierte Muster Funktionen wie Zellteilung, Differenzierung und Motilität. Ein wesentliches Merkmal der proteinbasierten Musterbildung ist, dass die Gesamtzahl der beteiligten Proteine auf der Zeitskala der Musterbildung konstant bleibt. Das übergreifende Thema dieser Arbeit ist es, den tiefgreifenden Einfluss dieser *Massenerhaltung* auf die Musterbildung zu untersuchen und Methoden zu entwickeln, die Massenerhaltung nutzen, um die zugrunde liegenden physikalischen Prinzipien von proteinbasierter Musterbildung zu verstehen.

Die zentrale Erkenntnis ist, dass Änderungen der lokalen Dichten lokale reaktive Gleichgewichte verschieben und somit Konzentrationsgradienten induzieren, die wiederum den diffusiven Transport von Masse antreiben. Für Zweikomponentensysteme kann dieses dynamische Wechselspiel durch einfache geometrische Objekte im (niedrigdimensionalen) Phasenraum der chemischen Konzentrationen erfasst werden. Auf dieser Phasenraumebene können physikalische Erkenntnisse durch geometrische Kriterien und grafische Konstruktionen gewonnen werden. Darüber hinaus führen wir den Begriff der regionalen (In-)stabilität ein, der es erlaubt, die Dynamik im hochgradig nichtlinearen Regime zu charakterisieren und einen inhärenten Zusammenhang zwischen Turing-Instabilität und stimulusinduzierter Musterbildung aufzuzeigen.

Die für konzeptionelle Zweikomponentensysteme gewonnenen Erkenntnisse können auf Systeme mit mehr Komponenten und mehreren erhaltenen

Massen verallgemeinert werden. In der minimalen Fassung von zwei diffusiv gekoppelten "Reaktoren" kann die gesamte Dynamik in den Phasenraum umverteilter Massen eingebettet werden, wobei der Phasenraumfluss durch Flächen lokaler reaktiver Gleichgewichte organisiert wird.

Aufbauend auf der Phasenraumanalyse für Zweikomponentensysteme entwickeln wir einen neuen Ansatz für die wichtige offene Fragestellung der Wellenängenselektion im hochgradig nichtlinearen Regime. Wir zeigen, dass "coarsening" (das stetige wachsen der charakteristischen Längenskala) von Mustern in Zweikomponentensystemen nie stoppt, wenn sie exakt massenerhaltend sind. Die Selektion einer endlichen Wellenlänge entsteht durch schwach gebrochene Massenerhaltung oder durch Kopplung an zusätzliche Komponenten. Diese Prozesse wirken der Masseumverteilung, die coarsening treibt, entgegen und stoppen so das coarsening.

Bei komplexen dynamischen Phänomenen wie Wellenmustern und dem Übergang zu raumzeitlichen Chaos bietet eine Analyse in Bezug auf lokale Gleichgewichte und deren Stabilitätseigenschaften ein leistungsstarkes Werkzeug, um Daten aus numerischen Simulationen und Experimenten zu interpretieren und die zugrunde liegenden physikalischen Mechanismen aufzudecken.

In Zusammenarbeit mit verschiedenen experimentellen Labors haben wir das Min-System von *Escherichia coli* untersucht. Eine zentrale Erkenntnis aus diesen Untersuchungen ist, dass die Kopplung zwischen Volumen und Oberfläche zu einer starken Abhängigkeit der Musterbildung von der räumlichen Geometrie führt. Das erklärt die qualitativ unterschiedliche Dynamik, die in Zellen im Vergleich zu *in vitro* Rekonstitutionen beobachtet wird. Durch die theoretische Untersuchung der Polarisationsmaschinerie in Hefezellen, kombiniert mit experimentellen Tests theoretischer Vorhersagen, haben wir herausgefunden, dass dieses Funktionsmodul mehrere redundante Polarisationsmechanismen implementiert, die von verschiedenen Untergruppen von Proteinen abhängen.

Zusammengenommen beleuchtet unsere Arbeit die vereinheitlichenden Prinzipien, die der intrazellulären Selbstorganisation zugrunde liegen, und zeigt, wie mikroskopische Interaktionsregeln und physikalische Bedingungen gemeinsam zu spezifischen biologischen Funktionen führen.

Summary

The curve is the divine object.
The parametrization is human
and thus meaningless.

— Detlef Dürr
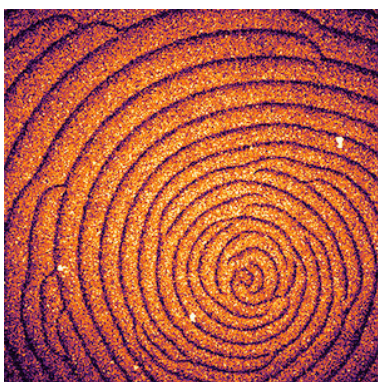
Biological systems perform functions by the orchestrated interplay of many small components without a "conductor." Such self-organization pervades life on many scales, from the subcellular level to populations of many organisms and whole ecosystems. On the intracellular level, protein-based pattern formation coordinates and instructs functions like cell division, differentiation and motility. A key feature of protein-based pattern formation is that the total numbers of the involved proteins remain constant on the timescale of pattern formation. The overarching theme of this thesis is the profound impact of this mass-conservation property on pattern formation and how one can harness mass conservation to understand the underlying physical principles. The central insight is that changes in local densities shift local reactive equilibria, and thus induce concentration gradients which, in turn, drive diffusive transport of mass. For two-component systems, this dynamic interplay can be captured by simple geometric objects in the (low-dimensional) phase space of chemical concentrations. On this phase-space level, physical insight can be gained from geometric criteria and graphical constructions. Moreover, we introduce the notion of regional (in)stabilities, which allows one to characterize the dynamics in the highly nonlinear regime reveals an inherent connection between Turing instability and stimulus-induced pattern formation.

The insights gained for conceptual two-component systems can be generalized to systems with more components and several conserved masses. In the minimal setting of two diffusively coupled "reactors," the full dynamics can be embedded in the phase-space of redistributed masses where the phase space flow is organized by surfaces of local reactive equilibria.

Building on the phase-space analysis for two component systems, we develop a new approach to the important open problem of wavelength selec-

tion in the highly nonlinear regime. We show that two-component reaction–diffusion systems always exhibit uninterrupted coarsening (the continual growth of the characteristic length scale) of patterns if they are strictly mass conserving. Selection of a finite wavelength emerges due to weakly broken mass-conservation, or coupling to additional components, which counteract and stop the competition instability that drives coarsening.

For complex dynamical phenomena like wave patterns and the transition to spatiotemporal chaos, an analysis in terms of local equilibria and their stability properties provides a powerful tool to interpret data from numerical simulations and experiments, and to reveal the underlying physical mechanisms.

In collaborations with different experimental labs, we studied the Min system of *Escherichia coli*. A central insight from these investigations is that bulk-surface coupling imparts a strong dependence of pattern formation on the geometry of the spatial confinement, which explains the qualitatively different dynamics observed inside cells compared to *in vitro* reconstitutions. By theoretically studying the polarization machinery in budding yeast and testing predictions in collaboration with experimentalists, we found that this functional module implements several redundant polarization mechanisms that depend on different subsets of proteins.

Taken together, our work reveals unifying principles underlying biological self-organization and elucidates how microscopic interaction rules and physical constraints collectively lead to specific biological functions.

CONTENTS

I | INTRODUCTION

The purpose of this introduction is to provide an overarching picture of our work. This includes a brief outline of the historical background as well as some discussion of our work to the broader context of the literature on pattern formation. In particular, we highlight how our work provides new and fruitful interconnections between different theoretical tools used to study spatially extended, nonlinear dynamics. More detailed summaries of the results of individual publications are given in Chapter II.

1 Protein-based pattern formation

A common feature of biological systems across many scales is that they perform functions by the orchestrated interplay of many small components without a "conductor." Such collective dynamics, or self-organization, is crucial for many biological functions and pervades life on many scales, from the subcellular level to populations of many organisms and whole ecosystems.

A striking example is intracellular organization. The interior of cells is highly structured and compartmentalized. This internal organization is key to many cellular functions, including cell division, motility, differentiation and the cell's response to external stimuli [1]. Finding the mechanisms underlying spatiotemporal coordination of cellular functions is therefore key to understanding some of the most fundamental processes of life.

Proteins, the elementary building blocks of cells are orders of magnitude smaller than the cell itself. Thus, the question arises how the internal structure of cells is established and maintained. Important examples for intracellular structures include the cytoskeleton [2], organelles (both membrane-bound and non-membrane bound liquid condensates [3], and concentration patterns of proteins [4]. Here we will focus on the latter: protein-based pattern formation.

An elementary case of intracellular organization is cell polarization — the establishment of a preferred spatial direction. Cell polarization is important for a large number of cellular functions. Examples include, but are not limited

to, asymmetric cell division (e.g. budding yeast) [5], cell motility [6, 7], axon growth and information propagation in neurons [8], and establishing distinct apical and basal surfaces in epithelial cells [9, 10]. Cell polarization is typically generated by an asymmetric distribution of proteins such as small GTPases [11]. As such, it is a paradigmatic example for a protein-based intracellular pattern [4, 12]. Conceptual models for cell polarization encompass several fundamental features of intracellular pattern formation. We will therefore develop the central concepts of our theoretical framework in this context.

Another, maybe more striking, example of an intracellular pattern are the pole-to-pole oscillations of the MinD and MinE proteins in *E. coli*. Due to these oscillations, the time averaged concentration of MinD is lowest at mid-cell, which provides the positional cue for the cell-division plane. The Min system has been reconstituted *in vitro*, where it displays a striking variety of patterns, predominantly traveling waves and spirals [13], but also "mushrooms", "snakes", "amoebas" and "bursts" [14, 15], chaotic patterns [16, 17], "homogeneous pulsing" [18–20] as well as quasi-stationary labyrinths, spots, and mesh-like patterns [17, 21]. The *in vitro* system allows precise control over experimental conditions. Hence, the reconstituted Min system has become the workhorse for studying protein-based pattern formation.

Other examples for intracellular protein-patterns are actin waves [22, 23] and excitable/oscillatory pulses/waves of Rho proteins observed in oocytes of *Caenorhabditis elegans* [24], *Xenopus laevis*, and starfish [25, 26], as well as *X. laevis* cell extracts [27].

Collectively, the above examples show the wide variety of patterns formed by protein-based systems. The underlying protein-reaction networks range from the (comparatively[1]) simple Min system, with only two players, MinD and MinE [13], to highly complex systems involving many players and feedback loops, e.g., the Cdc42-polarization machinery of budding yeast [28]. Notably, as the two above examples illustrate, the complexity of the interaction network does not correlate with the complexity and richness of the emerging patterns.

Spatiotemporal organization inside cells has been an area of intense research and the field is continually growing with each advance in experimental methods. Arguably the most important experimental advance has been the advent of fluorescence microscopy that gave us the possibility to precisely track the positions of proteins within cells, and thus provides access to observe intracellular spatial organization. The more recent development of op-

---

[1]Despite only having two players, the reaction kinetics of the Min system are in fact quite complex since both MinD and MinE have multiple interaction domains and different conformational states [16, 17].

togenetics has enabled experimentalists to not only observe but also locally perturb and modify intracellular dynamics with sub-micrometer resolution. The ongoing development of methods to image, probe, perturb, and modify intracellular dynamics with increasing temporal and spatial resolution is generating an ever-growing stream of experimental data.

The overarching challenges for theorists are two-fold. One is the development of models that reproduce the specific experimental observations for concrete biological systems. Such models give insight into the underlying physical mechanisms and provide quantitative predictions that can be verified in further experiments. The second challenge is to find unifying principles that encompass many different biological systems and the rich variety of phenomena they exhibit. Finding such principles is important because they have the potential to be generalized beyond the specific, experimentally studied systems. They also permit the design of new, synthetic biological systems.

Finding the unifying principles underlying protein-based pattern formation is the overarching goal of this thesis. More generally, we develop a theoretical framework, termed local equilibria theory, for mass-conserving pattern-forming systems. Protein-based systems are an important instance of such systems.

1.1 Fundamental processes and features of protein-based systems

The two elementary processes underlying protein-based pattern formation are spatial transport of proteins and local interactions between them. In this section, we briefly describe these processes and highlight several fundamental features that have important consequences for their emergent dynamics and that we will utilize to develop our theoretical framework.

Protein interactions. The essential kinetic processes driving pattern formation are state changes of proteins and interactions between them. These processes conserve the local total densities of proteins. Production and degradation of proteins, processes that break mass conservation, take place on timescales much larger than the timescales on which the concentration patterns form [29]. Thus, a fundamental feature of protein-based pattern formation is the conservation of mass. As we will see, mass conservation has important consequences for the pattern-formation dynamics. A central goal of our work is to investigate these consequences and develop a theoretical framework that utilizes mass conservation to gain insight into the principles underlying protein-based pattern formation.[2]

---

[2]Although mass conservation is a central pillar of our work, our results do not require strict mass conservation. Generalizations, such as accounting for production and degradation of

A common feature of protein kinetics is the cycling between different conformational states. Important examples are ATPases and GTPases, which cycle between ATP/GTP-bound (active) and ADP/GDP-bound (inactive) states (see e.g. [31, 32]). Another example is switching between different degrees of phosphorylation (see e.g. [33] and references therein). The different conformational states vary in their affinity for binding to interaction partners and to the membrane and, thus, have different functional roles. Transitions between the states are catalyzed by regulatory proteins: nucleotide exchange factors and activating proteins in the case of ATP/GTPases; phosphatases and kinases in the case of phosphorylation. In turn, these regulatory proteins are often part of complex feedback cycles and signaling pathways [34]. Feedback cycles in protein-interaction networks are an essential ingredient for protein-based pattern formation. In particular, they are responsible for establishing and maintaining self-organized concentration gradients that cause directed mass transport.

Proteins in their active state are often bound to the membrane which acts as a "substrate" for interactions with downstream effectors. In contrast, the inactive states are often cytosolic which allows them to diffuse quickly (see paragraph "Spatial transport" below). The attachment–detachment dynamics at the membrane plays a key role for protein-based pattern formation for two reasons. First, the different diffusivities of membrane-bound and cytosolic proteins are key for self-organized pattern formation (see Sec. I.2.1 below). Second, the attachment–detachment kinetics at the membrane generically lead to cytosolic gradients normal to the membrane. These gradients cause a strong dependence of the dynamics on the shape of the geometric confinement, e.g., the cell [35].

Finally, let us emphasize that ATP/GTPases cycles and phosphorylation cycles are driven by ATP and GTP, which acts as a chemical fuel. Therefore, protein dynamics is driven far from thermal equilibrium and the concentration patterns formed by proteins are non-equilibrium steady states. Typically, ATP and GTP are abundant at high concentrations [36], such that they can be assumed to be available as an unlimited reservoir that is not explicitly modeled.

Spatial transport. Spatial transport of proteins is essential for spatiotemporal organization within cells. Arguably the most important mode of transport is diffusion in the cytosol. One often thinks about diffusion as a process that removes concentration gradients. This intuition seems at odds with the fact that diffusive transport, in combination with chemical reactions, can drive

_____

proteins on slow timescales are discussed in Ref. [30].

pattern formation (see Sec. I.2.1). This conundrum is resolved if one thinks of diffusion as a mass-transport process that is driven and directed by concentration gradients. A persistent diffusive flux is sustained if gradient is maintained. Thus, a key question to understand protein-pattern formation is how concentration gradients are maintained by the local protein interactions.

Protein concentration patterns typically form on the cell membrane (or bound to other substrates) where diffusion is slow such that the concentration gradients can be easily maintained against diffusive dispersion. The membrane is coupled to the cytosol by the attachment–detachment kinetics of the proteins that we discussed above.

In addition to cytosolic diffusion, there are several other modes of transport in cells. This includes advective flows of the cytoplasm [37] and the cell cortex [38, 39], as well as vesicle-based transport along cytoskeletal filaments by molecular motors. In contrast to diffusion, transport along cytoskeletal filaments is active as the molecular motors consume ATP, and it is inherently directed along the orientation of the filaments. As we discuss in the outlook, incorporating orientational order and directed, advective transport is an important avenue for future generalizations of the concepts and ideas presented here.

1.2 Model development and model reduction

For chemical pattern-forming systems, such as the Belousov–Zhabotinsky (BZ) reaction [40–42], one has precise experimental control over the reagents and the reaction conditions which allows one to perform quantitative experiments like the measurement of reaction rates. This, in turn, has facilitated the development of detailed models [43, 44] that quantitatively reproduce the experimentally observed phenomena. Importantly, these models often have little or no fitting parameters.

In contrast, intracellular pattern formation takes place in the environment of the living cell, and thus in the face of full biological complexity. Typically, not all proteins participating in the dynamics are known. Even in cases where one knows the molecular players, e.g., for *in vitro* reconstitutions of the Min system, one faces the challenge that proteins are huge and complex compared to the molecules involved in chemical pattern-forming systems. Many proteins can change between different conformational states and have multiple functional domains for interacting with other proteins and with the membrane. The molecular details of protein-protein interactions are often not known and are not (yet) experimentally accessible. Thus, determining the key reaction steps and measuring reaction rates remains very difficult,

even if purified proteins are available. Even for the Min system, which has been reconstituted *in vitro*, the molecular details of key steps in the reaction network, like the self-recruitment of MinD to the membrane, are still in the dark.

Where biomolecular details are not available, such that development of quantitative models is not possible, it is particularly important to identify robust, qualitative characteristics of the dynamics that are independent of model details and can be generalized. These qualitative dynamical features, e.g., bistability, excitability, and oscillatory regimes, can be implemented by conceptual models.

In the development of such conceptual models, it is important to account for fundamental aspects of the underlying physical and biochemical processes. Examples are mass conservation, attachment–detachment dynamics that couple the membrane surface to the cytosolic volume, and the mass-action law for reaction kinetics. Incorporating these aspects lifts conceptual models above the purely phenomenological level and allows one to draw from them insight about underlying physical mechanisms.

Inherently connected to the challenge of finding the right model is that of choosing the parameters, such as diffusion constants and reaction rates. While the former can be determined for fluorescently labelled proteins using methods such as FRAP [45] and FCS [46], reaction rates are often not experimentally accessible. A common approach is to fit the unknown parameters to match experimental observables, e.g. characteristic length- and timescales, fractions of membrane-bound vs. cytosolic proteins, and response curves to experimental perturbations. Fitting is difficult for models with many parameters. Often, biochemical reaction networks with just a few components are already severely underdetermined, because not enough independent observable quantities are available. In fact, complex models generally have many sloppy parameters (or rather parameter combinations) that are only weakly constrained by observables [47]. Investigating the origins of this "sloppiness" and exploiting it for systematic model reduction are topics of increasing research interest [48, 49].

Fitting is only informative if a model is consistent on a mechanistic level. Therefore, the fundamental question of the (mesoscopic) mechanisms underlying a collective phenomenon must be answered first. This is not a trivial task. Systems exhibiting collective phenomena often exhibit multiple dynamical regimes where distinct mechanisms are at play. Moreover, different mechanisms can give rise to the same macroscopic phenomenon (see for instance the problem of local vs. lateral oscillations, discussed in Sec. I.2.2). One has to identify signatures of putative mechanisms that allow one to unambiguously

6

discern these mechanisms in the experimental system. Developing concepts that enable one to reveal and describe the mesoscopic, physical mechanisms underlying collective phenomena is a key theory challenge.

Brief discussion of several different approaches to modeling in the context of specific biological systems are given in Secs. II.6–II.8 and Sec. II.9.1, where we summarize several collaborative studies that combined theory with experiments. In each study, we adapted our modeling approach to the specific goals and the available experimental (biomolecular) data. In particular, we show how identifying the pattern-forming mechanisms of the Min system of *E. coli* has allowed us to reconcile the rich phenomenology found *in vitro* to the pole-to-pole and stripe oscillations in cells.

2 Reaction–diffusion systems

We are interested in protein-concentration patterns on scales on the order of micrometers, much larger than the size of individual proteins (on the order of nanometers). We therefore describe the protein concentrations by continuous fields governed by *reaction–diffusion* (RD) equations. Diffusion is described according to Fick's law. Protein interactions are described as chemical reactions, using the law of mass action.[3] This "mean-field" description neglects demographic fluctuations and correlations on the microscopic level.

A fundamental feature of protein-based systems, discussed in the previous section, is that the reaction kinetics are mass conserving. Thus, protein-based pattern formation is described by *mass-conserving reaction–diffusion* (MCRD) systems. A new theoretical framework for these systems that we developed in the course of this thesis will be presented in Sec. I.3.

Reaction–diffusion systems in general have been a topic of extensive research in the past decades. In the remainder of this section we give brief overview over central concepts and prevalent theoretical methods.

2.1 Turing instability

The investigation of pattern formation in reaction–diffusion systems goes back to Turing's pioneering work [50]. Turing was far ahead of his time and his contributions to the field cannot be overestimated.[4] His main insight was that a pattern-forming instability can arise from the interplay of two processes

---

[3]The law of mass action by Guldberg-Waage assumes that the rate of a chemical reaction is directly proportional to the product of the densities of the reacting species.

[4]Notably, a recent study [51] of Turing's unpublished notes has revealed that he had already come up with the paradigmatic "Turing–Swift–Hohenberg" equation that was later (re)discovered independently by Swift and Hohenberg.

that are stable by themselves. Namely, diffusion — a process that by itself always removes spatial gradients — and chemical reactions that are stable in a well-mixed system. Turing showed this by performing a stability analysis of a prototypic system with two components. An important, necessary requirement for the diffusion-driven instability revealed by Turing is that the chemical species have sufficiently different diffusivities.

Box 1. The terms "Turing instability" and "Turing pattern." Given Turing's deep and comprehensive insights, we find it unfortunate that most of the literature restricts the definition of "Turing instability" to those instabilities that give rise to stationary patterns whose final wavelength is determined by the fastest growing mode. In fact, Turing already classified the different types of instabilities, including oscillatory instabilities giving rise to standing and traveling waves. Importantly, he also noted that the linear analysis cannot predict the properties of fully developed patterns far from the homogeneous steady state. We will therefore adopt a much broader definition and call all diffusion-driven instabilities Turing instabilities. Accordingly, we will call the patterns that arise from such instability Turing patterns. In particular, this includes the patterns formed by mass-conserving two-component systems which exhibit coarsening and are reminiscent of phase-separation phenomena.

⌒

Twenty years after Turing's work, Segel and Jackson systematically analyzed linearized two-component RD systems and derived the heuristic criterion that a diffusion-driven instability requires the interplay of short-range activation and long-range inhibition [52]. In the same year, Gierer and Meinhardt formulated the same principle, based on heuristic arguments and numerical simulations, but notably without using linear stability analysis [53]. Thanks to its simplicity, the principle of short-range activation and long-range inhibition, or short "activator–inhibitor paradigm" has found widespread use as a heuristic explanation for pattern formation. It has been generalized beyond reaction–diffusion systems. Examples include pattern formation in neural tissues, zebrafish skin patterns, and ecological patterns (both in physical space and in trait space), which centrally involve non-local coupling [54, 55]. Unfortunately, the activator–inhibitor paradigm is imbued with several conceptual problems.[5] In particular, it is not well-suited to explain intracellu-

---

[5]A key problem with the activator–inhibitor paradigm that a species that biochemically has the role of an inhibitor is not necessarily an "inhibitor" in the sense of the activator–inhibitor paradigm. For instance, this is the case for MinE in the Min system of *E. coli* [56].

lar pattern formation as we have discussed in a recent review [4] (see also Refs. [56, 57]). In this thesis, we lay out a framework that is ideally suited for this setting and rooted in Turing's original work.

The relevance of Turing instability for pattern formation in nature, and more specifically biology, has long been questioned and is a matter of ongoing debate even today. One key issue is the requirement of (vastly) different diffusion constants. Indeed, due to this condition it took almost 40 years until the first experimental realization of a Turing pattern [58]. The breakthrough idea was binding one reactant to a gel-like substrate, thus substantially slowing its diffusion. In fact, for intracellular pattern formation, the cell membrane plays the role of such a substrate. In fact, the proteins that drive intracellular pattern formation often cycle between slow-diffusing, membrane-bound states and fast-diffusing cytosolic states. Therefore, the requirement of different diffusion constants is naturally fulfilled for protein-based pattern formation.

A related issue of Turing patterns is their parameter sensitivity (see e.g. [59, 60]. Turing instability is often only found in small parameter regimes. Finding systems that robustly give rise to Turing patterns is subject and goal of ongoing research. For instance, a recent mathematical analysis based on random matrix theory shows that the Turing instability might actually be more robust in systems with many components [61]. Studies accounting for noise find that noise-induced patterns appear outside the parameter regime of Turing instability and therefore extend the pattern-forming regime significantly [62, 63].

As we will see below, our work suggests that Turing patterns are easier to achieve and more robust in protein-based systems such as those underlying intracellular pattern formation. In fact, we show that the requirements for self-organized cell polarization are milder than those for bistability [57]. The latter is commonly found in protein-interaction networks (e.g. GTPase cycles and phosphorylation cycles) [34, 64]. From this perspective it appears that Turing instability should be rather common in intracellular systems.

To conclude this section, let us briefly mention some other instability mechanisms that generalize Turing's "diffusion–driven instability" to systems including other types of spatial coupling such as cross-diffusion, advective flows and non-local coupling. Cross-diffusion is found as a result of enzyme-ligand interactions [65] and electrostatic interactions between ions [66]. It also appears in coarse-grained models of cell-cell signaling that gives rise to skin patterns [67]. Advective flows are important for vegetation patterns in sloped terrain, which leads to water flow which advects nutrients. Inside cells, the cytoplasmic hydrodynamic flows (called cytoplasmic streaming) arise due to the activity of molecular motors. Finally, non-local coupling is often involved

in ecological pattern formation and neural tissues. Each of these processes can drive pattern-forming instabilities of a homogeneous steady state.

2.2 Bistable, excitable and oscillatory media

Turing instability and its generalizations are not the only mechanism for pattern formation in reaction–diffusion systems. Other classes of systems are so-called bistable, excitable and oscillatory media [68]; see [69] for a recent review from a biological perspective.

In bistable media, the local (reactive) dynamics at each point in space has two stable fixed points (and an unstable fixed point in-between them). These fixed points are stable homogeneous states of the spatially extended medium. Sufficiently strong perturbations can induce fronts that connect the two stable fixed points. These fronts, called trigger waves, are generically non-stationary. They therefore provide a means of signal propagation in biological systems [70, 71].

In excitable media, the local dynamics is (mono)stable, but close to a threshold. Local perturbations exceeding this threshold trigger a large excursion in the dynamics before the system returns to its stable steady state. Spatial coupling provides the stimulus that drives the local dynamics over the threshold. The resulting local excursion, in turn, triggers further neighbors that are in their excitable state. This subsequent triggering of local excitable dynamics leads to propagating pulses and wave trains; see [68, 72, 73] and references therein.

The defining property of oscillatory media is that the local dynamics at each point in space is oscillatory, independently of the spatial coupling. In other words, a patch of such a medium that is sufficiently small to be considered well-mixed and that is isolated from the surrounding medium is already oscillatory. Trivially, homogeneous oscillatory media exhibit homogeneous oscillations, since the diffusive coupling vanishes in the absence of gradients. In addition they exhibit traveling and standing waves as well as spatiotemporal chaos [74] in one spatial dimension. In two dimensions oscillatory media exhibit spiral waves, and target patterns, as well as chaotic dynamics such as defect-mediated turbulence [75].

Extensively studied, phenomenological models for excitable and oscillatory media are the FitzHugh–Nagumo model [76, 77] and the complex Ginzburg–Landau equation [74]. Owing to their simple mathematical form, these models lend themselves to systematic theoretical analysis. However, they cannot account for the specific features of concrete experimental and biological systems.

Arguably, the most widely-known and extensively studied experimental reaction–diffusion systems that constitute oscillatory and excitable media are the BZ reaction [40–42] and CO oxidation on Pt surfaces [78]. These systems have been subject to a vast number of studies, both experimental and theoretical using quantitative models [79–82].

In passing, let us note that the investigation of oscillatory media is related to the topic of oscillator synchronization, where instead of a continuous medium of oscillators, one considers discrete oscillators coupled in a network. Synchronization of coupled oscillators is a topic of broad interest pervasive in nonlinear systems [83]. Applications include self-organization of motile cells [84], cardiac calcium oscillations [85], neural tissues [86], and power grids [87, 88].

Relation to Turing patterns: lateral vs. local instability. The local oscillations driving an oscillatory medium persist if one isolates a small (i.e. well-mixed) of the system. In other words, the oscillations are driven by the local dynamics and are independent of lateral spatial coupling. We therefore say that an oscillatory medium is *locally unstable*.[6] In contrast, Turing instability arises as a consequence of the lateral spatial coupling in a system where a laterally isolated patch is stable. We refer to such instabilities as *lateral instabilities*.

Examples of protein-based patterns showing phenomenological similarity with excitable and oscillatory media include the reconstituted Min system *in vitro*, which prominently exhibits spiral waves [13], as well as actin waves [22, 23] and Rho waves and pulses observed in oocytes of *C. elegans* [24], *X. laevis*, and starfish [25, 26]. However, from the purely phenomenological perspective, one cannot conclude that these systems actually constitute oscillatory media, i.e. that their dynamics is driven by *local* oscillations. In fact, dynamic patterns such as traveling waves and standing waves can also arise from *lateral* (Turing) instabilities. In the dispersion relation obtained from LSA (see Sec. I.2.3), the formation of waves is indicated by a non-zero imaginary value of the growth rate. In principle, one could distinguish the two scenarios by making the system under consideration well-mixed, such that local oscillations would reveal themselves. Unfortunately, for living systems this is often not experimentally feasible. Instead, a systematic theoretical analysis can help to identify characteristic signatures of the oscillation modes underlying pattern formation in the experimental system. Performing such a theoretical investigation for the Min system, we have recently found that

---

[6]Note that a local instability automatically implies that the homogeneous steady state will be unstable against homogeneous perturbations. Thus, while these instabilities are *conceptually* different, the criteria for local instability and instability against homogeneous perturbations are actually identical.

depending on the parameters (specifically the bulk-surface ratio), there are different dynamical regimes where either lateral instability, local instability, or the interplay of both drive pattern formation (see Ref. [35] and Sec. II.6).

The above discussion raises the more general question how the dynamics of bistable, excitable and oscillatory media are related to Turing pattern formation and whether there is a unifying framework that encompasses both paradigms. Turing patterns are typically studied in the vicinity of a homogeneous state (in the linear and weakly nonlinear regime), while bistable, excitable and oscillatory media often operate far away from homogeneity in the strongly nonlinear regime. Hence, a key challenge for a unifying framework is to bridge this gap. Below, in Sec. I.3, we describe how local equilibria theory achieves this in the case of mass-conserving systems. As one key finding, we reveal a close relationship between Turing instability and bistability in two-component systems.

2.3 Theoretical methods and tools

In this section, we provide a brief overview of the main tools used to analyze pattern forming systems in general and reaction–diffusion systems specifically. Since these tools are well-established, we only explain the basic ideas in broad strokes and refer the interested reader to the pertinent (technical) literature.

Dynamical systems theory.   The primary challenge in analyzing the dynamics of RD equations lies in the nonlinear reaction terms. Nonlinear systems are prevalent in nature and exhibit a vast and often bewildering variety of phenomena, examples of which crop up in nearly every discipline of the natural sciences, engineering, and mathematics. These range from bistable switches and limit-cycle oscillations to propagating fronts and pulses, pattern formation, and (spatiotemporal) chaos [68, 89–92]. Closed mathematical solutions to nonlinear differential equations only exist in rare cases. In the vicinity of steady states, one can linearize the dynamics (see LSA). In the phase space spanned by the degrees of freedom of the system, steady states are fixed points and LSA provides *local* information about the phase space flow that encodes the dynamics in their vicinity. However, this analysis cannot answer questions about the long-term fate of a system that is driven away from an unstable steady state, or whose initial condition is far away from steady states. Answering such questions requires knowledge of the *global* structure of the phase space flow. The central insight of dynamical systems theory, going back to Poincaré [93], is that this flow is organized by geometric structures in phase

space, such as fixed points, nullclines, attractors, separatrices, and invariant manifolds. These geometric structures can provide qualitative information about the global dynamics without explicit solution of the differential equations. In other words, they reveal *the qualitative content of nonlinear equations.*

For example, dynamics described by ordinary differential equations (ODEs) with two variables can be characterized by a phase-portrait analysis based on the shapes of the nullclines, along which the right-hand side of one of the ODEs vanishes [89]. Important phenomena such as bistability, excitability, oscillations can be intuitively understood on this geometric level. This framework has found great success in explaining neuronal dynamics [90, 94] and biochemical oscillators [95] to name just two examples.

An important question is how the behavior of a system changes as one varies its control parameters. Generically, a small parameter variation will only lead to a small, quantitative change of the dynamics. Bifurcations occur when a small change in a parameter leads to a *qualitative* change in the phase space flow. Thus, bifurcations characterize the parameter dependence of a dynamical system and demarcate the transitions between distinct dynamical regimes in parameter space. Identifying the bifurcations of a system is one of the central goals of dynamical systems theory. Importantly, there is only a limited number of different types of bifurcations, enumerated by the number of dynamical variables and the number of parameters one has to tune for the bifurcation to occur. The dynamics close to each type of bifurcation is "universal" as described by the so-called normal form of the bifurcation [96, 97]. This means that systems governed by different underlying physics show the same behavior close to bifurcations.

A related notion for categorizing dynamics in phase space is that of *topological equivalence*. Two systems are are topologically equivalent if their phase space flows can be smoothly transformed into one another. This implies that they will show *qualitatively* analogous behavior. An example of local topological equivalence are the generic flows in the in the vicinity of fixed points in two-variable systems based on the eigenvalues of the linearized dynamics.

Unfortunately, phase-space geometric reasoning cannot generally be transferred to the *dynamics* of spatially extended systems, whose phase space is, in principle, infinite-dimensional. One strategy to overcome this difficulty is to focus on the vicinity of homogeneous steady states, where one can linearize the dynamics and use perturbative approaches to account for the effect of weak nonlinearities. Another approach uses phase-space geometric reasoning for the construction of *stationary* patterns and traveling waves (which appear stationary in a co-moving frame). Below we briefly outline these two approaches. The framework we develop for MCRD systems in Sec. I.3 com-

bines ideas from both approaches and bridges the gap between the linear and the strongly nonlinear regimes.

Linear stability analysis.   LSA is arguably the most important, and most commonly used mathematical tool to analyze pattern forming systems, specifically reaction–diffusion systems. Indeed, already Turing used this analysis in his pioneering work [50]. The basic idea is to linearize the dynamics around a homogeneous steady-state and to expand small spatial perturbations in the eigenfunctions of the differential (Laplace) operator encoding diffusion. On a one-dimensional domain, these spatial modes, characterized by their wavenumber q, are simply Fourier modes.[7] The linearized dynamics for each spatial mode is then described by a Jacobian matrix which depends on the mode's wavenumber. The Jacobian's eigenvalues indicate the growth rates of the modes, where a positive real part indicates unstable modes that grow in amplitude while a negative real part signifies stable modes that decay. A non-vanishing imaginary part indicates oscillatory dynamics. The relation between the wavenumber and the growth rates is called *dispersion relation* $\sigma(q)$.

If there is a band of unstable modes in the dispersion relation, spatial patterns will form from small random perturbations of the homogeneous steady state. The dispersion relation characterizes the initially growing, small amplitude patterns: The fastest-growing mode determines the wavelength of the initially growing pattern and a non-vanishing imaginary part indicates oscillatory modes that manifest as standing or traveling waves.

Amplitude equations.   Linearized equations only inform about the initial dynamics near a homogeneous steady state. The long-term fate of the patterns depends on the *nonlinearities*. If the only effect of the nonlinearities is to immediately stabilize the linear instability, the pattern growth will saturate at a small amplitude. In this *supercritical* case, the properties of the final pattern are dictated by the dispersion relation. Further one can perform a perturbative analysis called amplitude equation formalism or weakly-nonlinear analysis. Amplitude equations describe the slow variation of the pattern's amplitude (and potentially other slowly varying fields induced by symmetries and conservation laws) on scales much larger than its wavelength (see Box 2). They have been highly successful to explain pattern formation in the supercritical regime [74]. Unfortunately, if the nonlinearities are not immediately

---

[7]Finding the spatial eigenmodes that diagonalize the spatial differential operators becomes nontrivial in the presence of bulk-surface coupling and in geometries that break the spatial symmetries of the diffusion operator [35, 98].

stabilizing, the pattern amplitude will continue to grow into a regime where strong nonlinearities dominate. The characteristics of such fully developed, large-amplitude patterns cannot be inferred from the dispersion relation and perturbative approaches.

Biological patterns are often in this regime. In particular, our work shows that MCRD systems are generically subcritical [57]. This means that steady-state patterns exist outside the regime where the homogeneous state is linearly unstable and at the onset of instability, patterns immediately grow to large amplitudes. Moreover, in biological systems, patterns often form not from a homogeneous initial state but from one pattern to another, as already noted by Turing.

To study spatially extended dynamics in this strongly nonlinear regime, one is mostly limited to using numerical simulations. Hence, insights have largely remained restricted to specific models, and unifying physical principles have remained elusive. Moreover, numerical simulations of collective phenomena yield only limited insight into the underlying physical mechanisms and "organizational principles" of self-organization. Hence, there is a need for methods to visualize and interpret data from numerical simulations.

> **Box 2. Amplitude equations and mass conservation.** Amplitude equations are derived near the onset of pattern formation where they describe slowly varying fields on large scales. These "slow" (hydrodynamic) fields correspond to symmetries and conservation laws [74]. For non-oscillatory dynamics with translation and reflection symmetry the only slow field is the amplitude governed by the universal Ginzburg–Landau equation (GLE)
>
> $$\partial_t A = \partial_x^2 A + A - A^3,$$
>
> for the real amplitude A. Importantly, this equation captures the large-scale dynamics near a supercritical bifurcation independently of the details of the original dynamics (including the number of components).
>
> If the dynamics is oscillatory, there is symmetry under a global shift of the oscillator phase. Consequently, the phase appears as a slow field. The large scale dynamics is then described by the complex Ginzburg–Landau equation (CGLE),
>
> $$\partial_t A = (1 + i\alpha)\partial_x^2 A + A - (1 + i\beta)|A|^2 A$$
>
> where the complex amplitude A combines the real amplitude and the phase. The CGLE exhibits a rich dynamical behavior and has been stud-

ied in great detail [74]. In general, the structure of amplitude equations can be inferred on grounds of symmetries and conservation laws. However, relating the coefficients in the amplitude equation to the parameters of an underlying "microscopic model" requires explicit coarse-graining.

Conserved quantities induce additional slow fields that account for large-scale variations in the density. In the simplest case of non-oscillatory dynamics with one conserved quantity, the amplitude equations take the form

$$\partial_t A = \partial_x^2 A + A - A^3 - \rho A,$$
$$\partial_t \rho = \nu \, \partial_x^2 \rho + \mu \, \partial_x^2 (|A|^2).$$

This scenario of the GLE coupled to a conserved field was systematically studied in Ref. [99]. The analogous case for oscillatory dynamics, described by the CGLE coupled to a conservation law, appears, for instance, in coarse-grained phenomenological models for vibrated granular media [100]. An important consequence of the conserved field is the emergence of robust localized structures [99–104]. In general, additional slow fields significantly complicate the analysis of the amplitude equations. This might be one reason why amplitude equations for mass-conserving systems have remained a niche in the literature.

A striking example for the effect of additional slow fields in amplitude equations is observed for the so-called Nikoalevski equation where the presence of Galilean invariance requires an additional slow field describing a large-scale mean flow. In this case, turbulence appears at the supercritical onset of pattern formation [105, 106]. The reason is that all patterns that emerge from the linear instability are destabilized by the coupling to the additional field. In fact, this instability grows faster than the instability of the homogeneous state. This is in contrast to spatio-temporal chaos in the Ginzburg-Landau equation which emerges due to secondary bifurcations at a finite amplitude, beyond the so-called Benjamin–Feir instability [107]. The emergence of chaos at onset is also found in the *in vitro* Min system [108]. Here, mass-redistribution triggers local instabilities which drive spatio-temporal chaos. A remarkable feature of the Min system is that order emerges at a finite distance from onset when a "mass-redistribution mode" with half the wavelength of the fastest growing mode becomes unstable in the dispersion relation.

〜

Phase space geometry of stationary and propagating patterns. Consider a stationary (or propagating) pattern in a reaction–diffusion system in one spatial dimension with N components u_i. Stationarity implies that the time derivatives vanish, such that only the spatial derivatives remain. The stationary pattern is therefore described by N second-order ODEs. These can be converted to $2N$ first-order ODEs by introducing N auxiliary variables for the gradients $\partial_x u_i$.

In the $(u_i, \partial_x u_i)$ phase space, stationary patterns appear as trajectories that trace out the concentrations u_i and their gradients $\partial_x u_i$ along the spatial profile. For instance, periodic patterns are closed orbits and fronts connecting homogeneous states correspond to heteroclinic orbits connecting fixed points. This phase-space representation makes the powerful tools of dynamical systems theory available for the construction and investigation of stationary and propagating patterns and has found widespread use in the mathematical community [109]. An elementary example is the construction of propagating fronts in the Fisher-KPP equation [110, 111] as described in Ref. [112].

Unfortunately, the flow in the $(u_i, \partial_x u_i)$ phase-space is rather abstract, and the connection to physical intuition is often limited. Moreover, the mapping of a spatially extended system to this phase space is restricted to stationary states, such that reasoning about dynamics is not possible. In particular, one does not gain information about the stability of the constructed patterns.

Developing phase-space representations of spatially extended dynamics is an open challenge. In Sec. I.3, we will tackle this challenge by utilizing mass conservation.

Other methods. To conclude this section, let us briefly mention other methods that have been developed to study spatially extended, nonlinear dynamics. One category of methods uses the fact that these systems often exhibit coherent, localized structures [113], e.g., fronts in bistable media [68] or phase defects and spiral cores in oscillatory media [114, 115]. The motion of these structures and interactions admit effective, "particle"-like descriptions. Essentially, this relies on a separation of timescales between the rapidly relaxing "internal" degrees of freedom of the coherent structures and the slow dynamics of the "particle"-like degrees of freedom that parametrize them (e.g., position, orientation, topological charge). Put more abstractly, one constructs a parametrization of the slow invariant manifold of the spatially extended dynamics and obtains effective (approximate) equations for the motion within that manifold [116].

Where analytic progress is not possible, a range of methods has been developed to analyze and interpret data from numerical simulations and exper-

iments. Examples include, proper orthogonal decomposition [117], dynamic mode decomposition [118], and local causal states [119]. Increasingly, machine learning-based approaches are being developed for the "equation-free" characterization of complex systems. In the Outlook (Sec. I.6) we briefly discuss how these approaches could be combined with local equilibria theory.

3 A theoretical framework for MCRD dynamics

The two central, guiding ideas behind our theory for MCRD dynamics are:

(*i*) The essential dynamics is the spatial redistribution of conserved masses.

(*ii*) Qualitative insight can be gained from the central concepts of dynamical systems theory: phase space geometry, fixed points, stability, and bifurcations.

Conserved quantities naturally appear as slow ("hydrodynamics") variables in coarse-grained theories for the dynamics on large spatial and temporal scales, such as the amplitude equation formalism (see Box 2). We take a different perspective where we perform "coarse-graining" not in physical space and time but in phase space by using the concepts of dynamical systems theory. That is, we aim to identify the essential (qualitative) features of the phase-space flow that represents a system's dynamics. The geometric objects encoding these features — fixed points, nullclines, invariant manifolds, and bifurcation scenarios — provide a "coarse-grained" view of the phase-space flow. The key challenge is to transfer these concepts from ODE systems to spatially extended dynamics, described by PDEs. From a mathematical point of view, one would expect this to be a futile exercise, given that PDE phase spaces are infinite-dimensional while the geometric analysis is feasible only for low-dimensional ODE phase spaces.

Instead of focusing on the purely mathematical problem, we wish to decompose the dynamics into the key physical processes driving pattern formation: reaction and diffusion. It turns out that such a decomposition is particularly insightful in the case of mass-conserving systems. Put briefly, we imagine the system dissected into local compartments that are sufficiently small to be considered well-mixed. The dynamics within each compartment are governed by reaction kinetics and diffusive in- and out-fluxes of mass. If one were to isolate such a compartment, the *local masses* in the compartment would remain constant because the reaction kinetics are mass-conserving. Thus, the local masses in a compartment act as control parameters of the local reactive

dynamics within the compartment. In particular, the reactive equilibrium concentrations in each compartment depend on the total masses within each compartment. The properties (position and stability) of these *local reactive equilibria* act as proxies for the local phase-space flow. Diffusive coupling redistributes the globally conserved masses between neighboring compartments, such that the local masses in the compartments change over time. As a result, the local equilibria move and their stability may change, indicating changes in the local reactive phase-space flow. The local reactions, in turn, lead to concentration gradients that drive further diffusive redistribution of mass. Analyzing this interplay is the goal of local equilibria theory.

Concrete implementations of these overarching ideas have been developed in a series publications which we briefly summarize in the following paragraphs. Each of these publications focuses on a different aspect of the overarching ideas outlined above to answer specific, important questions. A self-contained, pedagogical introduction of local equilibria theory in the context of intracellular protein-based pattern formation is given Ref. [120]. The analysis of two-component MCRD systems (cf. Refs. [30, 57]) has recently been reviewed in a special issue on symmetry breaking in cells and tissues [121].

- *Rethinking pattern formation.* Ref. [108] introduces the idea to consider a system dissected into notional compartments and derives from this picture the concepts of moving local equilibria and their stability. These ideas are then used for the analysis of numerical simulations of the reconstituted Min system of *E. coli*, which exhibit intriguing behavior, in particular the emergence of spatiotemporal chaos near the onset of pattern formation and transition from chaos to order (standing and traveling waves) further away from the onset. Mapping the dynamics into the phase space of the redistributed masses, which is the parameter space for local equilibria, shows that chaos is a consequence of the destabilization of local equilibria. The transition of order is driven by a "control mode" that acts as a "pacemaker" for the local destabilization.[8] Taken together, Ref. [108] demonstrates how arguing in terms of mass redistribution and local equilibria is useful to gain insight into the organizational principles underlying complex dynamical phenomena and to build heuristics from numerical simulations.

- *Phase-space geometry.* In Ref. [57], we marry the two guiding ideas, stated at the beginning of this section, for the prototypical case of two-component

---

[8]Strikingly, this transition is marked by a specific ratio of two characteristic modes in the dispersion relation of the homogeneous steady state. Namely, the ratio of the right edge of the band of unstable modes q_{max} and the fastest growing mode q_c is exactly $q_{max}/q_c = 2$ at the transition. This is a particularly puzzling example for the broad observation that linear stability analysis is informative even far away from the homogeneous steady state.

MCRD systems in one spatial dimension

$$\partial_t m(x,t) = D_m \partial_x^2 m + f(m,c),$$
$$\partial_t c(x,t) = D_c \partial_x^2 c - f(m,c).$$

Such systems serve as important conceptual models for cell polarity, where m and c are the membrane-bound and cytosolic concentrations of a protein species and the nonlinear function $f(m,c)$ describes the attachment–detachment kinetics. For two-component MCRD systems, all concepts of local equilibria theory have simple geometric representations in the (m,c)-phase plane. The relation between reactive equilibria and total mass $n = m + c$ is encoded in the nonlinear shape of the reactive nullcline ($f(m,c) = 0$). To represent diffusion (i.e. spatial coupling) in the phase plane of the reaction kinetics, we introduce the concept of a *flux-balance subspace*. A phase-portrait analysis of the pattern-formation dynamics, the stationary patterns, and their bifurcations then becomes possible in terms of the reactive nullcline and flux-balance subspace. This analysis reveals the physical mechanism underlying pattern formation in MCRD systems — a *mass-redistribution instability* — and provides a simple geometric criterion for when it occurs. Moreover, we introduce the important notion of a *regional instability* which reveals an inherent connection between lateral (Turing) instability and stimulus-induced pattern formation and is employed in subsequent studies [30, 122, 123]. Taken together, Ref. [57] puts the concepts of local equilibria theory on a systematic foundation and introduces many notions that we use and generalize in subsequent studies. (A summary of this study is given in Sec. II.1, the manuscript is reproduced in Appendix A.1.)

- *Diffusively coupled compartments.* In Ref. [56], we make the concept of local compartments explicit and consider two diffusively-coupled, well-mixed compartments as the simplest "caricature" of a spatially extended system. This minimal setting eliminates the technical difficulties of spatially continuous systems and highlights the essential degrees of freedom: the redistribution of masses between the two compartments. We first revisit two-component systems with one conserved quantity to transfer the results for spatially continuous setting, studied in Ref. [57], to the setting of diffusively coupled compartments. We then turn to study models for concrete biological systems with more than one conserved mass, namely the Min system of *E. coli* [35, 98, 124], the PAR system of *C. Elegans* [38], and the Cdc42 system of budding yeast [5, 28, 125]. We show how the mass-redistribution dynamics can be fully understood in terms of simple geometric constructions based on surfaces of reactive equilibria, parametrized by the conserved masses. These

nullcline surfaces generalize the reactive nullcline used to study two-component systems (see Ref. [57]). For the example of the Min system, we explain how spatial oscillations arise from the diffusive coupling of reaction kinetics that are not oscillatory in a well-mixed setting. Such *lateral* oscillations are fundamentally different from the local oscillations underlying oscillatory media [35, 108]. This distinction turns out to be key to understanding the relationship between the *in vivo* and *in vitro* regimes of the Min system (see Sec. II.6 and Ref. [35]). From a broader perspective, the key achievement of this work is the demonstration of how insights from conceptual two-component models can be systematically transferred to concrete biological systems. (A summary of this study is given in Sec. II.2, the manuscript is reproduced in Appendix A.2.)

- *Coarsening and wavelength selection.* In Ref. [30] we build on the insights from Ref. [57] to make essential steps towards solving the critical problem of wavelength selection for fully developed nonlinear patterns. Our central insight is that wavelength selection in reaction–diffusion systems can be understood as a coarsening process (progressively increasing wavelength) that is put to a halt by counteracting processes at a certain wavelength. We develop a quantitative theory that generalizes the ideas of local equilibria theory to a large spatial scale, namely the mass-transport between the elementary patterns (single peaks or mesas) that constitute a periodic pattern. In particular, we show that neighboring elementary patterns compete for mass, which results in an instability that drives coarsening and that generalizes the mass-redistribution instability (see Ref. [57]). In particular, the criterion for this *mass-competition instability* is analogous that of mass-redistribution instability, where elementary steady-state patterns, parametrized by their total mass take the role of (local) reactive equilibria parametrized by the local mass. Notably, we find that patterns in two-component MCRD systems always fulfill the criterion for competition instability and, thus, generally exhibit uninterrupted coarsening. We then turn to systems with weak source terms that brake mass conservation and show how the production and degradation processes counteract the competition instability and stop coarsening at a finite wavelength. At even larger wavelength, the source terms can trigger regional lateral instabilities that lead to the splitting of elementary patterns and, thus, reverse the coarsening process. Demonstrating that local-equilibria equilibria theory is not restricted to strictly mass-conserving systems is an important achievement of this study. (A summary of this study is given in Sec. II.3, the manuscript is reproduced in Appendix A.3.)

- In Ref. [35], we use local equilibria theory in combination with numerical simulations and experiments to identify the mechanisms (mass-redistribution

modes) that drive pattern formation in the Min system in vitro and *in vivo*. This allows us to systematically connect these two settings (see Sec. I.4).

- In two further, technical studies, we explore how spatially heterogeneous re-action kinetics [122] and advective flows [123] impact pattern formation in conceptual two-component models for cell polarity. These studies demonstrate how the phase-space analysis developed in Ref. [57] can be further generalized. In particular, they show how concepts like regional lateral instabilities can be used to understand dynamics of highly nonlinear patterns, far away from a homogeneous steady state. (Summaries of these studies are given in Secs. II.4 and II.5; the manuscripts are reproduced in Appendices A.4 and A.5.)

4 Experimental collaborations

In the following, we briefly outline the studies we carried out in collaboration with several experimental labs. Here, we combined theoretical analysis of mathematical models with experiments to answer specific biophysical questions in concrete biological systems as briefly outlined below. For extended summaries of the results, including brief descriptions of the different modeling approaches used, see Chapter II.

- *How can we learn about the principles governing in vivo dynamics from in vitro experiments even though these two settings typically differ vastly in geometry and spatial scale?* We address this question by studying the mechanisms underlying pattern-formation in the reconstituted Min system of *E. coli* (Dekker Lab, TU Delft) [35]. A central insight of this work is that the same protein-protein interaction network in different spatial geometries (inside a cell vs. in an *in vitro* setup) can give rise to qualitatively different pattern-forming mechanisms associated with Turing and Hopf bifurcations, respectively. Controlling the spatial geometry in microfluidic devices, we are able to drive the transition between the *in vivo* and the *in vitro* regimes in the reconstituted system. Local equilibria theory was pivotal for the theoretical analysis in this study, which showcases the potential of this theoretical framework to interpret numerical and experimental data. (A summary of this study is given in Sec. II.6, the manuscript is reproduced in Appendix A.6.)

- *How do the functional domains of pattern-forming proteins contribute to their collective dynamics?* We approached this question in collaboration with experiments performed by the Schwille Lab (MPI for Biochemistry, Munich) using the reconstituted MinDE system [17]. Replacing MinE with several modularly constructed, synthetic substitutes, *in vitro* and *in silico* we have revealed the

role of MinE's functional domains (MinD-binding, dimerization, membrane-binding) for Min-protein pattern formation. Specifically, we find that the MinD-binding domain is essential and that least one other domain, either for dimerization or for membrane-binding, or a combination of both, is required for pattern formation. (A summary of this study is given in Sec. II.7, the manuscript is reproduced in Appendix A.7.)

- *How do the mechanisms underlying self-organized functions adapt to strong genetic perturbations and how do they evolve from more rudimentary ancestral mechanisms?* By theoretically studying the polarization machinery in budding yeast and testing theoretical predictions in collaboration with the Laan Lab at TU Delft, we found that this functional module implements several redundant polarization mechanisms that depend on different subsets of proteins [28]. This redundancy makes the polarization machinery both robust and evolvable as it relieves evolutionary constraints and, thus, allows for duplication and sub-functionalization of key players. Finally, we hypothesize how redundancy might have emerged from a rudimentary, ancestral mechanism through the incremental evolution of a scaffold protein. Taken together, this work exemplifies how a mechanistic understanding of self-organized cellular function can lead to fundamental insights into the way this function could have evolved from a more rudimentary ancestral form. (A summary of this study is given in Sec. II.8, the manuscript is reproduced in Appendix A.8.)

- *How can cells sense their own shape and adapt cellular functions to shape changes?* We addressed this question by studying the cortical contraction wave of starfish oocytes in experiments performed by the Fakhri Lab at MIT [126]. Our work shows how cell-shape information, encoded in a cytosolic concentration gradient, is decoded by a hierarchy of protein patterns on the membrane. The modules constituting this hierarchy implement bistable, excitable and oscillatory dynamics. This highlights how concepts from dynamical systems theory can be used to understand spatiotemporal information processing in cells.

The above works provide examples of how a systematic theoretical analysis can reveal the *relevant details* that matter in the context of concrete biological systems. We encountered relevant details on the biomolecular level of the functional domains of the proteins [17] and the protein-protein interaction network [28], as well as on the physical level of geometric confinement [35].

5 Conclusions

In summary, this thesis presents both theoretical investigations of conceptual models and studies that combine theory and experiments to address specific biological questions. It thus lays the groundwork for local equilibria theory and demonstrates how this framework can be applied to concrete biological systems.

The value of conceptual models is that they bring essential degrees of freedom and dynamical features into sharp focus. From the systematic analysis of conceptual models, one gains the intuition required for identifying these essential features in specific, complex biological systems. Specifically, the insights gained from conceptual models provide a unifying reference frame within which complex, concrete models can be placed and against which the particular, relevant details of specific biological systems stand out.

We adopted the perspective of dynamical systems theory, where the dynamical features of a system are studied in terms of phase-space geometry. Collectively, our work shows how unifying principles of protein-based pattern formation can be systematically formulated in the language of dynamical systems theory. Importantly, the notions of local (reactive) phase spaces and local (reactive) equilibria, determined by the local amounts of globally conserved quantities, solved the critical challenge of transferring the phase-space analysis to the dynamics of spatially extended systems. This central role of local equilibria is the motivation for the name *local equilibria theory*.

In the following, we elaborate on some concepts, insights, and ideas from this theoretical framework for MCRD systems.

5.1 Mass-redistribution instability

How can diffusive mass transport become self-amplifying and, thus, drive an instability? Consider particles switching between two (or more) different states with different diffusivities, say membrane-bound and cytosolic states. For the sake of simplifying the argument, let us assume that the slow state does not diffuse at all, so that mass is only redistributed due to gradients in the fast-diffusing component (let us call it cytosolic for specificity). Now suppose the switching dynamics (i.e. the kinetic reactions) is such that the cytosolic concentration decreases when the total density is increased. (This requires some feedback mechanism in the reaction kinetics such that switching from the fast to the slow state is self-enhancing.) Then, initial heterogeneities in the total density will induce cytosolic concentration gradients that result in particle fluxes from regions of low mass to regions of high mass. This mass redistribution will amplify the density fluctuations, which in turn, will further

amplify the cytosolic gradients that drive the fluxes. This self-amplification is the mechanism underlying mass-redistribution instability.

Geometrically, the criterion for this instability is a negative slope of the reactive nullcline, which encodes the shift of the reactive equilibrium to lower cytosolic concentration upon increasing total density. If, instead, the cytosolic concentration increases when the total density is increased (corresponding to positive nullcline slope), the signs of the cytosolic gradients will be opposite, such that the mass flux will remove the spatial heterogeneities.

Since the mass-redistribution instability is driven by diffusion, it is a Turing instability. In contrast to the prevalent activator-inhibitor rationale of pattern-formation instability, the reasoning in terms of mass redistribution is not restricted to two-component systems and can also be generalized to systems with multiple conserved masses [56].

Mass-redistribution instabilities are not limited to lateral transport along the membrane surface. They can also be driven by cytosolic gradients normal to the membrane that transport mass between two opposing membrane surfaces or between the membrane and a cytosolic "reservoir" [35]. Because these instabilities do not require lateral coupling (i.e. they appear in laterally isolated systems, comprising (a) small membrane patch(es) coupled to a cytosolic bulk column), they are *local instabilities*.

Finally, the notion of mass-redistribution instability unifies several other phenomena that are at first glance unrelated to Turing instability:

- *Ostwald ripening.* Consider two droplets of slightly different radius in a phase-separated system governed by a free-energy density. Owing to the interfacial tension the equilibrium chemical potential in local equilibrium is *lower* outside the *larger* droplet [127, 128]. Therefore, there will be a gradient in the chemical potential that drives flux of mass from the smaller droplet to the larger one and, thus, amplifies their size difference. This self-amplifying mechanism is analogous to the mass-redistribution instability. Indeed, there is an analog to the chemical potential for MCRD systems — the mass-redistribution potential [57]. In contrast to the chemical potential, it does not derive from a free-energy density but is governed by a dynamical equation. Gradients in the mass-redistribution potential drive not only the initial pattern-forming instability but also the coarsening process in two-component MCRD systems. This generalizes the Ostwald ripening mechanism to reaction–diffusion systems which are inherently far from thermal equilibrium.

- *Motility-induced phase separation* (MIPS) is a phenomenon exhibited by self-propelled particles interacting in such a way that they slow down in regions of high particle density [129] (this may be due to collisions or through some

"quorum sensing" mechanism [130]). In a concluding section of Ref. [57], we explain who MIPS can be understood as a mass-redistribution instability.

- *Rubber balloons.* Mass-redistribution instability also has simple analogs such as the "two-balloon experiment" [131] that may have pedagogical use to introduce Turing instability. The analog of the reactive nullcline is the volume–pressure relationship of an air-filled rubber balloon. This is due to the nonlinear material properties of rubber, this relationship is N-shaped, i.e. it has a section where the pressure in the balloon decreases upon an increase in response to a volume increase. In this regime, if two rubber balloons of equal volume are connected by a pipe, a symmetry-breaking instability will ensue which redistributes the air from one balloon to the other until they reach equal pressure at different volumes. This setup is analogous to two diffusively coupled compartments [56]. Indeed, in Chapter 7 of Ref. [131], the authors discuss a graphical construction of the instability and the final steady states of the two-balloon setup analogous to the one presented in Ref. [56].

5.2   The dual role of conserved masses

The conserved masses have a two-fold role in MCRD systems: they are control parameters and dynamical variables at the same time.[9] Specifically, the instantaneous, local masses are control parameters of the local reaction kinetics as becomes explicit through the dissection of the spatially extended system into small compartments. Correspondingly, the space spanned by the conserved masses is both a phase space where dynamics play out and a parameter space. As masses are dynamically redistributed, different points in physical space visit different regions in that parameter space. Therefore, the properties of (local) reactive equilibria in parameter space of the conserved masses contains information about the global phase-space flow of the spatially extended system.

As a concrete example, this reasoning explains why local instabilities can play an important role even if the homogeneous steady state is in a locally stable regime. For example, in the *in vitro* Min system, the triggering of local instabilities causes the emergence of spatiotemporal chaos [108]. The emergence of local instabilities qualitatively distinguishes the Min-protein dynamics in *in vitro* setups with large bulk volumes from the pole-to-pole oscillations in cells, which are driven by a lateral instability alone [35]. This is because for sufficiently low ratios of bulk volume to surface area, the regime of local instability disappears in the parameter space spanned by the total densities

---

[9]To express their dual role, the total densities were termed *control variables* in Ref. [108]. Correspondingly, the associated phase space was termed *control space*.

of MinD and MinE.

The notion of masses as local control parameters can be generalized by dissecting the system in to extended regions rather than small, well-mixed compartments. This generalization gives rise to the notion of regional dispersion relations which we discuss in the next section.

5.3 Regional dispersion relations

Since they recur several times in this thesis, let us briefly explain the ideas of a regional dispersion relation and regional lateral (in)stability.

Consider a mesa pattern in a two-component MCRD system dissected into three regions: the two plateaus and the interface that connects them (analogously, a half-peak pattern can be dissected into an interface and a low density plateau). One can then average the total density in each region and calculate the corresponding homogeneous steady state. The respective *regional dispersion relations* inform about the dynamics in each region. Importantly, the regionally averaged masses are generally different from the global average mass, and consequently the regional dispersion relations may be qualitatively different from dispersion relation of the global homogeneous steady state. In the case of a mesa pattern, the dispersion relation of the interface region has a band of unstable modes, and the right edge of this band determines the interface width of the pattern [57]. In contrast, the dispersion relations of the plateau regions have no band of unstable modes, i.e. they are laterally stable. If one introduces source terms that break mass conservation or couples the system to a third component, the plateau concentrations may be shifted into a regime of lateral instability, triggering a regional instability that results in the splitting of the plateau through the emergence of two new interfaces [30].

An argument based on regional instability precisely predicts the "nucleation threshold" for stimulus-induced pattern formation in two-component MCRD systems and establishes an inherent link between Turing instability and stimulus-induced pattern formation.

Moreover, a regional instability and regional dispersion relations also explain the emergence of localized peaks in systems with heterogeneous reaction kinetics [122], predict the velocity of peak propagation induced by advective flows [123], and predict the interface widths of standing wave patterns in the Min system (see Supplementary Information in Ref. [35]).

Taken together, the above examples show how one can gain insight about highly nonlinear, spatially extended dynamics from linear stability analysis.

5.4 Is Turing instability hard to achieve in mass-conserving systems?

The condition for a Turing instability (i.e. a mass-redistribution instability) in two-component MCRD systems is a nullcline segment whose negative slope is larger than the ratio of the diffusion constants. For intracellular systems, this ratio is very close to zero because diffusion in the cytosol is orders of magnitude faster than on the membrane. Thus, the criterion for Turing instability is essentially a nullcline segment with a negative slope. How hard is it to achieve this?

For a comparison, consider the condition for bistability, which is a nullcline segment with a slope more negative than -1. This is clearly more restrictive than the requirement of a negative nullcline slope for Turing instability. In general, a segment with a negative slope is found on N-shaped (or Λ-shaped) nullclines. Such nullclines encode the nonlinear feedback mechanisms that underlie relaxation oscillations, excitability, and bistability [69, 90, 95, 132, 133]. These phenomena are widespread phenomena in biological systems, suggesting that feedback mechanisms giving rise to N-shaped nullclines are rather common.

Together, the above arguments suggest that pattern forming systems based on proteins cycling between cytoslic and membrane-bound states, are ideally suited to robustly exhibit Turing patterns. In other words, Turing's ideas might have found their "true calling" in intracellular protein-based pattern formation.

5.5 The cytosol is not a well-mixed pool

The cytosol is often assumed to be a well-mixed "pool" (see, e.g., Refs. [134–139]). Unfortunately, this assumption is problematic for several reasons.

First, the picture of the cytosol as a pool obscures the physical process of mass transport: diffusive fluxes driven by cytosolic gradients. Indeed, this conceptual issue has led to confusion about the mechanism of pattern formation in MCRD systems and its relation to Turing instability [12, 134, 140, 141] (see Sec. I.5.6).

A second and more severe problem arises when one tries to systematically derive the well-mixed cytosol as the limit of infinitely fast cytosolic diffusion. If there is more than one cytosol component, the result of sending the diffusion constants to infinity is not unique but depends on how the limit is taken (e.g., with a fixed ratio of the diffusion constants, or the order if the limits are taken successively).[10] In other words, even shallow gradients can be sig-

---

[10]Even if there is just one component, the limit of infinitely fast diffusion, termed "shadow limit" [142] in the technical literature, may be singular, that is, the behavior at the limit may be

nificant, and therefore the behavior of a model with well-mixed cytosol is qualitatively different from a model with large but finite cytosolic diffusion constants. This is the case in the Min system, where the relative magnitude of the cytosolic diffusion constants of MinD and MinE determines whether or not patterns can form. If a well-mixed cytosol is assumed a priori, the model exhibits no patterns [35].

Finally, attachment–detachment kinetics at the membrane cause cytosolic gradients in the direction normal to the membrane. These gradients can be crucial for the dynamics. In the *in vitro* Min system, cytosolic gradients normal to the membrane (short, *vertical gradients*) drive local oscillation modes that are responsible for the characteristic *in vitro* patterns [35, 108]. In the cell and in reconstituted systems with sufficiently low bulk height (below ca. 10 μm), the geometric confinement constrains these the vertical gradients and, thus, suppresses the local oscillations. Moreover, in cells that have non-spherical shapes, vertical cytosol gradients play an important role in the orientation of patterns [17, 143, 144].

5.6 Wave-pinning, Turing instability, and bistability

In previous literature, a mechanism termed "wave-pinning" has been proposed as a new pattern-forming mechanism in MCRD systems [134, 140]. Specifically it has been claimed that (*i*) wave pinning is fundamentally different to pattern formation due to Turing instability and (*ii*) that wave-pinning requires bistable reaction kinetics. Our work shows that wave-pinning and Turing instability are, in fact, closely related. More precisely: all systems exhibiting wave-pinning also have a regime of Turing instability (and vice versa). The reason is simply that wave-pinning requires an N-shaped null-cline, which necessarily has a segment of negative slope which is the condition for Turing instability in MCRD systems. Actually, wave-pinning is simply a form of stimulus-induced pattern formation [12], which, as our work shows, can be understood in terms of a regional Turing instability.

The second claim in the "wave-pinning" literature is that this mechanism of pattern formation requires bistable reaction kinetics. This has led to some controversy and confusion. To disentangle this issue, let us first emphasize that by bistability we always refer to a property of the reaction kinetics *in a well-mixed system*, i.e. the steady states of sufficiently small, isolated compartment or the homogeneous steady states of a spatially extended system. Consider now reaction kinetics with an N-shaped nullcline whose slope is above −1 everywhere. Such a nullcline will intersect any reactive phase space

---

different from that for any arbitrarily large but finite value of the diffusion constant.

(i.e. linear subspace given by $m + c = n$) only once. Thus, for any given total density n, there is only a single fixed point. In other words, the system is monostable if one considers the total density as a control parameter. However, the N-shape of the nullcline implies that there is a regime where a line of constant cytosol concentration c intersects the nullcline three times. These intersection points correspond to different total densities. Thus, reaction kinetics with an N-shaped nullcline appear bistable if one holds the cytosolic density fixed and allows the total density to vary. In other words, fixing the cytosolic density requires coupling to a reservoir, such that the system is no longer closed. For closed systems the natural control parameter is the total density and the term *bistable* should only be used if there are two stable fixed points for the same total mass.

Importantly, in the spatially extended system, bistability of the reaction kinetics plays a secondary role, because spatial mass-redistribution shifts local equilibria and therefore provides the scaffold for patterns irrespective of local bistability.

Nonetheless it is interesting to note that there is a close geometric relationship between lateral (Turing) instability and local bistability. Both require N-shaped (or Λ-shaped) nullclines. While the former requires a nullcline section with negative slope, the latter requires a nullcline section where the slope is more negative than -1. The bifurcation at the transition between these two regimes is a Cusp, which serves as an "organizational center" in the bifurcation diagram [141].

5.7 Model development and model reduction

The central role of mass-redistribution for pattern formation in MCRD systems has several important consequences for model development and model reduction.

In general, it implies that a decomposition of the reaction kinetics into conservative and non-conservative terms, should precede model reductions when complex, many-component systems are studied. The reason is that model reductions in the well-mixed scenario (ODEs) — specifically the elimination of variables using conservation laws and separation of timescales — may obscure the role of mass redistribution in the spatially extended systems. As a specific example for this issue, we discuss the BZ reaction below (Sec. I.5.8).

Investigating the role of mass redistribution provides important information for model reduction and model classification [56, 57]. In systems with more than one conserved mass, important questions are: Which masses need

to be redistributed for patterns to emerge? How does mass transport impact the characteristics of the patterns, for instance, whether they are stationary or oscillatory? One strategy to answer these questions is to set the diffusive transport of the conserved species to different timescales. In the case of the Min system, this approach reveals that Min pole-to-pole oscillations are relaxation oscillations where MinE redistribution drives periodic switching of the MinD-polarization direction. The core pattern, a polarized MinD distribution, does not require MinE redistribution (see Ref. [56], summarized in Sec. II.2).

Pattern formation in eukaryotic cells often involves many protein species (typically GTPases and their regulators), coupled via intricate feedback loops. Studying these systems through the lens of local equilibria theory helps to disentangle these complex systems and to identify the specific roles of the individual protein in the self-organizing mechanisms.

The investigation of MCRD systems in terms of phase-space geometry shows that only a few features of the reaction kinetics matter and that these features are encoded in the nonlinear shape of the reactive nullcline (or, respectively, nullcline surfaces for systems with more than one conserved mass). The nullcline shape determines whether a system is capable of forming patterns and determines the characteristics of these patterns (peaks vs. mesas, stationary vs. oscillatory patterns). This geometric reasoning will guide model development. The central question becomes which features of the reaction kinetics qualitatively influence the shape of the nullcline. Importantly, reaction networks with different wiring topologies can give rise to the same nullcline shape, and vice versa the same reaction network can give rise to different nullcline shapes depending on the reaction rates.

From a different perspective, the central role of the nullcline shape suggests a new, data-driven approach to modeling. Rather than obtaining the nullcline from a concrete mathematical model for the reaction kinetics, one can try to directly measure the nullcline, i.e. the graph of reactive equilibria as a function of the total densities, in experiments. The experimentally measured nullcline could then serve as the basis for a data-driven model for the redistributed masses. In fact, a similar approach could be used to perform data-driven coarse-graining of agent-based computation models, by extracting the nullcline from simulations in small, well-mixed systems.

5.8 The BZ reaction as a (nearly) mass-conserving system

The BZ reaction exhibits a vast array of complex phenomena, including oscillations, bursting and chaos under well-mixed conditions; spiral waves in thin, laterally extended layers [42]; and a large variety of dynamic and stationary

patterns in micromulsions (BZ-AOT system) [145, 146]. For the well-mixed scenario, the BZ reaction is quantitatively described by a systematic reduction of the so-called FKN mechanism [43] to a seven-component ODE model [44]. At the core of the FKN mechanism is a cycle of bromine between a molecular form and a bromide ion. This cycle is driven by a reducing agent (typically malonic acid) and catalyzed by a metal ion (e.g. cerium). While the reducing agent is consumed as a chemical fuel, both bromine and the catalyst are (approximately) conserved in the reaction cycle. This suggests that the FKN mechanism has a mass-conserving core. However, theoretical studies of pattern formation in the BZ system often use reduced three- or two-component models (e.g. the so called Oregonator model [147]). The systematic reduction from the full FKN model to these reduced models is based on a rescaling of the variables (non-dimensionalization) and elimination of variables by conservation laws and separation of timescales (see e.g. Ref. [44, 147]). While these reductions preserve many qualitative and quantitative features of the BZ oscillations, they often conceal the inherent conservation laws. It may be more useful to preserve conservation laws in order to perform a geometric analysis based on shifting local equilibria, rather than using them to reduce the number of components.

More importantly, model reductions that exploit conservation laws to eliminate variables in the well-mixed dynamics, implicitly preclude spatial redistribution of mass. They are therefore no longer valid in situations where mass is redistributed, e.g. due to differential diffusion. As a specific example, let us take a closer look at the BZ-AOT system [145, 146]. In this microemulsion system, the diffusivities of polar and nonpolar components vary by an order of magnitude. Differential diffusion of multiple components, whose total density is conserved, generically leads to spatial redistribution of this conserved total density. Hence, we expect mass redistribution of the total bromine concentration in the BZ-AOT system. Interestingly, the BZ-AOT system exhibits localized patterns (both stationary and oscillatory), which have been previously linked to spatial redistribution of globally conserved quantities in other systems like vibrated granular media [99–102] and magnetoconvection [103, 104]. This suggests that redistribution of (approximately) conserved total densities may also play an important role in the BZ-AOT system. We hence believe that local equilibria theory may provide an exciting new perspective and new insights on this classic pattern-forming system.

6 Outlook

Going forward, we expect that local equilibria theory can be generalized to a theoretical framework for studying mass-conserving, spatially extended, dynamical systems. In the remainder of this section, we provide a brief outlook on forthcoming manuscripts, the critical open problem of evolution of self-organized mechanisms, and potential future generalizations of local equilibria theory. Specific outlooks on the particular subject of each publication are provided in Chapter II.

6.1 Forthcoming manuscripts

- *Reconstructing small-scale pattern characteristics from coarse-grained fields.* We perform simulations and experiments (collaboration with the Dekker Lab, TU Delft) of the reconstituted Min system in a large domain with a wedge-shaped bulk volume. A complex phenomenology on multiple spatial and temporal scales is observed where distinct types of patterns (chaos, standing waves, and traveling waves) coexist in different spatial regions and transition from one into another as time progresses. We first explain this phenomenology by building on a previously observed correlation between the pattern attractor and specific features of the dispersion relation. We show that this correlation indeed predicts the regional pattern attractors from the regional dispersion relations that are calculated based on the regionally averaged total densities in the simulation data. This shows how the transitions between different pattern types on long timescales are caused by the slow redistribution of masses. Using a local quasi-steady-state approximation, we derive a simple equation that governs mass-redistribution on large scales. This equation, together with the regional pattern prediction from the regional dispersion relation, allows us to make a long-term "pattern forecast" that is orders of magnitudes faster than the full numerical simulation. From a broader perspective, we provide a concrete example of how correlations can be utilized to recover information about the "microscopic" dynamics from the coarse-grained, hydrodynamics variables. In future studies, machine learning methods could be employed to extract the relevant correlations directly from data [148]. (This research was conducted in collaboration with Laeschkir Würthner, Jacob Halatek, and Erwin Frey.)
- *Filament bundle formation and polarity sorting through length regulation.* Based on an earlier study for single-filament length regulation [149], we develop a minimal model for a network of filaments whose length is regulated by polymerization and depolymerizing motors while the minus ends of the fila-

ments and their orientation remain fixed. Importantly, we explicitly account for the free motors and (tubulin) monomers that diffuse in the cytosol. Strikingly, agent-based simulations of this simple model show the formation of filament bundles. These bundles are characterized by sharply defined interfaces, where filament plus-ends co-localize, and segregated domains of net polarity, directed towards the interfaces. On longer timescales the bundles show a variety of phenomena, including coarsening through cytosolic mass exchange and spatiotemporal oscillations where bundles cyclically emerge and disintegrate. We identify three distinct stages in the dynamics and develop coarse-grained models that quantitatively describe the dynamics in each stage. Starting from a homogeneous state, the initial formation of heterogeneities is governed by a mass-redistribution instability which is driven by diffusive transport of monomers. At this stage, the filaments can be approximated as "point-like" i.e. their spatial extent and the directed transport of motor along filaments can be neglected. The mass-redistribution instability leads to segregated regions of growing and shrinking filaments. This causes filament-tip motion that results in polarity sorting and co-localization of filament tips. This second stage, where filament bundles start to form, is captured by a systematically coarse-grained model employing a gradient expansion in physical space and a moment expansion for the local length distributions. Finally, advective transport of motors caused by the net polarization further stabilizes the bundles. An effective model for filament bundles quantitatively explains the long-term dynamics of bundles observed in agent-based simulations. In particular, we develop a theoretical description for the coarsening dynamics using the insights from Ref. [56]. Taken together, our results show how phenomena typically attributed to mechanical interactions between filaments (caused, for example, by cross-linking motors) can emerge from filament-length regulation and the (diffusive) transport of limited resources in the cytosol alone. We expect that our minimal system can be realized in *in vitro* experiments. Going forward, it will be interesting to incorporate mechanical interactions between filaments into the model. (This study was conducted in collaboration with Moritz Striebel and Erwin Frey.)

- *Stability of periodic patterns in nearly mass-conserving reaction–diffusion systems.* In Ref. [56], we showed that coarsening in two-component MCRD systems is driven by a mass-redistribution instability and showed how weak source terms lead to wavelength selection by counteracting this instability. Expressions for the growth rate of the instability were obtained based on heuristic arguments in two limiting regimes (diffusion-limited and reaction-limited). Here, we rigorously derive the instability growth rates using a sharp interface approximation and a perturbative expansion in the source strength. The re-

sulting expression is validated against numerical stability analysis and agrees with the heuristically obtained growth rates in the limiting regimes. Moreover, these limits are shown to correspond to Cahn–Hilliard dynamics and conserved Allen–Cahn dynamics, respectively. This explains the strikingly similar phenomenology between two-component MCRD dynamics and these classical phase-separating systems. Importantly, we treat both peak-like and mesa-like patterns and our derivations, informed by physical insight, are independent of the mathematical form of the reaction kinetics, which is a significant advance over previous, mathematical approaches. (This work was carried out together with Henrik Weyer and Erwin Frey.)

- *Advective bulk-flow discriminates pattern-forming mechanisms in the in vitro Min system.* Previous experiments have shown upstream propagation of reconstituted Min-protein patterns in a microfluidic channel. In contrast, we find only downstream pattern-propagation in numerical simulations of the previously established minimal Min model. To reproduce the upstream propagation of patterns, an extended model of the Min system that accounts for switching of MinE between an active and an inactive state [16] is required. Interestingly, this model shows a transition downstream propagating patterns for low ratios of the MinE to MinD concentration (E:D ratio) — a prediction that we confirm experimentally (collaboration with the Dekker Lab, TU Delft). Numerical simulations further show hysteresis in the transition between upstream and downstream propagation and that downstream propagation leads to a coarsening process that culminates in a solitary wave. Systematic analysis and model reduction of the extended model show that pattern formation is driven by qualitatively different pattern forming mechanisms in the regimes of low E:D ratio and high E:D ratio where downstream and upstream propagation are observed, respectively. This suggests that the response of patterns to advective flows can be used as a probe to distinguish pattern-forming mechanisms that subtly depend on biomolecular details. (This research was conducted in as a master thesis project by Jernej Rudi Finžgar.)

6.2   Future questions in intracellular self-organization

In the following we highlight some important areas for future research.

Control of pattern formation.   We showed that mass-redistribution instability provides a general mechanism for protein-based pattern formation that generically emerges in mass-conserving systems with kinetics coupling the cytosol to the membrane (or other substrates), see Sec. I.5.4. An important question going forward is how cells utilize and functionalize this instability. This is the

question of how pattern formation is *controlled* and answering it requires to account for the heterogeneous and temporally changing environment within which protein-patterns form. Indeed, already Turing noted that "Most of an organism, most of the time is developing from one pattern into another, rather than from homogeneity into a pattern." [50]. For conceptual, two-component MCRD systems, we demonstrated that local equilibria theory provides new, powerful tools to analyze protein-pattern formation under such heterogeneous and dynamically changing conditions [57, 122, 122]. An important challenge going forward will be to understand how protein-based pattern formation is controlled in concrete biological systems [39, 126, 138, 150–152]. In fact, a similar question arises for cytoskeletal organization and morphogenesis, which fall into the broad class of active matter systems. Instabilities are common in these systems, and a central question in the field is how these instabilities can be controlled and "functionalized."

Intracellular membrane trafficking. Rho GTPases play a central role in organizing vesicle trafficking between the endoplasmatic reticulum (ER), the Golgi, endosomes, lysosomes, and the plasma membrane [153]. We therefore expect that protein-based patterns on these intracellular membranes will be an important future research area. Here, the complex and dynamically changing spatial geometries of the Golgi and the ER with highly curved membranes will play a key role [154–156].

Cytoskeletal self-organization. Diverse architectures of cytoskeletal structures emerge from the mechano-chemical interplay of filament nucleation, length regulation, and mechanical forces between filaments exerted by molecular motors. Many of these processes are spatiotemporally coordinated and regulated by protein-concentration patterns. For instance, active RhoA recruits myosin motors [157], Cdc42 initiates actin nucleation [158], and Ran regulates microtubule nucleation [159]. In turn, cytoskeletal structures feed back into the protein dynamics via active transport along filaments [160], mechanical deformations [126] and flows induced by motor activity [39, 161, 162] to name just few examples. The interplay between protein-based pattern formation and cytoskeletal dynamics is an exciting area for future research. Importantly, the resources for cytoskeletal structures (actin/tubulin monomers, molecular motors, nucleation factors, etc.) are limited, that is, their total masses are conserved. We therefore expect that the methods and insights from local equilibria theory will help to understand cytoskeletal self-organization.

6.3 Active matter

Reaction–diffusion systems are part of a broader class of non-equilibrium systems where energy is fed in on the microscopic scale. This class also encompasses active matter systems, which are driven by (self-)propulsive forces on the single-particle level [129, 163–165]. The propulsive forces are directed by the orientations of the particles which, in turn, are governed by local alignment rules that derive from the interactions between the particles. Orientational order parameters, both polar and nematic, therefore become important degrees of freedom on the coarse-grained level. This distinguishes active matter from reaction–diffusion systems. Yet from a broader perspective, both are instances of nonlinear, pattern-forming systems. Indeed, since particle-based systems are inherently mass conserving, we expect that the concepts of local equilibria theory can be generalized to study active-matter systems.

A central insight from local equilibria theory is that changes in local density can drive bifurcations of the local dynamics (e.g., a change of stability of the local equilibria). Analogously, in active matter systems, change in local density can drive transitions in local orientational order, e.g. induce local symmetry breaking. In turn, orientational order impacts the particle fluxes that redistribute density. This interplay gives rise to a rich dynamical behavior on the macroscopic level, including the coexistence and interconversion between polar flocks and nematic lanes [166]. This explains the striking observations from recent experiments and agent-based simulations [167].

6.4 Are local equilibria and local causal states?

Local causal states are a recently developed concept that aims to characterize complex spatiotemporal dynamics based on data [119, 168, 169]. The idea is that at a given instant of time, each point in space can be assigned one of a finite number of distinct dynamical states that characterize the instantaneous, local dynamics. As time progresses, transitions between these local states occur locally. The goal is then to identify a minimal set of states and a set of transition probabilities that predict the local state transitions at each point conditioned on the point's "short-term" past lightcone. Here, the lightcone reflects the fact that information only propagates at a finite speed through systems governed by local evolution laws. Because such a set of local states together with the conditional transition probabilities provide a causal link between the past and the future, they are called *local causal states*. In Refs. [168, 169] it is demonstrated that the local causal states can be inferred purely from data and that they reveal coherent spacetime structures in complex dynamical systems. More recently, it was shown how the conditional transition probabilities for

local causal states can be used to produce long-term forecasts of the dynamics [119].

We hypothesize that the properties of local equilibria (i.e. their position and stability) may be related to local causal states. Indeed, since they serve as proxies for the local dynamics, the properties of local equilibria encode information about the local, short-term time evolution. Moreover, the bifurcation diagram in the parameter space spanned by the total densities encodes information about the transitions of local equilibria between distinct dynamical regimes.

These parallels between local equilibria and local causal states suggest that one could find a mapping between them. This hypothesis could be tested by performing a local causal state analysis for a system where local equilibria theory has been applied successfully, e.g., the *in vitro* Min system. If a mapping between local equilibria and local causal states is indeed found, an analysis based on local causal states may be used to reconstruct the properties of local equilibria and the associated bifurcation scenarios purely from data. This would help to identify the underlying physical mechanisms and guide the development of models that capture the essential dynamical features on a "mesoscopic" level.

Local equilibria theory centrally builds on conserved masses and the insight that their spatial redistribution is an essential driver of the dynamics. Therefore, a key question is whether conservation laws can be built into the local causal state framework.

II | Publication summaries

1 Phase-space geometry of mass-conserving reaction–diffusion dynamics

This manuscript is reproduced as part of this thesis in Appendix A.1.

Journal reference. F. Brauns,[*] J. Halatek,[*] and E. Frey, *Phase-space geometry of mass-conserving reaction–diffusion dynamics.* Phys. Rev. X 10, 041036 (2020)

Author contributions. All authors conceptualized the study, performed the investigation and wrote the manuscript. FB performed numerical analysis and simulations.

[*] FB and JH contributed equally to this work.

An early version of this manuscript is part of Jacob Halatek's PhD thesis.

Abstract

Experimental studies of protein-pattern formation have stimulated new interest in the dynamics of reaction-diffusion systems. However, a comprehensive theoretical understanding of the dynamics of such highly nonlinear, spatially extended systems is still missing. Here, we show how a description in phase space, which has proven invaluable in shaping our intuition about the dynamics of nonlinear ordinary differential equations, can be generalized to mass-conserving reaction-diffusion (MCRD) systems. We present a comprehensive analysis of two-component MCRD systems, which serve as paradigmatic minimal systems that encapsulate the core principles and concepts of the local equilibria theory introduced in the paper. The key insight underlying this theory is that shifting local (reactive) equilibria—controlled by the local total density—give rise to concentration gradients that drive diffusive redistribution of total density. We show how this dynamic interplay

can be embedded in the phase plane of the reaction kinetics in terms of simple geometric objects: the reactive nullcline (line of reactive equilibria) and the diffusive flux-balance subspace. On this phase-space level, physical insight can be gained from geometric criteria and graphical constructions. The effects of nonlinearities on the global dynamics are simply encoded in the curved shape of the reactive nullcline. In particular, we show that the pattern-forming "Turing instability" in MCRD systems is a mass-redistribution instability and that the features and bifurcations of patterns can be characterized based on regional dispersion relations, associated to distinct spatial regions (plateaus and interfaces) of the patterns. In an extensive outlook section, we detail concrete approaches to generalize local equilibria theory in several directions, including systems with more than two components, weakly broken mass conservation, and active matter systems.

Background

A previous work, Ref. [108], has introduced local equilibria and suggested a new way of thinking about reaction–diffusion systems that focuses on the redistribution of globally conserved masses. It demonstrated the power of this way of thinking, which we term local equilibria theory, by explaining the complex phenomenology of a specific model. Here, we systematically build up local equilibria theory by means of a simple, prototypical example: two-component MCRD systems. The main advantage of these systems is that their phase space of the chemical concentrations is two-dimensional and, hence, lends itself to a phase-portrait analysis. The main ideas and concepts of local equilibria theory, which remained rather abstract in Ref. [108], find simple, geometric representations in this phase portrait. In the context of intracellular pattern formation, two-component MCRD systems play a central role as conceptual models for cell polarization. We therefore adopt the terms membrane-bound and cytosolic to refer to the slow-diffusing and fast-diffusing component, respectively.

Key results and conclusions

- The nonlinear reaction kinetics is encoded by the shape of the *reactive nullcline* in the phase plane of the chemical concentrations. Local reactive phase spaces encode the mass-conservation property of the local reaction kinetics. Their position in the phase plane is determined by the local total density. Intersection points between reactive phase spaces and nullcline determine the reactive equilibria. This graphical construction connects the spatially extended system to the phase plane and illustrates how mass redistribution shifts local reactive equilibria.

- A family of flux-balance subspaces encode a balance of diffusive fluxes and thus represent the diffusive spatial coupling in the phase plane of the reaction kinetics.

- Mass-redistribution is driven by gradients in the *mass-redistribution potential*. The mass-redistribution potential parametrizes the family of flux-balance subspaces and plays an analogous role to the chemical potential in equilibrium systems. However, in contrast to its equilibrium counterpart, it does not derive from a free energy density but is governed by its own dynamical equation.

- We introduce the concept of a mass-redistribution instability and show that it is the general physical mechanism underlying Turing instability in MCRD systems. The criterion for this instability is that the mass-redistribution potential in reactive equilibrium must decrease as a function of the total density (geometrically this implies a negative nullcline slope). If this is the case, diffusive mass transport, driven by the gradients in the mass-redistribution potential will amplify itself and thus drive the instability. In Ref. [56] we show that the mass-redistribution instability can be generalized to the level of elementary patterns that compete for mass.

- A stationary pattern is embedded in a single flux-balance subspace, whose position is determined by a balance of net reactive turnovers (which is graphically represented by an area balance, akin to a Maxwell-construction). Intersection points between the reactive nullcline and the flux-balance subspace mark the concentrations in the plateaus and at the inflection point of the spatial pattern profile. This geometric reasoning allows us to graphically construct the stationary patterns.

- The phase-portrait analysis based on the reactive nullcline and the flux-balance subspace yields the complete bifurcation diagram of two-component MCRD systems. This shows that two-component MCRD systems are generically subcritical, i.e. that stationary patterns exist outside the regime of Turing instability.

- Moreover, the bifurcation analysis reveals the connection between Turing instability and bistability of the reaction kinetics (see discussion in Sec. I.5.6) and shows that all two-component MCRD systems are *topologically equivalent*. (This is further strengthened by Ref. [30], where it is shown all two-component systems MCRD systems exhibit uninterrupted coarsening).

- Generalizing the idea of local equilibria to spatially extended *regions* we introduce the notion of a *regional lateral instability*. The interface of a stationary pattern is maintained by a regional lateral instability and its width is set by the marginally stable wavelength.

- An argument in terms of regional instability reveals an inherent connection between Turing instability and stimulus-induced pattern formation and predicts the critical stimulus threshold.

- We identify two elementary pattern types, peaks and mesas. Whether a system forms peaks or mesas and the transition from one pattern type to the other can be read-off from the phase portrait, and depends on the nullcline shape, the ratio of the diffusion constants (setting the flux-balance subspace's slope) and the total mass in the system. The distinction between peaks and mesas is important for the coarsening process of pattern composed of many elementary patterns (see Sec. II.3 and Ref. [30])

Outlook

- The complete characterization of two-component MCRD systems serves as the basis for future generalizations of the phase-portrait analysis and the reasoning in terms of local equilibria (see Refs. [30, 56, 122, 123] which are summarized in the following sections).

- The nullcline, i.e. the graph of reactive equilibria as a function of the total density, is, in principle, measurable in experiments or in agent based simulations and can be generalized beyond reaction–diffusion systems. A phase-portrait analysis based on a measured nullcline can then provide insight even when an explicit mathematical expression for the reaction kinetics is not available.

2 Diffusive coupling of two well-mixed compartments elucidates elementary principles of protein-based pattern formation

This manuscript is reproduced as part of this thesis in Appendix A.2.

Journal reference.   F. Brauns, J. Halatek, and E. Frey, *Diffusive coupling of two well-mixed compartments elucidates elementary principles of protein-based pattern formation.* Phys. Rev. Research 3, 013258 (2021)

Author contributions.   All authors conceptualized the study, performed the investigation and wrote the manuscript.

Abstract

Spatial organization of proteins in cells is important for many biological functions. In general, the nonlinear, spatially coupled models for protein-pattern formation are only accessible to numerical simulations, which has limited insight into the general underlying principles. To overcome this limitation, we adopt the setting of two diffusively coupled, well-mixed compartments that represents the elementary feature of any pattern—an interface. For intracellular systems, the total numbers of proteins are conserved on the relevant timescale of pattern formation. Thus, the essential dynamics is the redistribution of the globally conserved mass densities between the two compartments. We present a phase-portrait analysis in the phase-space of the redistributed masses that provides insights on the physical mechanisms underlying pattern formation. We demonstrate this approach for several paradigmatic model systems. In particular, we show that the pole-to-pole Min oscillations in *Escherichia coli* are relaxation oscillations of the MinD polarity orientation. This reveals a close relation between cell polarity and oscillatory patterns in cells. Critically, our findings suggest that the design principles of intracellular pattern formation are found in characteristic features in these phase portraits (nullclines and fixed points). These features are not uniquely determined by the topology of the protein-interaction network but depend on parameters (kinetic rates, diffusion constants) and distinct networks can give rise to equivalent phase portrait features.

Background

The fundamental, defining feature of a pattern are interfaces, separating regions of low and high concentrations. In the coarsest caricature, such an interface is described by two diffusively coupled, well-mixed compartments. This setting accounts for diffusive spatial coupling in a minimal, elementary form, while preserving the highly nonlinear character of the local reaction kinetics. In this setting, the notions of local equilibria theory find concrete geometric representations. While the phase space analysis performed in Ref. [57] was restricted to two-component systems, the setting of two compartments admits simple geometric constructions for systems with more components and conserved masses.

Key results and conclusions

- Utilizing mass conservation, we reduce the dynamics to the low-dimensional phase space of the redistributed masses. For systems with two conserved

masses, this phase space is two-dimensional, which admits a phase portrait analysis. The dynamics in mass-redistribution phase portrait can be derived from a simple geometric construction that explains the interplay between the local reaction kinetics and the diffusive spatial coupling.

- The central object in the geometric construction are surfaces of reactive equilibria as a function of the conserved masses. These surfaces generalize the reactive nullcline to systems with more than one conserved mass.

- We demonstrate our general approach for three paradigmatic model systems for intracellular pattern formation, the Min system of *E. coli*, the PAR system of *C. elegans* and the Cdc42 system of *S. cerevisiae* (a non-technical review of the self-organization principles in these systems is given in Ref. [4]). The mass-redistribution phase portraits of these systems yield several important and striking insights: Min pole-to-pole oscillations are spatial relaxation oscillations of the MinD polarization direction. Redistribution of MinE is not required for the formation of a polarized MinD concentration profile. This establishes a close mechanistic connection between oscillatory Min patterns and stationary cell polarity as exhibited by the Cdc42 system. In contrast, the stationary polarity patterns exhibited by the PAR system are based on a fundamentally different mechanism that explicitly requires the redistribution of both protein species.

Outlook

- Based on our results, we propose that the design principles underlying protein-based pattern formation can be systematically formulated in terms of phase-space geometry. This will help to better understand the relations between existing models and will guide future modeling efforts for intracellular pattern formation. Moreover, the phase portrait analysis in the phase space of the redistributed masses provides a new way to classify pattern-forming systems. This will complement existing network-centered approaches.

- From a different perspective, MinE mass redistribution can be seen as an endogenous control mechanism for MinD polarization. Indeed, control systems for switching cell polarity based on spatial relaxation oscillations were investigated in several recent studies [138, 139]. Going forward, control theory [170] might provide a new perspective on intracellular self-organization and could help to make sense of the complex intertwined feedback loops found in eukaryotic protein-protein interaction networks [31, 32, 34]. We expect that the setting of diffusively coupled compartments will, thanks to its conceptual simplicity, help investigating such complex many-component systems.

- In future work, the minimal setting of two diffusively coupled compartments could be particularly useful to study the link between phase-space geometry and parameter space topology. Another interesting task for future research is to enumerate all possible wirings of the two-protein interaction networks and classify them based on their phase portraits in the phase space of redistributed masses.

3 Wavelength selection by interrupted coarsening in reaction-diffusion systems

This manuscript is reproduced as part of this thesis in Appendix A.3.

Author contributions. FB, HW, JH and EF conceptualized the study; FB, HW and JY performed mathematical analysis and performed numerical simulations; FB, HW and EF wrote the manuscript.

[*] FB and HW contributed equally to this work.

This manuscript will also be part of the PhD thesis of Henrik Weyer.

Abstract

Wavelength selection in reaction–diffusion systems can be understood as a coarsening process that is interrupted by counteracting processes at certain wavelengths. We first show that coarsening in mass-conserving systems is driven by self-amplifying mass transport between neighboring high-density domains. We derive a general coarsening criterion and show that coarsening is generically uninterrupted in two-component systems that conserve mass. The theory is then generalized to study interrupted coarsening and anti-coarsening due to weakly-broken mass conservation, providing a general path to analyze wavelength selection in pattern formation far from equilibrium.

Background

Traditionally, wavelength selection in reaction–diffusion systems is studied in terms of the linearized dynamics in the vicinity of a homogeneous steady

state, where the fastest growing mode sets the prevailing wavelength. This reasoning, however, fails for fully developed patterns far away from the homogeneous steady state. To make progress in this highly nonlinear regime, we propose an entirely different approach.

Key results and conclusions

- We show that wavelength selection in reaction–diffusion systems can be understood as an (interrupted) coarsening process. Coarsening is driven by a competition for mass between neighboring elementary patterns (single peaks or mesas) due to gradients in the mass-redistribution potential (introduced in Ref. [57]). This competition can be framed in terms of an instability that generalizes the mass-redistribution instability that gives rise to patterns out of the homogeneous steady state. The competition instability between peaks occurs if the mass-redistribution potential of a single peak (or mesa) is a decreasing function of the total peak mass. This is analogous to the negative nullcline slope criterion for mass-redistribution instability.

- Arguments based on the phase-space analysis developed in Ref. [57], show that the criterion for competition instability is always fulfilled for two-component MCRD systems, that is, such systems always exhibit uninterrupted coarsening, independently of the specific reaction kinetics. This answers a long-standing question in the field.

- Depending on the rate of diffusive mass transport between neighboring peaks/ mesas compared to the rate at which the peaks/mesas profile adapts to changes in mass, there are two regimes. A *diffusion-limited regime* and a *reaction-limited regime*. In the former regime, each peak can be assumed to be in quasi-steady-state (akin to LSW theory for Ostwald ripening [127, 128]. In the latter regime, relaxation to the steady-state profile is the limiting process. The dynamics in this regime can be mapped to a conserved Allen–Cahn equation.

- Dynamic coarsening laws can be derived from the rate of the competition instability through a simple scaling analysis. The functional dependence of the mass-redistribution potential on the total mass determines the temporal coarsening law. Peak patterns exhibit non-universal coarsening exponents that depend on the reaction kinetics and on the spatial dimension. Mesa patterns exhibit logarithmic coarsening in 1D and classical $t^{1/3}$ in two and more spatial dimensions.

- How can the coarsening process be interrupted? As a minimal extension, we include weak source terms (production and degradation) that break mass conservation. These source terms counteract the competition instability that

drives coarsening. Since diffusive mass transport becomes slower with increasing length scale, the source terms eventually interrupt the coarsening process. Thus, a new length scale emerges from the balance of source terms and competition instability.

- Above a critical wavelength, typically much larger than the wavelength where coarsening stops, the source terms induce splitting of peaks/mesas. This splitting reduces the wavelength and is sometimes referred to as anti-coarsening. A phase-space analysis (see Ref. [57]), shows that splitting is triggered by a regional lateral instability and derive a relation for the critical wavelength above which splitting occurs.

- In-between the thresholds for interrupted coarsening and splitting, there is a large regime of stable wavelengths. If the initial wavelength is below the interrupted coarsening threshold, coarsening will proceed until it is interrupted at the threshold. In this case, the selected wavelength is the shortest stable wavelength. This might be different in the presence of noise [171, 172]. Whether noise selects a particular wavelength in the band of stable wavelengths is an important open question for future research.

Outlook

- In the diffusion-limited regime, the coarsening criterion based on the quasi-steady-state mass-redistribution potential holds independently of the number of components. If there is more than one conserved mass, there will be a corresponding mass-redistribution potential for each conservation law. The coarsening criterion then generalized analogously to the generalized slope criterion for mass-redistribution instability discussed in Ref. [56]. Important future challenges are cases where the quasi-steady-state approximation is not possible, including dynamic patterns such as traveling and standing waves [35].

- The analysis of two-component systems with weak source terms serves as a prototype for other scenarios that can give rise to interrupted coarsening; for instance, three-component systems with mass-conserving reactions [126, 173–175] and mass-conserving two-component systems coupled to a third component that is not conserved [22, 176]. In addition to (quasi-)stationary patterns, these systems exhibit dynamic patterns like standing and traveling waves. Coarsening and wavelength selection of such patterns is an important open issue (see Supplementary Discussion in [35]).

4 Pattern localization to a domain edge

This manuscript is reproduced as part of this thesis in Appendix A.4.

Author contributions. All authors conceptualized the study and wrote the manuscript; FB, MCW and TH performed the investigation; FB and TH performed numerical analysis and simulations.

[*] MCW, FB and TH contributed equally to this work.

This manuscript is also part of the PhD thesis of Manon Wigbers.

Abstract

The formation of protein patterns inside cells is generically described by reaction–diffusion models. The study of such systems goes back to Turing, who showed how patterns can emerge from a homogenous steady state when two reactive components have different diffusivities (e.g. membrane-bound and cytosolic states). However, in nature, systems typically develop in a heterogeneous environment, where upstream protein patterns affect the formation of protein patterns downstream. Examples for this are the polarization of Cdc42 adjacent to the previous bud-site in budding yeast, and the formation of an actin-recruiter ring that forms around a PIP3 domain in macropinocytosis. This suggests that previously established protein patterns can serve as a template for downstream proteins and that these downstream proteins can 'sense' the edge of the template. A mechanism for how this edge sensing may work remains elusive. Here, we demonstrate and analyze a generic and robust edge-sensing mechanism, based on a two-component mass-conserving reaction-diffusion (MCRD) model. Our analysis is rooted in a recently developed theoretical framework for MCRD systems, termed local equilibria theory. We extend this framework to capture the spatially heterogeneous reaction kinetics due to the template. This enables us to graphically construct the stationary patterns in the phase space of the reaction kinetics. Furthermore, we show that the protein template can trigger a regional mass-redistribution instability near the template edge, leading to the accumulation of protein mass, which eventually results in a stationary peak at the template edge. We show that simple geometric criteria on the reactive nullcline's shape predict when this edge-sensing mechanism is operational. Thus, our results

provide guidance for future studies of biological systems, and for the design of synthetic pattern forming systems.

Background

Already Turing noted that "most of an organism, most of the time, is developing from one pattern into another, rather than from homogeneity into a pattern." Indeed, in cells, upstream protein patterns can serve as a "template" by affecting the formation of protein patterns downstream. For example, in budding yeast, landmark proteins direct the polarization of the GTPase Cdc42, such that the Cdc42 cluster forms adjacent to previous bud-sites [177–179]. Furthermore, in macropinocytosis, it has been suggested that a high-density domain of PIP3 serves as a template for a ring of actin recruiters that forms around the PIP3 domain [180, 181]. In these examples, the downstream protein "senses" the edge between two spatial subdomains defined by the upstream pattern. A mechanism for how this edge sensing may work had remained elusive.

Key results and conclusions

- As an elementary scenario, we study a two-component MCRD system with a step-like heterogeneity in the reaction rates, partitioning the system into two subdomains. A conceptual and technical challenge is that such systems have a heterogeneous base state rather than a homogeneous steady state.

- The heterogeneous base state and stationary patterns can be constructed in the phase plane of the chemical concentration, by using and generalizing the analysis developed in Ref. [57]. Using the global average density as a control parameter, we find that the system is multistable and exhibits a hysteresis loop delimited by saddle-node bifurcations. At these bifurcations the system transitions from the heterogeneous base state to a stationary pattern. The results from this phase-portrait analysis are confirmed by a numerical bifurcation analysis using pseudo-arclength continuation and by finite element simulations.

- The transition from the base state to patterns is governed by a regional mass-redistribution instability (see Ref. [57]), which is localized to the edge between the two subdomains. This localized instability leads to the formation of a density peak at the subdomain edge, and thus positions the final stationary pattern.

- A simple geometric criterion based on the reactive nullcline shapes in the two subdomains predicts when this edge-sensing mechanism is operational.

Thus, our work shows how the phase-portrait analysis established in Ref. [57] can be used to design specific functions.

Outlook

- As a next step it will be interesting to explicitly model an upstream concentration profile that defines the spatial subdomains and introduce feedback coupling from the edge-localized pattern to this "upstream" pattern.

- The insights gained for a conceptual two-component model will guide future theoretical studies of concrete biological systems where localization of proteins to a domain edge has specific functions [177, 181, 182].

5 Flow induced symmetry breaking in a conceptual polarity model

This manuscript is reproduced as part of this thesis in Appendix A.5.

Author contributions.   All authors designed and carried out the research; MCW, FB, and EF wrote the paper; CYL visualized the findings.

[*] MCW, FB and CLY contributed equally to this work.

Abstract

Important cellular processes, such as cell motility and cell division, are coordinated by cell polarity, which is determined by the non-uniform distribution of certain proteins. Such protein patterns form via an interplay of protein reactions and protein transport. Since Turing's seminal work, the formation of protein patterns resulting from the interplay between reactions and diffusive transport has been widely studied. Over the last few years, increasing evidence shows that also advective transport, resulting from cytosolic and cortical flows, is present in many cells. However, it remains unclear how and whether these flows contribute to protein-pattern formation. To address this question, we use a minimal model that conserves the total protein mass to characterize the effects of cytosolic flow on pattern formation. Combining a

linear stability analysis with numerical simulations, we find that membrane-bound protein patterns propagate against the direction of cytoplasmic flow with a speed that is maximal for intermediate flow speed. We show that the mechanism underlying this pattern propagation relies on a higher protein influx on the upstream side of the pattern compared to the downstream side. Furthermore, we find that cytosolic flow can change the membrane pattern qualitatively from a peak pattern to a mesa pattern. Finally, our study shows that a non-uniform flow profile can induce pattern formation by triggering a regional lateral instability.

Background

In addition to transport by diffusion, proteins are advected by hydrodynamic flows of the cytoplasm ("cytoplasmic streaming") [37] and of the cell cortex [38, 39]. These flows are induced by cytoskeletal motors [162], cell-shape deformations [183], and acto-myosin contractility [184]. To study the effect of such flows on pattern formation, we study a conceptual two-component model that incorporates advection by cytoplasmic flow (i.e. advective flow in the fast-diffusing component).

Key results and conclusions

- We identify a lateral instability that is driven by the interplay of shifting local equilibria and mass transport by the advective flow. This instability generalizes the diffusion-driven mass-redistribution instability. In particular, we generalize the nullcline-slope criterion for this instability to account for advective flow. Since advective mass transport alone can drive instability, different diffusion constants of the two components are no longer required for pattern formation if the advective flow in the cytosol is sufficiently fast.

- Using linear stability analysis and numerical simulations, we show that cytoplasmic flow drives upstream propagation of the membrane-bound density peak. The mechanism of this propagation can be inferred from a phase-portrait analysis, and a regional linear stability analysis at the inflection point of the concentration profile predicts the propagation velocity of the peak. Heuristically, peak propagation is a result of asymmetric cytosolic fluxes into the peak. In a steady-state, the peak in the membrane-bound protein density is maintained against diffusion by attachment of proteins from the cytosol and thus acts as a cytosolic sink. In the absence of advection this sink is resupplied by diffusive influx, which is symmetric. Advection resupplies the cytosolic sink asymmetrically, where the resupply is increased on the upstream side and decreased on the downstream side of the peak. This asymmetry

leads to increased (decreased) attachment to the membrane on the upstream (downstream) side, resulting in an upstream motion of the membrane-bound concentration peak.

- We show how cytosolic flow can drive the transition from mesa patterns to peak patterns.
- Finally, we show how a heterogeneous flow velocity leads to mass accumulation which can trigger a regional lateral instability and, thus, induce pattern formation even when the homogeneous steady-state is stable. In the regime where the homogeneous steady state and stationary patterns coexist, the flow-induced pattern will remain once the flow is switched off.

Outlook

In future work it will be interesting to study the effect of advective flows in systems with more components. For instance, in systems with two cytosolic components that have antagonistic roles in the reaction dynamics (e.g. MinD and MinE in the Min system), flow may induce both downstream and upstream propagation of patterns (see Sec. I.6.1).

6 Bulk-surface coupling reconciles Min-protein pattern formation *in vitro* and *in vivo*

A preprint of this manuscript is reproduced as part of this thesis in Appendix A.6.

Note: Due to bioRxiv's policy of not allowing post-acceptance updates, the bioRxiv version if this manuscript referenced here is older than the accepted version reproduced in Sec. A.6.

Author contributions.   FB, GP, JH, EF, and CD designed and conceptualized the study; GP and CD designed and carried out the experiments; FB, JH, and EF designed the theoretical models and performed the mathematical analyses; FB, GP, and JK analyzed data; and FB, GP, JH, EF, and CD wrote the paper.

 [*]FB, GP, and JH contributed equally to this work.

Abstract

Self-organization of Min proteins is responsible for the spatial control of cell division in *Escherichia coli*, and has been studied both *in vivo* and *in vitro*. Intriguingly, the protein patterns observed in these settings differ qualitatively and quantitatively. This puzzling dichotomy has not been resolved to date. Using reconstituted proteins in laterally wide microchambers with a well-controlled height, we experimentally show that the Min protein dynamics on the membrane crucially depend on the micro chamber height due to bulk concentration gradients orthogonal to the membrane. A theoretical analysis shows that *in vitro* patterns at low microchamber height are driven by the same *lateral* oscillation mode as pole-to-pole oscillations *in vivo*. At larger microchamber height, additional *vertical* oscillation modes set in, marking the transition to a qualitatively different *in vitro* regime. Our work reveals the qualitatively different mechanisms of mass transport that govern Min protein-patterns for different bulk heights and thus shows that Min patterns in cells are governed by a different mechanism than those *in vitro*.

Background

The Min-protein system arguably is *the* paradigmatic model system for protein-based pattern formation, and has been studied extensively *in vivo* in cells [185, 186] and *in vitro* in minimal reconstituted systems on artificial membranes [13]. Yet, despite many studies, a key question has remained puzzling until recently; namely, how the plethora of patterns observed *in vitro* relates to the *in vivo* pole-to-pole oscillations. Based on previous theoretical results and experimental observations we hypothesize that the volume of the cytosolic bulk relative to the membrane surface is the key control parameter that distinguishes these settings.

Key results and conclusions

- In reconstitution experiments with Min proteins, we control the bulk-surface ratio using flat, laterally large microchambers with a range of different heights. We observe a striking variety of membrane-bound protein patterns depending on the chamber height.

- A minimal model for the Min system qualitatively reproduces these patterns and the phase diagram where the chamber height and the MinE-to-MinD concentration ratio are varied.

- Attachment and detachment of proteins at the membrane cause concentration gradients normal to the membrane. This bulk-surface coupling imparts a

strong dependence of the pattern forming dynamics on the spatial geometry.

- *Different mass-redistribution modes drive pattern formation depending on the bulk height*: For low bulk heights, only a lateral (Turing) mode is unstable. This is the same mode that drives pole-to-pole oscillations *in vivo* [56, 98]. In this regime, the geometric confinement (low bulk-surface ratio) constrains vertical gradients and thus suppresses local instabilities. For larger bulk heights, a regime of local instability appears in the stability diagram, indicating the onset of membrane-to-membrane oscillations. These oscillations are driven by vertical bulk gradients that transport mass from one membrane to the other and back. Finally, for very large bulk heights, the bulk far away from the membranes acts as a reservoir that facilitates membrane-to-bulk oscillations.

- Different types of synchronization of the patterns on the top and bottom surface of the microchambers provide characteristic signatures for the distinct mass-redistribution modes in the experimental system.

- Collectively, the experimental and theoretical results systematically connect the *in vivo* and the *in vitro* regime and thereby solve the puzzle of the qualitatively different patterns on the level of the pattern-forming mechanisms.

Modeling approach

We use a previously established [98, 108, 187], minimal model that accounts for basic interactions between MinD and MinE. This model is valid in the regime of low E:D concentration ratio where it qualitatively reproduces the experimentally observed phenomena in dependence of the bulk height. Importantly, the minimal model reveals the distinct mass-redistribution modes that drive pattern formation. This explains the qualitative difference between the *in vivo* and *in vitro* patterns and connects these two regimes. However, the minimal Min model cannot account for pattern formation in the high E:D regime where the switching of MinE between an open and closed confirmation becomes important [16]. The minimal model also does not account for various types of quasi-stationary patterns observed in recent experiments [21]. Finally, neither the minimal model nor the extended model that accounts for MinE switching, reproduce the correct length and timescales in the *in vitro* setting. We expect that further extensions of the model will be necessary to resolve these discrepancies.

Outlook

- The about five- to ten-times larger wavelengths observed in the reconstituted system compared to the *in vivo* setting remain an open problem. Understand-

ing the qualitative pattern-forming mechanisms is an important step towards a solution of this quantitative discrepancy.

- Our findings show how geometric confinement can be used to control pattern-forming mechanisms. Indeed, *E. coli* cells exhibit robust pole-to-pole oscillations precisely because other oscillation modes are suppressed by the cellular confinement. This will be important for future studies that aim to engineer [17] and functionalize [188] protein-based patterns.

- Bulk-surface coupling is not specific to Min proteins but a fundamental aspect of many systems for intracellular pattern formation, where proteins cycle between membrane-bound and cytosolic states. This suggests that geometric confinement will play an important role in many of these systems. In cells that actively change their shape through mechanical forces, bulk-surface coupling may provide a means of mechano-chemical feedback.

- Synchronization — both in-phase and anti-phase — of membrane-bound patterns across the bulk is an interesting phenomenon in itself that deserves more detailed experimental and theoretical investigation. Previous experiments using the BZ reaction have implemented coupling of surface patterns through a membrane separating two reaction domains [189] and artificially using a camera–projector setup [190, 191]. In-phase synchronization of spiral waves was found for sufficiently strong coupling. In our experiments with the Min system in flat microchambers, the coupling is inherent to the system and we find both in-phase and anti-phase synchronization. Future theoretical work, using, for instance, a phase-reduction approach [192], might provide further insight into the principles underlying these synchronization phenomena.

7 Design of biochemical pattern forming systems from minimal motifs

This manuscript is reproduced as part of this thesis in Appendix A.7.

Author contributions. All authors conceptualized the study; PG performed the experiments; FB and JH performed numerical simulations and the theoretical analysis; PG and FB wrote the manuscript; JH, EF and PS reviewed the manuscript.

* PG and FB contributed equally to this work.

Abstract

Although molecular self-organization and pattern formation are key features of life, only very few pattern-forming biochemical systems have been identified that can be reconstituted and studied *in vitro* under defined conditions. A systematic understanding of the underlying mechanisms is often hampered by multiple interactions, conformational flexibility and other complex features of the pattern forming proteins. Because of its compositional simplicity of only two proteins and a membrane, the MinDE system from *Escherichia coli* has in the past years been invaluable for deciphering the mechanisms of spatiotemporal self-organization in cells. Here we explored the potential of reducing the complexity of this system even further, by identifying key functional motifs in the effector MinE that could be used to design pattern formation from scratch. In a combined approach of experiment and quantitative modeling, we show that starting from a minimal MinE-MinD interaction motif, pattern formation can be obtained by adding either dimerization or membrane-binding motifs. Moreover, we show that the pathways underlying pattern formation are recruitment-driven cytosolic cycling of MinE and recombination of membrane-bound MinE, and that these differ in their *in vivo* phenomenology.

Background

How do the interactions, conformations and multiple functions of individual biomolecules relate to the emergence of self-organized patterns. Here, we approach this question by combining *in vitro* reconstitution and mathematical modeling of pattern-forming protein networks.

Key results and conclusions

- Using the two-protein Min system from *E. coli* as a base, we replaced MinE with a minimal, 19 amino acid peptide. This peptide alone cannot form patterns with MinD. We recover pattern formation in two biochemically, and importantly also mechanistically, distinct ways, namely by adding either dimerization domain or membrane-binding domain to the peptide. Strikingly, these domains don't need to be the native MinE-domains but can be exchanged for functionally equivalent domains from foreign proteins. Thus, we supply a modular reaction–diffusion platform in which the individual functional domains of a key player can be directly related to the patterns that emerge on the collective level.

- Mathematical modeling shows that membrane binding and dimerization fa-

56

cilitate distinct pathways for pattern formation: recombination of membrane-bound MinE and recruitment-driven cytosolic cycling of MinE, respectively. Importantly, linear stability analysis in elliptic geometry and numerical simulations show that these mechanisms differ in how the protein pattern aligns relative to the geometry of the rod-shaped *E. coli* bacteria. Only with the dimerization domain, the protein pattern is aligned to oscillate from pole-to-pole, which is key for the correct positioning of the cell division machinery.

Modeling approach

To model the synthetic MinE constructs incorporating different functional domains, we extend the minimal Min model to account for MinE membrane binding. To determine the role of these domains for pattern formation, we study the model in the phase diagram of the rate of MinE recruitment to the membrane (a process we hypothesize is enhanced by MinE dimerization) and the MinE membrane affinity (which is enhanced by the membrane-binding domain). This reveals distinct regimes in which different biochemical pathways drive pattern formation.

Outlook

Going forward, the modularity and tunability of the MinDE system open the road towards a modular toolbox for protein-based pattern formation. Close collaboration of experiment and theory will facilitate a design-oriented approach to engineer new proteins with tailored functions, sourcing functional domains from different proteins.

8 Adaptability and evolution of the cell polarization machinery in budding yeast

This manuscript is reproduced as part of this thesis in Appendix A.8.

Preprint reference. F. Brauns, L. M. Iñigo de la Cruz, W. K.-G. Daalman, I. de Bruin, J. Halatek, L. Laan, E. Frey, *Adaptability and evolution of the cell polarization machinery in budding yeast* bioRxiv, doi:10.1101/2020.09.09.290510 (2020)

Author contributions. FB, WKD, JH, LL, and EF conceptualized and designed the study; FB developed the model, performed mathematical analy-

sis, and numerical simulations; LIC, WKG, and IB performed experiments; FB, JH, LL, and EF wrote the manuscript.

Abstract

How can a self-organized cellular function evolve, adapt to perturbations, and acquire new sub-functions? To make progress in answering these basic questions of evolutionary cell biology, we analyze, as a concrete example, the cell polarity machinery of *Saccharomyces cerevisiae*. This cellular module exhibits an intriguing resilience: it remains operational under genetic perturbations and recovers quickly and reproducibly from the deletion of one of its key components. Using a combination of modeling, conceptual theory, and experiments, we show that multiple, redundant self-organization mechanisms coexist within the protein network underlying cell polarization and are responsible for the module's resilience and adaptability. Based on our mechanistic understanding of polarity establishment, we hypothesize how scaffold proteins, by introducing new connections in the existing network, can increase the redundancy of mechanisms and thus increase the evolvability of other network components. Moreover, our work suggests how a complex, redundant cellular module could have evolved from a more rudimental ancestral form.

Background

The two central questions of evolutionary biology are "How do cells work and how did cells come to be the way they are?" [193]. While intracellular pattern formation has been studied extensively, the question of how the underlying protein-reaction networks evolve remains open. The yeast polarization machinery is an ideal model system to tackle that question in a concrete biological context. Recent experiments have shown an intriguing adaptability of the cell polarization machinery in budding yeast against a strong genetic perturbation — the deletion Bem1, a key player of the wild-type polarization mechanism [194]. We provide a mechanistic understanding of the polarization machinery that explains this adaptability and argue that it provides hints for the evolutionary history of the yeast polarity machinery.

Key results and conclusions

- We develop an analyze a model for the cell polarization machinery in budding yeast that accounts for experimentally known interactions of the central

polarity protein Cdc42 with its regulators (GAPs and GEFs), the feedback mediator Bem1, and downstream effectors.

- *Redundant mechanisms for cell polarization.* In addition to the wild-type polarization mechanism, mediated by the scaffold protein Bem1, a latent mechanism is operational in bem1Δ cells below a critical GAP/Cdc42-concentration ratio. This explains why bem1Δ cells are rescued by loss of the GAP Bem3, and how in bem1Δ cells polarization can be induced by optogenetic GEF recruitment. Importantly, while the wild-type mechanism and the latent "rescue" mechanism share many components, the specific roles of these components in the pattern-forming mechanisms, and thus the constraints on them, differ between the two mechanisms.

- We experimentally confirm our theoretical predictions on how cell polarization in bem1Δ mutants and bem1Δ bem3Δ double mutants can be rescued by changing the Cdc42 expression level.

- *Hypothesis on the evolutionary pathway.* The mechanistic understanding of the cell polarization module in wild type and mutant cells, suggests a possible evolutionary scenario for the emergence of this self-organized cellular function. We argue that the redundancy of mechanisms arises due to stepwise evolution from a rudimentary, generic mechanisms to a more complex mechanism that relies on specialized components, here the scaffold protein Bem1. The evolution of this specialized feedback-mediator might have facilitated the duplication and subsequent sub-functionalization of Cdc42-GAPs.

Modeling approach

We combine key elements from several previous models and incorporate experimental evidence about the operation of the Cdc42-GAPs, specifically Bem3. The model accounts in detail for the interactions between Cdc42, Bem1, GEF and the GAPs — the key players in the polarization machinery. In addition, it accounts for additional feedback loops (such as actin-based vesicle trafficking and feedback loops via downstream effectors of Cd42) in a coarse-grained fashion. Key control parameters in the model are the expression levels (average total densities) of the four key players. This allows us to reveal the distinct pattern-forming mechanisms underlying cell polarization and the specific roles of the different proteins in each mechanism.

Choosing parameters was a particular challenge in this study. Out of the ca. 20 model parameters, only the total protein numbers and diffusion constants have been measured, while 13 reaction rates are not experimentally accessible. To systematically study the parameter dependence of the model, we sample 5×10^6 random sets of reaction rates over four orders of magni-

tude in each rate. Using LSA, we identify the sets consistent with qualitative experimental observations (different mutants and experimental conditions). We find that even the most constrained rate covers two orders of magnitude while the majority of rates cover the entire sampled range (four orders of magnitude).

Outlook

- Our hypotheses about the evolution of the polarization machinery can be tested in future work, using, for example, phylogenetic analysis.

- The mechanistic understanding of the polarization machinery can be integrated into cell cycle models and population dynamics models to predict evolutionary trajectories.

9 Other publications

9.1 A hierarchy of protein patterns robustly decodes cell shape information

Abstract. Many cellular processes, such as cell division, cell motility, wound healing and tissue folding, rely on the precise positioning of proteins on the membrane. Such protein patterns emerge from a combination of protein interactions, transport, conformational state changes and chemical reactions at the molecular level. Recent experimental and theoretical work clearly demonstrates the role of geometry, including membrane curvature and local cytosolic-to-membrane ratios, and advective cortical flow in modulating membrane protein patterns. However, it remains unclear how these proteins achieve robust spatiotemporal organization on the membrane during the dynamic cell shape changes involved in physiological processes. Here we use oocytes of the starfish *Patiria miniata* as a model system to elucidate a shape-adaptation mechanism that robustly controls spatiotemporal protein dynamics on the membrane in spite of cell shape deformations. By combining experiments with biophysical theory, we show how cell shape information contained in a cytosolic gradient can be decoded by a bistable regulator of the enzyme Rho, which is associated with contractility. This bistable front in turn controls a mechanochemical response by locally triggering excitable dynamics of Rho. We posit that such a shape-adaptation mechanism based

on a hierarchy of protein patterns may constitute a general physical principle for cell shape sensing and control.

Modeling approach. The main challenge in the model development was the sparse experimental information about the biomolecular interactions of the key players, Cdk1, Ect2, and Rho. In fact, it is likely that a number of additional interaction partners and regulators play a role that have not been identified in experiments yet. We therefore base our model on considerations about the dynamical features (Ect2 bistability and Rho excitability) that can explain the observed phenomena. These dynamical features are implemented in minimal models that are consistent with the known biochemical interactions and minimal additional assumptions.

9.2 Capping protein-controlled actin polymerization shapes lipid membranes

Journal reference. K. Dürre, F. C. Keber, P. Bleicher, F. Brauns, C. J. Cyron, J. Faix, and A. R. Bausch, *Capping protein-controlled actin polymerization shapes lipid membranes.* Nature Communications 9, 1630 (2018)

Abstract. Arp2/3 complex-mediated actin assembly at cell membranes drives the formation of protrusions or endocytic vesicles. To identify the mechanism by which different membrane deformations can be achieved, we reconstitute the basic membrane deformation modes of inward and outward bending in a confined geometry by encapsulating a minimal set of cytoskeletal proteins into giant unilamellar vesicles. Formation of membrane protrusions is favored at low capping protein (CP) concentrations, whereas the formation of negatively bent domains is promoted at high CP concentrations. Addition of non-muscle myosin II results in full fission events in the vesicle system. The different deformation modes are rationalized by simulations of the underlying transient nature of the reaction kinetics. The relevance of the regulatory mechanism is supported by CP overexpression in mouse melanoma B16-F1 cells and therefore demonstrates the importance of the quantitative understanding of microscopic kinetic balances to address the diverse functionality of the cytoskeleton.

9.3 Review: Self-organization principles of intracellular pattern formation

Journal reference. J. Halatek, F. Brauns, and E. Frey, *Self-organization principles of intracellular pattern formation.* Phil. Trans. R. Soc. B 373, 20170107 (2018).

Abstract. Dynamic patterning of specific proteins is essential for the spatio-temporal regulation of many important intracellular processes in prokaryotes, eukaryotes and multicellular organisms. The emergence of patterns generated by interactions of diffusing proteins is a paradigmatic example for self-organization. In this article, we review quantitative models for intracellular Min protein patterns in *Escherichia coli*, Cdc42 polarization in *Saccharomyces cerevisiae* and the bipolar PAR protein patterns found in *Caenorhabditis elegans*. By analysing the molecular processes driving these systems we derive a theoretical perspective on general principles underlying self-organized pattern formation. We argue that intracellular pattern formation is not captured by concepts such as 'activators', 'inhibitors' or 'substrate depletion'. Instead, intracellular pattern formation is based on the redistribution of proteins by cytosolic diffusion, and the cycling of proteins between distinct conformational states. Therefore, mass-conserving reaction–diffusion equations provide the most appropriate framework to study intracellular pattern formation. We conclude that directed transport, e.g. cytosolic diffusion along an actively maintained cytosolic gradient, is the key process underlying pattern formation. Thus, the basic principle of self-organization is the establishment and maintenance of directed transport by intracellular protein dynamics.

9.4 Book chapter: Self-organization of protein patterns

These notes are an account of a series of lectures given at the Les Houches Summer School "Active Matter and Non-equilibrium Statistical Physics" during August and September 2018.

Bibliography

[1] B. Alberts, editor. *Molecular Biology of the Cell*. Garland Science, New York, 5th ed edition, 2008. ISBN 978-0-8153-4105-5 978-0-8153-4106-2.

[2] D. A. Fletcher and R. D. Mullins. Cell mechanics and the cytoskeleton. *Nature*, 463(7280):485–492, 2010. doi:10.1038/nature08908.

[3] S. F. Banani, H. O. Lee, A. A. Hyman, and M. K. Rosen. Biomolecular condensates: Organizers of cellular biochemistry. *Nature Reviews Molecular Cell Biology*, 18(5):285–298, 2017. doi:10.1038/nrm.2017.7.

[4] J. Halatek, F. Brauns, and E. Frey. Self-organization principles of intracellular pattern formation. *Philosophical Transactions of the Royal Society B: Biological Sciences*, 373(1747):20170107, 2018. doi:10.1098/rstb.2017.0107.

[5] E. Bi and H.-O. Park. Cell Polarization and Cytokinesis in Budding Yeast. *Genetics*, 191(2):347–387, 2012. doi:10.1534/genetics.111.132886.

[6] A. J. Ridley, M. A. Schwartz, K. Burridge, R. A. Firtel, M. H. Ginsberg, G. Borisy, J. T. Parsons, and A. R. Horwitz. Cell Migration: Integrating Signals from Front to Back. *Science*, 302(5651):1704–1709, 2003. doi:10.1126/science.1092053.

[7] D. Schumacher and L. Søgaard-Andersen. Regulation of Cell Polarity in Motility and Cell Division in Myxococcus xanthus. *Annual Review of Microbiology*, 71(1):61–78, 2017. doi:10.1146/annurev-micro-102215-095415.

[8] M. N. Rasband. The axon initial segment and the maintenance of neuronal polarity. *Nature Reviews Neuroscience*, 11(8):552–562, 2010. doi:10.1038/nrn2852.

[9] J. Wu and M. Mlodzik. A quest for the mechanism regulating global planar cell polarity of tissues. *Trends in Cell Biology*, 19(7):295–305, 2009. doi:10.1016/j.tcb.2009.04.003.

[10] D. St Johnston and J. Ahringer. Cell Polarity in Eggs and Epithelia: Parallels and Diversity. *Cell*, 141(5):757–774, 2010. doi:10.1016/j.cell.2010.05.011.

[11] S. Iden and J. G. Collard. Crosstalk between small GTPases and polarity proteins in cell polarization. *Nature Reviews Molecular Cell Biology*, 9 (11):846–859, 2008. doi:10.1038/nrm2521.

[12] A. B. Goryachev and M. Leda. Many roads to symmetry breaking: Molecular mechanisms and theoretical models of yeast cell polarity. *Molecular Biology of the Cell*, 28(3):370–380, 2017. doi:10.1091/mbc.e16-10-0739.

[13] M. Loose, E. Fischer-Friedrich, J. Ries, K. Kruse, and P. Schwille. Spatial Regulators for Bacterial Cell Division Self-Organize into Surface Waves in Vitro. *Science*, 320(5877):789–792, 2008. doi:10.1126/science.1154413.

[14] V. Ivanov and K. Mizuuchi. Multiple modes of interconverting dynamic pattern formation by bacterial cell division proteins. *Proceedings of the National Academy of Sciences*, 107(18):8071–8078, 2010. doi:10.1073/pnas.0911036107.

[15] A. G. Vecchiarelli, M. Li, M. Mizuuchi, L. C. Hwang, Y. Seol, K. C. Neuman, and K. Mizuuchi. Membrane-bound MinDE complex acts as a toggle switch that drives Min oscillation coupled to cytoplasmic depletion of MinD. *Proceedings of the National Academy of Sciences*, 113 (11):E1479–E1488, 2016. doi:10.1073/pnas.1600644113.

[16] J. Denk, S. Kretschmer, J. Halatek, C. Hartl, P. Schwille, and E. Frey. MinE conformational switching confers robustness on self-organized Min protein patterns. *Proceedings of the National Academy of Sciences*, 115(18):4553–4558, 2018. doi:10.1073/pnas.1719801115.

[17] P. Glock, F. Brauns, J. Halatek, E. Frey, and P. Schwille. Design of biochemical pattern forming systems from minimal motifs. *eLife*, 8:e48646, 2019. doi:10.7554/eLife.48646.

[18] T. Litschel, B. Ramm, R. Maas, M. Heymann, and P. Schwille. Beating Vesicles: Encapsulated Protein Oscillations Cause Dynamic Membrane Deformations. *Angewandte Chemie International Edition*, 57(50): 16286–16290, 2018. doi:10.1002/anie.201808750.

[19] E. Godino, J. N. López, D. Foschepoth, C. Cleij, A. Doerr, C. F. Castellà, and C. Danelon. De novo synthesized Min proteins drive oscillatory liposome deformation and regulate FtsA-FtsZ cytoskeletal patterns. *Nature Communications*, 10(1):4969, 2019. doi:10.1038/s41467-019-12932-w.

[20] S. Kohyama, N. Yoshinaga, M. Yanagisawa, K. Fujiwara, and N. Doi. Cell-sized confinement controls generation and stability of a protein

wave for spatiotemporal regulation in cells. *eLife*, 8:e44591, 2019. doi:10.7554/eLife.44591.

[21] P. Glock, B. Ramm, T. Heermann, S. Kretschmer, J. Schweizer, J. Mücksch, G. Alagöz, and P. Schwille. Stationary Patterns in a Two-Protein Reaction-Diffusion System. *ACS Synthetic Biology*, 8(1):148–157, 2019. doi:10.1021/acssynbio.8b00415.

[22] E. Bernitt, H.-G. Döbereiner, N. S. Gov, and A. Yochelis. Fronts and waves of actin polymerization in a bistability-based mechanism of circular dorsal ruffles. *Nature Communications*, 8(1):15863, 2017. doi:10.1038/ncomms15863.

[23] N. Inagaki and H. Katsuno. Actin Waves: Origin of Cell Polarization and Migration? *Trends in Cell Biology*, 27(7):515–526, 2017. doi:10.1016/j.tcb.2017.02.003.

[24] J. B. Michaux, F. B. Robin, W. M. McFadden, and E. M. Munro. Excitable RhoA dynamics drive pulsed contractions in the early *C. elegans* embryo. *The Journal of Cell Biology*, 217(12):4230–4252, 2018. doi:10.1083/jcb.201806161.

[25] W. M. Bement, M. Leda, A. M. Moe, A. M. Kita, M. E. Larson, A. E. Golding, C. Pfeuti, K.-C. Su, A. L. Miller, A. B. Goryachev, and G. von Dassow. Activator–inhibitor coupling between Rho signalling and actin assembly makes the cell cortex an excitable medium. *Nature Cell Biology*, 17(11):1471–1483, 2015. doi:10.1038/ncb3251.

[26] T. H. Tan, J. Liu, P. W. Miller, M. Tekant, J. Dunkel, and N. Fakhri. Topological turbulence in the membrane of a living cell. *Nature Physics*, 16(6):657–662, 2020. doi:10.1038/s41567-020-0841-9.

[27] J. Landino, M. Leda, A. Michaud, Z. Swider, M. Prom, C. M. Field, W. M. Bement, A. G. Vecchiarelli, A. B. Goryachev, and A. L. Miller. Rho and F-actin self-organize within an artificial cell cortex. *bioRxiv*, page doi:10.1101/2021.04.09.438460, 2021. doi:10.1101/2021.04.09.438460.

[28] F. Brauns, L. M. Iñigo de la Cruz, W. K.-G. Daalman, I. de Bruin, J. Halatek, L. Laan, and E. Frey. Adaptability and evolution of the cell polarization machinery in budding yeast. *bioRxiv*, page doi:10.1101/2020.09.09.290510, 2020. doi:10.1101/2020.09.09.290510.

[29] M. Shamir, Y. Bar-On, R. Phillips, and R. Milo. SnapShot: Timescales in Cell Biology. *Cell*, 164(6):1302–1302.e1, 2016. doi:10.1016/j.cell.2016.02.058.

[30] F. Brauns, H. Weyer, J. Halatek, J. Yoon, and E. Frey. Wavelength Selection by Interrupted Coarsening in Reaction-Diffusion Systems. *Physical Review Letters*, 126(10):104101, 2021. doi:10.1103/PhysRevLett.126.104101.

[31] A. Wittinghofer, editor. *Ras Superfamily Small G Proteins: Biology and Mechanisms 1: General Features, Signaling*. Springer Vienna : Imprint: Springer, Vienna, 1st ed. 2014 edition, 2014. ISBN 978-3-7091-1806-1. doi:10.1007/978-3-7091-1806-1.

[32] A. Wittinghofer, editor. *Ras Superfamily Small g Proteins: Biology and Mechanisms. 2: Transport*. Springer, Cham, 2014. ISBN 978-3-319-07761-1 978-3-319-07760-4.

[33] D. Fisher, L. Krasinska, D. Coudreuse, and B. Novák. Phosphorylation network dynamics in the control of cell cycle transitions. *Journal of Cell Science*, 125(20):4703–4711, 2012. doi:10.1242/jcs.106351.

[34] B. N. Kholodenko. Cell-signalling dynamics in time and space. *Nature Reviews Molecular Cell Biology*, 7(3):165–176, 2006. doi:10.1038/nrm1838.

[35] F. Brauns, G. Pawlik, J. Halatek, J. Kerssemakers, E. Frey, and C. Dekker. Bulk-surface coupling identifies the mechanistic connection between Min-protein patterns in vivo and in vitro. *Nature Communications*, 12(1):3312, 2021. doi:10.1038/s41467-021-23412-5.

[36] T. W. Traut. Physiological concentrations of purines and pyrimidines. *Molecular and Cellular Biochemistry*, 140(1):1–22, 1994. doi:10.1007/BF00928361.

[37] R. E. Goldstein and J.-W. van de Meent. A physical perspective on cytoplasmic streaming. *Interface Focus*, 5(4):20150030, 2015. doi:10.1098/rsfs.2015.0030.

[38] N. W. Goehring, P. K. Trong, J. S. Bois, D. Chowdhury, E. M. Nicola, A. A. Hyman, and S. W. Grill. Polarization of PAR Proteins by Advective Triggering of a Pattern-Forming System. *Science*, 334(6059):1137–1141, 2011. doi:10.1126/science.1208619.

[39] P. Gross, K. V. Kumar, N. W. Goehring, J. S. Bois, C. Hoege, F. Jülicher, and S. W. Grill. Guiding self-organized pattern formation in cell polarity establishment. *Nature Physics*, 15(3):293–300, 2019. doi:10.1038/s41567-018-0358-7.

[40] B. P. Belousov. Periodically acting reaction and its mechanism. In *Collection of Short Papers on Radiation Medicine for 1958*, volume "", page 145. Moscow, 1959.

[41] A. M. Zhabotinsky. Periodical oxidation of malonic acid in solution (a study of the Belousov reaction kinetics). *Biofizika*, 9:306–311, 1964.

[42] R. J. Field and M. Burger, editors. *Oscillations and Traveling Waves in Chemical Systems*. Wiley, New York, 1985. ISBN 978-0-471-89384-4.

[43] R. J. Field, E. Koros, and R. M. Noyes. Oscillations in chemical systems. II. Thorough analysis of temporal oscillation in the bromate-cerium-malonic acid system. *Journal of the American Chemical Society*, 94(25): 8649–8664, 1972. doi:10.1021/ja00780a001.

[44] J. J. Tyson. Scaling and reducing the Field-Koros-Noyes mechanism of the Belousov-Zhabotinskii reaction. *The Journal of Physical Chemistry*, 86(15):3006–3012, 1982. doi:10.1021/j100212a039.

[45] D. Axelrod, D. E. Koppel, J. Schlessinger, E. Elson, and W. W. Webb. Mobility measurement by analysis of fluorescence photobleaching recovery kinetics. *Biophysical Journal*, 16(9):1055–1069, 1976.

[46] E. L. Elson and D. Magde. Fluorescence correlation spectroscopy. I. Conceptual basis and theory. *Biopolymers*, 13(1):1–27, 1974. doi:10.1002/bip.1974.360130102.

[47] M. K. Transtrum, B. B. Machta, and J. P. Sethna. Why are Nonlinear Fits to Data so Challenging? *Physical Review Letters*, 104(6):060201, 2010. doi:10.1103/PhysRevLett.104.060201.

[48] M. K. Transtrum and P. Qiu. Model Reduction by Manifold Boundaries. *Physical Review Letters*, 113(9):098701, 2014. doi:10.1103/PhysRevLett.113.098701.

[49] M. K. Transtrum, B. B. Machta, K. S. Brown, B. C. Daniels, C. R. Myers, and J. P. Sethna. Perspective: Sloppiness and emergent theories in physics, biology, and beyond. *The Journal of Chemical Physics*, 143(1): 010901, 2015. doi:10.1063/1.4923066.

[50] A. M. Turing. The chemical basis of morphogenesis. *Philosophical Transactions of the Royal Society of London. Series B, Biological Sciences*, 237(641):37–72, 1952. doi:10.1098/rstb.1952.0012.

[51] J. H. Dawes. After 1952: The later development of Alan Turing's ideas on the mathematics of pattern formation. *Historia Mathematica*, 43(1): 49–64, 2016. doi:10.1016/j.hm.2015.03.003.

[52] L. A. Segel and J. L. Jackson. Dissipative structure: An explanation and an ecological example. *Journal of Theoretical Biology*, 37(3):545–559, 1972. doi:10.1016/0022-5193(72)90090-2.

[53] A. Gierer and H. Meinhardt. A theory of biological pattern formation. *Kybernetik*, 12(1):30–39, 1972. doi:10.1007/BF00289234.

[54] N. F. Britton. Spatial Structures and Periodic Travelling Waves in an Integro-Differential Reaction-Diffusion Population Model. *SIAM Journal on Applied Mathematics*, 50(6):1663–1688, 1990. doi:10.1137/0150099.

[55] S. Gourley. Travelling front solutions of a nonlocal Fisher equation. *Journal of Mathematical Biology*, 41(3):272–284, 2000. doi:10.1007/s002850000047.

[56] F. Brauns, J. Halatek, and E. Frey. Diffusive coupling of two well-mixed compartments elucidates elementary principles of protein-based pattern formation. *Physical Review Research*, 3(1):013258, 2021. doi:10.1103/PhysRevResearch.3.013258.

[57] F. Brauns, J. Halatek, and E. Frey. Phase-Space Geometry of Mass-Conserving Reaction-Diffusion Dynamics. *Physical Review X*, 10(4): 041036, 2020. doi:10.1103/PhysRevX.10.041036.

[58] V. Castets, E. Dulos, J. Boissonade, and P. De Kepper. Experimental evidence of a sustained standing Turing-type nonequilibrium chemical pattern. *Physical Review Letters*, 64(24):2953–2956, 1990. doi:10.1103/PhysRevLett.64.2953.

[59] P. K. Maini, T. E. Woolley, R. E. Baker, E. A. Gaffney, and S. S. Lee. Turing's model for biological pattern formation and the robustness problem. *Interface Focus*, 2(4):487–496, 2012. doi:10.1098/rsfs.2011.0113.

[60] N. S. Scholes, D. Schnoerr, M. Isalan, and M. P. Stumpf. A Comprehensive Network Atlas Reveals That Turing Patterns Are Common but Not Robust. *Cell Systems*, 9(5):515–517, 2019. doi:10.1016/j.cels.2019.09.010.

[61] P. A. Haas and R. E. Goldstein. Turing's diffusive threshold in random reaction-diffusion systems. *arXiv:2011.04614 [cond-mat, physics:nlin, q-bio]*, 2020.

[62] T. Biancalani, F. Jafarpour, and N. Goldenfeld. Giant Amplification of Noise in Fluctuation-Induced Pattern Formation. *Physical Review Letters*, 118(1):018101, 2017. doi:10.1103/PhysRevLett.118.018101.

[63] D. Karig, K. M. Martini, T. Lu, N. A. DeLateur, N. Goldenfeld, and R. Weiss. Stochastic Turing patterns in a synthetic bacterial population. *Proceedings of the National Academy of Sciences*, 115(26):6572–6577, 2018. doi:10.1073/pnas.1720770115.

[64] A. Ehrmann, B. Nguyen, and U. Seifert. Interlinked GTPase cascades provide a motif for both robust switches and oscillators. *Journal of The Royal Society Interface*, 16(157):20190198, 2019. doi:10.1098/rsif.2019.0198.

[65] G. Giunta, H. Seyed-Allaei, and U. Gerland. Cross-diffusion induced patterns for a single-step enzymatic reaction. *Communications Physics*, 3(1):167, 2020. doi:10.1038/s42005-020-00427-w.

[66] V. K. Vanag and I. R. Epstein. Cross-diffusion and pattern formation in reaction–diffusion systems. *Phys. Chem. Chem. Phys.*, 11(6):897–912, 2009. doi:10.1039/B813825G.

[67] D. Bullara and Y. De Decker. Pigment cell movement is not required for generation of Turing patterns in zebrafish skin. *Nature Communications*, 6(1):6971, 2015. doi:10.1038/ncomms7971.

[68] A. S. Mikhailov. *Foundations of Synergetics I: Distributed Active Systems*. Springer Berlin Heidelberg, Berlin, Heidelberg, 1990. ISBN 978-3-642-97269-0 978-3-642-78556-6 978-3-642-78558-0.

[69] L. Gelens, G. A. Anderson, and J. E. Ferrell. Spatial trigger waves: Positive feedback gets you a long way. *Molecular Biology of the Cell*, 25 (22):3486–3493, 2014. doi:10.1091/mbc.e14-08-1306.

[70] J. B. Chang and J. E. Ferrell Jr. Mitotic trigger waves and the spatial coordination of the Xenopus cell cycle. *Nature*, 500(7464):603–607, 2013. doi:10.1038/nature12321.

[71] X. Cheng and J. E. Ferrell. Apoptosis propagates through the cytoplasm as trigger waves. *Science*, 361(6402):607–612, 2018. doi:10.1126/science.aah4065.

[72] J. J. Tyson and J. P. Keener. Singular perturbation theory of traveling waves in excitable media (a review). *Physica D: Nonlinear Phenomena*, 32(3):327–361, 1988. doi:10.1016/0167-2789(88)90062-0.

[73] V. Osipov. Criteria of spontaneous interconversions of traveling and static arbitrary dimensional dissipative structures. *Physica D: Nonlinear Phenomena*, 93(3-4):143–156, 1996. doi:10.1016/0167-2789(95)00296-0.

[74] M. C. Cross and P. C. Hohenberg. Pattern formation outside of equilibrium. *Reviews of Modern Physics*, 65(3):851–1112, 1993. doi:10.1103/RevModPhys.65.851.

[75] P. Coullet, L. Gil, and J. Lega. Defect-mediated turbulence. *Physical Review Letters*, 62(14):1619–1622, 1989. doi:10.1103/PhysRevLett.62.1619.

[76] R. FitzHugh. Impulses and Physiological States in Theoretical Models of Nerve Membrane. *Biophysical Journal*, 1(6):445–466, 1961. doi:10.1016/S0006-3495(61)86902-6.

[77] J. Nagumo, S. Arimoto, and S. Yoshizawa. An Active Pulse Transmission Line Simulating Nerve Axon. *Proceedings of the IRE*, 50(10):2061–2070, 1962. doi:10.1109/JRPROC.1962.288235.

[78] S. Jakubith, H. H. Rotermund, W. Engel, A. von Oertzen, and G. Ertl. Spatiotemporal concentration patterns in a surface reaction: Propagating and standing waves, rotating spirals, and turbulence. *Physical Review Letters*, 65(24):3013–3016, 1990. doi:10.1103/PhysRevLett.65.3013.

[79] M. Kim, M. Bertram, M. Pollmann, A. von Oertzen, A. S. Mikhailov, H. H. Rotermund, and G. Ertl. Controlling Chemical Turbulence by Global Delayed Feedback: Pattern Formation in Catalytic CO Oxidation on Pt(110). *Science*, 292(5520):1357–1360, 2001. doi:10.1126/science.1059478.

[80] R. M. Eiswirth, K. Krischer, and G. Ertl. Nonlinear dynamics in the CO-oxidation on Pt single crystal surfaces. *Applied Physics A Solids and Surfaces*, 51(2):79–90, 1990. doi:10.1007/BF00324269.

[81] A. S. Mikhailov and K. Showalter. Control of waves, patterns and turbulence in chemical systems. *Physics Reports*, 425(2-3):79–194, 2006. doi:10.1016/j.physrep.2005.11.003.

[82] G. Ertl. Non-Linear Dynamics: Oscillatory Kinetics and Spatio-Temporal Pattern Formation. In G. Ertl, H. Knözinger, F. Schüth, and J. Weitkamp, editors, *Handbook of Heterogeneous Catalysis*, page hetcat0080. Wiley-VCH Verlag GmbH & Co. KGaA, Weinheim, Germany, 2008. ISBN 978-3-527-31241-2 978-3-527-61004-4. doi:10.1002/9783527610044.hetcat0080.

[83] S. Strogatz. *Sync: The Emerging Science of Spantaneous Order*. Penguin Books, London, 2004. ISBN 978-0-14-100763-2.

[84] S. Sawai, P. A. Thomason, and E. C. Cox. An autoregulatory circuit for long-range self-organization in Dictyostelium cell populations. *Nature*, 433(7023):323–326, 2005. doi:10.1038/nature03228.

[85] A. T. Winfree. *When Time Breaks down: The Three-Dimensional Dynamics of Electrochemical Waves and Cardiac Arrhythmias*. Princeton University Press, Princeton, N.J, 1987. ISBN 978-0-691-08443-5 978-0-691-02402-8.

[86] F. Varela, J.-P. Lachaux, E. Rodriguez, and J. Martinerie. The brainweb: Phase synchronization and large-scale integration. *Nature Reviews Neuroscience*, 2(4):229–239, 2001. doi:10.1038/35067550.

[87] A. E. Motter, S. A. Myers, M. Anghel, and T. Nishikawa. Spontaneous synchrony in power-grid networks. *Nature Physics*, 9(3):191–197, 2013. doi:10.1038/nphys2535.

[88] M. Rohden, A. Sorge, M. Timme, and D. Witthaut. Self-Organized Synchronization in Decentralized Power Grids. *Physical Review Letters*, 109(6):064101, 2012. doi:10.1103/PhysRevLett.109.064101.

[89] S. H. Strogatz. *Nonlinear Dynamics and Chaos*. CRC Press, Boca Raton, second edition, 2015.

[90] E. M. Izhikevich. *Dynamical Systems in Neuroscience: The Geometry of Excitability and Bursting*. Computational Neuroscience. MIT Press, Cambridge, Mass, 2007. ISBN 978-0-262-09043-8.

[91] J. D. Murray. *Mathematical Biology: I. An Introduction*, volume 17 of *Interdisciplinary Applied Mathematics*. Springer New York, New York, NY, 2002. ISBN 978-0-387-95223-9 978-0-387-22437-4. doi:10.1007/b98868.

[92] E. A. Jackson. *Perspectives of Nonlinear Dynamics*. Cambridge University Press, Cambridge, first edition, 1989. ISBN 978-0-521-34504-0 978-0-521-42632-9 978-0-511-62397-4. doi:10.1017/CBO9780511623974.

[93] H. Poincaré. *Les Méthodes Nouvelles de La Mécanique Céleste*, volume 1–3. Gauthiers-Villars, Paris, 1892, 1893, 1899.

[94] E. M. Izhikevich. Neural excitability, spiking and bursting. *International Journal of Bifurcation and Chaos*, 10(06):1171–1266, 2000. doi:10.1142/S0218127400000840.

[95] B. Novák and J. J. Tyson. Design principles of biochemical oscillators. *Nature Reviews Molecular Cell Biology*, 9(12):981–991, 2008. doi:10.1038/nrm2530.

[96] J. Guckenheimer and P. Holmes. *Nonlinear Oscillations, Dynamical Systems, and Bifurcations of Vector Fields*, volume 42 of *Applied Mathematical Sciences*. Springer New York, New York, NY, 1983. ISBN 978-1-4612-7020-1 978-1-4612-1140-2. doi:10.1007/978-1-4612-1140-2.

[97] S. Wiggins. *Introduction to Applied Nonlinear Dynamical Systems and Chaos*. Number 2 in Texts in Applied Mathematics. Springer, New York, 2nd ed edition, 2003. ISBN 978-0-387-00177-7.

[98] J. Halatek and E. Frey. Highly Canalized MinD Transfer and MinE Sequestration Explain the Origin of Robust MinCDE-Protein Dynamics. *Cell Reports*, 1(6):741–752, 2012. doi:10.1016/j.celrep.2012.04.005.

[99] P. C. Matthews and S. M. Cox. Pattern formation with a conservation law. *Nonlinearity*, 13(4):1293–1320, 2000. doi:10.1088/0951-7715/13/4/317.

[100] L. S. Tsimring and I. S. Aranson. Localized and Cellular Patterns in a Vibrated Granular Layer. *Physical Review Letters*, 79(2):213–216, 1997. doi:10.1103/PhysRevLett.79.213.

[101] H. Riecke. Localized Structures In Pattern-Forming Systems. In W. Miller, M. Golubitsky, D. Luss, and S. H. Strogatz, editors, *Pattern Formation in Continuous and Coupled Systems*, volume 115, pages 215–229. Springer New York, New York, NY, 1999. ISBN 978-1-4612-7192-5 978-1-4612-1558-5. doi:10.1007/978-1-4612-1558-5_17.

[102] D. M. Winterbottom, S. M. Cox, and P. C. Matthews. Pattern Formation in a Model of a Vibrated Granular Layer. *SIAM Journal on Applied Dynamical Systems*, 7(1):63–78, 2008. doi:10.1137/06067540X.

[103] J. H. P. Dawes. Localized Pattern Formation with a Large-Scale Mode: Slanted Snaking. *SIAM Journal on Applied Dynamical Systems*, 7(1):186–206, 2008. doi:10.1137/06067794X.

[104] E. Knobloch. Localized structures and front propagation in systems with a conservation law. *IMA Journal of Applied Mathematics*, 81(3):457–487, 2016. doi:10.1093/imamat/hxw029.

[105] M. I. Tribelsky and K. Tsuboi. New Scenario for Transition to Turbulence? *Physical Review Letters*, 76(10):1631–1634, 1996. doi:10.1103/PhysRevLett.76.1631.

[106] P. C. Matthews and S. M. Cox. One-dimensional pattern formation with Galilean invariance near a stationary bifurcation. *Physical Review E*, 62(2):R1473–R1476, 2000. doi:10.1103/PhysRevE.62.R1473.

[107] B. Shraiman, A. Pumir, W. van Saarloos, P. Hohenberg, H. Chaté, and M. Holen. Spatiotemporal chaos in the one-dimensional complex Ginzburg-Landau equation. *Physica D: Nonlinear Phenomena*, 57(3-4):241–248, 1992. doi:10.1016/0167-2789(92)90001-4.

[108] J. Halatek and E. Frey. Rethinking pattern formation in reaction–diffusion systems. *Nature Physics*, 14(5):507, 2018. doi:10.1038/s41567-017-0040-5.

[109] C. Kuehn. *PDE Dynamics: An Introduction*. Number 23 in Mathematical Modeling and Computation. Society for Industrial and Applied Mathematics, Philadelphia, 2019. ISBN 978-1-61197-566-6.

[110] R. A. Fisher. The Wave of Advance of Advantageous Genes. *Annals of Eugenics*, 7:355–369, 1937.

[111] A. N. Kolmogorov, I. G. Petrovskii, and N. S. Piscounov. étude de l'équation de la diffusion avec croissance de la quantité de matiére et son application a un probléme biologique. *Moscou Univ. Bull. Math.*, 1: 1–25, 1937.

[112] D. S. Jones, M. J. Plank, and B. D. Sleeman. *Differential Equations and Mathematical Biology*. Chapman & Hall/CRC Mathematical and Computational Biology Series. Chapman & Hall/CRC, Boca Raton, FL, 2nd ed edition, 2010. ISBN 978-1-4200-8357-6.

[113] W. van Saarloos and P. C. Hohenberg. Fronts, pulses, sources and sinks in generalized complex Ginzburg-Landau equations. *Physica D: Nonlinear Phenomena*, 56(4):303–367, 1992. doi:10.1016/0167-2789(92)90175-M.

[114] D. Barkley. Euclidean symmetry and the dynamics of rotating spiral waves. *Physical Review Letters*, 72(1):164–167, 1994. doi:10.1103/PhysRevLett.72.164.

[115] B. Sandstede and A. Scheel. Defects in Oscillatory Media: Toward a Classification. *SIAM Journal on Applied Dynamical Systems*, 3(1):1–68, 2004. doi:10.1137/030600192.

[116] F. Vafa, M. J. Bowick, M. C. Marchetti, and B. I. Shraiman. Multidefect Dynamics in Active Nematics. *arXiv:2007.02947 [cond-mat, physics:physics]*, 2020.

[117] G. Berkooz, P. Holmes, and J. L. Lumley. The Proper Orthogonal Decomposition in the Analysis of Turbulent Flows. *Annual Review of Fluid Mechanics*, 25(1):539–575, 1993. doi:10.1146/annurev.fl.25.010193.002543.

[118] P. J. Schmid. Dynamic mode decomposition of numerical and experimental data. *Journal of Fluid Mechanics*, 656:5–28, 2010. doi:10.1017/S0022112010001217.

[119] A. Rupe and J. P. Crutchfield. Spacetime Autoencoders Using Local Causal States. *arXiv:2010.05451 [nlin, physics:physics]*, 2020.

[120] E. Frey and F. Brauns. Self-organisation of Protein Patterns. *arXiv:2012.01797 [nlin, physics:physics]*, 2020.

[121] A. B. Goryachev and M. Leda. Compete or Coexist? Why the Same Mechanisms of Symmetry Breaking Can Yield Distinct Outcomes. *Cells*, 9(9):2011, 2020. doi:10.3390/cells9092011.

[122] M. C. Wigbers, F. Brauns, T. Hermann, and E. Frey. Pattern localization to a domain edge. *Physical Review E*, 101(2):022414, 2020. doi:10.1103/PhysRevE.101.022414.

[123] M. C. Wigbers, F. Brauns, C. Y. Leung, and E. Frey. Flow Induced Symmetry Breaking in a Conceptual Polarity Model. *Cells*, 9(6):1524, 2020. doi:10.3390/cells9061524.

[124] K. C. Huang, Y. Meir, and N. S. Wingreen. Dynamic structures in Escherichia coli: Spontaneous formation of MinE rings and MinD polar zones. *Proceedings of the National Academy of Sciences*, 100(22):12724–12728, 2003. doi:10.1073/pnas.2135445100.

[125] B. Klünder, T. Freisinger, R. Wedlich-Söldner, and E. Frey. GDI-Mediated Cell Polarization in Yeast Provides Precise Spatial and Temporal Control of Cdc42 Signaling. *PLOS Computational Biology*, 9(12): e1003396, 2013. doi:10.1371/journal.pcbi.1003396.

[126] M. C. Wigbers, T. H. Tan, F. Brauns, J. Liu, S. Z. Swartz, E. Frey, and N. Fakhri. A hierarchy of protein patterns robustly decodes cell shape information. *Nature Physics*, pages 1–7, 2021. doi:10.1038/s41567-021-01164-9.

[127] I. Lifshitz and V. Slyozov. The kinetics of precipitation from supersaturated solid solutions. *Journal of Physics and Chemistry of Solids*, 19(1-2): 35–50, 1961. doi:10.1016/0022-3697(61)90054-3.

[128] C. Wagner. Theorie der Alterung von Niederschlägen durch Umlösen (Ostwald-Reifung). *Zeitschrift für Elektrochemie*, 65(7):581–591, 1961. doi:10.1002/bbpc.19610650704.

[129] M. E. Cates and J. Tailleur. Motility-Induced Phase Separation. *Annual Review of Condensed Matter Physics*, 6(1):219–244, 2015. doi:10.1146/annurev-conmatphys-031214-014710.

[130] A. I. Curatolo, N. Zhou, Y. Zhao, C. Liu, A. Daerr, J. Tailleur, and J. Huang. Cooperative pattern formation in multi-component bacterial systems through reciprocal motility regulation. *Nature Physics*, 16(11):1152–1157, 2020. doi:10.1038/s41567-020-0964-z.

[131] I. Müller and P. Strehlow. *Rubber and Rubber Balloons: Paradigms of Thermodynamics*. Lecture Notes in Physics. Springer-Verlag, Berlin Heidelberg, 2004. ISBN 978-3-540-20244-8. doi:10.1007/b93853.

[132] S. H. Strogatz. From Kuramoto to Crawford: Exploring the onset of synchronization in populations of coupled oscillators. *Physica D: Nonlinear Phenomena*, 143(1-4):1–20, 2000. doi:10.1016/S0167-2789(00)00094-4.

[133] J. E. Ferrell, T. Y.-C. Tsai, and Q. Yang. Modeling the Cell Cycle: Why Do Certain Circuits Oscillate? *Cell*, 144(6):874–885, 2011. doi:10.1016/j.cell.2011.03.006.

[134] Y. Mori, A. Jilkine, and L. Edelstein-Keshet. Wave-Pinning and Cell Polarity from a Bistable Reaction-Diffusion System. *Biophysical Journal*, 94(9):3684–3697, 2008. doi:10.1529/biophysj.107.120824.

[135] W. R. Holmes, M. A. Mata, and L. Edelstein-Keshet. Local Perturbation Analysis: A Computational Tool for Biophysical Reaction-Diffusion Models. *Biophysical Journal*, 108(2):230–236, 2015. doi:10.1016/j.bpj.2014.11.3457.

[136] R. Diegmiller, H. Montanelli, C. B. Muratov, and S. Y. Shvartsman. Spherical Caps in Cell Polarization. *Biophysical Journal*, 115(1):26–30, 2018. doi:10.1016/j.bpj.2018.05.033.

[137] B. Xu and A. Jilkine. Modeling the Dynamics of Cdc42 Oscillation in Fission Yeast. *Biophysical Journal*, 114(3):711–722, 2018. doi:10.1016/j.bpj.2017.12.007.

[138] M. Guzzo, S. M. Murray, E. Martineau, S. Lhospice, G. Baronian, L. My, Y. Zhang, L. Espinosa, R. Vincentelli, B. P. Bratton, J. W. Shaevitz, V. Molle, M. Howard, and T. Mignot. A gated relaxation oscillator mediated by FrzX controls morphogenetic movements in Myxococcus xanthus. *Nature Microbiology*, 3(8):948–959, 2018. doi:10.1038/s41564-018-0203-x.

[139] F. Tostevin, M. Wigbers, L. Søgaard-Andersen, and U. Gerland. Four different mechanisms for switching cell polarity. *PLOS Computational Biology*, 17(1):e1008587, 2021. doi:10.1371/journal.pcbi.1008587.

[140] L. Edelstein-Keshet, W. R. Holmes, M. Zajac, and M. Dutot. From simple to detailed models for cell polarization. *Philosophical Transactions of the Royal Society B: Biological Sciences*, 368(1629):20130003, 2013. doi:10.1098/rstb.2013.0003.

[141] P. K. Trong, E. M. Nicola, N. W. Goehring, K. V. Kumar, and S. W. Grill. Parameter-space topology of models for cell polarity. *New Journal of Physics*, 16(6):065009, 2014. doi:10.1088/1367-2630/16/6/065009.

[142] Y. Nishiura. Global Structure of Bifurcating Solutions of Some Reaction-Diffusion Systems. *SIAM Journal on Mathematical Analysis*, 13(4):555–593, 1982. doi:10.1137/0513037.

[143] D. Thalmeier, J. Halatek, and E. Frey. Geometry-induced protein pattern formation. *Proceedings of the National Academy of Sciences*, 113(3): 548–553, 2016. doi:10.1073/pnas.1515191113.

[144] R. Geßele, J. Halatek, L. Würthner, and E. Frey. Geometric cues stabilise long-axis polarisation of PAR protein patterns in C. elegans. *Nature Communications*, 11:539, 2020. doi:10.1038/s41467-020-14317-w.

[145] V. K. Vanag and I. R. Epstein. Pattern Formation in a Tunable Medium: The Belousov-Zhabotinsky Reaction in an Aerosol OT Microemulsion. *Physical Review Letters*, 87(22):228301, 2001. doi:10.1103/PhysRevLett.87.228301.

[146] I. R. Epstein and V. K. Vanag. Complex patterns in reactive microemulsions: Self-organized nanostructures? *Chaos: An Interdisciplinary Journal of Nonlinear Science*, 15(4):047510, 2005. doi:10.1063/1.2102447.

[147] R. J. Field and R. M. Noyes. Oscillations in chemical systems. IV. Limit cycle behavior in a model of a real chemical reaction. *The Journal of Chemical Physics*, 60(5):1877–1884, 1974. doi:10.1063/1.1681288.

[148] J. Pathak, Z. Lu, B. R. Hunt, M. Girvan, and E. Ott. Using machine learning to replicate chaotic attractors and calculate Lyapunov exponents from data. *Chaos: An Interdisciplinary Journal of Nonlinear Science*, 27(12):121102, 2017. doi:10.1063/1.5010300.

[149] M. Rank, A. Mitra, L. Reese, S. Diez, and E. Frey. Limited Resources Induce Bistability in Microtubule Length Regulation. *Physical Review Letters*, 120(14):148101, 2018. doi:10.1103/PhysRevLett.120.148101.

[150] N. Muller, M. Piel, V. Calvez, R. Voituriez, J. Gonçalves-Sá, C.-L. Guo, X. Jiang, A. Murray, and N. Meunier. A Predictive Model for Yeast Cell Polarization in Pheromone Gradients. *PLOS Computational Biology*, 12 (4):e1004795, 2016. doi:10.1371/journal.pcbi.1004795.

[151] K. Witte, D. Strickland, and M. Glotzer. Cell cycle entry triggers a switch between two modes of Cdc42 activation during yeast polarization. *eLife*, 6:e26722, 2017. doi:10.7554/eLife.26722.

[152] L. Hubatsch, F. Peglion, J. D. Reich, N. T. L. Rodrigues, N. Hirani, R. Illukkumbura, and N. W. Goehring. A cell-size threshold limits cell polarity and asymmetric division potential. *Nature Physics*, 15(10): 1078–1085, 2019. doi:10.1038/s41567-019-0601-x.

[153] E. Mizuno-Yamasaki, F. Rivera-Molina, and P. Novick. GTPase Networks in Membrane Traffic. *Annual Review of Biochemistry*, 81(1):637–659, 2012. doi:10.1146/annurev-biochem-052810-093700.

[154] M. Okamoto, K. Kurokawa, K. Matsuura-Tokita, C. Saito, R. Hirata, and A. Nakano. High-curvature domains of the ER are important for the organization of ER exit sites in Saccharomyces cerevisiae. *Journal of Cell Science*, 125(14):3412–3420, 2012. doi:10.1242/jcs.100065.

[155] M. G. Hanna, I. Mela, L. Wang, R. M. Henderson, E. R. Chapman, J. M. Edwardson, and A. Audhya. Sar1 GTPase Activity Is Regulated by Membrane Curvature * ♦. *Journal of Biological Chemistry*, 291(3):1014–1027, 2016. doi:10.1074/jbc.M115.672287.

[156] A. Goychuk and E. Frey. Protein Recruitment through Indirect Mechanochemical Interactions. *Physical Review Letters*, 123(17):178101, 2019. doi:10.1103/PhysRevLett.123.178101.

[157] S. Schonegg and A. A. Hyman. CDC-42 and RHO-1 coordinate acto-myosin contractility and PAR protein localization during polarity establishment in C. elegans embryos. *Development*, 133(18):3507–3516, 2006. doi:10.1242/dev.02527.

[158] H. Chen, C.-C. Kuo, H. Kang, A. S. Howell, T. R. Zyla, M. Jin, and D. J. Lew. Cdc42p regulation of the yeast formin Bni1p mediated by the effector Gic2p. *Molecular Biology of the Cell*, 23(19):3814–3826, 2012. doi:10.1091/mbc.e12-05-0400.

[159] D. Oh, C.-H. Yu, and D. J. Needleman. Spatial organization of the Ran pathway by microtubules in mitosis. *Proceedings of the National Academy of Sciences*, 113(31):8729–8734, 2016. doi:10.1073/pnas.1607498113.

[160] R. Wedlich-Soldner. Spontaneous Cell Polarization Through Actomyosin-Based Delivery of the Cdc42 GTPase. *Science*, 299(5610): 1231–1235, 2003. doi:10.1126/science.1080944.

[161] J. S. Bois, F. Jülicher, and S. W. Grill. Pattern Formation in Active Fluids. *Physical Review Letters*, 106(2):028103, 2011. doi:10.1103/PhysRevLett.106.028103.

[162] D. B. Stein, G. De Canio, E. Lauga, M. J. Shelley, and R. E. Goldstein. Swirling Instability of the Microtubule Cytoskeleton. *Physical Review Letters*, 126(2):028103, 2021. doi:10.1103/PhysRevLett.126.028103.

[163] M. C. Marchetti, J. F. Joanny, S. Ramaswamy, T. B. Liverpool, J. Prost, M. Rao, and R. A. Simha. Hydrodynamics of soft active matter. *Reviews of Modern Physics*, 85(3):1143–1189, 2013. doi:10.1103/RevModPhys.85.1143.

[164] H. Chaté. Dry Aligning Dilute Active Matter. *Annual Review of Condensed Matter Physics*, 11(1):189–212, 2020. doi:10.1146/annurev-conmatphys-031119-050752.

[165] M. Bär, R. Großmann, S. Heidenreich, and F. Peruani. Self-Propelled Rods: Insights and Perspectives for Active Matter. *Annual Review of Condensed Matter Physics*, 11(1):441–466, 2020. doi:10.1146/annurev-conmatphys-031119-050611.

[166] J. Denk and E. Frey. Pattern-induced local symmetry breaking in active-matter systems. *Proceedings of the National Academy of Sciences*, 117(50):31623–31630, 2020. doi:10.1073/pnas.2010302117.

[167] L. Huber, R. Suzuki, T. Krüger, E. Frey, and A. R. Bausch. Emergence of coexisting ordered states in active matter systems. *Science*, 361(6399): 255–258, 2018. doi:10.1126/science.aao5434.

[168] A. Rupe and J. P. Crutchfield. Local causal states and discrete coherent structures. *Chaos: An Interdisciplinary Journal of Nonlinear Science*, 28(7): 075312, 2018. doi:10.1063/1.5021130.

[169] A. Rupe, N. Kumar, V. Epifanov, K. Kashinath, O. Pavlyk, F. Schlimbach, M. Patwary, S. Maidanov, V. Lee, Prabhat, and J. P. Crutchfield. DisCo: Physics-Based Unsupervised Discovery of Coherent Structures in Spatiotemporal Systems. *arXiv:1909.11822 [physics]*, 2019.

[170] A. A. Agrachev and Y. Sachkov. *Control Theory from the Geometric Viewpoint*. Encyclopaedia of Mathematical Sciences, Control Theory and Optimization. Springer-Verlag, Berlin Heidelberg, 2004. ISBN 978-3-540-21019-1. doi:10.1007/978-3-662-06404-7.

[171] A. P. Solon, H. Chaté, and J. Tailleur. From Phase to Microphase Separation in Flocking Models: The Essential Role of Nonequilibrium Fluctuations. *Physical Review Letters*, 114(6):068101, 2015. doi:10.1103/PhysRevLett.114.068101.

[172] E. Tjhung, C. Nardini, and M. E. Cates. Cluster Phases and Bubbly Phase Separation in Active Fluids: Reversal of the Ostwald Process. *Physical Review X*, 8(3):031080, 2018. doi:10.1103/PhysRevX.8.031080.

[173] S. M. Murray and V. Sourjik. Self-organization and positioning of bacterial protein clusters. *Nature Physics*, 13(10):1006–1013, 2017. doi:10.1038/nphys4155.

[174] B. Jacobs, J. Molenaar, and E. E. Deinum. Small GTPase patterning: How to stabilise cluster coexistence. *PLOS ONE*, 14(3):e0213188, 2019. doi:10.1371/journal.pone.0213188.

[175] J.-g. Chiou, K. D. Moran, and D. J. Lew. How cells determine the number of polarity sites. *bioRxiv*, page doi:10.1101/2020.05.21.109520, 2020. doi:10.1101/2020.05.21.109520.

[176] C. Beta, N. S. Gov, and A. Yochelis. Why a Large-Scale Mode Can Be Essential for Understanding Intracellular Actin Waves. *Cells*, 9(6):1533, 2020. doi:10.3390/cells9061533.

[177] Z. Tong, X.-D. Gao, A. S. Howell, I. Bose, D. J. Lew, and E. Bi. Adjacent positioning of cellular structures enabled by a Cdc42 GTPase-activating protein–mediated zone of inhibition. *The Journal of Cell Biology*, 179(7):1375–1384, 2007. doi:10.1083/jcb.200705160.

[178] W.-C. Lo, M. E. Lee, M. Narayan, C.-S. Chou, and H.-O. Park. Polarization of Diploid Daughter Cells Directed by Spatial Cues and GTP Hydrolysis of Cdc42 in Budding Yeast. *PLoS ONE*, 8(2):e56665, 2013. doi:10.1371/journal.pone.0056665.

[179] K. E. Miller, W.-C. Lo, M. E. Lee, P. J. Kang, and H.-O. Park. Fine-tuning the orientation of the polarity axis by Rga1, a Cdc42 GTPase-activating protein. *Molecular Biology of the Cell*, 28(26):3773–3788, 2017. doi:10.1091/mbc.e17-01-0074.

[180] T. D. Williams, P. I. Paschke, and R. R. Kay. Function of small GTPases in Dictyostelium macropinocytosis. *Philosophical Transactions of the Royal Society B: Biological Sciences*, 374(1765):20180150, 2019. doi:10.1098/rstb.2018.0150.

[181] D. M. Veltman, T. D. Williams, G. Bloomfield, B.-C. Chen, E. Betzig, R. H. Insall, and R. R. Kay. A plasma membrane template for macropinocytic cups. *eLife*, 5:e20085, 2016. doi:10.7554/eLife.20085.

[182] E. M. Vaughan, A. L. Miller, H.-Y. E. Yu, and W. M. Bement. Control of Local Rho GTPase Crosstalk by Abr. *Current Biology*, 21(4):270–277, 2011. doi:10.1016/j.cub.2011.01.014.

[183] E. F. Koslover, C. K. Chan, and J. A. Theriot. Cytoplasmic Flow and Mixing Due to Deformation of Motile Cells. *Biophysical Journal*, 113(9): 2077–2087, 2017. doi:10.1016/j.bpj.2017.09.009.

[184] V. Ruprecht, S. Wieser, A. Callan-Jones, M. Smutny, H. Morita, K. Sako, V. Barone, M. Ritsch-Marte, M. Sixt, R. Voituriez, and C.-P. Heisenberg. Cortical Contractility Triggers a Stochastic Switch to Fast Amoeboid Cell Motility. *Cell*, 160(4):673–685, 2015. doi:10.1016/j.cell.2015.01.008.

[185] H. I. Adler, W. D. Fisher, A. Cohen, and A. A. Hardigree. Miniature Escherichia coli cells Deficient in DNA. *Proceedings of the National Academy of Sciences*, 57(2):321–326, 1967. doi:10.1073/pnas.57.2.321.

[186] P. A. de Boer, R. E. Crossley, and L. I. Rothfield. A division inhibitor and a topological specificity factor coded for by the minicell locus determine proper placement of the division septum in E. coli. *Cell*, 56(4): 641–649, 1989. doi:10.1016/0092-8674(89)90586-2.

[187] F. Wu, J. Halatek, M. Reiter, E. Kingma, E. Frey, and C. Dekker. Multistability and dynamic transitions of intracellular Min protein patterns. *Molecular Systems Biology*, 12(6):873, 2016. doi:10.15252/msb.20156724.

[188] B. Ramm, A. Goychuk, A. Khmelinskaia, P. Blumhardt, H. Eto, K. A. Ganzinger, E. Frey, and P. Schwille. A diffusiophoretic mechanism for ATP-driven transport without motor proteins. *Nature Physics*, pages 1–9, 2021. doi:10.1038/s41567-021-01213-3.

[189] D. Winston, M. Arora, J. Maselko, V. Gáspár, and K. Showalter. Cross-membrane coupling of chemical spatiotemporal patterns. *Nature*, 351 (6322):132–135, 1991. doi:10.1038/351132a0.

[190] M. Hildebrand, J. Cui, E. Mihaliuk, J. Wang, and K. Showalter. Synchronization of spatiotemporal patterns in locally coupled excitable media. *Physical Review E*, 68(2):026205, 2003. doi:10.1103/PhysRevE.68.026205.

[191] S. Weiss and R. D. Deegan. Weakly and strongly coupled Belousov-Zhabotinsky patterns. *Physical Review E*, 95(2):022215, 2017. doi:10.1103/PhysRevE.95.022215.

[192] H. Nakao, T. Yanagita, and Y. Kawamura. Phase-Reduction Approach to Synchronization of Spatiotemporal Rhythms in Reaction-Diffusion Systems. *Physical Review X*, 4(2):021032, 2014. doi:10.1103/PhysRevX.4.021032.

[193] M. Lynch, M. C. Field, H. V. Goodson, H. S. Malik, J. B. Pereira-Leal, D. S. Roos, A. P. Turkewitz, and S. Sazer. Evolutionary cell biology: Two origins, one objective. *Proceedings of the National Academy of Sciences*, 111(48):16990–16994, 2014. doi:10.1073/pnas.1415861111.

[194] L. Laan, J. H. Koschwanez, and A. W. Murray. Evolutionary adaptation after crippling cell polarization follows reproducible trajectories. *eLife*, 4:e09638, 2015. doi:10.7554/eLife.09638.

Acknowledgments
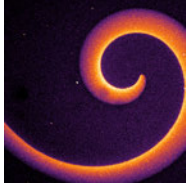
First of all, I want to express my gratitude to Erwin Frey. I deeply appreciate your support and the freedom you gave me in pursuing my scientific interests. Thank you for all the time and effort you invested in our projects, for the countless discussions we had, and for the guidance in navigating the jungle of scientific publishing and politics. I am especially grateful for the many opportunities to participate in conferences and summer schools, and for the chance to visit many scientists at various universities around the world. In particular, I immensely enjoyed the Les Houches Summer School in 2018. Thank you for always supporting and encouraging this active participation in the scientific life.

I also want to thank Jacob Halatek, for the countless, stimulating, and insightful discussions and for sharing the ideas that developed into local equilibria theory. I greatly enjoyed working with you. In the same spirit, I want to thank Henrik Weyer for picking up the torch on the question of wavelength selection and making rigorous, systematic progress much further than I could have hoped for. Thank you for your enthusiasm, all the inspiring discussions, and your critical feedback. Special thanks go to Manon Wigbers: I greatly enjoyed our numerous collaborations and always appreciated your critical feedback; to Laeschkir Würthner: thank you for your endless patience in babysitting and fixing COMSOL simulations; and to Moritz Striebel for the collaboration on an exciting, new pattern-forming system.

Thank you to all members of our group for the supportive, collaborative, and open atmosphere without which my time as a PhD student would not have been half as fun.

I want to thank my experimental collaborators Werner Daalman, Cees Dekker, Nikta Fakhri, Philipp Glock, Liedewij Laan, Grzegorz Pawlik, and Tzer Han Tan. Thank you for sharing your outstanding work and for the opportunity to put our theoretical ideas to the test in the real world. It was an honor and a great experience to work with all of you.

Ein ganz besonderer Dank gilt meinen Eltern und meine Schwester, die mich immer unterstützt und mir Zuspruch gegeben haben.

Und schließlich, Livi, danke für deine große Liebe.

Image credit for pages vi, viii, and 81: P. Glock, with permission.

A | Publication manuscripts

1   Phase-space geometry of mass-conserving reaction–diffusion dynamics

This section is a publication preprint of the following manuscript published in Phys. Rev. X 10, 041036 (2020)

Phase-space geometry of mass-conserving reaction–diffusion dynamics

F. Brauns,[1,*] J. Halatek,[1,*] and E. Frey[1]

[1] *Arnold Sommerfeld Center for Theoretical Physics and Center for NanoScience, Department of Physics, Ludwig-Maximilians-Universtiät München, Theresienstraße 37, D-80333 München, Germany*

[*]FB and JH contributed equally to this work.

Phase-space geometry of mass-conserving reaction–diffusion dynamics

Fridtjof Brauns, Jacob Halatek, and Erwin Frey

Arnold Sommerfeld Center for Theoretical Physics and Center for NanoScience,
Department of Physics, Ludwig-Maximilians-Universtiät München,
Theresienstraße 37, D-80333 München, Germany
(Dated: April 14, 2021)

Experimental studies of protein-pattern formation have stimulated new interest in the dynamics of reaction–diffusion systems. However, a comprehensive theoretical understanding of the dynamics of such highly nonlinear, spatially extended systems is still missing. Here we show how a description in phase space, which has proven invaluable in shaping our intuition about the dynamics of nonlinear ordinary differential equations, can be generalized to mass-conserving reaction–diffusion (MCRD) systems. We present a comprehensive analysis of two-component MCRD systems, which serve as paradigmatic minimal systems that encapsulate the core principles and concepts of the *local equilibria theory* introduced in the paper. The key insight underlying this theory is that shifting local (reactive) equilibria—controlled by the local total density—give rise to concentration gradients that drive diffusive redistribution of total density. We show how this dynamic interplay can be embedded in the phase plane of the reaction kinetics in terms of simple geometric objects: the reactive nullcline (line of reactive equilibria) and the diffusive flux-balance subspace. On this phase-space level, physical insight can be gained from geometric criteria and graphical constructions. The effects of nonlinearities on the global dynamics are simply encoded in the curved shape of the reactive nullcline. In particular, we show that the pattern-forming 'Turing instability' in MCRD systems is a mass-redistribution instability, and that the features and bifurcations of patterns can be characterized based on regional dispersion relations, associated to distinct spatial regions (plateaus and interfaces) of the patterns. In an extensive outlook section, we detail concrete approaches to generalize local equilibria theory in several directions, including systems with more than two-components, weakly-broken mass conservation, and active matter systems.

Keywords: mass conservation; reaction–diffusion; pattern formation; phase space; local equilibria; flux balance; self-organization

I. INTRODUCTION

A. Motivation and background

Nonlinear systems are as prevalent in nature as they are difficult to deal with conceptually and mathematically [1–7]. Cases in which the equations describing such systems can be solved in closed analytical form are rare, making nonlinear problems appear inaccessible to mathematical analysis at first sight. A key insight, going back to the work of Poincaré [8], was that geometric structures in the phase space of a system can provide qualitative information about the *global* dynamics (trajectories in phase space) without an explicit solution of the differential equations. The essence of this geometric reasoning can be understood by considering simple systems with only two independent variables; see e.g. Refs. [1, 2]. In this case, the key geometric objects are nullclines, defined as curves in phase space along which one of the system's two variables is in equilibrium. The points at which nullclines intersect mark equilibria (fixed points) of the system. These geometric objects organize phase-space flow, and thereby allow one to infer the qualitative dynamics from the shapes and intersections of the nullclines. Key concepts like linear stability, excitability, multi-stability, and limit cycles can be understood in the context of such a geometric analysis [1, 2]. Transitions (bifurcations) between qualitatively different regimes are

revealed by structural changes of the flow in phase space as the control parameters are varied. One key advantage of such a geometric approach to nonlinear dynamical systems is that it yields systematic physical insights into the processes driving dynamics without requiring the explicit solution of the full set of equations.

Generalizing these methods, developed for ordinary differential equations (ODEs), to phenomena that explicitly require a description on a spatially extended domain—and therefore involve partial differential equations (PDEs)—poses a huge, ongoing challenge. Instances where this has been successfully achieved are rare. One classical approach for nonlinear systems in one spatial dimension is the construction of steady-state patterns (including both stationary patterns and traveling-wave solutions in a co-moving frame). Mathematically, the steady state in this case is described by a set of ODEs, which can be analyzed based on their phase-space geometry (see e.g. Refs. [9, 10]). An elementary example of this is the phase-plane analysis of traveling waves of the Fisher-KPP equation [11, 12] as described in Ref. [13]. Here, we go beyond this approach, and gain physical insight into the *global dynamics* of spatially extended systems from the analysis of geometric objects in a low-dimensional phase space. Crucially, such a theory should be able to explain both, the dynamic process of pattern formation—initiated, for instance, by a lateral (Turing) instability—as well as the final stationary patterns in terms of the same concepts and principles.

In its full generality, this is likely a futile task. Here, we restrict ourselves to mass-conserving reaction–diffusion (MCRD) dynamics. A broad class of systems that can be described by MCRD dynamics are models for intracellular protein-pattern formation [14], which is essential for the spatiotemporal organization of many cellular processes, including cell division, motility and differentiation. Moreover, as we discuss in the Outlook, many pattern-forming systems are governed by a combination of mass-conserving dynamics and source terms that break mass conservation. Studying such systems in the *nearly* mass-conserving limit may help to tackle long-standing questions like pattern selection (wavelength selection) in the highly nonlinear regime [15].

Recent results have indicated ways of making progress towards a general theory rooted in mass-conservation [16]. Based on numerical simulations, this study suggests a new way of thinking about pattern formation, namely in terms of mass redistribution that gives rise to *moving local equilibria*: A dissection of space into (notional) local compartments allows the spatiotemporal dynamics to be characterized on the basis of the ODE phase space of local reactions. As (*globally* conserved) masses are spatially redistributed, the *local* masses in the compartments act as parameters for the reactive phase-space flow within them. The properties (position and stability) of the *local reactive equilibria* in the compartments are shown to depend on local masses and thus act as proxies for the local phase-space flow [17].

Diffusion acts to redistribute the conserved quantities between neighboring compartments and thereby induces changes in the local phase-space structure. This level of description proved to be very powerful in explaining chemical turbulence and transitions from chemical turbulence to long range order (standing and traveling waves) far from onset of the (subcritical) lateral instability. The prediction of chemical turbulence at onset, based on numerical simulations in Ref. [16], was recently confirmed experimentally [19]. Hence, the advances in this "proof-of-principle" study [16] suggest that a comprehensive theory of pattern formation in reaction–diffusion systems with conserved total densities (masses) can be developed based on the concept of mass-redistribution.

Here, we put this overarching idea on a general theoretical foundation. To this end, we develop a number of new theoretical concepts, exemplified by two-component mass-conserving reaction-diffusion (2C-MCRD) systems and based on simple geometric structures in the phase space of the reaction kinetics. From these concepts, general geometric criteria for lateral (Turing) instability and stimulus-induced pattern formation emerge and allow us to obtain the features and bifurcations of patterns from graphical constructions. Moreover, these advances reveal connections to other pattern forming phenomena like liquid-liquid phase separation and shear banding in complex fluids.

In our work, general two-component systems serve two purposes. First, as a paradigmatic and didactic example that encapsulates the core concepts and principles of our theory in a pedagogic and broadly accessible way. Second, they provide an elementary basis for further generalizations. Taken together, the role we envision for 2C-MCRD systems is similar to the role of two-variable systems in dynamical systems theory of ODEs.

The framework we present here has recently been employed and generalized to study the principles underlying coarsening and wavelength selection [15], as well as systems with spatially heterogeneous reaction rates [20] and the role of advective flow in the cytosol [21]—all in the context of two-component systems. Moreover, the concepts of local equilibria and regional instabilities have recently proven useful to disentangle the interplay of several distinct instabilities that give rise to Min-protein patterns *in vivo* and *in vitro* [22].

Potential future generalizations range from adding more components and more conserved quantities, to going beyond strictly mass-conserving systems (see Outlook). Mass conservation and, more generally, conserved quantities are inherent to the elementary processes underlying many pattern forming systems. We therefore believe that the local equilibria theory we present here offers a new perspective on a broad class of pattern-forming systems—including intracellular pattern formation, classical chemical systems such as the BZ reaction, and even agent-based active matter systems.

B. Structure of the paper

Put briefly, the paper is structured as follows. Section II introduces 2C-MCRD systems, and their applications, most prominently as conceptual models for cell polarization. The concepts introduced in Sec. III and Sec. IV form the foundation of the proposed framework and the subsequent analysis. The following two sections present results that are particularly relevant in the biological context of intracellular pattern formation: A characterization of the possible pattern types exhibited by 2C-MCRD systems (Sec. V) and a simple heuristic for the threshold perturbation required for stimulus-induced pattern formation (Sec. VI). Section VII delves into a more technical analysis of the generic bifurcation structure of 2C-MCRD systems. Here, we find striking similarities to the phase diagram of phase-separation phenomena (such as liquid-liquid phase separation and motility-induced phase separation). This technical section also includes weakly nonlinear analysis in the vicinity of the lateral instability onset that corresponding to a critical point in the language of phase transitions. Finally, in Sec. VIII, we provide an extensive discussion of the implications of our results and an outlook to future research directions.

II. TWO-COMPONENT MASS-CONSERVING REACTION–DIFFUSION SYSTEMS

Our goal is to find geometric structures in phase space that allow the characterization of mass-conserving reaction–diffusion (MCRD) systems. The simplest system of this type is a two-component reaction–diffusion system with two scalar densities, $m(x,t)$ and $c(x,t)$,

$$\partial_t m(x,t) = D_m \partial_x^2 m + f(m,c), \qquad (1a)$$
$$\partial_t c(x,t) = D_c \partial_x^2 c - f(m,c), \qquad (1b)$$

on a one-dimensional domain of length L with reflective (no-flux) boundary conditions $\partial_x m|_{0,L} = \partial_x c|_{0,L} = 0$; all results can straightforwardly be generalized to periodic boundary conditions. The global average $\bar{n}$ of total density $n(x,t) = m(x,t) + c(x,t)$ is conserved:

$$\bar{n} = \frac{1}{L} \int_0^L \mathrm{d}x \left(m(x,t) + c(x,t) \right). \qquad (1c)$$

We chose the above form for its conceptual simplicity. However, the principles that characterize pattern formation for this 'minimal' model can be generalized to more complex systems with more components and conserved species [16, 23], and even beyond strictly mass-conserving systems [15]; see also Sec. VIII D.

Two-component systems of the above form were widely studied as conceptual models for cell polarization [24–36], where Eq. (1) describes the dynamics of a protein species that cycles between membrane (slow diffusing, concentration $m(x,t)$) and cytosol (fast diffusing, concentration $c(x,t)$). In this biological context, the nonlinear kinetics term $f(m,c)$ is of the form

$$f_{\text{attach–detach}}(m,c) = a(m)c - d(m)m, \qquad (2)$$

where the non-negative terms $a(m)c$ and $d(m)m$ characterize the attachment of proteins from the cytosol to the membrane and the detachment back into the cytosol, respectively. This functional form results from the fact that in intracellular systems chemical reactions are mainly restricted to the cell membrane. We will use kinetics of the above form for illustration purposes; for specific examples see Appendix A. Importantly however, our results hold for general kinetics f, and are not restricted to models for intracellular pattern formation. Moreover, 2C-MCRD systems have also been studied for slime mold aggregation [37], cancer cell migration (glioma invasion) [38], precipitation patterns [39, 40], and simple contact processes [41, 42]. Finally, non-isothermal solidification models [43] can also be rewritten in the form Eq. (1); see e.g. Refs. [44, 45].

In the mathematical literature, 2C-MCRD systems with a specific form of the reaction kinetics, $f(m,c) = c - g(m)$, have been studied extensively [44, 46–48]. The dynamics of these systems can be mapped to a variational form (gradient flow of an effective free-energy density). In this form, the properties of the dynamics and the stationary patterns can be analyzed analogously to the Cahn–Hilliard equation which describes phase separation near *thermal* equilibrium (see e.g. Ref. [49]). In particular, one can prove that these systems always exhibit uninterrupted coarsening, i.e. the fully phase separated state is the only stable stationary state of the system [47, 48]. The theory we present here is fundamentally different from these previous mathematical approaches. Instead of an abstract mapping to a variational form, our approach is grounded in concepts with clear physical interpretation that are not restricted to specific reaction terms. Local equilibria, the overarching concept of our theory, can be generalized to systems with more than two components and more complex phenomena such as waves, oscillations and chaos [16, 22].

In closing this section we we would like to point out that systems which are not strictly mass conserving may have a mass-conserving subsystem (or 'core') that captures essential aspects of the system's pattern formation dynamics. An example is the Brusselator system [50], a widely used paradigmatic model to study pattern formation. It's reaction kinetics has a 'core' of the same form as Eq. (1) with additional linear production and degradation terms that break mass conservation. This broken mass conservation can give rise to interesting new phenomena, not present in the mass-conserving core. Still, the core dynamics can be useful in understanding these new phenomena by exploiting a time scale separation between (fast) mass-conserving processes and (slow) production/degradation processes [15, 51, 52]. In the Outlook, Sec. VIII D, we briefly discuss this example and the broader prospects of such an approach to non-conservative systems.

III. SETTING THE STAGE—GEOMETRIC STRUCTURES IN PHASE SPACE

In this section we introduce the basic geometric concepts in phase space, which we will later use for a full characterization of pattern formation, including pattern types, bifurcations, and the corresponding characteristic length and time scales. To this end, we will first study the spatially homogeneous (well-mixed) case where we can use the classical geometric tools for studying ordinary differential equations [1, 2, 5]. Subsequently, we will build on the phase-space structures obtained from the well-mixed case to also understand pattern formation in spatially extended systems in terms of flow in phase space.

A. Phase-space analysis of a well-mixed system

For a well-mixed system, the dynamics reduces to a set of ordinary differential equations

$$\partial_t m = f(m,c), \qquad \partial_t c = -f(m,c). \tag{3}$$

Since the reaction kinetics conserve total density (protein mass), $n = m + c$, the reactive flow in (m,c)-phase space is restricted to the *reactive phase space* where n is a constant of motion (i.e. $\partial_t n = 0$), as illustrated in Fig. 1a. The reaction kinetics are balanced at the reactive equilibria (fixed points) $\mathbf{u}^* = (m^*, c^*)$,

$$\mathbf{u}^*(n) : \begin{cases} f(\mathbf{u}^*) = & 0, \\ m^* + c^* = & n, \end{cases} \tag{4}$$

which are given by the intersection points between the reactive *reactive nullcline* (NC) (or 'line of reactive equilibria'), $f(m^*, c^*) = 0$, and the reactive phase space for a given mass n. The *reactive flow* in the respective phase space is organized by the location and (linear) stability of these fixed points (which are both functions of n); see Fig. 1a and discussion below. By varying the total density n, i.e. by shifting the reactive phase space, one can construct a bifurcation diagram of the (reactive) equilibrium $c^*(n)$ as a function of the total density n (Fig. 1b). The total density is a control parameter of the reactive equilibria. When the total density changes, the local equilibria shift. These *shifting (or moving) local equilibria*, introduced in Ref. [16], are the key to understanding the mass-conserving reaction–diffusion dynamics as we will see repeatedly throughout this paper.

In each reactive phase space, we can eliminate (the cytosolic density) $c(t)$ and write the dynamics in terms of (the membrane density) $m(t)$ alone: $\partial_t m(t) = f\big(m(t), n - m(t)\big)$; equally well could be eliminated. In the vicinity of an equilibrium m^* the linearized reactive flow reads $\partial_t m(t) \approx (f_m - f_c)(m(t) - m^*)$, with $f_i := \partial_i f|_{\mathbf{u}^*}, i \in \{m, c\}$. We can read off the eigenvalue $\sigma_{\mathrm{loc}}(n) := f_m - f_c$ for the local equilibrium and obtain to linear order in the vicinity of the reactive nullcline:

$$\begin{aligned} f(m,c) &\approx \sigma_{\mathrm{loc}}(n) \cdot \big[m - m^*(n)\big] \\ &= -\sigma_{\mathrm{loc}}(n) \cdot \big[c - c^*(n)\big]. \end{aligned} \tag{5}$$

The sign of σ_{loc}—and thereby stability of the reactive equilibria—can be inferred from the slope of the nullcline

$$s_{\mathrm{nc}}(n) := \partial_m c^*(m)\big|_n = -\frac{f_m}{f_c}\bigg|_n. \tag{6}$$

For $f_c > 0$, which is always the case for attachment–detachment kinetics where $f_c = a(m)$, local equilibria are stable, $\sigma_{\mathrm{loc}}(n) < 0$, if (and only if) the slope of the reactive nullcline is less steep than the slope of the reactive phase space:

$$s_{\mathrm{nc}}(n) = -1. \tag{7}$$

(∘) ● (un)stable reactive equilibria
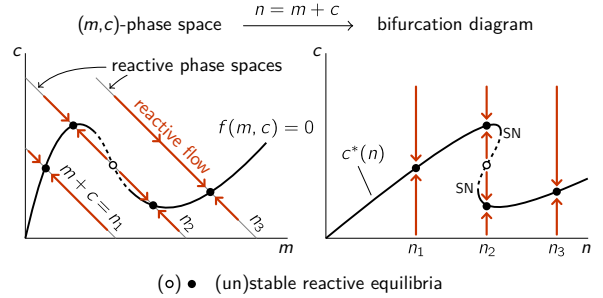
FIG. 1. Phase space and bifurcation structure of a well-mixed 2C-MCRD system. The conservation law $m + c = n$ is geometrically represented by 1-simplices in phase space, referred to as *reactive phase spaces*. Local reactions give rise to a flow in phase space (red arrows) which, due to mass conservation, is confined to the reactive phase spaces. The flow vanishes along the *reactive nullcline* $f(m,c) = 0$ (black line) which is a line of *reactive equilibria*. Each intersection of a reactive phase space with the reactive nullcline is a reactive equilibrium $\mathbf{u}^*(n)$ for a given total density n (shown as disks, ●/∘, for three different values $n_{1,2,3}$). The (m,c)-phase portrait can be transformed into a bifurcation diagram $c^*(n)$ by the skew transformation $n = m + c$. Because of the conservation law, the well-mixed system has only one degree of freedom, so the only possible bifurcations are saddle-node bifurcations (SN) where the reactive nullcline is tangential to a reactive phase space.

Figure 1a shows an example for reaction kinetics where the dynamics is monostable except for a window of protein masses exhibiting bistability with one unstable (∘) and two stable fixed points (●). (Note that the local eigenvalue σ_{loc} can be rewritten as $\sigma_{\mathrm{loc}} = f_c \cdot (-s_{\mathrm{nc}} - 1)$, which shows why the slope criterion, Eq. (7), for local stability is reversed for $f_c < 0$.)

B. Stationary patterns are embedded in a flux-balance subspace of phase space

To generalize the above approach to spatially extended systems, one has to understand the role of diffusive coupling. We start by studying stationary patterns. The insights gained from this analysis will later prove useful for studying the dynamics (instability of the homogeneous state and stimulus-induced pattern formation).

A *stationary pattern* $\widetilde{\mathbf{u}}(x) = [\widetilde{m}(x), \widetilde{c}(x)]$ is a solution to the steady-state equations,

$$D_m \partial_x^2 \widetilde{m} + f(\widetilde{m}, \widetilde{c}) = 0, \tag{8a}$$

$$D_c \partial_x^2 \widetilde{c} - f(\widetilde{m}, \widetilde{c}) = 0, \tag{8b}$$

under the constraint of a given average total density $\bar{n}$ (Eq. (1c)). Figure 2a shows the sketch of a typical stationary pattern $\widetilde{m}(x)$ (solid line) and the corresponding local equilibria $m^*(x)$ (black disks) obtained from a numerical solution of Eq. (8) with a reaction term as, for

instance, in Refs. [28, 34, 53] (see Appendix A). We study patterns with monotonic density profiles, which serve as elementary building blocks for more complex stationary patterns (see Section V). Figure 2a shows an example for a monotonic pattern profile exhibiting two plateau regions connected by an interface region with an inflection point at x_0. (We will later see that this type of pattern, termed 'mesa', is one of three elementary pattern types found in two-component reaction–diffusion systems; see Sec. V C).

Here we ask what can be learned about the stationary pattern by applying geometric concepts in phase space alone, i.e. without relying on an explicit numerical solution. Observe that Eqs. (8) imply that the diffusive fluxes of m and c have to balance locally at each position x in the spatial domain $[0, L]$ in steady state:

$$D_m \partial_x \widetilde{m}(x) = -D_c \partial_x \widetilde{c}(x). \qquad (9)$$

This local *flux-balance condition* is obtained by adding the two steady-state equations, Eq. (8a) and Eq. (8b), integrating over x and employing no-flux boundary conditions. Integrating this relation once more from the boundary to any point x in the domain yields that any stationary pattern obeys the linear relation

$$\frac{D_m}{D_c} \widetilde{m}(x) + \widetilde{c}(x) = \eta_0, \qquad (10)$$

where η_0 is a constant of integration. (An alternative derivation of this relation that directly generalizes to higher spatial dimensions (cf. Eq. (14b) is provided below.) Equation (10) defines a family of linear subspaces in the (m, c)-phase plane parametrized by η_0. We shall call these subspaces the *flux-balance subspaces* (FBS), since they represents the local balance between the diffusive fluxes on the membrane and in the cytosol. Any stationary pattern is confined to one such subspace; see Fig. 2b. We will learn later (Sec. III C), how the value of $\eta_0(\bar{n}, L)$ is determined by the balance of reactive processes.

Equation (10) has been previously used to mathematically simplify the construction and analysis of stationary patterns in two-component systems, by introducing the new phase-space coordinate (orthogonal to the flux-balance subspace)

$$\eta := \frac{D_m}{D_c} m + c, \qquad (11)$$

and describing the spatiotemporal dynamics in terms of the scalar fields $n(x, t)$ and $\eta(x, t)$ (cf. Refs. [25, 34]). The physical origin (diffusive flux balance) and the geometric interpretation (flux-balance subspace) discussed above explains why Eq. (10) has proven to be useful before (and why it will be central in our further analysis). In particular, note that by adding Eqs. (1a) and (1b) one finds that gradients in $\eta(x, t)$ drive mass redistribution:

$$\partial_t n(x, t) = D_c \partial_x^2 \eta(x, t). \qquad (12)$$

We will therefore call $\eta(x, t)$ the *mass-redistribution potential*. Substituting c using η, the reaction term reads

$$\tilde{f}(m, \eta) := f(m, \eta - m D_m/D_c), \qquad (13)$$

and the stationarity conditions, Eqs. (8a) and (8b), are replaced by

$$D_m \partial_x^2 \widetilde{m} + \tilde{f}(\widetilde{m}, \widetilde{\eta}) = 0, \qquad (14a)$$
$$D_c \partial_x^2 \widetilde{\eta} = 0. \qquad (14b)$$

From the second equation, we recover that in steady state, the mass-redistribution potential must be constant in space, $\widetilde{\eta} = \eta_0$, on a domain with no-flux or periodic boundary conditions. This result also holds in higher spatial dimensions, as one can see by analogy to the electric potential in a charge free space. The mass-redistribution potential plays a role analogous to the chemical potential in Model B dynamics [54]. However, it does not follow from a free energy density. Instead, it is determined by the local concentrations via Eq. (11), and its spatial gradients represent the local imbalance of diffusive fluxes. Finally, note that the equation for the mass-redistribution dynamics Eq. (12) is not closed. Later, in Sec. IV, we will introduce an approximate "closure relation" for Eq. (12).

The above analysis can be generalized to systems with N components whose total mass is conserved (describing, for instance, a single protein species with N conformational states). The mass-redistribution potential is the sum of the concentrations weighted by their respective diffusion constants. Respectively, the flux-balance subspace in the N-dimensional concentration phase space is a $N-1$ dimensional hyperplane orthogonal to the vector of diffusion constants $(D_1, D_2, \dots, D_N)$.

C. Stationary patterns are "scaffolded" by local equilibria

Whenever the diffusion constants D_m and D_c are unequal, the flux-balance subspace cannot coincide with any reactive phase space (which has slope -1). Hence, a non-uniform total density profile $\widetilde{n}(x) := \widetilde{m}(x) + \widetilde{c}(x)$ is innate to any stationary pattern (non-uniform $\widetilde{m}(x)$) whenever $D_m \neq D_c$.

As we will see next, this non-uniform total density profile is key understand the relationship between the stationary pattern in real space and the reactive nullcline in the phase plane.

Consider the system as being spatially dissected into notional *local* compartments [16]. Within each such compartment, local reaction kinetics induce a reactive flow $f(m, c)$ that lies in the *local phase space* $\{(m, c) : m + c = \widetilde{n}(x)\}$ which is determined by the respective local mass $\widetilde{n}(x)$. We define the *local equilibria*

$$f(\mathbf{u}^*(n(x, t))) = 0,$$
$$m^*(n(x, t)) + c^*(n(x, t)) = n(x, t), \qquad (15)$$
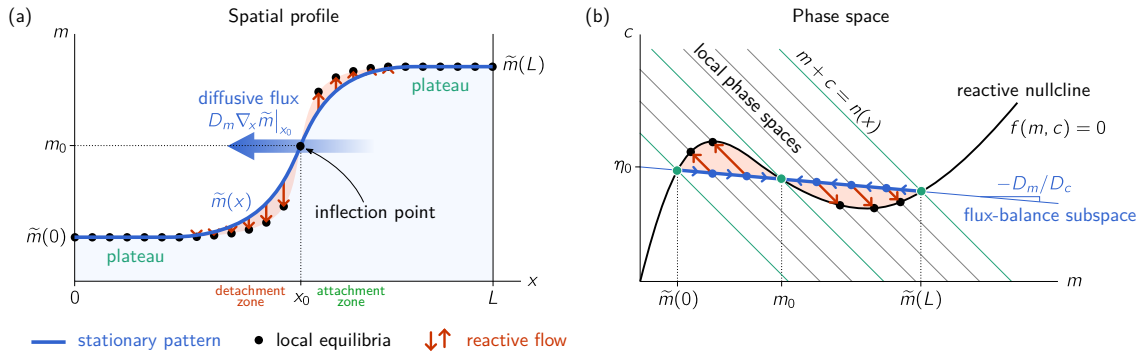
FIG. 2. Illustration of a stationary pattern and its embedding in phase space which motivates the flux-balance construction based on the reactive nullcline. (Movie 1 shows the dynamics that lead to such a stationary pattern). (a) Local (reactive) equilibria $m^*(\widetilde{n}(x))$ (•) act as a "scaffold" for the pattern profile which is tied to the equilibria by local reactive flows (red arrows). At the inflection point x_0 the flux-balance subspace intersects the reactive nullcline $\tilde{f}(m(x_0), \eta_0) = 0$. In a steady state, the diffusive flux on the membrane (blue arrow) is balanced by an equal and opposite flux in the cytosol. Together these fluxes exactly cancel the cumulative reactive turnover on either side of the inflection point (indicated by red shaded areas). (b) The phase-space trajectory corresponding to the stationary pattern is embedded in a flux-balance subspace (thin blue line). The local reactive flows (red arrows) are restricted to the local phase spaces where total density is conserved locally. The intersections between the local phase spaces and the reactive nullcline $f(m, c) = 0$ yield the local equilibria (•). Slow membrane diffusion (blue arrows) balances the reactive flows towards the equilibria in the vicinity of x_0 (cf. Eq. (20)). The regions left and right of x_0 can be intuitively characterized as attachment and detachment zones based on the direction of the reactive flow in them. A balance of total turnovers (red shaded areas between pattern and local equilibria in (a) and (b)) determines η_0 (cf. Eq. (19)).

analogously to Eq. (4), where we emphasize that the total density $n(x, t)$ is a function of position x and time t here. The local equilibria are geometrically determined by intersection points of the *local* phase space with the reactive nullcline. Together with their linear stability the local equilibria serve as proxies for the local reactive flow in each notional compartment (as in the well-mixed system discussed in Sec. III A; cf. Eq. (5)). Thus, by thinking about a system as dissected into small compartments coupled by diffusion, we can carry over the phase-space structure of the local reaction kinetics to the spatially extended system (Fig. 2b).

What is the relationship between the local equilibria $\mathbf{u}^*(\widetilde{n}(x))$ and the stationary pattern $\widetilde{\mathbf{u}}(x)$? To gain some intuition, suppose the compartments were isolated from each other, i.e. diffusive coupling between them were shut off. If we choose the compartments small enough to be well-mixed, then the concentrations m and c in each of them will simply relax to the local equilibrium (black disks in Fig. 2) determined by the total density $\widetilde{n}(x)$ that varies from compartment to compartment. In that sense, the local equilibria act as a *scaffold* to which the pattern is "tied" by local reactive flows. Because total density must be conserved individually in each of the (now uncoupled) compartments the approach (red arrows) to the local equilibria is confined to the reactive phase space (gray lines) given by the total density in the compartment.

Let us now consider diffusive coupling between these compartments. In essence, diffusion acts to remove spatial gradients (as indicated by the small blue arrows along the FBS in Fig. 2b) and is counteracted by reactive flows towards the local equilibria (indicated by the red arrows from the FBS to the local equilibria in Fig. 2a,b). How does this competition play out in detail? In steady state, the *net* diffusive flux in and out of the compartment is balanced by the deviation from local (reactive) equilibrium (it is instructive to compare Eq. (4) for reactive equilibria and Eqs. (8) for stationary pattern). If the gradient does not change across the compartment, such that the flux into and out of the compartment are identical, the net diffusive flux vanishes: $\partial_x[D_m \partial_x \widetilde{m}(x)] = 0$. (Thanks to the flux-balance condition Eq. (9), the same holds automatically for $\widetilde{c}(x)$.) In turn, the stationary pattern pattern must coincide with the local equilibria: $\widetilde{\mathbf{u}}(x) = \mathbf{u}^*(\widetilde{n}(x))$ when the gradient does not change across a compartment. This holds exactly at *inflection points* of the pattern. For *plateaus*, the gradient is small, $\partial_x \widetilde{\mathbf{u}}(x) \approx 0$, in a spatially extended region, and so is the local net flux, that is, $\partial_x^2 \widetilde{\mathbf{u}}(x) \approx 0$. Hence, for plateaus we have $f(\widetilde{\mathbf{u}}(x)) \approx 0$, such that the pattern can be locally approximated by the respective local equilibria, that is, $\widetilde{\mathbf{u}}(x) \approx \mathbf{u}^*(\widetilde{n}(x))$ in plateau regions.

D. The flux-balance construction on the reactive nullcline

Combining these insights with the fact that the stationary pattern must be embedded in a flux-balance sub-

space, we can identify plateaus and the inflection point as intersection points of a flux-balance subspace and the nullcline (FBS–NC intersections). As illustrated in Fig. 2, these *'landmark points'* in phase space enable us to graphically construct the spatial patterns in real space as two plateaus connected by an interface (*flux-balance construction*).

Near the interface the densities $\widetilde{\mathbf{u}}(x)$ of a stationary pattern will deviate from the corresponding local equilibria. The ensuing reactive flows (red arrows) left and right of the inflection point are of opposite sign and correspond to attachment and detachment zones for protein patterns (see Fig. 2a) [14]. Linearizing the phase-space flow around the landmark points will later enable us to further quantify the spatial profile of stationary patterns, i.e. to determine the relevant length scales.

E. Turnover balance determines η_0

Integrating one of the stationarity conditions, Eq. (14a), over the whole spatial domain $[0, L]$ yields that in steady state the total reactive turnover must vanish

$$\int_0^L \mathrm{d}x\, \tilde{f}(\widetilde{m}(x), \eta_0) = 0. \tag{16}$$

This *total turnover balance* determines the position η_0 of the flux-balance subspace in steady state. A mathematically more convenient form of turnover balance is obtained by multiplying Eq. (8a) with $\partial_x \widetilde{m}(x)$ before integrating:

$$\int_{\widetilde{m}(0)}^{\widetilde{m}(L)} \mathrm{d}m\, \tilde{f}(m, \eta_0) = 0. \tag{17}$$

In this form, it becomes evident that the total turnover balance does not depend on the full density profile $\widetilde{m}(x)$, but only on the densities at the boundaries, $\widetilde{m}(0)$ and $\widetilde{m}(L)$. Total turnover balance, Eq. (17), together with the stationarity condition for $\widetilde{m}(x)$, Eq. (14a), fully determine the stationary patterns.

Geometrically, total turnover balance can be interpreted as a kind of (approximate) Maxwell construction in the (m, c)-phase plane (balance of areas shaded in red in Fig. 2). This requires the following approximations. First, we linearize the reactive flow around the reactive nullcline (cf. Eq. (5)):

$$\tilde{f}(m, \eta_0) \approx \sigma_{\mathrm{loc}}(\tilde{n}(m)) \cdot [m - m^*(\tilde{n}(m))], \tag{18}$$

where $\tilde{n}(m) := \eta_0 + (1 - D_m/D_c)m$ because the pattern is embedded in the flux-balance subspace, cf. Eq. (10). The expression in the square brackets of Eq. (18) is simply the distance of the reactive nullcline from the flux-balance subspace measured along the respective local phase space. Further, suppose for the moment that the local eigenvalue $\sigma_{\mathrm{loc}}(n)$ is approximately constant in the range of total densities attained by the pattern. Turnover

balance, Eq. (17), is then represented by a balance of the areas between nullcline and flux-balance subspace on either side of the inflection point (see areas shaded in red (light gray) in Fig. 2b):

$$\int_{\widetilde{m}(0)}^{\widetilde{m}(L)} \mathrm{d}m\, [m - m^*(\tilde{n}(m))] = 0. \tag{19}$$

In the characterization of pattern profiles in Sec. V, we will use that for a spatial domain size L much larger than the interface width, one can approximate the plateau concentrations by FBS-NC intersections: $\widetilde{m}(0) \approx m_-(\eta_0)$ and $\widetilde{m}(L) \approx m_+(\eta_0)$. In this case, Eq. (17) is closed and can be solved for η_0, either numerically or geometrically using the approximate 'Maxwell construction,' Eq. (19).

Multiplying the stationarity condition, Eq. (14a), by $\partial_x \widetilde{m}(x)$ (as we did to obtain Eq. (17) for total turnover balance) and integrating over the spatial subinterval $[0, x_0]$), one obtains a relation that depends only on η_0 and the boundary concentrations $\widetilde{m}(0)$ and $\widetilde{m}(L)$:

$$\begin{aligned} \frac{1}{2} D_m \big(\partial_x \widetilde{m}\big|_{x_0}\big)^2 &= \int_{\widetilde{m}(0)}^{m_0(\eta_0)} \mathrm{d}m\, \tilde{f}(m, \eta_0) \\ &= -\int_{m_0(\eta_0)}^{\widetilde{m}(L)} \mathrm{d}m\, \tilde{f}(m, \eta_0). \end{aligned} \tag{20}$$

These equations state that the net turnover on either side of the pattern inflection point x_0, has to be balanced by the net diffusive flux across that point as illustrated by the blue arrow in Fig. 2a. Because the reactive flow changes sign at the inflection point, the reactive turnover (integrated flow) is extremal there and determines the maximal slope $\widetilde{m}'(x_0)$ of the pattern profile. Depending on how the reactive turnover saturates on either side of the inflection point, the system exhibits, as we will learn in Sec. V C, three distinct characteristic elementary pattern types, classified by the shape of the concentration profile $\widetilde{m}(x)$: mesas, peaks/troughs and nearly harmonic (or 'weakly nonlinear') patterns.

F. Summary of geometric structures in phase space

Let us pause for a moment and briefly summarize our findings so far. We have established three major geometric structures in (m, c)-phase space: First, the *reactive nullcline*, $f(m, c) = 0$, along which the local reaction kinetics are balanced; second, the *local phase spaces*, $m + c = \tilde{n}(x)$, determined by the local total densities $\tilde{n}(x)$—local equilibria $\mathbf{u}^*(\tilde{n}(x))$ are intersections of the reactive nullcline and the local phase spaces; third, the family of *flux-balance subspaces*, within which diffusive flows in membrane and cytosol balance each other. The position of the flux-balance subspace, η_0, of a stationary pattern is determined by total turnover balance, Eq. (17), which represents a balance of reactive processes.

This geometric picture underlies the key results we present in the remainder of the paper. Up to now, we

only discussed the embedding of the pattern in the (m, c)-phase plane. To study the possible pattern profile shapes $\widetilde{m}(x)$ in real space, we need to understand the dynamic process of pattern formation, in particular the factors determining the interface region. As we will see below (Sec. V), the interface of a pattern is inherently connected to lateral instability. We will therefore first analyze lateral instability and the dynamic process of pattern formation in the following section. With these tools at hand, we will then be able to characterize the distinct pattern types exhibited by 2C-MCRD systems.

IV. LATERAL INSTABILITY

How can the geometric structures introduced in the previous section help us to understand the physical process of pattern formation? Previous research [16] suggests that the total densities are the essential degrees of freedom and their redistribution is the key dynamic process. Building on this insight, we systematically connect the geometric structures established above (Sec. III) to the lateral instability, i.e. instability against spatially inhomogeneous perturbations, of a homogeneous steady state.

A. Mass-redistribution instability

Consider the dynamics of the local total density $n(x,t) = c(x,t) + m(x,t)$. Because the kinetics conserve local total density, the time evolution of $n(x,t)$ is driven only by diffusion due to spatial gradients in the concentrations $c(x,t)$ and $m(x,t)$:

$$\partial_t n(x,t) = D_c \partial_x^2 c(x,t) + D_m \partial_x^2 m(x,t). \qquad (21)$$

As a result of mass redistribution, the local equilibrium concentrations $\mathbf{u}^*(n(x,t))$ change. In turn, these locally shifted equilibrium concentrations induce changes in the local reactive flows and thereby result in altered spatial gradients in $\mathbf{u}(x,t)$. This intricate coupling between redistribution of total mass, reactive flows, and diffusive flows drives pattern formation.

Qualitatively, this coupling between reactive and diffusive flow can be understood by observing that the dynamics depends mainly on the direction in which the local equilibria shift due to increasing or decreasing local total density. Let us therefore posit that the relevant diffusive gradients can be (qualitatively) estimated by replacing the local concentrations by the (locally stable) local equilibrium

$$\mathbf{u}(x,t) \to \mathbf{u}^*\big(n(x,t)\big), \qquad (22)$$

such that the local mass $n(x,t)$ is the only remaining degree of freedom:

$$\partial_t n(x,t) \approx D_c \partial_x^2 c^*(n) + D_m \partial_x^2 m^*(n). \qquad (23)$$

We term this the *local quasi-steady state approximation*. Note that this approximation becomes exact in the long wavelength limit where diffusive redistribution is much slower than chemical relaxation; see Sec. IV B and Appendices C and D for a detailed discussion. Applying the chain rule once, we can rewrite the mass redistribution dynamics as

$$\partial_t n(x,t) \approx \partial_x \big[\big(D_c \, \partial_n c^* + D_m \, \partial_n m^*\big) \partial_x n\big] \qquad (24)$$

which is simply a diffusion equation for the total density $n(x,t)$. For locally stable equilibria, the effective diffusion constant will become negative (which entails anti-diffusion) if

$$\frac{\partial_n c^*}{\partial_n m^*} = s_{\mathrm{nc}}(n) = -\frac{f_m}{f_c} < -\frac{D_m}{D_c}, \qquad (25)$$

where $s_{\mathrm{nc}}(n) = \partial_m c^*(m)|_n$ is the slope of the reactive nullcline $c^*(m)$ (cf. Eq. (6) in Sec. III A; note that local stability ensures $\partial_n m^* > 0$ when $f_c > 0$, for $f_c < 0$ the inequality Eq. (25) is reversed). Hence, starting from a homogeneous steady state $\mathbf{u}^*(\bar{n})$, a *lateral instability* due to effective anti-diffusion takes place if (and only if)

$$s_{\mathrm{nc}}(\bar{n}) < -\frac{D_m}{D_c}. \qquad (26)$$

This condition for lateral instability has a simple geometric interpretation in the (m, c)-phase plane: A spatially homogeneous steady state with total density $\bar{n}$ is laterally unstable if the slope of the nullcline is steeper than the slope of the flux-balance subspace. We term the mechanism a *mass-redistribution instability* to emphasize the underlying physical process and to contrast this mechanism to the "activator–inhibitor mechanism" (see Sec. VIII B 3 in the Discussion). Importantly, the mass-redistribution instability in reaction–diffusion systems is a Turing instability [55], in the sense that it is a diffusion-driven instability of a system that is stable in a well-mixed situation (i.e. stable against spatially homogeneous perturbations) [56]. The bifurcation where a homogeneous steady state becomes laterally unstable, i.e. Turing unstable, will be referred to as a *Turing bifurcation*.

The mass-redistribution dynamics, Eq. (24), can be rewritten most compactly using the mass-redistribution potential, η, (cf. Eq. (12)):

$$\partial_t n(x,t) \approx D_c \partial_x \big[\partial_n \eta^*(n) \, \partial_x n\big]. \qquad (27)$$

This implies that a mass-redistribution instability occurs if an increase in total density entails a decrease of the mass-redistribution potential (i.e. $\partial_n \eta^*|_{\bar{n}} < 0$).

Importantly the instability condition, Eq. (25), can be related directly to an underlying physical mechanism. For illustration purposes let us disregard membrane diffusion ($D_m = 0$). Following a small modulation δn of the mass on a large length scale, the local reactive equilibrium within each compartment shifts (1 in Fig. 3a).
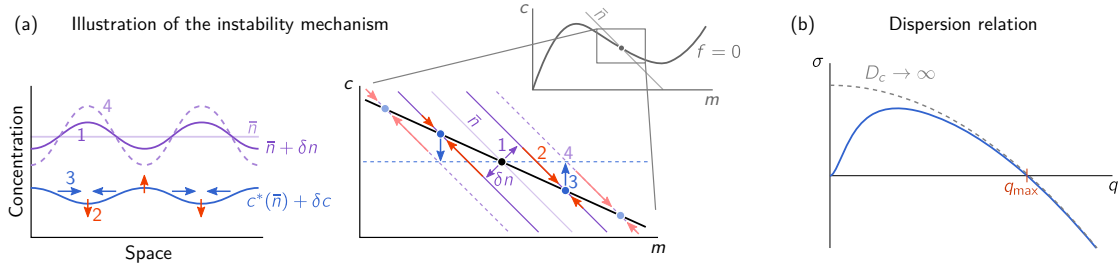
FIG. 3. Mass-redistribution instability. (a) Illustration of the underlying mechanism. Consider a small amplitude modulation of the total density (purple line in the real space plot) on a large length scale (1). As diffusion is slow on large scales, the system will locally relax to its reactive equilibrium (2). The resulting cytosolic density profile $\delta c(x) \approx \partial_n c^*(n)|_{\bar{n}} \delta n(x)$ is shown by the blue line in the real space plot. If the cytosolic equilibrium density decreases due to an increase of total density (i.e. if the nullcline slope, s_{nc}, is negative), the ensuing diffusive fluxes in the cytosol (3) will amplify the modulation of the total density profile (4), thus driving an instability. The membrane gradient is opposite to the cytosolic one, such that membrane diffusion counteracts the instability and suppresses it if $s_{nc} > -D_m/D_c$; cf. Eq. (25). (b) Dispersion relation (solid blue line). In the limit $D_c \to \infty$, the dispersion relation approaches the function $f_m - D_m q^2$ shown as gray, dashed line. This limit is discussed in Appendix C 3.

The instability criterion, Eq. (25), requires the slope of the reactive nullcline to be negative. In this case, the equilibrium shifts to lower cytosolic concentration $c^*(n)$ as total density n is increased. In other words, in regions with a higher total density, there will be a reactive flow onto the membrane (red arrows) as the shifted local equilibrium is approached—thus creating cytosolic sinks (2 in Fig. 3a). Conversely, the regions with lower total density become cytosolic sources. The ensuing cytosolic gradient leads to diffusive mass-redistribution (3), resulting in a further shift of the local equilibria (4), thus sustaining and amplifying the diffusive flux—the cycle feeds itself. Taken together, this shows that the *mass-redistribution instability is a self-amplifying mass redistribution cascade.* In contrast, when the cytosolic equilibrium density rises due to an increase in total density (i.e. for positive nullcline slope $\partial_n c^*|_{\bar{n}} > 0$) the compartment with more total density will become cytosolic source inducing mass redistribution that brings the system back to a homogenous state.

B. Diffusion- and reaction-limited regimes

On sufficiently large length scales, diffusive relaxation (transfer of mass) is slow compared to chemical relaxation $D_c q^2 \ll |\sigma_{loc}|$, such that the local quasi-steady state approximation Eq. (22) becomes exact—the concentrations are *slaved* to the local equilibria. This is the *diffusion-limited* regime: the growth rate of the lateral instability is limited by cytosolic redistribution via diffusion ($\sigma_{lat} \approx -\partial_n c^* \cdot D_c q^2$). In contrast, if cytosolic diffusion is much faster than chemical relaxation ($D_c q^2 \gg |\sigma_{loc}|$), the lateral instability is limited by the rate at which the shifting equilibria are approached ($\sigma_{lat} \approx \partial_n c^* \cdot \sigma_{loc} = f_m$). This is the *diffusion-limited*

regime. Importantly, the concept of shifting local equilibria still informs about the presence of the lateral instability in this regime. But it does no longer yield the growth rate quantitatively. A more detailed discussion of the local quasi-steady state approximation is provided in Appendix D.

The principle of shifting local equilibria provides insight into the spatial dynamics of systems with more than two components: In a five-component MCRD model for *in vitro* Min patterns, the concept of scaffolding allowed to predict the transition to chaos (qualitative change of the local attractors from stable fixed point to limit cycle) [16]. Notably, in this system, the onset of lateral instability is not a long wavelength instability but takes place for a band of unstable modes bounded away from $q = 0$, corresponding to 'type I' instability in the Cross–Hohenberg classification scheme. Thus, the principle of shifting local equilibria is not restricted to systems with a long wavelength ('type I') instability.

C. The marginal mode q_{max} reveals the role of membrane diffusion

Let us compare the instability criterion Eq. (25) to 'classical' linear stability analysis of Eq. (1) around the homogenous steady state (see Appendix C). There one obtains the dispersion relation $\sigma(q)$ for the growth rate σ of a mode with wavenumber q (see Fig. 3b). It exhibits a band of unstable modes, $\sigma(q) > 0$ for $0 < q < q_{max}$, with

$$q_{max}^2 := \frac{f_m}{D_m} - \frac{f_c}{D_c} = \frac{\tilde{f}_m}{D_m} \qquad (28)$$

if and only if $f_m/D_m > f_c/D_c$, i.e. exactly when the slope criterion, Eq. (25), is fulfilled. Equation (28) can be rewritten as $q_{max}^2 = f_c/D_m(-s_{nc} - D_m/D_c)$, which

shows why the slope criterion Eq. (25) is reversed for $f_c < 0$.

The instability condition Eq. (25) and the expression for the edge of the edge of the band of unstable modes Eq. (28) inform about the role of membrane diffusion as counteracting the cytosolic mass-redistribution that drives the instability. This is because the membrane gradient will always be opposed to the cytosolic gradient whenever the nullcline slope is negative ($-1 < \partial_n c^* < 0$) (because $\delta m = \delta n - \delta c$ and $\delta c^* = \delta n\, \partial_n c^*$).

The expression for q_{max} can be found quite easily by utilizing phase-space geometry. We start from the observation that q_{max} is a non-oscillatory marginal mode; it cannot be oscillatory for a locally stable fixed point, $\sigma_{loc} < 0$, as shown in Appendix C. Hence, the eigenvalue $\sigma(q_{max}) = 0$, so the mode $\sim \cos(q_{max} x)$ must fulfill the steady-state condition, Eq. (8), and the corresponding eigenvector must point along a flux-balance subspace $\propto (1, -D_m/D_c)^{\mathrm{T}}$ in phase space. The steady state condition in flux-balance subspace is given by Eq. (14a), which, in linearization around a homogeneous steady state reads

$$0 = D_m \partial_x^2 \delta m(x) + \left[f_m - \frac{D_m}{D_c} f_c \right]_{\bar{n}} \delta m(x). \qquad (29)$$

This equation is solved by the mode $\delta m(x) \propto \cos(q_{max} x)$ with $q_{max}^2 = f_m/D_m - f_c/D_c$ (cf. Eq. (28)). To conclude, the two effects of membrane diffusion are interlinked in the expression for q_{max}: (i) The condition $q_{max} = 0$ determines the critical NC-slope ($s_{nc}^{crit} = -D_m/D_c$) for the (long wavelength) onset of lateral instability. (ii) In the laterally unstable regime, q_{max} determines the smallest unstable length scale $\ell = q_{max}^{-1}$. In the limit of large D_c, this length scale is given by $\ell^2 \approx D_m/f_m$, i.e. a balance of membrane diffusion and reactive flows. In the next section, it will be shown that the marginal mode q_{max} *at the pattern inflection point* determines (to leading order) the interface width of a stationary pattern.

V. CHARACTERIZATION OF STATIONARY PATTERNS

With an intuitive picture of the principles underlying pattern formation in 2C-MCRD systems in hand, we now return to the spatially continuous system. We first study the characteristic types of stationary patterns exhibited by 2C-MCRD systems, focusing on *elementary* stationary patterns with monotonic concentration profiles on a domain with no-flux boundaries. More complex, nonmonotonic stationary patterns (also in domains with periodic boundary conditions) can always be dissected into such elementary patterns at their extrema (recall that due to the diffusive flux-balance condition, Eq. (9), extrema in $\widetilde{m}(x)$ and $\widetilde{c}(x)$ must coincide). Previous studies have observed that 2C-MCRD systems typically exhibit coarsening [24, 25, 34, 57]. In a follow-up work building on the concepts presented here, we show that coarsening

is indeed generic in all 2C-MCRD systems, independently of the specific form of the reaction kinetics [15].

A. Interface width

The width of the interfacial region, ℓ_{int}, is the only intrinsic length scale of the elementary patterns. Recall that the pattern inflection point, which defines the position of the interface region, is in local reactive equilibrium—geometrically determined by an FBS–NC intersection (m_0, c_0) (cf. Fig. 2 in Sec. III C). The interface is maintained by a balance of diffusion and the reactive flow in the vicinity of the inflection point. Therefore, the interface $\widetilde{m}(x - x_0) \approx m_0 + \delta\widetilde{m}(x)$ is to leading order determined by linearizing the steady-state equation, Eq. (14a), around the inflection point,

$$0 = D_m \partial_x^2 \delta\widetilde{m}(x) + \left[f_m - \frac{D_m}{D_c} f_c \right]_{n_0} \delta\widetilde{m}(x), \qquad (30)$$

where $n_0 = m_0 + c_0$, and we used the flux-balance subspace constraint, Eq. (10), to substitute the cytosol concentration $\delta\widetilde{c}(x)$. Equation (30) exactly resembles the equation that determines the marginal mode $\sin(q_{max} x)$ in the dispersion relation (right-hand edge of the band of unstable modes). Hence, the interface length scale is determined by the marginal mode of the dispersion relation *at the inflection point*:

$$\ell_{int} \simeq \pi/q_{max}(n_0) = \pi\sqrt{D_m/\tilde{f}_m|_{n_0}}. \qquad (31)$$

The interface shape is approximated by the corresponding eigenfunction $\delta\widetilde{m}(x) \propto \sin\big(q_{max}(n_0)x\big)$.

Let us pause for a moment to look at the interface region from the perspective of mass redistribution: the total density n_0 at the inflection point is such that the corresponding reactive equilibrium is *laterally* unstable, because the nullcline slope is steeper than the FBS-slope there; see Fig. 4 below, where we elaborate on this point in terms of spatial *regions*. From the spectrum of modes, only the marginally stable one, $q_{max}(n_0)$, fulfills the (linearized) stationarity condition. Thus, intuitively it must be the q_{max}-mode that determines the interface length scale. Importantly, because the pattern is formed by mass redistribution, the total density n_0 at the inflection point does not coincide in general with the average total density $\bar{n}$. The interface width is determined $q_{max}(n_0)$, not by $q_{max}(\bar{n})$. This also implies that the interface width depends on the FBS-position η_0 because the inflection point (m_0, c_0), and hence $n_0 = m_0 + c_0$, is determined geometrically as FBS-NC intersection point. We explicitly denote the interface width by $\ell_{int}(\eta_0)$ when we use this relationship in the following.

Finally, to approximate the stationary concentration profile of the interface, we use that its maximal slope $\widetilde{m}'(x_0)$ is attained at the pattern inflection point x_0 and can be calculated by flux-turnover balance (20). Together

with the harmonic mode $\delta\widetilde{m}(x) \propto \sin(\pi x/\ell_{\text{int}})$ obtained by linearizing phase space flow, we find

$$\widetilde{m}(x) \approx m_0 + \widetilde{m}'(x_0)\frac{\ell_{\text{int}}}{\pi}\sin\left(\pi\frac{x - x_0}{\ell_{\text{int}}}\right), \qquad (32)$$

in the vicinity of the inflection point. To go beyond this leading order approximations, one can perform a perturbative expansion of $\tilde{f}(m_0 + \delta m, \eta_0)$ and $\widetilde{m}(x_0 + \delta x)$ in Eq. (14a) around the pattern inflection point (m_0, η_0). The solution of this expansion can then be matched to the plateaus to obtain an approximation of the interface profile shape. Linearization around the plateaus yields exponential decay towards the plateaus ("exponential tails") $\sim \exp(-x/\ell_\pm)$, where the decay lengths are given by $\ell_\pm^2 = D_m/\tilde{f}_m(n_\pm)$.

B. Regions generalize the concept of local compartments

Not only the interfaces (n_0) but also the plateaus ($n_\pm$) of patterns correspond to FBS-NC intersection points in phase space (Fig. 4). However, in contrast to the interface, the plateaus lie on laterally stable sections of the nullcline where $s_{\text{nc}}(n_\pm) > -D_m/D_c$; recall the slope criterion for lateral instability Eq. (25). Put more precisely, the pattern profile becomes flat in the vicinity of $n_\pm$ *because* of regional lateral stability [58].

Thus, the FBS-NC intersection points act as "landmark points" that enable us to (notionally) dissect the pattern profile into spatial regions (plateaus and interface) in such a way that these spatial regions can be associated with regional phase spaces. The (linearized) properties of the reaction–diffusion dynamics—encoded in the *regional dispersion relations* (Fig. 4d)—in the vicinity of these landmark points can be used to determine the regional properties in real space. Within each of these regions, we can ask what would happen there if we were to isolate it from the rest of the system, akin to the question we asked in the context of local equilibria. Just as the local equilibria scaffold the interface, these regional "attractors" serve as scaffolds for the global pattern. The regional properties depend on the average regional mass which is redistributed between regions by diffusion, and the properties of the full pattern can be pieced together by (characteristically distinct) isolated regions (plateaus and interfaces).

Taken together, the nonlinear kinetics is encoded by the nullcline shape. The internal properties of the spatial regions are determined by *regionally linear* properties of phase space flow, encoded in the regional dispersion relations. We will therefore refer to this as the *method of regional phase-spaces and regional attractors*. This method bridges the gap between the linear and the highly nonlinear regime.

Finally, let us note that based on the region decomposition (cf. Fig. 4), the interface position—determining the global spatial structure—can be pictured as a collective degree of freedom. A conceptually similar, but technically more involved approach to study interfaces (also called 'kinks' or 'internal layers') and their dynamics is singular perturbation theory (specifically matched asymptotic expansion) where one uses an asymptotic separation of spatial scales, see e.g. Ref. [61] and references therein. Such methods also facilitate a phase-space geometric analysis [9].

C. Pattern classification

Employing the concept of regions we will now turn to the classification of patterns. We distinguish two generic pattern types: mesas and peaks. Mesa patterns are composed of plateaus (low density and high density) connected by an interface (Fig. 5a, c and d), while the term peak refers to an interface concatenated to a plateau only on the low density site (Fig. 5b) [62]. For small systems, close to onset, there is an additional pattern type comprising only an interface that spans the whole system; see Sec. VII D.

What are the conditions for the formation of a peak pattern versus the formation of a mesa pattern? A mesa pattern requires two plateau regions, each characterized by an FBS-NC intersection point, one at low density and one at high density. The low density plateau is generically present because the densities must be positive and thus are bounded from below. In contrast, the position of the FBS-NC intersection point at high density depends sensitively on the shape of the nullcline and the slope of the diffusive flux-balance subspace $-D_m/D_c$. Let us first consider the case of fast cytosol diffusion $D_c \gg D_m$. For an N-shaped nullcline, i.e. one that has an "upwards-pointing" tail (see Fig. 5a), the flux-balance construction presented in Sec. III C yields a mesa pattern. The situation is different for a "Λ-shaped" nullcline that has an asymptotically flat tail for large m (e.g. approaching $c^*(m) \to 0$ for $m \to \infty$); see Fig. 5b. In that case the third FBS-NC intersection point generically is far away from the first two; in Fig. 5b it lies out of frame. The requirement of total turnover balance (approximated by a balance of the areas shaded in light red in the Fig. 5) limits the maximum membrane concentration $\hat{m}$, such that there is no high density plateau and the pattern assumes a peak profile instead (Fig. 5b bottom). In the detailed analysis of peak patterns below, we will show that the FBS-position η_0, and thus the peak amplitude, is determined by the total mass in the system

Let us now consider what happens if the FBS is made steeper by lowering the ratio of diffusion constants D_c/D_m. As the FBS becomes steeper, the third FBS-NC intersection point moves towards lower membrane concentration. Eventually, this limits the total turnover on the right hand side of the inflection point, such that the peak amplitude saturates in a plateau, i.e. a mesa pattern forms (Fig. 5d). In the case of an N-shaped null-
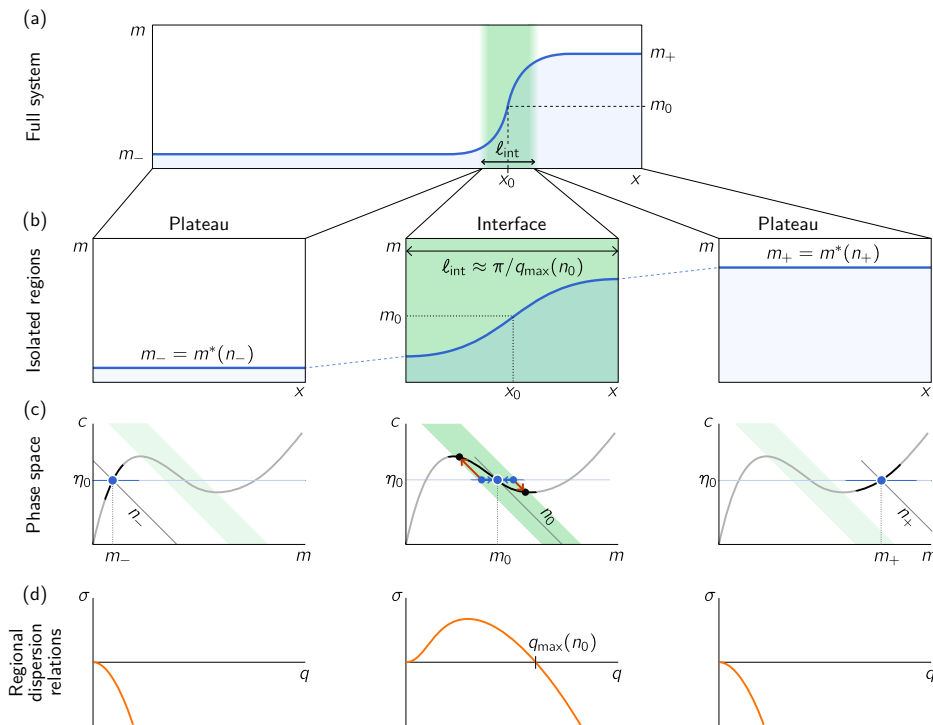
FIG. 4. Decomposition of a stationary pattern (a) into spatial regions that correspond to (m, c)-phase-space regions in the vicinity of landmark points. (b) Three characteristic spatial regions of the pattern (plateaus and the interface) can be notionally isolated. (c) The different average total densities n_-, n_0, and n_+ in three spatial regions determine the phase space regions corresponding to these spatial regions. The phase space region associated to laterally unstable nullcline segment is shaded in green. (d) Linearization of the reaction–diffusion dynamics around the reactive equilibria at n_-, n_0, and n_+ yields *regional dispersion relations* that determine the properties of the regions. The plateaus are laterally stable regions, while the interface region is necessarily laterally unstable. The interface width can be estimated by the marginally stable mode $q_{\max}(n_0)$ at the right-hand edge of the dispersion relation of the interface region: $\ell_{\text{int}} \simeq \pi/q_{\max}(n_0)$.

cline, lowering D_c reduces the concentration difference between the two plateaus, because the FBS-NC intersection points move closer together (Fig. 5c).

Taken together, the phase-plane analysis reveals how the interplay of nonlinear reactions (encoded in the nullcline shape) and diffusion (encoded in the FBS-slope) determine the pattern type and pattern amplitude.

1. Mesa patterns

To characterize mesa patterns in the limit $L \gg \ell_{\text{int}}$, we first determine the FBS-position, η_0, using total turnover balance, Eq. (17) (cf. Sec. III C). Since the plateaus are scaffolded by (laterally stable) local equilibria we can approximate the boundary concentrations

$$\widetilde{m}(0) \approx m_-(\eta_0), \quad \widetilde{m}(L) \approx m_+(\eta_0), \tag{33}$$

where the *plateau scaffolds* $m_\pm(\eta_0)$ are geometrically determined in phase space as intersection points $m_\pm(\eta_0)$ of

FBS and NC:

$$\tilde{f}(m_\pm, \eta_0) = 0. \tag{34}$$

With the approximation, Eq. (33), the total reactive turnover balance condition, Eq. (17), becomes:

$$\eta_0^\infty : \int_{m_-^\infty}^{m_+^\infty} \mathrm{d}m \, \tilde{f}(m, \eta_0^\infty) = 0, \tag{35}$$

where $m_\pm^\infty = m_\pm(\eta_0^\infty)$ and η_0^∞ denotes the FBS-position in the large system size limit. Equation (35) is closed and can be solved for η_0^∞. Once one has determined η_0^∞, the interface width $\ell_{\text{int}}(\eta_0^\infty)$ can be estimated with Eq. (31).

This *total turnover balance* condition implicitly determines the FBS-offset $\eta_0 = \eta_0^\infty$. Note that equation Eq. (35), and hence η_0^∞ depends only on the function f and the ratio of the diffusion constants, but not on the average mass $\bar{n}$ or the domain size L in the limit $L \gg \ell_{\text{int}}$. Instead, the average total density $\bar{n}$ determines the position x_0 of the interface. Again assuming an interface much narrower than the domain size,
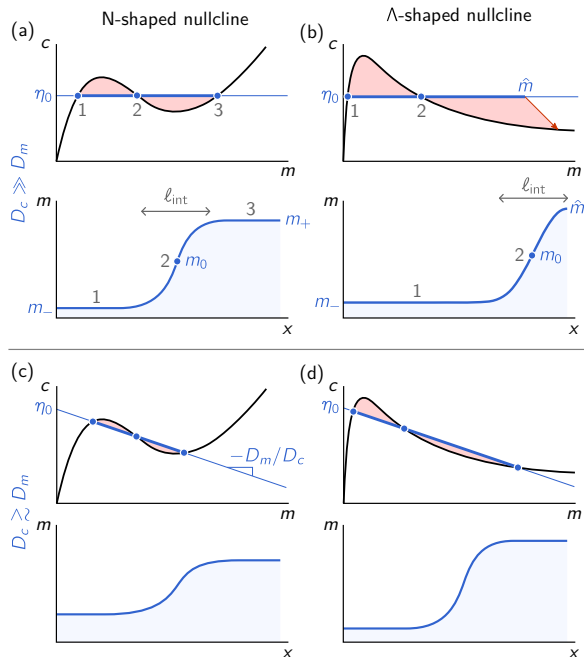
FIG. 5. Nullcline shape, and FBS-slope (diffusion constant ratio), and average total density determine wether a mesa or a peak pattern forms. Top row: fast cytosol diffusion; bottom row: slow cytosol diffusion. Each panel shows the pattern profile (top) and the respective phase portrait (bottom). (a,c and d) Mesa patterns; the average total density, $\bar{n}$, determines the position of the interface; see Eq. (36). (c) A peak pattern forms if the pattern amplitude does not saturate in a third FBS-NC intersection point. The peak amplitude is determined by the average total density, $\bar{n}$, via the interface width ℓ_{int}; see Eq. (39). As $\bar{n}$ is increased, the peak amplitude will grow, eventually reaching the third FBS-NC intersection point such that a mesa pattern forms.

the contribution of the interface region can be neglected, $L\bar{n} \approx n_-^\infty x_0 + n_+^\infty(L - x_0)$, which yields

$$x_0 \approx L \frac{n_+^\infty - \bar{n}}{n_+^\infty - n_-^\infty}, \qquad (36)$$

where n_+^∞ and n_-^∞ are the average total densities in the plateau regions:

$$n_\pm^\infty := \eta_0^\infty + (1 - D_m/D_c)\, m_\pm(\eta_0^\infty). \qquad (37)$$

This shows that the amplitude of mesa patterns is geometrically determined by the reactive nullcline alone and does not sensitively depend on average mass $\bar{n}$ or system size $L \gg \ell_{\text{int}}$. Moreover, far away from the critical point $D_c^{\min}$, cf. Sec. VII A the mesa-pattern amplitude becomes independent of the ratio of the diffusion constants. Adding mass to a mesa pattern shifts the interface position x_0 as the additional mass is redistributed between the two plateau regions.

Notably, a geometric argument shows that mesa patterns are the generic pattern for $L \to \infty$ when the ratio of the diffusion constants is nonzero $D_m/D_c > 0$, and $m \geq 0$, $c \geq 0$ (as must be the case for concentrations): The FBS intersects the m-axis ($c = 0$) at $(D_c/D_m)\eta_0$, and hence must intersect the nullcline at some finite value $m < (D_c/D_m)\eta_0$. For $L \to \infty$ keeping the average mass $\bar{n}$ constant, the pattern profile will eventually reach this third FBS–NC intersection point, and thus become a mesa pattern. Next, we will discuss the conditions under which peak/trough patterns occur.

The approximation Eq. (33) for the plateau densities, and in turn also Eq. (36) for the interface position, will break down when the distance of the interface to one of the system boundaries becomes smaller than the interface width $\ell_{\text{int}}(\eta_0^\infty)$. Then the stationary pattern no longer exhibits a plateau on that side and instead becomes a plateau–interface pattern, forming either a peak when $\bar{n}$ is close to n_-^∞, or a trough ('anti-peak') when $\bar{n}$ is close to n_+^∞. An estimate for these transition from mesa to peak/trough patterns can be obtained based on the approximated interface position, Eq. (36):

$$L\left|\bar{n} - n_\pm^\infty\right| \lesssim \ell_{\text{int}}(\eta_0^\infty)\left(n_+^\infty - n_-^\infty\right). \qquad (38)$$

2. Peak patterns

Let us now study these peak/trough patterns. Their defining characteristic is that a plateau, corresponding to laterally stable FBS-NC intersection point, forms only only on one side of the interface. Correspondingly, the reactive turnover saturates on the side where the plateau forms, while it depends on the variable pattern amplitude on the other side. For specificity, we focus on peak patterns here. As explained above, such a peak pattern forms when the nullcline is Λ-shaped, flux-balance subspace is very shallow ($D_c \gg D_m$); see Fig. 5b.

Suppose for a moment that we can freely choose the FBS-position, η_0, and that the total mass is not fixed. Given some η_0, the FBS-NC intersection point (1) determines the low-density plateau at the foot of the interface and thus the total turnover on this side, corresponding to the enclosed area in the interval between (1) and (2). This turnover must be balanced by an equal and opposite turnover on the right. Using again the (approximate) correspondence to the enclosed phase-plane area, it becomes obvious that this balance of areas determines the peak amplitude $\hat{m}$ (3). Using that the interface profile can be approximated as $\propto \sin((x - x_0)/\ell_{\text{int}})$, where ℓ_{int} is determined by the steady state equation linearized around the pattern inflection point (see Sec. V A), we can roughly estimate the total mass in a peak as [63]

$$N_{\text{peak}}(\eta_0) \approx \frac{1}{2}\ell_{\text{int}}(\eta_0)\left[\hat{m} - m_-(\eta_0)\right]. \qquad (39)$$

The sinusoidal shape of the interface furthermore mandates that the inflection point m_0 is approximately halfway between the plateau m_- and the maximum $\hat{m}$, such

that we can eliminate $\hat{m} \approx m_- + 2(m_0 - m_-)$ in Eq. (39). The remaining unknowns m_0 and m_- are determined geometrically (FBS–NC intersections) as functions of η_0. Thus we obtain a relation for the average total density $\bar{n}(\eta_0) \approx n_-(\eta_0) + N_{\mathrm{peak}}(\eta_0)/L$ as a function of η_0. The inverse of this relation yields the FBS-position $\eta_0(\bar{n})$ as a function the control parameter $\bar{n}$. This estimate will hold until the peak density $\hat{m}$ reaches the third FBS-NC intersection point $m_+(\eta_0)$, where a second plateau will start to form, such that the peak pattern transitions to a mesa pattern. In Appendix G we present the details of the peak approximation, and a comparison to numerical solutions.

Our estimate for the peak mass Eq. (39) and the resulting relation $\eta_0(\bar{n})$ show that, in contrast to mesa patterns, the amplitude of peak patterns sensitively depends on the total mass $N = L\bar{n}$ and the membrane diffusion constant (via $\ell_{\mathrm{int}}^2 \sim D_m/f_m$, cf. Eq. (31)). In addition, the position of the third FBS-NC intersection point $m_+(\eta_0)$ that limits the maximum peak density, sensitively depends on the FBS slope $-D_m/D_c$. In the limit $D_m/D_c \to 0$, the third FBS-NC intersection point m_+ moves to infinity. Hence, in this limit, a system with an asymptotically flat nullcline tail never exhibits mesa patterns.

3. More general nullcline shapes

Here we considered two types of nullcline shapes—N- and Λ-shaped—that both have a single maximum in the (m, c)-phase plane, but differ in their 'tail behavior'. Beyond these two prototypical nullcline shapes, more general nullcline shapes are possible. For instance, reaction kinetics of the attachment–detachment form, Eq. (2), with higher order nonlinearities (e.g. 5th-order polynomials) may exhibit nullclines with multiple maxima in the (m, c)-phase plane. For general reaction kinetics $f(m, c)$, more exotic shapes of the nullclines, e.g. with multiple disconnected branches, are possible. Our findings equally apply to such nullclines since our phase-space analysis is based on simple geometric properties such as slopes and intersection points with the FBS. Additional care is required if f_c changes sign along the nullcline, since the slope criteria for local and lateral stability, Eqs. (7) and (25), are reversed for $f_c < 0$. Conveniently, for reaction kinetics of the attachment–detachment form, Eq. (2), one has $f_c = a(m)$ which is generally positive for systems of biochemical origin.

D. Generic bifurcation structure under variation of the average mass $\bar{n}$

Now that we have classified the different types of stationary patterns exhibited by 2C-MCRD systems, we turn to study bifurcations where the patterns change structurally or in stability. The bifurcation parameter we study first is the average total density $\bar{n}$. This pa-
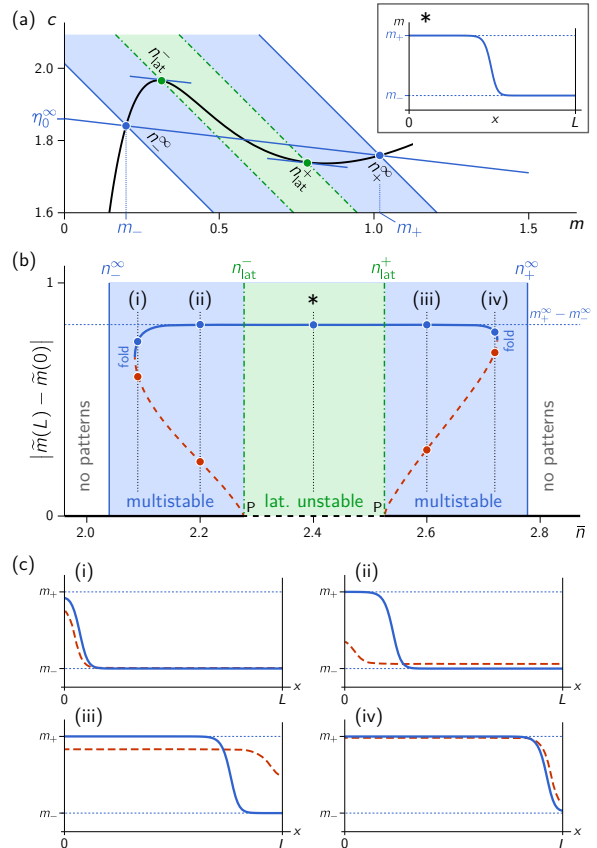
FIG. 6. Bifurcations of mesa patterns in the large system size limit ($L \to \infty$) can be constructed geometrically using the reactive nullcline. (a) Geometric construction of pattern bifurcation points for an example two-component system: Eq. (A1*) with $k = 0.07$, $D_m = 1$, and $D_c = 10$. The laterally unstable regime (shaded in green) is delimited by Turing bifurcations where the FBS is tangential to the NC (green dots, $n_\pm^{\mathrm{lat}}$). FBS-NC intersection points (blue dots, $n_\pm^\infty$), delimit the range of pattern existence (shaded in blue), where the FBS-position, η_0^∞, is determined by global turnover balance, Eq. (17). Inset in the top right corner: membrane density $\widetilde{m}(x)$ of a stable mesa pattern for $\bar{n} = 2.4$ (see star in (b)). (b) Bifurcation structure of the pattern amplitude $|\widetilde{m}(L) - \widetilde{m}(0)|$ for the control parameter $\bar{n}$ obtained by numerical continuation (cf. Appendix F) for a system size of $L = 100$. The branch of stable patterns (solid blue line) and the branches of unstable patterns (dashed red line) meet in fold bifurcations of patterns. Due to the finite system size, these fold bifurcations are offset from $n_\pm^\infty$ (vertical solid blue lines) by an amount $\sim \ell_{\mathrm{int}}(\eta_0^\infty)/L$. The unstable patterns emerge in subcritical pitchfork bifurcations (P) from the homogeneous steady state (black line) at the Turing bifurcations (vertical dash-dotted green lines). (c) Profiles $\widetilde{m}(x)$ of stationary patterns (solid blue: stable, dashed red: unstable) for the average total densities $\bar{n} = 2.09, 2.2, 2.6,$ and 2.72 (see thin dashed lines in (b)). The plateau scaffolds $m_\pm(\eta_0^\infty)$ are shown as thin black lines.

rameter does not affect the phase-space geometry (NC and FBS), which makes it particularly easy to study. Later, in Sec. VII, we generalize our findings to bifurcation parameters that change the phase-space geometry: diffusion constants change the FBS-slope, whereas kinetic rates affect the nullcline shape. For biological systems, the average total density $\bar{n}$ is a natural parameter as it can be tuned by up- or down-regulating the production of a protein.

Let us begin with the bifurcations where the homogenous steady state becomes laterally unstable. We already learned in Sec. IV that there is a band of unstable modes, $[0, q_{max}]$, if the NC-slope $s_{nc}(\bar{n})$ is negative and steeper than the FBS-slope, $-D_m/D_c$ (cf. Eq. (25) and Fig. 3a). Hence, a band of unstable modes exists if $\bar{n}$ is in the range (n_{lat}^-, n_{lat}^+), bounded by the points $n_{lat}^\pm$ where the flux-balance subspace is tangential to the reactive nullcline (dash-dotted green lines in Fig. 6a. (Note that a system of finite size L, is unstable if the longest wavelength mode lies in the band of unstable modes $\pi/L < q_{max}(\bar{n})$, where $q_{max}^2 = \tilde{f}_m/D_m$, as defined in Eq. (28) and $\tilde{f}_m = f_m - f_c D_m/D_c = (-D_m/D_c - s_{nc})f_c$.)

What about the range where stationary patterns exist? The plateau scaffolds $m_\pm(\eta_0)$ are geometrically determined by the reactive nullcline via the FBS–NC intersection points. The position η_0 of the flux-balance subspace generally depends on $\bar{n}$ and L via total turnover balance, Eq. (17). However, in the large system size limit $(L \to \infty)$, the FBS position η_0^∞ is independent of $\bar{n}$ and L (cf. Eq. (35)). For patterns to exist, the average total density $\bar{n}$ must lie in-between the plateau densities $n_\pm^\infty$; see Fig. 6a, cf. Eq. (36). Hence, in the limit $L \to \infty$, stationary patterns exist in the range $n_-^\infty < \bar{n} < n_+^\infty$.

Importantly the range of pattern existence generically extends beyond the range of lateral instability $(n_{lat}^- > n_-^\infty$ and $n_{lat}^+ < n_+^\infty)$ by geometric necessity for N-shaped nullclines; see Fig. 6a. This implies, that generically there are regions of multistability in parameter space, where stable stationary patterns exist, and the homogeneous steady state is stable (regions shaded in blue in Fig. 6).

To gain some intuition on the steady states in the multistable regimes, we performed numerical continuation (see Appendix F for details) of the stationary patterns for an example 2C-MCRD system using the attachment–detachment kinetics Eq. (A1*) from Ref. [28] which exhibit an N-shaped nullcline. Figure 6b shows the numerically obtained bifurcation structure where we plot the pattern amplitude $|\widetilde{m}(L) - \widetilde{m}(0)|$ against the bifurcation parameter $\bar{n}$. The star marks a typical stable mesa pattern (see inset in Fig. 6a) in the central region of the branch of stable patterns (solid blue line). As the plateaus are scaffolded by the FBS-NC intersections $m_\pm(\eta_0^\infty)$, the pattern amplitude stays approximately constant $(m_+ - m_-$, dotted blue line) across the whole range of $\bar{n}$ where patterns exist. Changing total average density simply shifts the interface position (cf. panels (ii) and (iii) in (c)). When the interface position is in the vicinity of a boundary, mesa pattern

transitions to peak patterns (see. panels (i) and (iv) in (c)) as we learned in the previous section (Eq. (38) in Sec. VC). The numerical continuation shows, that the peak/trough patterns are then annihilated in saddle-node bifurcations (SN), where the branch of stable patterns meets a branch of unstable patterns (dashed, red line). Due to the finite system size, the exact positions of the SN-bifurcation points are sightly offset from $n_\pm^\infty$ (by an amount $\sim \ell_{int}/L$). The branches of unstable patterns emerge from homogenous steady state in subcritical pitchfork bifurcations (P) at the Turing bifurcations $(n_{lat}^\pm)$. (In a finite sized system, the onset of lateral instability is offset by an amount $\sim L^2$ from the geometrically defined points $n_{lat}^\pm$, because the system is unstable only if the longest wavelength mode lies within the band of unstable modes; see Sec. VIID). In the multistable regions (shaded in blue), patterns can be triggered by a finite amplitude perturbation. The unstable patterns are "transition states" (or "critical nuclei") that lie on the separatrix separating the basins of attraction of the stable patterns and the stable homogeneous steady state. The actual separatrix is a complicated object in the high-dimensional PDE phase space. In the next section (VI), we will show that a heuristic can be inferred from the nullcline shape to estimate the threshold for stimulus-induced pattern formation for a prototypical class of spatial perturbation profiles.

Because the unstable patterns are peak/trough patterns, they can be approximated by the 'peak approximation' introduced in Sec. VC (see also Appendix G). Thus the qualitative structure of the branches of unstable patterns is determined by (m, c)-phase-space geometry independently of the details of the reaction term $f(m, c)$, as long as the reactive nullcline $f(m, c) = 0$ is N-shaped.

In summary, we conclude that the qualitative form of the bifurcation structure shown in Fig. 6b is determined by geometric relations in (m, c)-phase space. In particular, we find that 2C-MCRD systems generically have regions of multistability and that the onset of lateral instability is generically subcritical for large system size $L \gg \ell_{int}$. Further, this implies that such systems exhibit stimulus-induced pattern formation, and that there is hysteresis of stationary patterns when the total average density is varied.

VI. PERTURBATION THRESHOLD FOR STIMULUS-INDUCED PATTERN FORMATION

Before we delve into the more technical analysis of bifurcation structures, we would like to discuss one more important aspect of pattern formation: stimulus-induced pattern formation, i.e. the ability to induce the transition from one stable attractor (homogeneous steady state) to another (stationary pattern) by a large enough perturbation (stimulus). (In the context of phase separation, this is called *nucleation and growth*). Stimulus-induced pattern formation is a particularly important aspect of
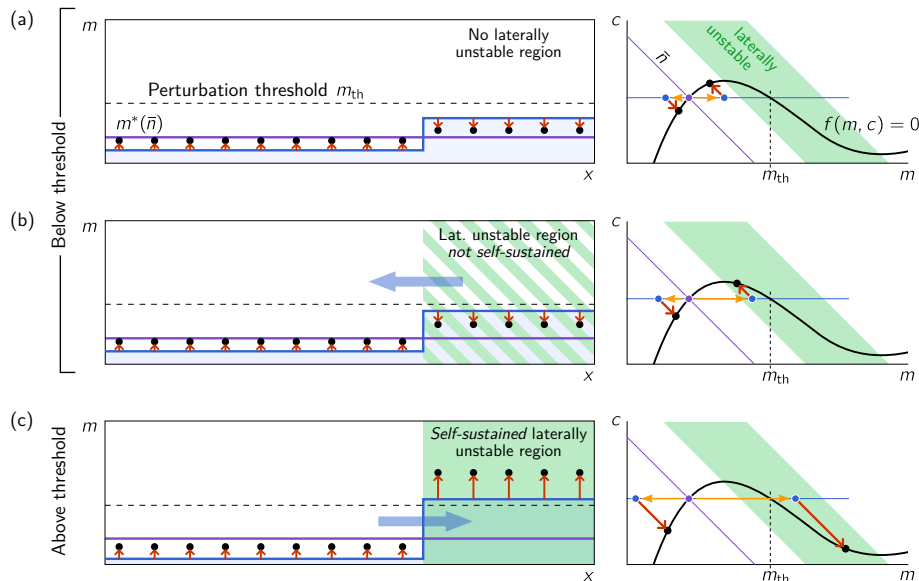
FIG. 7. Subcritical stationary patterns can be induced by perturbations above a threshold that can be heuristically estimated from the reactive nullcline. (a) After a small perturbation (blue profile, yellow arrows in phase space), that does not induce a laterally unstable region, the system returns to its uniform steady state (purple line). (b) A perturbation that creates a laterally unstable region, but does not cross the nullcline. Because the cytosolic concentration is lower in the laterally stable region, mass-redistribution (illustrated by the blue arrow) will disband the laterally unstable region. (c) A perturbation that crosses the nullcline will not only induce a laterally unstable region but also shifts the cytosolic equilibrium concentration in this region such that the lateral instability is (self-)sustained by mass redistribution from the stable into the unstable region (blue arrow).

2C-MCRD systems, because, as we have shown above, these systems generically have regions of multistability. Furthermore, biologically it is often desirable to be able to form a pattern following an external or internal stimulus that exceeds a certain threshold ("nucleation threshold") . As of yet, this threshold could only be determined numerically [29]. In the following, we will show how simple heuristic reasoning—based on *regional* lateral instability—yields a geometric criterion for the perturbation threshold in the (m, c)-phase plane.

As we have shown in the previous section, the hallmark of a stationary pattern is a laterally unstable region surrounding the pattern inflection point x_0 (even if the homogeneous state of the system is laterally stable). In the proposed framework, the phase-space dynamics are simply represented by the expansion of the system in the (m, c)-phase plane due to mass redistribution. Hence, to lead to a stationary pattern, a trajectory in the (high-dimensional) phase space of a partial differential equation (PDE) must enter and remain in a (linearly) laterally unstable region in the (m, c)-phase plane (shaded in green in Fig. 7). The laterally unstable region in (m, c)-space corresponds to a respective region in real space. If the homogenous state is laterally stable then a finite perturbation (stimulus) is required to create a laterally unstable region. Let us study a prototypical perturba-

tion able to induce a laterally unstable region: a step function that represents moving a 'block' of protein mass (total density) from one end of the system to the other; for an illustration of the spatial perturbation and the resulting flows in phase space see Fig. 7. Generalization to other perturbations is straightforward and based on analogous arguments. Such perturbations can be created by various means of 'active' mass redistribution, e.g. active transport in the cell cortex, along microtubules, and hydrodynamic cytosolic flows; see for instance Ref. [64].

Following a (large amplitude) perturbation, there are two distinct processes that are triggered in phase space as shown in Fig. 7. On the one hand, in the laterally unstable region (green shaded area), a mass-redistribution instability will start to form a pattern, thus further amplifying the perturbation. On the other hand, because the perturbation shifts the regional reactive equilibria (black disks), there will be reactive flows (red arrows) in the regions that induce a cytosolic gradient which leads to mass redistribution between the regions by cytosolic diffusion (large blue arrows). If the cytosolic density in the laterally stable region is lower than in the laterally unstable one, the regional instability may not be sustained and the system returns to homogenous steady state (Fig. 7b). Conversely, if the cytosolic density is lower in the laterally unstable region than in the later-

ally stable region, then the cytosolic flow between the regions (blue arrow) will sustain the regional instability (Fig. 7c). Because the mass-redistribution instability creates a self-organized and self-sustaining cytosolic sink, the laterally unstable region can be self-sustained. The heuristic criterion for a (self-)sustained laterally unstable region is that the perturbation must cross the nullcline (see Fig. 7c). Then, the overall cytosolic concentration in the laterally unstable region is decreased by reactive flows (red arrows) such that cytosolic diffusion (blue arrow) between the regions will sustain the laterally unstable region.

In Appendix H we show that this simple criterion already provides a very good approximation for the threshold in comparison to full numerical simulation. We conclude that the reactive nullcline provides the key information for understanding pattern formation dynamics, in a similar way as for the characterization of stationary patterns (Sec. V and the analysis of the linear mass-redistribution instability (Sec. IV). Specifically it enables one to estimate the basins of attraction of the uniform steady state and the polarized pattern. We further learned that regional lateral instability underlies stimulus-induced pattern formation from laterally stable homogeneous steady states.

The threshold estimate provided here might help to understand this "nucleation" of patterns from laterally stable homogeneous steady states. The unstable peak/trough patterns (dashed red lines in Fig. 6 are part of the separatrix between to the basin of attraction of stable stationary patterns, and can be pictured as canonical critical nucleus [65]. The peak approximation described in Sec. V C and compared to numerical continuation in Appendix G provides a simple estimate for this critical nucleus.

VII. COMPLETE BIFURCATION STRUCTURE

Bifurcation diagrams of 2C-MCRD systems were previously studied for specific choices of the reaction kinetics $f(m, c)$ using numerical methods [53]. Furthermore, based on numerical studies of various models, it was hypothesized that there might be a general bifurcation scenario underlying cell polarity systems [32]. Here we use the insight gained on phase-space geometry to systematically build the complete general bifurcation structure of 2C-MCRD systems. Our findings generalize previous results and unify them in the context of phase-space geometry. For large system size, the bifurcation structures are fully determined geometrically. We illustrate the effect of finite system size using numerically computed bifurcation diagrams shown in Appendix F.

Above, we studied the bifurcation diagram of stationary patterns for the bifurcation parameter $\bar{n}$ in a system with monostable kinetics; see Sec. V D and Fig. 6 therein. Recall, that in large systems ($L \to \infty$), the bifurcation points in $\bar{n}$ can be found based on geometric reasoning

in phase space: (i) Lateral instability is identified by a criterion on the nullcline slope: $s_{nc}(\bar{n}) < -D_m/D_c$. Hence, the range of lateral instability is bounded by points $n_{lat}^{\pm}$ where the FBS is tangential to the NC: $s_{nc}(n_{lat}^{\pm}) = -D_m/D_c$. ($ii$) FBS–NC intersection points $m_{\pm}(\eta_0^{\infty})$ provide the scaffold for the plateaus of mesa patterns, where the FBS-position, η_0^{∞}, is determined by total turnover balance, Eq. (35). Mesa patterns exist as long as the average total density can be distributed between two plateaus $n_{\pm}^{\infty}$, i.e. in the range $n_{-}^{\infty} < \bar{n} < n_{+}^{\infty}$; recall that $n_{\pm}^{\infty} = n_{\pm}(\eta_0^{\infty})$ depend on the position η_0^{∞} and slope $-D_m/D_c$ of the FBS (cf. Eq. (37)).

Both of these geometric bifurcation criteria depend on the diffusion constants via the slope of the flux-balance subspace $-D_m/D_c$. We keep D_m fixed—thus fixing the smallest characteristic length scale $\ell = \sqrt{D_m/f_m}$ where spatial structures can be maintained against membrane diffusion—and vary D_c to rotate the FBS in (m, c)-phase space.

A. Generic bifurcation structure of stationary patterns for monostable reaction kinetics

We construct the $(\bar{n}, D_c)$-bifurcation diagram by inferring $n_{lat}^{\pm}$ and $n_{\pm}^{\infty}$, as described above, as functions of D_c. Qualitatively, this can even be done manually with pen and paper in the spirit of a graphical construction (see e.g. Ref. [1]) based on the geometric criteria (i), (ii) above, as shown in Fig. 6. Figure 8a shows the qualitative structure obtained by this graphical construction. A quantitative construction of the bifurcation diagram can be performed with simple numerical implementation of the bifurcation criteria described above, e.g. in Mathematica (see SM File: "flux-balance-construction.nb", and Fig. 20 for figures of quantitative bifurcation structures). As we will see in the following, the structure of the bifurcation diagram is qualitatively the same for all monostable, N-shaped nullclines, independently of the details (nonlinearities and kinetic rates) of the reaction term $f(m, c)$. The bifurcation diagram is qualitatively different when the nullcline has a segment of bistability (where $s_{nc} < -1$, cf. Fig. 1). We will analyze this case and in particular the role of bistability further below in Sec. VII B.

As D_c is decreased, the flux balance subspace becomes steeper, and thus the bifurcation points $n_{lat}^{\pm}$ and $n_{\pm}^{\infty}$ start to converge (see Fig. 8; cf. Fig. 6). They meet in the inflection point of the reactive nullcline, n_{inf}, where the nullcline slope, s_{nc}^{inf}, is extremal ($\partial_n s_{nc}|_{n_{inf}} = 0$). The extremal nullcline slope at the nullcline inflection point determines the minimal cytosolic diffusion constant,

$$D_c^{min} := \frac{D_m}{-s_{nc}(n_{inf})}, \qquad (40)$$

above which there are three FBS–NC intersection points. When the 'critical' point (n_{inf}, D_c^{min}) is traversed in D_c-direction, the FBS–NC intersections bifurcate in a (supercritical) pitchfork bifurcation; see Fig. 8b. Since the
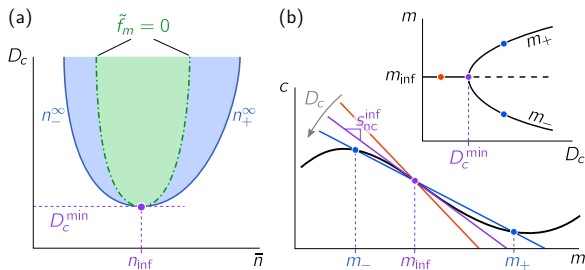
FIG. 8. $(\bar{n}, D_c)$-bifurcation diagram of stationary patterns for a system with monostable kinetics (same color code as in Fig. 6). (a) The bifurcation diagram for a large system $(L \to \infty)$ is obtained by tracking the geometrically constructed bifurcation points $n_{\mathrm{lat}}^{\pm}$ and $n_{\pm}^{\infty}$ as D_c, and thus the slope and position of the FBS, are varied (cf. Fig. 6). The onset of lateral instability (Turing bifurcation shown as green dash-dotted line) is generically subcritical since there exist stationary patterns outside the range of lateral instability $(n_{\mathrm{lat}}^{-}, n_{\mathrm{lat}}^{+})$; in the blue regions, the system is multistable (both the stationary patterns and the homogenous steady state are stable). The scaffolds for the low and high density plateaus $(n_{\pm}^{\infty})$ bifurcate supercritically from the homogenous steady state at the critical point $(n_{\mathrm{inf}}, D_c^{\mathrm{min}})$ (purple point). (b) The critical point in the $(\bar{n}, D_c)$-bifurcation diagram corresponds to the inflection point of the nullcline n_{inf}, where the nullcline slope $-f_m/f_c$ reaches its extremal value $s_{\mathrm{nc}}^{\mathrm{inf}}$ and thus determines the minimal cytosolic diffusion D_c^{min} (purple line); cf. Eq. (40). At D_c^{min}, the scaffolds of the plateaus, $m_{\pm}$, bifurcate in a supercritical pitchfork bifurcation from the nullcline inflection point m_{inf} (see inset).

FBS–NC intersection points $m_{\pm}$ are the scaffolds for the plateaus (in short: *plateau scaffolds*; cf. Fig. 2), this bifurcation at the critical point $(n_{\mathrm{inf}}, D_c^{\mathrm{min}})$ is a bifurcation of the scaffold itself. Importantly, the actual pattern is bounded by the plateau scaffolds. Thus, if there are no plateau scaffolds (i.e. only one FBS-NC intersection point), there cannot be stationary patterns. For $L \to \infty$, patterns emerge slaved to the plateau scaffold, such that the pattern bifurcation is supercritical at the nullcline inflection point $(\bar{n} = n_{\mathrm{inf}})$. Away from the nullcline inflection point $(n \neq n_{\mathrm{inf}})$, the lateral instability bifurcation is always subcritical for $L \to \infty$ because the range $(n_{-}^{\infty}, n_{+}^{\infty})$ where patterns exist always exceeds the range $(n_{\mathrm{lat}}^{-}, n_{\mathrm{lat}}^{+})$ of lateral instability, as we learned above in Sec. V D (cf. Fig. 6).

As we will see below in Sec. VII D, for finite L, the bifurcation is supercritical in the vicinity of the nullcline inflection point. The transition from super- to subcriticality depends on a subtle interplay of diffusive and reactive flow together with geometric factors like nullcline curvature.

Interestingly, the regimes and their interrelation in the $(\bar{n}, D_c)$-bifurcation diagram, as shown in Fig. 8a, are phenomenologically similar to the phase diagram of (near equilibrium) phase separation kinetics for binary mixtures, described by Cahn–Hilliard equation [66]. In a

previous study using the amplitude equation formalism, Ref. [67], a mapping from 2C-MCRD models to Model B has been found for the vicinity of the critical point, where the pattern emerges from the Turing bifurcation in a supercritical or weakly subcritical pitchfork bifurcation (see Sec. VII D).

Strikingly, our geometric reasoning shows that the physics implied by the bifurcation diagram is the same as in phase separation kinetics (binodal and spinodal regimes) *for all N-shaped nullclines*, and far away from the critical point. We discuss this finding in Sec. VIII C.

B. Locally bistable kinetics

Changing the kinetic rates deforms the nullcline shape. When the nullcline slope becomes smaller than -1, a regime of locally bistable reaction kinetics emerges (cf. Fig. 1).

1. Fronts in bistable media

To elucidate the role of bistability, let us first consider the case of equal diffusion constants $D_c = D_m =: D$. (Although this does not make sense in the intracellular context anymore, where typically $D_c > D_m$, we stick to the notation with concentrations m and c.) Then mass redistribution decouples from the kinetics $\partial_t n = D\partial_x^2 n$, i.e. the total density becomes uniform by diffusion (see the mass-redistribution dynamics, Eq. (12), and note that $\eta(x,t) = n(x,t)$ for equal diffusion constants). As a consequence, the system can be reduced to one component, for instance the membrane density

$$\partial_t m = D\partial_x^2 m + f(m, \bar{n} - m), \qquad (41)$$

where the local kinetics is bistable at every point in space (Fig. 9). This corresponds to a (classical) one-component model for bistable media which generically exhibits propagating fronts [3]. A standard calculation, commonly performed by 'Newton mapping' (briefly described in Sec. III C) or by phase-space analysis (in $(m, \partial_x m)$-phase space), shows that the propagation velocity v of a front is proportional to the imbalance in reactive turnover [3]: $v \propto \int_{m_-}^{m_+} \mathrm{d}m\, f(m, \bar{n} - m)$. Hence, a stationary front can only be realized by fine-tuning of parameters, e.g. the average total density $\bar{n}$, such that total turnover is balanced:

$$n_{\mathrm{stat}} : \int_{m_-}^{m_+} \mathrm{d}m\, f(m, n_{\mathrm{stat}} - m) = 0. \qquad (42)$$

The balanced (fine-tuned) case corresponds to the Allan–Cahn equation [68] (also called 'model A' dynamics [54]). (In a finite size system, there will be logarithmic coarsening, see Ref. [61] and references therein.)
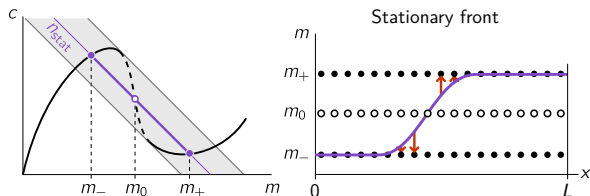
FIG. 9. Phase-space structure for bistable local kinetics in the case of equal diffusion constants, $D_m = D_c$, where there is no mass redistribution such that the system can be reduced to a one-component system, Eq. (41). The stable equilibria $m_\pm$ form a *static*, spatially homogenous scaffold; the equilibrium m_0 is locally unstable. Only if the local kinetics are fine-tuned such that the total turnover vanishes (e.g. by tuning $\bar{n} = n_{\text{stat}}$), the front is stationary (marginally stable).

With respect to the concept of local equilibria as scaffolds for patterns (cf. Sec. III C), the bistable local equilibria (fixed points $m_\pm$) can be regarded as a *static scaffold* for front solutions; see Fig. 9. Because there is no mass-redistribution, the scaffold must remain static and can not adapt to balance the total reactive turnover. Instead, fine-tuning of parameters (e.g. $\bar{n}$), is required to obtain a balance of total turnover and thus a stationary front. In the $(\bar{n}, D_c)$-bifurcation diagram, Fig. 10a, the stationary bistable front with a static scaffold appears only at a singular point $(\bar{n}, D_c) = (n_{\text{stat}}, D_m)$.

What happens when the diffusion constants are unequal $D_c \neq D_m$? Then, mass will be redistributed, leading to shifting of the local equilibria that scaffold the pattern. As we know from our analysis for monostable reaction terms, this dynamic scaffold is able to self-balance the total reactive turnover—fine-tuning of $\bar{n}$ is no longer required to obtain stationary patterns. Interestingly, for a bistable reaction term, stationary patterns can be constructed both for $D_m > D_c$ and for $D_m < D_c$, as we discuss next; see Fig. 10b,c. To determine the stability of these patterns, we will examine below (after the description of the bifurcation diagram) how the scaffold self-balances via mass redistribution.

2. Bifurcation diagram for locally bistable reaction kinetics

The bifurcation diagram, Fig. 10a, for the large system size limit ($L \to \infty$) is obtained using the same geometric criteria as for the case of locally monostable reaction kinetics (see Fig. 10b, cf. Fig. 6a). The presence of a bistable nullcline segment does not affect the feasibility of the geometric construction itself. However, the bifurcation diagram one obtains is qualitatively different from the monostable case, as we will see next. We discuss the regimes of stationary patterns (shaded in blue and red) first, before we analyze the regions of lateral instability (shaded in green and orange).

The region where stable stationary patterns exist (shaded in blue) is delimited by lines $n_\pm^\infty(D_c)$. These

lines converge in singular point $(n_{\text{stat}}, D_c = D_m)$, where a marginally stable front exists in a bistable medium without mass redistribution (Sec. VII B 1). Along the entire line, $D_c = D_m$, in the phase diagram Fig. 10a the dynamics can be reduced to a classical one-component system (Eq. (41)). Such a system exhibits propagating waves within the region of bistability located between the two saddle-node (SN) bifurcations of local equilibria (gray area in Fig. 10a); compare the bistable (gray) area in Fig. 9 and Fig. 10b,c, where the nullcline slope is more negative than -1. Only for the fine-tuned value right at $\bar{n} = n_{\text{stat}}$, the front velocity is zero (purple dot). At (n_{stat}, D_m), the dynamic scaffold that self-adapts via mass redistribution for $D_c \gtrless D_m$ bifurcates from the static scaffold $m_\pm(n_{\text{stat}})$ of the marginally stable front.

For bistable kinetics the slope at the inflection point of the nullcline, $s_{\text{nc}}^{\text{inf}}$, is necessarily more negative than -1 so stationary patterns may also exist for $D_c^{\text{min}} < D_m$ (cf. Eq. (40)), since they can be constructed from FBS-NC intersection points as shown in Fig. 10c. (We stick to the notation with concentrations m and c, although they are not meaningful as "membrane" and "cytosolic" concentrations, in the case $D_c < D_m$. Instead they should be understood as abstract concentrations [69]). The corresponding region where such stationary patterns exist is shaded in red in the bifurcation diagram shown in Fig. 10a. In the bottom half of this "balloon"-shaped region the equilibria that form the plateau of the constructed pattern are locally unstable. Hence these patterns cannot be stable. As we will see in the next subsection, *all* stationary patterns for $D_c < D_m$ are unstable (even if their plateaus are locally stable) since they are destabilized by the imbalance of reaction turnover induced by any (infinitesimal) perturbation. In contrast, stationary patterns for $D_c > D_m$ are stable because the self-adapting scaffold re-balances the reactive turnover.

The regions with a laterally unstable homogeneous steady state (NC-slope steeper than FBS-slope, cf. Eq. 25) are shaded in green and orange to distinguish in the bistable region which of the two locally stable reactive equilibria is laterally unstable; see Fig. 10b [70].

In conclusion, we found the generic $(\bar{n}, D_c)$-bifurcation diagram of stationary patterns for an N-shaped nullcline with a bistable segment using the same geometric arguments as for the case of a monostable nullcline. Since our analysis crucially relies on the flux-balance subspace, it is limited to stationary patterns. For the special case $D_c = D_m$ the existence of non-stationary patterns (traveling fronts) in the locally bistable regime is well known. By continuity, we expect that there will be traveling fronts also $D_c \neq D_m$. Furthermore, we speculate that there will be non-stationary patterns outside the regime of local bistability, because mass redistribution may dynamically create a *region* of bistability that travels through the system.
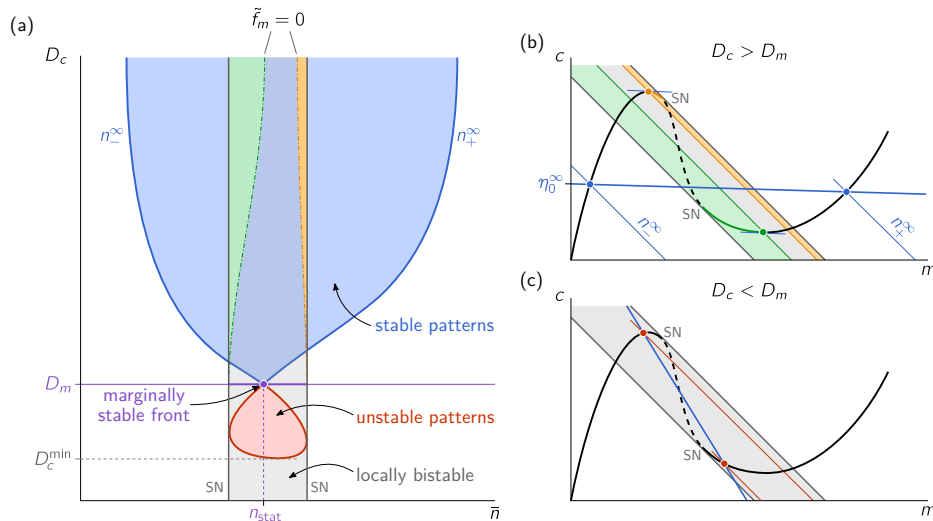
FIG. 10. Geometrically determined, schematic $(D_c, \bar{n})$-bifurcation diagram in the large system size limit for a system with bistable kinetics (the locally bistable region is shaded in gray in both the bifurcation diagram (a) and the phase-space plots (b)). (a) Bifurcation diagram: the regions where stationary patterns exist (shaded in red and blue) and where a homogenous steady state is laterally unstable (shaded in green and orange) are constructed based on the same geometric criteria as in the case of monostable kinetics (cf. Fig. 6). Along the purple line $D_c = D_m$ there is no mass redistribution, and the system exhibits classical traveling fronts within the bistable regime (cf. Fig. 9). A marginally stable front exists at the singular point at $(D_c = D_m, n_{stat})$ where total reactive turnover is balanced by fine-tuning $\bar{n}$ (cf. Eq. (42)). Outside the regions shaded in red and blue, there are no *stationary* patterns. There might however be non-stationary patterns like the traveling fronts in the bistable medium for $D_c = D_m$. Non-stationary patterns for $D_c \gtrless D_m$ are outside the scope of this study. (b) Phase-space plot showing the reactive nullcline (black line, dashed in the locally unstable region). The sections of the nullcline where homogenous steady state is laterally unstable (shaded in green and orange) are delimited by points where the FBS is tangential to the NC. Intersection points (blue dots) of the flux-balance subspace (thick blue line) with the reactive nullcline determine the range $n_\pm^\infty$ where stationary patterns exist. (c) Phase-space plot for the case $D_c < D_m$, where the slope of the FBS (thick red line) is more negative than -1. The plateau scaffolds of stationary patterns can be constructed via FBS-NC intersection points (red dots), as long as $D_c > D_c^{min}$ (cf. Eq. (40)). These patterns are unstable though (cf. Eq. (43)).

3. The dynamic scaffold self-balances by shifting the flux-balance subspace

In the following, we will assess the stability of the stationary (mesa) patterns found by the geometric construction above. (We only discuss the stability of mesa patterns, which are generic in the limit of large system size, $L \to \infty$.) The phase-portrait analysis in the phase space of chemical reactions facilitates a simple heuristic approach to study pattern stability: Instead of a full stability analysis of the stationary pattern, we consider only the stability of the FBS-position (mass-redistribution potential $\eta(x,t)$), as a proxy for the pattern stability. Intuitively, in the direction along the FBS, the pattern is quickly stabilized by due to scaffolding by local equilibria. In the following we present a simple stability criterion for stationary patterns, derived from this intuition. Details of the (ad hoc) derivation and a comparison to numerical analysis is presented in Appendix I. A mathematically rigorous stability analysis of stationary patterns (using, for instance, the "Singular Limit Eigenvalue Problem" introduced by [71], see [61] for a survey), is outside the

scope of this paper.

Recall that in steady state $\widetilde{\eta}(x) = \eta_0^\infty$ is spatially uniform and determined by total turnover balance, Eq. (17), that can be geometrically interpreted as a Maxwell construction (balance of the red-shaded areas in Figs. 2b and 11). How does the system evolve following a perturbation of the FBS-position η? Consider a spatially uniform shift, $\delta\bar{\eta} > 0$. Then the area between NC and FBS to the left of m_0 (inflection point of the pattern) will decrease, while the area on the right will increase; see Figs. 2b and 11. The net reactive flow ("sum of the arrows in the two areas") leads to a change of the average concentrations m and c (in the interface region) which amounts to a shift of the FBS-position, as shown in the insets in Fig. 11. Because the net reactive flow points along a reactive phase space (slope -1), the direction in which the FBS shifts due to turnover imbalance depends on its slope. For $D_c > D_m$, i.e an FBS-slope larger than -1, it will move down and, hence, relax back to η_0^∞ (recall that we considered an upwards shift as perturbation, the arguments work analogously for a downwards shift). In other words, the scaffold will adapt until total reactive
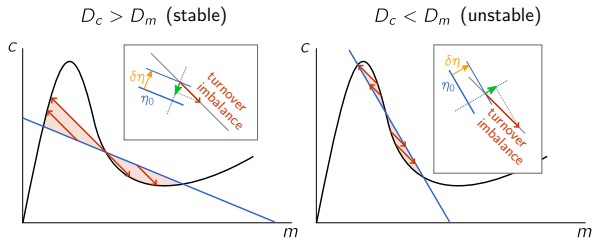
FIG. 11. Geometric construction of the stability of the FBS-position η_0 due to total turnover imbalance which serves as proxy for the stability of the pattern that is embedded in the FBS. In steady state, the reactive turnovers (illustrated by red arrows) on either side of the inflection point must be balanced. Inset boxes: A perturbation $\delta\eta$ (yellow arrow) that shifts the FBS-position η_0 will induce an imbalance of reactive turnovers (red arrow). Projecting this net reactive turnover onto the η-axis (dashed blue line) yields the movement of the FBS induced by the turnover imbalance (green arrow). For $D_c > D_m$, the FBS returns to its steady-state position η_0. Conversely, for $D_c < D_m$, the FBS is driven further away from its steady-state position, such that the initial perturbation is further amplified in a destabilizing feedback loop.

turnover is balanced again. We conclude that the scaffold is *self-balancing* when $D_c > D_m$. Conversely, when $D_c < D_m$, the FBS will move further in the direction of the perturbation, thus destabilizing the pattern.

This qualitative stability argument can be expressed mathematically, to obtain a quantitative approximation for the growth rate of perturbations $\delta\eta(x_0, t) := \eta(x_0, t) - \eta_0^\infty$ in the vicinity of a stationary mesa pattern $(\tilde{m}(x), \eta_0^\infty)$ (see Appendix I):

$$\partial_t \delta\eta(x_0, t) \approx \delta\eta(x_0, t) \frac{D_m/D_c - 1}{m_+ - m_-} \int_{m_-}^{m_+} \mathrm{d}m \, \tilde{f}_\eta(m, \eta_0^\infty)$$

$$(43)$$

where $\tilde{f}_\eta = \partial_\eta \tilde{f}$. Comparison to numerically computed linear stability (dominant eigenvalue) of stationary patterns confirms shows that Eq. (43) is a good lowest order approximation for pattern stability; see Appendix I and Fig. 25. The integral over $\tilde{f}_\eta$ is the turnover imbalance due to a shift of the FBS, and thereby captures the geometric intuition based on the 'Maxwell construction' (area balance) we outlined above. The prefactor $(D_m/D_c - 1)$ determines the direction in which FBS will shift because the integrand is always positive for $f_c > 0$ ($\tilde{f}_\eta(m, \eta_0^\infty) = f_c(m, \eta_0^\infty - m \, D_m/D_c) > 0$). We hence recover the stability criterion from our geometric argument above.

C. The cusp scenario is generic

In some previous literature, it was argued that bistability of the reaction kinetics is an essential prerequisite for polarization to emerge in 2C-MCRD systems [28, 29].
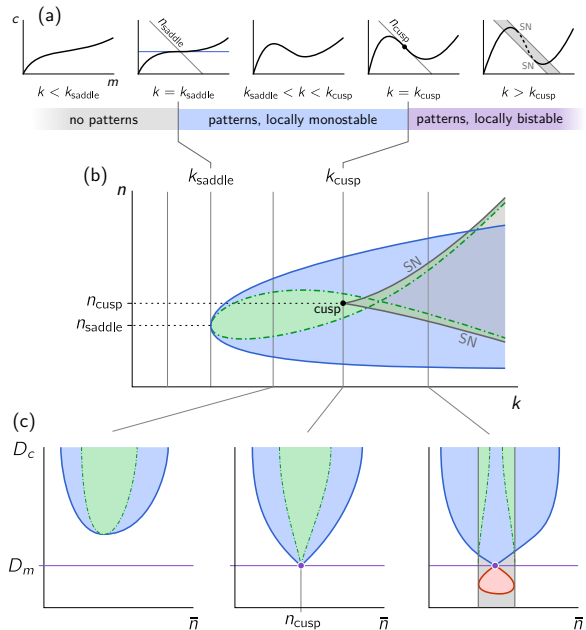
FIG. 12. Schematic of the cusp bifurcation scenario ("unfolding") in the $(k, \bar{n}, D_c)$-bifurcation diagram (same color code as Figs. 6, 8, and 10, Fig. 20). (a) We analyze the effect of a series of deformations of the reactive nullcline parametrized by the (notional) kinetic rate k. The respective (schematic) $(k, \bar{n})$-bifurcation diagram of stationary patterns (for $D_m/D_c \to 0$ and $L \to \infty$) is shown in (b). Initially, the nullcline is monotonic, and hence does not facilitate pattern formation. At k_{saddle} a segment of negative nullcline-slope, s_{nc}, emerges in a saddle point ($s_{\text{nc}} = 0$ at the inflection point), such that patterns can form for $D_m/D_c \to 0$ (generally, the critical nullcline slope $s_{\text{nc}}^{\text{crit}}$ for pattern formation is simply the ratio $-D_m/D_c$, cf. Eq. (40)). The regimes of lateral instability (green) and pattern existence (blue) emanate from this critical point. At k_{cusp}, a region of bistability (shaded in gray, bounded by saddle-node bifurcations) emanates from a cusp bifurcation ($s_{\text{nc}} = -1$ at the nullcline's inflection point). At this point, the topology of the $(\bar{n}, D_c)$-bifurcation diagram changes (see (c)). (In the small gray triangular region in the top-right corner of the (k, n)-bifurcation diagram, the system is locally bistable but does not exhibit stable stationary patterns.) (c) Schematic $(\bar{n}, D_c)$ bifurcation diagrams for $k_{\text{saddle}} < k < k_{\text{cusp}}$ (monostable kinetics, Fig. 8), at the cusp ($k = k_{\text{cusp}}$), and for $k > k_{\text{cusp}}$ (bistable kinetics, Fig. 10).

This claim was questioned recently [72].

Above, we conclusively showed that bistability is *not* necessary for pattern formation. Instead, in systems with conserved quantities, a (non-homogeneous) pattern scaffold can generically self-organize by due to shifting local equilibria when there is mass-redistribution ($D_c \neq D_m$). However, there is an interesting and more subtle connection between bistability and the ability to form patterns. This connection is revealed by studying the transition from monostable to bistable kinetics due to variation of

kinetic parameters.

Variations in the kinetic parameters will change the shape of the reactive nullcline. This may not only lead to quantitative but also qualitative changes in the $(\bar{n}, D_c)$-bifurcation diagram, namely if there is a transition from a monostable to a bistable reaction kinetics: Imagine that variation of some rate k in the reaction kinetics generates nullcline deformations as shown in Fig. 12a. Let us start with a nullcline that is strictly monotonically increasing with m. Then according to the geometric criterion, Eq. (25), there is no lateral instability and hence no stationary patterns; recall that we have shown in Sec. V A that an interface, the elementary element of a pattern, must be a laterally unstable region. Upon further changing the kinetic rate k there may eventually be a threshold value k_{saddle} beyond which the nullcline shows a region with a negative slope. A regime of lateral instability, and with it a regime where patterns can exist, emerges once the nullcline slope first becomes steeper than the slope of the FBS: $s_{\text{nc}}^{\text{crit}} = -D_m/D_c$. Eventually, at $k = k_{\text{cusp}}$, a further deformation of the nullcline may create a segment with slope $s_{\text{nc}} < -1$ where there is bistability of local equilibria. The bistable regime (shaded in gray) emanates in a cusp bifurcation where the two saddle-node (SN) bifurcations of the reactive equilibria meet in a single point, and the nullcline inflection point has slope $s_{\text{nc}}^{\text{inf}} = -1$ such that it is tangential to the reactive phase space $m + c = n_{\text{inf}} = n_{\text{cusp}}$; see Fig. 12b. The surface of reactive equilibria in the two-parameter bifurcation structure starts to fold over itself at the cusp point. Because the Turing bifurcations lie on different sheets of the folded surface of local equilibria, The Turing-bifurcation line (dash-dotted green line) crosses over itself in the bistable region of the bifurcation diagram.

At the cusp point, the topology of the $(\bar{n}, D_c)$-bifurcation diagram changes from the topology characteristic for monostable reaction kinetics (leftmost panel in Fig. 12c, cf. Fig. 8) to the one characteristic for bistable reaction kinetics (rightmost panel; cf. Fig. 10). At $k = k_{\text{cusp}}$, the bifurcation diagram has the singular topology shown in the center panel, with the cusp critical point at (n_{cusp}, D_m).

Interestingly, by changing kinetic rates, the reactive nullcline of any system that is able to form stationary patterns, can be deformed to undergo such a cusp bifurcation of (local) reactive equilibria. To see how this works, first recall that to obtain stationary patterns, there must be a segment where the nullcline slope is $s_{\text{nc}} < -D_m/D_c < 0$, i.e. necessarily negative. This segment can be deformed into a bistable region (slope $s_{\text{nc}} < -1$) by a dilation of the nullcline in the c-direction in phase space; see Fig. 13. Let us denote the scale factor by ζ, then the dilated nullcline is determined by $f(m, \zeta^{-1}c) = 0$. A slope s_{nc} of the original nullcline $f(m, c) = 0$ will become a slope $\zeta \cdot s_{\text{nc}}$ for the dilated nullcline. In particular, dilation by a factor $\zeta = |s_{\text{nc}}^{\text{inf}}|^{-1}$ leads to a nullcline with slope -1 at its inflection point, hallmark of a cusp bifurcation of the reactive equilibria (cf.
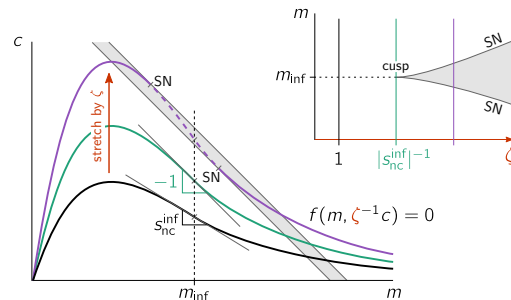
FIG. 13. Any nullcline with a segment of negative slope can be deformed by simple dilation to a exhibit cusp bifurcation where two saddle-node (SN) bifurcations of the reactive equilibria meet (see inset). The generic deformation to achieve this is a dilation in the c-direction by a scale factor ζ (i.e. replacing c in the reaction term $f(m, c)$ by $\zeta^{-1}c$, such that the dilated nullcline is given by: $f(m, \zeta^{-1}c) = 0$). Say the original nullcline (black curve, $\zeta = 1$) has a slope $s_{\text{nc}}^{\text{inf}} < 0$ at the inflection point m_{inf}. Then, the nullcline dilated by $\zeta = |s_{\text{nc}}^{\text{inf}}|^{-1}$ (green curve), will have the slope -1 at its inflection point, thus yielding a cusp point of reactive equilibria (see inset, cf. Fig. 12). Upon further dilation, the nullcline (purple curve) will have a segment with slope more negative than -1 (dashed line, region shaded in gray), where the reactive equilibria are bistable. Each of the three nullclines in the phase space corresponds a vertical line of the same color in the bifurcation diagram (inset).

Fig. 13). Any further dilatation leads to a bistable region (nullcline segment with slope more negative than -1). We conclude that the generic bifurcation scenario underlying all pattern-forming 2C-MCRD systems is a cusp bifurcation of reactive equilibria. Our geometric reasoning thus explains previous numerical observations [32].

D. Sub- and supercriticality of lateral instability in finite sized systems

So far, we have focused on the large system size limit $(L \to \infty)$ where bifurcation diagrams can be constructed from phase-space geometry. In particular, we found that the onset of a mass-redistribution instability is generically subcritical. To analyze sub- vs. super-criticality in the case of finite system size, we use a perturbative approach (weakly nonlinear analysis, see e.g. [73]) for the pattern close to onset. In the vicinity of the homogenous steady state (m^*, c^*), we expand a stationary state $(\widetilde{m}(x), \eta_0)$ in harmonic functions (eigenmodes of the Laplace operator under no-flux boundary conditions):

$$\widetilde{m}(x) = m^* + \sum_{k=0}^{\infty} \delta m_k \cos(k\pi x/L). \qquad (44)$$

As we have learned in Sec. IV, the band of unstable modes always extends to long wavelengths $(q \to 0)$ in

a 2C-MCRD system ('type II' instability, cf. Fig. 3b). Therefore, in a finite size system, the mode that becomes unstable first at the onset of the lateral instability is the longest wavelength mode: $\cos(\pi x/L)$. We want to study the steady-state amplitude of this mode in the vicinity of the onset bifurcation. It is not sufficient, though, to keep only this first harmonic in the mode expansion, Eq. (44), since higher harmonics couple to it through the nonlinear terms. For an expansion to third order in the first mode amplitude δm_1, one needs to include only the first and second harmonics in Eq. (44). Higher harmonics are not needed because they couple to δm_1 through higher nonlinearities $\mathcal{O}(\delta m_1^4)$. To leading order the ansatz thus reads

$$\widetilde{m}(x) \approx m^* + \delta m_0 + \delta m_1 \cos(\pi x/L) \tag{45a}$$
$$+ \delta m_2 \cos(2\pi x/L),$$
$$\eta_0 \approx \eta^* + \delta\eta_0, \tag{45b}$$

where (m^*, η^*) denotes the homogenous steady state: $\tilde{f}(m^*, \eta^*) = 0$. Using this ansatz in Eq. (14a) and keeping terms up to third order yields for the steady state pattern amplitude δm_1 (see Appendix J for details):

$$0 = F_1\, \delta m_1 + F_3\, \delta m_1^3 + \mathcal{O}(F_1 \delta m^3) + \mathcal{O}(\delta m_1^5). \tag{46}$$

The first order and third order coefficients read

$$F_1 = \tilde{f}_m - D_m \pi^2/L^2, \tag{47a}$$

$$F_3 = \frac{\tilde{f}_{mmm}}{8} + \frac{\tilde{f}_{mm}^2}{24} \frac{L^2}{\pi^2 D_m} - \frac{\tilde{f}_{mm}}{4} \frac{\tilde{\partial}_m \sigma_{\mathrm{loc}}}{\sigma_{\mathrm{loc}}}, \tag{47b}$$

where $\tilde{\partial}_m = \partial_m - \frac{D_m}{D_c}\partial_c$ is the derivative along the direction of the flux-balance subspace.

The first harmonic amplitude δm_1, solution to Eq. (46) undergoes a pitchfork bifurcation at $F_1 = 0$. This bifurcation is simply the Turing bifurcation as it coincides with the onset of lateral instability: the homogenous steady state, $\delta m_1 = 0$, is laterally unstable only if the longest wavelength mode, $q_1 = \pi/L$, is within the band of unstable modes: $\pi^2/L^2 < q_{\max}^2 = \tilde{f}_m/D_m$, i.e. if $F_1 > 0$ (cf. Eq. (47a)). Hence, the sign of the third order coefficient F_3, evaluated at the bifurcation point $F_1 = 0$, determines wether the bifurcation is supercritical ($F_3 < 0$) or subcritical ($F_3 > 0$); see Fig. 14b.

On the basis of this weakly nonlinear analysis, we can study the bifurcation at $F_1 = 0$ in any control parameter μ (for instance the average total density $\bar{n}$, the system size L, kinetic rates, and diffusion constants). With the critical value μ_c, defined by the condition $F_1(\mu_c) = 0$, we introduce the reduced control parameter $\delta\mu = \mu - \mu_c$, and linearize Eq. (46) to lowest order in $\delta\mu$:

$$0 = \partial_\mu F_1|_{\mu_c}\, \delta\mu\, \delta m_1 + F_3(\mu_c)\, \delta m_1^3. \tag{48}$$

To leading order, the branch of the solution that bifurcates at $F_1 = 0$ then reads

$$\delta m_1 = \sqrt{\left.\frac{\partial_\mu F_1}{-F_3}\right|_{\mu_c} \delta\mu}\,. \tag{49}$$
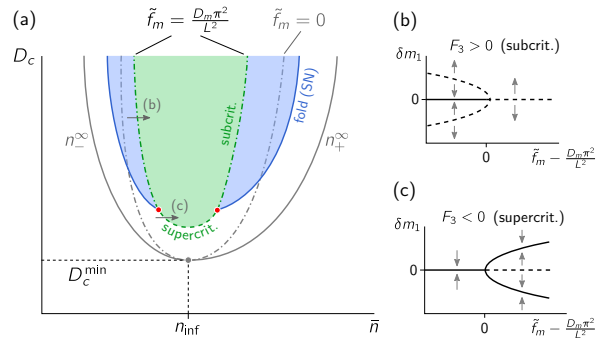
FIG. 14. Pattern bifurcation for finite domain size. (a) Schematic bifurcation structure for a system with monostable reaction kinetics (an analogous plot obtained by numerical continuation for a concrete reaction term, Eq. (A1*), is shown in Fig. 22, Appendix J). The gray lines indicate the bifurcation structure for $L \to \infty$ for comparison (cf. Fig. 8a). The Turing bifurcation (green dashed line, $\tilde{f}_m = D_m \pi^2/L^2$) is supercritical in the vicinity of n_{inf}, i.e. the nullcline inflection point. In the vicinity of onset (small pattern amplitude δm_1) the third order coefficient, F_3 (cf. Eq. (47b)), of a weakly nonlinear expansion (cf. Eq. (45)), determines if the bifurcation is super- or subcritical. The schmatica bifurcation diagrams (b) and (c), correspond to the small gray arrows in (a). Unstable patterns that emerge in a subcritical pitchfork bifurcation (see (b)) meet the stable patterns in a fold bifurcation (saddle-node of patterns, cf. Fig. 6). These fold bifurcations terminate in points where the lateral instability bifurcation switches from sub- to supercritical (red points), indicated by a vanishing third order coefficient $F_3 = 0$ in the weakly nonlinear expansion (cf. Eq. (46)). Along the line of supercritical lateral instability (dashed green line), stable patterns emerge directly in a supercritical pitchfork bifurcation; see (c).

At singular points where local stability and lateral stability change simultaneously, i.e. $\sigma_{\mathrm{loc}} = 0$ and $F_1 = 0$, the last term in F_3 diverges. Such codimension-two points require a more technically involved analysis (unfolding) that is outside the scope of this study (see e.g. Refs. [74, 75]).

From the third order coefficient F_3 (see Eq. (47b)), we can analyze the type of bifurcation in terms of geometric features (nullcline curvature $\kappa(n) \sim -\tilde{f}_{mm}|_n$, see Appendix K) together with the quantity that characterizes the relaxation rate to local equilibrium (σ_{loc}, cf. Eq. (5)). The first two terms in F_3 encode geometric properties of the reactive nullcline (curvature and its rate of change), i.e. how the local equilibria shift as mass redistribution shifts the local phase spaces. The last term in F_3 represents the rate of change of the timescale for relaxation σ_{loc} to the local equilibria. In the following, we discuss the various regimes that arise due to the interplay of the three terms in F_3. (To simplify notation, we will implicitly assume that all coefficients ($\tilde{f}_m$, etc.) in F_3 are evaluated at the bifurcation point μ_c.)

(i) At the nullcline inflection point $\tilde{f}_{mm} = 0$, only the first summand of F_3 remains: $F_3 = \tilde{f}_{mmm}/8$. The third derivative $\tilde{f}_{mmm}$ is proportional to the rate of change of the curvature ($\tilde{f}_{mmm} \sim -\partial_m \kappa$, see Appendix K). The curvature of a typical N-shaped nullcline must be positive (bent upwards) to the right of the inflection point and negative (bent downwards) to the left of it, otherwise it is impossible to smoothly connect laterally unstable regions ($\tilde{f}_m < 0$) to laterally stable regions ($\tilde{f}_m < 0$). This implies that $\tilde{f}_{mmm} < 0$, and we conclude that the bifurcation at the nullcline inflection point is supercritical. This confirms our geometric argument above (cf. Fig. 8, and thin gray lines in Fig. 14).

(ii) In the large system size limit ($L \to \infty$) away from the inflection point ($\tilde{f}_{mm} \neq 0$), the second term in Eq. (47b) dominates. Because this term is always positive, the Turing bifurcation in large systems is generically subcritical (cf. Fig. 14) as we have already concluded from geometric arguments in Sec. V D above.

(iii) In a finite-sized but still large system, the last two terms of F_3 are negligible sufficiently close to the nullcline inflection point where $\tilde{f}_{mm}$ vanishes. Hence, finite sized systems are supercritical in the vicinity of the nullcline inflection point, because $\tilde{f}_{mmm}$ must be negative as we argued above in point (i); (cf. Fig. 14). Solving the condition $F_3 = 0$ to to leading order in L^{-1} yields the estimate

$$\left| \tilde{f}_{mm} \right| < L^{-1} \sqrt{-\frac{3\pi^2}{2} D_m \tilde{f}_{mmm}}, \qquad (50)$$

for the range of supercriticality.

(iv) In small systems, the transition from supercriticality to subcriticality will depend also on the last term in F_3. It can contribute either positively or negatively to F_3, depending on the details of the reaction kinetics.

Importantly, the statements (i)–(iii), regarding large systems, follow from purely geometric arguments as they are determined by the first two terms in F_3. The reason for this is that at large wavelength, chemical relaxation is fast compared to diffusion, so the pattern is slaved to the scaffold, i.e. the reactive nullcline. For the same reason, the long wavelength onset of lateral instability is determined by a geometric criterion (slope of the nullcline) as we have shown in Sec. IV.

In conclusion, we comprehensively characterized the Turing bifurcation (sub- vs. supercritical) and the bifurcations of stationary patterns, using the (m, c)-phase-space geometry. Because of the inherent link between geometry and the physical concepts of mass-redistribution and shifting equilibria, we are able understand the physics underlying the patterns and their bifurcations.

The bifurcations in the large system size limit ($L \to \infty$)—determined by geometry—provide a good starting point to study the bifurcations in a finite sized system, e.g. by numerical continuation (see Appendix F).

VIII. CONCLUSIONS AND DISCUSSION

We have introduced a local equilibria theory that allows to analyze and characterize both the initial growth and the eventual stabilization (saturation) of patterns on the basis of geometric objects in phase space: the shape of the reactive nullcline and its intersections with the flux-balance subspace. Within this framework, many properties of the nonlinear dynamics of mass-conserving reaction-diffusion systems can now be directly addressed in terms of phase space geometry, which would otherwise only be accessible by numerical analysis. In the following we will summarize the key concepts of local equilibria theory and important findings for 2C-MCRD obtained from this theory. Subsequently, we address new perspectives for the investigation of reaction–diffusion systems with conserved masses. Protein-pattern forming systems *in vivo* (intracellular) and *in vitro* (reconstituted systems) will serve as the specific context for this part of the discussion. Finally, we will give a brief outlook on upcoming work, on questions that are currently under investigation, and on future research directions. In particular, we outline how local equilibria theory might provide a unifying geometric perspective on pattern formation in mass-conserving non-equilibrium systems and how it can be generalized to systems that are not strictly mass-conserving but contain a mass-conserving 'core'.

A. Summary of key concepts and results

Phase space analysis of (two-component) MCRD systems has shown that spatial variations in protein density give rise to spatially heterogeneous local equilibria. The relationship between mass and reactive equilibria is represented geometrically as a line of reactive equilibria (*reactive nullcline*) in phase space. Along the reactive nullcline, the reaction kinetics are balanced. We have shown that this nullcline is a central geometric object in phase space that organizes the spatiotemporal dynamics. Furthermore, we have identified a one-parameter family of (one-dimensional) manifolds in phase space on which diffusive fluxes balance. Any stationary pattern is embedded in one of these so-called *flux-balance subspaces*. The variable that parameterizes the family of flux-balance subspaces acts as a *mass-redistribution potential*: Its spatial gradients represent a local imbalance of diffusive fluxes that drives mass-redistribution. Thus, the mass-redistribution potential encapsulates the interplay between reactions and diffusion processes.

In this way, the spatiotemporal dynamics of the reaction–diffusion system is fully determined by geomet-

ric structures in phase space: (*i*) We introduced a *flux-balance construction*, based on intersection points between flux-balance subspace and reactive nullcline that enabled us to graphically construct stationary patterns and their complete bifurcation structure in the limit of large system size. Underlying this construction is the general insight that patterns are *scaffolded* by local equilibria which are, in turn, encoded by the reactive nullcline. This principle can be generalized to dynamics: (*ii*) The interplay between diffusive redistribution of mass and *shifting local equilibria* drives the pattern-forming instability that we termed *mass-redistribution instability*. Our analysis has shown that the slope of the nullcline provides a simple criterion for the occurrence of this instability. Importantly, we find that the onset of instability is generically subcritical in 2C-MCRD systems on a large domain. (*iii*) Generalizing the local equilibria concept, we have introduced a decomposition of the spatial domain into regions, such as plateaus and interfaces, which are characterized in terms of *regional dispersion relations*. This has enabled us to find simple heuristics for many properties of the pattern formation dynamics and stationary patterns. For instance, the width of the interface region can be approximated by the marginal mode of the regional dispersion relation at the interface. Building on this regional decomposition, one can characterize different pattern types and the transitions between them as control parameters are changed (Sec. V C). Furthermore, based on the concept of regional (in)stability we found an inherent connection between lateral (Turing) instability and stimulus-induced pattern formation ("nucleation and growth"), which enabled us to estimate the basin of attraction ("nucleation threshold") for stationary patterns by a simple heuristic using the reactive nullcline. As an additional advantage of such a characterization, we note that the reactive nullcline could in principle be determined experimentally for any given system in which the average total density can be controlled in a well-mixed "reactor".

Importantly, the concepts of scaffolding by local equilibria (*i*), mass-redistribution instability (*ii*) and regional dispersion relations (*iii*) are directly generalizable to systems with more components and more conserved quantities. We extensively discuss these future directions in the Outlook below.

B. Reaction–diffusion systems

For the sake of specificity, we will discuss the implications and application of our findings on mass-conserving reaction–diffusion systems with respect to protein pattern formation, which operates far from thermal equilibrium, and has received growing interest over the past two-decades. Intracellular, i.e. *in vivo*, protein pattern formation and self-organization have been subject to a large body of research, both experimentally (see Refs. [76, 77] for recent reviews) and theoretically (see Ref. [14] and

references therein.) Furthermore, the *in vitro* reconstitution of the MinDE system [78] has made it possible to study protein pattern formation experimentally under a wide range of externally controllable conditions; see Refs. [19, 79–88] and Ref. [89] for a recent review.

Taken together, these studies of both *in vivo* and *in vitro* systems have led to many important insights. However, many intriguing questions that are relevant to all reaction–diffusion systems far from equilibrium, remain open: What is the role of the (biomolecular) interaction network, and how can complex models be reduced to their essential components? What are the physical mechanisms underlying the pattern-forming instabilities and under which conditions do these instabilities arise? How can the dynamics of patterns far from the homogeneous steady state be studied systematically, i.e. how can we bridge the gap between the linear and the highly nonlinear regime? A particular question in this context is how different patterns and their characteristic length scales (interface width and wavelength) are selected in the highly nonlinear regime. In what follows, we discuss the implications of our work to these questions.

1. Model classification, network motifs and experimental accessibility

In recent years, several studies have employed high-throughput computational analyses of reaction–diffusion systems and graph theoretical analysis with the goal to infer the pattern-forming capabilities from the topology of the underlying reaction networks [90–93]. Our results offer an entirely new and distinct perspective on model classification and the role of the interaction-network topology for mass-conserving systems. We found a simple condition for the pattern-forming (mass-redistribution) instability in 2C-MCRD systems: The slope of the line of reactive equilibria (reactive nullcline) must be (sufficiently) negative. Broadly speaking, the reactive equilibrium of the faster diffusing (i.e. cytosolic) component has to decrease with increasing total density (cf. Sec. IV). Importantly, our approach goes beyond the classification based on linear (in)stability. It shows that the effect of nonlinearities on the dynamics is encoded in the curved shape of the nullcline. In particular, there is a direct connection between the nullcline shape and the characteristic spatial density profile of the pattern (cf. Sec. V C). The reactive equilibria, as represented by the reactive nullcline, might therefore provide an alternative approach to model classification. Hence, a key challenge for future research will be to study how specific reaction kinetics and model parameters affect the shape of the reactive nullcline.

Moreover, a major advantage of reactive equilibria as the essential criteria for model classification is their experimental accessibility. In principle, any line of reactive equilibria can be measured directly in experiments by using a single, isolated, and well-mixed reactor and

externally controlling the available conserved quantity (e.g. particle number). Such experiments would allow one to probe and classify the core mechanism quantitatively without any knowledge of the molecular details (which are irrelevant for such a classification).

The concepts that underlie local equilibria theory—mass redistribution and moving local equilibria—are not restricted to two-component systems with a single conservation law. They have previously been applied to the model of the (*in vitro*) MinDE system, which has two conserved protein species, MinD and MinE, and five components [16, 22]. We believe that the results presented here are foundational for the development of a more general theory. Our analysis constitutes the first step in a long-term project to find a geometric representation of the nonlinear dynamics of spatially extended systems. In the outlook, Section VIII D, we briefly describe various forthcoming works and future projects that build upon the present study and generalize its results.

2. Polarity patterns, bistability and the necessary condition for a Turing instability

Bistability is a generic feature of nonlinear systems, and its putative relation to polarity patterns has been controversially discussed in the literature [28, 32, 72, 94, 95]. In systems without mass conservation, bistable reaction kinetics facilitate traveling fronts that connect the two stable reactive equilibria (homogeneous steady states). (This scenario appears in mass-conserving systems as the special case of equal diffusion constants, which entails the lack of lateral mass redistribution; see Sec. VII B.) The stable equilibria of such a bistable medium can be pictured as scaffold for the traveling front. Because this scaffold is static in systems without mass redistribution, fine-tuning is required to achieve a stationary front (cf. Sec. VII B 1). Our results show that, in mass-redistributing systems (i.e. systems with unequal diffusion constants), the scaffold becomes dynamic and thereby supports stable, stationary polarity patterns in an extended parameter regime (cf. Sec. VII B). Most importantly, we found that, even in a monostable system, mass redistribution can facilitate the formation of a scaffold for stationary polarity patterns. Hence, bistability of the reaction kinetics is neither required nor sufficient for the formation of such patterns.

A central finding of our work is the physical mechanism by which the scaffold of a pattern emerges dynamically from a homogeneous steady state: the mass-redistribution instability (Sec. IV). Diffusive mass-redistribution requires that the diffusivities of the two components are different ("differential diffusion"); already a ratio D_m/D_c slightly different than unity is sufficient. This mass-redistribution drives an *instability* under the condition that the reactive nullcline in the phase space of the reaction kinetics includes a segment of negative slope. More precisely, the negative slope must be steeper

than the flux-balance subspace, whose slope is determined by the negative ratio of the diffusivities $-D_m/D_c$. As membrane–bound proteins are significantly less mobile than cytosolic proteins, i.e. $D_m \ll D_c$, a small negative slope of the reactive nullcline is already sufficient for a Turing instability in the intracellular context. Recall also that the criterion for bistability is a NC-slope more negative ("steeper") than -1 (cf. Sec. III A), which is obviously a more restrictive condition than that for lateral instability. Hence, a bistable region is generally surrounded by a larger region of lateral instability in parameter space (cf. Fig. 12).

One might wonder how generic nullclines with a segment of negative slope are. In fact, they are frequently encountered as N-shaped nullclines in a broad range of classical nonlinear systems [1, 2, 4, 96]. Typically, these nullclines encode some nonlinear feedback mechanisms that give rise to widespread phenomena such as relaxation oscillations, excitability and bistability. Feedback loops in intracellular signaling networks (e.g. GTPase and phosphorylation cycles) generically lead to these phenomena [97]. From this perspective, it appears that N-shaped nullclines should be rather common in biological systems.

Finally, the condition for mass-redistribution instability shows that, contrary to popular belief, Turing instability in a mass-conserving system can already arise for a ratio D_m/D_c only slightly below unity when the reactive nullcline has sufficiently steep segment (i.e. in the vicinity of saddle-node bifurcations of the reactive equilibria, cf. Fig. 12).

3. Mass-redistribution instability is mechanistically distinct from the activator–inhibitor paradigm

A key finding of our work is the physical mechanism of mass-redistribution instability: Shifting local equilibria induce gradients and hence (diffusive) mass-redistribution which, in turn, leads to further shifting of the local equilibria. Notably, mass-redistribution instability is a Turing instability in the original sense: a lateral instability due to diffusive coupling of a system that is locally stable in the absence of this coupling.

Importantly, the mechanism underpinning the mass-redistribution instability is distinct from the paradigm of short range activation and long range inhibition [98, 99]. The latter, termed "activator–inhibitor" mechanism, innately relies on some form of "production" and "degradation" processes, either of "morphogens" via gene-regulatory networks (e.g. in cell-cell signaling [100] and tissue patterning [101–103]), or of electric signals coupling excitory and inhibitory neurons (e.g. in the visual cortex where lateral instability may underlie hallucinations due to long range coupling of inhibitory neurons [104]). In contrast, intracellular pattern formation is often driven by (nearly) mass-conserving dynamics [14] and, hence, is necessarily based on a mass-redistribution

instability. Because, as we emphasized above, mass-redistribution instability is a Turing instability, self-organized intracellular protein-patterns (see Ref. [14] for a review) are examples for Turing patterns (in the sense of patterns that arise from a Turing instability [56]) in biological systems.

In general, it might not always be obvious whether the instability underlying pattern formation in a given system is either a mass-redistribution instability or one that essentially requires production and degradation. In the outlook Sec. VIII D 3, we propose a general definition to answer this question.

4. Subcriticality and stimulus-induced pattern formation

An important results of our analysis is that the onset of pattern formation in 2C-MCRD systems is generically subcritical (cf. Secs. V D and VII D). Subcriticality may be beneficial in a biological context, as it confers robustness: Once a pattern is established, it is robust towards parameter variations due to hysteresis [32, 64, 105].

Moreover, subcriticality implies the existence of parameter regimes where pattern formation can be triggered by sufficiently large perturbations (akin to "nucleation and growth" in the binodal regime of phase-separating systems). Such stimulus-induced pattern formation has been suggested as a new mechanism for pattern formation (under the term "wave-pinning"), which—it was argued—is fundamentally distinct from a lateral (Turing) instability [28, 29, 31]. This claim has been disputed in recent works [72, 106]. Indeed, our results show that linear instability and stimulus-induced pattern formation are inherently connected: the latter is possible only where there is an adjacent regime of linear lateral instability and the underlying mechanism is a *regional* (linear) lateral instability; see Sec. VI. Concretely, our results show that an interface—the elementary building block of a pattern—must necessarily be a laterally unstable region (cf. Sec. V A). Hence, the creation of a laterally unstable region is a necessary condition for the formation of a stationary pattern. This implies that, any two-component system that has a regime of stimulus-induced pattern formation, must also exhibit a regime where the homogenous steady state is laterally unstable, and this regime can always be reached by simply changing the average total density. Conversely, this suggests that subcriticality may be a generic feature of mass conserving systems since regional instability will facilitate stimulus-induced pattern formation adjacent to regimes where the homogeneous steady state is laterally unstable.

Finally, building on the concept of regional instability insights, we provided a simple geometric argument for the perturbation threshold for stimulus-induced pattern formation ("nucleation threshold") based on the reactive nullcline.

5. Length scale selection

An important consequence of subcriticality is that well-known mathematical results for systems near a *supercritical* instability may not apply anymore. Potentially the most prominent of such results is the existence of a *characteristic wavelength*, determined by the fastest growing mode in the dispersion relation. This is often considered as a defining property of "Turing patterns". However, for subcritical systems, the wavelength of the pattern cannot be inferred from a linear stability analysis of the uniform steady state in general—not even at onset. Indeed, 2C-MCRD systems always exhibit uninterrupted coarsening [15], i.e. the wavelength selected by the fastest growing mode at onset is observed only transiently and the final steady state is fully "phase separated."

Note, however, that coarsening is *not* a generic feature of all mass-conserving systems. Multicomponent MCRD models show (multi-)stable patterns with finite wavelengths [16, 107, 108]. We believe that identifying and understanding mechanisms of nonlinear wavelength selection that bring the coarsening processes to a halt and stabilize patterns with finite wavelength are among the most important tasks for future research on multicomponent models. While some rather general criteria have been found for one-component systems [109, 110], a comprehensive understanding of multicomponent systems remains out of reach for now.

In addition to the wavelength, patterns have a second characteristic length scale—the width of interfaces. While the wavelength of patterns far from the homogeneous steady state is not determined by the dispersion relation, we have shown in Section V A that the interface width is determined by the marginal mode (q_{max}) of the interface's *regional dispersion relation*. The more general insight underlying this finding is that highly nonlinear patterns can be decomposed into spatial regions and studied in terms of regional phase-spaces and regional attractors (cf. Sec. V B). In a follow-up work [22], we use this region decomposition to classify the different types of instabilities that govern Min-protein pattern formation *in vivo* and *in vitro*. In particular, we find that the interface width of standing wave patterns is also determined by the marginal mode of the regional dispersion relation.

6. Pattern types are determined by the nullcline shape

Two-component MCRD systems are found to exhibit two generic pattern types, referred to as mesas and peaks. In a recent numerical study of 2C-MCRD models [34], a phenomenological "saturation point" was found to mark the peak- to mesa-pattern transition. Our geometric analysis has now revealed the phase-space structure that underlies this "saturation point": It corresponds to an intersection point between reactive nullcline and diffusive flux-balance subspace; hence, its position dictated by the nullcline shape and the ratio of the diffusion constants.

Based on this insight, have shown that the nullcline shape serves as a simple criterion that to predicts the type of patterns formed by a given 2C-MCRD system; see Fig. 5.

Put briefly, we distinguish Λ- and N-shaped nullclines, based on their tail behavior for large densities. In the case of a Λ-shaped nullcline (e.g. nullclines that asymptotically approach the m-axis for large m; see Figs. 5b and 17) and a shallow flux-balance subspace ($D_m/D_c \ll 1$), a mesa pattern forms only when the average mass is sufficiently large. For lower densities, the system exhibits peak patterns instead. Their amplitude depends sensitively on the total mass and the membrane diffusion constant. The approximation of the peak pattern amplitude provided in Sec. VC (details in Appendix G), provides a simple estimate of the total (protein) mass at which peak patterns transition to mesa patterns. Notably, the amplitude of peak patterns and the transition to mesa patterns depends sensitively on the ratio of the diffusion constants. In the case of an N-shaped nullcline (see Figs. 2 and 5a), mesa patterns are generic, because the high-density plateau is already formed at low average mass (even if $D_m/D_c \ll 1$). (Peak patterns are also possible for such nullclines, but require fine tuning of the average mass to the vicinity of bifurcation points (see Fig. 6).)

These findings have important biological consequences because the characteristic features of a pattern dictate the positional information it can convey, and therefore the biological function it can facilitate [14, 111–114]. For example, cell division in budding yeast (*S. cerevisiae*) requires the formation of a single, narrow polarity site marked by a high density of the protein Cdc42, to uniquely determine the future bud site [115, 116]. This requirement is met by peak patterns. Mesa-like patterns, in contrast, sharply separate two spatial domains. This is, for instance, a feature of PAR-protein patterns in *C. elegans* [64, 117–119]. Interestingly, the stem cells that polarize via PAR-protein pattern formation become smaller after each cell division during morphogenesis of the *C. elegans* embryo [36]. As the cell size approaches the interface width, the patterns transition from the mesa to the 'weakly nonlinear' type (cf. Sec. VII D). Finally the system size becomes so small that the Turing instability is suppressed (see discussion of the marginal mode $q_{\max}$ in Sec. IV). This size-dependent loss of cell polarization has been shown to be important for stem-cell fate decision [36].

An important difference between peak and mesa patterns is how they respond to changes in average total protein density, e.g. owing to up- or down-regulation of gene expression, or system size, e.g. due to growth. An increase in average mass makes peak patterns grow in amplitude, while for mesa patterns it leads to a shift in the interface position. Upon an increase in system size, peak patterns grow in amplitude, because the total number of proteins in the system increases. In contrast, amplitude and the relative interface position of mesa patterns remain unchanged. Hence, mesa patterns inher-

ently scale with the system size—a property that is desirable in developmental systems. Note, however, that the interface width of mesa patterns does *not* scale with the system size, and is independent of the average total density (Sec. VC).

Another difference between patterns composed of peaks vs patterns composed of mesas is their rate of coarsening by competition for mass. Peak patterns coarsen significantly faster than mesa patterns [15, 34]. Fast coarsening is important if the biological function requires selection of a single polarity site, as for instance cell division of budding yeast [115, 116].

C. Non-equilibrium phase separation

On the phenomenological level, the dynamics of 2C-MCRD systems closely resembles a phase separation process, as exhibited by binary mixtures that undergo liquid-liquid phase separation near *thermal* equilibrium. We showed that the bifurcation diagram of 2C-MCRD systems (Fig. 8), obtained by the flux-balance construction on the reactive nullcline, resembles the phase diagram of phase separation with spinodal and binodal lines that meet in a critical point. The analogous process to spinodal decomposition is the mass-redistribution instability (Sec. IV). In both cases, the condition for instability is that a potential decreases as a function of the total density. In the former case, it is the *chemical* potential, derived from a free energy functional, while in the latter case it is the mass-redistribution potential $\eta^*(n)$ derived from the reactive nullcline. Moreover, nucleation in the binodal regime of binary-mixture phase separation corresponds to stimulus-induced pattern formation in 2C-MCRD systems (Sec. VI). In addition to their equivalent phase diagrams, binary-mixture phase separation and 2C-MCRD systems and both exhibit uninterrupted coarsening [15].

This phenomenological equivalence between binary-mixture phase separation and 2C-MCRD dynamics is quite remarkable, since the former describes systems close to thermal equilibrium, while the latter is inherently far from thermal equilibrium (driven by a chemical fuel like ATP/GTP in the case of proteins). In fact, segregation into domains of high and low density is observed in many other non-equilibrium systems, most prominently self-propelled particles that exhibit formation of polar waves and nematic lanes [120, 121] and motility-induced phase separation (MIPS) [122]. Further examples include active contractility [123], motile bacteria [124], and shear banding [125]. Some authors have used the term "active phase separation" [67, 126, 127] for such phenomena.

One interesting feature shared by many phase-separating systems is that they exhibit interrupted coarsening ('micro-phase separation') once the mass conservation is weakly broken by additional production and degradation terms. The strength of these terms determines the length scale where coarsening arrests. This

holds true both near thermal equilibrium [128, 129] and for MIPS of self-propelled particles subject to a birth–death process [130, 131]. In a followup work to the present manuscript, we show that the same holds true for two-component reaction–diffusion systems with weakly-broken mass conservation [15]. Interestingly, interrupted coarsening can also occur as a consequence of non-reciprocal coupling that destroys the variational nature of the Cahn–Hilliard model [132].

Given the phenomenological equivalence to phase separation near thermal equilibrium, one might be tempted to search for a mapping to an effective thermodynamic language or develop an entirely phenomenological thermodynamic description. In fact, for 2C-MCRD systems with a specific form of reaction kinetics, $f = c - g(m)$, an effective free-energy functional can be constructed [44, 46, 47], giving a gradient-flow structure to the 2C-MCRD dynamics with such a reaction term. In this specific case, some of the results presented here, like the phase diagram with binodals and spinodals, can be inferred directly from the mapping to equilibrium phase separation (see e.g. Ref. [46]). Moreover, the mapping implies uninterrupted coarsening for this specific form of reaction kinetics.

However, such an approach disregards the actual underlying non-equilibrium physics. Our analysis of 2C-MCRD systems shows how a framework can be developed that is rooted in the underlying physics (here chemical reactions and diffusion) and not subject to the restrictions of a mapping to an effective thermodynamic description. Concretely, we show in a followup work that uninterrupted coarsening is generic in 2C-MCRD systems independently of the specific reaction kinetics [15]. Moreover, a thermodynamic description cannot account for the rich phenomenology, including and oscillatory patterns and waves [16, 22, 51, 52, 133–135], that arises once coupling to additional components or source terms breaking mass-conservation are included. In contrast, local equilibria theory has proven useful also in these more complex scenarios [15, 16, 22]. We further discuss this perspective in the final two subsections of the Outlook.

Instead of describing attachment and detachment of proteins at a membrane, Eq. (1) can be interpreted as the mean field equation for particles undergoing Brownian motion and switching between two states with different velocities/tumbling rates. Then the reaction term $f = f(n)$ describes the switching dynamics that depends on the local density of particles (e.g. by some quorum sensing mechanism), and m and c are the concentrations of slow and fast diffusing particles, respectively. This system constitutes a minimal example for MIPS and shows that MIPS and Turing instability are analogous on the mean field level. MIPS is typically studied for particles with continually varying velocity that depends on the local particle density. For particles switching between two states with different velocities, the mean velocity varies continuously as a function of the total density.

Hence, we define the average diffusion constant

$$\bar{D} = \frac{D_m m + D_c c}{m + c}, \tag{51}$$

which is directly connected to the mass-redistribution potential via the identity $\eta = n\bar{D}/D_c$. With this, the nullcline-slope condition for lateral instability, $\partial_n \eta^* < 0$, can be recast as

$$\frac{\partial_n \bar{D}^*}{\bar{D}^*} < -\frac{1}{n}. \tag{52}$$

(As always, the star denotes evaluation at the reactive equilibrium; the function $\bar{D}^*(n)$ can be obtained from the reactive nullcline, $\eta^*(n)$, via the relation $\bar{D}^*(n) = D_c \eta^*(n)/n$.) Notably, the condition for MIPS has exactly the same form as Eq. (52), where the density dependent particle velocity $v(n)$ takes the place of the average diffusivity $\bar{D}^*(n)$.

This reveals the *common underlying principle* of Turing instability in MCRD systems and the instability driving MIPS of self-propelled particles: slowing down of particles in regions of high density. For an instability to occur, particles have to slow down enough in response to an increase in density, cf. Eq. (52).

Another phenomenon that can be pictured as a phase separation process is shear banding in complex fluids. In Appendix L, show how one can establish an analogy between our flux-balance construction on the reactive nullcline for 2C-MCRD systems and the "common total stress" construction on the *constitutive* relation employed to analyze shear banding [125, 136]. This analogy shows that these physically distinct systems are *topologically equivalent*, i.e. share the same phase space geometry.

D. Outlook

Based on the theoretical concepts presented in this work for 2C-MCRD systems there are several promising directions for future research. First of all, for 2C-MCRD systems several follow-up works elucidate the principles at work during wavelength selection [15] and address how self-organization may be controlled by spatiotemporal "templates" [20] and by advective flows [21]. Going forward, it will be interesting to explore various avenues toward generalization to MCRD systems with more components and conserved species, including applications to various specific physical and biological systems as outlined shortly below. The long-term perspective is a generalization toward a geometric theory of MCRD systems. Below, we discuss some possible routes towards such a generalization in more detail.

In a broader context, reaction–diffusion systems are part of a large class of non-equilibrium systems that are able to form self-organized patterns. This includes models for living matter where molecular motors generate

active flows [123, 137] and active visco-/poroelastic deformations of the medium [134, 138], as well as particle-based active matter [120, 122, 139] and granular media [140]. Ultimately, it may be fruitful to apply the concepts presented here to such systems.

1. Generalization to more complex phenomena

The 2C-MCRD system studied here has a comparatively simple phenomenology, exhibiting only steady states that are stationary (no oscillations) and no wavelength selection (uninterrupted coarsening). In a previous study [16], and recently in Ref. [22], the concepts of mass redistribution and local equilibria have already been successfully employed to analyze a multicomponent multispecies MCRD model (for MinDE *in vitro* pattern formation) that exhibits much more complex phenomena, like spatiotemporal chaos (chemical turbulence) at onset and a transition to order (standing and traveling waves). These phenomena, observed in numerical simulations, can be understood in terms of the changing local stability of local equilibria due to mass redistribution.

In particular, this study revealed intriguing, highly non-trivial, connections between the nonlinear pattern dynamics far from the homogeneous steady state and the dispersion relation that characterizes the linearized dynamics in the vicinity of the homogeneous steady state. However, these findings are model specific, and rely on numerical simulations. In contrast, the characterization of the 2C-MCRD systems presented here is independent of the specific model (reaction term) and enables us to predict the pattern formation dynamics from a simple graphical analysis, without the need to perform numerical simulations. The obvious next step is to generalize this level of understanding to more complex phenomena by studying three-component MCRD systems. Such models have recently been employed to model various (bio-)physical phenomena in numerical studies [108, 141]. Studying these models using local equilibria theory might reveal the principles underlying their dynamics and provide a good starting point for a generalization of the theory presented here.

For ODE dynamics, the seemingly small step from two to three variables increases the diversity of phenomena dramatically. We expect a similar situation for spatially extended systems. Note in particular that, with three components and one conserved quantity, the reactive phase space will be two-dimensional. This allows for more complex local dynamics and attractors, such as limit cycle oscillations. A fully general study of three-component MCRD systems will therefore probably not be possible from the outset. Instead we propose to focus on cases where a time-scale separation enables one to build on the results for two-component systems. A good starting point is to study cases where the coupling to the additional third component is slow (the model investigated in Ref. [108] is of that form) using, for instance,

a singular perturbation analysis. Closely related to such three-component MCRD systems are *nearly* mass-conserving two-component systems that contain production/degradation terms on a slow timescale (see next subsection). Making use of such timescale separations is has proven to be a powerful strategy to study complex phenomena in dynamical systems; see for instance Ref. [142] for a comprehensive overview of three-variable ODE systems in the context of neural excitability.

The benefit of such an approach is that the effects of strong nonlinearities may be captured by a geometric phase-portrait analysis of the fast two-variable subsystem. More complex behavior arises as the slow dynamics modifies the fast subsystem, driving it through bifurcations. Analogously, in reaction–diffusion systems, the effects of the strong nonlinearities are encoded in the shape of the nullcline, which enables one to construct the elementary patterns (mesas, peaks). Much richer phenomenology can arise by the modification of these elementary patterns due to additional *linear* (or weakly nonlinear) terms, whose effects could be studied using the method of regional phase spaces (Sec. V B). This can be viewed as a dual ("strong coupling") approach to the amplitude equation formalism (weakly nonlinear analysis), where the elementary pattern originates in the narrow band of unstable modes, and the modification of the pattern due nonlinearities that couple these modes perturbatively.

Another promising direction of study is the role of noise in stochastic MCRD systems. Noise-induced phenomena in reaction–diffusion systems have previously been studied for models with (e.g. [27, 30]) and without conserved quantities (e.g. [100, 143–146]). Importantly, noise in reaction–diffusion systems is not constrained by the fluctuation-dissipation theorem, but must be inferred from the stochasticity of the chemical processes by explicit coarse graining, using, for instance, path integral approaches [135].

2. Model reduction and classification

While multicomponent, multispecies models can exhibit complex phenomenology, as discussed above, this is not *necessarily* the case. For instance, cell polarization of eukaryotic cells is often brought about by a large number of interacting protein species. Well-studied examples are the Cdc42 system of *S. cerevisiae* [26, 34, 147, 148] and the PAR system of *C. elegans* [32, 64, 118, 119]. Despite the complexity of these systems, their phenomenology—cell polarization—is simple and can already be captured by two-component systems as studied here. This raises the question whether complex models can be reduced to an underlying minimal 'core' that captures their essential phenomenology. The finding that redistribution of conserved quantities is the essential driver of pattern formation in MCRD systems suggests that such a reduction might be possible in the phase space of conserved

quantities—the *control space*. Note that such reduced 'core' systems may comprise more than two components and more than a single conserved mass. As we detail in the next subsection, even non-conservative models can have a mass-conserving 'core'.

The central theme of local equilibria theory is that conserved quantities are control parameters for reactive equilibria. Hence, the bifurcation scenario of reactive equilibria in the control space may serve as a criterion for classifying models. One example of such a class is the cusp bifurcation scenario, found by numerical analysis of various cell-polarization models in Ref. [32], and identified here as the general bifurcation scenario underlying pattern formation in 2C-MCRD systems. In a forthcoming work, we will use our theory to elucidate the control-space geometry underlying the pole-to-pole oscillations of the *in vivo* MinDE system [23]). As there are two conserved quantities, the total densities of MinD and MinE respectively, the control space is two-dimensional and there are surfaces (instead of lines) of reactive equilibria. Using the local quasi-steady state approximation, these *nullcline surfaces* allow for a geometric analysis of the *in vivo* MinDE dynamics. We propose this geometrically motivated approach as an alternative to algebraically motivated model reduction methods, such as the quasi-steady-state approximation of slowly diffusing components [149] or (extended) center-manifold reduction [150, 151]. Such an approach offers the advantage that it does not require abstract mathematical calculations and instead enables one to gain physical intuition from elementary geometric objects and graphical constructions. Furthermore, as pointed out earlier, reactive equilibria in principle allow one to assess phase-space geometry experimentally. This could ultimately make it possible to infer theoretical models from experimental data at a mesoscopic level, especially in situations where access to more molecular information (at the protein level) is not available yet.

3. Beyond strict mass conservation

What can we learn from local equilibria theory about systems without strict mass conservation?

Non-equilibrium systems are dissipative, that is, they consume some sort of chemical fuel (e.g. ATP in biological systems and malonic acid in the Belousov–Zhabotinsky (BZ) reaction [152]) that drives them far from thermal equilibrium. The chemical fuel often drives cycling of components between different states, as illustrated in Fig. 15. Examples are cycling of NTPase proteins between active and inactive states [153]; phosphorylation–dephosphorylation [154, 155] and membrane attachment–detachment of proteins [14]; and cycling between molecular bromine and bromide ions and cycling of a metal catalyst (e.g. cerium) in the BZ reaction [152, 156, 157]. While such cycles consume a fuel (and produce a waste), they conserve the total density of the
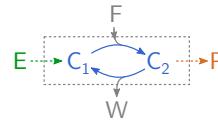
FIG. 15. Basic elements of a (chemical) system with a mass-conserving 'core'. The cycling of the 'core' between two states, C_1 and C_2, is driven out of thermal equilibrium by consumption of a fuel F and production of a waste W. If the fuel is abundant, and replenished from the outside it can be assumed to be present at constant concentration. The cycling components are produced from a precursor E and irreversibly degraded to a product P. When production and degradation are slow compared to the rate of cycling between C_1 and C_2, the system inside the dashed box may be treated as mass-conserving on the fast timescale of cycling.

cycling components (C_1 and C_2 in Fig. 15). The chemical fuels are quite generally assumed to be supplied from a large reservoir and hence are not explicitly modeled. Several recent works study explicitly the role of a finite fuel supply in the framework of stochastic thermodynamics [158–160]. In particular, in Ref. [160], the bifurcations of bistable and oscillatory well-mixed systems are studied as they approach thermal equilibrium where detailed balances holds (vanishing chemical potential difference between fuel and waste).

In addition, there may be production and (irreversible) degradation processes that break the (strict) conservation of the cycling components. To dissect the roles of conserving and non-conserving processes, any reaction kinetics can be split up into the respective functional terms. For a general two-component reaction–diffusion system, such a splitting would take the form

$$\partial_t m(x,t) = D_m \partial_x^2 m + f(m,c) \ + \ \gamma\, s_1(m,c), \quad (53\text{a})$$

$$\partial_t c(x,t) = \ D_c \partial_x^2 c \ - f(m,c) \ + \ \gamma\, s_2(m,c). \quad (53\text{b})$$

where γ describes the ratio of the timescale of mass-conserving reactions encoded in f and the timescale of production/degradation processes encoded in the source terms $s_{1,2}$ [161]. If γ is small, one can study the mass-conserving subsystem (limit $\gamma \to 0$) using the theory presented here. In particular the capacity for pattern formation of the mass-conserving subsystem can be directly read off from the shape of the f-nullcline. The remaining effect of the source terms in this limit is to set the total average mass $\bar{n}$, which is no longer a control parameter when $\gamma \neq 0$, but is controlled by the parameters in $s_{1,2}$ instead. Geometrically, this corresponds to setting the center of mass of a pattern in the (m,c)-phase plane.

A decomposition into mass-conserving and non-conserving terms of the form Eq. (53) can be carried out for systems with any number of components. (Note that this should be done *before* model reductions like non-dimensionalization and variable eliminations that affect the mass-conserving terms.) Linear stability analysis can then be used to determine whether the mass-conserving

subsystem is able to form patterns by setting $\gamma = 0$. This defines two classes of systems, (i) those where pattern-forming instability is preserved in the mass-conserving case $\gamma = 0$, and (ii) those that inherently depend on production and degradation (i.e. don't exhibit lateral instability for $\gamma = 0$). Put differently, class (i) systems do have a *pattern-forming*, mass-conserving core, while class (ii) systems don't. Of course, the distinction between these two classes will be limited if γ is too large such that production-degradation dynamics dominate over the mass-conserving core.

The mass-conserving 'core' of systems (or regimes) in class (i) can be analyzed using the local equilibria theory. An immediate conclusion is that their lateral instability is driven by a mass-redistribution cascade. This insight may inform model reduction of many-component models as we have discussed in the previous subsection. Furthermore, one can then study how the 'core patterns' are qualitatively and quantitatively modified by $0 \neq \gamma \ll 1$. Importantly, $\gamma \neq 0$ might be a singular perturbation, i.e. weakly broken mass conservation might cause a qualitative change in the dynamics, such as interrupted coarsening and oscillations; see example (i) below. Importantly, for $\gamma \ll 1$ these qualitatively new phenomena will play out at large length- and timescales, whereas the behavior at short scales is still determined by the mass conserving core; see e.g. Ref. [15]. In the language of bifurcation theory, the mass-conserving 'core' would take the role of an "organizing center" from which the various dynamical regimes of the system "unfold" (see e.g. section 30 in Ref. [74] and chapter 3 in Ref. [75]). Let us provide examples for the two classes of systems defined above.

Example for class (i): Brusselator model. — Let us exemplify the reduction to a mass-conserving core for a classical model, the Brusselator [50]. This early, qualitative model for the BZ reaction can be written in the form Eq. (53) where $f(m, c) = m^2 c - m$, $s_1 = k_{\text{in}} - k_{\text{out}} m$, $s_2 = 0$. The nullcline of f has two segments, $m = 0$ and $c^*(m) = 1/m$, which is a singular case of an N-shaped nullcline. Thus, it is immediately clear that pattern formation of the Brusselator is driven by a mass-conserving core and that its elementary stationary patterns are mesa patterns when $D_c \gtrsim D_m$ and peak patterns when $D_c \gg D_m$. Slow production and degradation lead to interrupted coarsening and splitting of the mesa patterns at length scales that depend on γ as has been studied using singular perturbation methods in the limit $\gamma \ll 1$ [162–165]. Local equilibria theory, in particular the phase-portrait analysis of spatially extended systems that it facilitates, provides a new, intuitive approach that explains the physics underlying interrupted coarsening and mesa splitting [15]. Moreover, in the oscillatory regime of the Brusselator, the limit cycle oscillations can be constructed as relaxation oscillations on the basis of the nullcline of the mass-conserving core (f-nullcline) in the limit $\gamma \ll 1$ [52]. The oscillation period depends on γ and diverges in the limit $\gamma \to 0$.

Example for class (ii): Gierer–Meinhardt model. —

An example for a two-component system without a mass-conserving core (class (ii)) is the "Gierer–Meinhardt" model [98]. This model describes an "activator" which enhances its own production and the production of an "inhibitor" which impedes the "activator's" production. Both "activator" and "inhibitor" are degraded at constant rates. Written in the form Eq. (53), using $\{a, h\}$ for the "activator" and "inhibitor" concentrations instead of $\{m, c\}$, one has $f = 0$, $s_1 = k_a^+ + k_{\text{fb}} a^2/h - k_a^- a$, $s_2 = k_h^+ + k_{\text{fb}} a^2 - k_h^- h$. Clearly, this system does not possess a mass-conserving core capable of pattern formation. Generally, systems in class (ii) are those where production (from a reservoir or substrate) and irreversible degradation are the dominant processes; for instance, during tissue patterning (morphogenesis) [101–103] or cell-cell signaling in bacterial colonies [100].

The role of (nearly) conserved quantities in classical pattern-forming systems. — Many chemical systems contain a mass-conserving 'core' of components that rapidly cycle between different states and are produced and degraded only on a much slower timescale. An example is the cycling of bromine between a molecular form and a bromide ion in the BZ reaction. It is an interesting question whether this core alone is able to produce some non-trivial behavior like oscillations or patterns (assuming that the chemical fuel driving the cycling of the core components is abundant, as e.g. ATP in protein-based pattern formation). Systems where this is the case can then be analyzed using local equilibria theory (potentially extended to account for slow production and degradation, see e.g. [15]). Above, we showed that this is true for the Brusselator, which is a conceptual model for the BZ reaction. We hypothesize that a similar approach might/will also work for more detailed models such as the so-called FKN mechanism [157], whose mass-conserving core presumably contains more than two components.

Such a program might eventually lead to a perspective that unifies "classical" pattern-forming systems such as the BZ reaction and the more recently discovered biological systems, including the Min system [16, 22, 78], intracellular actin waves [133, 166], and Rho excitability [167–170].

4. Beyond reaction–diffusion systems

In the systems discussed so far (excluding Sec. VIII C), energy is fed into the system via the reaction kinetics alone, while the spatial transport process, diffusion, is passive. Such systems are part of a broader class of so-called *active* systems where energy is fed in on the microscopic scale. This comprises systems where the transport processes are active, driven e.g. by molecular motors such as myosin. Examples include systems with active flows generated by cortical contractions [123, 137], as well as actively deforming visco- and poroelastic media [134, 138]. On a more conceptual level, several non-equilibrium generalization of the Cahn–Hilliard equation have been studied recently [132, 171–173]. The phenom-

ena exhibited by the above systems include (micro-)phase separation and more complex phenomena like waves and turbulence. Another broad sub-class of active systems are self-propelled particles that exhibit a huge variety of collective phenomena, including MIPS ([122], see Sec. VIII C above) and flocking [120, 121, 174].

What all these systems have in common with MCRD systems is the presence of conserved quantities that serve both as macroscopic variables and as local parameters of the microscopic dynamics. We therefore expect that the ideas on mass redistribution and local equilibria put forward in this article can be broadly applied to understand emergent behavior in these systems. As a concrete example, the self-organized interplay between total density and emergent orientational order (polar or nematic) was investigated recently for self-propelled particles with microscopic alignment interactions that are continuously tunable between polar and nematic symmetry [174]. Here, the *local* particle density controls the emergent orientational order, i.e. induces local symmetry breaking. In turn, the orientational order leads to particle currents that redistribute the particle density. Strikingly, this interplay explains the coexistence of different macroscopic structures, such as polar flocks and nematic lanes, and the continual interconversion between them as recently observed in experiments and agent-based numerical simulations [121].

ACKNOWLEDGMENTS

Appendix A: Models used for illustration and numerical studies

To visualize the our findings on pattern formation in 2C-MCRD systems we use two prototypical reaction terms, $f(m, c)$, that exhibit two distinct nullcline shapes. Both variants effectively model attachment–detachment dynamics as used to describe cell-polarization systems:

(*i*) The reaction kinetics used in Ref. [28], to conceptually describe cell-polarization based on autocatalytic recruitment (Michaelis-Menten kinetics with Hill coefficient 2) and linear detachment:

$$f(m, c) = \left(k_{\text{on}} + k_{\text{fb}} \frac{m^2}{K_{\text{d}}^2 + m^2}\right) c - k_{\text{off}} m. \qquad \text{(A1)}$$
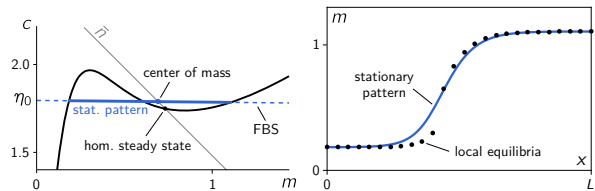
FIG. 16. Left: numerically phase-space distribution (thick blue line) of a computed stationary pattern embedded in the flux balance subspace (dashed blue line). The thin gray line shows the reactive phase space corresponding to the average total density $\bar{n}$. Right: spatial profile (solid blue line) together with numerically determined local equilibria ($\bullet$). Parameters: $k = 0.07$, $\bar{n} = 2.48$, $D_m = 0.1$, $D_c = 10$, $L = 10$.

We can non-dimensionalize by expressing time in units of k_{off}^{-1} and densities in units of K_{d}. Furthermore, for specificity we set the (non-dimensional) feedback rate $k_{\text{fb}}/k_{\text{off}} =: \hat{k}_{\text{fb}} = 1$, leaving only $k := k_{\text{on}}/k_{\text{off}}$ as free parameter in the non-dimensional reaction term:

$$f(m, c) = \left(k + \frac{m^2}{1 + m^2}\right) c - m. \qquad \text{(A1*)}$$

Fig. 16 shows the nullcline in the (m, c)-phase plane of the reaction kinetics Eq. (A1*) for $k = 0.07$, together with a numerically determined stationary pattern (steady-state solution to Eq. (1)) and the local equilibria (spatial profile on the right).

(*ii*) Dynamics due to attachment together with linear self-recruitment and enzyme driven detachment (described by first order Michaelis–Menten kinetics):

$$f(m, c) = (k_{\text{on}} + k_{\text{fb}} m)c - k_{\text{off}} \frac{m}{K_{\text{d}} + m}. \qquad \text{(A2)}$$

We non-dimensionalize by expressing time in units of the attachment rate k_{on} and densities in units of the dissociation constant K_{d} of the detachment kinetics. The two remaining parameters are the (non-dimensional) feedback rate $\hat{k}_{\text{fb}} := K_{\text{d}} k_{\text{fb}}/k_{\text{on}}$ and detachment rate $\hat{k}_{\text{off}} := k_{\text{off}}/(k_{\text{on}} K_{\text{d}})$:

$$f(m, c) = (1 + k_{\text{fb}} m)c - k_{\text{off}} \frac{m}{1 + m}, \qquad \text{(A2*)}$$

where we suppressed the hats. Fig. 17 shows a typical reactive nullcline for the reaction term Eq. (A2*) together with a stationary peak pattern and the local equilibria that scaffold it.

a. Length scale. — For convenience, we do not specify a unit of length in the domain size L and the diffusion constants $D_{m,c}$. In an intracellular context a typical size would be $L \sim 10\,\mu\text{m}$, and typical diffusion constants $D_m \sim 0.01-0.1\,\mu\text{m}^2\,\text{s}^{-1}$ on the membrane and $D_c \sim 10\,\mu\text{m}^2\,\text{s}^{-1}$ in the cytosol. Rescaling to different spatial dimensions is straightforward.
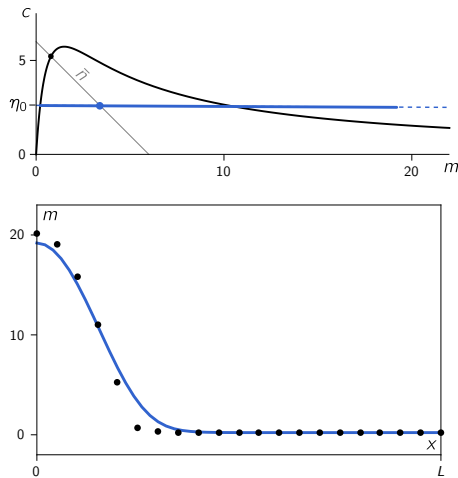
FIG. 17. Above: Numerically determined phase space distribution and stationary pattern profile and for an MCRD system with the reaction kinetics Eq. (A2*). Below: stationary pattern together with local equilibria (●). Parameters: $k_{\mathrm{fb}} = 0.45$, $k_{\mathrm{off}} = 16$, $\bar{n} = 6$, $D_m = 1$, $D_c = 200$, $L = 10$

b. Nullcline shape predicts the pattern type. — Important for the distinction between peak-forming vs. mesa-forming systems is the behavior of the reactive nullcline for large n. If it approaches the m-axis monotonically for large n, then peak patterns are will form in a large range of $\bar{n}$ for $D_m/D_c \ll 1$ (see Fig. 23). Otherwise, mesa patterns are typical while peak/trough patterns only form in narrow regimes at the edges of the range of pattern existence $[n_-^\infty, n_+^\infty]$. For attachment–detachment kinetics, one can study the nullcline behavior for large n by comparing the largest powers in the denominator and numerator of the functional form $c^*(m) = m\,d(m)/a(m)$ of the nullcline. For the reaction term Eq. (A1*), one obtains $c^*(m \to \infty) \to m$, i.e. typically mesa patterns. For the reaction kinetics Eq. (A2*), one has $c^*(m \to \infty) \to 0$, favoring peak patterns for $D_c \gg D_m$.

Appendix B: Numerical simulations

The reaction–diffusion dynamics were simulated on a domain with no-flux boundaries using the numerical PDE-solver routine `NDSolve[]` provided by Mathematica (see Supp. File "PDE-solver_minimal-setup.nb" for an example setup). In the videos we show the density distribution in phase space and the real space profile $m(x,t)$ together with local equilibria.

Appendix C: Linear stability analysis

This section provides the technical details of linear stability analysis.
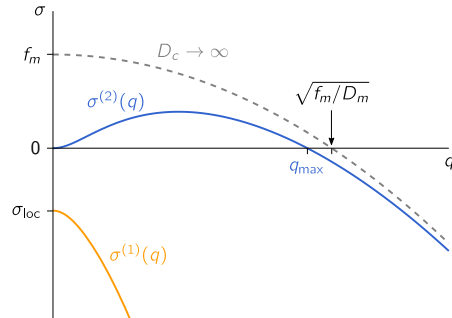
FIG. 18. Generic dispersion relation of the 2C-MCRD system in a laterally unstable regime. The two branches $\sigma_q^{(1,2)}$ of the eigenvalue problem for $J(q)$ are shown in blue and yellow. At $q \to 0$, the branches connect to the eigenvalues $\sigma_{\mathrm{loc}} = f_m - f_c$ and 0 of the local stability problem. For $D_c \to \infty$, the second branch approaches $\sigma_q^{(2)} \to f_m - D_m q^2$ for $q > 0$. Accordingly, $q_{\max}$ approaches $\sqrt{f_m/D_m}$. "Parameters": $f_m = 0.7$, $f_c = 1$, $D_m = 1$, $D_c = 10$.

1. Canonical linear stability analysis

Linear stability analysis of a reaction–diffusion system is performed by expanding a spatial perturbation in the eigenbasis of the diffusion operator (Laplacian) in the geometry of the system. In a line geometry with reflective boundary conditions at $x = 0, L$, the eigenfunctions of the Laplacian are the discrete Fourier modes $\cos(k\pi x/L)$ with $k \in \mathbb{N}$. Linearization of the dynamics of a mass-conserving two-component system around a homogeneous steady state (m^*, c^*) yields the linear dynamics

$$\partial_t \begin{pmatrix} \delta m_q(t) \\ \delta c_q(t) \end{pmatrix} = J(q) \begin{pmatrix} \delta m_q(t) \\ \delta c_q(t) \end{pmatrix} \tag{C1}$$

with the Jacobian

$$J(q) = \begin{pmatrix} -D_m q_k^2 + f_m & f_c \\ -f_m & -D_c q_k^2 - f_c \end{pmatrix}, \tag{C2}$$

where we use the abbreviations $q_k = k\pi/L$ for the (discrete) wavenumbers and $f_{m,c} = \partial_{m,c} f\big|_{(m^*,c^*)}$ for the linearized kinetics at the homogeneous steady state. The eigenvalues of the Jacobian yield the growth rates $\sigma_q^{(i)}$ of the respective eigenmodes such that a perturbation in the spatial eigenfunction $\cos(qx)$ evolves in time as

$$\begin{pmatrix} \delta m_q(t) \\ \delta c_q(t) \end{pmatrix} = \sum_{i=1,2} A_q^{(i)}\, \mathbf{e}_q^{(i)} \exp(\sigma_q^{(i)} t) \cos(qx), \tag{C3}$$

with the eigenvectors $\mathbf{e}_q^{(i)}$. For a given initial condition (perturbation), the coefficients $A_q^{(i)}$ are determined by projecting initial condition the onto the eigenbasis $\mathbf{e}_q^{(i)} \cos(qx)$.

To calculate the eigenvalues of the Jacobian, we use that the eigenvalues of a 2×2-matrix can be expressed in terms of its trace τ and determinant δ:

$$\sigma^{(1,2)} = \tau/2 \pm \sqrt{\tau^2/4 - \delta}, \qquad (C4)$$

where the indices $\{1, 2\}$ correspond to $\{-, +\}$ on the RHS.

The trace and determinant of the Jacobian $J(q)$ can be written as

$$\tau_q = f_m - f_c - (D_m + D_c)q^2,$$
$$= \sigma_{\text{loc}} - (D_m + D_c)q^2, \qquad (C5a)$$

$$\delta_q = q^2 D_m D_c \left(q^2 + \frac{f_c}{D_c} - \frac{f_m}{D_m} \right),$$
$$= q^2 D_m D_c \left(q^2 - q_{\max}^2 \right), \qquad (C5b)$$

where we used the expression Eq. (28) for $q_{\max}$.

From Eq. (C5a), it follows that for a locally stable hom. steady state ($\sigma_{\text{loc}} < 0$) the trace τ_q is negative for all q. Hence, the only way to get lateral instability is a negative determinant $\delta_q < 0$. This implies that eigenvalues with positive real part must be purely real, since the term under the square root in Eq. (C4) is positive. This means that there cannot be oscillatory lateral instability for a locally stable hom. steady state. Moreover, the instability condition $\delta_q < 0$ immediately yields the band of unstable modes $[0, q_{\max}]$.

Figure 18 shows the two branches of eigenvalues, $\sigma_q^{(1,2)}$, for a laterally unstable case. In the limit $q \to 0$, the first branch connects to the eigenvalue of a well-mixed system $\sigma_0^{(1)} = \sigma_{\text{loc}}$ (cf. Sec. III A). The corresponding eigenvector lies in the reactive phase space for $q = 0$, and hence fulfills mass conservation.

The second branch, $\sigma_q^{(2)}$, smoothly approaches zero in the limit $q \to 0$. The eigenvector $\mathbf{e}_0^{(2)}$ corresponding to the marginal eigenvalue $\sigma_0^{(2)} = 0$ points along the reactive nullcline. It represents a perturbation that changes the total density and thus shifts the reactive equilibrium. For the stability of a closed, well-mixed system (i.e. the stability against homogeneous perturbations) such a perturbation is not relevant since it breaks mass conservation. For $q \neq 0$, the perturbation is spatially inhomogeneous, and therefore redistributes mass in the system. This mass redistribution shifts the local equilibria. That the eigenvector points along the reactive nullcline reflects the fact that , the concentrations are slaved to the local equilibria in the long wavelength limit. As one goes towards shorter wavelengths (i.e. larger q) the eigenvector begins to deviate from being tangential to the nullcline (see Supplementary Material of Ref. [16]). In particular, the eigenvalue of the marginal mode $q_{\max}$ points along the flux-balance subspace, $\mathbf{e}_{q_{\max}}^{(2)} \propto (1, -D_m/D_c)^{\mathrm{T}}$.

We found that the band of unstable modes for the 2C-MCRD system always extends down to long wavelength ($q \to 0$), a situation called "type II" instability in the Cross–Hohenberg classification scheme [175].

In systems with more components and/or multiple conserved species, this is no longer true—the band of unstable modes can be bound away from zero ("type I" in Cross–Hohenberg scheme), see e.g. Ref. [16].

2. Approximation close to the onset of lateral instability

The eigenvalues of a 2×2-matrix, Eq. C4, to leading order in $\delta/\tau \ll 1$ are given by

$$\sigma^{(1)} = \tau - \delta/\tau + \mathcal{O}(\delta^2/\tau^2), \qquad (C6a)$$
$$\sigma^{(2)} = \delta/\tau + \mathcal{O}(\delta^2/\tau^2). \qquad (C6b)$$

We will now use this approximation for the 2C-MCRD dynamics where the trace and determinant of the Jacobian for a mode q are given by Eqs. (C5). A straightforward calculation shows that δ_q reaches its extremum at $q^* = q_{\max}/\sqrt{2}$, with a minimal value of $\delta_{q^*} = -\tilde{f}_m^2 D_c/(4D_m)$. Furthermore, the trace $\tau_q \approx \sigma_{\text{loc}}$ is approximated by the local eigenvalue for $\tilde{f}_m \ll \sigma_{\text{loc}}$. Hence, the above approximation is valid in the vicinity of *lateral* instability onset ($\tilde{f}_m \approx 0$), far away from the *local* instability onset (which takes place at $\sigma_{\text{loc}} = 0$). The dispersion relation then reads

$$\sigma_q^{(1)} \approx \sigma_{\text{loc}} - (D_m + D_c)q^2, \qquad (C7a)$$
$$\sigma_q^{(2)} \approx \frac{D_m D_c}{-\sigma_{\text{loc}}} q^2 \left(q_{\max}^2 - q^2 \right), \qquad (C7b)$$

for $\tilde{f}_m^2 D_c/D_m \ll |\sigma_{\text{loc}}|$. The first branch, $\sigma_q^{(1)}$, simply represents relaxation to local equilibrium. The laterally unstable branch, $\sigma_q^{(2)}$, shown in Fig. 19a, is the identical to the dispersion relation of the Cahn–Hilliard equation [176] (and the more general class of Model B dynamics). We can rewrite Eq. (C7b) as

$$\sigma_q^{(2)} \approx -D_c q^2 \left(\partial_n \eta^* |_{\bar{n}} - \frac{D_m}{-\sigma_{\text{loc}}} q^2 \right). \qquad (C7b^*)$$

The two terms of this expression reflect the shifting of local equilibria (dominating at large wavelengths) driving the instability for $\partial_n \eta^* |_{\bar{n}} < 0$ and the competition of local reactive flow towards equilibrium and membrane diffusion that re-stabilizes the system on short length scales. (To recast Eq. (C7b) as (C7b*), one uses the relation $\partial_n c^*(n) = \partial_m c^*(m)/[1 + \partial_m c^*(m)]$.)

Figure 19 gives an overview of the various regimes of mass-redistribution instability and their interrelation. A typical dispersion relation (solid green line) deep in the laterally unstable regime (i.e. far from onset) is shown in Fig. 19b, together with various limiting cases (see caption for details). One can distinguish diffusion- and reaction-limited regimes. The former (i.e. long wavelength limit) was studied in detail in the main text. In the next subsection, we briefly analyze the two limits of fast cytosol diffusion and vanishing membrane diffusion.
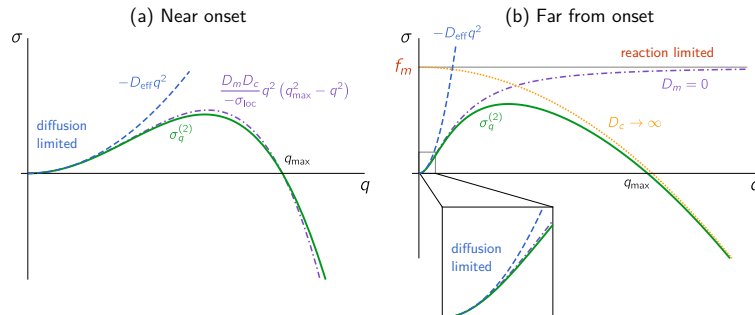
FIG. 19. Overview of the regimes of mass-redistribution instability and their interrelations. (a) Near onset ($D_m/D_c \approx -s_{\mathrm{nc}}$ and therefore $q_{\max} \ll \sqrt{f_m/D_m}$), the laterally unstable branch ($\sigma_q^{(2)}$, green solid line) of the dispersion relation is approximated by a fourth-order polynomial (purple, dash-dotted line; cf. Eq. (C7)(b)) that corresponds to the dispersion relation of Model B dynamics. For $q \ll q_{\max}$, the instability is *diffusion limited* (blue dashed line) and effectively described by anti-diffusion with the effective diffusion constant $D_{\mathrm{eff}} = D_c \partial_n \eta^*$ (see Sec. IV). (b) Dispersion relation far from onset ($D_m/D_c \ll |s_{\mathrm{nc}}|$). The case without membrane diffusion ($D_m = 0$, purple dash-dotted line) clearly shows the diffusion-limited and the reaction-limited regimes for $q^2 \ll |\sigma_{\mathrm{loc}}/D_c|$ and $q^2 \gg |\sigma_{\mathrm{loc}}/D_c|$, respectively. Finite membrane diffusion suppresses the instability at short wavelength in the reaction-limited regime ($q \gtrsim \sqrt{|\sigma_{\mathrm{loc}}|/D_c}$). There, the dispersion relation is approximated by $f_m - D_m q^2$ (yellow dotted line, note in particular $q_{\max} \approx \sqrt{f_m/D_m}$, the approximation becomes exact in the limit $D_c \to \infty$). The diffusion-limited regime ($q \ll \sqrt{|\sigma_{\mathrm{loc}}|/D_c}$, blue dashed line) has the same behavior as in the vicinity of onset (a) with the additional simplification that far from onset, the effective diffusion constant $D_{\mathrm{eff}} \approx D_c \partial_n c^*$. "Parameters": $f_m = 0.5, f_c = 1$ (i.e. $s_{\mathrm{nc}} = -0.5$, $\sigma_{\mathrm{loc}} = -0.5$), $D_m = 1$, $D_c = 2.1$ for (a) and $D_c = 50$ for (b).

3. Limits in the diffusion constants

a. Fast cytosol diffusion. — In the limit $D_c \to \infty$, the dispersion relation approaches the function $f_m - D_m q^2$ for wavenumbers $q \gg |\sigma_{\mathrm{loc}}/D_c|$; see dashed gray line in Fig. 19b). This shape of the dispersion relation reflects the fact that the growth rate of instability is limited by the rate of chemical relaxation to the shifting local equilibria ($\partial_n c^* \cdot \sigma_{\mathrm{loc}} = f_m$) and counteracted by membrane diffusion on short scales ($-D_m q^2$).

Somewhat deceptively, this shape of the dispersion relation resembles that of a locally unstable system for $q > 0$, even though the system is locally stable. In the strict limit, $D_c \to \infty$, the dispersion relation becomes discontinuous at $q = 0$, because the zero eigenvalue at $q = 0$ corresponding to the homogeneous perturbation breaking mass conservation is always present. (Recall that for the stability of a closed system against homogeneous perturbations, this mode is not relevant.)

It is important to keep in mind that the lateral instability is always driven by cytosolic mass redistribution. From this perspective the strict asymptotic limit $D_c \to \infty$ (and the common approximation to treat the cytosol as well mixed) is pathological as it masks the core dynamics underlying lateral instability in MCRD systems: the formation of gradients in the fast diffusing component(s) and the ensuing diffusive fluxes that redistribute total density. Furthermore, in systems with more than two components, the subtle interplay of multiple fast diffusing components might play an important role for pattern formation [19]. Such aspects would be missed if fast diffusing components are assumed to be well-mixed

at all times (which corresponds to setting their diffusion constants to infinity).

b. Vanishing membrane diffusion. — In the limit $D_m \to 0$, the band of unstable modes extends to arbitrarily small wavelengths (i.e. $q_{\max} \to \infty$); see purple, dash-dotted line in Fig. 19. For short wavelengths, the growth rate is reaction limited ($\sigma_q^{(2)} \approx f_m$) because cytosol diffusion is fast. For long wavelengths, the growth rate is diffusion limited, $\sigma_q^{(2)} \approx D_c q^2 \partial_n c^*$.

Appendix D: Remarks on the local quasi-steady state approximation

The local quasi-steady state approximation (LQSSA), i.e. slaving of the chemical concentrations to the local (reactive) equilibria, becomes exact when the timescales of diffusion and local reactions are separated. Specifically, let us scale the reaction terms in the reaction–diffusion dynamics Eq. (1) by ε^{-1}:

$$\partial_t m = D_m \partial_x^2 m + \varepsilon^{-1} f(m, c), \quad \text{(D1a)}$$

$$\partial_t c = D_c \partial_x^2 c \ - \varepsilon^{-1} f(m, c). \quad \text{(D1b)}$$

In the limit $\varepsilon \to 0$, relaxation to local equilibria becomes arbitrarily fast compared to diffusive redistribution—the concentrations will be at a local quasi-steady state (a stable local equilibrium). The characteristic spatial scale(s) of the dynamics and of stationary patterns are given by a balance of reaction and diffusion. In particular, in Sec. V A, we learned that the interface width is determined by $\pi(D_m/\tilde{f}_m)^{1/2}$. Under the scaling of reaction

rates by ε^{-1}, this length scale will go to zero as $\propto \varepsilon^{1/2}$. Hence, in the LQSSA, there is no "microscopic" length scale. This behavior is characteristic for a singular perturbation problem where some physics is lost when the small parameter ε is set to zero [5, 61]. A rigorous analysis of Eqs. (D1) could be performed in terms of singular perturbation theory. To lowest order in ε, any series of jumps (sharp interfaces) between two plateaus $n_\pm$ that fulfill $\eta^*(n_+) = \eta^*(n_-)$, such that $\eta^*(\tilde{n}(x)) = \eta_0$ is constant in space, is a valid steady state of Eq. (23). However, to be consistent with Eq. (D1) in the limit $\varepsilon \to 0$, the FBS-position must be $\eta_0 = \eta_0^\infty$ as determined by total-turnover balance Eq. (35). In addition, the given total density $\bar{n}$ constrains the spatial average $\langle \tilde{n}(x) \rangle_{[0,L]} = L_+ n_+ + L_- n_- = \bar{n}$, where $L_\pm$ are the aggregate lengths of the high and low density regions.

One may compare the LQSSA to the approach used to analyze limit cycle attractors of relaxation oscillators. There the N-shaped nullcline allows an analytic construction of the limit cycle in the asymptotic timescale separation limit. Moreover, even without the timescale separation the qualitative phase-space structure that underlies the oscillations can be deduced from the nullcline shapes. Note that treating such a timescale separation in a mathematically rigorous way requires singular perturbation theory (see Appendix D).

The LQSSA can also be understood as a closure relation. In that picture, $n(x,t)$ corresponds to a "coarse-grained order parameter" with the microscopically correct dynamics given by Eq. (21). This equation is not closed, because $m(x,t)$ and $c(x,t)$ are not known. Equation. (22) is a closure for Eq. (21) at the price of losing the "microscopic" length scale. One could try construct higher order closures that also take into account deviations from the local equilibria owing to diffusion on short length scales [177].

In a forthcoming publication, we choose a less technical way to qualitatively illustrate the elementary pattern formation dynamics: we consider the dynamics not on a continuous domain but in two diffusively coupled compartments. In this 'coarse grained' setting, the LQSSA is well-posed because a "microscopic" length scale as been imposed externally by the discretization into two-compartments.

Appendix E: Geometric construction of bifurcations

In Sec. V D and Sec. VII we describe how the bifurcations diagrams of stationary pattern can be constructed geometrically using the reactive nullcline and the flux-balance subspace. We implemented this procedure in Mathematica (see Supp. File "flux-balance-construction.nb" to find quantitative bifurcation structures. As an illustrative example, we present the results for the reaction kinetics Eq. (A1*); see Figs. 20 and 22. Figure 20a shows the shape of the reactive nullcline for a range of the kinetic rate parameter k (non-dimensional

attachment rate). For $k > k_{\text{saddle}}$, the nullcline is monotonic, such that pattern formation is impossible. (Recall that we set the non-dimensional feedback rate to 1, so k effectively describes the relative strength of basal attachment vs. feedback due to recruitment.) At $k = k_{\text{saddle}}$ a section of negative slope emerges on the nullcline, giving rise to lateral instability for $D_c/D_m \to \infty$. Further lowering k increases the range of negative nullcline slope and increases the maximal negative nullcline slope (thus decreasing $D_c^{\min}$, cf. Eq. (40)). Figure 20b shows the regimes of lateral instability and pattern existence for $D_c = 10 D_m$. At $k = k_{\text{cusp}}$ the maximal negative nullcline slope becomes -1, indicating a cusp bifurcation of the reactive equilibria. From this cusp point (black dot on the red nullcline in (a)), a regime of bistability emerges, section of unstable equilibria shown as dashed line in (a)). The locally bistable regime (shaded in gray in (b) is delimited by two saddle-node bifurcations (SN) which emerge from the cusp point, shown as black dot in (b). In the locally bistable regime, there exist *unstable* stationary patterns for $D_c < D_m$. These patterns can be constructed in the same way as stable stationary patterns for $D_c > D_m$. Their range of existence for $D_c = 0.9 D_m$ is shaded in red in (b), delimited by a dashed red line.

Figure 20c shows the geometrically constructed $(\bar{n}, D_c)$-bifurcation diagram for $k = 0.045$, i.e. for a bistable nullcline (corresponding to the schematic bifurcation diagram shown in Fig. 10 in the main text). The $(\bar{n}, D_c)$-bifurcation diagram for a monostable nullcline is shown in Fig. 22 in Appendix F, where we also show the bifurcation structure for finite domain size, L, obtained by numerical continuation.

Appendix F: Numerical continuation of stationary patterns

To calculate steady states and their bifurcation structures for systems with finite size, we use a standard numerical continuation scheme (pseudo-arclength continuation, see e.g. chapter 4 in Ref. [178]). The stationarity condition Eq. (14a) was discretized using finite differences, yielding a set of equations for the concentrations at the grid points. These equations, together with the flux-balance subspace Eq. (10) and the constraint of average total density Eq. (1c), are used to numerically determine the stationary patterns and their bifurcations (in the Mathematica software). To continue the fold bifurcations of stationary patterns, we use a bordered matrix method [178].

To determine the stability of the stationary patterns, we use a finite difference discretization of the reaction–diffusion dynamics (1) linearized around the steady state. The resulting eigenvalue problem is solved with Mathematica. The eigenvalue with the largest real part ("dominant eigenvalue") determines the pattern stability (see Fig. 25, which is discussed in Appendix I).
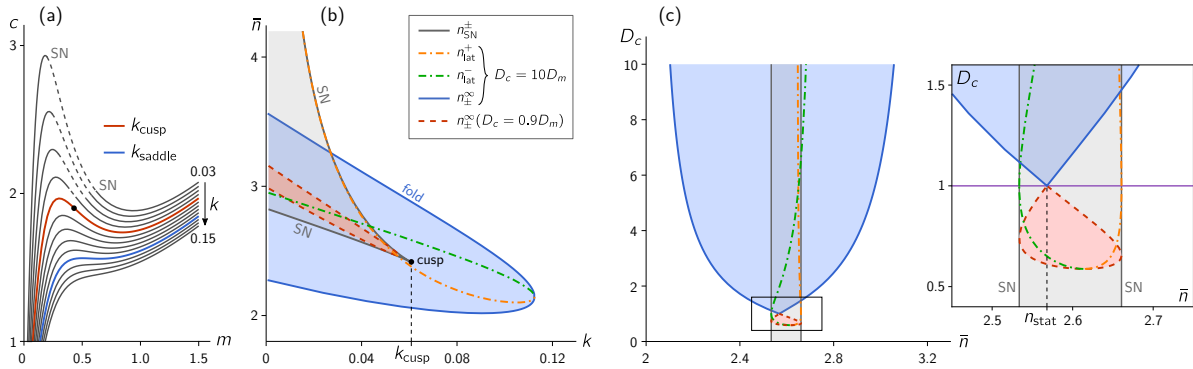
FIG. 20. Bifurcation diagrams obtained by the flux-balance construction (reaction term Eq. (A1*) from Ref. [28]). (a) Deformation of the reactive nullcline under variation of the kinetic rate k from 0.03 to 0.015. Dashed sections indicate local instability in the regime of bistability, that emanates from the cusp bifurcation at k_{cusp} (red nullcline, inflection point marked by black dot). The nullcline exhibiting a saddle point is shown in blue. (b) $(k, \bar{n})$-bifurcation diagram (compare Fig. 12b in the main text) where the lateral instability bifurcation lines ($n_{\mathrm{lat}}^{\pm}$, dash-dotted in orange and green) and the regime of pattern existence (shaded in blue, delimited by $n_{\pm}^{\infty}$ shown as solid blue line) are shown for $D_c = 10D_m$. Additionally, the region where unstable stationary patterns exist for $D_c = 0.9D_m$ is shaded in red, delimited by a dashed red line. Note the region in the top-right corner, where the local reaction kinetics are bistable, but no stationary patterns exist. (c) $(\bar{n}, D_c)$-bifurcation diagram for $k = 0.045$, where the reaction kinetics Eq. (A1*) exhibit a region of bistability; the inset shows a blow-up of the boxed region around $\bar{n} \approx n_{\mathrm{stat}}$ and $D_c \approx D_m$. The bifurcation diagrams (b) and (c) were constructed based on following the geometric reasoning presented in Sec. VII with the help of a Mathematica script (see Supp. File "flux-balance-construction.nb").

a. Bifurcation structure for $\bar{n}$

Figure 6 in the main text shows the $\bar{n}$-bifurcation structure of stationary patterns determined by numerical continuation for the reaction kinetics (A1*). In Fig 6, the pattern amplitude is plotted against $\bar{n}$. For the same bifurcation structure, Fig. 21, shows additional plots of the maximum and minimum concentrations in (a) and the FBS-position, η_0, in (b). For mesa patterns $\widetilde{m}(0)$ and $\widetilde{m}(L)$ are the plateau concentrations and therefore slaved to $m_{\pm}^{\infty} = m_{\pm}(\eta_0^{\infty})$, while the FBS-position η_0^{∞} is almost constant. At the boundaries of the range where patterns exist (limited by $[n_{-}^{\infty}, n_{+}^{\infty}]$, for $L \to \infty$), the mesa patterns undergo fold bifurcations where they meet the branches of unstable peak/trough patterns (dashed lines) that emanate from the homogeneous steady state (black line, dash-dotted in the regime of lateral instability). In both plots, the prediction from the analytic approximation of (unstable) peak/trough patterns (see Appendix G) is shown as red solid lines.

b. Two-parameter $(\bar{n}, D_c)$-bifurcation diagram

Figure 22 shows the two-parameter $(\bar{n}, D_c)$-bifurcation diagram for a monostable reactive nullcline (corresponding to the schematic diagram in Fig. 14a; the fixed parameters are the same as in Fig. 6). The fold-bifurcation lines (solid blue lines) of stationary patterns at finite domain size were obtained by numerical continuation. The respective bifurcation lines in the infinite system size limit,

$n_{\pm}^{\infty}$ (solid gray lines), were geometrically constructed (cf. Appendix E. The laterally unstable regime, bounded by the dash-dotted green line, was determined by linear stability analysis. On the right, a blow-up of the region around the critical point $(\bar{n}_{\mathrm{inf}}, D_c^{min})$. The finite sized system,

The tip of the laterally unstable regime in a finite-sized system is shifted upwards by an amount $\sim L^{-2}$ because of the stability condition $\tilde{f}_m = \pi^2 D_m / L^2$. Close to critical point, the patterns emerge in a supercritical pitchfork bifurcation (dashed green line). The points where the onset becomes sub-critical are marked by in red disks. At these points the two lines of fold bifurcations of stationary patterns originate. The sub-critical lateral instability bifurcation is shown as green dash-dotted line.

Appendix G: Approximation of peak/trough patterns

In the following, we detail the construction of approximate peak/trough patterns that was briefly introduced in Sec. V C. For specificity, we present the construction for peak patterns—generalization to trough patterns is straight forward.

In our analysis of pattern types (Sec. V C), we characterized peak patterns as composed of an interface region at a system boundary connected to a plateau region (cf. Fig. 5b). We have also characterized interfaces by linearization around the inflection point in Sec. V A which yielded a sinusoidal interface shape with a width $\ell_{\mathrm{int}}(\eta_0)$ (cf. Eq. (31)). We now construct a peak pattern by piec-
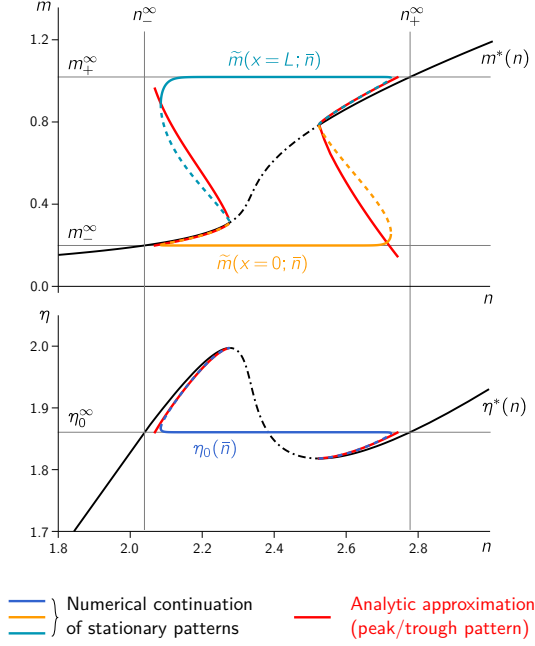
FIG. 21. Numerically determined bifurcation diagram for a 2C-MCRD system with the reaction kinetics Eq. (A1*) for the control parameter $\bar{n}$ (average total density). The figure supplements Fig. 6 in the main text, where the bifurcation structure is shown for the pattern amplitude $|\widetilde{m}(L) - \widetilde{m}(0)|$. The homogeneous steady state is shown as black line, dash-dotted in the regime of lateral instability (note that the slope criterion, Eq. (25), can be written as $\partial_n \eta^* < 0$). For stationary patterns, concentrations at the domain boundaries $\widetilde{m}(0)$ and $\widetilde{m}(L)$ (yellow and teal lines in the top panel), and the FBS-position η_0 (blue line in the bottom panel) are shown. Thin gray lines indicate the plateau densities $m_\pm^\infty$ and the FBS-position, η_0^∞, in the large system size limit $L \to \infty$. Red lines show the heuristic approximation of peak/trough patterns Eq. (G1), which are the unstable transition states in the multistable regimes (cf. Fig. 6). Note the almost perfect agreement of analytic approximation and numerical solutions for the FBS-position η_0.

ing together such an (approximate) interface at the left domain boundary and a plateau at $m_-(\eta_0)$ in the reminder of the system:

$$\widetilde{m}_{\mathrm{peak}}(x) \approx \begin{cases} m_0 + A \sin \pi \left(\dfrac{x}{\ell_{\mathrm{int}}} - \dfrac{1}{2} \right) & x < \ell_{\mathrm{int}} \\ m_- & x > \ell_{\mathrm{int}} \end{cases}.$$
(G1)

Within this approximation, the pattern inflection point is always at $x_0 = \ell_{\mathrm{int}}/2$. To match the interface to the plateau continuously at $x = \ell_{\mathrm{int}}$, the amplitude must be $A = m_- - m_0$. The plateau $m_-(\eta_0)$ and inflection point $m_0(\eta_0)$ are geometrically determined. To close the approximation, one has to find the FBS-position consis-

tent with the given average total density $\bar{n}$ (to fulfill the constraint Eq. (1c)). From Eq. (G1), one obtains the approximate total density average

$$\bar{n}(\eta_0, L) \approx \eta_0 + (1 - D_m/D_c)\Big[m_-(\eta_0) +$$
$$+ \frac{\ell_{\mathrm{int}}(\eta_0)}{L}\big(m_0(\eta_0) - m_-(\eta_0) \big) \Big].$$
(G2)

This relation can be inverted to obtain a relation $\eta_0(\bar{n}, L)$ for peak patterns with a density-profile approximated by Eq. (G1).

Peak/trough patterns are encountered in two contexts. First, stable peak patterns are typical for reaction kinetics that exhibit a strongly asymmetric nullcline shape, e.g. Eq. (A2*), when $D_m \ll D_c$ (see Fig. 17 for a typical peak pattern). Secondly, *unstable* peak/trough patterns form the unstable branches that connect the subcritical Turing bifurcation with the stable pattern branch (see Fig. 6). These unstable peak/trough patterns play the role of 'transition' states since they lie on the separatrix that separates the basins of attraction of the homogeneous steady state and the stationary pattern in the multistable regimes.

For both scenarios, we compared the analytic approximation Eq. (G1), where η_0 is determined via Eq. (G2), with numerical numerical continuation of the stationary patterns.

The approximation of unstable peak/trough patterns for the reaction kinetics Eq. (A1*) is shown in the bifurcation structure Fig. 21.

Figure 23 shows the $\bar{n}$-bifurcation diagram of station-
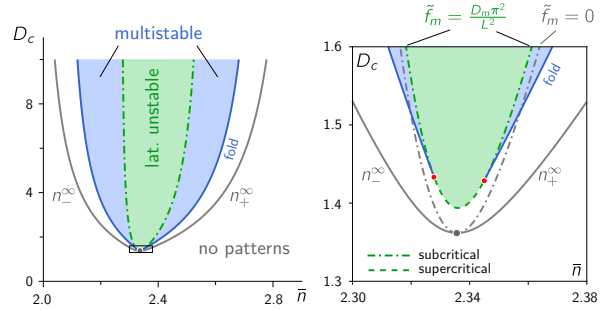
FIG. 22. Right: Numerically determined $(\bar{n}, D_c)$-bifurcation structure of stationary patterns in a finite sized domain; left: blow-up of the vicinity of the critical point. The continuous blue line marks the fold bifurcation of stationary patterns where stable and unstable stationary patterns meet (cf. Fig. 6b). The geometrically constructed bifurcation lines for $L \to \infty$ are shown in gray. The fold bifurcation where stable and unstable patterns merge terminates in the points where the Turing bifurcation switches from sub- to supercritical ($F_3 = 0$, cf. Eq. (46)). Along the line of supercritical Turing bifurcation (dashed green line), stable patterns emerge directly in a supercritical pitchfork bifurcation. Reaction term: Eq. (A1*); see Fig. 16 for the nullcline shape and a typical pattern profile. Parameters: $k = 0.07$, $D_m = 1$, $L = 100$.
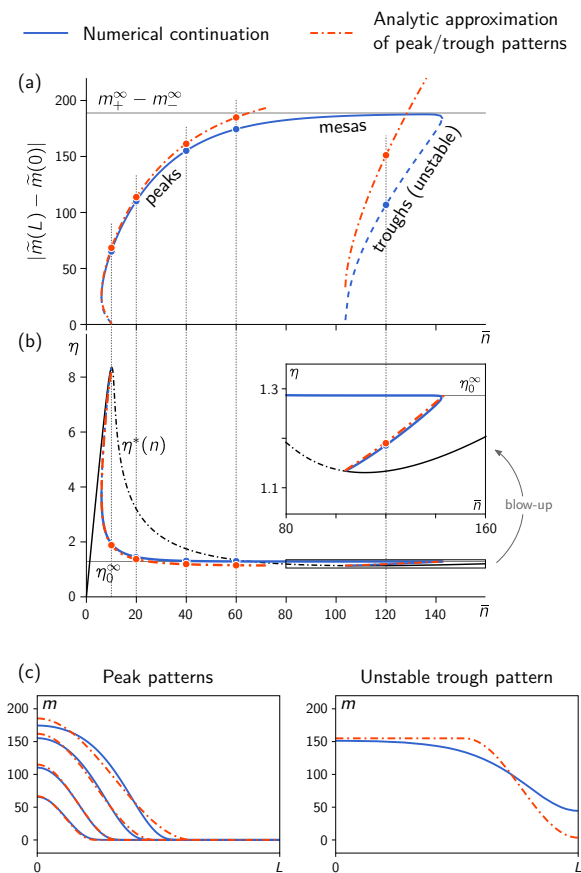
FIG. 23. Numerically determined $\bar{n}$-bifurcation structure of stationary patterns for the reaction term Eq. (A2*) (see Fig. 17a for the nullcline shape). (a) Amplitude $|\widetilde{m}(L) - \widetilde{m}(0)|$ and FBS-position η_0 (b) of stationary patterns from numerical continuation (blue line, dashed for unstable patterns) and the analytic peak-approximation Eq. (G1) (dash-dotted red line). Peak-type patterns transition to mesa patterns as total average density is increased. The transition threshold can be estimated by the point where the peak approximation (red, dash-dotted line) for the pattern amplitude exceeds the (geometrically determined) plateau amplitude $|m_+^\infty - m_-^\infty|$ (thin gray line). In the $(\bar{n}, \eta_0)$-plot (b), the homogeneous steady states (equivalent to the reactive nullcline via $\eta^* = c^* + m^* D_m/D_c$) are shown as solid black line (dash-dotted where laterally unstable). Inset: blowup of the η-axis in the trough pattern region. (c) Stationary pattern profiles from numerical continuation (solid blue lines) and from the analytic approximation (dash-dotted red lines) for various total average densities, corresponding to the dots in (a). Left: $n = 10, 20, 40, 60$, stable peak patterns; right: $\bar{n} = 120$, unstable trough pattern. Fixed parameters: $k_{\text{fb}} = 0.3$, $k_{\text{off}} = 20$, $L = 20$, $D_m = 1$, and $D_c = 200$.

ary patterns for the reaction kinetics Eq. (A2*). There is a large regime of peak patterns where the pattern amplitude keeps increasing with average total density $\bar{n}$. Peak patterns transition to mesa patterns when peak saturates in the third FBS-NC intersection point m_+. The amplitude of mesa patterns is almost independent of $\bar{n}$, because a change of total density merely shifts the interface position of mesa patterns (compare Fig. 6). Ultimately, mesa patterns transition to trough patterns which then undergo a fold bifurcation where they meet with the unstable branch of trough patterns that emerges from the homogeneous steady state. The asymmetry of the reactive nullcline (Fig. 17a) is reflected by the asymmetry of the bifurcation structure. The dot-dashed red lines in Fig. 23 show the analytic approximation for pattern amplitude (a), the FBS-position (b) and pattern profiles (c). The approximation of peak patterns becomes less accurate as the average total density increases and ultimately breaks down at the transition to mesa patterns (around $\bar{n} \approx 60$ in Fig. 23). The approximation of trough patterns is less accurate because the trough saturates more "abruptly" in m_-: Recall that the approximation underlying Eq. (G2) is a linearization of the interface region around the inflection point (cf. Sec. V A). This approximation breaks down in regions of high nullcline curvature, indicative of high nonlinearities. Interestingly, even though the pattern profile is not well approximated for troughs (see Fig. 23c), the estimate for the FBS-position η_0 is close to the true value (see inset in Fig. 23c), indicating that the relevant physics (total turnover balance) is still captured.

Appendix H: Stimulus-induced pattern formation

In Sec. VI, we argued that to trigger pattern formation from a laterally stable homogenous steady state, a perturbation (stimulus) must induce a (self-)sustained laterally unstable region. Based on this intuition we provided a simple geometric heuristic for the perturbation threshold: a perturbation of the membrane concentration profile must be such that concentrations in a spatial region are pushed beyond the laterally unstable part of the nullcline in phase space. Hence, the intersection point of the line $c = c^*(\bar{n})$ with the laterally unstable section of the nullcline, provides an estimate $m_{\text{th}}(\bar{n})$ for the threshold that the membrane perturbation has to exceed in a spatial region (see Fig. 24b, cf. Fig. 7). This criterion does not take into account the spatial shape of a perturbation, but only its characteristics in phase space. We tested how robust the estimate is against different spatial profiles using numerical simulations of the reaction–diffusion dynamics Eqs. (1) with the reaction term Eq. (A1*). We consider prototypical perturbations with a 'step-like' profile (see Fig. 24a):

$$m_{\text{pert}}(x) = \begin{cases} m^*(\bar{n}) - a & x < L - w \\ m^*(\bar{n}) + b & x > L - w. \end{cases} \tag{H1}$$

For the perturbation to conserve the global average total density, we must set $b = a\frac{L-w}{w}$. The 'step-like' profiles therefore form a two-parameter family of perturbations with the shape parameters w (width of the region where density is increased) and a (density removed uniformly from the rest of the system). Because the concentration may not drop below zero, only perturbations with $a < m^*(\bar{n})$ are physically sensible. The (heuristic) threshold in phase space $m_{\text{th}}(\bar{n})$ (see Fig. 24b) is exceeded in the (high density) region $x > L - w$ when

$$a > a_{\text{th}}(w; \bar{n}) := \frac{w}{L-w}[m_{\text{th}}(\bar{n}) - m^*(\bar{n})]. \qquad \text{(H2)}$$

Note that the threshold $m_{\text{th}}(\bar{n})$ in phase space is a function of the average total density. We tested various total average densities $\bar{n}$ across the multistable regime $n_-^\infty < \bar{n} < n_{\text{lat}}^-$, and varied the 'shape parameters' of the perturbation—amplitude a and width w—throughout their respective maximal ranges: $0 < a < m^*(\bar{n})$ and $0 < w < L$. Figure 24 shows that there is good agreement between the geometrically estimated threshold and the actual basins of attraction determined by numerical simulation.

Appendix I: Stability of stationary patterns

In our analysis of stationary patterns, we have touched the question of stability of these patterns only peripherally in Sec. VII B. Coarsening, i.e. the instability of multi-peak / multi-mesa patterns, in 2C-MCRD systems has been studied before both numerically [25, 34] and semi-analytically [24] for specific choices for the reaction kinetics $f(m, c)$. For specific reaction terms $f(m, c)$ that allow a mapping of the reaction–diffusion dynamics to an effective gradient dynamics, stability of patterns can be analyzed with the help of the effective free energy that is minimized by the stationary pattern [44, 46]. In the broader class of two-component systems without conserved total density, stability of stationary patterns has been subject to numerous mathematical studies, see e.g. Refs. [71, 164, 179].

Instead of the technical tools typically employed there, we choose a more heuristic approach here, building on the physical intuition we have gained throughout this work. We restrict our analysis to the case of mesa patterns with a small interface width compared to the system size ($\ell_{\text{int}} \ll L$).

Our starting point is the insight that the stationary pattern $(\widetilde{m}(x), \widetilde{c}(x))$ is embedded in a flux-balance subspace, Eq. (10), whose position η_0^∞ is determined by total turnover balance, Eq. (17). We hence write the stationary pattern as a pair $(\widetilde{m}(x), \eta_0^\infty)$, where only $\widetilde{m}(x)$ depends on x. Next, recall that the pattern itself is scaffolded by local equilibria. In particular, the plateaus are slaved to the plateau scaffolds $m_\pm(\eta_0^\infty)$, and the pattern inflection point is determined by $m_0(\eta_0^\infty)$. Following a perturbation $\delta m(x, t)$ of the stationary pattern profile,
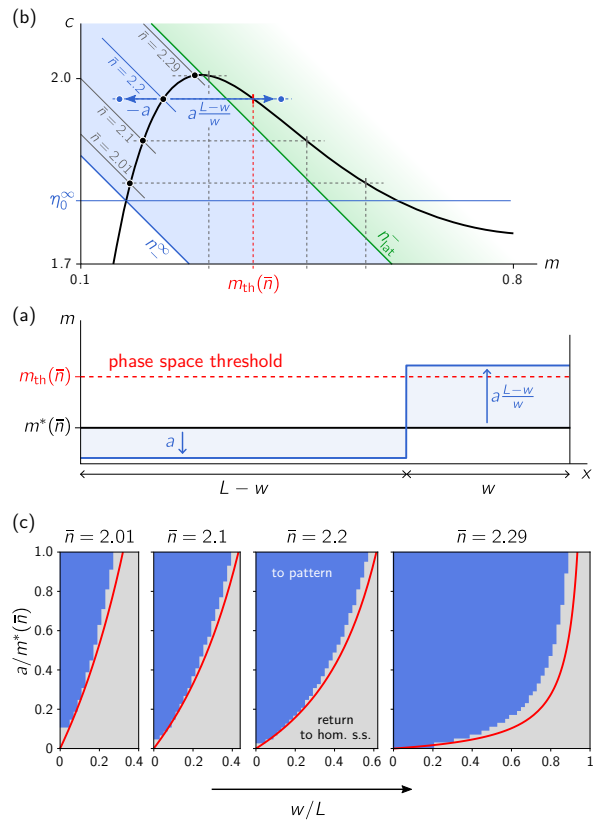
FIG. 24. Test of the geometric heuristic for the perturbation threshold perturbation by numerical simulations. (a) We consider a prototypical type of perturbation of the homogenous steady state $m^*(\bar{n})$: a 'step function' profile moving membrane density from the region $x < L - w$ into the region $x > L - w$; cf. Eq. (H1). Membrane density is lowered by an amount a on the left and increased by an amount $a\frac{L-w}{w}$ so that total mass is conserved. (b) In phase space, the threshold $m_{\text{th}}(\bar{n})$ for a perturbation of membrane density is determined by the intersection point of the line $c = c^*(\bar{n})$ with the laterally unstable section of the nullcline. Colored dashed lines show this construction for various total densities $\bar{n} = 2.01, 2.1, 2.2, 2.29$ in the range of multistability $n_-^\infty < \bar{n} < n_{\text{lat}}^-$ (shaded in blue). The laterally unstable region is shaded in green. (c) The geometrically determined threshold $m_{\text{th}}(\bar{n})$ predicts (red line, $a_{\text{th}}(w; \bar{n})$) which 'shapes' of perturbations, parametrized by amplitude a and width w, trigger formation of a stationary pattern. This prediction is in good agreement with the basins of attraction of stationary pattern (shaded in blue) and homogeneous state (shaded in gray) in the parameter space of perturbation 'shapes'. (Reaction term: Eq. (A1*), parameters: $k = 0.067$, $D_m = 0.1$, $D_c = 10$, $L = 20$.)

the plateaus will quickly return to their stable local equilibria, the plateau scaffolds $m_\pm$. On the other hand, a perturbation of the mass-redistribution potential ("FBS-position") $\delta\eta$, will not only shift the plateau scaffolds, but also cause an imbalance of total reactive turnover. This imbalance drives the dynamics of $\eta(x,t)$ and thus determines the stability of the pattern, as we will see in the following.

The dynamics of $\eta(x,t) = c(x,t) + m(x,t)D_m/D_c$ follows straightforwardly from the reaction–diffusion dynamics Eq. (1) and read:

$$\begin{aligned}
\partial_t \eta(x,t) &= D_c\partial_x^2\eta + (D_m/D_c - 1)\,\partial_t m \\
&= D_c\partial_x^2\eta + D_m(D_m/D_c - 1)\partial_x^2 m \\
&\quad + (D_m/D_c - 1)\tilde{f}(m,\eta) \qquad (\text{I1})
\end{aligned}$$

In linearization around a stationary pattern $(\widetilde{m}(x), \eta_0^\infty)$, we have

$$\begin{aligned}
\partial_t\delta\eta(x,t) &= D_c\partial_x^2\delta\eta + D_m(D_m/D_c - 1)\partial_x^2\delta m \\
&\quad + (D_m/D_c - 1)\big[\tilde{f}_m\delta m + \tilde{f}_\eta\delta\eta\big]_{(\widetilde{m}(x),\eta_0^\infty)}, \qquad (\text{I2})
\end{aligned}$$

where the membrane perturbation $\delta m = \delta m(x,t)$ is governed by the linearization of the reaction–diffusion dynamics Eq. (1a). The intuition is that $\delta m(x,t)$ quickly relaxes to the scaffold of local equilibria. We therefore focus on the dynamics of $\delta\eta(x,t)$, which will affect the scaffold itself by shifting local equilibria, in particular the plateau scaffolds $m_\pm(\eta)$.

Reactive turnover balance is primarily determined in the interfacial region (cf. Fig. 2) around the pattern inflection point x_0. We therefore focus on the interface region to learn how an imbalance of total reactive turnover affects the perturbation of the mass-redistribution potential ("FBS-shift") $\delta\eta(x,t)$. To that end, we use that the gradient of the membrane profile, $\partial_x\widetilde{m}(x)$, is negligible in the plateaus and whereas it peaks at the inflection point x_0. We hence multiply Eq. (I2) by $\partial_x\widetilde{m}(x)$ and integrate over the whole domain $[0,L]$ to obtain

$$\begin{aligned}
\partial_t\delta\eta(x_0,t) &\approx \delta\eta(x_0,t)\frac{D_m/D_c - 1}{m_+ - m_-}\int_{m_-}^{m_+}\mathrm{d}m\,\tilde{f}_\eta(m,\eta_0^\infty) \\
&\quad + D_c\partial_x^2\delta\eta(x_0,t) + \mathcal{O}\big(\delta m(x,t)\big). \qquad (\text{I3})
\end{aligned}$$

We neglect contributions $\mathcal{O}(\delta m(x,t))$ that correspond to perturbation along the direction of the FBS and quickly relax to the scaffold on the timescale $|\sigma_{\mathrm{loc}}|^{-1}$, fast compared to the contribution by the first term in Eq. (I3). Furthermore, because mass-redistribution $\eta(x,t)$ quickly homogenizes in the (small) interface region, we can neglect the second term $\partial_x^2\delta\eta(x_0,t)$.

Fig. 25 shows a comparison of the heuristic estimates of perturbation growth/decay rate based on Eq. (43) to numerically determined dominant eigenvalues $\sigma_{\max}(D_c)$ (linear stability analysis of stationary patterns determined by numerical continuation). The dominant eigenvalue $\sigma_{\max}(D_c)$ crosses over from system size independent growth rate of perturbations for $D_c < D_m$ to system size dependent decay of perturbations for $D_c > D_m$.

The instability is well estimated by turnover imbalance term in Eq. (43) (dashed red line in the inset in (b)), while the rate at which perturbations decay in the stable regime ($D_c > D_m$) is limited by diffusive transport $\sigma_{\mathrm{diff}} \sim D_c/L^2$ between the far ends of the system. Reactive timescales will become limiting in the stable regime only when $\sigma_{\mathrm{diff}} \approx \sigma_{\mathrm{loc}}$, that is, for fast enough cytosolic diffusion or a small system.

Appendix J: Weakly nonlinear analysis

Our goal is to find the stationary pattern in the vicinity of the onset of lateral instability (Turing bifurcation). To that end, we expand the stationary state $(\widetilde{m}(x), \eta_0)$ in harmonic functions (eigenmodes of the Laplace operator under no-flux boundary conditions):

$$\begin{aligned}
\widetilde{m}(x) &\approx m^* + \delta m_0 + \delta m_1\cos(\pi x/L) \\
&\quad + \delta m_2\cos(2\pi x/L), \qquad (\text{J1a}) \\
\eta_0 &\approx \eta^* + \delta\eta_0, \qquad (\text{J1b})
\end{aligned}$$

where $\eta^* = D_m/D_c m^* + c^*$ is the FBS position of the homogenous steady state. Mass conservation necessitates $\delta m_0 + \delta\eta_0 - D_m/D_c\delta m_0 = 0$, hence

$$\delta\eta_0 = (D_m/D_c - 1)\,\delta m_0$$

We plug the ansatz Eq. (J1a) into the stationarity condition, Eq. (14a), Taylor expand $\tilde{f}$, and project onto the zeroth harmonic (this is most conveniently done in CAS software, e.g Wolfram Mathematica)

$$\begin{aligned}
0 &= \big(\tilde{f}_m + (1 - D_m/D_c)\tilde{f}_\eta\big)\delta m_0 + \frac{1}{4}\tilde{f}_{mm}\delta m_1^2 \\
&\quad + \mathcal{O}(\delta m_0^2, \delta m_1^2\delta m_2, \delta m_0\delta m_1^2, \delta m_0\delta m_2^2), \qquad (\text{J2})
\end{aligned}$$

and and onto the second harmonic

$$\begin{aligned}
0 &= \big(\tilde{f}_m - 4D_m\pi^2/L^2\big)\delta m_2 + \frac{1}{4}\tilde{f}_{mm}\delta m_1^2 \\
&\quad + \mathcal{O}(\delta m_2^2, \delta m_0\delta m_1^2, \delta m_0^2\delta m_2, \delta m_1^2\delta m_2). \qquad (\text{J3})
\end{aligned}$$

Solving for δm_0 and δm_2 we get

$$\delta m_0 = \frac{1}{4}\frac{\tilde{f}_{mm}}{\tilde{f}_m + (1 - D_m/D_c)\tilde{f}_\eta}\delta m_1^2 + \mathcal{O}(\delta m_1^4), \quad (\text{J4a})$$

$$\delta m_2 = \frac{1}{4}\frac{\tilde{f}_{mm}}{\tilde{f}_m - 4D_m\pi^2/L^2}\delta m_1^2 + \mathcal{O}(\delta m_1^4). \qquad (\text{J4b})$$

These equations describe how asymmetry of the nullcline shape (and thereby reactive turnover) influences the pattern profile. For $\tilde{f}_{mm} = 0$ the turnovers on either side of the inflection point grow symmetrically (with opposite sign) as the amplitude δm_1 of the pattern increases. This symmetry of the turnovers only occurs at the inflection point of the nullcline where its shape is point-symmetric. Away from the inflection point of the nullcline, its shape

(a) Pattern amplitude

(b) Pattern stability (dominant eigenvalue)

(c)
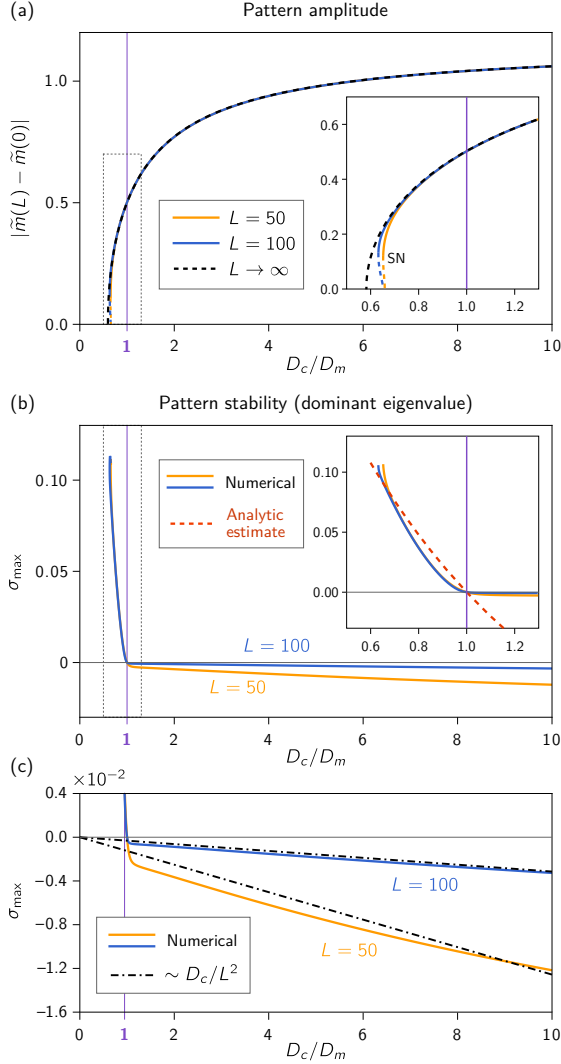
FIG. 25. Stability of stationary patterns as a function of D_c. (a) Pattern amplitude for a D_c-sweeps at constant $\bar{n} = n_{\text{stat}}$ for two system sizes $L = 50$ (yellow) and $L = 100$ (blue), obtained by numerical continuation, and geometric construction (corresponding to $L \to \infty$, dashed black line). The fixed parameters are the same as in Fig. 6. Finite size affects the stationary pattern amplitude only in the vicinity of the saddle-node bifurcation at $\approx D_c^{\min}$ (see inset: zoom on gray box). The purple line marks $D_c = D_m$. (b) Numerically determined dominant eigenvalues (maximal real part shown as solid lines) indicating linear stability of the patterns. Patterns are stable for $D_c > D_m$ and unstable for $D_c < D_m$, as predicted by the geometric arguments. The dominant eigenvalue for the unstable patterns is almost independent of system size. The approximation based on this geometric intuition of turnover imbalance (first term in Eq. (43)) is shown as red, dashed line in the inset. (c) Blow-up of the σ-axis, for negative values. For stable patterns ($D_c > D_m$), decay of perturbations is mainly determined by the timescale $\sim D_c/L^2$ of mass-transfer from one end of the system to the other. (The dot-dashed lines show the relation $-\alpha D_c/L^2$, where the prefactor $\alpha \approx 3.1$ that depends on the system specifics has been fitted by eye.)

is no longer symmetric around the steady state (m^*, c^*), and, respectively, the turnovers grow asymmetrically in the two halves of the system. This asymmetry creates an imbalance of the total turnover that is compensated by two effects: (i) the flux-balance subspace shifts (i.e. η_0 will deviate from η^*), and (ii) the pattern itself becomes asymmetric as the second harmonic will have a non-zero amplitude δm_2. Together, these two effects compensate the asymmetry of the turnovers, such that total turnover balance is reached.

The amplitude δm_1 of the stationary pattern is obtained by projecting (14a) onto the first harmonic $\cos(\pi x/L)$

$$0 = F_1 \, \delta m_1 + F_3 \, \delta m_1^3 + \mathcal{O}(\delta m_1^5), \qquad (J5)$$

where

$$F_1 = \tilde{f}_m - D_m \pi^2/L^2, \qquad (J6)$$

and

$$F_3 = \frac{\tilde{f}_{mmm}}{8} - \frac{\tilde{f}_{mm}}{8} \frac{\tilde{f}_{mm}}{\tilde{f}_m - 4D_m\pi^2/L^2}$$
$$- \frac{\tilde{f}_{mm}}{4} \frac{\tilde{f}_{mm} - (1 - D_m/D_c)\tilde{f}_{m\eta}}{\tilde{f}_m - (1 - D_m/D_c)\tilde{f}_\eta}. \qquad (J7)$$

Since there is no second order term in Eq. (J5), patterns always originate in a pitchfork bifurcation. At the bifurcation point, the first order coefficient vanishes ($F_1 = 0$). The system is laterally unstable if F_1 is positive (cf. Eq. (28)). Hence, only if $F_3 < 0$, the third order coefficient can saturate the pattern amplitude (supercritical bifurcation). For $F_3 > 0$ the bifurcation is subcritical.

The third order coefficient can be simplified further: A simple calculation shows that

$$\tilde{f}_m - (1 - D_m/D_c)\tilde{f}_\eta = f_m - f_c = \sigma_{\text{loc}}, \qquad (J8)$$

and therefore

$$\tilde{f}_{mm} - (1 - D_m/D_c)\tilde{f}_{m\eta} = \partial_m \sigma_{\text{loc}}(m, \eta - m \, D_m/D_c)$$
$$= \tilde{\partial}_m \sigma_{\text{loc}}(m, \eta) \qquad (J9)$$

where $\tilde{\partial}_m = \partial_m - (D_m/D_c)\partial_c$ is the derivative along the flux-balance subspace. With that, the second summand in the brackets in F_3 (cf. Eq. (J7)) can be rewritten and we obtain

$$F_3 = \frac{\tilde{f}_{mmm}}{8} - \frac{\tilde{f}_{mm}}{2} \left(\frac{\tilde{f}_{mm}/2}{\tilde{f}_m - 4D_m\pi^2/L^2} + \frac{\tilde{\partial}_m \sigma_{\text{loc}}}{\sigma_{\text{loc}}} \right). \qquad (J10)$$

We further rewrite the denominator of the first summand in the brackets as $F_1 - 3D_m\pi^2/L^2$, and use that F_1 vanishes at the bifurcation point (i.e. is small in its vicinity). We thus have

$$F_3 = \frac{\tilde{f}_{mmm}}{8} + \frac{\tilde{f}_{mm}^2}{24} \frac{L^2}{\pi^2 D_m} - \frac{\tilde{f}_{mm}}{4} \frac{\tilde{\partial}_m \sigma_{\text{loc}}}{\sigma_{\text{loc}}} + \mathcal{O}(F_1). \quad (J11)$$

Note that in weakly nonlinear approximation Eq. (46) in the main text, we have pulled the $\mathcal{O}(F_1)$ out from F_3 to simplify notation. The role and physical interpretation of the three terms in F_3, as written in the form Eq. (J11), are discussed in the main text in Sec. VII D.

Appendix K: Nullcline curvature approximation

In the following, we show that the nullcline curvature κ can be approximated by

$$\kappa \approx -\frac{f_c^2}{(f_m^2 + f_c^2)^{3/2}}\,\tilde{f}_{mm}, \qquad \text{(K1)}$$

in the vicinity of the Turing bifurcation (onset of lateral instability; recall the slope criterion Eq. (25)). Start by rewriting the second derivative $\tilde{f}_{mm}$ in terms of derivatives of f:

$$\tilde{f}_{mm} = \partial_m^2 f\left(m, \eta - \frac{D_m}{D_c} m\right)$$
$$= f_{mm} - 2\frac{D_m}{D_c} f_{mc} + \left(\frac{D_m}{D_c}\right)^2 f_{cc} \qquad \text{(K2)}$$

In the vicinity of the Turing bifurcation, we have $-D_m/D_c \approx -f_m/f_c$ (from the slope criterion for lateral instability, Eq. (25)), so we obtain

$$\tilde{f}_{mm} \approx f_c^{-2}\left[f_c^2 f_{mm} - 2 f_m f_c f_{mc} + f_m^2 f_{cc}\right]. \qquad \text{(K3)}$$

Comparing to the formula for the curvature κ of an implicitly determined curve $f(m, c) = 0$

$$\kappa = -\frac{f_c^2 f_{mm} - 2 f_m f_c f_{mc} + f_m^2 f_{cc}}{(f_m^2 + f_c^2)^{3/2}}, \qquad \text{(K4)}$$

one sees that the numerator of the curvature formula is identical to the term in the square brackets in Eq. (K3). Thus, by combining Eqs. (K3) and (K4), we obtain the approximation Eq. (K1).

Appendix L: Topological equivalence of 2C-MCRD systems shear banding in complex fluids

Analogies between the shear banding in complex fluids, phase separation near thermal equilibrium, and reaction–diffusion systems have been drawn before on mathematical grounds, i.e. using similarity of the equations used describe these phenomena [180, 181]. The phase space analysis of MCRD pattern formation presented in the present work establishes a connection to shear banding on the basis of phase space geometry. More specifically, these two phenomena can be regarded as *topologically equivalent*, i.e. they can be understood in terms of equivalent geometric objects in phase space. We shall briefly outline this connection in the following.

Complex fluids can exhibit a non-monotonic *constitutive* relationship $\Sigma(\dot{\gamma})$ between the total stress Σ and the (homogeneous) strain rate $\dot{\gamma}$ [125, 136]. When the total stress decreases upon an increase in strain rate, $\partial_{\dot{\gamma}}\Sigma < 0$, a mechanical instability results, which leads to a separation of a sheared fluid into "shear bands" with different viscosities and strain rates, which coexist at a common total stress. The "common total stress" construction on the *constitutive* curve $\Sigma(\dot{\gamma})$ employed to analyze this phenomenon (in a one-dimensional system) is analogous to our flux-balance construction on the reactive nullcline for 2C-MCRD systems (see Sec. III C), by means of a mapping $(n, \eta) \leftrightarrow (\dot{\gamma}, \Sigma)$ between the phase space variables. The average strain rate $\bar{\dot{\gamma}} = L^{-1}\int_0^L \mathrm{d}x\,\dot{\gamma}$ is analogous to the average total density $\bar{n}$. The constitutive $\Sigma(\dot{\gamma})$ curve is analogous to the reactive nullcline. The steady state conditions are spatially uniform total stress and flux-balance (spatially uniform mass-redistribution potential; see III B) respectively. The selection of the common total stress generally depends on the details of the model [182], in particular on stress diffusion [183]. For simple models, it can be pictured similarly to a Maxwell-construction (cf. total turnover balance in a 2C-MCRD system illustrated in Fig. 2). Furthermore, momentum propagation due to stress gradients in complex fluids is equivalent to mass redistribution due to concentration gradients in MCRD systems. Accordingly, the low Reynolds number limit is analogous to the $D_c \to \infty$ limit in the 2C-MCRD system.

Taking these analogies together, we conclude that these physically distinct phenomena are topologically equivalent and can be studied with similar phase-space geometric tools. Such a connection might benefit both fields as more involved scenarios are investigated, for instance coupling to additional degrees of freedom: For models of complex fluids, additional spatial dimensions [184], and coupling to internal structure of the fluid [185, 186], can lead to a variety of intricate spatiotemporal patterns; for mass-conserving reaction–diffusion systems, additional components or additional conserved species can equally lead to a broad range of phenomena [16, 108, 141]. Studying such systems in terms of local equilibria theory offers an exciting new perspective for future research.

---

[1] S. H. Strogatz, *Nonlinear Dynamics and Chaos*, 2nd ed. (Westview Press, 2014).

[2] E. M. Izhikevich, *Dynamical systems in neuroscience: the geometry of excitability and bursting* (The MIT

Press, Cambridge, Massachusetts, 2007).

[3] A. S. Mikhailov, *Foundations of Synergetics I: Distributed Active Systems*, 2nd ed., Springer Series in Synergetics 51 (Springer-Verlag Berlin Heidelberg, 1994).

[4] J. D. Murray, *Mathematical Biology I. An Introduction*, 3rd ed., Interdisciplinary Applied Mathematics, Vol. 17 (Springer, New York, 2002).

[5] E. A. Jackson, *Perspectives of Nonlinear Dynamics*, Vol. 1 (Cambridge University Press, 1989).

[6] M. Cross and H. Greenside, *Pattern Formation and Dynamics in Nonequilibrium Systems* (Cambridge University Press, 2009).

[7] E. Ott, *Chaos in Dynamical Systems*, 2nd ed. (Cambridge University Press, 2002).

[8] H. Poincaré, *Les méthodes nouvelles de la mécanique céleste*, Vol. 1–3 (Gauthiers-Villars, Paris, 1892, 1893, 1899) english translation edited by D. Goroff, published by the American Institute of Physics, New York, 1993.

[9] C. K. R. T. Jones, *Geometric singular perturbation theory*, edited by R. Johnson, Dynamical Systems. Lecture Notes in Mathematics, Vol. 1609 (Springer, New York, 1994) pp. 44–118.

[10] B. S. Kerner and V. V. Osipov, *Autosolitons: A New Approach to Problems of Self-Organization and Turbulence*, Fundamental Theories of Physics No. v. 61 (Kluwer Academic, Dordrecht; Boston, 1994).

[11] R. Fisher, "The wave of advance of advantageous genes," Annals of Eugenics **7**, 355–369 (1937).

[12] A. Kolmogorov, I. Petrovsky, and N. Piscounov, "étude de l'équation de la diffusion avec croissance de la quantité de matièr et son application à un probléme biologique," Moscou Univ. Bull. Math. **1**, 1–25 (1937).

[13] D. Jones, M. Plank, and B. Sleeman, *Differential Equations and Mathematical Biology*, 2nd ed., Chapman & Hall/CRC Mathematical and Computational Biology Series (Taylor & Francis, 2009).

[14] J. Halatek, F. Brauns, and E. Frey, "Self-organization principles of intracellular pattern formation," Philosophical Transactions of the Royal Society B: Biological Sciences **373**, 20170107 (2018).

[15] F. Brauns, H. Weyer, J. Halatek, J. Yoon, and E. Frey, "Wavelength selection by interrupted coarsening in reaction–diffusion systems," arXiv:2005.01495 [nlin, physics:physics] (2020), arXiv:2005.01495 [nlin, physics:physics].

[16] J. Halatek and E. Frey, "Rethinking pattern formation in reaction–diffusion systems," Nature Physics **14**, 507–514 (2018).

[17] The reactive equilibria are *not* thermal equilibria but *non-equilibrium steady states*. Specifically, the concept local reactive equilibria should not be confused with the concept of local thermal equilibria in Onsager's theory of systems close to thermal equilibrium [18]. We use the term "equilibrium" in the original, broad meaning of the term, namely the balance of opposing "forces". The specifier "reactive" emphasizes that the balance is between chemical "reactions," or more general kinetic processes if the equations are not interpreted in terms of chemical but a broader class of agents.

[18] L. Onsager, "Reciprocal relations in irreversible processes. I." Physical Review **37**, 405–426 (1931).

[19] J. Denk, S. Kretschmer, J. Halatek, C. Hartl, P. Schwille, and E. Frey, "MinE conformational switching confers robustness on self-organized Min protein patterns," Proc. Natl. Acad. Sci. U.S.A. **115**, 4553–4558 (2018).

[20] M. C. Wigbers, F. Brauns, T. Hermann, and E. Frey, "Pattern localization to a domain edge," Physical Review E **101**, 022414 (2020).

[21] M. C. Wigbers, F. Brauns, C. Y. Leung, and E. Frey, "Flow induced symmetry breaking in a conceptual polarity model," Cells **9**, 1524 (2020).

[22] F. Brauns, G. Pawlik, J. Halatek, J. Kerssemakers, E. Frey, and C. Dekker, "Bulk-surface coupling reconciles Min-protein pattern formation in vitro and in vivo," Preprint on bioRxiv (2020), DOI: 10.1101/2020.03.01.971952.

[23] F. Brauns, J. Halatek, and E. Frey, (unpublished).

[24] S. Ishihara, M. Otsuji, and A. Mochizuki, "Transient and steady state of mass-conserved reaction-diffusion systems," Phys. Rev. E **75**, 015203(R) (2007).

[25] M. Otsuji, S. Ishihara, C. Co, K. Kaibuchi, A. Mochizuki, and S. Kuroda, "A mass conserved reaction–diffusion system captures properties of cell polarity," PLoS Computational Biology **3**, e108 (2007).

[26] A. B. Goryachev and A. V. Pokhilko, "Dynamics of Cdc42 network embodies a Turing-type mechanism of yeast cell polarity," FEBS Letters **582**, 1437–43 (2008).

[27] S. J. Altschuler, S. B. Angenent, Y. Wang, and L. F. Wu, "On the spontaneous emergence of cell polarity," Nature **454**, 886–889 (2008).

[28] Y. Mori, A. Jilkine, and L. Edelstein-Keshet, "Wave-pinning and cell polarity from a bistable reaction-diffusion system," Biophysical Journal **94**, 3684–3697 (2008).

[29] A. Jilkine and L. Edelstein-Keshet, "A comparison of mathematical models for polarization of single eukaryotic cells in response to guided cues," PLoS Computational Biology **7**, e1001121 (2011).

[30] A. Jilkine, S. B. Angenent, L. F. Wu, and S. J. Altschuler, "A density-dependent switch drives stochastic clustering and polarization of signaling molecules," PLoS Computational Biology **7**, e1002271 (2011).

[31] L. Edelstein-Keshet, W. R. Holmes, M. Zajac, and M. Dutot, "From simple to detailed models for cell polarization," Philosophical Transactions of the Royal Society B: Biological Sciences **368**, 20130003–20130003 (2013).

[32] P. K. Trong, E. M. Nicola, N. W. Goehring, K. V. Kumar, and S. W. Grill, "Parameter-space topology of models for cell polarity," New Journal of Physics **16**, 065009 (2014).

[33] S. Seirin Lee and T. Shibata, "Self-organization and advective transport in the cell polarity formation for asymmetric cell division," Journal of Theoretical Biology **382**, 1–14 (2015).

[34] J.-G. Chiou, S. A. Ramirez, T. C. Elston, T. P. Witelski, D. G. Schaeffer, and D. J. Lew, "Principles that govern competition or co-existence in Rho-GTPase driven polarization," PLoS Computational Biology **14**, e1006095 (2018).

[35] R. Diegmiller, H. Montanelli, C. B. Muratov, and S. Y. Shvartsman, "Spherical caps in cell polarization," Biophysical Journal **115**, 26–30 (2018).

[36] L. Hubatsch, F. Peglion, J. D. Reich, N. T. L. Rodrigues, N. Hirani, R. Illukkumbura, and N. W. Goehring, "A cell-size threshold limits cell polarity and asymmetric division potential," Nature Physics , 1078–

1085 (2019).

[37] E. F. Keller and L. A. Segel, "Initiation of slime mold aggregation viewed as an instability," Journal of Theoretical Biology **26**, 399–415 (1970).

[38] K. Pham, A. Chauviere, H. Hatzikirou, X. Li, H. M. Byrne, V. Cristini, and J. Lowengrub, "Density-dependent quiescence in glioma invasion: instability in a simple reaction–diffusion model for the migration/proliferation dichotomy," Journal of Biological Dynamics **6**, 54–71 (2012).

[39] A. Scheel, "Robustness of liesegang patterns," Nonlinearity **22**, 457–483 (2009).

[40] D. Hilhorst, R. van der Hout, M. Mimura, and I. Ohnishi, "Fast reaction limits and liesegang bands," Free Boundary Problems , 241–250 (2006).

[41] F. van Wijland, K. Oerding, and H. Hilhorst, "Wilson renormalization of a reaction–diffusion process," Physica A: Statistical Mechanics and its Applications **251**, 179–201 (1998).

[42] D. A. Kessler and H. Levine, "Fluctuation-induced diffusive instabilities," Nature **394**, 556–558 (1998).

[43] G. Caginalp, "An analysis of a phase field model of a free boundary," Archive for Rational Mechanics and Analysis **92**, 205–245 (1986).

[44] Y. Morita and T. Ogawa, "Stability and bifurcation of nonconstant solutions to a reaction–diffusion system with conservation of mass," Nonlinearity **23**, 1387–1411 (2010).

[45] A. Pogan and A. Scheel, "Layers in the presence of conservation laws," J. Dyn. Differ. Equ. **24**, 249–287 (2012).

[46] R. N. Goh, S. Mesuro, and A. Scheel, "Spatial wavenumber selection in recurrent precipitation," SIAM Journal on Applied Dynamical Systems **10**, 360–402 (2011).

[47] S. Jimbo and Y. Morita, "Lyapunov function and spectrum comparison for a reaction–diffusion system with mass conservation," Journal of Differential Equations **255**, 1657–1683 (2013).

[48] E. Latos, Y. Morita, and T. Suzuki, "Stability and spectral comparison of a reaction–diffusion system with mass conservation," Journal of Dynamics and Differential Equations **30**, 823–844 (2018).

[49] L. Pismen, *Patterns and Interfaces in Dissipative Dynamics*, Springer Series in Synergetics (Springer-Verlag Berlin Heidelberg, 2006).

[50] I. Prigogine and R. Lefever, "Symmetry breaking instabilities in dissipative systems. II," The Journal of Chemical Physics **48**, 1695–1700 (1968).

[51] M. Kuwamura and Y. Morita, "Perturbations and dynamics of reaction-diffusion systems with mass conservation," Physical Review E **92**, 012908 (2015).

[52] M. Kuwamura and H. Izuhara, "Diffusion-driven destabilization of spatially homogeneous limit cycles in reaction-diffusion systems," Chaos: An Interdisciplinary Journal of Nonlinear Science **27**, 033112 (2017).

[53] Y. Mori, A. Jilkine, and L. Edelstein-Keshet, "Asymptotic and bifurcation analysis of wave-pinning in a reaction-diffusion model for cell polarization," SIAM Journal on Applied Mathematics **71**, 1401–1427 (2011).

[54] P. C. Hohenberg and B. I. Halperin, "Theory of dynamic critical phenomena," Reviews of Modern Physics **49**, 435–479 (1977).

[55] A. M. Turing, "The chemical basis of morphogenesis," Philosophical Transactions of the Royal Society B: Biological Sciences **237**, 37–72 (1952).

[56] We will use the terms lateral instability and Turing instability interchangeably. This means we take the term Turing instability slightly more general than it is typically done in the literature, where Turing instability became exclusively associated with instabilities that have a characteristic wavelength at onset, called 'type I' in the Cross–Hohenberg classification scheme [175].

[57] K. Kang, T. Kolokolnikov, and M. J. Ward, "The stability and dynamics of a spike in the 1D Keller–Segel model," IMA Journal of Applied Mathematics **72**, 140–162 (2007).

[58] In MCRD systems with more than two-components, the coupling to additional components can lead to destabilization of the plateaus [15]; such processes have been referred to as 'anti-coarsening' [59], 'peak-splitting' [60, 108], or 'self-replication' [163] in the literature.

[59] M. Ivanov, V. Popkov, and J. Krug, "Anticoarsening and complex dynamics of step bunches during sublimation on vicinal surfaces," Phys. Rev. E **82**, 011606 (2010).

[60] E. J. Crampin, E. A. Gaffney, and P. K. Maini, "Mode-doubling and tripling in reaction-diffusion patterns on growing domains: A piecewise linear model," Journal of Mathematical Biology **44**, 107–128 (2002).

[61] M. J. Ward, "Asymptotic methods for reaction-diffusion systems: Past and present," Bulletin of Mathematical Biology **68**, 1151–1167 (2006).

[62] The complement to a peak is a 'trough' pattern, composed of an interface connected to a high density plateau.

[63] Given η_0, and the boundary condition $m(x \to -\infty) \to m_-(\eta_0)$ one can determine the entire peak profile using the rolling-ball analogy: The profile corresponds to the Newtonian trajectory $m(x)$ of a mass point in a potential $V(m) = -\int dm\, f$, where m is the "position" of the mass point and x is "time".

[64] N. W. Goehring, P. K. Trong, J. S. Bois, D. Chowdhury, E. M. Nicola, A. A. Hyman, and S. W. Grill, "Polarization of PAR proteins by advective triggering of a pattern-forming system," Science **334**, 1137–1141 (2011).

[65] P. W. Bates and P. C. Fife, "The dynamics of nucleation for the Cahn–Hilliard equation," SIAM Journal on Applied Mathematics **53**, 990–1008 (1993).

[66] M. E. Cates and E. Tjhung, "Theories of binary fluid mixtures: from phase-separation kinetics to active emulsions," Journal of Fluid Mechanics **836**, P1 (2017).

[67] F. Bergmann, L. Rapp, and W. Zimmermann, "Active phase separation: A universal approach," Physical Review E **98**, 020603(R) (2018).

[68] S. M. Allen and J. W. Cahn, "Ground state structures in ordered binary alloys with second neighbor interactions," Acta Metallurgica **20**, 423 (1972).

[69] For a simple contact process with noise, the case $D_c < D_m$ (i.e. the self-recruiting component is the faster diffusing one), shows interesting correlations, while a first order phase transition has been conjectured for $D_m < D_c$ [41]. Note, however, that the simple contact process under consideration in Ref. [41] does not exhibit bistability.

[70] The slope s_{nc} of a continuous reactive nullcline smoothly approaches the slope -1 at the saddle-node bifurcations of the reactive equilibria. Hence, as D_c is decreased,

the laterally unstable regions shrink, but disappear fully only at $D_c = D_m$. In the vicinity of the saddle-node bifurcations for sufficiently small $D_c \gtrsim D_m$, no stationary patterns exist, but there are still small regions of lateral instability.

[71] Y. Nishiura and H. Fujii, "Stability of singularly perturbed solutions to systems of reaction-diffusion equations," SIAM Journal on Mathematical Analysis **18**, 1726–1770 (1987).

[72] A. B. Goryachev and M. Leda, "Many roads to symmetry breaking: molecular mechanisms and theoretical models of yeast cell polarity," Molecular Biology of the Cell **28**, 370–380 (2017).

[73] P. Manneville, *Dissipative structures and weak turbulence*, edited by P. Manneville (Academic Press, Boston, 1990).

[74] V. I. Arnold, *Geometrical Methods in the Theory of Ordinary Differential Equations*, 2nd ed., edited by M. Levi (Springer, New York, 1988).

[75] J. Murdock, *Normal Forms and Unfoldings for Local Dynamical Systems*, Springer Monographs in Mathematics (Springer, New York, 2003).

[76] J. P. Campanale, T. Y. Sun, and D. J. Montell, "Development and dynamics of cell polarity at a glance," Journal of Cell Science **130**, 1201–1207 (2017).

[77] J.-g. Chiou, M. K. Balasubramanian, and D. J. Lew, "Cell polarity in yeast," Annual Review of Cell and Developmental Biology **33**, 77–101 (2017).

[78] M. Loose, E. Fischer-Friedrich, J. Ries, K. Kruse, and P. Schwille, "Spatial regulators for bacterial cell division self-organize into surface waves in vitro," Science **320**, 789–792 (2008).

[79] V. Ivanov and K. Mizuuchi, "Multiple modes of interconverting dynamic pattern formation by bacterial cell division proteins," Proceedings of the National Academy of Sciences **107**, 8071–8078 (2010).

[80] K. Zieske and P. Schwille, "Reconstitution of self-organizing protein gradients as spatial cues in cell-free systems," eLife **3**, e03949 (2014).

[81] A. G. Vecchiarelli, M. Li, M. Mizuuchi, and K. Mizuuchi, "Differential affinities of MinD and MinE to anionic phospholipid influence Min patterning dynamics in vitro," Molecular Microbiology **93**, 453–463 (2014).

[82] Y. Caspi and C. Dekker, "Mapping out Min protein patterns in fully confined fluidic chambers," eLife **5**, e19271 (2016).

[83] S. Kretschmer, K. Zieske, and P. Schwille, "Large-scale modulation of reconstituted Min protein patterns and gradients by defined mutations in MinE's membrane targeting sequence," PLOS ONE **12**, e0179582 (2017).

[84] P. Glock, J. Broichhagen, S. Kretschmer, P. Blumhardt, J. Mücksch, D. Trauner, and P. Schwille, "Optical control of a biological reaction-diffusion system," Angewandte Chemie International Edition **57**, 2362–2366 (2018).

[85] T. Litschel, B. Ramm, R. Maas, M. Heymann, and P. Schwille, "Beating vesicles: Encapsulated protein oscillations cause dynamic membrane deformations," Angewandte Chemie International Edition **57**, 16286–16290 (2018).

[86] B. Ramm, P. Glock, J. Mücksch, P. Blumhardt, D. A. García-Soriano, M. Heymann, and P. Schwille, "The MinDE system is a generic spatial cue for membrane protein distribution in vitro," Nature Communications **9**, 3942 (2018).

[87] S. Kohyama, N. Yoshinaga, M. Yanagisawa, K. Fujiwara, and N. Doi, "Cell-sized confinement controls generation and stability of a protein wave for spatiotemporal regulation in cells," eLife **8**, e44591 (2019).

[88] P. Glock, F. Brauns, J. Halatek, E. Frey, and P. Schwille, "Design of biochemical pattern forming systems from minimal motifs," eLife **8**, e48646 (2019).

[89] K. J. A. Vendel, S. Tschirpke, F. Shamsi, M. Dogterom, and L. Laan, "Minimal in vitro systems shed light on cell polarity," Journal of Cell Science **132**, jcs217554 (2019).

[90] A. H. Chau, J. M. Walter, J. Gerardin, C. Tang, and W. A. Lim, "Designing synthetic regulatory networks capable of self-organizing cell polarization," Cell **151**, 320–332 (2012).

[91] L. Marcon, X. Diego, J. Sharpe, and P. Müller, "High-throughput mathematical analysis identifies Turing networks for patterning with equally diffusing signals," eLife **5**, e14022 (2016).

[92] S. S. Sugai, K. L. Ode, and H. R. Ueda, "A design principle for an autonomous post-translational pattern formation," Cell Reports **19**, 863–874 (2017).

[93] X. Diego, L. Marcon, P. Müller, and J. Sharpe, "Key features of Turing systems are determined purely by network topology," Physical Review X **8**, 021071 (2018).

[94] D. Cusseddu, L. Edelstein-Keshet, J. Mackenzie, S. Portet, and A. Madzvamuse, "A coupled bulk-surface model for cell polarisation," Journal of Theoretical Biology **481**, 119–135 (2018).

[95] A. Gamba, I. Kolokolov, V. Lebedev, and G. Ortenzi, "Universal features of cell polarization processes," Journal of Statistical Mechanics: Theory and Experiment **2009**, P02019 (2009).

[96] B. Novák and J. J. Tyson, "Design principles of biochemical oscillators," Nature Reviews Molecular Cell Biology **9**, 981–991 (2008).

[97] B. N. Kholodenko, "Cell-signalling dynamics in time and space," Nature Reviews Molecular Cell Biology **7**, 165–176 (2006).

[98] A. Gierer and H. Meinhardt, "A theory of biological pattern formation," Kybernetik **12**, 30–39 (1972).

[99] L. A. Segel and J. L. Jackson, "Dissipative structure: An explanation and an ecological example," Journal of Theoretical Biology **37**, 545–559 (1972).

[100] D. Karig, K. M. Martini, T. Lu, N. A. DeLateur, N. Goldenfeld, and R. Weiss, "Stochastic Turing patterns in a synthetic bacterial population," Proceedings of the National Academy of Sciences **115**, 6572–6577 (2018).

[101] L. Manukyan, S. A. Montandon, A. Fofonjka, S. Smirnov, and M. C. Milinkovitch, "A living mesoscopic cellular automaton made of skin scales," Nature **544**, 173–179 (2017).

[102] M. Watanabe and S. Kondo, "Is pigment patterning in fish skin determined by the Turing mechanism?" Trends in Genetics **31**, 88–96 (2015).

[103] S. Kondo and R. Asai, "A reaction–diffusion wave on the skin of the marine angelfish pomacanthus," Nature **376**, 765–768 (1995).

[104] G. B. Ermentrout and J. D. Cowan, "A mathematical theory of visual hallucination patterns," Biological Cybernetics **34**, 137–150 (1979).

[105] A. Eldar, B.-Z. Shilo, and N. Barkai, "Elucidating mechanisms underlying robustness of morphogen gra-

dients," Current Opinion in Genetics & Development **14**, 435–439 (2004).

[106] N. Verschueren and A. Champneys, "A model for cell polarization without mass conservation," SIAM Journal on Applied Dynamical Systems **16**, 1797–1830 (2017).

[107] J. Halatek and E. Frey, "Highly canalized MinD transfer and mine sequestration explain the origin of robust MinCDE-protein dynamics," Cell Reports **1**, 741–752 (2012).

[108] S. M. Murray and V. Sourjik, "Self-organization and positioning of bacterial protein clusters," Nature Physics **13**, 1006–1013 (2017).

[109] P. Politi and C. Misbah, "When does coarsening occur in the dynamics of one-dimensional fronts?" Physical Review Letters **92**, 090601 (2004).

[110] P. Politi and C. Misbah, "Nonlinear dynamics in one dimension: A criterion for coarsening and its temporal law," Physical Review E **73**, 036133 (2006).

[111] L. Wolpert, "Positional information and the spatial pattern of cellular differentiation," Journal of Theoretical Biology **25**, 1–47 (1969).

[112] B. Alberts, A. Johnson, J. Lewis, M. Raff, K. Roberts, and P. Walter, *Molecular Biology of the Cell*, 5th ed. (Garland Science, New York, 2007).

[113] J. Lutkenhaus, "Assembly dynamics of the bacterial mincde system and spatial regulation of the z ring," Annual Review of Biochemistry **76**, 539–562 (2007).

[114] F. O. Bendezu and S. G. Martin, "Cdc42 oscillations in yeasts," Science Signaling **5**, pe53 (2012).

[115] H.-O. Park and E. Bi, "Central roles of small gtpases in the development of cell polarity in yeast and beyond," Microbiology and Molecular Biology Reviews **71**, 48–96 (2007).

[116] S. G. Martin and R. A. Arkowitz, "Cell polarization in budding and fission yeasts," FEMS Microbiology Reviews **38**, 228–253 (2014).

[117] C. Hoege and A. A. Hyman, "Principles of PAR polarity in caenorhabditis elegans embryos," Nature Reviews Molecular Cell Biology **14**, 315–322 (2013).

[118] P. Gross, K. V. Kumar, N. W. Goehring, J. S. Bois, C. Hoege, F. Jülicher, and S. W. Grill, "Guiding self-organized pattern formation in cell polarity establishment," Nature Physics **15**, 293–300 (2018).

[119] R. Geßele, J. Halatek, L. Würthner, and E. Frey, "Geometric cues stabilise long-axis polarisation of PAR protein patterns in C. elegans," Nature Communications **11**, 539 (2020).

[120] H. Chaté, "Dry aligning dilute active matter," Annual Review of Condensed Matter Physics **11**, 189–212 (2020).

[121] L. Huber, R. Suzuki, T. Krüger, E. Frey, and A. R. Bausch, "Emergence of coexisting ordered states in active matter systems," Science **361**, 255–258 (2018).

[122] M. E. Cates and J. Tailleur, "Motility-induced phase separation," Annual Review of Condensed Matter Physics **6**, 219–244 (2015).

[123] J. S. Bois, F. Jülicher, and S. W. Grill, "Pattern formation in active fluids," Physical Review Letters **106**, 028103 (2011).

[124] G. Liu, A. Patch, F. Bahar, D. Yllanes, R. D. Welch, M. C. Marchetti, S. Thutupalli, and J. W. Shaevitz, "Self-driven phase transitions drive *myxococcus xanthus* fruiting body formation," Physical Review Letters **122**, 248102 (2019).

[125] P. D. Olmsted, "Perspectives on shear banding in complex fluids," Rheologica Acta **47**, 283–300 (2008).

[126] K. John and M. Bär, "Alternative mechanisms of structuring biomembranes: Self-assembly versus self-organization," Physical Review Letters **95**, 198101 (2005).

[127] J. Agudo-Canalejo and R. Golestanian, "Active phase separation in mixtures of chemically interacting particles," Physical Review Letters **123**, 018101 (2019).

[128] S. C. Glotzer, E. A. Di Marzio, and M. Muthukumar, "Reaction-controlled morphology of phase-separating mixtures," Physical Review Letters **74**, 2034–2037 (1995).

[129] Y. Oono and Y. Shiwa, "Computationally efficient modeling of block copolymer and benard pattern formations," Modern Physics Letters B **01**, 49–55 (1987).

[130] M. E. Cates, D. Marenduzzo, I. Pagonabarraga, and J. Tailleur, "Arrested phase separation in reproducing bacteria creates a generic route to pattern formation," Proceedings of the National Academy of Sciences **107**, 11715–11720 (2010).

[131] A. I. Curatolo, N. Zhou, Y. Zhao, C. Liu, A. Daerr, J. Tailleur, and J. Huang, "Engineering cooperative patterns in multi-species bacterial colonies," Preprint on bioRxiv (2019), DOI: 10.1101/798827.

[132] S. Saha, J. Agudo-Canalejo, and R. Golestanian, "Scalar active mixtures: The non-reciprocal Cahn-Hilliard model," arXiv:2005.07101 [cond-mat.stat-mech] (2020).

[133] E. Bernitt, H.-G. Döbereiner, N. S. Gov, and A. Yochelis, "Fronts and waves of actin polymerization in a bistability-based mechanism of circular dorsal ruffles," Nature Communications **8**, 15863 (2017).

[134] M. Radszuweit, S. Alonso, H. Engel, and M. Bär, "Intracellular mechanochemical waves in an active poroelastic model," Physical Review Letters **110**, 138102 (2013).

[135] M. F. Weber and E. Frey, "Master equations and the theory of stochastic path integrals," Reports on Progress in Physics **80**, 046601 (2017).

[136] T. Divoux, M. A. Fardin, S. Manneville, and S. Lerouge, "Shear banding of complex fluids," Annual Review of Fluid Mechanics **48**, 81–103 (2016).

[137] K. V. Kumar, J. S. Bois, F. Jülicher, and S. W. Grill, "Pulsatory patterns in active fluids," Physical Review Letters **112**, 208101 (2014).

[138] C. A. Weber, C. H. Rycroft, and L. Mahadevan, "Differential activity-driven instabilities in biphasic active matter," Physical Review Letters **120**, 248003 (2018).

[139] M. C. Marchetti, J. F. Joanny, S. Ramaswamy, T. B. Liverpool, J. Prost, M. Rao, and R. A. Simha, "Hydrodynamics of soft active matter," Reviews of Modern Physics **85**, 1143–1189 (2013).

[140] I. S. Aranson and L. S. Tsimring, "Patterns and collective behavior in granular media: Theoretical concepts," Reviews of Modern Physics **78**, 641–692 (2006).

[141] S. Alonso and M. Bär, "Phase separation and bistability in a three-dimensional model for protein domain formation at biomembranes," Physical Biology **7**, 046012 (2010).

[142] E. M. Izhikevich, "Neural excitability, spiking and bursting," International Journal of Bifurcation and Chaos **10**, 1171–1266 (2000).

[143] F. Sagués, J. M. Sancho, and J. Garcia-Ojalvo, "Spa-

tiotemporal order out of noise," Reviews of Modern Physics **79**, 829–882 (2007).

[144] L. J. Schumacher, T. E. Woolley, and R. E. Baker, "Noise-induced temporal dynamics in Turing systems," Physical Review E **87**, 042719 (2013).

[145] T. Biancalani, F. Jafarpour, and N. Goldenfeld, "Giant amplification of noise in fluctuation-induced pattern formation," Physical Review Letters **118**, 018101 (2017).

[146] M. F. Adamer, H. A. Harrington, E. A. Gaffney, and T. E. Woolley, "Coloured noise from stochastic inflows in reaction-diffusion systems," arXiv:1810.12663 (2018).

[147] R. Wedlich-Soldner, "Spontaneous cell polarization through actomyosin-based delivery of the Cdc42 GTPase," Science **299**, 1231–1235 (2003).

[148] B. Klünder, T. Freisinger, R. Wedlich-Söldner, and E. Frey, "GDI-Mediated cell polarization in yeast provides precise spatial and temporal control of Cdc42 signaling," PLoS Computational Biology **9**, e1003396 (2013).

[149] S. Smith and N. Dalchau, "Model reduction enables Turing instability analysis of large reaction–diffusion models," Journal of The Royal Society Interface **15**, 20170805 (2018).

[150] L. Sewalt, A. Doelman, H. Meijer, V. Rottschäfer, and A. Zagaris, "Tracking pattern evolution through extended center manifold reduction and singular perturbations," Physica D: Nonlinear Phenomena **298-299**, 48–67 (2015).

[151] A. Doelman, L. Sewalt, and A. Zagaris, "The effect of slow spatial processes on emerging spatiotemporal patterns," Chaos **25**, 036408 (2015).

[152] A. M. Zhabotinsky, "Periodical oxidation of malonic acid in solution (a study of the belousov reaction kinetics)," Biofizika , 306–311 (1964).

[153] S. R. Neves, "G protein pathways," Science **296**, 1636–1639 (2002).

[154] S. D. Hansen, W. Y. C. Huang, Y. K. Lee, P. Bieling, S. M. Christensen, and J. T. Groves, "Stochastic geometry sensing and polarization in a lipid kinase–phosphatase competitive reaction," Proceedings of the National Academy of Sciences **116**, 15013–15022 (2019).

[155] S. Alonso and M. Bär, "Modeling domain formation of MARCKS and protein kinase C at cellular membranes," EPJ Nonlinear Biomedical Physics **2** (2014), 10.1140/epjnbp14.

[156] B. P. Belousov, "Periodically acting reaction and its mechanism," Collection of Short Papers on Radiation Medicine , 145 (1959).

[157] R. J. Field, E. Koros, and R. M. Noyes, "Oscillations in chemical systems. II. Thorough analysis of temporal oscillation in the bromate-cerium-malonic acid system," Journal of the American Chemical Society **94**, 8649–8664 (1972).

[158] R. Rao and M. Esposito, "Conservation laws shape dissipation," New Journal of Physics **20**, 023007 (2018).

[159] F. Avanzini, G. Falasco, and M. Esposito, "Thermodynamics of chemical waves," The Journal of Chemical Physics **151**, 234103 (2019).

[160] A. Ehrmann, B. Nguyen, and U. Seifert, "Interlinked GTPase cascades provide a motif for both robust switches and oscillators," Journal of The Royal Society Interface **16**, 20190198 (2019).

[161] Alternatively, one may introduce $\gamma \in [0,1]$ as an interpolation parameter to interpolate between the original system ($\gamma = 1$) and the mass-conserving subsystem ($\gamma = 0$). One can then use analytic or numeric methods to continue the solution of the mass-conserving subsystem to the original system and thus systematically study the effect of the source terms.

[162] T. Kolokolnikov, T. Erneux, and J. Wei, "Mesa-type patterns in the one-dimensional Brusselator and their stability," Physica D: Nonlinear Phenomena **214**, 63–77 (2006).

[163] T. Kolokolnikov, M. Ward, and J. Wei, "Self-replication of mesa patterns in reaction–diffusion systems," Physica D: Nonlinear Phenomena **236**, 104–122 (2007).

[164] R. McKay and T. Kolokolnikov, "Stability transitions and dynamics of mesa patterns near the shadow limit of reaction-diffusion systems in one space dimension," Discrete & Continuous Dynamical Systems - B **17**, 191–220 (2012).

[165] J. C. Tzou, Y. Nec, and M. J. Ward, "The stability of localized spikes for the 1-d Brusselator reaction–diffusion model," European Journal of Applied Mathematics **24**, 515–564 (2013).

[166] V. Khamviwath, J. Hu, and H. G. Othmer, "A continuum model of actin waves in dictyostelium discoideum," PLoS ONE **8**, e64272 (2013).

[167] W. M. Bement, M. Leda, A. M. Moe, A. M. Kita, M. E. Larson, A. E. Golding, C. Pfeuti, K.-C. Su, A. L. Miller, A. B. Goryachev, and et al., "Activator–inhibitor coupling between rho signalling and actin assembly makes the cell cortex an excitable medium," Nature Cell Biology **17**, 1471–1483 (2015).

[168] M. Graessl, J. Koch, A. Calderon, D. Kamps, S. Banerjee, T. Mazel, N. Schulze, J. K. Jungkurth, R. Patwardhan, D. Solouk, and et al., "An excitable rho gtpase signaling network generates dynamic subcellular contraction patterns," Journal of Cell Biology **216**, 4271–4285 (2017).

[169] J. B. Michaux, F. B. Robin, W. M. McFadden, and E. M. Munro, "Excitable RhoA dynamics drive pulsed contractions in the early C. elegans embryo," The Journal of Cell Biology **217**, 4230–4252 (2018).

[170] T. H. Tan, J. Liu, P. W. Miller, M. Tekant, J. Dunkel, and N. Fakhri, "Topological turbulence in the membrane of a living cell," Nature Physics **16**, 657–662 (2020).

[171] D. Zwicker, A. A. Hyman, and F. Jülicher, "Suppression of Ostwald ripening in active emulsions," Physical Review E **92**, 012317 (2015).

[172] E. Tjhung, C. Nardini, and M. E. Cates, "Cluster phases and bubbly phase separation in active fluids: Reversal of the Ostwald process," Physical Review X **8**, 031080 (2018).

[173] C. A. Weber, D. Zwicker, F. Jülicher, and C. F. Lee, "Physics of active emulsions," Reports on Progress in Physics **82**, 064601 (2019).

[174] J. Denk and E. Frey, "Pattern-induced local symmetry breaking in active matter systems," arXiv:2005.12791 [cond-mat.soft] (2020).

[175] M. C. Cross and P. C. Hohenberg, "Pattern formation outside of equilibrium," Reviews of Modern Physics **65**, 851–1112 (1993).

[176] J. W. Cahn, "On spinodal decomposition," Acta Metallurgica **9**, 795–801 (1961).

[177] H. Weyer, F. Brauns, and E. Frey, (unpublished).

[178] B. Fiddler, ed., *Handbook of Dynamical Systems*, Vol. 2 (Elsevier, 2002).

[179] T. Kolokolnikov, M. J. Ward, and J. Wei, "The existence and stability of spike equilibria in the one-dimensional gray-scott model: The low feed-rate regime," Studies in Applied Mathematics **115**, 21–71 (2005).

[180] O. Radulescu, P. D. Olmsted, and C.-Y. D. Lu, "Shear banding in reaction-diffusion models," Rheologica Acta **38**, 606–613 (1999).

[181] M. A. Fardin, T. J. Ober, C. Gay, G. Grégoire, G. H. McKinley, and S. Lerouge, "Potential "ways of thinking" about the shear-banding phenomenon," Soft Matter **8**, 910–922 (2012).

[182] J. K. G. Dhont and W. J. Briels, "Gradient and vorticity banding," Rheologica Acta **47**, 257–281 (2008).

[183] M.-A. Fardin, O. Radulescu, A. Morozov, O. Cardoso, J. Browaeys, and S. Lerouge, "Stress diffusion in shear banding wormlike micelles," Journal of Rheology **59**, 1335–1362 (2015).

[184] S. M. Fielding, "Viscoelastic taylor-couette instability of shear banded flow," Physical Review Letters **104**, 198303 (2010).

[185] S. M. Fielding, "Complex dynamics of shear banded flows," Soft Matter **3**, 1262 (2007).

[186] M. Turcio, A. E. Chávez, J. E. López-Aguilar, R. O. Vargas, A. Capella, and O. Manero, "Dissipative structures in shear-thickening complex fluids," Physics of Fluids **30**, 114104 (2018).

2 Diffusive coupling of two well-mixed compartments elucidates elementary principles of protein-based pattern formation

This section is a publication preprint of the following manuscript published in Phys. Rev. Research 3, 013258 (2021)

Diffusive coupling of two well-mixed compartments elucidates elementary principles of protein-based pattern formation

F. Brauns,[1] J. Halatek,[2] and E. Frey[1]

[1] *Arnold Sommerfeld Center for Theoretical Physics and Center for NanoScience, Department of Physics, Ludwig-Maximilians-Universtiät München, Theresienstraße 37, D-80333 München, Germany*

[2] *Biological Computation Group, Microsoft Research, Cambridge CB1 2FB, UK*

Diffusive coupling of two well-mixed compartments elucidates elementary principles of protein-based pattern formation

Fridtjof Brauns,[1] Jacob Halatek,[2] and Erwin Frey[1, *]

[1] *Arnold Sommerfeld Center for Theoretical Physics and Center for NanoScience,*
Department of Physics, Ludwig-Maximilians-Universität München,
Theresienstraße 37, D-80333 München, Germany
[2] *Biological Computation Group, Microsoft Research, Cambridge CB1 2FB, UK*

Spatial organization of proteins in cells is important for many biological functions. In general, the nonlinear, spatially coupled models for protein-pattern formation are only accessible to numerical simulations, which has limited insight into the general underlying principles. To overcome this limitation, we adopt the setting of two diffusively coupled, well-mixed compartments that represents the elementary feature of any pattern—an interface. For intracellular systems, the total numbers of proteins are conserved on the relevant timescale of pattern formation. Thus, the essential dynamics is the redistribution of the globally conserved mass densities between the two compartments. We present a phase-portrait analysis in the phase-space of the redistributed masses that provides insights on the physical mechanisms underlying pattern formation. We demonstrate this approach for several paradigmatic model systems. In particular, we show that the pole-to-pole Min oscillations in *Escherichia coli* are relaxation oscillations of the MinD polarity orientation. This reveals a close relation between cell polarity and oscillatory patterns in cells. Critically, our findings suggest that the design principles of intracellular pattern formation are found in characteristic features in these phase portraits (nullclines and fixed points). These features are not uniquely determined by the topology of the protein-interaction network but depend on parameters (kinetic rates, diffusion constants) and distinct networks can give rise to equivalent phase portrait features.

I. INTRODUCTION

The spatial intracellular organization of proteins by reactions (protein-protein interactions) and diffusion has received growing attention in recent years; for recent reviews see Refs. [1–8]. Gaining intuition and theoretical insight into the spatiotemporal protein dynamics remains challenging owing to the complexity arising from the spatial coupling and nonlinear reaction terms. Therefore, insights often remain restricted to specific mathematical models. A systematic understanding is hard to achieve, in particular if there are multiple protein species with several conformational states involved (complex interaction network). Thus, finding the elementary principles underpinning protein-based pattern formation still remains a largely open question.

To simplify the analysis on a technical level, systems of two diffusively coupled, well-mixed compartments (also called 'boxes', 'reactors', 'cells', or 'patches') have been widely used in earlier literature. In fact Turing himself used the setting of diffusively coupled compartments (called "cells") in his pioneering work to show that diffusion can destabilize otherwise stable reactions, thus leading to spatial pattern formation [9]. Physically, the two-compartment setting represents the elementary feature of any pattern—an interface connecting a low density region to a high density region. In the context of intracellular pattern formation, the two compartments typically represent the polar zones of rod-shaped cells, such as *E. coli*

bacteria (see Fig. 1a), *M. xanthus* bacteria [10, 11], and fission yeast (*S. pombe*) [12, 13].

In a broader context, two-compartment systems also have been realized in experiments, using diffusively coupled CSTRs (continuously stirred tank reactors) [14] and recently using nanometer scale microfluidic devices [15, 16]. Furthermore, in population dynamics, they are known as "two-patch systems" and have been used to study toe role of spatial coupling and patterning in ecology, see e.g. [17–19].

In this manuscript, we focus on protein-based pattern formation in cells. A key property of such intracellular pattern formation is that the total number of proteins is conserved on the relevant time scale of pattern formation [6, 20–23]. Recent works [24, 25] suggest that (diffusive) mass redistribution is the key physical process driving pattern formation in mass-conserving reaction–diffusion systems. Based on this insight, a framework termed *local equilibria theory* has been developed [25]. The basic idea of this framework is to consider the system as decomposed into (notional) compartments, small enough to be effectively well-mixed. Within each compartment, the reactive dynamics conserves the mass(es). The reactive equilibria (steady states) of the reactions within an isolated compartment, controlled by these local masses, serve as proxies for the local dynamics. Diffusive coupling of the compartments redistributes masses between them. In turn, the changing local masses shift the local reactive equilibria and potentially change their stability. Thinking about reaction–diffusion systems in terms of this interplay between mass-redistribution and shifting local equilibria has proven a powerful approach to study their complex nonlinear dynamics [24–28].
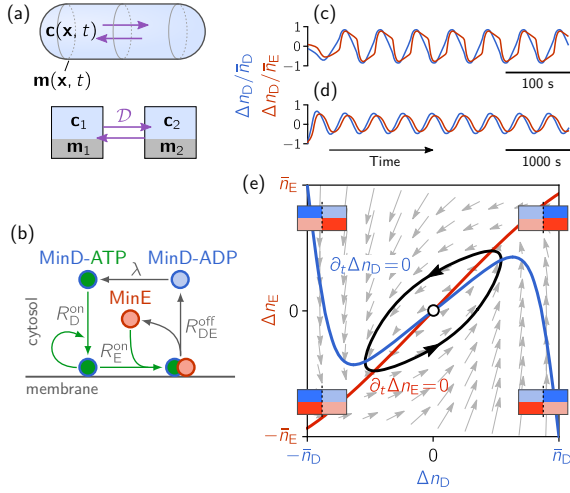
---

* frey@lmu.de

FIG. 1. Reduction from the full dynamics in cell-geometry to the phase portrait of mass-redistribution dynamics. (a) Spherocylinder geometry of a rod-shaped *E. coli* cell (top) and reduced two-compartment setting representing the two cell halves (bottom). Purple arrows illustrate diffusive mass transport. (b) Protein-interaction network of the Min system of *E. coli* (see main text Sec. III for details. (c) Time traces of the protein mass in the compartments relative to the mean, $\Delta n_{\mathrm{D,E}}$ defined via $n_{\mathrm{D,E}}^{(1,2)} = \bar{n}_{\mathrm{D,E}} \pm \Delta n_{\mathrm{D,E}}$, showing the pole-to-pole oscillations in three-dimensional cell geometry. (d) Oscillations persist in the two-compartment setting, with diffusive exchange rates set to a slow time scale. (e) Phase portrait of the mass-redistribution dynamics showing the flow field (gray arrows) and the nullclines of MinD and MinE redistribution (blue and red lines). The origin $(0,0)$ corresponds to the homogeneous state which is unstable against perturbations redistributing mass. The limit cycle trajectory (black) corresponds to pole-to-pole oscillations. The cartoons in the four corners illustrate the two-compartments (separated by a vertical dashed line) where the color intensity indicates the mass distribution of MinD (blue) and MinE (red) in the respective quadrant of the phase portrait.

Here we adopt the two-compartment setting and show how this way of thinking can be made explicit in the form of simple graphical constructions and a phase portrait analysis in the phase space of the redistributed masses. This will enable us to gain insights on the physical mechanisms underlying pattern formation that would otherwise remain hidden. Importantly, and in contrast to previous works [10, 11, 29–31], we do *not* assume the fast diffusing (cytosolic) components to be well mixed. In other words, we explicitly allow for cytosolic gradients between the two compartments. As we will see later, this is important understand the physical mechanisms underlying pattern formation. In particular, it is key to explain the pole-to-pole oscillations of Min proteins in *E. coli*.

a. Motivation. Let us present the main motivation for this work using the pole-to-pole oscillations of Min

proteins in *E. coli* as a concrete example without going into technical details (which will be presented below). Put briefly, the pole-to-pole oscillations are driven by two types of proteins, MinD and MinE, which cycle between membrane-bound and cytosolic states and interact with each other on the membrane (Fig. 1b), while the total masses of MinD and MinE (n_{D} and n_{E}) remain conserved. A key insight from previous works is that spatial redistribution of such globally conserved masses constitutes the essential degrees of freedom of mass-conserving reaction diffusion systems [24]. Indeed, mapping the Min system to the two-compartment setting and tuning the diffusive exchange rates to a slow time scale retains the qualitative features of the pole-to-pole oscillations (Fig. 1c,d). On the slow time scale, only the masses in the two compartments $n_{\mathrm{D,E}}^{(1,2)}$ remain as dynamic variables. Because of mass conservation, the average masses $\bar{n}_{\mathrm{D,E}}$ remain constant. Defining the redistributed masses, Δn_{D} and Δn_{E}, via $n_{\mathrm{D,E}}^{(1,2)} = \bar{n}_{\mathrm{D,E}} \pm \Delta n_{\mathrm{D,E}}$, we can visualize the dynamics in the two-dimensional $(\Delta n_{\mathrm{D}}, \Delta n_{\mathrm{E}})$-phase space, Fig. 1e, where we plot the flow field and its nullclines. Along the nullclines the rate of mass-exchange between the compartments vanishes. We hence refer to them as mass-redistribution nullclines. The phase portrait shows the characteristics of relaxation oscillations. In this paper, we show that the Min pole-to-pole oscillations are indeed *spatial* relaxation oscillations of the MinD polarity orientation.

This example shows how important qualitative features of mass-conserving reaction–diffusion (MCRD) systems can be obtained from a phase portrait analysis in the phase space of the redistributed masses. In the following, we show how this phase portrait can be constructed systematically, starting from the reaction–diffusion equations. We show what determines the structure of the phase space flow and derive a simple geometric relation between the *mass-redistribution* nullclines and the *reactive* nullclines of the local reaction kinetics.

b. Structure of the paper. To introduce the basic elements of our analysis, we first study MCRD systems with two components, e.g. the membrane-bound and cytosolic state of a single protein species (see Sec. II). We then generalize the nullcline-based approach to systematically derive the phase portrait of the Min system of *E. coli* shown in Fig. 1e. This construction then allows us to study the role of diffusive mass redistribution of MinD and MinE for the formation of Min-protein patterns. Finally, we apply the same approach to two other paradigmatic model systems: PAR polarity of *C. elegans* and Cdc42 polarity of budding yeast. Comparing the different nullcline geometries of these systems allows one to classify their pattern-forming mechanisms (see Sec. IV). Such a nullcline-based classification provides intuition for the role of various elements in the biochemical network. Moreover, it might guide model building and serve as a first step of analysis for systems that are biochemically not as well characterized as the aforementioned exam-

ples. In the Conclusions, Sec. V, we discuss important implications of our work, both specific to the Min system and in a broader context, and give an outlook to promising future research directions.

II. TWO-COMPONENT MCRD SYSTEMS

Two-component MCRD systems have been previously used as conceptual models for cell polarity [20, 29, 32, 33]. In this section, we apply local equilibria theory [24, 25] to these systems in the two-compartment setting. In this simplified setting, the formulation of local equilibria theory is technically simpler than in spatially continuous systems [34]. Importantly, the approach developed below for two-component MCRD systems can be generalized to systems with more components and more conserved masses such as those studied in Sections III and IV, where the new approach yields novel insights.

Let us denote the concentrations of the two components in compartment $i \in \{1, 2\}$ by $\mathbf{u}_i = (m_i, c_i)$, where m_i and c_i are the concentration of membrane-bound and cytosolic proteins, respectively. The reaction kinetics $\boldsymbol{f} = (f, -f)$ within each compartment account for the attachment and detachment to and from the membrane. Importantly, they conserve the local total density (mass) $n_i = m_i + c_i$ in each of the two compartments individually. Mass is transferred between the compartments by a diffusive exchange process that acts to even out concentration differences. Denoting the diffusive exchange rates in the matrix $\mathfrak{D} = \mathrm{diag}(\mathcal{D}_m, \mathcal{D}_c)$, we have the coupled compartment dynamics in vector notation

$$
\begin{aligned}
\partial_t \mathbf{u}_1 &= \mathfrak{D}(\mathbf{u}_2 - \mathbf{u}_1) + \boldsymbol{f}(\mathbf{u}_1), \\
\partial_t \mathbf{u}_2 &= \mathfrak{D}(\mathbf{u}_1 - \mathbf{u}_2) + \boldsymbol{f}(\mathbf{u}_2).
\end{aligned} \tag{1}
$$

Since both the local reactions and the diffusive exchange are mass conserving, the average total density $\bar{n} = (n_1 + n_2)/2$ is a constant of motion. In Appendix A, it is shown how the (diffusive) exchange rates $\mathcal{D}_{m,c}$ can be related to the diffusion constants $D_{m,c}$ in a spatially continuous system, in such a way that the linearized dynamics of Eq. (1) near a homogeneous steady state is identical to the linearized dynamics of a single Fourier mode $\sim \cos(\pi x/L)$ in the spatially continuous system on the interval $[0, L]$ with no-flux boundary conditions. For patterns with large amplitudes, nonlinearities lead to mode coupling in a spatially continuous system. This is not captured by the two-component system which only describes the dynamics at a single length scale. Nonetheless, one can gain a good qualitative understanding of the full nonlinear pattern formation process, including the termination of the pattern-forming instability in a stationary pattern.

A. Setting the stage: phase-space geometry of two-component MCRD systems

In the following, we present the key concepts of local equilibria theory in the two-compartment setting. Because of mass conservation, only the mass density difference with respect to the mean $\Delta n := (n_1 - n_2)/2$ is a dynamic variable, while $\bar{n}$ is a *control parameter*. Thus, we can rewrite the local masses as $n_{1,2}(t) = \bar{n} \pm \Delta n(t)$. Adding the equations for $\partial_t m_1$ and $\partial_t c_1$ (Eq. (1) yields $\partial_t n_1$, and thus

$$
\partial_t \Delta n(t) = -\mathcal{D}_m \Delta m - \mathcal{D}_c \Delta c, \tag{2}
$$

where $\Delta \mathbf{u} = (\Delta m, \Delta c) := \mathbf{u}_1 - \mathbf{u}_2$ and we used that $\partial_t \bar{n} = 0$. Observe that the reaction terms cancel because they conserve the mass in each compartment individually. Thus, the dynamics of the total density is solely determined by concentration differences in m and c between the two compartments. These concentration differences approximate the gradients in the spatially continuous system.

To understand how these concentration differences are governed by the reaction kinetics, consider the (m, c)-phase plane of the reaction kinetics (see Fig. 2a). While this phase plane is two-dimensional, mass conservation also implies that reactive flow $(f, -f)$ in each compartment i is constrained to a respective linear subspace $m_i + c_i = n_i$. We term these subspaces the *local phase spaces* of each compartment [22, 25]. Here, and in the following, the term *local* always refers to the properties of a single (notionally isolated) compartment. Correspondingly, we define as *local reactive equilibrium* the point within the local phase space where the reaction kinetics are balanced, i.e. where the reactive flow vanishes ($f = 0$):

$$
\mathbf{u}^*(n_i) : \begin{cases} \boldsymbol{f}(\mathbf{u}^*) = 0, \\ m^* + c^* = n_i. \end{cases} \tag{3}
$$

Geometrically, the local equilibria are the intersection points between the local phase spaces and the reactive nullcline (see Fig. 2) [35]. These local equilibria determine the steady state (reactive equilibrium) in each compartment that would be reached if, given the local masses n_1 and n_2, the two compartments were isolated, i.e. if the diffusive exchange between the compartments was shut off. Thus, the local equilibria serve as proxies for the local reactive flow within each of the compartments (red arrows in Fig. 2a).

Diffusive coupling between the compartments redistributes mass between the compartments. This is reflected in the shifting of the local phase spaces *in the (m, c)-phase plane*, as indicated by the purple arrows in Fig. 2a,b). As a result, the local reaction kinetics change since the local equilibria move in the (m, c)-phase plane. In the following we will elucidate this interplay between diffusive mass-redistribution and shifting local equilibria in the most elementary form.
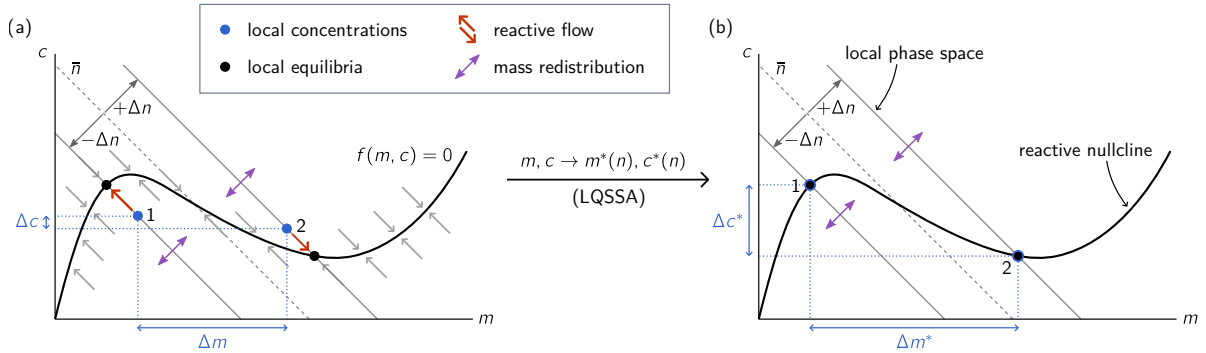
FIG. 2. Phase space structure of a two-compartment two-component MCRD system, with reaction and diffusion on the same time scale (a) and with diffusion set to a slower time scale (b). The concentrations (m_i, c_i) in the two compartments are marked by blue dots, labelled 1 and 2, respectively. The local phase spaces corresponding to the masses in the two compartments $n_{1,2} = \bar{n} \pm \Delta n$ are shown as gray lines. Gray arrows indicate the reactive flow towards the reactive nullcline $f = 0$ (solid black line). Black dots mark the local equilibria (intersection points between reactive nullcline and local phase spaces) and red arrows indicate the reactive flow towards these local equilibria. (b) When diffusion is set to a slower time scale, the local concentrations adiabatically follow the reactive nullcline. Thus, the only remaining degree of freedom is the mass difference Δn, whose dynamics is governed by the concentration differences $\Delta m^*(\Delta n)$ and $\Delta c^*(\Delta n)$ (see Eq. (2)).

B. Limit of slow mass exchange

To separate the roles of local reactions and diffusive mass redistribution, we consider a situation where the latter occurs on a much slower time scale than the former [36]. In this limit, the cytosolic and membrane concentrations in each compartment adiabatically follow the local equilibria that depend on the local masses n_i, as encoded by the shape of the reactive nullcline in the (m, c)-phase plane (see Fig. 2b). We can, therefore, approximate the densities by their respective equilibrium values

$$\mathbf{u}_i(t) \approx \mathbf{u}^*\big(n_i(t)\big). \tag{4}$$

We term this the *local quasi-steady state approximation* (LQSSA). The dynamics of the mass difference Δn is then governed by a closed equation

$$\partial_t \Delta n(t) \approx -\mathcal{D}_m \Delta m^*(\Delta n) - \mathcal{D}_c \Delta c^*(\Delta n), \tag{5}$$

with the shorthand notation for the concentration differences between the two compartments:

$$\Delta \mathbf{u}^*(\Delta n) := \mathbf{u}^*(\bar{n} + \Delta n) - \mathbf{u}^*(\bar{n} - \Delta n). \tag{6}$$

In this approximation, the roles of local reactive dynamics and diffusive mass exchange are clearly separated. The concentrations only change if the local phase spaces shift due to mass redistribution. In turn, the mass fluxes from one compartment to the other are determined by the concentration gradients $\Delta \mathbf{u}^*(\Delta n)$, weighted by the respective exchange rates $\mathcal{D}_{m,c}$. This nonlinear feedback between shifting equilibria and mass redistribution is the basic mechanism underlying pattern formation in mass-conserving reaction diffusion systems [24, 25]. Importantly, the role of the reaction kinetics is fully encoded

in the shape of the reactive nullcline, i.e. the functional dependence of the reactive equilibrium concentrations $\mathbf{u}^*(n)$ on the total density n.

The local masses n_i within each compartment play the role of *control variables* [24] that determine the position of the local phase spaces (and thus the position of the reactive equilibria) within the (m, c)-phase plane. At the same time the local masses are also dynamic variables that change by means of diffusive mass redistribution between the compartments. Accordingly, we refer to the phase space of the redistributed masses as *control space*. In the two-component MCRD system, the only control variable is the mass difference Δn, such that the control space is one-dimensional.

Typically, diffusion on the membrane is orders of magnitude slower than in the cytosol, $D_m \ll D_c$ such that its contribution to mass redistribution can be neglected; see e.g. Refs. [37, 38]. Hence, to simplify the following analysis, we neglect the slow membrane diffusion (i.e. we set $D_m = 0$), such that

$$\begin{aligned} \partial_t \Delta n(t) &= -\mathcal{D}_c \Delta c^*(\Delta n) \\ &= -\mathcal{D}_c \big[c^*(\bar{n} + \Delta n) - c^*(\bar{n} - \Delta n) \big]. \end{aligned} \tag{7}$$

Generalization to account for the effect of membrane diffusion is straightforward by changing variables from c to the 'mass-redistribution potential' $\eta := c + (D_m/D_c)m$ [39].

Equation (7), has a simple geometric interpretation as shown in Fig. 3b,c. The term in the brackets in Eq. (7) expresses the difference between the nullcline (solid, black line) and its mirror image (dashed gray line) reflected at the point $\bar{n}$. Depending on the nullcline slope at $\bar{n}$, the resulting dynamics $\partial_t \Delta n$, indicated by the blue arrows, is qualitatively different. For a posi-
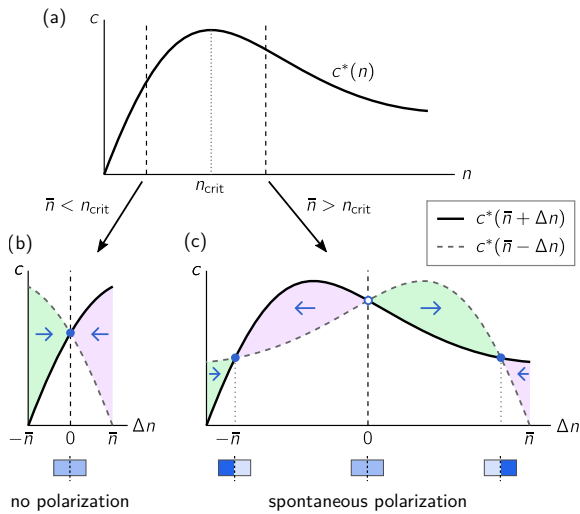
FIG. 3. Graphical construction of the control-space dynamics for two-component MCRD systems. (a) Reactive nullcline (line of reactive equilibria) $c^*(n)$. (b) For $\bar{n} < n_{\mathrm{crit}}$, the lines $c^*(\bar{n} + \Delta n)$ (black solid line) and $c^*(\bar{n} - \Delta n)$ (gray dashed line) only intersect once at $\Delta n = 0$, corresponding to the homogeneous steady state. The flow direction in control space (indicated by blue arrows) is determined by the sign of the difference between $c^*(\bar{n} + \Delta n)$ and $c^*(\bar{n} + \Delta n)$, as indicated by the green and purple shading; cf. Eq. (7). (c) For $\bar{n} > n_{\mathrm{crit}}$, there are two additional intersection points between $c^*(\bar{n} + \Delta n)$ and $c^*(\bar{n} - \Delta n)$, corresponding polarized steady states. The flow in control space is directed away from the homogeneous state $\Delta n = 0$, which is therefore unstable, and drives the system towards one of the stable polarized states.

tive slope, $\partial_n c^*(n)|_{\bar{n}} > 0$, following a small perturbation from the "homogeneous" state $\Delta n = 0$ the system returns to the $\Delta n = 0$; see Fig. 3b. In contrast, for a negative slope, $\partial_n c^*(n)|_{\bar{n}} < 0$, the homogeneous state is unstable; see Fig. 3c. This criterion for a lateral instability (instability against spatially inhomogeneous perturbations) was previously derived in Ref. [25] for spatially continuous systems. The physical mechanism for this *mass-redistribution instability* is that the reactive equilibrium shifts to lower concentration of the fast diffusing (cytosolic) component, $c^*(n)$, when the total density n is increased, and vice versa. Hence, a small perturbation δn results in a gradient Δc that transports mass from the compartment with lower mass to the compartment with higher mass. This amplification mechanism drives the instability.

The growth of the mass difference Δn will stop once the cytosolic gradient $\Delta c^*(\Delta n)$ vanishes, i.e. when the cytosolic concentration is the same in both compartments, $c^*(\bar{n} + \Delta n) = c^*(\bar{n} - \Delta n)$. Thus, stationary states can be determined graphically as the intersection points of the nullcline $c^*(n)$ with its own mirror image, mirrored at $\bar{n}$, as illustrated in Fig. 3c. The intersection point at

$\Delta n = 0$ always exists by construction, and corresponds to the homogeneous steady state. The two intersection points at $\Delta n \neq 0$ represent polarized steady states.

In summary, we have shown how one can graphically construct the mass-redistribution dynamics of two-compartment systems with one conserved mass simply based on the reactive nullcline $\mathbf{u}^*(n)$. In the next section, we will generalize this construction to systems with two conserved masses.

III. TWO-CONSERVED MASSES: THE EXAMPLE OF MIN-PROTEIN OSCILLATIONS

The Min-protein system is a paradigmatic model system for intracellular pattern formation. It was discovered in *E. coli*, where the pole-to-pole oscillations of the proteins MinD and MinE allow the cell to position its division machinery at midcell [40, 41]. This spatial oscillation, i.e. the alternating accumulation of the proteins at the two cell poles is driven by cycling of MinD and MinE between cytosolic and membrane bound states, fuelled by ATP (details described below). Subsequent to its reconstitution *in vitro* [42], the Min system has been studied in great detail, both experimentally [26, 42–53] and theoretically [22, 24, 26, 49, 52, 54–57]. This research has revealed a bewildering zoo of patterns, including traveling waves, standing waves, spatiotemporal chaos, and defect mediated turbulence, observed in different experimental setups (including microfluidic devices [26, 46] and vesicles [50, 51]). Recent works employing local-equilibria theory to interpret data from numerical simulations and experiments have provided insights on the mechanisms underlying these patterns and their relationships among each other [6, 26].

Here, we revisit the comparatively simple pole-to-pole oscillation employing the local-equilibria theory in the two-compartment setting. This offers a fresh perspective on the Min-protein dynamics as it allows us to understand this elementary dynamic pattern in terms of phase space geometry, independently of numerical simulations. In future work, this could serve as a starting point to systematically understand more complex patterns, like "stripe oscillations" (standing waves) in filamentous cells [22, 41] and the zoo of patterns found *in vitro* [26, 53, 58].

Intuitively, the two-compartment system represents the two cell poles (or cell halves) of the rod-shaped *E. coli* bacterium, as shown in Fig. 1a (see Appendix B 1 for a systematic reduction starting from the full three-dimensional cell geometry). Figure 1c,d shows that the key qualitative features of Min pole-to-pole oscillations are still captured by the two-compartment model (see also Fig. 7 in Appendix B). While this two-compartment model cannot be expected to give a detailed quantitative description of Min oscillations, it has the advantage of informing about the basic underlying mechanism. This complements earlier quantitative studies of the *in vivo* dynamics [22, 57]. Moreover, the two-compartment

model serves as a minimal system for an oscillation mode recently reported for an *in vitro* reconstitution of the Min system in microfluidic devices [26]. There, the oscillations go back and forth between two membrane surfaces through the bulk solution in-between them (see Fig. 8 in Appendix. B). The analogy between this *in vitro* oscillation mode and pole-to-pole oscillations *in vivo* is further discussed in the conclusions, Sec. III D.

We use a well-established minimal model for the Min-protein interactions that has been shown to successfully reproduce and predict a large range of experimental findings, quantitatively *in vivo* and qualitatively *in vitro* [6, 22, 27, 49, 56]. For a detailed description of the model, we refer the reader to Refs. [22, 27]. In short, the minimal model employs mass-action law kinetics to account for the attachment and detachment of MinD and MinE to and from the membrane and for their interactions there (see Fig. 1b): Membrane-bound MinD amplifies the attachment of further MinD from the cytosol with rate k_{dD} and also recruits MinE from the cytosol with rate k_{dE} to form MinDE complexes on the membrane. In these complexes, MinE stimulates MinD hydrolysis with rate k_{de}, leading to the dissociation of the complex and detachment of both proteins to the cytosol. In the cytosol, MinD undergoes nucleotide exchange from the ADP-bound form to the ATP-bound form, which can then attach to the membrane again.

Mathematically, the above reaction kinetics are described by the system of equations of the form Eq. (1) with $\mathbf{u} = (m_d, m_{de}, c_{DT}, c_{DD}, c_E)$, $\mathfrak{D} = \mathrm{diag}(\mathcal{D}_d, \mathcal{D}_{de}, \mathcal{D}_D, \mathcal{D}_D, \mathcal{D}_E)$ and

$$\boldsymbol{f}(\mathbf{u}) = \begin{pmatrix} R_D^{on}(\mathbf{u}) - R_E^{on}(\mathbf{u}) \\ R_E^{on}(\mathbf{u}) - R_{DE}^{off}(\mathbf{u}) \\ -R_D^{on}(\mathbf{u}) + \lambda c_{DD} \\ R_{DE}^{off}(\mathbf{u}) - \lambda c_{DD} \\ -R_E^{on}(\mathbf{u}) + R_{DE}^{off}(\mathbf{u}) \end{pmatrix}, \qquad (8)$$

where the reaction terms

$$R_D^{on}(\mathbf{u}) = (k_D + k_{dD} m_d) c_{DT}, \qquad (9a)$$

$$R_E^{on}(\mathbf{u}) = k_{dE} m_d c_E, \qquad (9b)$$

$$R_{DE}^{off}(\mathbf{u}) = k_{de} m_{de}, \qquad (9c)$$

account, respectively, for MinD attachment and self-recruitment to the membrane, MinE recruitment by MinD, and dissociation of MinDE complexes with subsequent detachment of both proteins to the cytosol. The term λc_{DD} accounts for nucleotide exchange, i.e. conversion from c_{DD} to c_{DT}, in the cytosol. Importantly, these reaction kinetics conserve the total number of MinD and MinE proteins, $\bar{n}_D$ and $\bar{n}_E$, individually, i.e. there are *two* globally conserved masses that are redistributed between the two compartments (cell halves) [59].

Numerically integrating the above set of ordinary differential equations using the parameters from Ref. [22] yields pole-to-pole oscillations in good qualitative agreement with the oscillations found in the full three-dimensional geometry (see Fig. 7a,b in Appendix B). Importantly, these oscillations persist if diffusive exchange between the compartments is set to a slow time scale compared to the reaction kinetics (see Fig. 7c) In this limit, the concentrations in the two compartments adiabatically follow the equilibrium concentrations that depend on the local masses $n_{D,i}, n_{E,i}$ in the two compartments. Hence, we can again apply the LQSSA, Eq. (4), substituting the concentrations $\mathbf{u}$ by the reactive equilibria $\mathbf{u}^*$. A discussion of the validity of this approximation and potential generalizations is deferred to the Conclusions, Sec. V.

The reactive equilibria as a function of the masses n_D and n_E are (for each compartment) determined by (cf. Eq. (3))

$$\mathbf{u}^*(n_D, n_E) : \begin{cases} \boldsymbol{f}(\mathbf{u}^*) = 0, \\ c_D^* + m_d^* + m_{de}^* = n_D, \\ c_E^* + m_{de}^* = n_E, \end{cases} \qquad (10)$$

where we introduced the total cytosolic MinD concentration $c_D = c_{DD} + c_{DT}$. For each component in the concentration vector $\mathbf{u}^*$ this defines a surface parametrized by n_D and n_E, as shown in Figure 4a,b for c_D^* and c_E^* (the respective surfaces for the membrane concentrations m_d^* and m_{de}^* are shown in Fig. 10 in Appendix B). We will term these *reactive nullcline surfaces*. In the following, we show how the dynamics of the local masses $n_{D,i}, n_{E,i}$ can be inferred from these surfaces, analogously to the construction shown in Fig. 3 for two-component MCRD systems.

Because the total number of MinD and MinE proteins are conserved, only the protein masses redistributed between the two polar zones, $\Delta n_{D,E}(t)$, are time dependent and the mass densities of MinD and MinE in the right and left polar zone are given by

$$n_{\alpha,1/2}(t) = \bar{n}_\alpha \pm \Delta n_\alpha(t), \quad \alpha = D, E. \qquad (11)$$

Analogously to the two-component system, we call the redistributed masses $\Delta n_{D,E}(t)$ the *control variables* and the $(\Delta n_D, \Delta n_E)$-phase plane the *control space*. The dynamics in control space are governed by

$$\partial_t \Delta n_D(t) = -\mathcal{D}_D \, \Delta c_D^* - \mathcal{D}_d \, \Delta m_d^* - \mathcal{D}_{de} \, \Delta m_{de}^*, \quad (12a)$$

$$\partial_t \Delta n_E(t) = -\mathcal{D}_E \, \Delta c_E^* - \mathcal{D}_{de} \, \Delta m_{de}^*, \qquad (12b)$$

where the concentration gradients (differences between the two polar zones) of the local equilibria are defined as (cf. Eq. (6))

$$\Delta \mathbf{u}^*(\Delta n) := \mathbf{u}^*(\bar{n} + \Delta n) - \mathbf{u}^*(\bar{n} - \Delta n). \qquad (13)$$

A. From reactive nullcline surfaces to mass-redistribution nullclines

To understand the qualitative structure of the control-space dynamics Eq. (12), we first consider the lines along
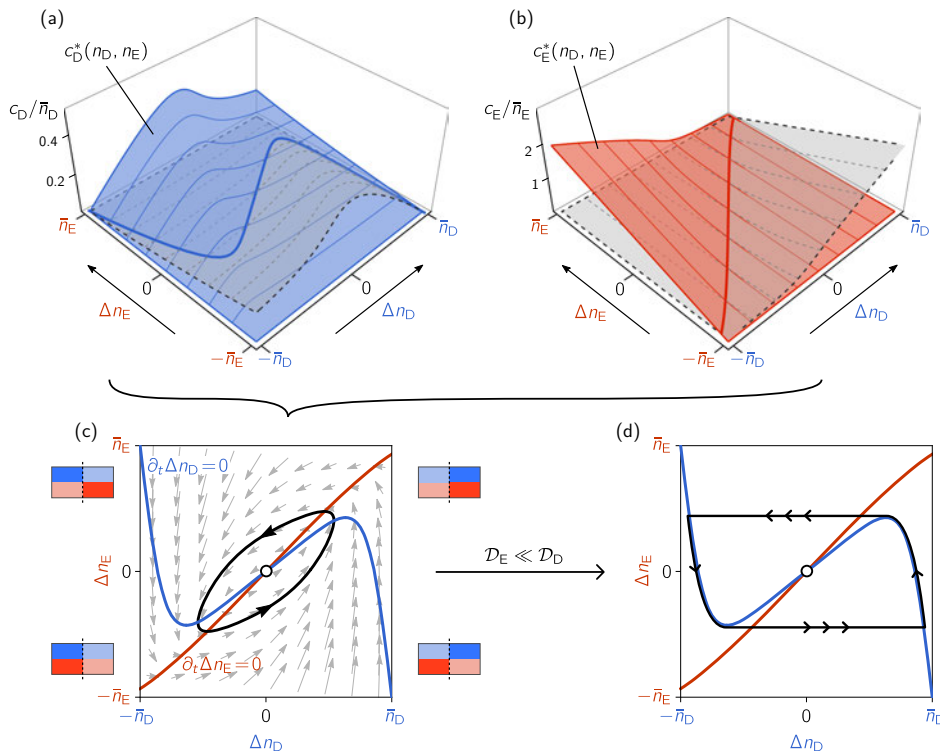
FIG. 4. Graphical construction of the dynamics in control space from the reactive nullcline surfaces. (a,b) Reactive nullcline surfaces showing MinD and MinE cytosol concentration (shaded blue and red respectively) as a function of the mass differences $\Delta n_D, \Delta n_E$. The intersection of each surface with its point reflection (shaded in gray with dashed outlines) determine the mass-redistribution nullclines (see text for details). These nullclines are a generalization of the fixed points shown in Fig. 3b,c. (c) Phase portrait of the dynamics Eq. (14) with the MinD and MinE mass-redistribution nullclines obtained by the construction in (a) and (b) and the limit cycle trajectory (black) corresponding to pole-to-pole oscillations (cf. Fig. 1e). (d) Setting MinE diffusion to a slower time scale transforms the limit cycle trajectory to the shape characteristic for relaxations oscillations.

which there is no mass-redistribution of MinD/E respectively, $\partial_t \Delta n_{D,E} = 0$. We term these *mass-redistribution* nullclines. Importantly, these are not to be confused with the *reactive* nullcline (line of reactive equilibria) along which the reactive flow vanishes within a single compartment.

As we shall see in Sec. III B, one can neglect the slow membrane diffusion to understand the basic oscillation mechanism of the Min system. We therefore consider this simpler case, $\mathcal{D}_d = \mathcal{D}_{de} = 0$, first. Equation (12) then reduces to

$$\partial_t \Delta n_D(t) = -\mathcal{D}_D \, \Delta c_D^*(\Delta n_D, \Delta n_E), \qquad (14a)$$

$$\partial_t \Delta n_E(t) = -\mathcal{D}_E \, \Delta c_E^*(\Delta n_D, \Delta n_E), \qquad (14b)$$

describing how mass redistribution is driven by the gradients in the cytosolic protein densities, which are slaved to the local equilibria. Thus, the mass-redistribution nullclines are simply given by $\Delta c_D^* = 0$ and $\Delta c_E^* = 0$. Geometrically, this corresponds to the intersection lines between the reactive nullcline surfaces $c_{D,E}^*(n_D, n_E)$, and their respective point reflections, reflected at the

point $(\bar{n}_D, \bar{n}_E)$; see gray surfaces with dashed outlines in Fig. 4a,b. In other words, the shape of reactive nullcline surfaces encodes the essential information about the nonlinear reaction kinetics for the dynamics of the spatially coupled system.

This construction is the analog to the construction for the two-component system shown in Fig. 3. In fact, in slices with $n_E = $ const, the line $c_D^*(n_D)$ has the same shape as the nullcline shown in Fig. 3. This "hump shape" gives rise to the N-shaped MinD-redistribution nullcline ($\partial_t \Delta n_D = 0$, see blue line in Fig. Fig. 4a,c). The two outer branches of this N-shaped nullcline represent polarized MinD states, corresponding to the two outer fixed points in the analogous two-component system construction Fig. 3c. We will make this more concrete below in Sec. III C. If $\bar{n}_D$ lies to the left of the crest of $c_D^*(n_D, n_E)$, the resulting MinD-redistribution nullcline is monotonic, analogous to the single fixed point in Fig. 3b. The crest of the c_D^* surface defined by $\partial_{n_D} c_D^*(n_D, n_E) = 0$ approximately follows the line $n_E/n_D \approx k_{dD}/k_{dE}$ for sufficiently large n_E (specifically

in the limit $n_\mathrm{E}^2 \gg k_\mathrm{D} k_\mathrm{dD} k_\mathrm{de}/k_\mathrm{dE}^3$). This relation is found by applying the implicit function theorem to evaluate the derivative $\partial_{n_\mathrm{D}} c_\mathrm{D}^*$ using the definition Eq. (10) for the reactive equilibria.

In contrast to the non-trivial MinD-redistribution nullcline, the monotonicity of the surface $c_\mathrm{E}^*(n_\mathrm{D}, n_\mathrm{E})$ gives rise to a monotonic MinE-redistribution nullcline (red line in Fig. 4b,c) for all $\bar{n}_\mathrm{D}, \bar{n}_\mathrm{E}$.

Mass-redistribution potentials. In passing, let us introduce an alternative formulation of the mass-redistribution dynamics Eq. (12) that allows one to generalize the graphical construction presented in Fig. 4 to arbitrary values of all diffusion constants (including $\mathcal{D}_\mathrm{d,de} > 0$). Using the mass-redistribution potentials (cf. Ref. [25]), $\eta_\mathrm{D} = c_\mathrm{D} + (\mathcal{D}_\mathrm{d}/\mathcal{D}_\mathrm{D})m_\mathrm{d} + (\mathcal{D}_\mathrm{de}/\mathcal{D}_\mathrm{D})m_\mathrm{de}$ and $\eta_\mathrm{E} = c_\mathrm{E} + (\mathcal{D}_\mathrm{de}/\mathcal{D}_\mathrm{E})m_\mathrm{de}$, Eq. (12) can be written as

$$\partial_t \Delta n_\mathrm{D}(t) = -\mathcal{D}_\mathrm{D}\, \Delta \eta_\mathrm{D}^*, \tag{15a}$$

$$\partial_t \Delta n_\mathrm{E}(t) = -\mathcal{D}_\mathrm{E}\, \Delta \eta_\mathrm{E}^*. \tag{15b}$$

Since these equations have the same form as Eq. (14), the construction shown in Fig. 4 can be generalized by exchanging $c_\mathrm{D,E}^*$ for $\eta_\mathrm{D,E}^*$. The surfaces η_D^* and η_E^* can be interpreted as "superpositions" of the local-equilibrium surfaces of the individual components weighted by the respective exchange rates $\mathcal{D}_i$. The effect of reaction rates or diffusion constants on the spatial dynamics is encoded in the deformation of these surfaces under variation of these parameters (see Movies 1 and 2).

B. Min pole-to-pole oscillations are relaxation oscillations

The nullclines enable one to read off the qualitative structure of the dynamics in the $(\Delta n_\mathrm{D}, \Delta n_\mathrm{E})$-phase plane [60, 61]. Specifically, one immediately recognizes the characteristic scenario of a relaxation oscillator [62]. Recalling that the two outer branches of the N-shaped MinD-redistribution nullcline correspond to polarized MinD states, this shows that Min pole-to-pole oscillations are *relaxation oscillations of the MinD-polarity direction* driven by mass-redistribution of MinE between the two cell halves.

The limit cycle of relaxation oscillators can be graphically constructed in the limit where the variable with the N-shaped nullcline evolves on a much faster time scale compared to the other variable [61]. In the Min system, this corresponds to setting MinE redistribution to a much slower time scale than MinD redistribution ($\mathcal{D}_\mathrm{D} \gg \mathcal{D}_\mathrm{E}$). In this limit, the limit cycle deforms into a "trapezoidal" trajectory; see Fig. 4d. The dynamics slowly follows the N-shaped MinD-redistribution nullcline (polarized MinD states), driven by MinE redistribution, and rapidly switches between the left and right branches at the extrema of this nullcline, driven by MinD redistribution.

In a broader context, the above analysis demonstrates how the reactive nullcline surfaces and their intersection lines—which are the mass-redistribution nullclines—are helpful tools to explore the ability of systems to show nontrivial spatial dynamics without the need to perform a full scale finite element simulation. The shape of the reactive nullcline surfaces and thus the mass-redistribution nullclines are ultimately a consequence of the nonlinear feedback in the reaction kinetics. In the specific case of the Min system, these are the recruitment terms $k_\mathrm{dD} m_\mathrm{d} c_\mathrm{D}$ and $k_\mathrm{dE} m_\mathrm{d} c_\mathrm{D}$. It is important to recall that the shape of the nullclines resulting from the reaction kinetics, and not the specific reaction kinetics per se, determines the spatial (mass-redistribution) dynamics. Hence, different reaction terms can give rise to same nullcline geometry, and thus the same spatial dynamics. Rather than classifying dynamics based on their reaction network topology, this suggests that a classification might be possible in terms of the shapes of their reactive nullcline surfaces and the resulting mass-redistribution nullclines. We demonstrate this in Sec. IV, where we analyze two further paradigmatic models for intracellular pattern formation.

C. The role of diffusive MinE transport

So far, we have neglected membrane diffusion to elucidate the basic Min-oscillation mechanism. We now relax that approximation and first consider the role of MinE membrane diffusion. Using the conservation law $m_\mathrm{de} + c_\mathrm{E} = n_\mathrm{E}$, Eq. (12b) can be recast as

$$\partial_t \Delta n_\mathrm{E} = -(\mathcal{D}_\mathrm{E} - \mathcal{D}_\mathrm{de})\Delta c_\mathrm{E}^*(\Delta n_\mathrm{D}, \Delta n_\mathrm{E}) - \mathcal{D}_\mathrm{de}\Delta n_\mathrm{E}. \tag{16}$$

This shows that diffusive transport on the membrane always counteracts cytosolic transport. In particular, if one were to set $\mathcal{D}_\mathrm{E} = \mathcal{D}_\mathrm{de}$, there would be no MinE mass-redistribution since Eq. 16 would reduce to $\partial_t \Delta n_\mathrm{E} = -\mathcal{D}_\mathrm{de}\Delta n_\mathrm{E}$, such that Δn_E would simply relax to the homogeneous state $\Delta n_\mathrm{E} = 0$. Thus, in control space, the MinE-redistribution nullcline would simply be given by $\Delta n_\mathrm{E} = 0$, which intersects the N-shaped MinD nullcline at three points, representing the unstable homogeneous steady state in the center and two stable polarized states on the left and right, respectively. Hence, the dynamics would reduce to the one-dimensional control space for MinD redistribution which, corresponding to the scenario shown in Fig. 3. From this Gedankenexperiment, we conclude that the elementary pattern-forming mechanism of the Min system is MinD polarization and does not require spatial redistribution of MinE. The specific function of MinE in MinD polarization is that of a "local catalyst" that provides nonlinear feedback essential in shaping the non-monotonic reactive MinD nullcline $c_\mathrm{D}^*(n_\mathrm{D})$. Thus, while redistribution of MinE is not required for the formation of a polarized MinD pattern, it causes the emergence of oscillations by periodically inducing switching of the MinD polarization direction as we showed in the previous section.

Physiologically, $\mathcal{D}_E = \mathcal{D}_{de}$ would actually correspond to a scenario where free MinE remains membrane bound, i.e. MinE would cycle between the MinD-bound and the free conformation on the membrane and c_E would then denote the concentration of free MinE. The stationary patterns resulting in this case provide a potential hint for the possible biomolecular features of MinE responsible for the (quasi-)stationary patterns reported in recent experiments using MinE purified with a His-tag at the C-terminus instead of the N-terminus [53]. Compared to his-MinE, MinE-his might have a strong membrane affinity causing free MinE to remain membrane-bound after the dissociation of MinDE complexes. Free MinE on the membrane diffuses much slower than in the cytosol thus suppresses the MinE redistribution that gives rise to dynamic patterns (waves and oscillations). This hypothesis suggests that increasing the MTS strength of MinE might cause a transition from dynamic to quasi-stationary patterns.

To elucidate the role of MinE transport more quantitatively, we now study the transition from stationary to oscillatory patterns as a function of the diffusion constants $\mathcal{D}_E$ and $\mathcal{D}_{de}$. Varying these diffusion constants results in a deformation of the MinE-redistribution nullcline in control space. Specifically, the shape of the MinD-redistribution nullcline only depends on the difference $\mathcal{D}_E - \mathcal{D}_{de}$, i.e. the balance of co-polarizing diffusion of free MinE compared to the contra-polarizing diffusion of MinDE complexes. In the relaxation-oscillation limit where MinE-redistribution is much slower than MinD redistribution ($\mathcal{D}_{de}, \mathcal{D}_E \ll \mathcal{D}_D$), the locations of the intersection points between the MinD's and MinE's mass-redistribution nullclines determine whether the system is oscillator or exhibits stationary polarity (see Fig. 5b). The transition case separating these two regimes is when the MinE-redistribution nullcline intersects the MinD-redistribution nullcline at its extrema. In addition, the stability of the homogeneous steady state can be obtained by a linear stability analysis in LQSSA (see Appendix C 2). The resulting "phase diagram" is shown in Fig. 5a.

This phase diagram obtained using LQSSA can be compared to the phase diagram of the full model obtained by numerical simulations (see Fig. 5b). The fact that the topology of the two phase diagrams agrees shows that the reduced dynamics, Eq. (12), accounts for the relevant physics of the *in vivo* Min system.

D. Concluding remarks on the Min system.

We have shown that dynamics underlying Min pole-to-pole oscillations can be reduced to the redistribution of MinD and MinE mass between the two cell poles. A simple geometrical construction yields the qualitative phase space structure of the mass-redistribution dynamics. Specifically, we recovered the paradigmatic N-shaped nullcline that underlies general relaxation oscil-

lations. This systematic reduction immediately allowed us to transfer the knowledge on relaxation oscillations to the Min pole-to-pole oscillations. The outer legs of the N-shaped MinD-redistribution nullcline correspond to oppositely polarized MinD states. MinE redistribution drives cyclic switching between these two states, giving rise to the pole-to-pole oscillations. In the absence of MinE redistribution (achieved by setting $\mathcal{D}_E = \mathcal{D}_{de}$), MinD forms stationary polarized patterns instead. This shows that the elementary pattern underlying for pole-to-pole oscillations in the *in vivo* Min system is not oscillatory but generic cell polarity. We conclude that the oscillatory dynamics are not a direct property of the kinetic interaction network, which is the same for the oscillatory and non-oscillatory regime. Instead, oscillations arise as consequence of MinE redistribution "downstream" of MinD polarization. MinE redistribution is not necessary for MinD polarization while MinD redistribution is strictly required. This links pole-to-pole oscillation in the Min system and generic cell polarity and suggests a hierarchy of species in large multi-species multi-component systems. Notably, this also shows that the functional role of MinE for pattern formation cannot be considered to be that of an inhibitor in the sense of the "activator–inhibitor" mechanism [63, 64].

The above analysis of the mass-redistribution dynamics elucidates the different roles of MinD and MinE redistribution for Min-protein pattern formation. In Sec. IV, we apply the same reduction approach to two other intracellular systems. This will allow us to compare the underlying pattern-forming mechanisms on the level of their mass-redistribution nullcline geometries.

a. Min oscillations in vitro. Let us emphasize again that the pole-to-pole oscillations emerge due to the diffusive coupling of two compartments, representing the two cell halves. An isolated compartment exhibits only stable, stationary states. In other words, the *in vivo* Min system is not an "oscillatory medium" of coupled oscillators. Remarkably, this is in stark contrast to the Min-protein pattern dynamics observed in classical *in vitro* setups with a large cytosolic bulk volume on top of a flat membrane surface. Here, a single (laterally isolated) membrane patch is coupled to an extended cytosolic reservoir, and it is this coupling that gives rise to *local* oscillations [6, 26]. This shows that on a mechanistic level, Min protein patterns in cells are distinct from patterns in reconstituted systems with a large bulk.

In a recent work, the Min system was studied in microfluidic chambers with two flat membrane surfaces separated by a bulk solution [26] (see Fig. 8 in Appendix B). This limits the bulk volume above each membrane patch and thus suppresses the local oscillations for sufficiently low bulk height. Interestingly, for intermediate bulk height, experiments and a theoretical analysis have revealed an oscillation mode that transports mass between the two opposite membrane surfaces through the bulk in-between them. This oscillation is analogous to the *in vivo* pole-to-pole oscillation where the two opposite
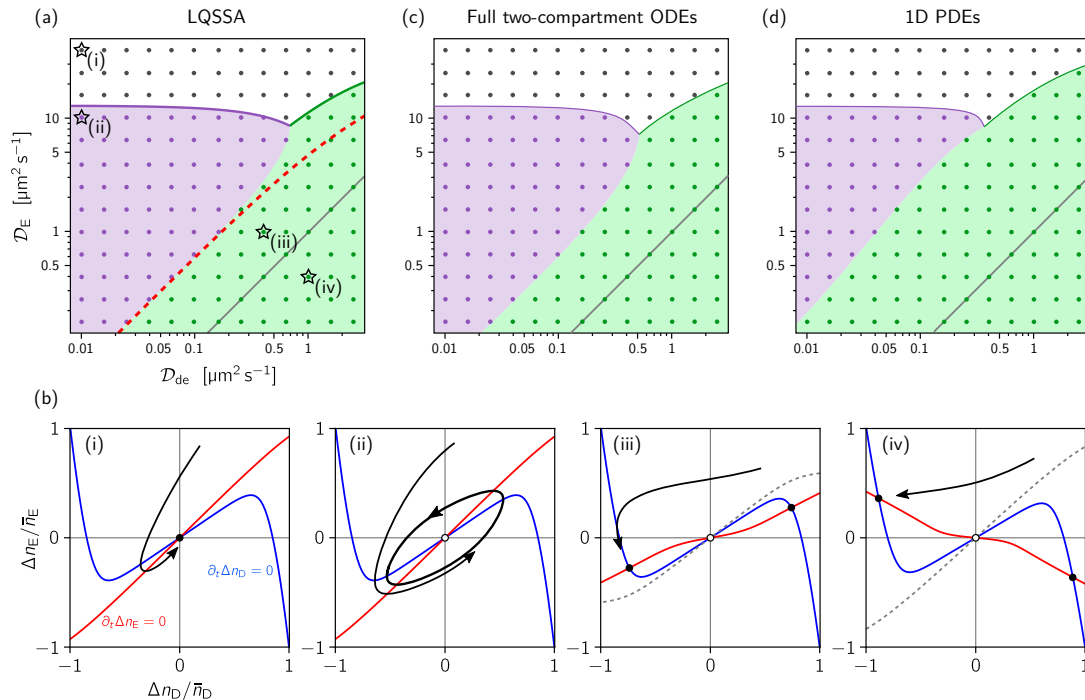
FIG. 5. Phase diagrams of Min protein dynamics. In each panel, the points and shaded background indicate the results from numerical simulations, distinguishing no patterns (gray), oscillations (purple) and stationary polarity (green). (a) Phase diagram for the LQSSA dynamics Eq. (12). The solid purple and green line indicate the Hopf and pitchfork bifurcations found by linear stability analysis of the LQSSA dynamics. Along the dashed red line, the MinE-redistribution nullcline intersects MinD-redistribution nullcline at the latter's extrema. In the limit $\mathcal{D}_\mathrm{E}, \mathcal{D}_\mathrm{de} \ll \mathcal{D}_\mathrm{D}$, this marks the transition between relaxation oscillations and stationary polarity. The gray line indicates the line $\mathcal{D}_\mathrm{E} = \mathcal{D}_\mathrm{de}$. (b) Example trajectories in the $(\Delta n_\mathrm{D}, \Delta n_\mathrm{E})$-phase plane (cf. Fig. 4c): (i) no instability, (ii) pole-to-pole oscillations, (iii) stationary polarity for $\mathcal{D}_\mathrm{E} > \mathcal{D}_\mathrm{de}$, (iv) stationary polarity for $\mathcal{D}_\mathrm{E} < \mathcal{D}_\mathrm{de}$ (note the opposite slope of the MinE-redistribution nullcline). In (iii) and (iv), the dashed gray line shows the separatrix, that separates the basins of attraction of the two polarized states. (c) Phase diagram from numerical simulations of the full two-compartment dynamics, Eq. (1). Note the excellent agreement with LQSSA (a). (d) Phase diagram from numerical simulations of the PDEs on a line (varying D_E in full three-dimensional cell geometry affects also the vertical gradients rather than just lateral diffusion).

membrane patches play the role of the cell poles *in vivo*. Correspondingly, with regard to the *in vitro* geometry, the two-compartment system serves as a minimal system to represent single vertical bulk column and the membrane patches at its top and bottom; see Fig. 8.

b. Historic note: Oscillations driven by diffusive coupling of two "dead" cells. Intriguingly, the Min-oscillation mechanism described above has some parallels to a conceptual model for diffusion-driven oscillations studied by Smale already in 1974 [65]. Smale's motivation, inspired by Turing's pioneering work [9], was to show how two identical reactors that exhibit only a stable stationary state when isolated, start oscillating (in anti-phase) when coupled diffusively. Or, as Smale put it: "One has two dead (mathematically dead) cells interacting by a diffusion process which has a tendency in itself to equalize the concentrations. Yet in interaction, a state continues to pulse indefinitely." As we showed

above, the *in vivo* Min system also has that property.

Remarkably, Smale used a relaxation oscillator as starting point to construct the diffusion driven two-compartment oscillator. In a broader view, this demonstrates how structures in phase space, like fixed points and nullclines, are powerful tools to understand and design nonlinear systems. For instance, they have been used to great success in the study of neuronal dynamics [66] and biochemical oscillators [67, 68].

IV. CONTROL SPACE FLOW OF THE PAR AND CDC42 SYSTEMS

The above investigation of the Min system demonstrates that the key characteristics of the spatio-temporal protein dynamics, and the underlying pattern-forming mechanisms, can be inferred from the shapes of the re-
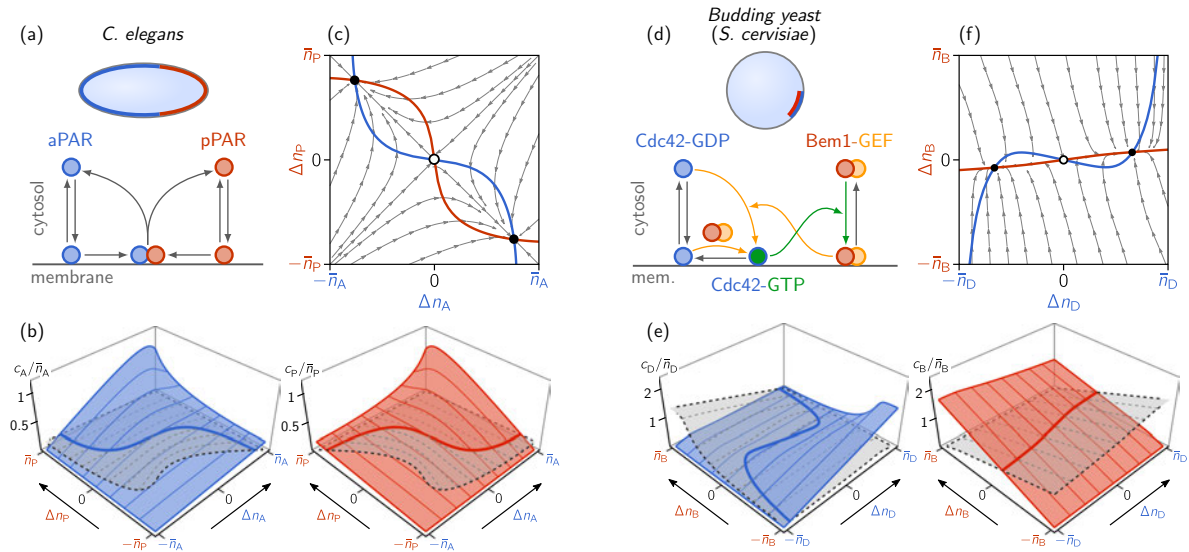
FIG. 6. Reaction networks, reactive nullcline surfaces and control-space phase portraits for the PAR system of *C. elegans* (a–c) and the Cdc42 system of *S. Cerevisiae* (d–f). (a) Cartoon of a *C. elegans* embryo showing the segregated aPAR and pPAR domains which as a result of mutual detachment of aPAR and pPAR proteins from the membrane. (b) Reactive nullcline surfaces of aPARs (blue, left) and pPARs (red, right). Note the symmetry under the exchange A↔P. (c) Control-space phase portrait showing the mass-redistribution dynamics and the mass-redistribution nullclines of aPARs (blue) and pPARs (red). Both mass-redistribution nullclines intersect the lines $\Delta n_{A,P} = 0$ only once, indicating that pattern formation requires redistribution of both protein species. (d) Cartoon of a budding yeast cell showing a polar cluster of co-localized Cdc42 and Bem1-GEF complexes. In WT cells, Cdc42 and Bem1-GEF complexes (homologous to Scd1-Scd2 complexes in fission yeast) mutually recruit each other to the membrane and are therefore co-localized in the resulting pattern. (e) Reactive nullcline surfaces of Cdc42 (blue, left) and Bem1-GEF (red, right). (f) Control-space phase portrait showing the mass-redistribution dynamics and the mass-redistribution nullclines of Cdc42 (blue) and Bem1-GEF (red). The N-shaped Cdc42-redistribution nullcline intersects the line $\Delta n_B = 0$ three times, indicating that redistribution of Bem1-GEF complexes is not required for pattern formation. In contrast to MinE in the Min system, where cytosolic MinE redistribution drives oscillations, the cytosolic redistribution of Bem1-GEF complexes has a stabilizing effect on stationary patterns.

active nullcline surfaces. In the following, we use the approach introduced above to two paradigmatic model systems for intracellular self-organization: the PAR system of *C. elegans* and the Cdc42 system of budding yeast (*S. cerevisiae*). Starting from previously established mathematical models on spatially continuous domains, we follow the same reduction procedure as for the Min system; details on the models, parameter choices and the reduction procedure are described in Appendix D. Put briefly, the spatially continuous dynamics is mapped to the two-compartment setting, and the LQSSA is applied such that only the redistributed masses remain as dynamic variables. The mass-redistribution dynamics can then be analyzed in terms of the reactive nullcline surfaces and the resulting phase portraits as shown in (Fig. 6). This allows us to compare the pattern forming mechanisms underlying these different systems.

a. PAR system. The first division of *C. elengans* embryos is asymmetric, where the fate of the daughter cells is defined by proteins called aPARs and pPARs that segregate along the long axis of the ellipsoidal cells [4]. A model for the formation of these segregated do-

mains was introduce in Ref. [21], based on the mutual antagonism between cortex-bound A- and pPARs (see Fig. 6a). Here, we adopt this model here, to illustrate the phase portrait structure that is characteristic of the mutual-antagonism mechanism. Model details and the parameters are given in Appendix D. Since, the reaction network (and the parameters used) are symmetric, so are the reactive nullcline surfaces (Fig. 6b). From the resulting mass-redistribution nullclines (Fig. 6c), we can immediately see that the patterns form by segregation into domains where pPAR concentration is high while aPAR concentration is low and vice versa. Notably, the mass-redistribution nullclines do not intersect the lines $\Delta n_A = 0$ and $\Delta n_P = 0$ away from the origin, indicating that PAR-pattern formation the requires the redistribution of both protein species. Moreover, the topology of the phase portrait is such that oscillations cannot occur. We expect that these qualitative insights generalize to more detailed models for PAR-protein polarity, see e.g. Ref. [69].

b. Cdc42 system. Budding yeast cells divide asymmetrically by budding and growing a daughter cell. The

division site is determined by the polarization of GTP-bound Cdc42 to a "spot" on the membrane [70]. In wild-type cells, Cdc42 polarization is driven by a mutual-recruitment mechanism that is facilitated by the scaffold protein Bem1. Bem1 is recruited to the membrane by Cdc42-GTP. Membrane-bound Bem1 then recruits Cdc42's GEF, Cdc24, forming Bem1-GEF complexes. In turn, Bem1-GEF complexes recruit Cdc42-GDP from the cytosol and catalyze its conversion to Cdc42-GTP, thus closing the feedback loop. To illustrate the phase portrait structure that is characteristic of this mutual recruitment mechanism, we adopt a simplified form of the detailed, quantitative model introduced in Ref. [71]; see Appendix D. In the simplified model, Bem1-GEF complexes are described as a single species with a membrane-bound and a cytosolic state (see Fig. 6d). Figure 6e,d shows the reactive nullcline surfaces and the resulting phase portrait of this model. The location of the mass-redistribution nullcline intersection points, corresponding to stationary polarized states, indicates that Cdc42 and Bem1-GEF complexes co-polarize as expected. Moreover, the N-shaped Cdc42-redistribution nullcline that intersects the line $\Delta n_{\mathrm{B}} = 0$ three times, indicating that polarization does not require spatial redistribution of Bem1-GEF complexes. Still, the enzymatic action of Bem1-GEF complexes in the local reaction kinetics is essential for Cdc42 polarization as they provide the nonlinear feedback that shapes the Cdc42-redistribution nullcline. In this sense, Bem1-GEF complexes play an analogous but inverse role to MinE in the Min system. In the physiological case, Bem1-GEF complexes they stabilize polarity by co-polarizing with Cdc42. In the unphysiological case that free Bem1-GEF complexes diffuse slower that membrane-bound ones ($\mathcal{D}_{\mathrm{b}} > \mathcal{D}_{\mathrm{B}}$), contra-polarization of Bem1-GEF complexes drives cycling switching of Cdc42 polarity. Thus, the Cdc42 system and the Min system can be regarded as two complementary versions of the same mechanism in which the enzymatic function of the "secondary protein" (Bem1-GEF/MinE) is reversed such that its spatial redistribution has opposite effects in the two systems.

The above analysis has a striking implication: On the level of the pattern forming mechanisms, the Cdc42 system is closely related to the Min system, while the PAR system operates based on a fundamentally different mechanism. From the perspective of the phenomenology exhibited for physiological parameters, this is highly surprising since the Cdc42 system and the PAR system exhibit stationary polarity patterns, while the Min system exhibits pole-to-pole oscillations.

V. CONCLUSIONS

Quantitative models of biological systems are typically multi-component multi-species systems with a high-dimensional parameter space. It is therefore particularly challenging to find a unifying level of description where the mechanisms underlying different models can be compared.

Here, we presented a reduction method to obtain a phase-portrait representation of mass-conserving pattern forming systems which crystallizes their key qualitative features. This reduction is based on two steps. First, a reduction of the spatially continuous domain to two well-mixed compartments coupled by diffusion. This approximation assumes that the pattern of interest is a single "interface" connecting a high density region to a low density region. This is rather the rule than the exception for protein patterns observed in cells, especially bacterial cells due to their small size. Moreover, such an interface can also be interpreted as the elementary building block of more complex patterns with many interfaces. Second, the local quasi-steady-state approximation (LQSSA), which assumes that the relaxation of the concentrations in the compartments to a reactive equilibrium (local quasi-steady state) is fast compared to slow diffusive mass exchange between the compartments. This approximation is motivated by the insights that the essential degree of freedom is the spatial redistribution of the conserved masses and that the key information about the reaction kinetics is encoded in the dependence of the reactive equilibria on these masses. Limitations and potential extensions of the LQSSA are discussed in the Outlook, Sec. V A.

After these two reduction steps, the only remaining degrees of freedom are the differences in globally conserved masses between the two compartments. In this reduced system, the dynamics of these mass differences can simply be inferred from the reactive nullcline (hyper-)surfaces. Specifically, the intersection lines of *reactive* nullcline surfaces act as *mass-redistribution* null-clines in the phase space of the redistributed masses. The mass-redistribution nullclines depend on the diffusion constants and thus inform about the role of mass-redistribution in the observed phenomena. Thus, they allow a classification of pattern-forming systems, as we demonstrated by comparing the phase portraits of three different protein-pattern forming systems. Attempts to classify pattern-forming systems based on the topology of the protein interaction network face the difficulty that many networks can give rise to similar phenomena, and the same network can produce different phenomena depending on parameters (e.g. stationary and oscillatory patterns in the Min system). In contrast, here we have demonstrated that the geometry of the reactive nullcline surfaces informs on the key qualitative features of the observed dynamics. This suggests that one can identify geometric design principles based on the shape of the reactive nullcline surfaces and the resulting mass-redistribution nullclines. Such design principles might guide future model building efforts in a similar way as the design principles that have been identified for neural excitability [66] and well-mixed biochemical oscillators [67, 68].

The phase-portrait analysis in terms of mass-

redistribution nullclines also shows that not all species need to be redistributed for patterns to form in the first place. One can construct a "core" pattern-forming system, where these species are considered non-diffusible and their kinetics absorbed into effective kinetics of the redistributed species. In the Min system and the Cdc42 system, the (local) *enzymatic action* of MinE / Bem1-GEF complexes is part of the core pattern-forming mechanism, whereas their *cytosolic redistribution* is not. Redistribution of MinD / Cdc42 is sufficient for the formation of (stationary) MinD / Cdc42 patterns. Thus, the elementary polarization mechanism is equivalent in the Min system and the Cdc42 system. The difference of these system lies in the effect of the mass redistribution of the "secondary proteins" MinE and Bem1-GEF respectively. In the Min system, redistribution of MinE by cytosolic diffusion system drives cyclic switching of the MinD polarity axis and thus gives rise to pole-to-pole oscillations. In contrast, redistribution of Bem1-GEF complexes stabilizes stationary Cdc42 polarization.

Taken together, the shape of the reactive nullcline surfaces and the resulting mass-redistribution nullclines inform about important qualitative features of a model and thus bridge the gap between nonlinear reaction kinetics and the observed phenomena. In particular, they allow one to disentangle the functional roles of each protein species in the pattern-forming mechanisms.

a. Assuming a well-mixed cytosol misses important physics. The assumption of a well-mixed cytosol is often made a priori, justified by the observation that diffusive transport on cellular scales is fast compared to membrane diffusion (and reaction kinetics); see e.g. [10, 11, 13, 29–31]. This reasoning overlooks that the relative rates of transport can be important if there is more than one protein species diffusing in the cytosol. Or put differently, setting the cytosol concentrations well-mixed neglects that the cytosol gradients of different species can have different amplitudes, which may be mechanistically relevant, even if the cytosol gradients are shallow compared to membrane gradients.

In fact, for the Min system, we find that increasing the diffusion of free MinE eventually always suppresses pattern formation in the Min system (see phase diagram Fig. 5a and Appendix B 4). This shows that the relative rate of cytosolic transport of MinD vs MinE (and, the relative amplitude of the cytosolic gradients, respectively) is important for the dynamics. This shows that one misses important physics if one assumes a well-mixed cytosol a priori.

In general, the time scales of cytosol diffusion—even if fast— and, correspondingly, the relative amplitudes of cytosolic gradients—even if shallow—can be important if there is more than one cytosolic (fast-diffusing) species. Approaches, such as the so called "local-perturbation analysis" [30], that rely on the a priori approximation to treat fast diffusing components as well-mixed, may therefore miss important features of the dynamics.

In passing, we note that explicit cytosol diffusion is also important to account for effects due to cell geometry. This is relevant for the axis selection of polarity patterns in rod-shaped or ellipsoidal cells [52, 69, 72]. Compartment-based models—although requiring more than two compartments—have also been employed successfully to study such geometry effects [72].

A. Outlook

a. Future applications and generalizations. Going forward, it will be interesting to apply the reduction method and phase-portrait analysis presented here to other model systems, e.g. the oscillatory Cdc42-polarization in fission yeast [12, 13]. The phase portrait analysis might be particularly helpful to study genuinely nonlinear phenomena like stimulus induced pattern formation and stimulus-induced polarity switching [11] which are not accessible to linear stability analysis.

Potential obvious generalizations of the two-compartment setting are systems with asymmetric exchange rates, and those with heterogeneous compartments (reaction kinetics, bulk-surface ratio, size). Indeed, setting the redistribution of one species to a slow time scale in the models with two conserved masses (e.g. Min system), makes the system heterogeneous from the point of view of the fast species. The heterogeneity is determined by distribution of the slow species between the two compartments and changes on the slow time scale. Concrete application for heterogeneous two-compartment models might be Ran-GTPase driven nuclear transport, where the two compartments represent the cytoplasm and nucleoplasm, with transport between them through pores in nuclear envelope [73–76]. More broadly, two-compartment systems with asymmetric exchange rates and heterogeneous compartments have been studied in ecology [17, 19], where interesting new effects compared to the symmetric case were found.

Another route of generalization is to study more than two coupled compartments. In this case, the phase space of the mass differences becomes high-dimensional and thus impractical for a phase-portrait analysis [72]. Instead, one can plot all local masses into one graph, as was done in Ref. [6]. This way, the spatial information is lost, but one can still gain insight about the role of the control space structure (surface of local equilibria and their stability) for the dynamics of the spatially coupled system.

b. Relation to parameter-space topology. A previous work on reaction–diffusion models for cell polarity has identified generic topological features of their parameter spaces [23]. In the specific case of two-component systems, the origin of these features was recently traced back to the phase space geometry, specifically the shape of the reactive nullcline of pattern forming systems (see Sec. VII in Ref. [25]). Two-compartment systems are a promising setting to generalize these findings to systems with more components and phenomena like pole-to-pole oscillations.

Indeed, the way the mass-redistribution nullclines deform due to the variation of parameters (kinetic rates, diffusion constants, average masses) determines the bifurcations in parameter space. Thus, we expect a close relation between the geometry of mass-redistribution nullclines and phase space topology.

c. Relaxing the local quasi-steady state assumption. The analysis presented here relied crucially on the stability of the local equilibria and a time scale separation between reactive relaxation to the local equilibria and diffusive mass redistribution. This allowed us to make the LQSSA Eq. (4). In the absence of this time scale separation, the concentrations will deviate from the local equilibria due to the diffusive flows in the individual components. For two-component systems, this deviation from the local equilibria has only a quantitative effect but does not change the dynamics qualitatively. This is because the local phase spaces are one-dimensional such that the reactive flow is always directed straight towards the local equilibrium (see Fig. 2a). In contrast, in systems with more components, explicitly accounting for the relaxation towards local equilibria may be important to capture the salient features of the full dynamics. One potential approach is to allow for small deviations from the local equilibria along the direction of the slowest decaying eigenvector. Moreover, local equilibria may become unstable, driving the concentrations away from them [24, 77]. This qualitative change of the local reaction dynamics can have profound consequences on the dynamics of the spatially extended system, as was studied in detail in Refs. [24, 26]. There, it was found that destabilization of the local equilibria gives rise to chaos near the onset of pattern formation.

Even if a systematic reduction in terms of a (generalized) LQSSA is not possible, visualizing the trajectories from full numerical simulations in control space can be a powerful tool to gain insight into the underlying mechanisms [6, 26].

Appendix A: Relating diffusive exchange rates to diffusion constants

The diffusive exchange rates $\mathcal{D}_\alpha$ can be related to the diffusion constants D_α in a spatially continuous system in two alternative ways. First, a finite volume approximation of the Laplace operator on a line with reflective boundary conditions yields

$$\mathcal{D}_\alpha^{(\mathrm{FV})} = \frac{4}{L^2} D_\alpha. \tag{A1}$$

Second, we can choose the exchange rates such that the linearization of Eq. (1) for an antisymmetric perturbation $\mathbf{u}_{1,2} = \mathbf{u}^* \pm \delta\mathbf{u}$ is identical to the linearization of a spatially continuous MCRD system for a Fourier mode $\sim \cos qx$ with $q = \pi/L$:

$$\mathcal{D}_\alpha^{(\mathrm{LSA})} = \frac{\pi^2}{2L^2} D_\alpha. \tag{A2}$$

The factor 2 in the denominator originates from the linearization of the exchange terms in Eq. (1) for the antisymmetric mode where any perturbation in compartment 1 is balanced by an equal and opposite perturbation in compartment 2. For symmetric perturbations $\mathbf{u}_{1,2} = \mathbf{u}^* + \delta\mathbf{u}$, corresponding to homogeneous perturbations of the continuous system, the exchange term in Eq. (1) cancels. For the exchange rates Eq. (A2), the small amplitude dynamics of antisymmetric perturbations of the two-compartment system exactly represent the linearized dynamics of a single mode $q = \pi/L$ in the spatially continuous system, and one can use the system size L as a bifurcation parameter to sample the whole dispersion relation $\sigma(q = \pi/L)$.

The two options above differ by a factor $\mathcal{D}_\alpha^{(\mathrm{LSA})}/\mathcal{D}_\alpha^{(\mathrm{FV})} = \pi^2/8 \approx 1.23$. This can be interpreted as an effective rescaling of the system size L by a factor $\pi/(2\sqrt{2}) \approx 1.11$ due to the finite difference discretization. Throughout this study, we used the exchange rate defined by Eq. (A2).

Appendix B: Min system: Geometry reduction, parameter choice, numerical simulations and phase diagram

1. Reduction from three-dimensional spherocylinder to two-comparmetment system

We model the three-dimensional cell geometry as a spherocylinder of length $L = 3\,\mu\mathrm{m}$ and radius $R = 0.5\,\mu\mathrm{m}$. The surface of this spherocylinder represents the cell membrane and is the domain for the protein densities m_d, m_de, while its three-dimensional bulk is the domain of the cytosolic components $c_\mathrm{DT}, c_\mathrm{DD}$ and c_E. Reactive boundary conditions at the surface account for attachment and detachment of proteins at the membrane. The mathematical implementation of the Min-skeleton model in this three-dimensional bulk-surface coupled setting can be found in [26].

To reduce this geometry to the two-compartment system, we cut the spherocylinder at midplane and assume that the cytosol and membrane in both halves are well mixed. That is, we only account for concentration differences between the two cell halves which serve as a proxy

TABLE I. Parameters for the Min-skeleton model adapted from [22]. ζ is the bulk-surface ratio that appears because we express cytosol concentrations in units of surface density $\mathrm{\mu m}^{-2}$, as explained in the text (Appendix. B 1).

Parameter	Value	Unit
D_D	16	$\mathrm{\mu m}^2\,\mathrm{s}^{-1}$
D_E	10	$\mathrm{\mu m}^2\,\mathrm{s}^{-1}$
D_d	0.013	$\mathrm{\mu m}^2\,\mathrm{s}^{-1}$
D_de	0.013	$\mathrm{\mu m}^2\,\mathrm{s}^{-1}$
n_D	5.0	$\mathrm{\mu m}^{-2}$
n_E	2.0	$\mathrm{\mu m}^{-2}$
λ	6.0	s^{-1}
k_D	$0.1/\zeta$	s^{-1}
k_dD	$0.108/\zeta$	$\mathrm{\mu m}^2\,\mathrm{s}^{-1}$
k_dE	$0.435/\zeta$	$\mathrm{\mu m}^2\,\mathrm{s}^{-1}$
k_de	0.4	s^{-1}

for the concentration gradients along the cell. Moreover, we express the cytosol concentrations in units of surface density, $\hat{c} = \zeta c$, where ζ is the ratio of cytosolic bulk volume to membrane area (short bulk-surface ratio). This allows us to collect all concentrations in a vector that does not mix units. Substituting $c \to \hat{c}/\zeta$, all reaction rates for reaction terms involving a cytosol concentration are rescaled by the bulk-surface ratio: $\hat{k} = k/\zeta$. In the following, we drop the hats.

The bulk-surface ratio of a spherocylinder is given by

$$\zeta = \frac{\pi R^2 L + 4\pi R^3/3}{2\pi RL + 4\pi R^2} = \frac{RL + 4R^2/3}{L + 4R}, \qquad \text{(B1)}$$

which, with $L \approx 3\,\mathrm{\mu m}$ and $R \approx 3\,\mathrm{\mu m}$ for *E. coli*, gives $\zeta \approx 0.23$.

For the *in vitro* setup using flat microchambers whose top and bottom surfaces are covered by lipid bilayers that mimic the cell membrane, the bulk-surface ratio is simply $H/2$, where H is the height of the microchamber; see Fig. 8. With respect to this microchamber geometry, the two-compartment system represents a single, laterally isolated cytosol column with two membrane patches at its top and bottom. Only vertical gradients in the cytosol on the scale of the microchamber height are accounted for by the two compartments.

2. Parameter choice

For the physiological parameters from [22], the densities enter a regime where the reaction kinetics is bistable (i.e. where there are two stable reactive equilibria for given local total densities, see Fig. 9a). This "local bistability" does not change the dynamics of the spatially coupled system qualitatively. However, it complicates the analysis in terms of LQSSA to deal with the branch switching that happens when the dynamics leaves the

locally bistable region: Upon passing the saddle-node bifurcations that delimit the bistable region, the concentrations jump to the remaining branch of stable equilibria. To avoid these technical subtleties, we reduce the total densities to values where the local system no longer becomes bistable (inset in Fig. 9a). Because this also increases the minimal domain size for instability, we increase the domain length by a factor 8. The oscillation period increases due to this, but the limit cycle in control space does not change qualitatively (see Fig. 9b,c). For the parameter values used here, see Table I.

3. Simulations on 1D domain

In Figure. 5, we compare simulations of the two-compartment system to simulations in a spatially continuous domain (1D line) with no-flux boundary conditions. The dynamics in this domain is given by

$$\partial_t \mathbf{u}(x,t) = \mathbf{D}\partial_x^2 \mathbf{u} + \boldsymbol{f}(\mathbf{u}), \qquad \text{(B2)}$$

$\mathbf{D} = \mathrm{diag}(\{D_i\})$ is the diffusion matrix. (As in the two-compartment setting, the concentrations are measured in units of surface density, $\mathrm{\mu m}^{-2}$. To convert the bulk concentrations to volume densities, they must be divided by the bulk-surface ratio ζ.)

The reason that we do not perform the simulations in the three-dimensional cell geometry is that we are interested in the role of *lateral* MinE transport, which we study by tuning the diffusion constants D_E and D_de. Bulk-surface coupling induces bulk-concentration gradients in the direction normal to the membrane. Those gradients control the flux onto and off the membrane (attachment–detachment dynamics). Hence, changing the cytosol diffusion constants in the bulk-surface coupled 3D system affects both transport and the reaction kinetics. Reducing the system to a 1D line geometry, which effectively amounts to neglecting vertical gradients, allows us to tune the cytosol diffusion constants to study the role of lateral mass transport alone.

4. No instability for well-mixed cytosol

In the limit $\mathcal{D}_\mathrm{D}, \mathcal{D}_\mathrm{E} \to \infty$, the cytosol is well mixed, i.e. $\mathbf{c}^{(1)} = \mathbf{c}^{(2)} = \mathbf{c}$. Defining

$$f_i^{(j)} = f_i(m_\mathrm{d}^{(j)}, m_\mathrm{de}^{(j)}, c_\mathrm{DD}, c_\mathrm{DT}, c_\mathrm{E}),$$
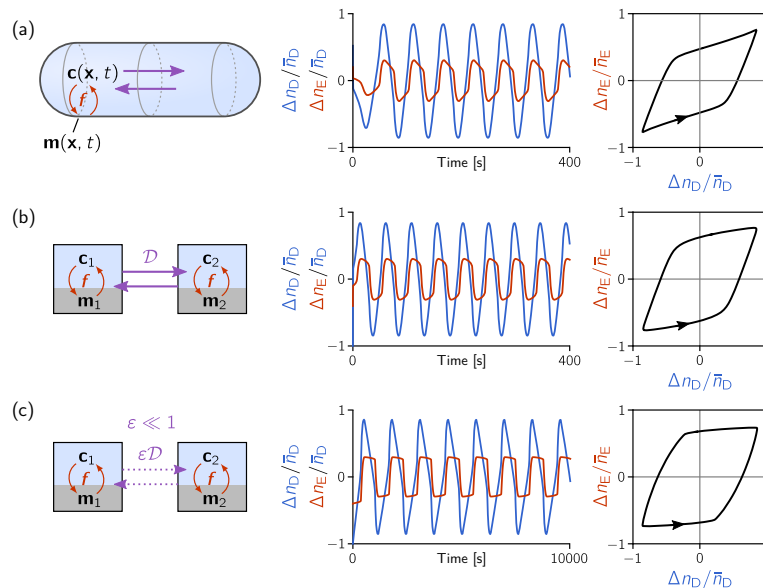$$i \in \{\mathrm{d, de, DD, DT, E}\}, \; j = 1, 2, \qquad \text{(B3)}$$

FIG. 7. Comparison of the Min-protein dynamics in the full 3D geometry of an *E. coli* cell (a) to the two-compartment system (b,c) representing the two cell-halves (poles); see Sec. III for details. Nonlinear reactions (f, red arrows) account for cycling between membrane-bound and cytosolic states (concentrations m and c). Diffusive exchange is indicated by purple arrows. Time traces (center) and phase-space trajectories (right) of the redistributed masses $\Delta n_{\mathrm{D,E}}$ between the two cell-halves/compartments show good qualitative agreement between the full 3D simulation and the two-compartment system. Importantly, setting the diffusive exchange rates to a much slower time scale ($\mathcal{D} \to \varepsilon \mathcal{D}$, here $\varepsilon = 10^{-2}$) does not qualitatively alter the pole-to-pole oscillation (c).
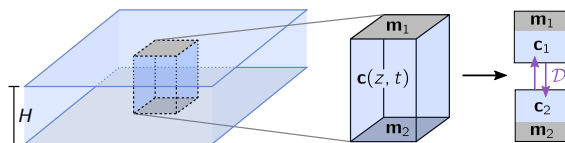

FIG. 8. Illustration of an *in vitro* setup using a flat microchamber with two membrane surfaces (gray planes) on top and bottom of a bulk volume [26]. An individual column of that system, comprising two membrane patches and the bulk volume in-between them can be pictured as an analog to the cell geometry, where the two membrane patches correspond to the cell poles. The analogous approximation by two compartments, as shown on the right, is valid as long as the vertical bulk gradient is approximately linear. Comparing to Fig. 1a, the analogy between pole-to-pole oscillations in cells and vertical membrane-to-membrane oscillations in microchambers becomes immediately evident.

with $\boldsymbol{f}$ given by Eq. (8), the dynamics is governed by

$$\partial_t m_{\mathrm{d}}^{(1,2)} = \pm \mathcal{D}_{\mathrm{d}} \left(m_{\mathrm{d}}^{(2)} - m_{\mathrm{d}}^{(1)} \right) + f_{\mathrm{d}}^{(1,2)}, \tag{B4a}$$

$$\partial_t m_{\mathrm{de}}^{(1,2)} = \pm \mathcal{D}_{\mathrm{de}} \left(m_{\mathrm{de}}^{(2)} - m_{\mathrm{de}}^{(1)} \right) + f_{\mathrm{de}}^{(1,2)}, \tag{B4b}$$

$$\partial_t c_{\mathrm{DD}} = f_{\mathrm{DD}}^{(1)} + f_{\mathrm{DD}}^{(2)}, \tag{B4c}$$

$$\partial_t c_{\mathrm{DT}} = f_{\mathrm{DT}}^{(1)} + f_{\mathrm{DT}}^{(2)}, \tag{B4d}$$

$$\partial_t c_{\mathrm{E}} = f_{\mathrm{E}}^{(1)} + f_{\mathrm{E}}^{(2)}. \tag{B4e}$$

We now perform a linear stability analysis of the homogeneous steady states ($\mathbf{m}^{(1)} = \mathbf{m}^{(2)} = \mathbf{m}^*$, $\boldsymbol{f}(\mathbf{u}^*) = 0$) of these equations and show that they never exhibit a symmetry breaking instability. Because of the parity symmetry, $1 \leftrightarrow 2$, of the homogeneous steady state, even and odd perturbations are decoupled. Even perturbations correspond to the stability against homogeneous perturbations. Odd perturbations correspond lateral stability, i.e. stability against spatially inhomogeneous perturbations. These are the relevant perturbations for pattern formation. For odd perturbations, mass conservation of MinD and MinE enforces $\delta c_{\mathrm{DD}} = -\delta c_{\mathrm{DT}}$ and $\delta c_{\mathrm{E}} = 0$. Thus, we obtain the eigenvalue problem

$$\partial_t \begin{pmatrix} \delta m_{\mathrm{d}} \\ \delta m_{\mathrm{de}} \\ \delta c_{\mathrm{DT}} \end{pmatrix} = J_{\mathrm{odd}} \begin{pmatrix} \delta m_{\mathrm{d}} \\ \delta m_{\mathrm{de}} \\ \delta c_{\mathrm{DT}} \end{pmatrix} \tag{B5}$$
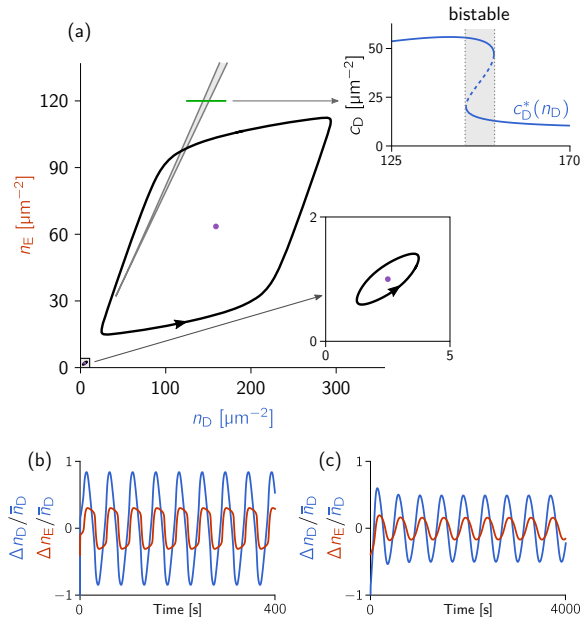
(a)

(b)

(c)

FIG. 9. Qualitative equivalence of the Min dynamics at physiological protein densities and with scaled down densities. (a) Parameter space of the protein densities n_D, n_E showing the regime of bistable reaction kinetics in gray and trajectories from simulations of the two compartment model. The inset on the top right shows a curve of reactive equilibria (blue) in a slice through the bistable region at constant n_E. The inset on the bottom right shows a blow-up of the trajectory in the low density regime. Purple dots mark the average masses. (b,c) Timetraces of the mass differences corresponding to the two trajectories in (a). Note the differently scaled time axes.
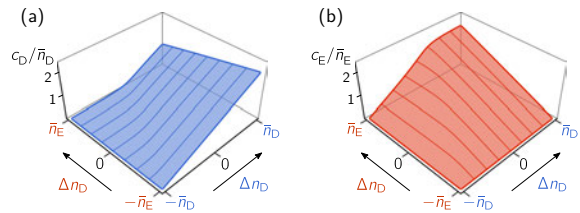
FIG. 10. Reactive equilibrium surfaces showing the membrane concentrations m_d and m_{de}.

with the Jacobian

$$J_{\text{odd}} = \begin{pmatrix} k_{dD}c_{DT} - k_{dE}c_E - 4\mathcal{D}_d & 0 & k_D + k_{dD}m_d \\ k_{dE}c_E & -k_{de} - 4\mathcal{D}_{de} & 0 \\ 0 & 0 & -2k_D - 2k_{dD}m_d - 2\lambda \end{pmatrix}. \tag{B6}$$

The eigenvalues of J_{odd} are

$$\sigma_1 = k_{dD}c_{DT} - k_{dE}c_E - 4\mathcal{D}_d,$$
$$\sigma_2 = -k_{de} - 4\mathcal{D}_{de}, \tag{B7}$$
$$\sigma_3 = -2k_D - 2k_{dD}m_d - 2\lambda.$$

One immediately sees that only the first eigenvalue, σ_1, may become positive. A necessary condition for this is

$$k_{dD}c_{DT} - k_{dE}c_E > 0. \tag{B8}$$

The Jacobian is evaluated at the homogeneous steady state where $\boldsymbol{f}(\mathbf{u}^*) = 0$. In particular,

$$f_d = (k_{dD}c_{DT}^* - k_{dE}c_E^*)m_d^* + k_D c_D^* = 0, \tag{B9}$$

which implies $k_{dD}c_{DT}^* < k_{dE}c_E^*$ for all steady states. Therefore, the necessary condition for instability,

Eq. (B8), is never fulfilled. In conclusion, the Min skeleton model with well-mixed cytosol cannot exhibit a lateral instability (instability against spatially inhomogeneous perturbations). This result, derived in the two-compartment setting also holds in spatially continuous domains thanks to the correspondence between these two setting; see Sec. A.

Appendix C: LQSSA

1. General setup and notation

Consider a system with N components, $\mathbf{u} = \{u_i\}_{i=1..N}$, governed by local reactions $\boldsymbol{f}(\mathbf{u})$ that con-

serve M masses, $\mathbf{n} = \{n_\alpha\}_{\alpha=1..M}$. The conserved masses are given in terms of the component vector via $n_\alpha = \mathbf{s}_\alpha^\mathsf{T} \mathbf{u}$ where $\mathbf{s}_\alpha$ are "stoichiometric" vectors fulfilling $\mathbf{s}_\alpha^\mathsf{T} \boldsymbol{f} = 0$. Denoting the diffusive exchange rates by the matrix $\mathfrak{D} = \mathrm{diag}\{\mathcal{D}_i\}$, the dynamics in LQSSA is given by

$$\Delta n_\alpha = -\mathbf{s}_\alpha^\mathsf{T} \mathfrak{D} \Delta \mathbf{u}^*(\Delta \mathbf{n}), \qquad \text{(C1)}$$

where the slaved concentration gradients $\Delta \mathbf{u}^*$ are defined in terms of the reactive equilibria as $\Delta \mathbf{u}^* = \mathbf{u}^*(\bar{\mathbf{n}} + \Delta \mathbf{n}) - \mathbf{u}^*(\bar{\mathbf{n}} - \Delta \mathbf{n})$; cf. Eq. (6). The reactive equilibria $\mathbf{u}^*(\mathbf{n})$ are defined by

$$0 \stackrel{!}{=} \mathbf{F}(\mathbf{u}^*; \mathbf{n}) = \begin{pmatrix} \{\mathbf{s}_\alpha^\mathsf{T} \mathbf{u}^* - n_\alpha\}_\alpha \\ \boldsymbol{f}(\mathbf{u}^*) \end{pmatrix}. \qquad \text{(C2)}$$

The factor $s_\alpha^\mathsf{T} \mathfrak{D}$ determines the diffusive mass flux of species α that results from slaved concentration gradients. We now define the "mass-redistribution potentials" [25] $\eta_\alpha := \mathbf{s}_\alpha^\mathsf{T} \mathfrak{D} \mathbf{u}$, which allows us to write the mass-redistribution dynamics as

$$\partial_t \Delta n_\alpha = -\Delta \eta_\alpha^*(\Delta \mathbf{n}). \qquad \text{(C3)}$$

2. Linear stability analysis

For small perturbations δn around the homogeneous steady state $\Delta \mathbf{n} = 0$, the dynamics is given by

$$\partial_t \delta n_\alpha = -2 \sum_\beta \partial_{n_\beta} \eta_\alpha^*|_{\bar{\mathbf{n}}} \, \delta n_\beta,$$
$$= \sum_\beta \mathcal{J}_{\alpha\beta} \, \delta n_\beta, \qquad \text{(C4)}$$

where, in the second line, we introduced the mass-redistribution Jacobian

$$\mathcal{J}_{\alpha\beta} := -2 \partial_{n_\beta} \eta_\alpha^*|_{\bar{\mathbf{n}}} = -2 \mathbf{s}_\alpha^\mathsf{T} \mathfrak{D} \, (\partial_{n_\beta} \mathbf{u}^*|_{\bar{\mathbf{n}}}). \qquad \text{(C5)}$$

The eigenvalues of this Jacobian determine the stability of the homogeneous steady state in LQSSA.

Before we continue to calculate the derivatives $\partial_{n_\beta} \eta_\alpha^*$ in terms of the linearized reaction kinetics, let us take moment to interpret the Jacobian $\mathcal{J}$. In the case of one conserved mass n, we have the 1×1 Jacobian $\mathcal{J} = -2 \partial_n \eta*|_n$. Hence, we recover the nullcline-slope criterion for lateral instability $\partial_n \eta*|_n < 0$ (cf. Eq. (27) in Ref. [25]). For more than one conserved mass, the entries of $\mathcal{J}$ are the slopes of the nullcline (hyper-)surfaces $\eta * (\mathbf{n})$ along the directions of the conserved masses in parameter space. The eigenvalue problem for $\mathcal{J}$ can therefore be interpreted as a generalized slope criterion.

To find the nullcline slopes $\partial_{n_\beta} \eta_\alpha^*$, we take the derivative of the defining equation for the reactive equilibria

Eq. (C2) with respect to n_α which gives (implicit function theorem)

$$\partial_{n_\alpha} \mathbf{u}^* = -(D_\mathbf{u} \mathbf{F}|_{\mathbf{u}^*})^{-1} \partial_{n_\alpha} \mathbf{F} = (D_\mathbf{u} \mathbf{F}|_{\mathbf{u}^*})^{-1} \mathbf{e}_\alpha, \quad \text{(C6)}$$

where $\mathbf{e}_\alpha$ is the unit vector with entry 1 in the αth component. Substituting this in Jacobian yields

$$\mathcal{J}_{\alpha\beta} = -2 \mathbf{s}_\alpha^\mathsf{T} \mathfrak{D} \, (D_\mathbf{u} \mathbf{F}|_{\mathbf{u}^*(\bar{\mathbf{n}})})^{-1} \mathbf{e}_\beta. \qquad \text{(C7)}$$

This can easily be implemented numerically to obtain the Jacobian and calculate its eigenvalues.

a. Equivalence to perturbation theory in long-wavelength limit. The Jacobian derived above for the two-compartement system in LQSSA can also be obtained by a long-wavelength perturbation theory for linear stability analysis on a continuous domain. To see why this is, consider the Jacobian on a spatially continuous domain

$$J_q = D_\mathbf{u} \boldsymbol{f}|_{\bar{\mathbf{n}}} - q^2 \mathbf{D}, \qquad \text{(C8)}$$

where $\mathbf{D} = \mathrm{diag}(\{D_i\})$ is the diffusion matrix, and q is the wavenumber (i.e. $-q^2$ are the eigenvalues of the Laplace operator). In the long wavelength limit $q \to 0$, we can find the eigenvalues of J_q by solving the degenerate perturbation problem with q^2 as perturbation parameter. We are interested in the eigenvalue branches that emanate from 0 at $q = 0$, corresponding to the conservation laws. The associated left eigenvectors, (spanning the left nullspace of $D_\mathbf{u} \boldsymbol{f}$) are the "stochiometric vectors" $\mathbf{s}_\alpha^\mathsf{T}$. The right eigenvectors of $D_\mathbf{u} \boldsymbol{f}$ associated to the eigenvalue 0 are $\partial_{n_\alpha} \mathbf{u}^*$. This follows immediately from the defining equation $\boldsymbol{f}(\mathbf{u}^*) = 0$ by taking the derivative w.r.to n_α and using that $\boldsymbol{f}$ does not explicitly depend on n_α. The first order perturbation of the degenerate 0 eigenvalues is given by eigenvalues of the matrix

$$M_{\alpha\beta}^{(1)} = -\mathbf{s}_\alpha^\mathsf{T} \mathbf{D} \, (\partial_{n_\beta} \mathbf{u}^*), \qquad \text{(C9)}$$

where we used $\mathbf{s}_\alpha^\mathsf{T} \partial_{n_\beta} \mathbf{u}^* = \partial_{n_\beta} (\mathbf{s}_\alpha^\mathsf{T} \mathbf{u}^*) = \partial_{n_\beta} n_\alpha = \delta_{\alpha\beta}$. Substituting the diffusion matrix $\mathbf{D}$ by the exchange rate matrix via Eq. (A2) yields the desired result

$$\mathcal{J}_{\alpha\beta} = q^2 M_{\alpha\beta}^{(1)}. \qquad \text{(C10)}$$

b. Example: Min system. For the Min system as defined in the main text we have

$$\mathbf{u} = (m_\mathrm{d}, m_\mathrm{de}, c_\mathrm{DT}, c_\mathrm{DD}, c_\mathrm{E})^\mathsf{T},$$
$$\mathbf{s}_\mathrm{D}^\mathsf{T} = (1, 1, 1, 1, 0), \quad \mathbf{s}_\mathrm{E}^\mathsf{T} = (0, 1, 0, 0, 1),$$
$$\mathbf{F} = (\mathbf{s}_\mathrm{D}^\mathsf{T} \mathbf{u} - n_\mathrm{D}, \, \mathbf{s}_\mathrm{E}^\mathsf{T} \mathbf{u} - n_\mathrm{E}, \, f_\mathrm{d}(\mathbf{u}), f_\mathrm{de}(\mathbf{u}), f_\mathrm{DD}(\mathbf{u})),$$
$$\mathfrak{D} = \mathrm{diag}(\mathcal{D}_\mathrm{d}, \mathcal{D}_\mathrm{de}, \mathcal{D}_\mathrm{D}, \mathcal{D}_\mathrm{D}, \mathcal{D}_\mathrm{E}),$$
$$\text{(C11)}$$

where $\boldsymbol{f}$ is given in Eq. (8). Note that we eliminated to components from $\boldsymbol{f}$ because the system would otherwise be overdetermined owing to the two conserved masses. This gives the derivative matrix

$$D_{\mathbf{u}}\mathbf{F} = \begin{pmatrix} 1 & 1 & 1 & 1 & 0 \\ 0 & 1 & 0 & 0 & 0 \\ k_{\mathrm{dD}}c_{\mathrm{DT}} - k_{\mathrm{dE}}c_{\mathrm{E}} & 0 & k_{\mathrm{D}} + k_{\mathrm{dD}}m_{\mathrm{d}} & 0 & -k_{\mathrm{dE}}m_{\mathrm{d}} \\ k_{\mathrm{dE}}c_{\mathrm{E}} & -k_{\mathrm{de}} & 0 & 0 & k_{\mathrm{dE}}m_{\mathrm{d}} \\ 0 & k_{\mathrm{de}} & 0 & -\lambda & 0 \\ -k_{\mathrm{dE}}c_{\mathrm{E}} & k_{\mathrm{de}} & 0 & 0 & -k_{\mathrm{dE}}m_{\mathrm{d}} \end{pmatrix}. \tag{C12}$$

Note that the first to rows are simply $\mathbf{s}_{\mathrm{D}}^{\mathsf{T}}$ and $\mathbf{s}_{\mathrm{E}}^{\mathsf{T}}$, which follows immediately from the definition of $\mathbf{F}$.

c. Inhomogeneous (asymmetric) steady states. The derivation presented above for homogeneous steady sates can be generalized to inhomogeneous steady states $\Delta\tilde{\mathbf{n}}$ defined by $\Delta\mathbf{u}^*(\Delta\tilde{\mathbf{n}}) = 0$. The resulting Jacobian reads

$$\tilde{\mathcal{J}}_{\alpha\beta} = \mathbf{s}_\alpha^{\mathsf{T}}\,\mathfrak{D} \cdot \left[(D_{\mathbf{u}}\mathbf{F}|_{\bar{\mathbf{n}}+\Delta\tilde{\mathbf{n}}})^{-1} + (D_{\mathbf{u}}\mathbf{F}|_{\bar{\mathbf{n}}-\Delta\tilde{\mathbf{n}}})^{-1}\right]\mathbf{e}_\beta. \tag{C13}$$

Appendix D: PAR and Cdc42 models

1. PAR polarity model

We adopt the model introduced in [21] and further analyzed in [23] which accounts for the membrane-bound and cytosolic concentrations of aPARs and pPARs $\mathbf{u} = (m_{\mathrm{a}}, m_{\mathrm{p}}, c_{\mathrm{A}}, c_{\mathrm{P}})$ with the reaction kinetics

$$\boldsymbol{f} = \begin{pmatrix} k_{\mathrm{A}}c_{\mathrm{A}} - k_{\mathrm{a}}m_{\mathrm{a}} - k_{\mathrm{ap}}m_{\mathrm{p}}^2 m_{\mathrm{a}} \\ k_{\mathrm{P}}c_{\mathrm{P}} - k_{\mathrm{p}}m_{\mathrm{p}} - k_{\mathrm{pa}}m_{\mathrm{a}}^2 m_{\mathrm{p}} \\ -k_{\mathrm{A}}c_{\mathrm{A}} + k_{\mathrm{a}}m_{\mathrm{a}} + k_{\mathrm{ap}}m_{\mathrm{p}}^2 m_{\mathrm{a}} \\ -k_{\mathrm{P}}c_{\mathrm{P}} + k_{\mathrm{p}}m_{\mathrm{p}} + k_{\mathrm{pa}}m_{\mathrm{a}}^2 m_{\mathrm{p}} \end{pmatrix}. \tag{D1}$$

These reactions conserve the total densities of aPARs $n_{\mathrm{A}} = m_{\mathrm{a}} + c_{\mathrm{A}}$ and pPARs $n_{\mathrm{P}} = m_{\mathrm{p}} + c_{\mathrm{P}}$, respectively. Since the reaction network is symmetric under the exchange A$\leftrightarrow$P, we use reaction rates that also respect this symmetry for simplicity [23]. The diffusion matrix reads $\mathfrak{D} = 4/L^2 \operatorname{diag}(D_m, D_m, D_c, D_c)$, where $L \approx 15\,\mu\mathrm{m}$ is the long half-axis of the ellipsoidal cells. For the model parameters, see Table II. Note that in LQSSA, this length only contributes to the overall time scale but does not affect the phase portrait structure.

2. Cdc42 polarity model

We use a simplified form of the quantitative model proposed in [71]. This model describes the dynamics of the GTPase Cdc42, its guanine nucleotide exchange factor

(GEF) Cdc24 and the scaffold protein Bem1. The critical feedback loop is constituted by mutual recruitment between membrane-bound Cdc42-GTP and Bem1-GEF complexes. While the full model accounts for Bem1 and GEF separately, we lump these species into a complex species here. This retains the salient features of the model, in particular the mutual recruitment mechanism.

TABLE II. Parameters for the PAR model adapted from [23].

Parameter	Value	Unit
D_c	10	$\mu\mathrm{m}^2\,\mathrm{s}^{-1}$
D_m	0.1	$\mu\mathrm{m}^2\,\mathrm{s}^{-1}$
n_{A}	3.0	$\mu\mathrm{m}^{-2}$
n_{P}	3.0	$\mu\mathrm{m}^{-2}$
k_{a}	0.1	s^{-1}
k_{A}	1.0	s^{-1}
k_{ap}	0.1	$\mu\mathrm{m}^2\,\mathrm{s}^{-1}$
k_{p}	0.1	s^{-1}
k_{P}	1.0	s^{-1}
k_{pa}	0.1	$\mu\mathrm{m}^2\,\mathrm{s}^{-1}$

The variables of this simplified model are $\mathbf{u} = (m_{\mathrm{t}}, m_{\mathrm{d}}, m_{\mathrm{b}}, c_{\mathrm{D}}, c_{\mathrm{B}})$, accounting, respectively, for membrane-bound Cdc42-GTP, Cdc42-GTP and Bem1-GEF complexes as well as cytosolic Cdc42-GDP and Bem1-GEF complexes. The reaction kinetics, describing attachment and detachment of Cdc42 at the membrane, hydrolysis and nucleotide exchange of Cdc42 of membrane-bound Cdc42, as well recruitment of Bem1-GEF complexes to the membrane by Cdc42-GTP are given by

$$\boldsymbol{f} = \begin{pmatrix} k_{\mathrm{dt}}m_{\mathrm{d}} + k_{\mathrm{bd}}m_{\mathrm{b}}m_{\mathrm{d}} + k_{\mathrm{bD}}m_{\mathrm{b}}c_{\mathrm{D}} - k_{\mathrm{td}}m_{\mathrm{t}} \\ k_{\mathrm{D}}c_{\mathrm{D}} + k_{\mathrm{td}}m_{\mathrm{t}} - (k_{\mathrm{d}} + k_{\mathrm{dt}} + k_{\mathrm{bd}}m_{\mathrm{b}})m_{\mathrm{d}} \\ k_{\mathrm{B}}c_{\mathrm{B}} + k_{\mathrm{tB}}m_{\mathrm{t}}c_{\mathrm{B}} - k_{\mathrm{b}}m_{\mathrm{b}} \\ -k_{\mathrm{D}}c_{\mathrm{D}} - k_{\mathrm{bD}}m_{\mathrm{b}}c_{\mathrm{D}} + k_{\mathrm{d}}m_{\mathrm{d}} \\ -k_{\mathrm{B}}c_{\mathrm{B}} - k_{\mathrm{tB}}m_{\mathrm{t}}c_{\mathrm{B}} + k_{\mathrm{b}}m_{\mathrm{b}} \end{pmatrix}. \tag{D2}$$

These reactions conserve the total densities of Cdc42 $n_{\mathrm{D}} = m_{\mathrm{t}} + m_{\mathrm{d}} + c_{\mathrm{D}}$ and Bem1-GEF complexes $n_{\mathrm{B}} = m_{\mathrm{b}} + c_{\mathrm{B}}$, respectively.

The parameter values, given in Table III are adapted from [71]. The values of k_{b}, k_{B} and k_{tB} are chosen to account for the lumped Bem1-GEF complexes species.

[1] Andrew B. Goryachev and Marcin Leda, "Many roads to symmetry breaking: Molecular mechanisms and theoret- ical models of yeast cell polarity," Molecular Biology of

TABLE III. Parameters for the Cdc42 model adapted from [71]. $\zeta = R/3$ is the bulk-surface ratio of the spherical cell.

Parameter	Value	Unit
D_c	10	$\mu m^2 s^{-1}$
D_m	0.01	$\mu m^2 s^{-1}$
R	4.0	μm
n_D	$3000/(4\pi R^2)$	μm^{-2}
n_B	$6500/(4\pi R^2)$	μm^{-2}
k_{bd}	0.2	$\mu m^2 s^{-1}$
k_{td}	1.0	s^{-1}
k_{dt}	0.002	s^{-1}
k_{bD}	$0.266/\zeta$	$\mu m^2 s^{-1}$
k_d	1.0	s^{-1}
k_D	$0.28/\zeta$	s^{-1}
k_B	$0.001/\zeta$	$\mu m^2 s^{-1}$
k_{tB}	$0.009/\zeta$	$\mu m^2 s^{-1}$
k_b	0.35	s^{-1}

the Cell **28**, 370–380 (2017).

[2] Wouter-Jan Rappel and Leah Edelstein-Keshet, "Mechanisms of cell polarization," Current Opinion in Systems Biology **3**, 43–53 (2017).

[3] Jian-geng Chiou, Mohan K. Balasubramanian, and Daniel J. Lew, "Cell Polarity in Yeast," Annual Review of Cell and Developmental Biology **33**, 77–101 (2017).

[4] Charles F. Lang and Edwin Munro, "The PAR proteins: From molecular circuits to dynamic self-stabilizing cell polarity," Development **144**, 3405–3416 (2017).

[5] Erwin Frey, Jacob Halatek, Simon Kretschmer, and Petra Schwille, "Protein Pattern Formation," in *Physics of Biological Membranes*, edited by Patricia Bassereau and Pierre Sens (Springer International Publishing, Cham, 2018) pp. 229–260.

[6] Jacob Halatek, Fridtjof Brauns, and Erwin Frey, "Self-organization principles of intracellular pattern formation," Philosophical Transactions of the Royal Society B: Biological Sciences **373**, 20170107 (2018).

[7] Seán M. Murray and Martin Howard, "Center Finding in E. coli and the Role of Mathematical Modeling: Past, Present and Future," Journal of Molecular Biology **431**, 928–938 (2019).

[8] Yougan Cheng, Bryan Felix, and Hans G. Othmer, "The Roles of Signaling in Cytoskeletal Changes, Random Movement, Direction-Sensing and Polarization of Eukaryotic Cells," Cells **9**, 1437 (2020).

[9] Alan M. Turing, "The chemical basis of morphogenesis," Philosophical Transactions of the Royal Society of London. Series B, Biological Sciences **237**, 37–72 (1952).

[10] Mathilde Guzzo, Seán M. Murray, Eugénie Martineau, Sébastien Lhospice, Grégory Baronian, Laetitia My, Yong Zhang, Leon Espinosa, Renaud Vincentelli, Benjamin P. Bratton, Joshua W. Shaevitz, Virginie Molle, Martin Howard, and Tâm Mignot, "A gated relaxation oscillator mediated by FrzX controls morphogenetic movements in Myxococcus xanthus," Nature Microbiology **3**, 948–959 (2018).

[11] Filipe Tostevin, Manon Wigbers, Lotte Søgaard-Andersen, and Ulrich Gerland, "Four different mecha-

[12] M. Das, T. Drake, D. J. Wiley, P. Buchwald, D. Vavylonis, and F. Verde, "Oscillatory Dynamics of Cdc42 GTPase in the Control of Polarized Growth," Science **337**, 239–243 (2012).

[13] Bin Xu and Alexandra Jilkine, "Modeling the Dynamics of Cdc42 Oscillation in Fission Yeast," Biophysical Journal **114**, 711–722 (2018).

[14] K. Bar-Eli and W. Geiseler, "Mixing and relative stabilities of pumped stationary states," The Journal of Physical Chemistry **85**, 3461–3468 (1981).

[15] Thomas Litschel, Michael M. Norton, Vardges Tserunyan, and Seth Fraden, "Engineering reaction–diffusion networks with properties of neural tissue," Lab on a Chip **18**, 714–722 (2018).

[16] Michael M. Norton, Nathan Tompkins, Baptiste Blanc, Matthew Carl Cambria, Jesse Held, and Seth Fraden, "Dynamics of Reaction-Diffusion Oscillators in Star and other Networks with Cyclic Symmetries Exhibiting Multiple Clusters," Physical Review Letters **123**, 148301 (2019).

[17] Robert D. Holt, "Population dynamics in two-patch environments: Some anomalous consequences of an optimal habitat distribution," Theoretical Population Biology **28**, 181–208 (1985).

[18] Bernd Blasius, Amit Huppert, and Lewi Stone, "Complex dynamics and phase synchronization in spatially extended ecological systems," Nature **399**, 354–359 (1999).

[19] Yacov Salomon, Sean R. Connolly, and Lance Bode, "Effects of asymmetric dispersal on the coexistence of competing species," Ecology Letters **13**, 432–441 (2010).

[20] Andrew B. Goryachev and Alexandra V. Pokhilko, "Dynamics of Cdc42 network embodies a Turing-type mechanism of yeast cell polarity," FEBS Letters **582**, 1437–1443 (2008).

[21] N. W. Goehring, P. K. Trong, J. S. Bois, D. Chowdhury, E. M. Nicola, A. A. Hyman, and S. W. Grill, "Polarization of PAR Proteins by Advective Triggering of a Pattern-Forming System," Science **334**, 1137–1141 (2011).

[22] Jacob Halatek and Erwin Frey, "Highly Canalized MinD Transfer and MinE Sequestration Explain the Origin of Robust MinCDE-Protein Dynamics," Cell Reports **1**, 741–752 (2012).

[23] Philipp Khuc Trong, Ernesto M Nicola, Nathan W Goehring, K Vijay Kumar, and Stephan W Grill, "Parameter-space topology of models for cell polarity," New Journal of Physics **16**, 065009 (2014).

[24] J. Halatek and E. Frey, "Rethinking pattern formation in reaction–diffusion systems," Nature Physics **14**, 507 (2018).

[25] Fridtjof Brauns, Jacob Halatek, and Erwin Frey, "Phase-Space Geometry of Mass-Conserving Reaction-Diffusion Dynamics," Physical Review X **10**, 041036 (2020).

[26] Fridtjof Brauns, Grzegorz Pawlik, Jacob Halatek, Jacob Kerssemakers, Erwin Frey, and Cees Dekker, "Bulk-surface coupling identifies the mechanistic connection between Min-protein patterns in vivo and in vitro," Nature Communications **12**, 3312 (2021).

[27] Fridtjof Brauns, Henrik Weyer, Jacob Halatek, Junghoon Yoon, and Erwin Frey, "Wavelength Selection by Interrupted Coarsening in Reaction-Diffusion Systems," Physical Review Letters **126**, 104101 (2021).

nisms for switching cell polarity," PLOS Computational Biology **17**, e1008587 (2021).

[28] Manon C. Wigbers, Fridtjof Brauns, Tobias Hermann, and Erwin Frey, "Pattern localization to a domain edge," Physical Review E **101**, 022414 (2020).

[29] Yoichiro Mori, Alexandra Jilkine, and Leah Edelstein-Keshet, "Wave-Pinning and Cell Polarity from a Bistable Reaction-Diffusion System," Biophysical Journal **94**, 3684–3697 (2008).

[30] William R. Holmes, May Anne Mata, and Leah Edelstein-Keshet, "Local Perturbation Analysis: A Computational Tool for Biophysical Reaction-Diffusion Models," Biophysical Journal **108**, 230–236 (2015).

[31] Rocky Diegmiller, Hadrien Montanelli, Cyrill B. Muratov, and Stanislav Y. Shvartsman, "Spherical Caps in Cell Polarization," Biophysical Journal **115**, 26–30 (2018).

[32] Mikiya Otsuji, Shuji Ishihara, Carl Co, Kozo Kaibuchi, Atsushi Mochizuki, and Shinya Kuroda, "A Mass Conserved Reaction–Diffusion System Captures Properties of Cell Polarity," PLoS Computational Biology **3**, e108 (2007).

[33] Jian-Geng Chiou, Samuel A. Ramirez, Timothy C. Elston, Thomas P. Witelski, David G. Schaeffer, and Daniel J. Lew, "Principles that govern competition or co-existence in Rho-GTPase driven polarization," PLOS Computational Biology **14**, e1006095 (2018).

[34] A detailed analysis of two-component MCRD systems in a spatially continuous setting can be found in Ref. [25].

[35] Depending on the nullcline shape, there can be several reactive equilibria for a given total density [25]. We focus here on the case where only one, stable equilibrium exists.

[36] More specifically, this means $\mathcal{D}_{m,c} \ll \sigma_{loc}$, where σ_{loc} is the eigenvalue of the linearized local reaction kinetics with the smallest absolute real part. In the case of a two-component system, $\sigma_{loc} = f_c - f_m$, with $f_\alpha = \partial_\alpha f|_{\mathbf{u}^*}$.

[37] G Meacci, J Ries, E Fischer-Friedrich, N Kahya, P Schwille, and K Kruse, "Mobility of Min-proteins in *Escherichia coli* measured by fluorescence correlation spectroscopy," Physical Biology **3**, 255–263 (2006).

[38] Felipe O. Bendezú, Vincent Vincenzetti, Dimitrios Vavylonis, Romain Wyss, Horst Vogel, and Sophie G. Martin, "Spontaneous Cdc42 Polarization Independent of GDI-Mediated Extraction and Actin-Based Trafficking," PLOS Biology **13**, e1002097 (2015).

[39] Dan Bracha, Mackenzie T. Walls, Ming-Tzo Wei, Lian Zhu, Martin Kurian, José L. Avalos, Jared E. Toettcher, and Clifford P. Brangwynne, "Mapping Local and Global Liquid Phase Behavior in Living Cells Using Photo-Oligomerizable Seeds," Cell **175**, 1467–1480.e13 (2018).

[40] Joe Lutkenhaus, "Assembly Dynamics of the Bacterial MinCDE System and Spatial Regulation of the Z Ring," Annual Review of Biochemistry **76**, 539–562 (2007).

[41] D. M. Raskin and P. A. J. de Boer, "Rapid pole-to-pole oscillation of a protein required for directing division to the middle of Escherichia coli," Proceedings of the National Academy of Sciences **96**, 4971–4976 (1999).

[42] M. Loose, E. Fischer-Friedrich, J. Ries, K. Kruse, and P. Schwille, "Spatial Regulators for Bacterial Cell Division Self-Organize into Surface Waves in Vitro," Science **320**, 789–792 (2008).

[43] V. Ivanov and K. Mizuuchi, "Multiple modes of interconverting dynamic pattern formation by bacterial cell division proteins," Proceedings of the National Academy of Sciences **107**, 8071–8078 (2010).

[44] Katja Zieske and Petra Schwille, "Reconstitution of Pole-to-Pole Oscillations of Min Proteins in Microengineered Polydimethylsiloxane Compartments," Angewandte Chemie International Edition **52**, 459–462 (2013).

[45] Katja Zieske and Petra Schwille, "Reconstitution of self-organizing protein gradients as spatial cues in cell-free systems," eLife **3**, e03949 (2014).

[46] Anthony G. Vecchiarelli, Min Li, Michiyo Mizuuchi, and Kiyoshi Mizuuchi, "Differential affinities of MinD and MinE to anionic phospholipid influence Min patterning dynamics *in vitro*: Flow and lipid composition effects on Min patterning," Molecular Microbiology **93**, 453–463 (2014).

[47] Katja Zieske, Grzegorz Chwastek, and Petra Schwille, "Protein Patterns and Oscillations on Lipid Monolayers and in Microdroplets," Angewandte Chemie International Edition **55**, 13455–13459 (2016).

[48] Yaron Caspi and Cees Dekker, "Mapping out Min protein patterns in fully confined fluidic chambers," eLife **5**, e19271 (2016).

[49] Jonas Denk, Simon Kretschmer, Jacob Halatek, Caroline Hartl, Petra Schwille, and Erwin Frey, "MinE conformational switching confers robustness on self-organized Min protein patterns," Proceedings of the National Academy of Sciences **115**, 4553–4558 (2018).

[50] Shunshi Kohyama, Natsuhiko Yoshinaga, Miho Yanagisawa, Kei Fujiwara, and Nobuhide Doi, "Cell-sized confinement controls generation and stability of a protein wave for spatiotemporal regulation in cells," eLife **8**, e44591 (2019).

[51] Elisa Godino, Jonás Noguera López, David Foschepoth, Céline Cleij, Anne Doerr, Clara Ferrer Castellà, and Christophe Danelon, "De novo synthesized Min proteins drive oscillatory liposome deformation and regulate FtsA-FtsZ cytoskeletal patterns," Nature Communications **10**, 4969 (2019).

[52] Philipp Glock, Fridtjof Brauns, Jacob Halatek, Erwin Frey, and Petra Schwille, "Design of biochemical pattern forming systems from minimal motifs," eLife **8**, e48646 (2019).

[53] Philipp Glock, Beatrice Ramm, Tamara Heermann, Simon Kretschmer, Jakob Schweizer, Jonas Mücksch, Gökberk Alagöz, and Petra Schwille, "Stationary Patterns in a Two-Protein Reaction-Diffusion System," ACS Synthetic Biology **8**, 148–157 (2019).

[54] Martin Howard, Andrew D. Rutenberg, and Simon de Vet, "Dynamic Compartmentalization of Bacteria: Accurate Division in *E. Coli*," Physical Review Letters **87**, 278102 (2001).

[55] Karsten Kruse, "A Dynamic Model for Determining the Middle of Escherichia coli," Biophysical Journal **82**, 618–627 (2002).

[56] K. C. Huang, Y. Meir, and N. S. Wingreen, "Dynamic structures in Escherichia coli: Spontaneous formation of MinE rings and MinD polar zones," Proceedings of the National Academy of Sciences **100**, 12724–12728 (2003).

[57] Fabai Wu, Jacob Halatek, Matthias Reiter, Enzo Kingma, Erwin Frey, and Cees Dekker, "Multistability and dynamic transitions of intracellular Min protein patterns," Molecular Systems Biology **12**, 873 (2016).

[58] Anthony G. Vecchiarelli, Min Li, Michiyo Mizuuchi, Ling Chin Hwang, Yeonee Seol, Keir C. Neuman, and Kiyoshi Mizuuchi, "Membrane-bound MinDE complex acts as a toggle switch that drives Min oscillation coupled

to cytoplasmic depletion of MinD," Proceedings of the National Academy of Sciences **113**, E1479–E1488 (2016).

[59] In the most general form, each such conservation law can be written as $\mathbf{s}^{\mathsf{T}} \cdot \boldsymbol{f} = 0$, where the entries in the "stoichiometric" vector $\mathbf{s}$ account for the components whose sum is conserved. In the case of the Min system, we have $\mathbf{s}_{\mathrm{D}}^{\mathsf{T}} = (1, 1, 1, 1, 0)$ and $\mathbf{s}_{\mathrm{E}}^{\mathsf{T}} = (0, 1, 0, 0, 1)$ for the conservation of MinD and MinE respectively.

[60] Steven H. Strogatz, *Nonlinear Dynamics and Chaos*, 2nd ed. (CRC Press, Boca Raton, 2015).

[61] E. Atlee Jackson, *Perspectives of Nonlinear Dynamics*, 1st ed. (Cambridge University Press, Cambridge, 1989).

[62] Relaxation oscillators are often encountered in simple two-component models of (biological) oscillators and switches; see e.g. the FitzHugh–Nagumo model [78, 79] and Chapter 5 in Ref. [80].

[63] A. Gierer and H. Meinhardt, "A theory of biological pattern formation," Kybernetik **12**, 30–39 (1972).

[64] Lee A. Segel and Julius L. Jackson, "Dissipative structure: An explanation and an ecological example," Journal of Theoretical Biology **37**, 545–559 (1972).

[65] Stephen Smale, "A mathematical model of two cells via Turing's equation," in *Some Mathematical Questions in Biology*, V. American Mathematical Society Lectures on Mathematics in the Life Sciences, Vol. 6 (American Mathematical Society, Providence, 1974) pp. 15–26.

[66] Eugene M. Izhikevich, *Dynamical Systems in Neuroscience: The Geometry of Excitability and Bursting*, Computational Neuroscience (MIT Press, Cambridge, Mass, 2007).

[67] Béla Novák and John J. Tyson, "Design principles of biochemical oscillators," Nature Reviews Molecular Cell Biology **9**, 981–991 (2008).

[68] James E. Ferrell, Tony Yu-Chen Tsai, and Qiong Yang, "Modeling the Cell Cycle: Why Do Certain Circuits Oscillate?" Cell **144**, 874–885 (2011).

[69] Raphaela Geßele, Jacob Halatek, Laeschkir Würthner, and Erwin Frey, "Geometric cues stabilise long-axis polarisation of PAR protein patterns in C. elegans," Nature Communications **11**, 539 (2020).

[70] Erfei Bi and Hay-Oak Park, "Cell Polarization and Cytokinesis in Budding Yeast," Genetics **191**, 347–387 (2012).

[71] Ben Klünder, Tina Freisinger, Roland Wedlich-Söldner, and Erwin Frey, "GDI-Mediated Cell Polarization in Yeast Provides Precise Spatial and Temporal Control of Cdc42 Signaling," PLOS Computational Biology **9**, e1003396 (2013).

[72] Dominik Thalmeier, Jacob Halatek, and Erwin Frey, "Geometry-induced protein pattern formation," Proceedings of the National Academy of Sciences **113**, 548–553 (2016).

[73] Gregory R. Smith, Scott A. Givan, Paul Cullen, and George F. Sprague Jr., "GTPase-Activating Proteins for Cdc42," Eukaryotic Cell **1**, 469–480 (2002).

[74] Dirk Görlich, Michael J. Seewald, and Katharina Ribbeck, "Characterization of Ran-driven cargo transport and the RanGTPase system by kinetic measurements and computer simulation," The EMBO Journal **22**, 1088–1100 (2003).

[75] Sanghyun Kim and M. Elbaum, "A Simple Kinetic Model with Explicit Predictions for Nuclear Transport," Biophysical Journal **105**, 565–569 (2013).

[76] Ogheneochukome Lolodi, Hiroya Yamazaki, Shotaro Otsuka, Masahiro Kumeta, and Shige H. Yoshimura, "Dissecting in vivo steady-state dynamics of karyopherin-dependent nuclear transport," Molecular Biology of the Cell **27**, 167–176 (2016).

[77] Tobias Reichenbach, Mauro Mobilia, and Erwin Frey, "Mobility promotes and jeopardizes biodiversity in rock–paper–scissors games," Nature **448**, 1046–1049 (2007).

[78] Richard FitzHugh, "Impulses and Physiological States in Theoretical Models of Nerve Membrane," Biophysical Journal **1**, 445–466 (1961).

[79] J. Nagumo, S. Arimoto, and S. Yoshizawa, "An Active Pulse Transmission Line Simulating Nerve Axon," Proceedings of the IRE **50**, 2061–2070 (1962).

[80] J. D. Murray, *Mathematical Biology: I. An Introduction*, Interdisciplinary Applied Mathematics, Vol. 17 (Springer New York, New York, NY, 2002).

3 Wavelength selection by interrupted coarsening in reaction-diffusion systems

This section is a publication preprint of the following manuscript published in Phys. Rev. Lett. 126, 104101 (2021)

Wavelength selection by interrupted coarsening in reaction-diffusion systems

F. Brauns,[1,*] H. Weyer,[1,*] J. Halatek,[2] J. Yoon,[1] and E. Frey[1]

[1] *Arnold Sommerfeld Center for Theoretical Physics and Center for NanoScience, Department of Physics, Ludwig-Maximilians-Universtiät München, Theresienstraße 37, D-80333 München, Germany*

[2] *Biological Computation Group, Microsoft Research, Cambridge CB1 2FB, UK*

[*]FB and HW contributed equally to this work.

Wavelength selection by interrupted coarsening in reaction–diffusion systems

Fridtjof Brauns,[1, *] Henrik Weyer,[1] Jacob Halatek,[2] Junghoon Yoon,[1] and Erwin Frey[1, †]

[1] *Arnold Sommerfeld Center for Theoretical Physics and Center for NanoScience,*
Department of Physics, Ludwig-Maximilians-Universität München,
Theresienstraße 37, D-80333 München, Germany
[2] *Biological Computation Group, Microsoft Research, Cambridge CB1 2FB, UK*

Wavelength selection in reaction–diffusion systems can be understood as a coarsening process that is interrupted by counteracting processes at certain wavelengths. We first show that coarsening in mass-conserving systems is driven by self-amplifying mass transport between neighboring high-density domains. We derive a general coarsening criterion and show that coarsening is generically uninterrupted in two-component systems that conserve mass. The theory is then generalized to study interrupted coarsening and anti-coarsening due to weakly-broken mass conservation, providing a general path to analyze wavelength selection in pattern formation far from equilibrium.

To predict the wavelength of patterns in highly non-linear systems is a critical open problem as wavelength selection is ubiquitous in a large range of non-equilibrium systems [1–7]. While the amplitude equation formalism and weakly nonlinear analysis have been highly successful in the vicinity of onset [8], these approaches are not informative for large amplitude patterns far away from onset. For one-component systems, a theory for wavelength selection based on a multiple-scale analysis has been developed [9, 10], but generalizations to multi-component systems have remained elusive.

In this Letter, we propose that wavelength selection in reaction–diffusion systems can be understood as a coarsening process that is interrupted and even reversed by counteracting processes at certain wavelengths. Specifically, we study two-component systems and develop a theory for the mass-conserving case first where coarsening is uninterrupted. We then generalize this theory to account for source terms that break mass conservation and counteract the coarsening process.

While coarsening is well understood as minimization of the free energy for systems relaxing to thermal equilibrium (such as binary mixtures [11, 12]), this reasoning is generally not applicable for non-equilibrium systems such as most reaction–diffusion systems. Two-component mass-conserving reaction–diffusion (MCRD) systems serve as paradigmatic models for intracellular pattern formation [13–19], and are used as phenomenological models for a wide range of systems including precipitation patterns [20], granular media [21], and braided polymers [22]. It has long been speculated that two-component MCRD systems generically exhibit uninterrupted coarsening [16, 19, 23, 24]. However, it has remained unclear whether coarsening always goes to completion in two-component MCRD systems, largely owing to a lack of insight into the underlying physical processes.

Here, we show that coarsening is driven by positive feedback in the competition for mass, derive a simple and quantitative description of coarsening dynamics, and explain why coarsening is generically uninterrupted in two-component MCRD systems. As they are grounded in a phase-space analysis [25], our results are independent of the specific mathematical form of the reaction kinetics.

Building on the insights into the coarsening process in the mass-conserving case, we elucidate and quantify the physical mechanisms underlying wavelength selection in the presence of weak source terms (weakly broken mass conservation). Coarsening arrests when mass competition is balanced by production and degradation. Moreover, domain splitting—owing to the destabilization of plateaus—reverses coarsening. Both are graphically understood by a generalization of the phase-space analysis. Since our approach builds on studying the spatial redistribution of a nearly conserved quantity, we expect that it can be generalized beyond two-component reaction–diffusion systems; for instance, to systems with more components and to hydrodynamic models for active matter systems [3, 26–29].

The general form of a reaction–diffusion system with two components, u and v, can be written as

$$\partial_t u(x,t) = D_u \nabla^2 u + f(u,v) + \varepsilon\, s_1(u,v), \qquad \text{(1a)}$$

$$\partial_t v(x,t) = D_v \nabla^2 v - f(u,v) + \varepsilon\, s_2(u,v), \qquad \text{(1b)}$$

on a domain Ω, with either no-flux or periodic boundary conditions [30]. For specificity, we choose $D_u < D_v$ [31]. The reaction term f describes conversion between u and v while the source terms $s_{1,2}$ with a (small) dimensionless source strength ε break mass conservation.

Let us first analyze the mass-conserving case $\varepsilon = 0$. Then, the total density $\rho = u + v$ is conserved such that the average $\bar\rho = |\Omega|^{-1} \int_\Omega \mathrm{d}x\, \rho(x,t)$ remains constant. The time evolution of ρ is given by [13, 22, 23, 25]

$$\partial_t \rho(x,t) = D_v \nabla^2 \eta(x,t) \qquad \text{(2)}$$

with the *mass-redistribution potential* defined by $\eta := v + (D_u/D_v)u$; the corresponding dynamical equation for $\eta(x,t)$ is given in the SM [32], Sec. 1.1. For stationary patterns $[\tilde u(x), \tilde v(x)]$, the mass-redistribution potential must be spatially uniform, $\eta(x) = \eta_{\text{stat}}$. Based on this one can analyze two-component MCRD systems in the (u,v) phase plane [25]: There, stationary patterns are
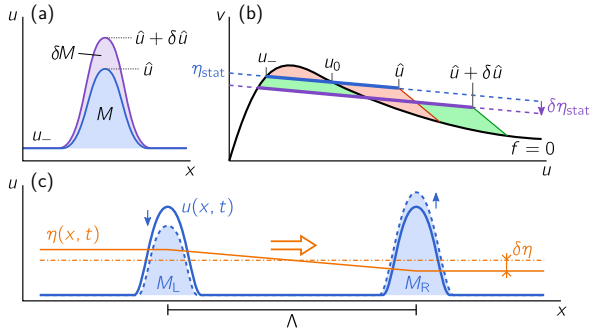
FIG. 1. (a) Illustration of a stationary peak with peak mass M. Increasing the mass to $M + \delta M$ increases the peak amplitude to $\hat{u} + \delta\hat{u}$. (b) Representation of the stationary peak in phase space (thick blue line), which is constrained to the FBS (dashed blue line). The FBS-offset $\eta_{\text{stat}}(M)$ is determined by a balance of total reactive turnovers (areas shaded in red). For a peak with increased mass $M + \delta M$, and thus increased peak amplitude $\delta\hat{u}$, the FBS shifts downwards $\delta\eta_{\text{stat}}$ until total turnover balance is restored (balance of green-shaded areas). (c) After a perturbation of two identical stationary peaks, the gradient in the mass-redistribution potential η (orange line) drives mass-transport between the peaks (orange arrow) such that the larger (smaller) peak grows (shrinks) further (blue arrows).

constrained to a linear subspace, $v + (D_u/D_v)u = \eta_{\text{stat}}$, called *flux-balance subspace* (FBS); see Fig. 1b. The intercept η_{stat} is determined by the balance of the spatially integrated reactive flows (*total turnover balance*), corresponding (approximately) to a balance of areas (shaded in red in Fig. 1b) enclosed by the FBS and the *reactive nullcline* ($f = 0$, NC). The FBS-NC intersection points correspond to the plateau(s) and inflection point(s) of a stationary pattern. Two types of patterns can be distinguished—mesas and peaks. The elementary mesa pattern is composed of two plateaus, connected by an interface (or "kink"), while a peak forms when the maximum density does not saturate in a high-density plateau (Fig. 1a, compare Fig. 2a) [25][33]. We begin the analysis with peak patterns and then generalize the results to mesas.

A mass-competition instability drives coarsening. Coarsening requires the transport of mass between peaks. Because mass transport is diffusive, it is fastest on the shortest length scales; hence, the dominant process is competition for mass between neighboring peaks (Fig. 1a). Thus, as an elementary case, we study two peaks in a 'box' with no-flux boundary conditions. Consider a situation ("coarsening limit") where the peaks are well separated, such that diffusive transport is limiting. We can then approximate the peaks to be in (regional) quasi-steady state (QSS), such that $\eta = \eta_{\text{stat}}(M)$ at a given peak with total mass M. This approximation is commonly applied in thin film theory [34, 35] and Ost-

wald ripening [11, 12].

Starting from two identical, stationary peaks, each with total mass M_0, the dynamics of the mass difference between them ($M_{\text{R,L}} = M_0 \pm \delta M$)—obtained by integration of Eq. (2) over a single peak—is determined by the η-gradients in the plateau between them (indicated by the orange arrow in Fig. 1c). Using QSS at each peak separately, the mass-redistribution potential at the peaks is given by $\eta_{\text{R,L}} = \eta_{\text{stat}} \pm (\partial_M \eta_{\text{stat}}|_{M_0}) \delta M$. Between the peaks, η obeys $\partial_x^2 \eta = 0$ because diffusive relaxation within the plateau is fast compared to the peak evolution (see SM Sec. 2 for details). Thus in 1D, the resulting gradient in η is linear and determined by $\eta = \eta_{\text{R,L}}$ at the peak positions. For a given peak separation Λ, this approximation determines the dynamics of mass redistribution

$$\partial_t \delta M \approx -\frac{2D_v}{\Lambda}\left(\partial_M \eta_{\text{stat}}\big|_{M_0}\right)\delta M =: \sigma_{\text{D}}\,\delta M. \quad (3)$$

The subscript D denotes the diffusion-limited regime. If the growth rate σ_{D} is positive, an instability driven by positive feedback in competition for mass results in coarsening. Hence, the condition for uninterrupted coarsening reads

$$\partial_M \eta_{\text{stat}}(M) < 0, \quad (4)$$

i.e. that $\eta_{\text{stat}}(M)$ is a strictly monotonically decreasing function for all stable stationary single-peak solutions. This recovers a previous, mathematically derived coarsening condition [13, 23]. Importantly, the analysis presented here gives insight into the underlying physical mechanism and shows that not only the criterion for coarsening, but the entire *temporal evolution* of coarsening is determined by $\partial_M \eta_{\text{stat}}$ via Eq. (3) [36]. We learn that the functional dependence of the *mass-redistribution potential* on the peak mass, $\eta_{\text{stat}}(M)$, plays a role analogous to the functional dependence of the chemical potential on the droplet size that drives Ostwald ripening or to the film height in dependence of droplet size that drives coarsening of unstable thin films [34, 35].

Generic coarsening laws for mass-conserving systems. To show that coarsening is uninterrupted, we need to show that the criterion Eq. (4) holds, and continues to hold as small peaks disappear causing the mass of the remaining peaks to increase. For an intuitive argument, consider a single stationary peak with mass M (see Fig. 1a) and its representation in phase space, the blue line in Fig. 1b. Add an amount δM of mass and hold η_{stat} fixed for the moment (for the sake of argument). Fixing η_{stat} also fixes the plateau u_-. Therefore, the additional mass will increase the peak amplitude $\hat{u}$ (Fig. 1b), causing the reactive turnover to the right of u_0 to increase. The resulting imbalance of total turnover entails a net reactive flow that shifts the flux-balance subspace downwards, i.e. lowers η_{stat}, to restore total turnover balance.
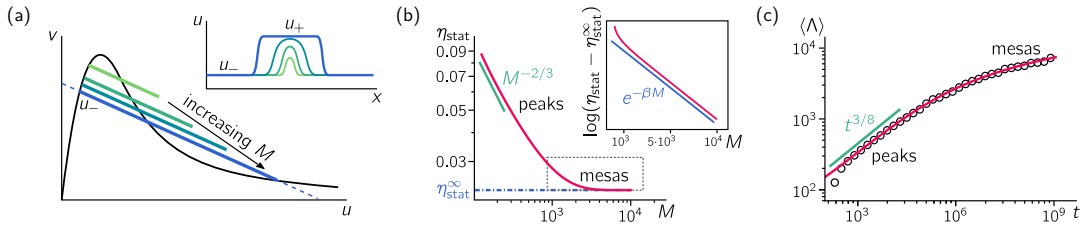
FIG. 2. (a) Illustration of the peak to mesa transition as the total mass M is increased. (b) The function $\eta_{\text{stat}}(M)$ obtained by numerical continuation of the stationary solutions for the reaction kinetics f_{ex}. Crossover from power law for peak patterns (amplitude not saturated) to exponential approach to $\eta_{\text{stat}}^\infty$ for mesa patterns. (c) Coarsening dynamics from finite element simulations for f_{ex} (black circles; mean peak distance averaged over four independent runs started from random initial conditions; parameters: $D_u = 1, D_v = 10^4, \bar\rho = 1.5$ and system size $|\Omega| = 2 \times 10^5$, periodic boundary conditions). The red line shows the analytic prediction based on σ_{D} from $\eta_{\text{stat}}(M)$, shown in (b), via Eq. (3). After an initial transient, power-law coarsening $\Lambda \sim t^{3/8}$ for peaks is observed, which flattens into logarithmic coarsening for mesas.

We conclude that, $\eta_{\text{stat}}(M)$ is generically a monotonically decreasing function. (More rigorous arguments are given in SM Secs. 4 and 5).

Let us now turn to the dynamic coarsening laws. As an example, consider $f_{\text{ex}} = (1+u)v - u/(1+u)$, where the first and second terms may, for instance, describe protein recruitment and first-order enzymatic detachment, respectively. A simple scaling argument [37] yields a power-law relation $\eta_{\text{stat}}(M) \sim M^{-\alpha}$, where the exponent depends on the specific reaction kinetics ($\alpha = 2/3$ for the example above); see Fig. 2b. In a large system containing multiple peaks, the average peak separation $\langle\Lambda\rangle$ is linked to the characteristic peak mass by $\langle M\rangle = (\bar\rho - \rho_-)\langle\Lambda\rangle$, where ρ_- is the total density in the low density plateau between the peaks, and $\langle\cdot\rangle$ denotes an average over the entire system. As peaks collapse, with a typical time given by the inverse growth rate of the mass-competition instability $t \sim \sigma_{\text{D}}^{-1}$, the average peak separation $\langle\Lambda\rangle$ will increase. Combining $\sigma_{\text{D}} \sim -\langle\partial_M\eta_{\text{stat}}\rangle/\langle\Lambda\rangle$ with $\langle\partial_M\eta_{\text{stat}}\rangle \sim \langle M\rangle^{-\alpha-1} \sim (\bar\rho\langle\Lambda\rangle)^{-\alpha-1}$ yields power-law coarsening with $\langle\Lambda\rangle(t) \sim t^{1/(2+\alpha)}$; see Fig. 2c and Fig. S4. Moreover, using appropriate scaling amplitudes, the coarsening trajectories for different average masses $\bar\rho$ can be collapsed onto a single master curve obtained from $\partial_M\eta_{\text{stat}}$ (see SM Sec. 3). Power-law coarsening in 1D has previously been found for peak-like droplets formed during the dewetting of thin liquid films [34].

As peaks collapse, those remaining grow in mass and height. When the density at the peak maximum saturates in a high-density plateau (corresponding to a FBS-NC intersection point in phase space), a mesa pattern starts to form (Fig. 2a, Fig. S3) [38]. For such mesas, somewhat more subtle arguments show that $\eta_{\text{stat}}(M)$ remains a monotonically decreasing function (see SM Sec. 5). In essence, changing M shifts the interface positions and thus changes the width of a mesa's plateau. As the density profile approaches the limiting plateaus $u_\pm(\eta_{\text{stat}}^\infty)$ through exponential tails, $\eta_{\text{stat}}(M)$ approaches $\eta_{\text{stat}}^\infty$ exponentially slowly (see inset in Fig. 2b) where

we define $\eta_{\text{stat}}^\infty$ as the limit of η_{stat} for the stationary pattern on an infinite domain (see SM Sec. 5.1). Using the same scaling arguments as for peaks, one obtains a logarithmic coarsening law for all mesa patterns, as in the one-dimensional Cahn–Hilliard model [40]. For the concrete example f_{ex}, we find excellent agreement between finite-element simulations and $\langle\Lambda\rangle(t)$ obtained from $\eta_{\text{stat}}(M)$ by these scaling arguments (see Fig. 2c). Based on the physical insights presented above, a generalization to more than one spatial dimension is straightforward. For mesa-like droplets with radius R one finds $\eta_{\text{stat}} - \eta_{\text{stat}}^\infty \sim R^{-1}$ which yields power law coarsening with the universal exponent $1/3$ (see SM Sec. 5.4). For peak-like droplets, we expect system-dependent exponents as in 1D.

The limit of large D_v. For $D_v \to \infty$, mass redistribution by v-diffusion becomes instantaneous, such that the reactive conversion between u and v, which drives the growth/shrinking of mesas or peaks, becomes limiting. In this *reaction-limited* case, we find $\sigma_{\text{R}} \approx (\partial_M\eta_{\text{stat}})\, \ell_{\text{int}}\langle f_v\rangle_{\text{int}}$, where ℓ_{int} is the interface width and $\langle\cdot\rangle_{\text{int}}$ denotes the average over the interface region (see SM Sec. 6 for details and numerical verification). Comparing with Eq. (3) shows that the coarsening criterion Eq. (4) holds in both regimes, and the crossover from diffusion- to reaction-limited coarsening occurs at $D_v/\Lambda \approx \ell_{\text{int}}\langle f_v\rangle_{\text{int}}$.

Weakly broken mass conservation. With an understanding for the coarsening dynamics in the strictly mass-conserving system, we now consider the effect of slow production and degradation for $0 < \varepsilon \ll 1$. We will see that these additional processes interrupt coarsening [1, 2, 26, 41] and can reverse it by inducing peak/mesa splitting [5, 7, 42], thus selecting a range of stable pattern wavelengths. In the presence of source terms, the time evolution of the total density ρ is governed by

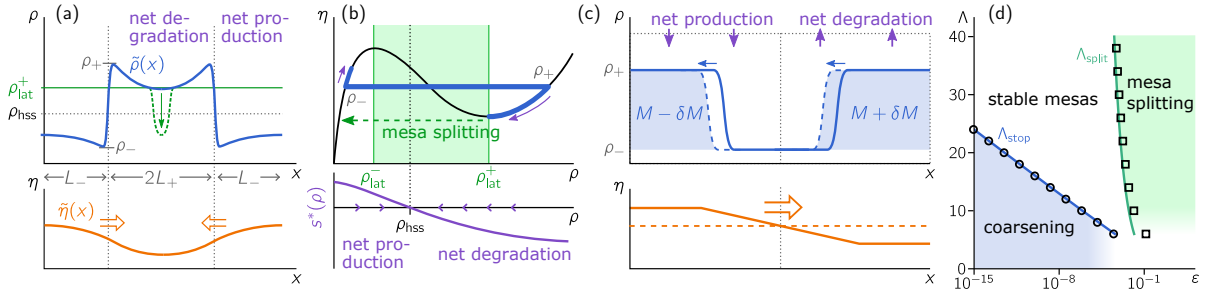$$\partial_t\rho = D_v\partial_x^2\eta + \varepsilon\, s(u,v), \tag{5}$$

FIG. 3. Wavelength selection by weakly broken mass conservation. (a,b) Mesa splitting: (a) real space profiles of $\tilde{\rho}(x)$ and $\tilde{\eta}(x)$, (b) phase space in (ρ, η) coordinates, with the source term in local equilibrium approximation plotted below. The green shaded area indicates the region of lateral instability. (c) Interrupted coarsening due to a balance of production, degradation, and mass redistribution between neighboring mesas. (d) Regimes separated by interrupted coarsening (squares) and mesa splitting (circles) as well as analytic approximations (blue, green lines) for large Λ and small ε. While in the coarsening regime (blue) stationary patterns are unstable, no stationary patterns exist in the mesa-splitting regime (green). In the regime of small Λ and large ε, corrections become large and the approximations do not hold (see SM Sec. 7). Parameters: $D_u = 0.1, D_v = 1, p = 2$.

with the total source $s := s_1 + s_2$. Hence, the average mass $\langle \rho \rangle$ is no longer a control parameter but a time-dependent variable that is determined indirectly by a balance of production and degradation (in short: *source balance*). In phase space, there are now two reactive nullclines, one each for u and v, which both converge to $f = 0$ for $\varepsilon \to 0$. Their intersection point(s) determine(s) the homogeneous steady state (HSS) ρ_{hss} that balances the total source term.

In the following, we restrict ourselves to mesa patterns. To lowest order in ε, source balance determines the 'half lengths' $L_\pm$ of the upper and lower plateaus (see SM Sec. 7). Along the plateaus, the spatial gradients induced by slow production–degradation (ε small) are shallow, such that the dynamics is (approximately) slaved to the nullcline $f = 0$ (see Fig. 3b). This justifies a local equilibrium approximation $s(u, v) \approx s[u^*(\rho), v^*(\rho)] \equiv s^*(\rho)$ in Eq. (5), where the local equilibria are defined by $f(u^*, v^*) = 0$ and $u^* + v^* = \rho$. On the short scale of the interface width, the weak source term is negligible and each interface constrained to a flux-balance subspace. We are now in a position to generalize the phase-space analysis introduced in Ref. [25] and analyze interrupted coarsening and mesa splitting.

(*i*) *Peak/mesa splitting.* Consider the fully coarsened state for $\varepsilon = 0$ and add a small source term such that $s^*(\rho_+) < 0$ and $s^*(\rho_-) > 0$ (i.e. $\rho_- < \rho_{\mathrm{hss}} < \rho_+$, see Fig. 3b) [43]. The upper plateau is depressed by net degradation and is refilled by inflow from the interfaces that connect to the lower plateau where net production prevails. The longer the plateaus (and the larger ε), the more they curve towards ρ_{hss}. Since $\rho_- < \rho_{\mathrm{hss}} < \rho_+$, $\rho(x)$ will eventually enter the interval of lateral instability $[\rho_{\mathrm{lat}}^-, \rho_{\mathrm{lat}}^+]$ (where $\partial_\rho \eta^* < 0$), triggering a nucleation event that results the splitting of the mesa (see Fig. 3a and Movie 2). A simple approximation for the threshold

wavelength $\Lambda_{\mathrm{split}}(\varepsilon)$ where this happens is derived in the SM, Sec. 7.1. Comparison with numerical simulations shows excellent agreement (see Fig. 3d).

(*ii*) *Interrupted coarsening.* Intuitively, production and degradation can counteract the mass-competition instability. To determine the corresponding length scale Λ_{stop} where coarsening arrests, we consider the stability of two neighboring, symmetric mesas. A perturbation that moves a small amount of mass from one mesa to the other (Fig. 3c) has two effects: First, it shifts the mass-redistribution potential at the interfaces, leading to mass transport that further amplifies the perturbation with rate $\sigma_{\mathrm{D}}(\Lambda)\delta M$ as in the strictly mass-conserving situation; cf. Eq. (3). Second, the changed lengths $\delta L = \delta M/(\rho_+ - \rho_-)$ of the two mesas result in net production (degradation) in the shorter (longer) mesa with rate $\varepsilon |s^*(\rho_{\mathrm{outer}})|\delta L$ (indicated by the purple arrows in Fig. 3c). Here ρ_{outer} denotes the total density of the outer plateau (the inner plateau shifts as a whole and does not change in length, see Fig. 3b). Together, the balance of both processes determines Λ_{stop} (see SM Sec. 7.2 for details)

$$\sigma_{\mathrm{D}}(\Lambda_{\mathrm{stop}}) \approx \varepsilon \frac{|s^*(\rho_{\mathrm{outer}})|}{\rho_+ - \rho_-}. \tag{6}$$

As a concrete example, we apply Eq. (6) to the "Brusselator" model [44] ($f = u^2 v - u, s = p - u$), and find excellent agreement with numerics (Fig. 3c). Notably, the simple estimate given by Eq. (6) generalizes a previous, mathematically obtained results [41, 45].

Our analysis shows that the mechanisms underlying mesa splitting and interrupted coarsening are distinct. Notably, the length scale where coarsening stops is much smaller than the length scale where mesas/peaks split (see Fig. 3d). This implies that there are stable periodic patterns for a large, continuous range of wavelengths

(multistability), as was shown previously for the 'Brusselator' [41, 42, 44]. Similarly, multistability of wavelengths was recently found in a hydrodynamic model for flocking [3]. Interestingly, a unique length scale is selected once noise is accounted for [4]. Noise-driven wavelength selection was also observed in an "active Model B" [46]. It would be interesting to study whether this phenomenon is also found in reaction–diffusion systems.

Another interesting open problem are systems with cross diffusion and density-dependent diffusion coefficients (see e.g. Refs. [47–50]). We also expect that our approach can be generalized to systems with more than two components, higher spatial dimensions and also beyond reaction–diffusion systems. In particular, conserved densities (particle numbers) are a generic feature of many active matter systems in which coarsening and length-scale selection ("micro-phase separation") are of growing interest [3, 26–29, 46, 51–57].

FB and HW contributed equally to this work.

---

* fridtjof.brauns@lmu.de
† frey@lmu.de

[1] Fong Liu and Nigel Goldenfeld, "Dynamics of phase separation in block copolymer melts," Physical Review A **39**, 4805–4810 (1989).
[2] Sharon C. Glotzer, Edmund A. Di Marzio, and M. Muthukumar, "Reaction-Controlled Morphology of Phase-Separating Mixtures," Physical Review Letters **74**, 2034–2037 (1995).
[3] Jean-Baptiste Caussin, Alexandre Solon, Anton Peshkov, Hugues Chaté, Thierry Dauxois, Julien Tailleur, Vincenzo Vitelli, and Denis Bartolo, "Emergent Spatial Structures in Flocking Models: A Dynamical System Insight," Physical Review Letters **112**, 148102 (2014).
[4] Alexandre P. Solon, Hugues Chaté, and Julien Tailleur, "From Phase to Microphase Separation in Flocking Models: The Essential Role of Nonequilibrium Fluctuations," Physical Review Letters **114**, 068101 (2015).
[5] Seán M. Murray and Victor Sourjik, "Self-organization and positioning of bacterial protein clusters," Nature Physics **13**, 1006–1013 (2017).
[6] Jian-geng Chiou, Kyle D. Moran, and Daniel J. Lew, "How cells determine the number of polarity sites," bioRxiv , doi:10.1101/2020.05.21.109520 (2020).
[7] Chunyi Gai, David Iron, and Theodore Kolokolnikov, "Localized outbreaks in an S-I-R model with diffusion," Journal of Mathematical Biology (2020), 10.1007/s00285-020-01466-1.
[8] M. C. Cross and P. C. Hohenberg, "Pattern formation outside of equilibrium," Reviews of Modern Physics **65**, 851–1112 (1993).
[9] Paolo Politi and Chaouqi Misbah, "When Does Coarsening Occur in the Dynamics of One-Dimensional Fronts?" Physical Review Letters **92**, 090601 (2004).
[10] Paolo Politi and Chaouqi Misbah, "Nonlinear dynamics in one dimension: A criterion for coarsening and its temporal law," Physical Review E **73**, 036133 (2006).
[11] C. Wagner, "Theorie der Alterung von Niederschlägen durch Umlösen (Ostwald-Reifung)," Zeitschrift für Elektrochemie **65**, 581–591 (1961).
[12] I.M. Lifshitz and V.V. Slyozov, "The kinetics of precipitation from supersaturated solid solutions," Journal of Physics and Chemistry of Solids **19**, 35–50 (1961).
[13] Mikiya Otsuji, Shuji Ishihara, Carl Co, Kozo Kaibuchi, Atsushi Mochizuki, and Shinya Kuroda, "A Mass Conserved Reaction–Diffusion System Captures Properties of Cell Polarity," PLoS Computational Biology **3**, e108 (2007).
[14] Andrew B. Goryachev and Alexandra V. Pokhilko, "Dynamics of Cdc42 network embodies a Turing-type mechanism of yeast cell polarity," FEBS Letters **582**, 1437–1443 (2008).
[15] Steven J. Altschuler, Sigurd B. Angenent, Yanqin Wang, and Lani F. Wu, "On the spontaneous emergence of cell polarity," Nature **454**, 886–889 (2008).
[16] Yoichiro Mori, Alexandra Jilkine, and Leah Edelstein-Keshet, "Wave-Pinning and Cell Polarity from a Bistable Reaction-Diffusion System," Biophysical Journal **94**, 3684–3697 (2008).
[17] Alexandra Jilkine and Leah Edelstein-Keshet, "A Comparison of Mathematical Models for Polarization of Single Eukaryotic Cells in Response to Guided Cues," PLoS Computational Biology **7**, e1001121 (2011).
[18] Philipp Khuc Trong, Ernesto M Nicola, Nathan W Goehring, K Vijay Kumar, and Stephan W Grill, "Parameter-space topology of models for cell polarity," New Journal of Physics **16**, 065009 (2014).
[19] Jian-Geng Chiou, Samuel A. Ramirez, Timothy C. Elston, Thomas P. Witelski, David G. Schaeffer, and Daniel J. Lew, "Principles that govern competition or co-existence in Rho-GTPase driven polarization," PLOS Computational Biology **14**, e1006095 (2018).
[20] Arnd Scheel, "Robustness of Liesegang patterns," Nonlinearity **22**, 457–483 (2009).
[21] Igor Aranson and Lev Tsimring, *Granular Patterns* (Oxford University Press, 2008).
[22] Giada Forte, Michele Caraglio, Davide Marenduzzo, and Enzo Orlandini, "Plectoneme dynamics and statistics in braided polymers," Physical Review E **99**, 052503 (2019).
[23] Shuji Ishihara, Mikiya Otsuji, and Atsushi Mochizuki, "Transient and steady state of mass-conserved reaction-diffusion systems," Physical Review E **75**, 015203(R) (2007).
[24] Yoshihisa Morita and Toshiyuki Ogawa, "Stability and bifurcation of nonconstant solutions to a reaction–diffusion system with conservation of mass," Nonlinearity **23**, 1387–1411 (2010).
[25] Fridtjof Brauns, Jacob Halatek, and Erwin Frey, "Phase-Space Geometry of Mass-Conserving Reaction-Diffusion Dynamics," Physical Review X **10**, 041036 (2020).
[26] M. E. Cates, D. Marenduzzo, I. Pagonabarraga, and J. Tailleur, "Arrested phase separation in reproducing bacteria creates a generic route to pattern formation," Proceedings of the National Academy of Sciences **107**,

11715–11720 (2010).

[27] Michael E. Cates and Julien Tailleur, "Motility-Induced Phase Separation," Annual Review of Condensed Matter Physics **6**, 219–244 (2015).

[28] Benno Liebchen and Demian Levis, "Collective Behavior of Chiral Active Matter: Pattern Formation and Enhanced Flocking," Physical Review Letters **119**, 058002 (2017).

[29] Hugues Chaté, "Dry Aligning Dilute Active Matter," Annual Review of Condensed Matter Physics **11**, 189–212 (2020).

[30] We discuss the dispersion relation of Eq. (1) linearized around a homogeneous steady state in Fig. S1 in the SM.

[31] Our findings immediately generalize to systems with density-independent cross-diffusion, see SM Sec. 1.2.

[32] See Supplemental Material for Movies 1 and 2 as well as technical background information.

[33] Diffusive flux balance ensures that any stationary pattern can be dissected by inserting no-flux boundaries at its extrema.

[34] K. B. Glasner and T. P. Witelski, "Coarsening dynamics of dewetting films," Physical Review E **67**, 016302 (2003).

[35] Len M. Pismen and Yves Pomeau, "Mobility and interactions of weakly nonwetting droplets," Physics of Fluids **16**, 2604–2612 (2004).

[36] For mesa patterns in 1D, $\partial_M \eta_{stat}$ must be calculated for the high- and low-density plateaus separately (see SM Sec. 5).

[37] For a back of the envelope calculation we use density at the pattern inflection point u_0 and the interface width approximation $\ell_{int} \approx \pi/q_{max}|_{u_0,\eta_{stat}}$ [25], and $\hat{u} \approx 2u_0$ to estimate the peak mass $M = \int dx[\tilde{\rho}(x) - \rho_-] \approx \hat{u} \cdot \ell_{int} \approx u_0 \cdot 2\pi/q_{max}|_{\eta_{stat}} \approx 2\pi u_0 \sqrt{D_u/f_u}|_{\eta_{stat}}$. For the example f_{ex}, one finds $f_u \approx \eta_{stat}$ and $u_0 \approx \eta_{stat}^{-1}$, and thus $M \sim \eta_{stat}^{-3/2} = \eta_{stat}^{-1/\alpha}$, for sufficiently large M and $D_v \gg D_u$. Other reaction terms, e.g. with different nonlinearities in the recruitment term, yields other exponent.

[38] If u,v describe (shifted) concentrations (u,v bounded from below) and D_u/D_v is finite, mesas inevitably form at high densities (cf. Fig. 2a). Arbitrarily large peaks form if no third FBS-NC intersection point exists; as, for example, in "Model II" in Ref. [13]. The peak-to-mesa transition has previously been observed for unstable thin films subject to gravity [39].

[39] M. B. Gratton and T. P. Witelski, "Coarsening of unstable thin films subject to gravity," Physical Review E **77**, 016301 (2008).

[40] J.S Langer, "Theory of spinodal decomposition in alloys," Annals of Physics **65**, 53–86 (1971).

[41] T. Kolokolnikov, T. Erneux, and J. Wei, "Mesa-type patterns in the one-dimensional Brusselator and their stability," Physica D: Nonlinear Phenomena **214**, 63–77 (2006).

[42] T. Kolokolnikov, M.J. Ward, and J. Wei, "Self-replication of mesa patterns in reaction–diffusion systems," Physica D: Nonlinear Phenomena **236**, 104–122 (2007).

[43] In steady state, net degradation in high-density regions ($\rho > \rho_{hss}$) and net production in low-density regions ($\rho < \rho_{hss}$) must balance.

[44] I. Prigogine and R. Lefever, "Symmetry Breaking Instabilities in Dissipative Systems. II," The Journal of Chemical Physics **48**, 1695–1700 (1968).

[45] Rebecca McKay and Theodore Kolokolnikov, "Stability transitions and dynamics of mesa patterns near the shadow limit of reaction-diffusion systems in one space dimension," Discrete & Continuous Dynamical Systems - B **17**, 191–220 (2012).

[46] Elsen Tjhung, Cesare Nardini, and Michael E. Cates, "Cluster Phases and Bubbly Phase Separation in Active Fluids: Reversal of the Ostwald Process," Physical Review X **8**, 031080 (2018).

[47] Vladimir K. Vanag and Irving R. Epstein, "Cross-diffusion and pattern formation in reaction–diffusion systems," Phys. Chem. Chem. Phys. **11**, 897–912 (2009).

[48] Federico Rossi, Vladimir K. Vanag, and Irving R. Epstein, "Pentanary Cross-Diffusion in Water-in-Oil Microemulsions Loaded with Two Components of the Belousov-Zhabotinsky Reaction," Chemistry - A European Journal **17**, 2138–2145 (2011).

[49] Amitava Giri, Shreyans Pramod Jain, and Sandip Kar, "Alteration in Cross Diffusivities Governs the Nature and Dynamics of Spatiotemporal Pattern Formation," ChemPhysChem **21**, 1608–1616 (2020).

[50] Giovanni Giunta, Hamid Seyed-Allaei, and Ulrich Gerland, "Cross-diffusion induced patterns for a single-step enzymatic reaction," Communications Physics **3**, 167 (2020).

[51] Q.-X. Liu, A. Doelman, V. Rottschafer, M. de Jager, P. M. J. Herman, M. Rietkerk, and J. van de Koppel, "Phase separation explains a new class of self-organized spatial patterns in ecological systems," Proceedings of the National Academy of Sciences **110**, 11905–11910 (2013).

[52] Raphael Wittkowski, Adriano Tiribocchi, Joakim Stenhammar, Rosalind J. Allen, Davide Marenduzzo, and Michael E. Cates, "Scalar Φ4 field theory for active-particle phase separation," Nature Communications **5**, 4351 (2014).

[53] Giuseppe Gonnella, Davide Marenduzzo, Antonio Suma, and Adriano Tiribocchi, "Motility-induced phase separation and coarsening in active matter," Comptes Rendus Physique **16**, 316–331 (2015).

[54] Syeda Sabrina, Matthew Spellings, Sharon C. Glotzer, and Kyle J. M. Bishop, "Coarsening dynamics of binary liquids with active rotation," Soft Matter **11**, 8409–8416 (2015).

[55] Guannan Liu, Adam Patch, Fatmagül Bahar, David Yllanes, Roy D. Welch, M. Cristina Marchetti, Shashi Thutupalli, and Joshua W. Shaevitz, "Self-Driven Phase Transitions Drive *Myxococcus xanthus* Fruiting Body Formation," Physical Review Letters **122**, 248102 (2019).

[56] A. I. Curatolo, N. Zhou, Y. Zhao, C. Liu, A. Daerr, J. Tailleur, and J. Huang, "Engineering cooperative patterns in multi-species bacterial colonies," bioRxiv, doi:10.1101/798827 (2019).

[57] Yuting I. Li and Michael E. Cates, "Non-equilibrium phase separation with reactions: A canonical model and its behaviour," arXiv:2001.02563 [cond-mat] (2020), arXiv:2001.02563 [cond-mat].

4 Pattern localization to a domain edge

This section is a publication preprint of the following manuscript published in

Pattern localization to a domain edge

M. C. Wigbers,[1,*] F. Brauns,[1,*] T. Hermann,[1,*] and E. Frey[1]

[1] *Arnold Sommerfeld Center for Theoretical Physics and Center for NanoScience, Department of Physics, Ludwig-Maximilians-Universtiät München, Theresienstraße 37, D-80333 München, Germany*

[*] MW, FB, and TH contributed equally to this work.

Pattern localization to a domain edge

Manon C. Wigbers,* Fridtjof Brauns,* Tobias Hermann,* and Erwin Frey†

Arnold Sommerfeld Center for Theoretical Physics (ASC) and Center for NanoScience (CeNS),
Department of Physics, Ludwig-Maximilians-Universität München,
Theresienstraße 37, D–80333 München, Germany

(Dated: April 14, 2021)

The formation of protein patterns inside cells is generically described by reaction–diffusion models. The study of such systems goes back to Turing, who showed how patterns can emerge from a homogenous steady state when two reactive components have different diffusivities (e.g. membrane-bound and cytosolic states). However, in nature, systems typically develop in a heterogeneous environment, where upstream protein patterns affect the formation of protein patterns downstream. Examples for this are the polarization of Cdc42 adjacent to the previous bud-site in budding yeast, and the formation of an actin-recruiter ring that forms around a PIP3 domain in macropinocytosis. This suggests that previously established protein patterns can serve as a template for downstream proteins and that these downstream proteins can 'sense' the edge of the template. A mechanism for how this edge sensing may work remains elusive.

Here we demonstrate and analyze a generic and robust edge-sensing mechanism, based on a two-component mass-conserving reaction-diffusion (McRD) model. Our analysis is rooted in a recently developed theoretical framework for McRD systems, termed local equilibria theory. We extend this framework to capture the spatially heterogeneous reaction kinetics due to the template. This enables us to graphically construct the stationary patterns in the phase space of the reaction kinetics. Furthermore, we show that the protein template can trigger a regional mass-redistribution instability near the template edge, leading to the accumulation of protein mass, which eventually results in a stationary peak at the template edge. We show that simple geometric criteria on the reactive nullcline's shape predict when this edge-sensing mechanism is operational. Thus, our results provide guidance for future studies of biological systems, and for the design of synthetic pattern forming systems.

I. INTRODUCTION

A. Background and motivation

Many cellular processes, such as cell division and cell motility, rely crucially on the localization of proteins in space and time. Strikingly, these protein localization patterns can emerge from the collective coordination of transport and local molecular interactions of proteins. Diffusion in the cytosol is a simple means of protein transport that accounts for many self-organization processes [1]. To analyze how the interplay of diffusive protein transport and protein-protein interactions on a nanometer scale influences the protein patterns on the cellular scale, mass-conserving reaction–diffusion models have proven useful [2–18]. The study of reaction–diffusion systems in general goes back to Turing [19], who showed how patterns can emerge from a homogenous steady state when two reactive components have different diffusivities. In cells, differential diffusivities are generic because many proteins have membrane-bound and cytosolic states, where diffusion on the membrane is orders of magnitude slower than in the cytoplasm. Turing's pioneering work [19] has led to vast advances in the field on how protein patterns arise from homogeneous (initial) steady states on spatially homogeneous domains. However, as Turing already pointed out [19], "most of an organism, most of the time, is developing from one pattern into another, rather than from homogeneity into a pattern."

For example, previously formed protein patterns can control pattern formation of proteins downstream by affecting their local interactions, such that the upstream pattern acts as a *spatial template* for the downstream proteins. A biological system where such "templating" has been suggested is macropinocytosis [20]. Here, a high density domain of PIP3 (a charged phospholipid) and a Ras-GTPase[1] have been suggested to serve as a template for a ring of actin recruiters (SCAR complex, Arp2/3), that forms around the PIP3 domain edge [21]. Recruitment of an actomyosin ring, controlled by GTPases, is also key for single-cell wound healing. Following the rupture of the cell wall, two GTPases– Abr and Cdc42 – are recruited to the wound edge, where they organize into two concentric rings of high protein concentration [22]. Cdc42 in turn recruits actomyosin which contracts to close the wound and repair the underlying cytoskeleton. Mutations of Abr, which forms the inner ring, leads to a loss of the outside Cdc42 ring, suggesting hierarchical interaction between Abr and Cdc42 [22]. Thus,

---

* These three authors contributed equally
† frey@lmu.de

---

[1] GTPases are hydrolase enzymes that can bind and hydrolyze guanosine triphosphate (GTP). Ras is a subfamily of small GTPases.

the inner Abr-ring may be pictured as a template for the outer Cdc42-ring. Yet another example where protein patterns act as a spatial template, can be found during cell division in budding yeast. Here, landmark proteins direct the polarization of the GTPase Cdc42, such that the Cdc42 cluster emerges either adjacent to the previous bud-site, or at the opposite cell pole, depending on the cell-type [23]. Various mutations or deletions of individual landmark proteins lead to Cdc42 clusters right on top of the previous bud-site or at a random position [24–26]. Hence, the landmark proteins may be pictured as a template that controls Cdc42 pattern formation. Common to all the above examples is that the downstream proteins localize at the edge of some template. Both the specific (molecular) mechanisms, and the general principles underlying this 'edge sensing' remain elusive.

Here, we present a pattern-forming mechanism capable of robust edge sensing and provide criteria for its operation based on simple geometric relations in the phase space of the reaction kinetics. To find these criteria, we use a recently developed framework, termed *local equilibria theory* which enables us to gain insight into the dynamics of *mass-conserving reaction–diffusion* (McRD) systems [27, 28]. We briefly review the key elements of the local equilibria theory for a paradigmatic model for cell polarization in Section I B. We then introduce a step-like template that imposes heterogeneity in the reaction kinetics, and generalize the framework to study the dynamics of such systems. This enables us to explain why and under which conditions a density peak forms at the edge of the template. Thus, our results may provide guidance for the design of patterns in synthetic systems and may help to identify molecular mechanisms underlying edge-sensing in biological systems.

B.   Local equilibria theory

We consider the dynamics of one protein species on a one-dimensional domain of length L, as in Ref. [28]. The proteins can cycle between a membrane-bound state (concentration $m(x,t)$) and a cytosolic state (concentration $c(x,t)$), with diffusion constants D_m and D_c respectively. In cells, the diffusion constants of membrane-bound proteins and cytosolic proteins are typically widely different, such that $D_m \ll D_c$. The reaction–diffusion equations for the membrane density m and the cytosolic density c read

$$\partial_t m(x,t) = D_m \partial_x^2 m + f(m,c), \qquad (1a)$$

$$\partial_t c(x,t) = D_c \partial_x^2 c \; - f(m,c), \qquad (1b)$$

where the reaction term $f(m,c)$ describes the attachment–detachment dynamics of the proteins. Specific examples of such systems exhibiting self-organized pattern formation can be found in [4, 6, 7, 17]. At the boundaries, we impose no-flux conditions $D_c \partial_x c|_{0,L} = D_m \partial_x m|_{0,L} = 0$. The dynamics conserves total protein density

$$\bar{n} = \frac{1}{L} \int_0^L \mathrm{d}x \; n(x,t), \qquad (2)$$

with the local total density $n(x,t) = m(x,t) + c(x,t)$.

To characterize the dynamics and steady states of McRD systems, we recently introduced a framework, termed *local equilibria theory* [27, 28]. This theory proposes to analyze spatially extended systems as a collection of small diffusively coupled compartments. The local reaction kinetics inside each of the compartments, then serves a proxy for the spatially extended dynamics, enabling a quantitative phase portrait analysis of the spatially extended system in the phase space of reaction kinetics [28]. In the following we briefly review the key results of local equilibria theory for the two-component McRD system and generalize this framework to analyze pattern formation in the presence of a spatial template. For a comprehensive analysis of the two-component McRD system on a homogeneous domain, we refer to Ref. [28].

The reaction kinetics of McRD systems conserves total protein mass, which implies that the reactive flow must point along the reactive phase spaces $n = c+m$, indicated by the gray lines in Fig. 1(a). The reactive flow vanishes along the *reactive nullcline* (NC), given by $f(m,c) = 0$. Intersections of the reactive nullcline with reactive phase spaces, given by the total density (mass) n, determine the reactive equilibria $(m^*(n), c^*(n))$ shown as black dots in Fig. 1(a). Hence, the shape of the nullcline encodes how the reactive equilibria move when total density n is changed, highlighting that the total density n is a *control parameter* for the reaction dynamics. Within each reactive phase space, the flow is directed towards a stable reactive equilibrium, as illustrated by the red arrows in Fig. 1(a).

In a spatially extended system, the total density $n(x,t) = m(x,t) + c(x,t)$ is generically inhomogeneous, and its dynamics is driven by diffusion, as can be seen by adding Eqs. (1a) and (1b)

$$\partial_t n(x,t) = D_c \partial_x^2 \eta(x,t), \qquad (3)$$

where we introduced the *mass-redistribution potential*, defined as [28]

$$\eta(x,t) := c(x,t) + \frac{D_m}{D_c} m(x,t). \qquad (4)$$

To study the interplay of local reactions and diffusive mass-transport in spatially extended systems, local equilibria theory proposes to analyze such systems as a collection of diffusively coupled compartments. These notional compartments are chosen small enough that each of them can be regarded as well-mixed. Thus, local dynamics within each compartment can be characterized in the ODE phase space of reactions which is determined by the density $n(x,t)$ within that compartment. In this
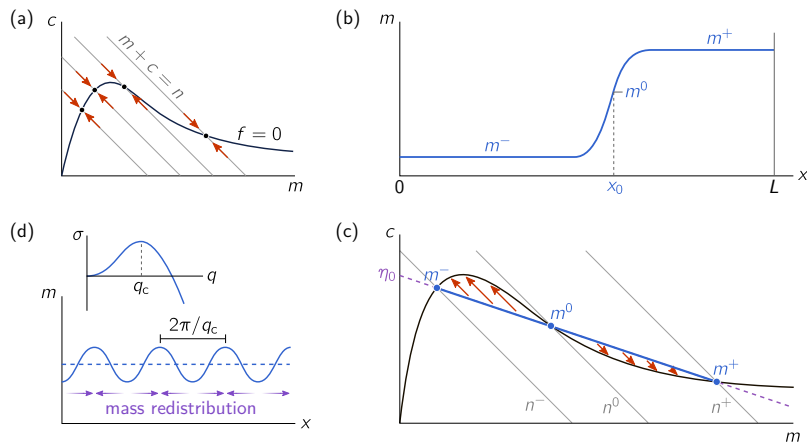
FIG. 1. Illustration of the phase-space geometric analysis for two-component McRD systems. (a) The reactive equilibria (black dots) are given by the intersections between the reactive subspaces $m+c=n$ (grey lines) and the reactive nullcline $f=0$ (black line) in the (m,c)-phase space. Hence, the reactive nullcline encodes the qualitative structure of the reactive flow as illustrated by the red arrows. (b) Sketch of the membrane profile of a mesa pattern composed of a high- and low-density domains, m^+ and m^-, connected by a diffusive interface around the inflection point x_0. (c) Flux-balance construction of the mesa pattern in phase space (cf. (a)). The intersections of the flux-balance subspace (FBS) (purple dashed line) and the reactive nullcline yield the concentrations at the plateaus $m^\pm$ and the inflection point m^0. The balance of net reactive flows in the system (red arrows) determines the FBS-offset η_0. In the regime where the slope of the reactive nullcline is steeper than the slope of the FBS, an homogenous steady state is laterally unstable. (d) Linearization of the dynamics in the vicinity of the homogeneous steady state, yields a dispersion relation for growth rates of the eigenfunctions (Fourier modes indexed by wavenumber q). The fastest growing mode, q_c, dominates the length scale of the initial dynamics.

characterization, the *local (reactive) equilibria* and their stability in each local phase space serve as proxies for the reactive dynamics in each compartment. This becomes clear when one imagines the compartments as isolated, for a given total density profile $n(x)$. Then each compartment will approach a stable local equilibrium, parametrized by the local density $n(x)$. In the spatially coupled system, the total density $n(x,t)$ is diffusively redistributed due to concentration gradients between the compartments (cf. Eq. (3)). Consequently, the local equilibria shift and their stability may change [1, 28]. This interplay between shifting local equilibria and mass transport is at the core of *local equilibria theory*.

In the remainder of this section, we recapitulate two key results from the phase-portrait analysis of two-component McRD systems [28]. We will later generalize this analysis to systems on a spatially heterogeneous domain.

Flux-balance construction. — From the dynamics of the total mass Eq. (3)–(4) it follows that, for any stationary pattern (denoted by $\widetilde{m}(x)$, $\widetilde{c}(x)$), $\widetilde{\eta}(x)$ must be constant in space on a domain with no-flux (or periodic) boundary conditions [28]:

$$\eta_0 = \widetilde{c}(x) + \frac{D_m}{D_c}\widetilde{m}(x) = \text{const.} \tag{5}$$

This relationship defines a linear subspace, termed *flux-balance subspace* (FBS), of the (m,c)-phase space of re-

action kinetics (purple dashed line in Fig. 1(c)). Any stationary pattern must be embedded in a single FBS. This reflects that, in steady state, the diffusive fluxes in m and c are balanced against each other such that there is no net transport of mass.

We can use this condition, Eq. (5), to geometrically construct the steady state density profile in the (m,c)-phase space and from that estimate the real space density profile. The key insight is that we can approximate the concentrations at the plateaus, and the inflection point of the pattern by the local equilibria at the FBS-NC intersections (see Fig. 1(b)). We denote these intersection points by m^-, m^0 and m^+, where $m^\pm$ correspond to the concentrations at the plateaus and m^0 to the concentration at the inflection point of the pattern (Fig. 1(b,c)). Thus, the FBS-offset, η_0, fully determines these concentrations.

To determine the FBS-offset, η_0, one uses that in steady state the net reactive flow within the whole system must be balanced[2]:

$$\int_{m^-(\eta_0)}^{m^+(\eta_0)} \mathrm{d}m\, f\left(m, \eta_0 - \frac{D_m}{D_c}m\right) = 0, \tag{6}$$

---

[2] Note that before integration, Eq. (1a) is multiplied with $\partial_x \widetilde{m}(x)$ as a mathematical trick to substitute the integral over space by an integral over m.

where the plateau concentrations far away from the interface are approximated by the FBS-NC intersections $m^{\pm}(\eta_0)$. This *total turnover balance* condition implicitly determines the FBS-offset η_0. Note that on a large domain (much larger than the interface width, where the approximation $m(0, L) \approx m_{\pm}$ holds), total turnover Eq. (6), and hence η_0, depends only on the function f and the ratio of the diffusion constants. This implies that η_0 is not dependent on the average mass $\bar{n}$ in this approximation.

We will show next that the average mass $\bar{n}$ determines the relative size of the low- and high-density regions and with that the position of the pattern's interface. This interface is marked by the position of the inflection point x_0 of the pattern profile. For a domain size much larger than the interface width, we can neglect the finite width of the interface region, such that the average mass can be approximated by

$$L \bar{n} \approx x_0 \, n^-(\eta_0) + (L - x_0) \, n^+(\eta_0). \qquad (7)$$

Conversely, x_0 can be determined for a given $\bar{n}$. Thus, this geometric construction, termed *flux-balance construction*, shows that significant features of the steady state profile are determined by the shape of the nullcline.

Mass-redistribution instability. — In addition to the construction of stationary patterns, it was shown in Ref. [28] that the nullcline shape determines the stability of a homogeneous steady state, and that the mechanism underlying lateral ("Turing") instability is a mass-redistribution cascade. Specifically, it was found that a homogenous steady state is laterally unstable when the *slope* of the nullcline $\chi(\bar{n}) := \partial_m c^*|_{\bar{n}}$ is steeper than the slope of the FBS (see Section II.D1 in Ref. [28] for a derivation),

$$\chi(\bar{n}) < -\frac{D_m}{D_c}, \qquad (8)$$

which, using the mass-redistribution potential, Eq. (4), is equivalent to $\partial_n \eta^* < 0$. If this condition is fulfilled, high-density regions act as cytosolic sinks, leading to further accumulation of mass and hence a mass-redistribution cascade. This motivates the corresponding name *mass-redistribution instability*.

Starting from a homogeneous steady state with a small random perturbation, the initial dynamics is dominated by the fastest growing eigenfunction of the linearized dynamics. At the onset of this instability there is a dominant eigenfunction that determines the initial dynamics of the system. We can find this dominant eigenfunction by linearizing the system around its homogenous steady state (linear stability analysis). For a homogenous steady state, these eigenfunction are Fourier modes and their growth rates are given by the dispersion relation, shown as inset in Fig. 1(d). The fastest growing mode, q_c, determines the length scale of the initially growing pattern as illustrated in Fig. 1(d)). Subsequently the pattern coarsens into a single peak [6, 7, 17, 28].

C.   Pattern formation with a step-like template

A common feature of the biological examples we discussed in Section I A is that the templates have a sharp edge, and that a downstream protein pattern localizes to this edge. To obtain a conceptual understanding of how such an edge-sensing mechanism might work, we study how an idealized step-like template affects the pattern formation of the two-component McRD model as a paradigmatic example.

We consider a step-like template profile $\theta(x)$ with a sharp edge at x_{E}

$$\theta(x) := \begin{cases} \theta_{\mathrm{A}} & x \leq x_{\mathrm{E}} \\ \theta_{\mathrm{B}} & x > x_{\mathrm{E}} \end{cases}, \qquad (9)$$

as illustrated in Fig. 2(a). Such a template defines two spatial subdomains (labelled A and B). Here, we consider a template that couples to the downstream pattern forming system via the local reactions $f(m, c; \theta(x))$, such that different reactive dynamics

$$f_{\mathrm{A,B}}(m, c) := f(m, c; \theta_{\mathrm{A,B}}), \qquad (10)$$

govern the system in the two subdomains (see Fig. 2(b)).

Pattern forming systems with a step-like (also called "jump-type") heterogeneity have a rich history in the mathematical literature (see e.g. [29–38]) where, they have been studied in the context of front-pinning [36], pulse localization [37], and wavenumber selection [38], to name a few recent examples. These studies predominantly focussed on excitable media and the models studied are not mass-conserving. Furthermore, the prevalent methods employed in these studies are singular perturbation theory (Refs. [39, 40] may serve as general introductions) and normal form theory (see e.g. Ref. [41]). The former method uses matched asymptotics and is based on a separation of spatial scales; the latter applies in the vicinity of a bifurcation.

Here, we choose a conceptually different approach building on the recently developed local equilibria theory [27, 28], specifically the phase-portrait analysis outlined in Sec. I B and introduced in detail in [28]. Our starting point is to use the reactive nullclines of the two subdomains as proxies for the respective reactive flows (Fig. 2(c)). For this purpose, we combine the phase portraits of the subdomains into a single phase portrait as shown in Fig. 2(d). This 'overlaying' of the phase portraits facilitates a geometric analysis of the system with a step-like template based on the approach presented previously for the two-component system on a homogeneous domain [28] (see recap in Sec. I B). Throughout the paper we will use nullcline shapes as illustrated in Fig. 2(d) (see Appendix A for the specific equations and parameters). A different nullcline 'arrangement', and the general role of the nullcline shapes are discussed in Appendix B.

The remainder of the paper is structured as follows. In Sec. II A, we first discuss how the spatial template leads
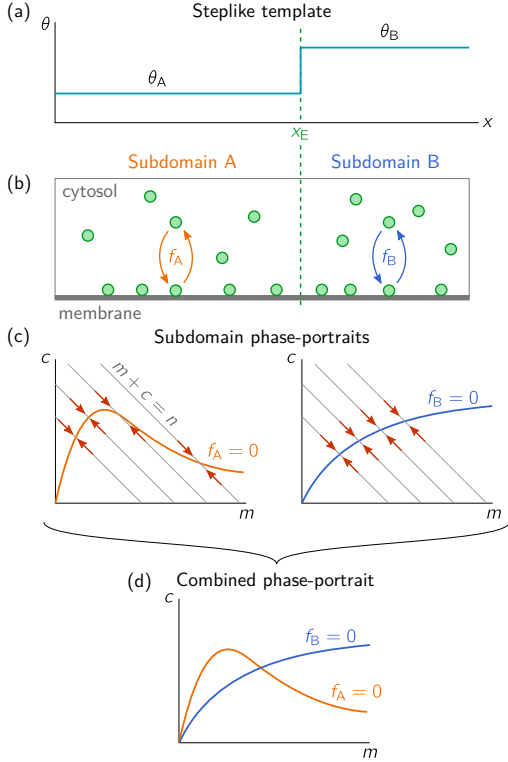
FIG. 2. Illustration of a step-like template (a) that acts on the reaction kinetics defines two subdomains, labelled A and B, with respective reaction kinetics f_A and f_B. (b) We consider a two-component system describing, for example, a single protein species that cycles between a membrane bound and a cytosolic state. (c) The reactive flow due to the reaction kinetics can be visualized in the (m, c)-phase space of concentrations. Due to mass-conservation, the flow points along the reactive phase spaces $m + c = n$ (indicated by gray lines). Along the nullclines $f_{A,B}$, the flow vanishes. Therefore, the reactive flow in each subdomain is qualitatively captured by the shape of the respective nullcline. (d) With the reactive flow encoded by the nullclines, the phase portraits of the two subdomains can be combined ('overlaid') into a single phase space. This combined phase space will be used for the construction of stationary states.

to steady states with a monotonic density profile, which we call *spatially heterogeneous base states*. We analyze these base states in the phase space of reaction kinetics and show that they are determined by a balance of reactive turnovers. Importantly, we find that this balance can break down, such that there are regimes where no base state (i.e. monotonic steady state) exists. In Sec. II B we show that, in these regimes, *stationary patterns* (i.e. non-monotonic steady states) emerge, with a density peak either at the system boundary or at the template edge. Specifically, we show that the peak at the template edge exist if the nullclines intersect at a point where only one of them has negative slope, as illustrated in Fig. 2(d). In

Sec. II C, we introduce the concept of *regional instability* to understand the transition between the monotonic base states to the non-monotonic patterns and the conditions under which a peak emerges at the template edge ('edge sensing'). Importantly, we find simple geometric criterion for edge sensing: The reactive nullclines of the two subdomains have to intersect at a point where only one of them has negative slope. Finally, in Sec. III, we ask how the peak responds to a moving template edge and show that this can lead to depinning or suppression of the peak when the template edge moves too fast.

II. CONSTRUCTION OF STEADY STATES AND THEIR BIFURCATIONS

The goal of this section is to characterize the steady states of the two-component McRD system with a step-like template. These systems generically don't exhibit spatially homogenous states. Non-homogeneous steady states can be categorized based on the monotonicity of their density profiles. In Sec. II A, we characterize the monotonic steady states, which consist of two plateaus connected by a monotonic interface at the template edge x_E, as shown in Fig. 3(a). We call these monotonic steady states the *(spatially) heterogenous base-states*. In subsection B we extend our analysis to non-monotonic steady states which are the 'genuine' self-organized patterns of the system.

Note that we restrict our construction to the nullcline shapes shown in Fig. 2(d) here. Generalizations to other arrangements follow the same principles and can be worked out analogously.

A. Monotonic steady states (base states)

In steady state, the net diffusive flux that redistributes mass must vanish and reactive flows in m and c must be balanced. This balance is encoded in the constraint that a stationary pattern's phase space distribution must be embedded in a flux-balance subspace (cf. Eq. (5)). This constraint is independent of the local reactions, and, hence, also holds when the local reaction are heterogeneous due to a template (purple dotted line in Fig. 3(b)).

Analogously to the construction of mesa patterns in Sec. I B, we can graphically construct the steady-state density profile in real space, as illustrated in Fig. 3(b, e). To that end, we approximate the density profile at the plateaus—where diffusive fluxes cancel everywhere— by the concentration at the FBS-NC intersections, such that the concentration at the plateaus is fully determined by the FBS-offset, η_0. Let us denote the membrane concentration at the FBS-NC intersections as $m_A^-(\eta_0)$, $m_A^0(\eta_0)$ and $m_A^+(\eta_0)$ for subdomain A (orange nullcline) and as $m_B(\eta_0)$ for subdomain B (blue nullcline). For specificity, we consider in the following a base state that approaches the plateaus m_A^- and m_B far away from the
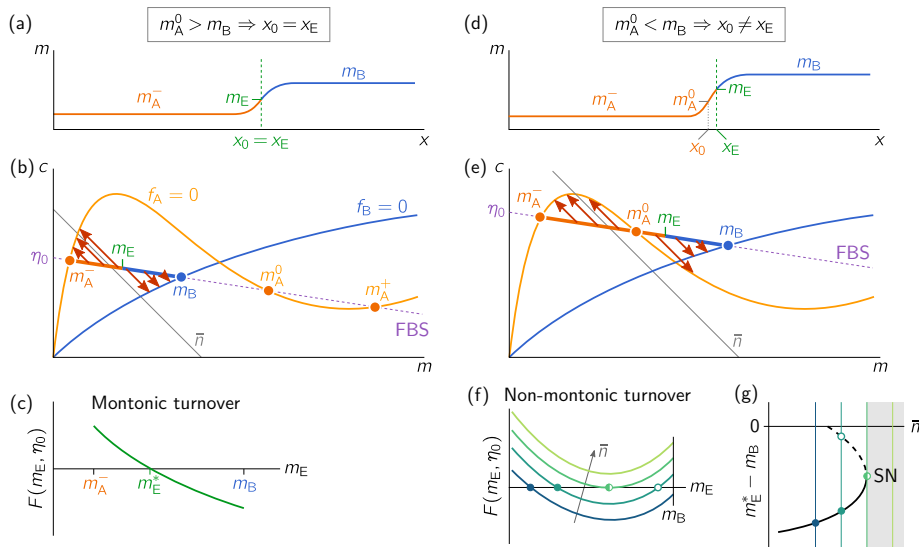
FIG. 3. Illustration of the construction of monotonic steady states (*heterogeneous base states*) in (m, c)-phase space. (a) Density profile with the inflection point at the template edge x_E. (b) Phase space including the reactive nullclines of subdomain A (orange) and B (blue) with the corresponding density distribution (thick orange and blue line). (c) Total turnover as a function of the membrane density at the template edge m_E. Total turnover balance determines the steady state value m_E^*. (d) Density profile for a case where the inflection point of the profile, x_0, lies within subdomain A, that is, when $m_A^0 > m_B$ as illustrated in the corresponding phase space representation (e). (f) In this case, the total turnover becomes a non-monotonic function of m_E, such that total turnover balance may have multiple solutions, or no solution at all. These different cases are sketched here for different average global total densities $\bar{n}$. (g) Bifurcation diagram of the base state, showing the saddle-node bifurcation due to breakdown of total-turnover balance. In the region beyond the saddle-node bifurcation (shaded in gray) no monotonic base state exists. Note that monotonicity enforces $m_E^* - m_B < 0$ here.

template edge. An analogous construction can be made for a monotonic state that connects m_A^+ and m_B.[3]

The conservation of average total density $\bar{n}$ enforces a constraint on the construction of the base state. This constraint can be used to estimate η_0 from the average total density $\bar{n}$. For a domain much larger than the profile interface, the interface region can be neglected and the average total density can be approximated by the weighted average of the plateau densities in the two subdomains

$$\bar{n} \approx x_E \, n_A^-(\eta_0) + (L - x_E) \, n_B(\eta_0), \qquad (11)$$

with n_A^- and n_B the total density at the plateaus in subsystem A and B respectively. This determines an implicit, approximate relation between the control parameter $\bar{n}$ and the FBS-offset η_0.

Upon changing $\bar{n}$, the plateau concentrations of the density profile must change, and hence, η_0 must shift (cf.

Eq. (11)). For the laterally stable plateaus, the nullcline slope at the corresponding FBS-NC intersections (m_A^- and m_B) is larger than the FBS-slope ($\partial_n \eta_{A,B}^*(n) > 0$, cf. NC-slope criterion Eq. (8)). Hence, the relationship $\eta_0(\bar{n})$ must be monotonically increasing for stable base states, as one sees by taking the derivative of Eq. (11) w.r.t η_0, and using that monotonicity of a function implies monotonicity of its inverse.

Note that, even though the base state looks similar to a mesa pattern in a system on a homogeneous domain, the relationship between η_0 and $\bar{n}$ makes a key difference between the two cases. As we discussed in the introduction (Sec. IB), in a system on a homogeneous domain, changing $\bar{n}$ does not affect η_0 in a system much larger than the interface width, but instead shifts the pattern interface (cf. Eq. (7)). In contrast, the interface position of a heterogeneous base state is determined by the position of the template edge x_E. Hence, to accommodate a given average mass $\bar{n}$ the plateau concentrations $n_A^-(\eta_0)$ and $n_B(\eta_0)$, determined by FBS-NC intersection points, must adapt (cf. Eq. (11)). Thus, η_0 of a heterogeneous base state depends directly on $\bar{n}$.

So far we have estimated the concentration at the two plateaus of the monotonic steady state profile. To determine how these two plateaus are connected at the template edge position x_E, we use the condition that in

---

[3] Furthermore, note that we ignore potential intersection points of FBS and B-nullcline at higher masses. In this regime, subdomain B will also exhibit lateral instability. Here, we restrict ourselves to the regime where only subdomain A becomes laterally unstable.

steady state the total reactive turnover in the system must vanish. In the vicinity of the template edge at x_E, the concentrations deviate from the local equilibria, such that there are reactive flows (illustrated by red arrows in Fig. 3(b)). Since the template introduces two subdomains with different reaction kinetics, the total reactive turnover in a system with a template is given by the sum over the turnover in the two subdomains,

$$F(m_E; \eta_0) = F_A(m_E; \eta_0) + F_B(m_E; \eta_0)$$
$$= \int_{m_A^-}^{m_E} dm \, f_A(m, \eta_0 - \frac{D_m}{D_c}m) \qquad (12)$$
$$+ \int_{m_E}^{m_B} dm \, f_B(m, \eta_0 - \frac{D_m}{D_c}m),$$

where m_E is the membrane concentration at the template edge. In steady state, the total turnover $F(m_E; \eta_0)$ must vanish such that all reactive flows in the system balance. Thus, the solution of $F(m_E^*; \eta_0) = 0$ (see Fig. 3(c)) determines the steady state concentration at the template edge $\widetilde{m}(x_E) = m_E^*$. Note that, due to monotonicity, η_0 and m_E^* uniquely identify a base state of a given system.

For small enough $\bar{n}$, the second FBS-NC intersection m_A^0 for the A-nullcline is larger than the FBS-NC intersection for the B-nullcline m_B as illustrated in Fig. 3(b). In this case, both summands of Eq. (12) are monotonic in $m_E \in [m_A^-, m_B]$ because the reactive flow does not change sign within either subdomain, i.e. the inflection point of the profile coincides with the template edge. Hence, there is only a single solution m_E^* that fulfills total turnover balance. For larger $\bar{n}$ (and thus η_0, cf. Eq. (11)), m_A^0 can become smaller than m_B, as illustrated in the sketch in Fig. 3(d,e). This entails that the position where the reactive flows change sign (i.e. inflection point) lies in subdomain A (see Fig. 3(d,e)). Thus, $F_A(m_E; \eta_0)$, and thereby also the total turnover F as a function of m_E becomes non-monotonic and may thus have multiple roots. Indeed, for increasing $\bar{n}$, our flux-balance construction predicts three different regimes: (i) A regime where there is one solution in the interval $[m_A^-, m_B]$, (ii) a regime with two solutions, and (iii) a regime with no solution (as illustrated in the sketch in Fig. 3(f)). In the last regime, total turnover balance becomes impossible for a *monotonic* steady state (base state). In Sec. II B, we will see how total turnover balance can be reached in this regime by a *non-monotonic* steady state.

The roots of F correspond to different base states which we characterize by the amplitude of the density profile in Subdomain B, $m_E^* - m_B$; see Fig. 3(g). For monotonic states (i.e. base states), $m_E^* - m_B$ is negative[4]. At the transition from regime (ii) to (iii), the base state undergoes a saddle-node bifurcation at $\bar{n}_{SN}$. From the flux-balance construction and total turnover balance,

we can estimate the position of this bifurcation. At the saddle-node bifurcation point, the minimum of F coincides with the root of F. From Eq. (12) it follows that F reaches its minimum at $f_A(m_{min}, \eta) = f_B(m_{min}, \eta)$. Thus, this condition, together with $F(m_{min}; \eta_{SN}) = 0$ implicitly determines the value of η_{SN} at the saddle-node bifurcation. From this we can then estimate $\bar{n}_{SN}$ via (11).

To test this approximate construction of steady states, we use specific reaction terms f_A and f_B as specified in Appendix A and compare the steady state profiles obtained from the flux-construction to the profiles obtained from numerical continuation (see Appendix E for a short description of numerical continuation and the comparison of steady states. A more detailed explanation of continuation methods can be found in Ref. [42]). We find that the flux-balance construction gives a estimate of the steady states profiles for sufficiently large system sizes (see Appendix E).

As we noted above, there is also a family of base states which connects a plateau at m_A^+ (instead of m_A^-) in subdomain A to m_B in subdomain B. These base states have a high average mass, and we will refer to them as 'high-mass' base states. Following the same arguments as above, we find that these base states undergo a saddle-node bifurcation when the average total mass is decreased below a critical average mass, analogously to the saddle-node bifurcation of 'low-mass' base states discussed in this section.

In summary, we have shown how to find monotonic steady states (base states) with a flux-balance construction. Notably, we found that for a range of total mass $\bar{n}$, this flux-balance construction has no solution, and hence, there exist no monotonic steady states. In this regime, the steady states must be non-monotonic. We next study these non-monontonic steady states, which we refer to as *patterns*.

B. Non-monotonic steady states (patterns)

To gain some intuition about the structure of the stationary patterns, we first calculate them numerically as a function of the average total density $\bar{n}$ using numerical continuation[5] for a specific choice of the reaction term $f(m, c; \theta)$ specified in Appendix A. The resulting one-parameter bifurcation structure shows that the system exhibits two stable patterns, one with a peak (high density region) at the template edge and one with a peak at the system boundary, respectively (see Fig. 4(a)). In the bifurcation structure, the two branches of stable patterns are connected by a cascade of unstable patterns exhibiting multiple peaks; see Fig. 13 in Appendix E. Their instability can heuristically be understood as a coarsening

---

[4] Note that for high-mass base states, monotonicity enforces $m_E^* - m_B > 0$, in the case of a nullcline arrangement as shown in Fig. 2.

[5] See Appendix E for a brief description of the core idea behind numerical continuation. An excellent overview is provided in Ref. [42].
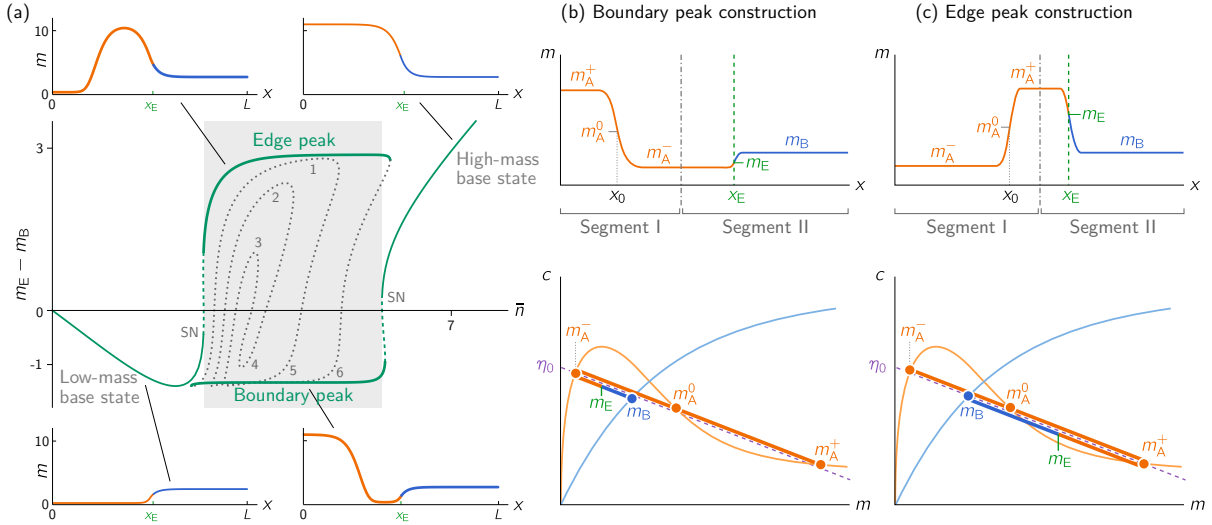
FIG. 4. Bifurcation structure and phase space construction of stationary patterns. (a) Bifurcation structure of stationary states for the average mass, $\bar{n}$, obtained by numerical continuation, together with spatial profiles for the stable steady states (montonic base states and non-monotonic patterns). In the area shaded in gray, no monotonic base states exist. Solid (dashed) lines indicate stable (unstable) branches. The unstable branches in the central region, marked by numbers correspond to unstable patterns with multiple inflection points in subdomain A (see Fig. 13 in Appendix E). In Supplementary Movies 1 and 2 we show finite element simulations in which we adiabatically increase and decrease the mass through the low- and high-mass saddle-node bifurcations. (b,c) Sketches of stable, non-monotonic, stationary patterns together with the corresponding phase space constructions. At the density profile's extremum, marked by the dash dotted vertical line, there are no gradients ($\partial_x \tilde{m} = 0 = \partial_x \tilde{c}$), such that a notional no-flux boundary can be introduced. Thus, the resulting two segments (labelled I and II), can now be studied separately. In the phase portraits, the density distributions of the two segments connect at the extremal concentrations m_A^- and m_A^+, in (a) and (b) respectively. They are shown slightly offset from the FBS (dashed purple line) for visual clarity. The true density distribution must of course be embedded in a single FBS to fulfill diffusive flux-balance. Parameters for the bifurcation diagram: $D_m = 0.01$, $D_c = 0.5$, $\hat{k}_{fb} = 0.25$, $\hat{k}_{off} = 4$, $\theta_B = 20$, $\theta_A = 2$, $L = 10$, $x_E = 5$.

process due to a competition for total density, similarly as in a system on a homogeneous domain [28]. Some more technical aspects of this bifurcation structure are discussed in Appendix E.

Can we use the flux-balance construction to construct non-monotonic steady states as well? At the extrema of any stationary pattern in a two-component McRD system, the gradients (and hence diffusive flux) in *both* membrane and cytosol concentration vanish simultaneously (cf. diffusive flux-balance Eq. (5)). This allows us to place notional reflective boundaries at extrema, effectively splitting the non-monotonic profile into monotonic segments. Thus, we can use the flux-balance construction as described in Sec. II A to construct the steady states in the two segments separately, with the additional constraint of continuity at the boundaries connecting the segments.

The stable patterns in the two-component McRD system with a step-like template have only a single peak, and hence only a single extremum within the domain that splits the system into two segments (labelled I and II; see Fig. 4(b,c)). Segment I is fully embedded in subdomain A, i.e. it is a system on a homogeneous (sub)domain. Hence, for sufficiently large domain size, its

steady state is a mesa pattern[6] as introduced in Sec. I B. The orientation of the mesa pattern in segment I determines whether the density peak is located at the left domain boundary or at the template edge. segment II contains the template edge, such that the steady state in segment II is a heterogeneous base state.

By continuity, the FBS-offset η_0 must be identical in both segments. Recall that for a mesa pattern, η_0 is determined by total turnover balance, and independent of the average mass and domain size in the large domain size limit (see Sec. I B and Ref. [28]). We can thus find η_0 solely by total-turnover balance in segment I, without specifying the position of the boundary between the segments, and without specifying the average masses in the two segments respectively. Instead, given η_0, we find the average mass in segment II, $\bar{n}_{II}$, via Eq. (11), which depends on the choice for the orientation of the mesa pattern in segment I. In segment II, subdomain B plays

---

[6] In the vicinity of the saddle-node bifurcations of these patterns, segment I exhibits a peak pattern instead of a mesa pattern. To obtain an approximation for this case, one would need to generalize the peak approximation as discussed in Ref. [28].

the role of a mass-reservoir that absorbs a fraction of the total average mass and thus reduces the mass available to the mesa pattern in segment I, $\bar{n}_\mathrm{I} = \bar{n} - \bar{n}_\mathrm{II}$. Finally, $\bar{n}_\mathrm{I}$ determines the position of the mesa pattern's interface in segment I via Eq. (7). Similarly, we can construct the (unstable) patterns with multiple peaks by splitting the system into more than two segments.

We conclude that the flux-balance construction fully characterizes the stationary patterns of the system with a step-like template. These steady states exhibit density peaks similar to a system on a homogeneous domain, however, the position of the density peak depends on the template edge position.

We next ask which of the two stable patterns emerges as the base state ceases to exist. To that end, we use finite element simulations and adiabatically increase the total average density in a system such that it passes through the base-state bifurcation (Supplementary Movie 1). The system evolves into a pattern with a peak at the template edge (corresponding to the upper branch in Fig. 4(a)). Upon further increase of $\bar{n}$ the peak widens and eventually transitions into a mesa pattern at the template edge. The right hand interface of the mesa patter remains localized at the template edge while the left hand interface moves into subdomain A to accommodate the additional mass (cf. Eq. 7). Eventually for even larger $\bar{n}$, the mesa pattern ceases to exist as its interface hits the left boundary of the domain. The system then transitions to the 'high-mass' base state which connects the FBS-NC intersection points m_A^+ and m_B. Going backwards by adiabatically decreasing $\bar{n}$, the system passes through the 'high-mass' base state's saddle-node bifurcation. The corresponding regional instability leads to the formation of a trough, rather than a peak, at the template edge. The resulting stationary pattern has a minimum at the template edge and a maximum at the left boundary (corresponding to the lower branch in Fig. 4(a)) (Supplementary Movie 2). Upon further decrease of $\bar{n}$, the interface of this pattern will reach the left boundary of the domain such that the system transitions back into the low-mass base state.

These transitions also take place when the average mass is changed non-adiabatically but still so slow that mass-transport across the system by cytosolic diffusion ($\sim L^2/D_c$) is faster than the rate at which mass is added or removed. Interestingly, when we increase the mass on a non-adiabatic timescale we observe multiple transient patterns, which we characterize in Appendix D. Furthermore, we show that we can get similar transitions between the base state and the patterns if, instead of increasing the average mass, the local reactions $f_\mathrm{A,B}$ in the two subdomains are varied over time (Appendix C).

Taken together, we have shown that the flux-balance construction can be used to construct non-monotonic steady states by splitting the density profile into monotonic segments. This is possible because, the stationary pattern profile can be split at extrema, where all diffusive fluxes vanish. We found that the system can exhibit two patterns, with a density peak either at the system boundary or at the template edge. The peak at the template edge only exists when the two nullclines intersect at a point where only one of them has negative slope. Furthermore, our finite element simulations show that increasing the mass, starting from the low-mass base state, leads to a peak at the template edge. Vice versa, decreasing mass, starting from the high-mass base state leads to a peak at the system boundary. In the next Section we provide a heuristic argument to understand under which conditions the peak emerges at the template edge.

C. Template-induced regional instability

We next want to understand the mechanism of pattern selection as the system goes through the saddle-node bifurcation(s) where the base state ceases to exist. We first show that a (numerical) linear stability analysis explains why either a peak or a trough pattern grows at the template edge, as the system goes through the bifurcation. We then provide a heuristic argument to explain this edge-sensing mechanism, and formulate a geometric criterion under which this mechanism works, based on the shape of the nullclines.

To study how the base state develops into a pattern, as the system goes through the saddle-node bifurcation, we consider a base state $(\widetilde{m}(x), \widetilde{c}(x))$ in the vicinity of the bifurcation point and analyze the dynamics of a small perturbation $(\delta m(x,t), \delta c(x,t))$. The dynamics of the perturbed state, up to linear order is given by:

$$\partial_t \delta m(x,t) = D_m \partial_x^2 \delta m + \tilde{f}_m(x)\delta m + \tilde{f}_c(x)\delta c, \quad (13a)$$

$$\partial_t \delta c(x,t) = D_c \partial_x^2 \delta c - \tilde{f}_m(x)\delta m - \tilde{f}_c(x)\delta c. \quad (13b)$$

The linearized reaction coefficients

$$\tilde{f}_{m,c}(x) = \partial_{m,c} f \big|_{(\widetilde{m}(x), \widetilde{c}(x))} \quad (14)$$

are not homogeneous in space and hence Eq. (13) is a set of linear PDEs with nonconstant coefficients. We seek solutions of the form $\delta m(x,t) = \Phi_m(x)e^{\sigma t}$, $\delta c(x,t) = \Phi_c(x)e^{\sigma t}$. With this ansatz, Eq. (13) turns into the Sturm–Liouville eigenvalue problem

$$\sigma \Phi_m(x) = D_m \partial_x^2 \Phi_m + \tilde{f}_m(x)\Phi_m + \tilde{f}_c(x)\Phi_c, \quad (15a)$$

$$\sigma \Phi_c(x) = D_c \partial_x^2 \Phi_c - \tilde{f}_m(x)\Phi_m - \tilde{f}_c(x)\Phi_c, \quad (15b)$$

for the eigenvalues σ and the associated eigenfunctions $(\Phi_m, \Phi_c)(x)$.

The defining feature of a a saddle-node bifurcation is that one eigenvalue vanishes exactly at the bifurcation point. The associated eigenfunction reveals the flow structure of the dynamics on the slowest timescale close to the bifurcation point (center manifold, see e.g. Ref. [41]). From this we can gain intuition about the fate of the system upon passing through the bifurcation.
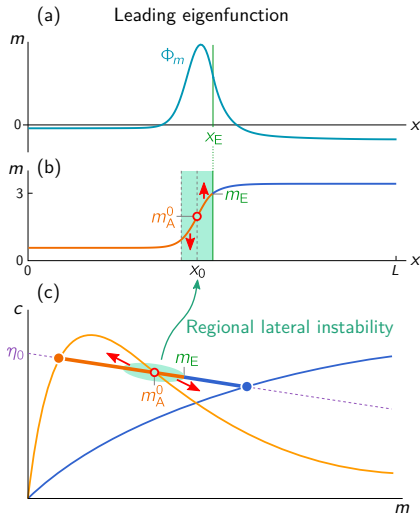
FIG. 5. Regional lateral instability at the base state's saddle-node bifurcation. (a) The numerically calculated eigenfunction, Φ_m, associated to the vanishing eigenvalue at the saddle-node bifurcation is localized at the template edge. (Parameters as in Fig. 4 at the saddle-node bifurcation $\bar{n} \approx 2.65541$). (b) The concentration profile $\widetilde{m}(x)$ of the base state at the saddle-node bifurcation. A spatial region that is fully contained in subdomain A and centered around the profile's inflection point x_0 is marked in green. (c) This spatial region corresponds to a phase space region where the dynamics is guided by a section of the nullcline with a negative slope, i.e. where the system is laterally unstable. (The phase space is shown as a sketch for visual clarity. See Fig. 8(a) in Appendix B for a plot from numerical simulation.)

At the base-state saddle-node bifurcation (marked SN in Fig. 4(a)), the numerically calculated[7] eigenfunction is peaked in the vicinity of the template edge (see Fig. 5(a)). This localized eigenfunction indicates that the density profile will change most in the vicinity of the template edge, giving rise to either a peak or a trough as the system goes through the saddle-node bifurcation.

An intuition why the neutral eigenfunction at the base-state saddle-node bifurcation is peaked at the template edge can be gained from the phase portrait as sketched in Fig. 5(c)). Recall, that the inflection point of the base state's density profile $m_A^0 = \widetilde{m}(x_0)$ lies within subdomain A (cf. Fig. 3(d,e)). Consider a region centered around x_0, fully contained within subdomain A, as indicated in green in Fig. 5(b). In phase space this point lies on a section of the A-nullcline with a slope steeper

than the FBS. Suppose for a moment that this region is isolated from the rest of the system. Then, as the slope of the nullcline at m_A^0 is steeper than the slope of the FBS, the homogeneous equilibrium in this region will be unstable due to a mass-redistribution instability. This instability will set in when the region is large enough to contain the shortest growing mode[8]. We call this a *regional (mass-redistribution) instability*.

A necessary condition to trigger a regional instability at the template edge is that the nullclines of the two subdomains cross at a point where the the A-nullcline fulfills the nullcline-slope criterion for lateral instability, Eq. (8) (see Fig. 6(a)). When this edge-sensing criterion is not fulfilled, as shown in Fig. 6(b), the regional instability sets in at the system boundary first, giving rise to a peak at the system boundary and not at the template edge (as illustrated in Fig. 8(b) in Appendix B). Because the shapes of the nullclines in the two subdomains relative to each other depend on how the template affects the reaction kinetics, the edge-sensing criterion constrains models that can exhibit edge sensing. In Appendix F we demonstrate that the edge-sensing criterion precisely predicts the regime of edge sensing for a phenomenological model of Cdc42. We furthermore show that edge sensing only works if the template increases both the attachment and detachment rate of Cdc42 in one of the subdomains. This may help to identify the relevant molecular players in biological systems.
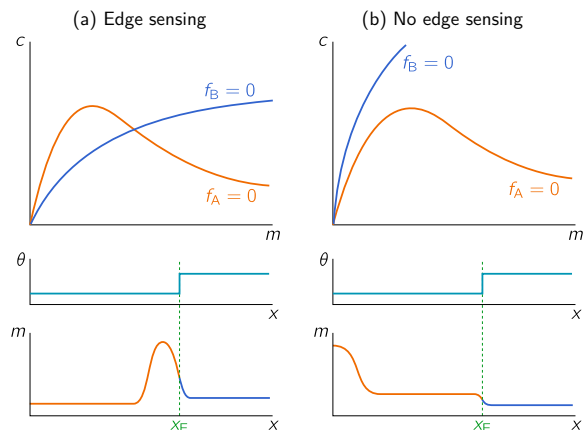

FIG. 6. Nullcline criterion for edge sensing, i.e. the emergence of a stable density peak at the template edge. Edge sensing is possible is the nullclines intersect in a point where one of them has negative slope (a). If they don't intersect (b) or intersect in a point where they have both positive (or both negative) slope, stable peaks only exist at a system boundary, and hence, edge sensing is not possible.

---

[7] The Sturm–Liouville eigenvalue problem at the numerically calculated base-state saddle-node bifurcation is solved by discretizing the spatial derivatives (Laplace operator) and solving the resulting eigenvalue problem numerically in Mathematica. For further details see e.g. Ref. [43].

[8] More precisely, the size of the region centered around the inflection point, $2(x_E - x_0)$, must be larger than the wavelength of the shortest growing mode $\pi/q_{\min}(n_0)$.

The concept of regional instability was already discussed in Ref. [28] in the context of excitability ("nucleation and growth") for a homogeneous domain. There, a stable homogeneous steady state is perturbed by moving mass from the system into small region. When this region contains sufficient mass, it can become laterally unstable and thus formation of a peak pattern is "nucleated." With that, the regional instability at the template edge can also be understood in terms of lateral excitability. From the perspective of subdomain A, the differing reaction kinetics in subdomain B induces a perturbation at the subdomain interface, that is, the template edge (orange line in Fig. 5(b)). In that sense, the base state is a perturbed homogeneous steady state in each subdomain. If in subdomain A, this perturbation becomes large enough to cross the nullcline in a section of negative slope (Fig. 5(c)), it triggers a lateral instability and thus the formation of density peak at the template edge. This relationship to excitability highlights that it is the spatial *gradient* of the reaction kinetics due to the template that localizes the instability. Heuristically this can be pictured as sensing the spatial derivative of the template. Here we focussed on a sharp template edge. For future work, it will be interesting to study also a smooth template edge. Intuitively, if the template gradient is too shallow, it will not induce a laterally unstable region, because the induced deviation from the local equilibria that effectively acts as the perturbation in the analogy to excitability will be too small.

In conclusion, we showed in this section that the template localizes the patterns and determines the position of the instability from which they emerge. Importantly, this instability determines which of the two stable stationary patterns forms when the system passes through a bifurcation of the base state. Finally, we presented a simple geometric criterion, shown in Fig. 6, that determines when the regional instability is localized at the template edge.

III. MOVING TEMPLATE EDGE

Until now we considered pattern formation with a fixed template edge position x_{E}. We next ask what happens when x_{E} moves after a peak at the template edge has been established (Fig. 7).

When the template edge moves, the peak must adapt to the new template edge position. In order to reach the new stationary state, mass must be transported from one side of the peak to the other. Thus, we expect that the peak follows the template edge position as long as the mass is transported faster than the velocity v_{E} at which the template edge moves, i.e. for $v_{\mathrm{E}} \ll D_c/w$, where w is the width of the peak. To test the intuition for this adiabatic case, and study what happens in the non-adiabatic case of a fast-moving template edge, we turn to numerical simulations. To probe a range of template velocities v_{E}, we quadratically increase the template edge
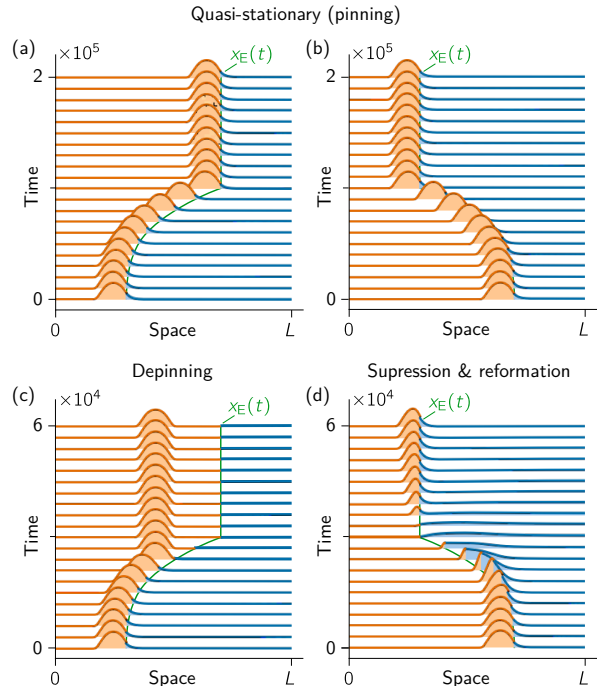

FIG. 7. Time evolution of m-profile due to dynamic template interface position. The supplementary material contains a movie for each of the four scenarios. (a) Slow pull (the template edge moves away from the peak): This results in pinning of the peak to the template edge (see SI Movie 3). (b) Slow push (the template edge moves towards the peak): This results in pinning of the peak to the template edge (see SI Movie 4). (c) Fast pull: This results in depinning as the peak cannot follow the template edge. However, the peak stays where it depins as it is quasi-stable in region A on the observed timescale (see SI Movie 5). (d) Fast push: This results in suppression as the peak is not stable in region B. As the peak dissipates the average mass at the new edge position slowly increases and potentially (if there is enough total mass in the system) leads to to a re-entrance of the peak (see SI Movie 6).

Parameters: $D_m = 0.01$, $D_c = 10$, $k_{\mathrm{on}} = 1$, $\hat{k}_{\mathrm{fb}} = 1$, $k_{\mathrm{off}} = 2$, $\hat{K}_{\mathrm{d}} = 1$, $\bar{n} = 5$, $\theta_{\mathrm{B}} = 20$, $\theta_{\mathrm{A}} = 0.5$, $L = 20$, $x_{\mathrm{E}} = 3/5\,L$, $v_{\mathrm{E}}(t) = \pm 2.4 \times 10^{-14}\,t^2$ in (a) and (b), $v_{\mathrm{E}}(t) = \pm 8.9 \times 10^{-13}\,t^2$ in (c) and (d).

velocity during the simulation. At a distance $0.3\,L$ from the system boundary, the template movement is stopped. Furthermore, we move the interface either to the right, away from the peak Fig. 7(a,c) or to the left, towards the peak Fig. 7(b,d). In the adiabatic case, we find—in agreement with our expectation—that the peak remains pinned to the template edge position (see Fig. 7(a,b) and SI Movies 3 and 4).

In the non-adiabatic case, when the template edge moves faster than the peak can follow by diffusive mass transfer, the peak position will shift relative to the template edge. We find that, when the template moves away

from the peak ('pulling'), the peak depins at a critical velocity and stops moving (see Fig. 7(c) and SI Movie 5). In contrast, when the template moves towards the peak ('pushing'), the peak is suppressed at some critical edge-velocity (see Fig. 7(d) and SI Movie 6). Interestingly, the critical velocity for depinning while pulling is much lower than the critical velocity for suppression while pushing.

To heuristically understand this difference of critical velocities, we take a closer look at how the peak adapts to a shifted template position. Suppose for a moment that we keep the peak profile frozen while shifting the template edge x_{E} by a small amount δx_{E}. This will change the local reactions in the vicinity of the template edge. When the peak profile is now "released", these reactions will lead to changes in the concentrations m and c, and hence in the mass-redistribution potential $\eta(x,t)$ between the original and shifted edge positions x_{E} and $x_{\mathrm{E}} + \delta x_{\mathrm{E}}$. The resulting η gradient leads to mass transport (Eqs. (3)), which in turn causes a movement of the peak.[9] The difference between pulling and pushing, i.e. moving the template edge away from the peak or towards it, is the amplitude of the η gradient that builds up as the template edge is shifted. In the case of pulling, the template edge moves into the flat tail of the peak, such that the η gradient decreases with increasing distance between peak and template edge. In contrast, while pushing, the template edge moves into the steep interface of the peak, leading to an continually increasing η gradient. Only when the template edge has shifted beyond the maximum of the peak, the induced η gradient starts decreasing again.

This effect qualitatively explains the different critical velocities for depinning (while pulling) and suppression (while pushing). In the former case the induced gradients in η, and hence, the rate of mass transport that shift the peak towards the moving template edge are small and decreasing with peak-to-edge distance. Therefore, depinning is self-enhancing. In the case of pushing, the η gradient keeps increasing as the peak-to-edge distance decreases. This in turn, increases the speed of the peak due to faster mass transport. Only when the template edge has crossed the peak maximum, the peak will be suppressed because it then lies mostly within the laterally stable subdomain B that does not support a stable peak.

In summary, we showed that in the case of an adiabatically slow template motion, the peak stays pinned at template edge. In the non-adiabatic case we found a qualitatively and quantitatively different behavior between pushing and pulling. Pulling leads to depinning, while pushing eventually leads to suppression. Furthermore, we heuristically explained why critical velocity for

pulling (depinning) is lower than the critical velocity for pushing (suppresion). Going forward, it would be interesting to study this behavior more systematically, both in numerical simulations and on an analytic level. For example, concepts like response functions [44], projection onto slow manifolds [33] and singular perturbation theory [36, 37] may help to estimate the critical velocities for depinning and suppression.

IV. DISCUSSION

We showed how protein pattern formation can be controlled by a spatial template (e.g. an upstream protein pattern), which acts on the proteins interaction kinetics. In particular, we demonstrated for two-component McRD systems how a step-like template—which defines two subdomains with different reaction kinetics—can localize the formation of a peak pattern to the template edge. We explained this edge-sensing mechanism by a regional (mass-redistribution) instability that emerges at the template edge position. This is in contrast to pattern formation on a homogeneous domain, where the instability is generically "delocalized" (Fourier modes, cf. Fig. 1(d)), such that noisy initial conditions have a strong impact on pattern formation process.

Our analysis is based on a recently developed theoretical framework [27, 28], termed local equilibria theory. This theory proposes to analyze McRD systems as dissected into diffusively coupled compartments, so small that each of the compartments can be considered as well-mixed. For the paradigmatic (minimal) case of two-component systems, this framework enables one to to perform phase-portrait analysis of the interplay between local reactions and diffusive transport in the phase space of the reaction kinetics. Here, we have extended this phase-portrait analysis to incorporate the effect of a step-like heterogeneity of the reaction kinetics in the spatial domain. We were able to construct the bifurcation diagram for the average mass $\bar{n}$, which is a natural control parameter as it can be controlled by production or degradation/sequestration of proteins in cells (e.g. in a cell cycle dependent manner). We found that, at a critical average mass, the system's base state undergoes a saddle-node bifurcation, such that the system transitions to a stationary pattern, with either a peak at the template edge or at the system boundary. The peak forms at the template edge if the template triggers a regional (mass-redistribution) instability at the template edge. The phase-portrait analysis enables us to formulate a geometric criterion for this edge-sensing mechanism. In particular, we show that the step-like template can trigger a regional instability at the template edge, if the nullclines of the reaction kinetics in the two subdomains intersect at a point where one of them has a negative slope (more precisely, a slope steeper than the negative ratio of the diffusion constants, $-D_m/D_c$), as illustrated in Fig. 6. Finally, we showed that the edge-localized

---

[9] A geometric analysis in phase space, similar to the one presented in Figs. 3 and 4, shows that the η gradient is always such that the peak moves in the direction that the template edge was shifted, until it reaches it's new stationary (pinned) position at the shifted edge position.

peak is stable when the template edge is slowly moved and demonstrated that qualitatively different processes—depinning vs. suppression—lead to the loss of the edge-localized peak when the template is shifted too rapidly away from the peak ('pulling') or towards it ('pushing').

We speculate that the edge-sensing mechanism studied here might underly formation of the actomysin ring during macropinocytosis and cellular wound healing, as well as the direction of Cdc42 polarization in budding yeast adjacent to the previous bud-site. In macropinocytosis a high density PIP3 domain has been suggested to act as a template for a ring of actin nucleators that localize to its periphery [21]. Similarly, during cellular wound healing, the inside Abr could act as a template for the outside Cdc42 ring which then drives recruitment of actin via formins [22]. Finally, in budding yeast, landmark proteins that localize to the previous bud-site can be pictured as a template that suppresses Cdc42 accumulation at the previous bud-site and simultaneously localizes Cdc42 cluster to its vicinity [23–26]. Furthermore, the spatio-temporal organization of intracellular membranes, like the Golgi apparatus, endosomes, and the endoplasmatic reticulum, involves cascades of coupled GTPases [45–47]. Hence, we speculate that this organization may rely on similar domain-edge sensing mechanisms.

The edge-sensing criterion (cf. Fig. 6) based on the shape of the nullcline, may provide guidance for the mathematical modeling of these systems and thereby help to identify the key bio-molecular players and processes. The nullcline shapes of a given model constrain the ability of this model for edge-sensing. As an example, we showed for an phenomenological two-component model for Cdc42 pattern formation [4] that edge sensing requires a template which increases both the attachment and detachment rate of Cdc42 in one subdomain. Indeed in single-cell wound healing, the protein Abr could provide such a template for Cdc42 since it is both a guanine exchange factor (GEF) and a GTPase-activation protein (GAP) for Cdc42 [22].

Beyond the understanding of living systems, our results may also advance the field of synthetic biology. Previous studies have explored mechanisms by which a gradient can position a sharp front pattern via a bistable reaction-diffusion system [48, 49]. The edge-sensing mechanism, presented in this paper, is a candidate for a further building block to design spatial protein patterns.

In future studies, it would be interesting to generalize our results beyond the paradigmatic case of a single, stationary, step-like template in one spatial dimension. Templates with multiple steps may be dissected into segments with single steps that can then be studied separately. Furthermore, it has been shown that the geometry of a cell indirectly affect the attachment–detachment kinetics via the ratio of bulk-volume to surface-area [50, 51], and curvature sensing proteins [52]. Another promising direction is to incorporate the dynamics of the template itself as a self-organized pattern-forming system, and include a feedback from the downstream pattern to the template. Such feedback may give rise to complex spatio-temporal behavior like oscillatory patterns and traveling waves that can then be characterized by building on the phase-portrait analysis presented here. Our results on the moving template (Sec. III) and non-adiabatic upregulation of average mass (Appendix D) indicate that the edge sensing works beyond the adiabatic regime.

Finally, even for the elementary case studied here, many important questions remain open. We showed that a moving template will lead to a loss of the edge-localized peak due to depinning (while pulling) or suppression (while pushing) at different critical edge-velocities. In future work, these transitions should be studied in more detail both numerically and analytically, e.g. using a response function formalism [44]. Furthermore, an analytic approach employing asymptotic methods like singular perturbation theory [33, 36, 37, 40] may help to cast our heuristic explanation of the localized eigenfunction, based on the concept of regional instability, into a more rigorous argument. Similarly, such an approach may elucidate the transition from edge-localized peaks to boundary-localized peaks for too fast mass upregulation (cf. Appendix D, Fig. 11). In general, we expect that combining mathematical tools like singular perturbation theory with the local equilibria framework will be a fruitful approach to systematically study complex pattern-forming systems.

Appendix A: Reaction kinetics and template definition

Throughout this paper we use a two-component McRD model on a one-dimensional domain with one protein species (cf. Eq. (1a) and (1b)). The proteins cycle between a cytosolic state (concentration $c(x,t)$) and membrane bound state (concentration $m(x,t)$) as specified by the reaction term $f(m,c)$. Importantly, our results are based on the shape of the reactive nullclines and, hence, don't depend on the specific choice for $f(m,c)$. To illustrate our findings, we use biochemically motivated reaction kinetics, comprising attachment, $a(m)$, and detach-

ment, $d(m)$, reactions

$$f(m,c) := a(m)c - d(m)m .$$ (A1)

Specifically we use

$$a(m) := (k_{on} + k_{fb}\, m) ,$$ (A2a)

$$d(m) := \frac{k_{off}}{K_d + m},$$ (A2b)

as introduced before in Ref. [28]. These reaction kinetics describe a protein species that can attach from the cytosol to the membrane with a rate k_{on} and get recruited from the cytosol to the membrane by membrane bound proteins with a rate k_{fb}. Membrane bound proteins detach from the membrane via an enzymatic process described by first order Michaelis-Menten kinetics, parameterized by the rate k_{off} and the dissociation constant K_d.

We consider systems were the reaction rates are different in subdomains A and B. This externally imposed heterogeneity was introduced as a step-like template in Sec. I C (cf. Eq. (9)). For specificity, we choose a template that affects the reaction rates, such that the reactive nullcline in subdomain B is stretched along the m-axis with respect to the reactive nullcline in subdomain A. To that end, we rescale the feedback rate and the dissociation constant scale with the template value, such that these rates become space dependent

$$k_{fb}(x) := \hat{k}_{fb}/\theta(x),$$ (A3a)

$$K_d(x) := \hat{K}_d\, \theta(x).$$ (A3b)

The reaction term then becomes

$$f(m,c;\theta) = \left(k_{on} + \hat{k}_{fb}\, \frac{m}{\theta(x)}\right) c - \frac{k_{off}\, \frac{m}{\theta(x)}}{\hat{K}_d + \frac{m}{\theta(x)}} .$$ (A4)

For convenience, we do not specify units of length and time. In an intracellular context a typical size would be $L \sim 10\ \mu$m, and typical diffusion constants are $D_m \sim 0.01-0.1\ \mu\text{m}^2\text{s}^{-1}$ on the membrane and $D_c \sim 10\ \mu\text{m}^2\text{s}^{-1}$ in the cytosol. Rescaling to different spatial dimensions is straightforward. To fix a timescale, the kinetic rates can be rescaled with respect to the attachment rate k_{on}. In an intracellular context, typical attachment timescales are on the order of seconds, i.e. $k_{on} \sim \text{s}^{-1}$.

Appendix B: Nullclines without edge-sensing

In Sec. II C in the main text, we analyzed the edge-sensing mechanism based on the reactive nullclines in phase space. In this analysis, the effect of the heterogeneous reaction kinetics, i.e. the template, is captured by the shapes of the reactive nullclines. From our analysis, we found a criterion for the edge-sensing mechanism, as illustrated in Fig. 5. The nullclines need to intersect

at a point where only one nullcline is steeper than FBS (cf. Eq. (8)).

In this appendix, we discuss a case where the criterion for edge sensing is not fulfilled, such that a localization of the regional instability to the edge is not possible, and a peak at the template edge does not exist (cf. Fig. 6(b)). As an example, we consider a template, affecting the reaction kinetics such that the nullcline is stretched along the c-axes instead of the m-axis, as shown in Fig. 8(b).

For the specific attachment–detachment reaction kinetics (Eq. (A2)), the nullclines is stretched along the c-axis via the off-rate while keeping all other rates constant:

$$k_{off}(x) := \hat{k}_{off}\, \theta(x).$$ (B1)

The resulting reaction term then reads

$$f(m,c;\theta) = (k_{on} + k_{fb}\, m)\, c - \theta(x)\frac{\hat{k}_{off}\, m}{K_d + m}.$$ (B2)

Following the same arguments as presented in Sec. II A, we can construct the base states (monotonic steady state). Starting from the low-mass base state, illustrated in Fig. 8(a), and increasing the average mass $\bar{n}$ results in an upwards shift of the FBS by the same argument as presented in Sec. II A. When the mass is further increased the FBS moves to the level where the two FBS-NC intersection points on the A-nullcline, m_A^- and m_A^0, annihilate in a saddle-node bifurcation, as shown in Fig. 8(b). If η_0 increases beyond that point, the base state vanishes. Note that the origin of the saddle-node bifurcation lies in the annihilation of the two FBS-NC intersection points. This is different from the saddle-node bifurcation that occurs for the nullclines we analyzed in Sec. II A in the main text. There, the base state vanishes due to a breakdown of total turnover balance which becomes apparent by the 'annihilation' of the two solutions for m_E of Eq. (12); cf. Fig. 3.

To study the dynamics in the vicinity of the base state bifurcation, we use the concept of regional instability (cf. Sec. II C). The part of the density distribution that enters the laterally unstable region in phase space corresponds to the concentration at the left hand system boundary ($x = 0$) (Fig. 8(b)). Hence, upon crossing the base state's saddle-node bifurcation, a regional instability emerges at this system boundary, and a peak forms there.

Moreover, for nullclines shown in Fig. 8, there is only one way to construct a stationary pattern with a single interface (inflection point) within subdomain A (in addition to the interface imposed by the template step). This pattern always has a density peak at the system boundary ($x = 0$) and decreases monotonically in space towards $x = L$. A stable peak localized to the template edge does not exist in this case.
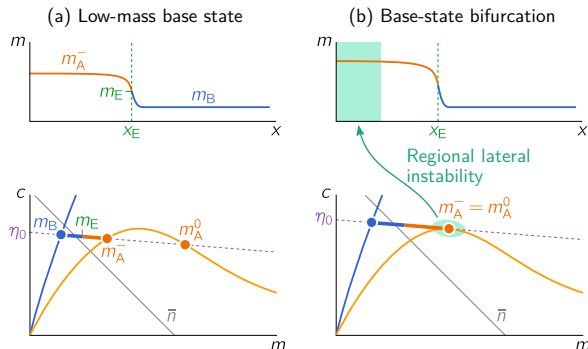
FIG. 8. Base states for nullclines shapes that do not facilitate edge-sensing. (a) The low-mass base state with a high-concentration plateau in subdomain A and a low-concentration plateau in subdomain B. (b) At a critical average mass, the base state undergoes a saddle-node bifurcation. The bifurcation arises from the 'annihilation' of the FBS-NC intersection point m_A^- and m_A^0, and not from the break down of turnover balance as discussed in Sec. II C the main text. In this case, a regional instability is triggered at the system boundary. An adiabatic sweep of $\bar{n}$ through the saddle-node bifurcation of the FBS-NC intersection points is shown in Supplementary Movie 7.

Appendix C: Temporal variation of the template

In Sec. II in the main text, we considered upregulation of average mass $\bar{n}$ while the spatial template was kept constant. One can perform a similar analysis for a varying template, while keeping the average mass constant. In this scenario, not $\bar{n}$ but the parametrization of the template (e.g. θ_A) serves as a bifurcation parameter. In the biological context, this corresponds to a dynamically varying upstream protein pattern.

To demonstrate that varying the template induces equivalent bifurcations as variation of the average mass, we use the template as in the main text (cf. Eq. (A4)) and perform a numeric simulation where we let the template $\theta(x, t)$ slowly vary with time (for simplicity only in subdomain A):

$$\theta(x, t) = \begin{cases} \theta_A(t) & x \leq x_E, \\ \theta_B & x > x_E. \end{cases} \quad \text{(C1)}$$

We initialize the template value in subdomain A at $\theta_A(0) = \theta_B$ and let it change via a sinusoidal ramp to its final value $\theta_A(t_f) = \theta_A^f$.

An exemplary simulation is shown in Fig. 9 and Supplementary Movie 8. At the start of the simulation, the reaction rates, and thus the reactive nullclines, are the same in subdomain A and subdomain B, which is illustrated by the overlapping nullclines in Fig. 9(a). The template is homogeneous, and the corresponding steady state is a homogeneous density profile for sufficiently low average mass. Upon decreasing θ_A, the reaction rates in

subdomain A change, leading to a change in the shape of the reactive nullcline (Fig. 9(b)). The resulting base state is equivalent to the low-mass base state, similar to the case for mass upregulation analyzed in Sec. II A. When θ_A is further decreased, the density profile becomes regionally unstable at the template edge(Fig. 9(c)), which triggers a peak at the template edge (Fig. 9(d)). This shows that the pattern formation process as discussed in the main text can also be realized with a dynamic template.

Appendix D: Non-adiabatic mass upregulation

In Sec. II in the main text, we analyzed the steady states as a function of average mass and found that the system undergoes a transition from base states to patterns through a saddle-node bifurcation. To analyze how the patterns emerge as the system goes through this bifurcation, we performed numerical simulations where we adiabatically increased the average mass by a global cytosolic source with rate κ_s

$$\partial_t c = D_c \, \partial_x^2 c - f(m, c) + \kappa_s, \quad \text{(D1)}$$

which entails $\partial_t \bar{n} = \kappa_s$. In this appendix, we explore the emergence of patterns when the average mass is non-adiabatically increased beyond the base-state bifurcation. We initialize the system at zero mass and increase mass up to a value $\bar{n}_f$ within the regime where no base state exists. Varying the rate of mass inflow κ_s, we find six regimes with qualitatively different transient dynamics (see Supplementary Movies 9-14). Below, we briefly describe the observed dynamics of the density profile in real space in these regimes going from slow to fast κ_s. We then use the (m, c)-phase space and the concept of regional instability (cf. Sec. II C) to heuristically explain the observed dynamics.

1. *Template-edge peak.* For small κ_s, a density peak emerges at the template edge, even though the density profile does not relax to a quasi-steady state. This highlights that the edge-sensing mechanism is robust against rate of mass inflow. (Supplementary Movie 9)

2. *Transition regime.* Here, we observe two peaks emerging simultaneously, one at the outer boundary of subdomain A and one at the template edge. This is an intermediate regime between the boundary peak regime (3) and the template edge peak regime (1), as both peaks emerge simultaneously. (Supplementary Movie 10)

3. *System-boundary peak.* Here, we observe one peak forming at the system boundary at $x = 0$. (Supplementary Movie 11)

4. *Sequential peak formation.* First, a peak forms at the domain boundary of subdomain A, as in the
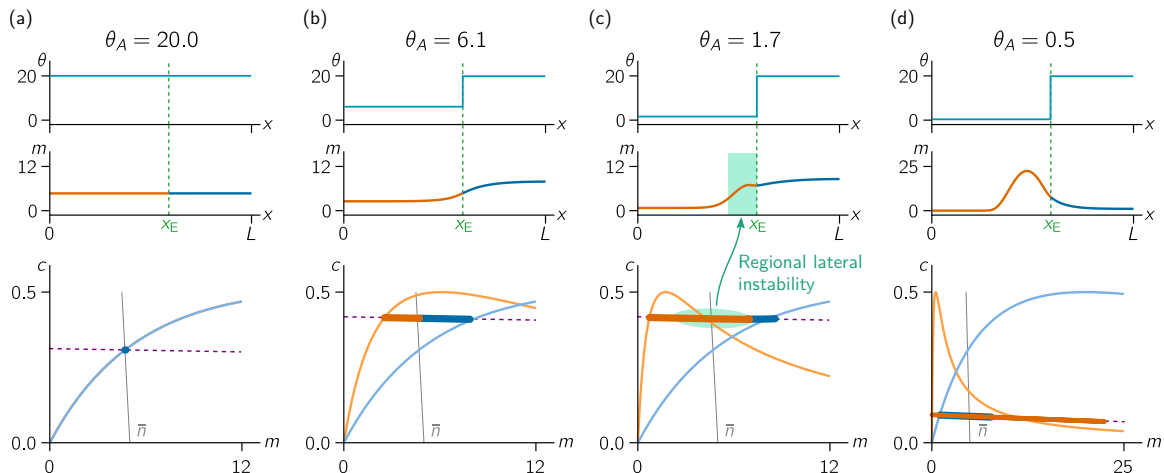
FIG. 9. An adiabatically changing template triggers peak formation at the template edge. See also Supplementary Movie 8. (a) Initial state with a homogeneous template profile $\theta_A = \theta_B$. (b) Base state analogous to Fig. 3. (c) Base state right before the saddle-node bifurcation. The region that becomes laterally unstable in the bifurcation is highlighted in light green in the spatial profile and in phase space (cf. Fig. 5). (d) Peak pattern state after the system transitioned through the bifurcation. This state is qualitatively the same as sketched in Fig. 4(c).
Parameters as in Fig. 7 but with $L = 5$, $\theta_B = 20$, and $\theta_A^f = 0.5$.

system-boundary peak regime (3). Then, after the first peak already formed, another peak forms at the template edge as in regime (1).(Supplementary Movie 12)

5. *Multiple peaks.* Here, the pattern-formation process is very similar to the system-boundary peak regime (3). However, multiple peaks form at the outer boundary of subdomain A simultaneously. (Supplementary Movie 13)

6. *Quenched system.* Here the mass is upregulated almost instantaneously, $\kappa_s^{-1} \to 0$, which is equivalent to a system initialized with the complete mass in the cytosol. This results in a sequence of peaks forms in subdomain A, starting from the template edge in a process akin to front invasion into an unstable state [53]. (Supplementary Movie 14)

Note that all states with multiple peaks (corresponding to multiple inflection points of the pattern profile in subdomain A) are unstable due to coarsening. The final steady state is always a pattern with a peak either at the template edge or at the system boundary $x = 0$.

In Sec. II C and Appendix B, we showed that the formation of a density peak is determined by the position of a regional instability, when the system is in quasi-steady state. The position of the regional instability can be found from a phase portrait analysis, since the nullcline slope criterion (cf. Eq. (8)) determines which part of the density profile becomes unstable. To use the same heuristic for understanding the formation of these transient peaks, we analyze the density distribution in phase space obtained from numerical simulations in these non-adiabatic regimes. When mass is added to the system on a faster timescale than it can relax to its steady state, the density distribution in phase space is no longer embedded in a single FBS. Instead, the density distribution in phase space follows a 'zig-zag' shape, as illustrated in Fig. 10. This indicates that the density in the vicinity of the template edge is still embedded in a FBS, with offset η_{int}, but the density far away from the template edge deviates from this FBS. Instead, these 'quasi-plateaus' are slaved to the nullcline which indicates that they are locally close to reactive equilibrium, and that their relaxation is limited by diffusive mass transport. Accordingly, for faster inflow of mass, the zig-zag shape is more pronounced—that is, the quasi-plateaus deviate more from η_{int}. If inflow of mass is faster than diffusive transport across the quasi-plateaus, a region at the system boundary in subdomain A enters the lateral unstable region in phase space first, as illustrated in Fig. 10(b). This leads to the emergence of a peak at the system boundary in regime (3), and to more complex pattern formation in regimes (4)–(6). In the transition regime (2), mass inflow and mass transport roughly balance, such that a region at the system boundary and a region at the template edge enter the laterally unstable region in phase space at the same time.

The $(L^2/D_c, \kappa_s^{-1})$-phase diagram shown in Fig. 11 confirms the intuition that pattern emergence depends on the competition between the time scales of mass inflow, κ_s, and diffusive mass transport across the system $\sim L^2/D_c$. Indeed, the regime boundaries in the phase diagram are roughly straight lines emanating from the
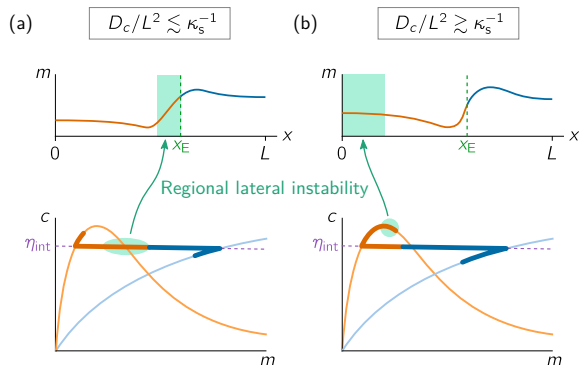
FIG. 10. Effect of non-adiabatic mass upregulation on the pattern formation dynamics. (a) Peak formation at the template edge: The density distribution is not embedded in a single FBS, leading to the 'zig-zag'-shaped density distribution in phase space. The regional instability is still triggered at the template edge, as highlighted by the (green) shaded region. (b) Peak formation at the system boundary: The faster mass-inflow leads to a more pronounced 'zig-zag'-shaped density distribution in phase space. The regional instability is now first triggered at the system boundary. This results in a peak forming at the system boundary as shown in Fig. 4(b).

FIG. 11. Phase diagram for the timescale of mass upregulation (global cytosolic inflow κ_s^{-1}) against the timescale of mass-redistribution across the entire domain (L^2/D_c). Edge sensing, i.e. formation of a single density peak a the template edge, is operational in regime (1), see Supplementary Movie 9. In regimes (2)-(6) a peak at the system boundary ($x = 0$) or multiple peaks form, see Supplementary Movies 10-14. Parameters: $D_m = 0.01$, $D_c = 10$, $k_{on} = 1$, $\hat{k}_{fb} = 1$, $k_{off} = 2$, $\hat{K}_d = 1$, $\theta_A = 0.5$, $\theta_B = 20$, $x_E = 3/5 L$, $\bar{n}_f = 5$.

origin. In particular, the transition from a 'template-edge peak' to a 'system-boundary peak' corresponds to a line $\kappa_s^{-1} \approx L^2/D_c$. This confirms the intuition that edge sensing is only possible when the inflow of mass into the system is slower than the timescale of diffusive mass transport. For comparison, in an intracellular context one has $L \approx 10 \ \mu m$ and $D_c \approx 10 \ \mu m^2 s^{-1}$, such that the timescale of mass transport across the cell is on the order of seconds. This is fast compared to changes in average protein concentrations (for instance, due to protein expression or release from the nucleus). Hence, the edge-sense mechanism is a realistic candidate for template guided intracellular pattern formation.

Appendix E: Numerical continuation, steady state construction and bifurcation scenarios

Numerical continuation. — To numerically calculate steady state solutions of the two-component McRD system (Eq. (1)), we choose a finite-difference discretization of the PDEs. For steady states, this yields an algebraic system of equations that can be solved with an iterative Newton method. The basic idea of numerical continuation is to follow a solution branch through parameter space (see for instance, Ref. [42] for an excellent overview over continuation methods). This "path-following" is often performed by emplying a predictor-corrector scheme: Starting from one solution, the next solution along the branch is predicted from the tangent space of the solution branch which can be obtained from the Jacobian.
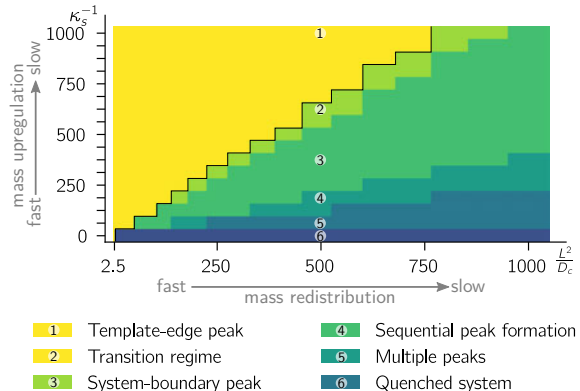
Steady state construction and finite domain size effects. — In order to test the geometric constructions introduced in Sec. II we characterize the steady state of the system with the quantity $m_E^* - m_B$, which must be negative for low-mass base states (monotonic steady states in the low-mass regime, cf. Sec. II A) and positive for non-monotonic steady states (stationary peak pattern localized at the template edge, cf. Sec. II B). We perform numerical continuation and compare the results from the simulation (solid lines in Fig. 12) with the approximation from the geometric construction (red dots and dash-dotted line). The geometric construction serves as a good approximation for the steady for sufficiently large system sizes.

Also note that for small system sizes the base state smoothly transitions into the pattern state (purple line corresponding to $L = 5$ in Fig. 12).

Bifurcation scenario. — The bifurcation scenario connecting the base state and the patterns can be understood as a series of imperfect subcritical pitchfork bifurcations. The imperfection is caused by the template that breaks mirror symmetry of the system. On a homogeneous domain (i.e. without a template), the bifurcations from homogeneous steady state to patterns are subcritical pitchfork bifurcation that become supercritical for small system sizes / large wavenumbers [28]. A more detailed analysis of the bifurcation scenario induced by the step-like template is left for future work. One interesting starting point would be to analyze the two-parameter bifurcation diagram in the $(\bar{n}, \theta_A)$-plane, where the line $\theta_A = \theta_B$ correspond to the homogeneous domain. Alternatively, one can investigate the bifurcation scenario
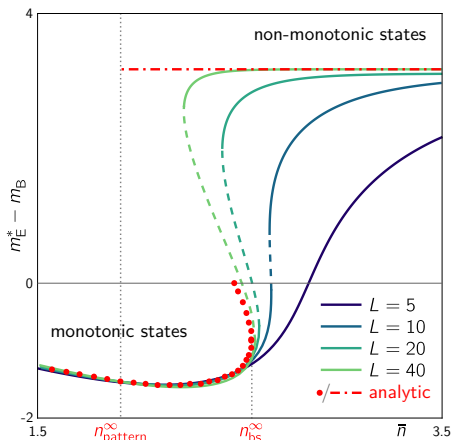
FIG. 12. One-parameter bifurcation structure in $\bar{n}$ (average mass) connecting the low-mass base state (monotonic, i.e. $m_\mathrm{E} < m_\mathrm{B}$ and the peak pattern at the template edge (non-monotonic, i.e. $m_\mathrm{E} > m_\mathrm{B}$). Solid (dashed) lines indicate stable (unstable) branches from numerical continuation for different domain sizes (increasing from dark to light lines). Solutions from the analytic construction of base states in the large domain size limit ($L \to \infty$) are shown as red dots and (position of the saddle-node bifurcation denoted by n_bs^∞). Note that for small domain size ($L = 5$), the saddle-node bifurcations vanish and the base state smoothly transitions into a stable peak pattern upon increasing $\bar{n}$. The red, dash dotted line indicates the analytically constructed edge-localized pattern (limit $L \to \infty$). The lower bound in average mass for the existence of these patterns is denoted by $n_\mathrm{pattern}^\infty$. Fixed parameters as in Fig. 4(a).

in the template edge position (i.e. the $(\bar{n}, x_\mathrm{E})$ parameter plane), where $x_\mathrm{E} = 0$ and $x_\mathrm{E} = L$ correspond to homogeneous domains.

Unstable multi-interface patterns. — The dotted branches in the bifurcation structure Fig. 4(a) correspond to patterns with multiple self-organized interfaces (i.e. more than two inflection points in the spatial profile, since the template edge enforces one inflection point at x_E). Figure 13 shows spatial profiles at the numbered points in Fig. 4(a) representative for the respective branches. The spiral structure of the bifurcation structure reflects an increasing number of of peaks from the outside to the center of the spiral. For the branches numbered 1-3 (4-6) the concentration difference $m_\mathrm{E}^* - m_\mathrm{B}$ is positive (negative), corresponding to a peak (trough) at the template edge.

All multi-interface patterns are unstable due to a competition for mass and decay into one of the two stable patterns, with a peak either at the system boundary or at the template edge, in a coarsening process.
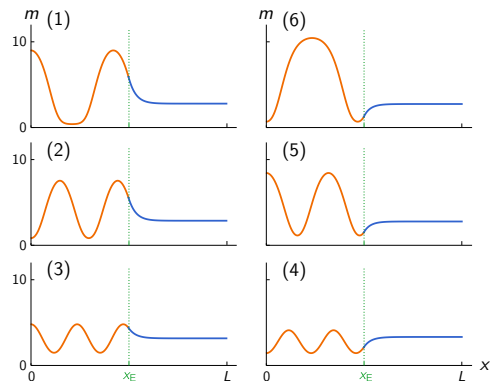

FIG. 13. Spatial profiles representative of the unstable branches numbered (1-6) in the $\bar{n}$-bifurcation diagram Fig. 4(a).

Appendix F: Demonstration of the edge-sensing criterion

To illustrate how the edge sensing criterion might help in modeling of biological systems we consider a concrete biological example. Cdc42 pattern formation is described by a phenomenological two-component model of the form Eq. (1) with the reaction kinetics [4]

$$f(m,c) = \left(k_\mathrm{on} + k_\mathrm{fb} \frac{m^2}{1+m^2}\right)c - k_\mathrm{off}m \qquad (\mathrm{F1})$$

The nullcline $c^*(m)$ determined by $f(m,c^*(m)) = 0$ has a section of negative slope for $k_\mathrm{fb} > 8k_\mathrm{on}$ in the interval $[m_\mathrm{max}, m_\mathrm{min}]$ given by

$$m_\mathrm{min,max} = \sqrt{\frac{1}{1+k_\mathrm{on}/k_\mathrm{fb}}\left(\frac{1 \mp \nu}{2} - \frac{k_\mathrm{on}}{k_\mathrm{fb}}\right)} \qquad (\mathrm{F2})$$

with

$$\nu = \sqrt{1 - 8\frac{k_\mathrm{on}}{k_\mathrm{fb}}}. \qquad (\mathrm{F3})$$

Since cytosolic diffusion is multiple orders of magnitude faster than diffusion of membrane bound Cdc42, we consider the limit $D_c \gg D_m$ where the FBS-slope is zero. Then the criterium for lateral instability is that the nullcline slope be negative $\partial_m c^*(m) < 0$; and the edge-sensing criterion is that nullclines must intersect at a point where one of them has negative slope.

In cellular wound healing, Abr forms a ring of high concentration around the wound edge, followed by the formation of a Cdc42 ring around the Abr ring [22]. Cdc42 then activates the actomyosin machinery that drives the contraction of the cell membrane to close the wound. Protein mutation on Abr and Cdc42 studies suggest that the high density Abr ring acts as a template for Cdc42
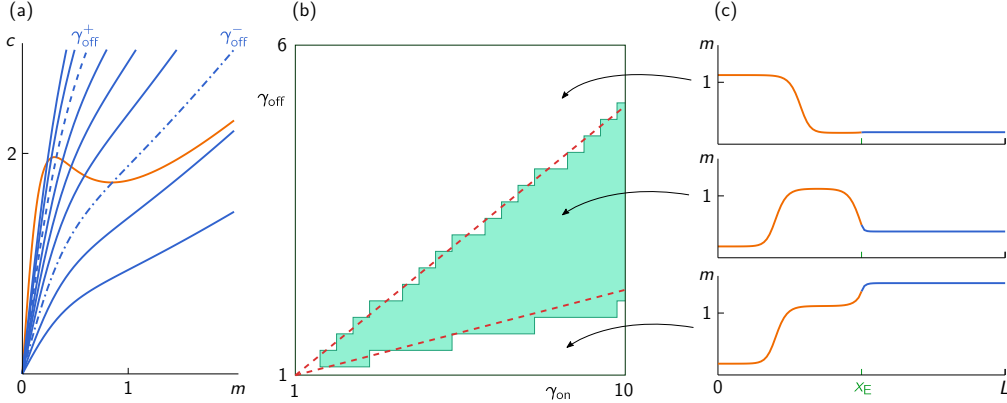
FIG. 14. Demonstration of the edge-sensing criterion for a phenomenological model for Cdc42 pattern formation. (a) Nullclines of the reaction kinetics Eq. (F1) in subdomains A (orange) and B (blue), defined by the reaction rates in Eq. (F4). Multiple B-nullclines are shown for off-rate factors $\gamma_{off} = 1, 1.5, \ldots, 5$ while the on-rate factor is fixed at $\gamma_{on} = 8$. The critical values $\gamma_{off}^{\pm}$ between which the A-nullcline is intersected at negative slope (i.e. the edge-sensing criterion is fulfilled) are shown as dashed and dash-dotted lines respectively. (b) Phase diagram of on- and off-rate factors $(\gamma_{on}, \gamma_{off})$. The shaded region shows the regime where edge-sensing is observed in numerical simulations with adiabatically increasing average mass (cf. Eq. (D1)). Dashed red lines show the curves $\gamma_{off}^{\pm}(\gamma_{on})$, cf. Eq. (F6), between which the edge-sensing criterion is fulfilled. (c) Quasi-stationary density profiles obtained from numerical simulations with adiabatically increasing average mass $\bar{n}$ illustrating the typical pattern emerging from the base-states's saddle-node bifurcation in the three regimes of the $(\gamma_{on}, \gamma_{off})$ phase diagram $(\gamma_{on} = 8;$ top: $\gamma_{off} = 5.5, \bar{n} = 2.9;$ $\gamma_{off} = 3, \bar{n} = 2.35;$ bottom: $\gamma_{off} = 1.5, \bar{n} = 2.24.$). Fixed parameters: $k_{fb} = 1, k_{on} = 0.07, k_{off} = 1, D_m = 10^{-4}, D_c = 0.1, L = 1, x_E = 0.5, \kappa_s = 10^{-5}$.

[22]. Furthermore, it has been shown that Abr acts as both a nucleotide exchange factor (GEF) and a GTPase-activating protein (GAP) for Cdc42 [22]. We therefore model the effect of Abr on the Cdc42 kinetics as a factor increasing both the attachment rate k_{on} and the detachment rate k_{off}. The reaction terms in the two subdomains with low and high Abr density, are thus defined as $f_{A,B}(m, c) = f(m, c; k_{on}^{A,B}, k_{off}^{A,B})$ with

$$k_{on}^A = k_{on}, \qquad k_{on}^B = \gamma_{on} k_{on}, \qquad \text{(F4)}$$
$$k_{off}^A = k_{off}, \qquad k_{off}^B = \gamma_{off} k_{off}, \qquad \text{(F5)}$$

where the factors $\gamma_{on}, \gamma_{off} > 1$ encode the relative enhancement of attachment and detachment rates in subdomain B compared to subdomain A.

The edge-sensing criterion (nullclines intersect at a point where the A-nullcline has negative slope) is fulfilled when the intersection point (m_i, c_i) of the two nullclines, defined by $f_A(m_i, c_i) = 0$ & $f_B(m_i, c_i) = 0$, lies in the range $[m_{max}, m_{min}]$ (see Fig. 14(a)). Solving these equations for γ_{off}, we find that nullclines fulfill the edge-sensing criterion when γ_{off} lies in the range $[\gamma_{off}^-, \gamma_{off}^+]$ as a function of γ_{on}:

$$\gamma_{off}^{\pm}(\gamma_{on}) = \frac{1}{1 + k_{fb}/k_{on}} \left(\frac{k_{fb}}{k_{on}} + \frac{2}{\nu \mp 1} + \gamma_{on} \frac{\nu \mp 3}{\nu \mp 1} \right).$$
$$\text{(F6)}$$

Note that $\gamma_{off}^{\pm}(1) = 1$ corresponds to the singular case where the template has no effect, i.e. the reaction kinetics in the two subdomains are identical. The dashed, red lines in Fig. 14(b) show the curves $\gamma_{off}^{\pm}(\gamma_{on})$ that delineate the regime where the edge-sensing criterion is fulfilled.

To test the criterion, we ran numerical simulations, for different combinations $(\gamma_{on}, \gamma_{off})$. In each simulation, the average mass is adiabatically increased at a rate $\kappa_s = 10^{-5}$, cf. Eq. (D1).

We find three different types of patterns emerging from the base-states's saddle-node bifurcation. Examples of these are shown in Fig. 14(c). The regime where we find edge-localized peaks agrees well with the prediction from the geometric edge-sensing criterion (shown as dashed, red lines in (b)).

Interestingly, the $(\gamma_{on}, \gamma_{off})$-phase diagram shows that both attachment and detachment need to be enhanced in subdomain B. This implies that proteins, like Abr, that have both GEF- and GAP-catalytic domains may play a crucial role for edge sensing by GTPases.

[1] J. Halatek, F. Brauns, and E. Frey, Philosophical Transactions of the Royal Society B: Biological Sciences **373**, 20170107 (2018).

[2] M. Howard, A. D. Rutenberg, and S. de Vet, Physical Review Letters **87** (2001), 10.1103/PhysRevLett.87.278102.

[3] K. C. Huang, Y. Meir, and N. S. Wingreen, Proceedings of the National Academy of Sciences **100**, 12724 (2003).

[4] Y. Mori, A. Jilkine, and L. Edelstein-Keshet, Biophysical Journal **94**, 3684 (2008).

[5] A. B. Goryachev and A. V. Pokhilko, FEBS Letters **582**, 1437 (2008).

[6] S. Ishihara, M. Otsuji, and A. Mochizuki, Physical Review E **75** (2007), 10.1103/PhysRevE.75.015203.

[7] M. Otsuji, S. Ishihara, C. Co, K. Kaibuchi, A. Mochizuki, and S. Kuroda, PLoS Computational Biology **3**, e108 (2007).

[8] J. Halatek and E. Frey, Cell Reports **1**, 741 (2012).

[9] B. Klünder, T. Freisinger, R. Wedlich-Söldner, and E. Frey, PLOS Computational Biology **9**, e1003396 (2013).

[10] P. K. Trong, E. M. Nicola, N. W. Goehring, K. V. Kumar, and S. W. Grill, New Journal of Physics **16**, 065009 (2014).

[11] S. Alonso and M. Bär, EPJ Nonlinear Biomed Phys **2**, 1 (2014).

[12] F. Wu, J. Halatek, M. Reiter, E. Kingma, E. Frey, and C. Dekker, Molecular Systems Biology **12**, 873 (2016).

[13] A. B. Goryachev and M. Leda, Molecular Biology of the Cell **28**, 370 (2017).

[14] S. M. Murray and V. Sourjik, Nature Physics **13**, 1006 (2017).

[15] J. Denk, S. Kretschmer, J. Halatek, C. Hartl, P. Schwille, and E. Frey, Proc Natl Acad Sci USA **115**, 4553 (2018).

[16] D. Cusseddu, L. Edelstein-Keshet, J. Mackenzie, S. Portet, and A. Madzvamuse, Journal of Theoretical Biology (2018), 10.1016/j.jtbi.2018.09.008.

[17] J.-G. Chiou, S. A. Ramirez, T. C. Elston, T. P. Witelski, D. G. Schaeffer, and D. J. Lew, PLOS Computational Biology **14**, e1006095 (2018).

[18] P. Glock, F. Brauns, J. Halatek, E. Frey, and P. Schwille, bioRxiv (2019), 10.1101/666362.

[19] A. M. Turing, Philosophical Transactions of the Royal Society of London. Series B, Biological Sciences **237**, 37 (1952).

[20] T. D. Williams, P. I. Paschke, and R. R. Kay, Philosophical Transactions of the Royal Society B: Biological Sciences **374**, 20180150 (2019).

[21] D. M. Veltman, T. D. Williams, G. Bloomfield, B.-C. Chen, E. Betzig, R. H. Insall, and R. R. Kay, eLife **5**, e20085 (2016).

[22] E. M. Vaughan, A. L. Miller, H.-Y. E. Yu, and W. M. Bement, Current Biology **21**, 270 (2011).

[23] J. Chant and J. R. Pringle, J. Cell Biol. **129**, 751 (1995).

[24] Z. Tong, X.-D. Gao, A. S. Howell, I. Bose, D. J. Lew, and E. Bi, J Cell Biol **179**, 1375 (2007).

[25] W.-C. Lo, M. E. Lee, M. Narayan, C.-S. Chou, and H.-O. Park, PLoS ONE **8**, e56665 (2013).

[26] K. E. Miller, W.-C. Lo, M. E. Lee, P. J. Kang, and H.-O. Park, Molecular Biology of the Cell **28**, 3773 (2017).

[27] J. Halatek and E. Frey, Nature Physics **14**, 507 (2018).

[28] F. Brauns, J. Halatek, and E. Frey, arXiv:1812.08684

[29] P. K. Maini, D. L. Benson, and J. A. Sherratt, Math Med Biol **9**, 197 (1992).

[30] G. B. Ermentrout and J. Rinzel, SIAM Journal on Applied Mathematics **56**, 1107 (1996).

[31] M. Bär, A. K. Bangia, I. G. Kevrekidis, G. Haas, H.-H. Rotermund, and G. Ertl, The Journal of Physical Chemistry **100**, 19106 (1996).

[32] X. Yuan, T. Teramoto, and Y. Nishiura, Phys. Rev. E **75**, 036220 (2007).

[33] Y. Nishiura, T. Teramoto, X. Yuan, and K.-I. Ueda, Chaos: An Interdisciplinary Journal of Nonlinear Science **17**, 037104 (2007).

[34] J. Miyazaki and S. Kinoshita, Physical Review E **76** (2007), 10.1103/PhysRevE.76.066201.

[35] K. Nishi, Y. Nishiura, and T. Teramoto, Japan Journal of Industrial and Applied Mathematics **30**, 351 (2013).

[36] A. Doelman, P. van Heijster, and F. Xie, SIAM Journal on Applied Dynamical Systems **15**, 655 (2016).

[37] P. van Heijster, C.-N. Chen, Y. Nishiura, and T. Teramoto, J Dyn Diff Equat **31**, 153 (2019).

[38] A. Scheel and J. Weinburd, Philosophical Transactions of the Royal Society A: Mathematical, Physical and Engineering Sciences **376**, 20170191 (2018).

[39] C. K. R. T. Jones, in *Dynamical Systems*, Vol. 1609, edited by R. Johnson (Springer, Berlin, Heidelberg, 1995) pp. 44–118.

[40] M. J. Ward, Bulletin of Mathematical Biology **68**, 1151 (2006).

[41] J. Guckenheimer and P. Holmes, *Nonlinear Oscillations, Dynamical Systems, and Bifurcations of Vector Fields*, Applied Mathematical Sciences, Vol. 42 (Springer New York, New York, NY, 1983).

[42] B. Krauskopf, H. M. Osinga, and J. Galan-Vioque, eds., *Numerical Continuation Methods for Dynamical Systems: Path Following and Boundary Value Problems*, Understanding Complex Systems (Springer Netherlands, Dordrecht, 2007).

[43] J. D. Pryce, *Numerical Solution of Sturm-Liouville Problems*, Monographs on Numerical Analysis (Clarendon Press, Oxford; New York, 1993).

[44] A. Ziepke, S. Martens, and H. Engel, J. Chem. Phys. **145**, 094108 (2016).

[45] S. R. Pfeffer, Biochemical Society Transactions **40**, 1373 (2012).

[46] P. Novick, Small GTPases **7**, 252 (2016).

[47] L. C. Noack and Y. Jaillais, Current Opinion in Plant Biology **40**, 22 (2017).

[48] S. Rulands, B. Klünder, and E. Frey, Phys. Rev. Lett. **110**, 038102 (2013).

[49] A. S. Zadorin, Y. Rondelez, G. Gines, V. Dilhas, G. Urtel, A. Zambrano, J.-C. Galas, and A. Estevez-Torres, Nature Chemistry **9**, 990 (2017).

[50] D. Thalmeier, J. Halatek, and E. Frey, Proc Natl Acad Sci USA **113**, 548 (2016).

[51] A. Ziepke, S. Martens, and H. Engel, SIAM J. Appl. Dyn. Syst. **18**, 1015 (2019).

[52] A. Haupt and N. Minc, Journal of Cell Science **131**, jcs214015 (2018).

[53] W. van Saarloos, Physics Reports **386**, 29 (2003).

(2018), arXiv:1812.08684.

5 Flow Induced Symmetry Breaking in a Conceptual Polarity Model

This section is a publication preprint of the following manuscript published in

Flow Induced Symmetry Breaking in a Conceptual Polarity Model

M. C. WIGBERS,[1,*] F. BRAUNS,[1,*] C. Y. LEUNG,[1,*] AND E. FREY[1]

[1] *Arnold Sommerfeld Center for Theoretical Physics and Center for NanoScience, Department of Physics, Ludwig-Maximilians-Universtiät München, Theresienstraße 37, D-80333 München, Germany*

[*]MW, FB, and CYL contributed equally to this work.

Cytosolic flow induced symmetry breaking in a conceptual polarity model

Manon C. Wigbers[†] , Fridtjof Brauns[†] , Ching Yee Leung[†] and Erwin Frey*

Arnold Sommerfeld Center for Theoretical Physics (ASC) and Center for NanoScience (CeNS), Department of Physics, Ludwig-Maximilians-Universität München, Theresienstraße 37, D–80333 München, Germany

*   Correspondence: frey@lmu.de;
†   These authors contributed equally to this work.

Abstract: Important cellular processes, such as cell motility and cell division, are coordinated by cell polarity, which is determined by the non-uniform distribution of certain proteins. Such protein patterns form via an interplay of protein reactions and protein transport. Since Turing's seminal work, the formation of protein patterns resulting from the interplay between reactions and diffusive transport has been widely studied. Over the last few years, increasing evidence shows that also advective transport, resulting from cytosolic and cortical flows, is present in many cells. However, it remains unclear how and whether these flows contribute to protein-pattern formation. To address this question, we use a minimal model that conserves the total protein mass to characterize the effects of cytosolic flow on pattern formation. Combining a linear stability analysis with numerical simulations, we find that membrane-bound protein patterns propagate *against* the direction of cytoplasmic flow with a speed that is maximal for intermediate flow speed. We show that the mechanism underlying this pattern propagation relies on a higher protein influx on the upstream side of the pattern compared to the downstream side. Furthermore, we find that cytosolic flow can change the membrane pattern qualitatively from a peak pattern to a mesa pattern. Finally, our study shows that a non-uniform flow profile can induce pattern formation by triggering a regional lateral instability.

Keywords: symmetry breaking; cytoplasmic flow; phase-space analysis; protein pattern formation

1. Introduction

Many biological processes rely on the spatiotemporal organization of proteins. Arguably one of the most elementary forms of such organization is cell polarization — the formation of a "cap" or spot of high protein concentration that determines a direction. Such a polarity axis then coordinates downstream processes including motility [1,2], cell division [3], and directional growth [4]. Cell polarization is an example for *symmetry breaking* [5], as the orientational symmetry of the initially homogeneous protein distribution is broken by the formation of the polar cap.

Intracellular protein patterns arise from the interplay between protein interactions (chemical reactions) and protein transport. Diffusion in the cytosol serves as the most elementary means of transport. Pattern formation resulting from the interplay of reactions and diffusion has been widely studied since Turing's seminal work [6]. In addition to diffusion, proteins can be transported by fluid flows in the cytoplasm and along cytoskeletal structures (vesicle trafficking, cortical contractions) driven by molecular motors [7,8]. These processes lead to *advective* transport of proteins.

Recently, it has been shown experimentally that advective transport (caused by cortical flows) induces polarization of the PAR system in the *C. elegans* embryo [9–11]. Furthermore, *in vitro* studies with the MinDE system of *E. coli*, reconstituted in microfluidic chambers, have shown that the flow of the bulk fluid has a strong effect on the protein patterns that form on the membrane [12,13]. Increasing evidence shows that cortical and cytosolic flows (also called "cytoplasmic streaming") are present in many cells [14–19]. In addition, cortical contractions can drive cell-shape deformations [20], inducing flows in the incompressible cytosol [21,22]. However, the role of flows for protein-pattern formation

remains elusive. This motivates to study the role of advective flow from a conceptual perspective, with a minimal model. The insights thus gained will help to understand the basic, principal effects of advective flow on pattern formation and reveal the underlying elementary mechanisms.

The basis of our study is a paradigmatic class of models for cell polarization that describe a single protein species which has a membrane-bound state and a cytosolic state. Such two-component mass-conserving reaction–diffusion (2cMcRD) systems serve as conceptual models for cell polarization [23–27]. Specifically they have been used to model Cdc42 polarization in budding yeast [28,29] and PAR-protein polarity [30]. 2cMcRD systems generically exhibit both spontaneous and stimulus-induced polarization [5,27,30]. In the former case, a spatially uniform steady state is unstable against small spatial perturbations ("Turing instability" [6]). Adjacent to the parameter regime of this lateral instability, a sufficiently strong, localized stimulus (e.g. an external signal) can induce the formation of a pattern starting from a stable spatially uniform state. The steady state patterns that form in two-component McRD systems are generally stationary (there are no travelling or standing waves). Moreover, the final stationary pattern has no characteristic wavelength. Instead, the peaks that grow initially from the fastest growing mode ("most unstable wavelength") compete for mass until only a single peak remains ("winner takes all") [26,28,31]. The location of this peak can be controlled by external stimuli (e.g. spatial gradients in the reaction rates) [28,32].

Recently, a theoretical framework, termed *local equilibria theory*, has been developed to study these phenomena using a geometric analysis in the phase plane of the protein concentrations [27,33]. With this framework one can gain insight into the mechanisms underlying the dynamics of McRD systems both in the linear and in the strongly nonlinear regime, thereby bridging the gap between these two regimes.

Here, we show that cytosolic flow in two-component systems always induces upstream propagation of the membrane-bound pattern. In other words, the peak moves against the cytosolic flow direction. This propagation is driven by a higher protein influx on the upstream side of the membrane-concentration peak compared to its downstream side. Using this insight, we are able to explain why the propagation speed becomes maximal at intermediate flow speeds and vanishes when the rate of advective transport becomes fast compared to the rate of diffusive transport or compared to the reaction rates. We first study a uniform flow profile using periodic boundaries. This effectively represents a circular flow, which is observed in plant cells (where this phenomenon is called cytoplasmic streaming or cyclosis) [34]. It also represents an *in vitro* system in a laterally large microfluidic chamber. We then study the effect of a spatially non-uniform flow profile in a system with reflective boundaries, as a minimal system for flows close to the membrane [9,11,25], e.g. in the actin cortex. We show that a non-uniform flow profile redistributes the protein mass, which can trigger a regional lateral instability and thereby induce pattern formation from a stable homogeneous steady state.

The remainder of the paper is structured as follows. We first introduce the model in Sec. 2. We then perform a linear stability analysis in Sec. 3 to show how spatially uniform cytosolic flow influences the dynamics close to a homogeneous steady state. In Sec. 4, we use numerical simulations to study the fully nonlinear long-term behavior of the system. Next, we show that upon increasing the cytosolic flow velocity, the pattern can qualitatively change from a mesa pattern to a peak pattern in Sec. 5. Finally, in Sec. 6, we study how a spatially non-uniform cytosolic flow can trigger a regional lateral instability and thus induce pattern formation. Implications of our findings and links to earlier literature are briefly discussed at the end of each section. We conclude with a brief outlook section.

2. Model

We consider a spatially one-dimensional system of length L. The proteins can cycle between a membrane-bound state (concentration $m(x, t)$) and a cytosolic state (concentration $c(x, t)$), and diffuse with diffusion constants D_m and D_c, respectively (Fig. 1). In cells, the diffusion constant on the membrane is typically much smaller than the diffusion constant in the cytosol. In the cytosol, the
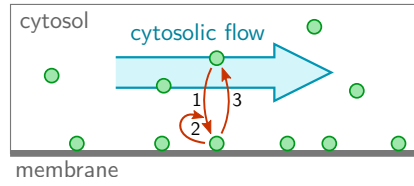
Figure 1. One-dimensional two-component system with cytosolic flow into the positive x direction. The reaction kinetics include (1) attachment, (2) self-recruitment and (3) enzyme-driven detachment.

proteins are assumed to be advected with a speed $v_f(x)$, as indicated by the blue arrow in Fig. 1. Thus, the reaction-diffusion-advection equations for the cytosolic density and membrane density read

$$\partial_t c + \partial_x(v_f c) = D_c \partial_x^2 c - f(m,c), \tag{1a}$$
$$\partial_t m = D_m \partial_x^2 m + f(m,c), \tag{1b}$$

with either periodic or reflective boundary conditions. The nonlinear function $f(m,c)$ describes the reaction kinetics of the system. Attachment–detachment kinetics can generically be written in the form

$$f(m,c) = a(m)c - d(m)m, \tag{2}$$

where $a(m) > 0$ and $d(m) > 0$ denote the rate of attachment from the cytosol to the membrane and detachment from the membrane to the cytosol, respectively. The dynamics given by Eq. (1) conserve the average total density

$$\bar{n} = \frac{1}{L} \int_0^L dx \, n(x,t). \tag{3}$$

Here, we introduced the *local* total density $n(x,t) := m(x,t) + c(x,t)$.

For illustration purposes, we will use a specific realization of the reaction kinetics [27],

$$a(m) = k_{on} + k_{fb}m \quad \text{and} \quad d(m) = \frac{k_{off}}{K_D + m}, \tag{4}$$

describing attachment with a rate k_{on}, self-recruitment with a rate k_{fb}, and enzyme-driven detachment with a rate k_{off} and the Michaelis-Menten constant K_D, respectively. However, our results do not depend on the specific choice of the reaction kinetics. Unless stated otherwise, we use the parameters: $k_{on} = 1\,\text{s}^{-1}, k_{fb} = 1\,\mu\text{m s}^{-1}, k_{off} = 2\,\text{s}^{-1}, K_D = 1\,\mu\text{m}^{-1}, \bar{n} = 5\,\mu\text{m}^{-1}, D_m = 0.01\,\mu\text{m}^2/\text{s}, D_c = 10\,\mu\text{m}^2/\text{s}$.

3. Linear stability analysis

3.1. Linearized dynamics and basic results

To study how cytosolic flow affects the formation of protein patterns, we first consider a spatially uniform flow profile (i.e. constant $v_f(x) = v_f$) and perform a linear stability analysis of a spatially homogeneous steady state $\mathbf{u}^* = (m^*, c^*)$:

$$f(m^*, c^*) = 0, \quad m^* + c^* = \bar{n}. \tag{5}$$

Following the standard procedure, we linearize the dynamics for small perturbations $\mathbf{u}(x,t) = \mathbf{u}^* + \delta\mathbf{u}(x,t)$ around the homogeneous steady state. Expanding $\delta\mathbf{u}(x,t)$ in exponentially growing (or decaying) Fourier modes $\delta\mathbf{u} = \hat{\mathbf{u}}_q e^{\sigma t} e^{iqx}$ leads to the eigenvalue problem

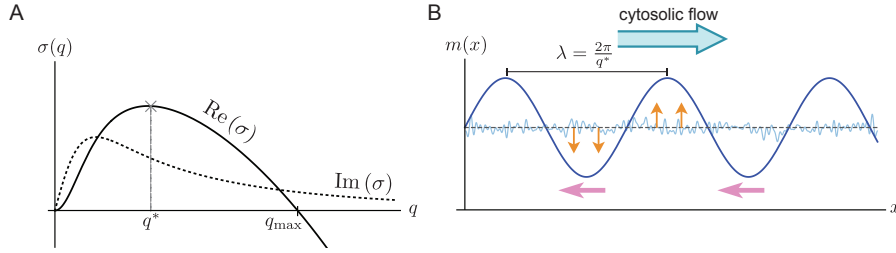$$\mathcal{J}\hat{\mathbf{u}}_q = \sigma\hat{\mathbf{u}}_q, \tag{6}$$

Figure 2. (A) Sketch of real (solid) and imaginary (dotted) part of a typical dispersion relation with a band $[0, q_{max}]$ of unstable modes. (B) The initial dynamics of a spatially homogeneous state with a small random perturbation (blue thin line). The direction of cytosolic flow is indicated by a blue arrow. The typical wavelength (λ) of the initial pattern is determined by the fastest growing mode q^* and the phase velocity is determined by the value of the imaginary part of dispersion relation at the fastest growing mode ($v_{phase} = \mathrm{Im}\,\sigma(q^*)/q^*$). The growth of the pattern is indicated by orange arrows, while the travelling direction is indicated by pink arrows.

with the Jacobian

$$\mathcal{J} = \begin{pmatrix} -D_c q^2 - i v_{\mathrm{f}} q - f_c & -f_m \\ f_c & -D_m q^2 + f_m \end{pmatrix},$$

where $f_c = \partial_c f|_{\mathbf{u}^*}$ and $f_m = \partial_m f|_{\mathbf{u}^*}$ encode the linearized reaction kinetics. Note that for reaction kinetics of the form Eq. (2), $f_c = a(m) > 0$ and we consider this case in the following.

For each mode with wavenumber q, there are two eigenvalues $\sigma_{1,2}(q)$. The case $q = 0$ corresponds to spatially homogeneous perturbations, where the two eigenvalues are given by $\sigma_1 = f_m - f_c$ and $\sigma_2 = 0$ [27]. Here, we restrict our analysis to homogeneously stable states ($\sigma_1 < 0$). The second eigenvalue ($\sigma_2 = 0$) corresponds to perturbations that change the average mass $\bar{n}$ and therefore shift the homogeneous steady state $\mathbf{u}^*(\bar{n})$ along the nullcline $f = 0$. Because these perturbations break mass-conservation, they are not relevant for the stability of a closed system as considered here. The modes $q > 0$ determine the stability of the system against spatially inhomogeneous perturbations (*lateral stability*). The eigenvalue with the larger real part determines the stability and will be denoted by $\sigma(q)$, suppressing the index.

A typical dispersion relation with a band of unstable modes is shown in Fig. 2A. The real part (solid line), indicating the mode's growth rate, has a band of unstable modes $[0, q_{max}]$ where $\mathrm{Re}\,\sigma(q) > 0$. The fastest growing mode q^* determines the wavelength λ of the pattern that initially grows, triggered by a small, random perturbation of the spatially homogeneous steady state. For $v_{\mathrm{f}} = 0$, the imaginary part of $\sigma(q)$ vanishes, for locally stable steady states ($\sigma(0) \leq 0$). [27]. However, in the presence of flow, the imaginary part of $\sigma(q)$ is non-zero (dashed line in Fig. 2A), which implies a propagation of each mode with the phase velocity $v_{phase}(q) = -\mathrm{Im}\,\sigma(q)/q$. This means that a mode q not only grows over time (orange arrows in Fig. 2B), but also propagates as indicated by the pink arrows in Fig. 2B. Further below, in Sec. 3.4, we will show that $\mathrm{Im}\,\sigma(q)$ always has the same sign as the flow velocity v_{f}, such that all modes propagate *against* the flow direction.

To gain physical insight into the mechanisms underlying the growth and propagation of perturbations (modes) we will first give an intuitive explanation of a lateral instability in McRD systems, building on the concepts of local equilibria theory [27,33]. We then provide a more detailed analysis in the limits of long wavelength as well as fast and slow flow.

3.2. Intuition for the flow-driven instability and upstream propagation of the unstable mode

Lateral instability in McRD systems can be understood as a *mass-redistribution instability* [27]. Let us briefly recap the mechanism underlying this instability for a system without flow. To this end, we first discuss the effect of reactions and diffusion separately, and explain how these effects together

drive the mass-redistribution instability. We then explain how this instability is affected by cytosolic flow.

Consider a spatially homogeneous steady state, perturbed by a slight redistribution of the *local* total density $n(x,t)$. The dashed orange line in Figure 3A shows such a perturbation where the membrane concentration (Fig. 3A top) is slightly perturbed in a sinusoidal fashion. In phase space this is represented by a density distribution that slightly deviates from the spatially homogeneous steady state (marked by the orange dashed line). Here, the open star and open circle mark the minimum and maximum of the local total density, respectively. The local total density determines the local reactive equilibrium concentrations $m^*(n)$ and $c^*(n)$ (cf. Eq. (5), replacing the average mass $\bar{n}$ by the local mass $n(x,t)$). In phase space (Fig. 3A bottom) these local equilibria can be read off from the intersections (marked by black circles) of the reactive subspaces $n(x,t) = m(x,t) + c(x,t)$ (gray solid lines) and the reactive nullcline (black solid lines). A slight redistribution of the local total density shifts the reactive equilibria, leading to reactive flows towards these shifted equilibria (red and green arrows in Fig. 3A). Thus, the reactive equilibria, and thereby the reactive flows, are encoded in the shape of the reactive nullcline in phase space. If the nullcline slope is negative, increasing the total density leads to a decreasing equilibrium cytosolic concentration and therefore to *attachment* (green arrows in Fig. 3A). Conversely, in regions of lower total density, the equilibrium cytosolic concentration increases via *detachment* (red arrows in Fig. 3A). Hence, regions of high total density become *self-organized attachment zones* and regions of low total density become *self-organized detachment zones* [33] (green and red areas in Fig. 3 top and middle).

These attachment and detachment zones act as sinks and sources for diffusive mass-transport on the membrane and in the cytosol: The attachment zone acts as a cytosolic sink and membrane source, and the detachment zone acts as a cytosolic source and a membrane sink (blue arrows in Fig. 3B). As diffusion in the cytosol is much faster than in the membrane, mass is transported faster in the cytosol than on the membrane, as indicated by the size of the blue arrows in Fig. 3B top and middle. This leads to net mass transport from the detachment zone to the attachment zone. As the local total density increases in the attachment zone, it facilitates further attachment and thereby the growth of the pattern on the membrane. In short, the mechanism underlying the mass-redistribution instability is a cascade of attachment–detachment kinetics (Fig. 3A) and net mass-transport towards attachment zones (Fig. 3B).

How does cytosolic fluid flow affect the mass-redistribution instability? Cytosolic flow transports proteins advectively. This advective transport shifts the cytosolic density profile downstream relative to the membrane density profile (dashed to solid orange line in Fig. 3C middle). This shift leads to an increase of the cytosolic density on the upstream (cyan) side of the membrane peak and a decrease on the downstream (magenta) side, in Fig. 3C (middle), respectively. In phase space, this asymmetry is reflected as a 'loop' shape of the phase space trajectory that corresponds to the real space pattern (Fig. 3C bottom). The higher cytosolic density on the upstream side increases attachment relative to the downstream side. This leads to a propagation of the membrane concentration profile in the upstream direction.

3.3. Long wavelength limit

To complement this intuitive picture we consider the long wavelength limit $q \rightarrow 0$.[1] In this limit, the dispersion relation expanded to second order in q reads

$$\sigma(q) \approx -\frac{1}{1+s_{\mathrm{nc}}} \left[is_{\mathrm{nc}} v_{\mathrm{f}} q + (D_m + s_{\mathrm{nc}} D_c) q^2 + \frac{s_{\mathrm{nc}} v_{\mathrm{f}}^2}{f_c (1+s_{\mathrm{nc}})^2} q^2 \right], \tag{7}$$

---

[1] In principle, the dispersion relation can be easily obtained in closed form using the formula for eigenvalues of 2×2 matrices: $\sigma_{1,2} = \frac{1}{2} \operatorname{tr} \mathcal{J} \mp \frac{1}{2} \sqrt{(\operatorname{tr} \mathcal{J})^2 - 4 \det \mathcal{J}}$ where $\operatorname{tr} \mathcal{J}$ and $\det \mathcal{J}$ are the Jacobian's trace and determinant, respectively. Because the resulting expression is rather lengthy, we don't write it out it explicitly here.
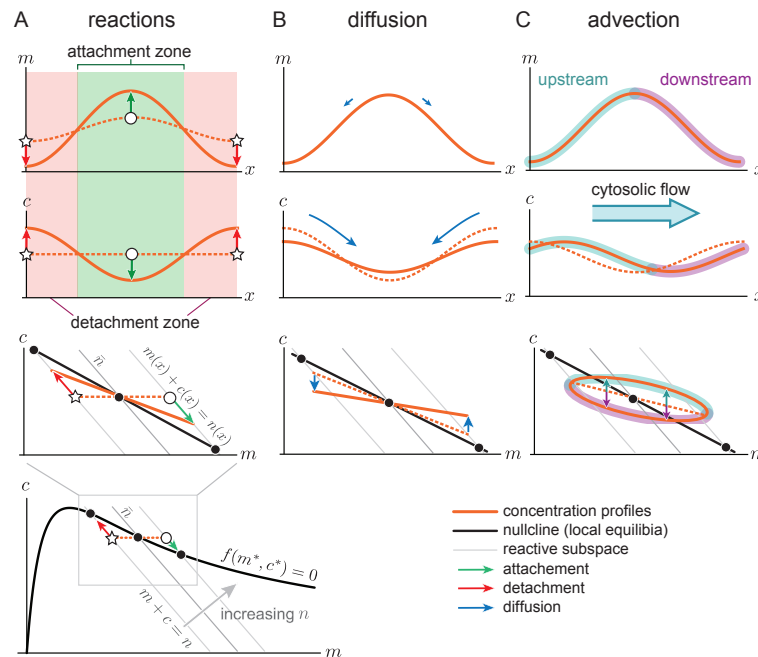
Figure 3. Sketch of the initial dynamics of an laterally unstable spatially homogeneous steady state. The role of reactions (A), diffusion (B) and advection (C) for a mass-redistribution instability are presented for the membrane (top) and cytosolic (middle) concentration profiles and in phase space (bottom). (A) A small perturbation of the spatially homogeneous membrane concentration (orange dashed lines in top panel) leads to a spatially varying local total density $n(x)$, with a larger total density at the maximum of the membrane profile (open circle) and a smaller total density at the minimum (open star). These local variations in total density lead to attachment zones (green region) and detachment zones (red region). The reactive flow, indicated by the red and green arrows, points along the reactive subspace (gray lines) in phase space towards the shifted local equilibria (black circles). These reactive flows lead to the solid orange density profiles after a small amount of time. (B) Faster diffusion in the cytosol compared to the membrane (indicated by the large and small blue arrows in the middle and top panel, respectively), lead to net mass transport from the detachment zone to the attachment zone. Again, dashed and solid lines indicate the state before and after a short time interval of diffusive transport. (C) Cytosolic flow shifts the cytosolic concentration with respect to the membrane concentration (orange dashed to orange solid lines), increasing the cytosolic concentration on the upstream side of the pattern and decreasing the cytosolic concentration on the downstream side . In phase space, the trajectory of this density profile forms a 'loop'.

where $s_{nc} = -f_m/f_c$ is the slope of the reactive nullcline. The imaginary part $\text{Im}\,\sigma(q)$ is linear in q to lowest order, implying a phase velocity $v_{\text{phase}} = v_f s_{nc}/(1 + s_{nc})$ that is independent of the wavelength. The growth rate $\text{Re}\,\sigma(q)$ is quadratic in q to lowest order. If this quadratic term is positive, there is a band of unstable modes.[2] Hence, the criterion for a mass-redistribution instability can be expressed in terms of the nullcline slope [27]

$$s_{nc} < -\frac{D_m}{D_c}\left[1 + \frac{v_f^2}{(1+s_{nc})^2 D_c f_c}\right]^{-1}. \tag{8}$$

In the absence of flow, $v_f = 0$, we recover the slope criterion $s_{nc} < -D_m/D_c$ for a mass-redistribution instability driven by cytosolic diffusion [27]. We find that flow always increases the range of instability since the second term in the square brackets monotonically increases with flow speed $|v_f|$. Furthermore, the instability criterion becomes independent of the diffusion constants in the limit of fast flow ($|v_f| \gg \sqrt{D_c f_c}$). The criterion for the (flow-driven) mass-redistribution instability then simply becomes $s_{nc} < 0$, independently of the ratio of the diffusion constants. This has the interesting consequence that, for sufficiently fast flow, a mass-redistribution instability can be driven solely via cytoplasmic flow, independent of diffusion.

3.4. Limits of slow and fast flow

To analyze the effect of flow for wavelengths away from the long wavelength limit it is instructive to consider the limit cases of slow and fast flow speed.

We first consider a limit where advective transport $(qv_f)^{-1}$ is slow compared either to the chemical reactions or to diffusive transport. To lowest order in v_f, the dispersion relation is given by (see Appendix A)

$$\sigma(q) \approx \sigma^{(0)}(q) + i\frac{v_f q}{2}A(q), \tag{9}$$

where the zeroth order term, $\sigma^{(0)}(q)$, is the dispersion relation in the absence of flow, which has no imaginary part [27] (cf. Eq. (A1)). The function $A(q)$ is positive for all laterally unstable modes ($\text{Re}\,\sigma(q) > 0$). Equation (9) shows that to lowest order (linear in v_f) the effect of cytosolic flow is to induce propagation of the modes with the phase velocity $v_{\text{phase}}(q) = \text{Im}\,\sigma(q)/q \approx -v_f A(q)$. Since $A(q) > 0$ for laterally unstable modes, all growing perturbations propagate against the direction of the flow (as illustrated in Fig. 2B).

In the limit of fast flow (compared either to reactions or to cytosolic transport) we find that the dispersion relation (given by the eigenvalue problem Eq. (6)) reduces to

$$\sigma(q) \approx f_m - D_m q^2 + i\frac{f_c f_m}{v_f q} \tag{10}$$

for non-zero wavenumbers. The real part of the dispersion relation in this fast flow limit becomes identical to the dispersion relation in the limit of fast diffusion [27]. In both limits, cytosolic transport becomes (near) instantaneous. In particular, in the limit of fast flow, advective transport completely dominates over diffusive transport in the cytosol such that the dispersion relation becomes independent of the cytosol diffusion constant D_c.

From the imaginary part of $\sigma(q)$, we obtain the phase velocity $v_{\text{phase}} = -f_c f_m/(v_f q^2)$. In other words, an increase in cytosolic flow leads to a *decrease* of the phase velocity. This is opposite to the slow flow limit discussed above, where the phase velocity increased linearly with the flow speed.

---

[2] Homogeneous stability implies that the nullcline slope s_{nc} is larger than -1 [27], such that the prefactor $(1 + s_{nc})^{-1}$ is positive.

To rationalize these findings, we recall the propagation mechanism as discussed above. There, we argued that a phase shift between the membrane and the cytosol pattern is responsible for the pattern propagation, as it leads to an asymmetry in the attachment–detachment balance upstream and downstream. This phase shift increases with the flow velocity and eventually saturates at $\pi/4$.[3] On the other hand, the cytosol concentration gradients become shallower the faster the flow. To understand why this is, imagine a small volume element in the cytosol being advected with the flow. The faster the flow, the less time it has to interact with each point on the membrane it passes. Therefore, for faster advective flow, the attachment–detachment flux at the membrane is effectively diluted over a larger cytosolic volume. This leads to a flattening of the cytosolic concentration profile (see Movie 2), and therefore a reduction in the upstream–downstream asymmetry of attachment. As a result, in the limit of fast flow, the pattern propagates *slower* the faster the flow, whereas, in the limit of slow flow, the pattern propagates *faster* the faster the flow. Thus, comparing these two limits, we learn that the phase velocity reaches a maximum at intermediate flow speeds.

3.5. Summary and discussion of linear stability

Let us briefly summarize our main findings from linear stability analysis. We found that the leading order effect of cytosolic flow is to induce upstream propagation of patterns. This propagation is driven by the faster resupply of protein mass on the upstream side of the pattern compared to the downstream side. A similar effect was previously found for vegetation patterns which move uphill because nutrients are transported downhill by water flow [35]. Even though these systems are not strictly mass conserving, their pattern propagation underlies the same principle: The nutrient uptake in regions of high vegetation density creates a nutrient sink which is resupplied asymmetrically due to the downhill flow of water and nutrients.

Moreover, we used a phase-space analysis to explain how flow extends the range of parameters where where patterns emerge spontaneously, i.e. where the homogeneous steady state is laterally unstable. This was previously shown mathematically for general two-component reaction–diffusion systems (not restricted to mass-conserving ones) [35,36]. Our analysis in the long wavelength limit explains the physical mechanism of this instability for mass-conserving systems: The flow-driven instability is a mass-redistribution instability, driven by a self-amplifying cascade of (flow-driven) mass transport and the self-organized formation of attachment and detachment zones (shifting reactive equilibria). This shows that the instability mechanism is identical to the mass-redistribution instability that underlies pattern formation in systems without flow (i.e. where only diffusion drives mass transport) [27]. For these systems, the instability strictly requires $D_c > D_m$. In contrast, we find that for sufficiently fast flow, there can be a mass-redistribution instability even in the absence of cytosolic diffusion ($D_c = 0$). While the case $D_c = 0$ is not physiologically relevant in the context of intracellular pattern formation, it may be relevant for the formation of vegetation patterns on sloped terrain [37], where c and m are the soil-nutrient concentration and plant biomass density, respectively. In conclusion, advective flow can fully replace diffusion as the mass-transport mechanism driving the mass-redistribution instability.

4. Pattern propagation in the nonlinear regime

So far we have analyzed how cytosolic flow affects the dynamics of the system in the vicinity of a homogeneous steady state, using linear stability analysis. However, patterns generically don't saturate at small amplitudes but continue to grow into the strongly nonlinear regime [27] (see Movie 1 for an example in which a small perturbation of the homogeneous steady state evolves into a large amplitude pattern in the presence of flow).

---

3   The phase shift can be read off from the real and imaginary parts of the eigenvectors in the linear stability analysis.
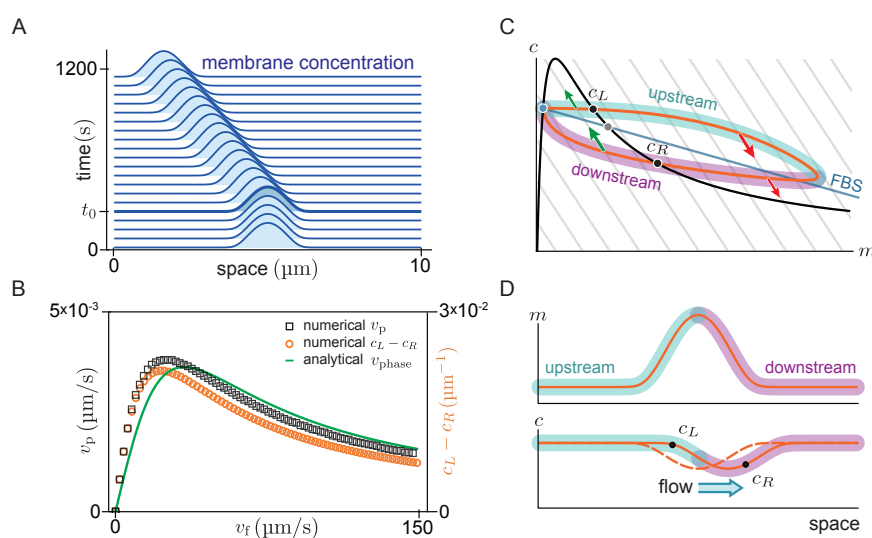
Figure 4. Pattern dynamics far from the spatially homogeneous steady state. (A) Time evolution of the membrane-bound protein concentration. At time $t_0 = 240\,\text{s}$ a constant cytosolic flow with velocity $v_f = 20\,\mu\text{m/s}$ towards the right is switched on (cf. Movie 3). (B) Relation between the peak speed (v_p) and flow speed (v_f). Results from finite element simulations (black open squares) are compared to the phase velocity of the mode $q_{\max}$ obtained from linear stability analysis (green solid line) and to an approximation (orange open circles) of the area enclosed by the density distribution trajectory in phase space (area enclosed by the 'loop' in D). (The domain size, $L = 10\,\mu\text{m}$, is chosen large enough compared to the peak width such that boundary effects are negligible.) (C) A schematic of the phase portrait corresponding to the pattern in D. The density distribution in the absence of flow is embedded in the FBS (blue straight line). In the presence of flow, the density distribution trajectory forms a 'loop' in phase space. The upstream and downstream side of the pattern are highlighted in cyan and magenta, respectively. Red and green arrows indicate the direction of the reactive flow in the attachment and detachment zones, respectively. At intersection points of the density distribution with the nullcline (c_L and c_R) the system is at its local reactive equilibrium. (D) Sketch of the membrane (orange solid line, top) and cytosolic (orange dashed line, bottom) concentration profiles for a stationary pattern in the absence of cytosolic flow. Flow shifts the cytosol profile downstream (orange solid line, bottom).

To study the long time behavior (steady state) far away from the spatially homogeneous steady state, we performed finite element simulations in Mathematica [38]. To interpret the results of these numerical simulations, we will use *local equilibria theory*, building on the phase-space analysis introduced in Refs. [27,33].

Figure 4A shows the space-time plot (kymograph) of a system where there is initially no flow ($t < t_0$), such that the system is in a stationary state with a single peak. For such a stationary steady state, diffusive fluxes on the membrane and in the cytosol have to balance exactly. This diffusive flux balance imposes the constraint that in the (m, c)-phase plane, the trajectory corresponding to the pattern lies on a straight line with slope $-D_m/D_c$, called '*flux-balance subspace*' (FBS) [27] (see light blue line in Fig. 4C). At the plateaus of the pattern, diffusive flow vanishes and attachment and detachment are balanced, i.e. the system is locally in reactive equilibrium. Hence, plateaus corresponds to points in the (m, c)-phase plane where the FBS intersects the reactive nullcline on a segment with slope larger than $-D_m/D_c$ (blue point in Fig. 4C). The intersection point between the FBS and the nullcline where the nullcline slope is smaller than $-D_m/D_c$ (gray point in Fig. 4C) corresponds inflection points of the pattern profile. An in depth analysis of stationary patterns based on these geometric relations in phase space can be found in Ref. [27]. Here we ask how the phase portrait changes in the presence of flow.

At time $t = t_0$, a constant cytosolic flow in the positive x-direction is switched on. Consistent with the expectation from linear stability analysis, we find that the peak propagates against the flow direction in the negative x-direction (solid lines in Fig. 4A). The diffusive fluxes no longer balance for this propagating steady state, such that the phase-space trajectory is no longer embedded in the FBS. Instead, as advective flow shifts the cytosol concentration profile relative to the membrane profile, the phase-space trajectory becomes a 'loop' (Fig. 4C). On the upstream side of the peak, the cytosolic density is increased, such that net attachment — which is proportional to the cytosolic density — is increased relative to net detachment. Conversely, the reactive balance is shifted towards detachment on the downstream side. Because the reactive flow is approximately proportional to the distance from the reactive nullcline in phase space, the asymmetry between net attachment and detachment on the upstream and downstream side of the peak can be estimated by the area enclosed by the loop-shaped trajectory in phase space.

To test whether the attachment–detachment asymmetry explains the propagation speed of the peak, we estimate the enclosed area in phase space by the difference in cytosolic concentrations at the points c_L and c_R (black dots in Fig. 4C and D) where the loop intersects the reactive nullcline ($f = 0$ black line Fig. 4C). At these points, the system is in a local reactive equilibrium. Indeed, we find that the propagation speed of the pattern obtained from numerical simulations (black open squares in Fig. 4B) is well approximated by the difference in cytosolic density ($v_p \propto c_L - c_R$) for all flow speeds (orange open circles in Fig. 4B). Furthermore, in the limit of slow and fast flow, the peak propagation speed is well approximated by the propagation speed of the unstable traveling mode with the longest wavelength, as obtained from linear stability analysis.[4] For small flow speeds, the pattern's propagation speed v_p increases linearly with v_f (cf. Eq. 7) and for large flow speeds the pattern speed is proportional to $1/v_f$ (cf. Eq. 10).

In summary, we found that the peak propagation speed in the slow and fast flow limits is well described by the propagation speed of the linearly unstable mode with the longest wavelength (i.e. the right edge of the band of unstable modes q_{max}). Moreover, we approximated the asymmetry of protein attachment by the area enclosed by the density distribution in phase space, and found that this is proportional to the peak speed for all flow speeds.

---

[4] The phase velocity depends on the mode's wavelength. The relevant length scale for the peak's propagation is its width, which is approximately given by $2\pi/q_{max}$ at the pattern's inflection point [27]. Thus, we infer the peak propagation speed from $\text{Im}\,\sigma(q_{max})/q_{max}$ at the inflection point of the stationary peak.
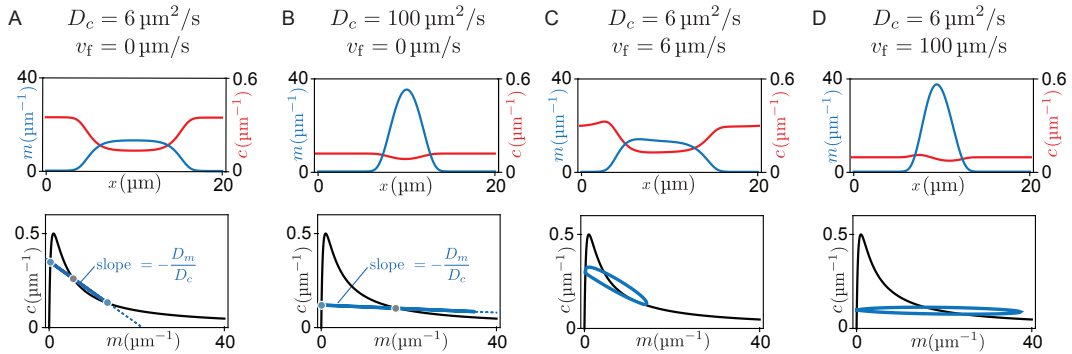
Figure 5. Demonstration of the transition from a mesa pattern to a peak pattern. Each panel shows a snapshot from finite element simulations in steady state. Top concentration profiles in real space; bottom: corresponding trajectory (blue solid line) in phase space. (A) Mesa pattern in the case of slow cytosol diffusion and no flow. The two plateaus (blue dots) and the inflection point (gray dot) of the pattern correspond to the intersection points of the FBS (blue dashed line) with the reactive nullcline (black line). (B) For fast cytosol diffusion, the third intersection point between FBS and nullcline lies at much higher membrane concentration such that it no longer limits the pattern amplitude. Therefore, a peak forms whose amplitude is limited by the total protein mass in the system. (C) Slow flow only slightly deforms the mesa pattern, compare to (A). Fast cytosolic flow leads to formation of a peak pattern (D), similarly to fast diffusion. Parameters: $\bar{n} = 7\,\mu\text{m}^{-1}$, $D_m = 0.1\,\mu\text{m}^2/\text{s}$ and $L = 20\,\mu\text{m}$.

5. Flow-induced transition from mesa to peak patterns

So far we have studied the propagation of patterns in response to cytosolic flow. Next, we will show how cytosolic flow can also drive the transition between qualitatively different pattern types. We distinguish two pattern types exhibited by McRD systems, peaks and mesas [26,27]. Mesa patterns are composed of plateaus (low density and high density) connected by interfaces, while a peak can be pictured as two interfaces concatenated directly (cf. Fig. 4). Mesa patterns form if protein attachment saturates in regions of high total density, while peaks form if the attachment rate does not saturate at high density [26,27]. Thus, while the amplitude of mesa patterns is determined by the attachment–detachment balance in the two plateaus, the amplitude (maximum concentration) of a peak is determined by the total mass available in the system [27].

How does protein transport affect whether a peak or a mesa forms? As we argued above, a peak pattern forms if protein attachment in regions of high density does not saturate. In general, this will happen if attachment to the membrane depletes proteins from the cytosol slower than lateral transport can resupply proteins (see Fig. 5A). Let us first recap the situation without flow, where proteins are resupplied by diffusion from the detachment zone to the attachment zone across the pattern's interface with width ℓ_{int}. Thus, a peak pattern forms if the rate of transport by cytosolic diffusion is faster than the attachment rate ($D_c/\ell_{\text{int}}^2 \gg \tau_{\text{react}}^{-1}$). Further using that the interface width is given by a balance of membrane diffusion and local reactions ($\ell_{\text{int}}^2 \sim \tau_{\text{react}} D_m$), we obtain the condition $D_c \gg D_m$ for the formation of peak patterns.

In terms of phase space geometry, this means that the slope $-D_m/D_c$ of the flux-balance subspace in phase space must be sufficiently shallow. For a steep slope $-D_m/D_c$ of the FBS, the membrane concentration saturates at the point where the FBS intersects with the reactive nullcline blue dots in Fig. 5A. There, attachment and detachment balance such that a mesa forms (Fig. 5A). For faster cytosol diffusion, the flux-balance subspace is shallower such that the third FBS-NC intersection point shifts to higher densities. Thus, for sufficiently fast cytosol diffusion a peak forms (Fig. 5B).

Adding slow cytosolic flow does not significantly contribute to the resupply of the cytosolic sink (i.e. attachment zone) and therefore does not alter the pattern type (Fig. 5C). In contrast, when cytosolic protein transport (by advection and/or diffusion) is fast compared to the reaction kinetics, the cytosolic

sink gets resupplied quickly, leading to a flattening of the cytosolic concentration profile. Accordingly, the density distribution in phase space approaches a horizontal line, both for fast cytosolic diffusion (Fig. 5B) and for fast cytosolic flow (Fig. 5D). As a consequence, the point where the density distribution meets the nullcline shifts towards larger membrane concentrations, resulting in an increasing amplitude of the mesa pattern. Eventually, when the amplitude of the pattern can not grow any further due to limiting total mass, a peak pattern forms (Fig. 5B,D). Hence, an increased flow velocity can cause a transition from a mesa pattern to a peak pattern (see Movie 4).

In summary, we found that cytosolic flow can qualitatively change the membrane-bound protein pattern from a small-amplitude, wide mesa pattern to a large-amplitude, narrow peak pattern. In cells, such flows could therefore promote the precise positioning of polarity patterns on the membrane. Furthermore, we hypothesize that flow can contribute to the selection of a single peak by accelerating the coarsening dynamics of the pattern via two distinct mechanisms. First, flow accelerates protein transport that drives coarsening. Second, as peak patterns coarsen faster than mesa patterns [26,39], flow can accelerate coarsening via the flow-driven mesa-to-peak transition. Such fast coarsening may be important for the selection of a single polarity axis, e.g. a single budding site in *S. cerevisiae* [4], for axon formation in neurons [40], and to establish a distinct front and back in motile cells [2,41].

6. Flow-induced pattern formation

So far we have studied how a uniform flow profile affects pattern formation on a domain with periodic boundary conditions, representing circular flows along the cell membrane and bulk flows in microfluidic *in vitro* setups.

However, flows in the vicinity of the membrane can be non-uniform. We will discuss examples of such non-uniform flows at the end of this section. A non-uniform flow transports the proteins at different speeds along the membrane. Starting from a spatially homogeneous initial state, this leads to a redistribution of mass. It has been demonstrated in previous work that this non-uniform flow can induce pattern formation even if the homogeneous steady state is laterally stable (i.e. there is no spontaneous pattern formation) [9,11,25]. Based on numerical simulations, a transition from flow-guided to self-organized dynamics has been reported [11]. However, the physical mechanism underlying this transition, and what determines the transition point have remained unclear.

As a minimal system to address this question, we consider a one-dimensional domain with no-flux boundaries and a parabolic speed profile that vanishes at the system boundaries (Fig. 6A, top). In the following, we describe the flow-induced dynamics starting from a spatially homogeneous steady state to the final polarity pattern observed in numerical simulations (see Movie 5). Figure 6 visualizes these dynamics in real space (A) and in the (m, c)-phase plane (B). To relate our findings to the previous study Ref. [11], we also visualize the dynamics in an abstract representation of the state space (comprising all concentration profiles) used in this previous study. In this state space, steady states are points and the time evolution of the system is a trajectory (thick blue/orange line in Fig. 6C).

Starting from the homogeneous steady state (*i*), the non-uniform advective flow redistributes mass in the cytosol (*ii*). Due to this redistribution of mass, the local reactive equilibria shift as we have seen repeatedly here and in earlier studies of mass-conserving systems [27,42]. In fact, as long as the gradients of both the membrane and cytosol profiles are shallow, the concentrations remain close to the local equilibria, as evidenced by the density distribution in phase space spreading along the reactive nullcline (see profile (ii) in Fig. 6A,B). Eventually, the region where mass accumulates (here the right edge of the domain), enters the laterally unstable regime (see profile *iii*). In the phase plane (Fig. 6B) this regime corresponds to the range of total densities $\bar{n}$ where the nullcline slope has a steeper negative than the flux-balance subspace ($s_{\mathrm{nc}} < -D_m/D_c$)[5]. The mass-redistribution instability

---

[5]   More precisely, the size of the laterally unstable region must be larger than the shortest unstable mode (corresponding to the right edge of the band of unstable modes in the dispersion relation (Fig. 2A)).
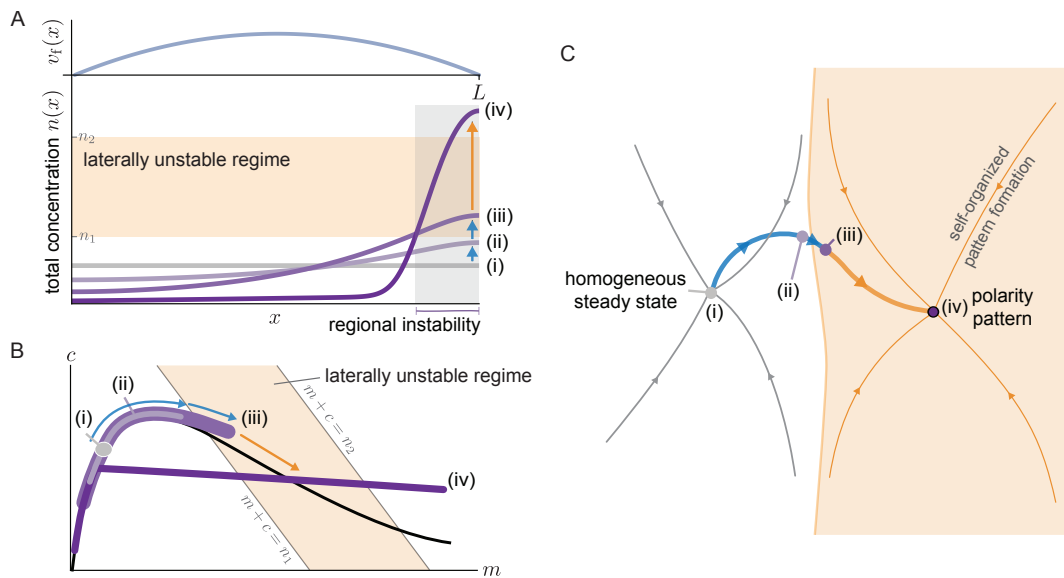
Figure 6. Flow-driven protein mass accumulation can induce pattern formation by triggering a regional lateral instability. (A) Top: quadratic flow velocity profile: $v_f = -v_{\max} \left(x/L - 1/2 \right)^2$. Bottom: illustration of the total density profiles at different time points starting from a homogeneous steady state (*i*) to the final pattern (*iv*); see Movie 5. Mass redistribution due to the non-uniform flow velocity drives mass towards the right hand side of the system, as indicated by the blue arrows. The range of total densities shaded in orange indicates the laterally unstable regime determined by linear stability analysis. Once the total density reaches this regime locally, a regional lateral instability is triggered resulting in the self-organized formation of a peak (orange arrow). (B) Sketch of the phase space representation corresponding to the profiles shown in A. Note that the concentrations are slaved to the reactive nullcline (black line) until the regional lateral instability is triggered. (C) Schematic representation of the state space of concentration patterns in a case where both the homogeneous steady state and a stationary polarity pattern are stable. Thin trajectories indicate the dynamics in the absence of flow and the pattern's basin of attraction is shaded in orange. The thick trajectory connecting both steady states shows the flow-induced dynamics, corresponding to the sequence of states (i)–(iv) shown in A and B.

in this region, based on the self-organized formation of attachment and detachment zones (cf. Sec. 3.2) will lead to the formation of a polarity pattern there (*iv*). Thus, the onset of a *regional lateral instability* marks the transition from flow-guided dynamics to self-organized dynamics.

In the abstract state space visualization (Fig. 6C) the area shaded in orange indicates the polarity pattern's basin of attraction comprising all states (concentration profiles) where a spatial region in the system is laterally unstable. In the absence of flow, states that do not exhibit such a laterally unstable region return to the homogeneous steady state (thin gray lines). Non-uniform cytosolic flow induces mass-redistribution, that can drive an initially homogeneous system (i) into the polarity pattern's basin of attraction. From there on, self-organized pattern formation takes over, leading to the formation of a polarity pattern (iv), essentially independently of the advective flow (orange trajectory).

Similar pattern forming mechanisms based on a regional instability have previously been shown to also underlie stimulus-induced pattern formation following a sufficiently strong initial perturbation [27] and peak formation at a domain edge where the reaction kinetics abruptly change [32]. Thus, an overarching principle for stimulus-induced pattern formation emerges: To trigger (polarity) pattern formation, the stimulus, be it advective flow or heterogeneous reaction kinetics, has to redistribute protein mass in a way such that a regional (lateral) instability is triggered.

It remains to be discussed what happens once the cytoplasmic flow is switched off after the polarity pattern has formed. In general, the polarity pattern will persist (see Movie 5), since it is maintained by self-organized attachment and detachment zones, largely independent of the flow. However, as long as there is flow, the average mass on the right hand side of the system (downstream of the flow) is higher than on the left hand side. Hence, flow can maintain a polarity pattern even if the average mass in the system as a whole is too low to sustain polarity patterns in the absence of flow (see bifurcation analysis in Ref. [27]). If this is the case, the peak disappears once the flow is switched off (see Movie 6).

In summary, the redistribution of the protein mass is key to induce (polarity) pattern formation starting from a stable homogeneous state. There are different scenarios how intracellular flows can lead to such mass redistribution: First, one (or more) components of the pattern forming system may be embedded in the cell cortex [9,11,43] which is a contractile medium driven by myosin-motor activity. Indeed, it was previously demonstrated that advection of proteins in the cell cortex can induce a polarity pattern in a conceptual 2cMcRD model [25] and more quantitative models for the PAR-system [9,11]. Second, three-dimensional flows in the cytoplasm can result in local accumulation of protein mass on the membrane due to flow in the direction normal to the membrane. Thus, the 3D flow field of the cytosol, which is incompressible, can have a similar effect as compressible cortex flows [44].

7. Conclusions and outlook

Inside cells, proteins are transported via diffusion and fluid flows, which, in combination with reactions, can lead to the formation of protein patterns on the cell membrane. To characterize the role fluid flows play in pattern formation, we studied the effect of flow on the formation of a polarity pattern, using a generic two-component model. We found that flow leads to propagation of the polarity pattern *against* the flow direction with a speed that is maximal for intermediate flow speeds, i.e. when the rate of advective transport is comparable to either the reaction rates or to the rate diffusive transport in the cytosol. Using a phase-space analysis, we showed that the propagation of the pattern is driven by an asymmetric influx of protein mass to a self-organized protein-attachment zone. As a consequence, attachment is stronger on the upstream side of the pattern compared to the downstream side, leading to upstream propagation of the membrane bound pattern. Furthermore, we have shown that flow can qualitatively change the pattern from a wide mesa pattern (connecting two plateaus) to a narrow peak pattern. Finally, we have presented a phase-space analysis to elucidate the interplay between flow-guided dynamics and self-organized pattern formation. This interplay was previously studied numerically in the context of PAR-protein polarization [9,11]. Our analysis reveals

the underlying cause for the transition from flow-guided to self-organized dynamics: the regional onset of a mass-redistribution instability.

We discussed implications of our results and links to earlier literature at the end of each section. Here, we conclude with a brief outlook. We expect that the insights obtained from the minimal two-component model studied here generalize to systems with more components and multiple protein species. For example, *in vitro* studies of the reconstituted MinDE system of *E. coli* show that MinD and MinE spontaneously form dynamic membrane-bound patterns, including spiral waves [45] and quasi-stationary patterns [46]. These patterns emerge from the competition of MinD self-recruitment and MinE-mediated detachment of MinD [47,48]. In the presence of a bulk flow, the traveling waves were found to propagate upstream [12]. Our analysis based on a simple conceptual model suggests that this upstream propagation is caused by a larger influx of the self-recruiting MinD on the upstream flanks compared to the downstream flanks of the travelling waves. However, the bulk flow also increases the resupply of MinE on the upstream flanks. As MinE mediates the detachment of MinD and therefore effectively antagonizes MinD's self-recruitment, this may drive the membrane-bound patterns to propagate downstream instead of upstream. Which one of the two processes dominates — MinD-induced upstream propagation or MinE-induced downstream propagation — likely depends on the details of their interactions. This interplay will be the subject of future work.

A different route of generalization is to consider advective flows that depend on the protein concentrations. In cells, such coupling arises, for instance, from myosin-driven cortex contractions [11,49] and shape deformations [21,22]. Myosin-motors, in turn, may be advected by the flow and their activity is controlled by signalling proteins such as GTPases and kinases [50]. This can give rise to feedback loops between flow and protein patterns. Previous studies show that such feedback loops can give rise to mechano-chemical instabilities [51], drive pulsatile (standing-wave) patterns [52,53] or cause the breakup of traveling waves [54]. We expect that our analysis based on phase-space geometry can provide insight into the mechanisms underlying these phenomena.

Abbreviations

The following abbreviations are used in this manuscript:

McRD	mass-conserving reaction–diffusion
2cMcRD	two-component mass-conserving reaction–diffusion
FBS	flux-balance subspace

Appendix A. Limit of slow flow and timescale comparison

The dispersion relation in the absence of flow ($v_f = 0$) reads

$$\sigma^{(0)} = -\frac{1}{2}\left[(D_m + D_c)\,q^2 + f_c - f_m\right] + \frac{B(q)}{2A(q)},\tag{A1}$$

with $A(q) = \left[1 - 4f_c f_m/B(q)^2\right]^{-1/2} - 1$ and $B(q) = f_m + f_c + (D_c - D_m)q^2$. To find the effect of slow flow, we first need to identify the relevant timescales such that we can define a dimensionless small parameter to expand in. Because pattern formation is driven by transport in the cytosol (diffusive and advective) and attachment from the cytosol to the membrane, there are three relevant timescales: (*i*) The the rate of advective transport on length scale q^{-1} is given by qv_f; (*ii*) The rate of diffusive

transport on that scale, given by $D_c q^2$; and (*iii*) the attachment rate $f_c = a(m)$ (cf. Eq. (2)). To compare these timescales, we form two dimensionless numbers: the Peclét number $\mathrm{Pe} = v_\mathrm{f}/(D_c q)$ and the Damköhler number $\mathrm{Da} = f_c/(v_\mathrm{f} q)$. Flow can either be slow compared to reactions ($\mathrm{Da} \gg 1$) or slow compared to diffusion ($\mathrm{Pe} \ll 1$). In both cases, expanding the the dispersion relation $\sigma(q)$ to first order yields

$$\sigma(q) = \sigma^{(0)}(q) + i \frac{v_\mathrm{f} q}{2} A(q) + \mathcal{O}(\varepsilon^2), \tag{A2}$$

where $\varepsilon = \min(\mathrm{Pe}, \mathrm{Da}^{-1})$. By elementary algebra using the assumptions $D_c > D_m$ and $f_c > 0$ made above, it follows that $A(q)$ is positive when $s_\mathrm{nc} < 0$. As Eq. (8) in Sec. 3.3 shows, the condition $s_\mathrm{nc} < 0$ is necessary for a band of unstable modes to exist. Therefore, $A(q)$ is positive for all unstable modes.

Appendix B. Movie descriptions

1. Growth of a pattern from a homogeneous steady state in the presence of flow. Top: concentration profiles in space; bottom: corresponding density distribution in the phase space. (Parameters: $D_m = 0.1\,\mu\mathrm{m}^2/\mathrm{s}$, $\bar{n} = 3\,\mu\mathrm{m}^{-1}$, $L = 20\,\mu\mathrm{m}$ and $v_\mathrm{f} = 20\,\mu\mathrm{m/s}$.)
2. Simulation with adiabatically increasing flow speed from $v_\mathrm{f} = 0\,\mu\mathrm{m/s}$ to $v_\mathrm{f} = 100\,\mu\mathrm{m/s}$. Note the flattening of the cytosolic concentration profile as the flow speed increases. (Fixed parameters as for Movie 1.)
3. Corresponds to the space-time plot in Fig. 4A.
4. Pattern transformation from a mesa pattern to a peak pattern as flow speed is adiabatically increased from $v_\mathrm{f} = 0$ to $v_\mathrm{f} = 45\,\mu\mathrm{m/s}$. (Fixed parameters as for Movie 1.)
5. Pattern formation triggered by mass-redistribution due to a spatially non-uniform flow (parabolic flow profile shown in Fig. 6A). After the flow is switched off at $t = 200\,\mathrm{s}$, the pattern is maintained. (Parameters: $D_m = 0.1\,\mu\mathrm{m}^2/\mathrm{s}$, $L = 30\,\mu\mathrm{m}$, $v_\mathrm{max} = 1\,\mu\mathrm{m/s}$, and $\bar{n} = 1\,\mu\mathrm{m}^{-1}$.)
6. As Movie 5, but with lower average mass, $\bar{n} = 0.8\,\mu\mathrm{m}^{-1}$. This mass is not sufficient to maintain a stationary peak in the absence of flow. Therefore, the peak disappears after the flow is switched off ($t > 200\,\mathrm{s}$).

References

1. Weiner, O.D. Regulation of Cell Polarity during Eukaryotic Chemotaxis: The Chemotactic Compass. *Current Opinion in Cell Biology* **2002**, *14*, 196–202. doi:10.1016/S0955-0674(02)00310-1.
2. Keilberg, D.; Søgaard-Andersen, L. Regulation of Bacterial Cell Polarity by Small GTPases. *Biochemistry* **2014**, *53*, 1899–1907. doi:10.1021/bi500141f.
3. Bi, E.; Park, H.O. Cell Polarization and Cytokinesis in Budding Yeast. *Genetics* **2012**, *191*, 347–387. doi:10.1534/genetics.111.132886.
4. Chiou, J.g.; Balasubramanian, M.K.; Lew, D.J. Cell Polarity in Yeast. *Annual Review of Cell and Developmental Biology* **2017**, *33*, 77–101. doi:10.1146/annurev-cellbio-100616-060856.
5. Goryachev, A.B.; Leda, M. Many Roads to Symmetry Breaking: Molecular Mechanisms and Theoretical Models of Yeast Cell Polarity. *Molecular Biology of the Cell* **2017**, *28*, 370–380. doi:10.1091/mbc.e16-10-0739.
6. Turing, A.M. The Chemical Basis of Morphogenesis. *Philosophical Transactions of the Royal Society of London. Series B, Biological Sciences* **1952**, *237*, 37–72. doi:10.1098/rstb.1952.0012.
7. Hawkins, R.J.; Bénichou, O.; Piel, M.; Voituriez, R. Rebuilding Cytoskeleton Roads: Active-Transport-Induced Polarization of Cells. *Physical Review E* **2009**, *80*, 040903. doi:10.1103/PhysRevE.80.040903.
8. Calvez, V.; Lepoutre, T.; Meunier, N.; Muller, N. Non-Linear Analysis of a Model for Yeast Cell Communication. *ESAIM: Mathematical Modelling and Numerical Analysis* **2020**, *54*, 619–648. doi:10.1051/m2an/2019065.
9. Goehring, N.W.; Trong, P.K.; Bois, J.S.; Chowdhury, D.; Nicola, E.M.; Hyman, A.A.; Grill, S.W. Polarization of PAR Proteins by Advective Triggering of a Pattern-Forming System. *Science* **2011**, *334*, 1137–1141. doi:10.1126/science.1208619.
10. Illukkumbura, R.; Bland, T.; Goehring, N.W. Patterning and Polarization of Cells by Intracellular Flows. *Current Opinion in Cell Biology* **2020**, *62*, 123–134. doi:10.1016/j.ceb.2019.10.005.

11. Gross, P.; Kumar, K.V.; Goehring, N.W.; Bois, J.S.; Hoege, C.; Jülicher, F.; Grill, S.W. Guiding Self-Organized Pattern Formation in Cell Polarity Establishment. *Nature Physics* **2019**, *15*, 293–300. doi:10.1038/s41567-018-0358-7.

12. Ivanov, V.; Mizuuchi, K. Multiple Modes of Interconverting Dynamic Pattern Formation by Bacterial Cell Division Proteins. *Proceedings of the National Academy of Sciences* **2010**, *107*, 8071–8078. doi:10.1073/pnas.0911036107.

13. Vecchiarelli, A.G.; Li, M.; Mizuuchi, M.; Mizuuchi, K. Differential Affinities of MinD and MinE to Anionic Phospholipid Influence Min Patterning Dynamics *in Vitro*: Flow and Lipid Composition Effects on Min Patterning. *Molecular Microbiology* **2014**, *93*, 453–463. doi:10.1111/mmi.12669.

14. Grill, S.W.; Gönczy, P.; Stelzer, E.H.K.; Hyman, A.A. Polarity Controls Forces Governing Asymmetric Spindle Positioning in the Caenorhabditis Elegans Embryo. *Nature* **2001**, *409*, 630–633. doi:10.1038/35054572.

15. Munro, E.; Nance, J.; Priess, J.R. Cortical Flows Powered by Asymmetrical Contraction Transport PAR Proteins to Establish and Maintain Anterior-Posterior Polarity in the Early C. Elegans Embryo. *Developmental Cell* **2004**, *7*, 413–424. doi:10.1016/j.devcel.2004.08.001.

16. Hecht, I.; Rappel, W.J.; Levine, H. Determining the Scale of the Bicoid Morphogen Gradient. *Proceedings of the National Academy of Sciences* **2009**, *106*, 1710–1715. doi:10.1073/pnas.0807655106.

17. Mayer, M.; Depken, M.; Bois, J.S.; Jülicher, F.; Grill, S.W. Anisotropies in Cortical Tension Reveal the Physical Basis of Polarizing Cortical Flows. *Nature* **2010**, *467*, 617–621. doi:10.1038/nature09376.

18. Goldstein, R.E.; van de Meent, J.W. A Physical Perspective on Cytoplasmic Streaming. *Interface Focus* **2015**, *5*, 20150030. doi:10.1098/rsfs.2015.0030.

19. Mogilner, A.; Manhart, A. Intracellular Fluid Mechanics: Coupling Cytoplasmic Flow with Active Cytoskeletal Gel. *Annual Review of Fluid Mechanics* **2018**, *50*, 347–370. doi:10.1146/annurev-fluid-010816-060238.

20. Bischof, J.; Brand, C.A.; Somogyi, K.; Májer, I.; Thome, S.; Mori, M.; Schwarz, U.S.; Lénárt, P. A Cdk1 Gradient Guides Surface Contraction Waves in Oocytes. *Nature Communications* **2017**, *8*, 1–10. doi:10.1038/s41467-017-00979-6.

21. Koslover, E.F.; Chan, C.K.; Theriot, J.A. Cytoplasmic Flow and Mixing Due to Deformation of Motile Cells. *Biophysical Journal* **2017**, *113*, 2077–2087. doi:10.1016/j.bpj.2017.09.009.

22. Klughammer, N.; Bischof, J.; Schnellbächer, N.D.; Callegari, A.; Lénárt, P.; Schwarz, U. Cytoplasmic Flows in Starfish Oocytes Are Fully Determined by Cortical Contractions. *PLoS computational biology* **2018**, *14*, e1006588. doi:10.1371/journal.pcbi.1006588.

23. Mori, Y.; Jilkine, A.; Edelstein-Keshet, L. Wave-Pinning and Cell Polarity from a Bistable Reaction-Diffusion System. *Biophysical Journal* **2008**, *94*, 3684–3697. doi:10.1529/biophysj.107.120824.

24. Jilkine, A.; Edelstein-Keshet, L. A Comparison of Mathematical Models for Polarization of Single Eukaryotic Cells in Response to Guided Cues. *PLoS Computational Biology* **2011**, *7*, e1001121. doi:10.1371/journal.pcbi.1001121.

25. Diegmiller, R.; Montanelli, H.; Muratov, C.B.; Shvartsman, S.Y. Spherical Caps in Cell Polarization. *Biophysical Journal* **2018**, *115*, 26–30. doi:10.1016/j.bpj.2018.05.033.

26. Chiou, J.G.; Ramirez, S.A.; Elston, T.C.; Witelski, T.P.; Schaeffer, D.G.; Lew, D.J. Principles That Govern Competition or Co-Existence in Rho-GTPase Driven Polarization. *PLOS Computational Biology* **2018**, *14*, e1006095. doi:10.1371/journal.pcbi.1006095.

27. Brauns, F.; Halatek, J.; Frey, E. Phase-Space Geometry of Reaction–Diffusion Dynamics. *arXiv:1812.08684* **2018**, [1812.08684].

28. Otsuji, M.; Ishihara, S.; Co, C.; Kaibuchi, K.; Mochizuki, A.; Kuroda, S. A Mass Conserved Reaction–Diffusion System Captures Properties of Cell Polarity. *PLoS Computational Biology* **2007**, *3*, e108. doi:10.1371/journal.pcbi.0030108.

29. Goryachev, A.B.; Pokhilko, A.V. Dynamics of Cdc42 Network Embodies a Turing-Type Mechanism of Yeast Cell Polarity. *FEBS Letters* **2008**, *582*, 1437–1443. doi:10.1016/j.febslet.2008.03.029.

30. Trong, P.K.; Nicola, E.M.; Goehring, N.W.; Kumar, K.V.; Grill, S.W. Parameter-Space Topology of Models for Cell Polarity. *New Journal of Physics* **2014**, *16*, 065009. doi:10.1088/1367-2630/16/6/065009.

31. Ishihara, S.; Otsuji, M.; Mochizuki, A. Transient and Steady State of Mass-Conserved Reaction-Diffusion Systems. *Physical Review E* **2007**, *75*, 015203. doi:10.1103/PhysRevE.75.015203.

32. Wigbers, M.C.; Brauns, F.; Hermann, T.; Frey, E. Pattern Localization to a Domain Edge. *Physical Review E* **2020**, *101*, 022414. doi:10.1103/PhysRevE.101.022414.

33. Halatek, J.; Brauns, F.; Frey, E. Self-Organization Principles of Intracellular Pattern Formation. *Philosophical Transactions of the Royal Society B: Biological Sciences* **2018**, *373*, 20170107. doi:10.1098/rstb.2017.0107.

34. Allen, N.S.; Allen, R.D. Cytoplasmic Streaming in Green Plants. *Annual Review of Biophysics and Bioengineering* **1978**, *7*, 497–526. doi:10.1146/annurev.bb.07.060178.002433.

35. Siero, E.; Doelman, A.; Eppinga, M.; Rademacher, J.D.; Rietkerk, M.; Siteur, K. Striped Pattern Selection by Advective Reaction-Diffusion Systems: Resilience of Banded Vegetation on Slopes. *Chaos: An Interdisciplinary Journal of Nonlinear Science* **2015**, *25*, 036411.

36. Perumpanani, A.J.; Sherratt, J.A.; Maini, P.K. Phase Differences in Reaction-Diffusion-Advection Systems and Applications to Morphogenesis. *IMA Journal of Applied Mathematics* **1995**, *55*, 19–33. doi:10.1093/imamat/55.1.19.

37. Samuelson, R.; Singer, Z.; Weinburd, J.; Scheel, A. Advection and Autocatalysis as Organizing Principles for Banded Vegetation Patterns. *Journal of Nonlinear Science* **2019**, *29*, 255–285. doi:10.1007/s00332-018-9486-6.

38. Mathematica. Wolfram Research, Inc., 2019.

39. Brauns, F.; Weyer, H.; Halatek, J.; Yoon, J.; Frey, E. Coarsening in (Nearly) Mass-Conserving Two-Component Reaction Diffusion Systems. *arXiv:2005.01495 [nlin, physics:physics]* **2020**, [arXiv:nlin, physics:physics/2005.01495].

40. Fivaz, M.; Bandara, S.; Inoue, T.; Meyer, T. Robust Neuronal Symmetry Breaking by Ras-Triggered Local Positive Feedback. *Current Biology* **2008**, *18*, 44–50. doi:10.1016/j.cub.2007.11.051.

41. Wang, Y.; Ku, C.J.; Zhang, E.R.; Artyukhin, A.B.; Weiner, O.D.; Wu, L.F.; Altschuler, S.J. Identifying Network Motifs That Buffer Front-to-Back Signaling in Polarized Neutrophils. *Cell Reports* **2013**, *3*, 1607–1616. doi:10.1016/j.celrep.2013.04.009.

42. Halatek, J.; Frey, E. Rethinking Pattern Formation in Reaction–Diffusion Systems. *Nature Physics* **2018**, *14*, 507–514. doi:10.1038/s41567-017-0040-5.

43. Wang, S.C.; Low, T.Y.F.; Nishimura, Y.; Gole, L.; Yu, W.; Motegi, F. Cortical Forces and CDC-42 Control Clustering of PAR Proteins for Caenorhabditis Elegans Embryonic Polarization. *Nature Cell Biology* **2017**, *19*, 988–995. doi:10.1038/ncb3577.

44. Mittasch, M.; Gross, P.; Nestler, M.; Fritsch, A.W.; Iserman, C.; Kar, M.; Munder, M.; Voigt, A.; Alberti, S.; Grill, S.W.; Kreysing, M. Non-Invasive Perturbations of Intracellular Flow Reveal Physical Principles of Cell Organization. *Nature Cell Biology* **2018**, *20*, 344–351. doi:10.1038/s41556-017-0032-9.

45. Loose, M.; Fischer-Friedrich, E.; Ries, J.; Kruse, K.; Schwille, P. Spatial Regulators for Bacterial Cell Division Self-Organize into Surface Waves in Vitro. *Science* **2008**, *320*, 789–792. doi:10.1126/science.1154413.

46. Glock, P.; Ramm, B.; Heermann, T.; Kretschmer, S.; Schweizer, J.; Mücksch, J.; Alagöz, G.; Schwille, P. Stationary Patterns in a Two-Protein Reaction-Diffusion System. *ACS Synthetic Biology* **2019**, *8*, 148–157. doi:10.1021/acssynbio.8b00415.

47. Huang, K.C.; Meir, Y.; Wingreen, N.S. Dynamic Structures in Escherichia Coli: Spontaneous Formation of MinE Rings and MinD Polar Zones. *Proceedings of the National Academy of Sciences* **2003**, *100*, 12724–12728. doi:10.1073/pnas.2135445100.

48. Halatek, J.; Frey, E. Highly Canalized MinD Transfer and MinE Sequestration Explain the Origin of Robust MinCDE-Protein Dynamics. *Cell Reports* **2012**, *1*, 741–752. doi:10.1016/j.celrep.2012.04.005.

49. Deneke, V.E.; Puliafito, A.; Krueger, D.; Narla, A.V.; De Simone, A.; Primo, L.; Vergassola, M.; De Renzis, S.; Di Talia, S. Self-Organized Nuclear Positioning Synchronizes the Cell Cycle in Drosophila Embryos. *Cell* **2019**, *177*, 925–941.e17. doi:10.1016/j.cell.2019.03.007.

50. Iden, S.; Collard, J.G. Crosstalk between Small GTPases and Polarity Proteins in Cell Polarization. *Nature Reviews Molecular Cell Biology* **2008**, *9*, 846–859. doi:10.1038/nrm2521.

51. Bois, J.S.; Jülicher, F.; Grill, S.W. Pattern Formation in Active Fluids. *Physical Review Letters* **2011**, *106*, 028103. doi:10.1103/PhysRevLett.106.028103.

52. Radszuweit, M.; Alonso, S.; Engel, H.; Bär, M. Intracellular Mechanochemical Waves in an Active Poroelastic Model. *Physical Review Letters* **2013**, *110*, 138102. doi:10.1103/PhysRevLett.110.138102.

53. Kumar, K.V.; Bois, J.S.; Jülicher, F.; Grill, S.W. Pulsatory Patterns in Active Fluids. *Physical Review Letters* **2014**, *112*. doi:10.1103/PhysRevLett.112.208101.

54. Nakagaki, T.; Yamada, H.; Ito, M. Reaction–Diffusion–Advection Model for Pattern Formation of Rhythmic Contraction in a Giant Amoeboid Cell of thePhysarumPlasmodium. *Journal of Theoretical Biology* **1999**, *197*, 497–506. doi:10.1006/jtbi.1998.0890.

6   Bulk-surface coupling reconciles Min-protein pattern formation in vitro and in vivo

This section is a publication preprint of the following manuscript published in Nature Communications 12, 3312 (2021)

Bulk-surface coupling reconciles Min-protein pattern formation in vitro and in vivo

F. Brauns,[1,*] G. Pawlik,[2,*] J. Halatek,[3,*], J. Kerssemakers,[2] E. Frey,[1] and C. Dekker[2]

[1] *Arnold Sommerfeld Center for Theoretical Physics and Center for NanoScience, Department of Physics, Ludwig-Maximilians-Universtiät München, Theresien-straße 37, D-80333 München, Germany*

[2] *Department of Bionanoscience, Kavli Institute of Nanoscience Delft, Delft University of Technology, Van der Maasweg 9, 2629 HZ Delft, the Netherlands*

[3] *Biological Computation Group, Microsoft Research, Cambridge CB1 2FB, UK*

[*] FB, GP, and JH contributed equally to this work.

Supplementary material is available online:
https://www.nature.com/articles/s41467-021-23412-5#Sec24

Bulk-surface coupling identifies the mechanistic connection between Min-protein patterns *in vivo* and *in vitro*

Fridtjof Brauns[1,*], Grzegorz Pawlik[2,*], Jacob Halatek[3,*], Jacob Kerssemakers[2], Erwin Frey[1,†], Cees Dekker[2,†]

[1]Arnold Sommerfeld Center for Theoretical Physics and Center for NanoScience, Department of Physics, Ludwig-Maximilians-Universität München, Theresienstraße 37, D-80333 München, Germany

[2]Department of Bionanoscience, Kavli Institute of Nanoscience Delft, Delft University of Technology, Van der Maasweg 9, 2629 HZ Delft, the Netherlands

[3]Biological Computation Group, Microsoft Research, Cambridge CB1 2FB, UK

[*]F.B., G.P., and J.H. contributed equally to this work. [†]Corresponding authors. Email: frey@lmu.de, c.dekker@tudelft.nl

Abstract

Self-organisation of Min proteins is responsible for the spatial control of cell division in *Escherichia coli*, and has been studied both *in vivo* and *in vitro*. Intriguingly, the protein patterns observed in these settings differ qualitatively and quantitatively. This puzzling dichotomy has not been resolved to date. Using reconstituted proteins in laterally wide microchambers with a well-controlled height, we experimentally show that the Min protein dynamics on the membrane crucially depend on the micro chamber height due to bulk concentration gradients orthogonal to the membrane. A theoretical analysis shows that *in vitro* patterns at low microchamber height are driven by the same *lateral* oscillation mode as pole-to-pole oscillations *in vivo*. At larger microchamber height, additional *vertical* oscillation modes set in, marking the transition to a qualitatively different *in vitro* regime. Our work reveals the qualitatively different mechanisms of mass transport that govern Min protein-patterns for different bulk heights and thus shows that Min patterns in cells are governed by a different mechanism than those *in vitro*.

Introduction

The Min-protein system was discovered in *E. coli* [1, 2], where pole-to-pole oscillations—that is, the periodically alternating accumulation of the Min proteins on either pole of the cylindrical cell—positions the cell-division machinery. The purification and reconstitution of the Min system *in vitro*, showed that only two proteins, MinD and MinE, a lipid bilayer that mimics the cell membrane and ATP as chemical fuel are required for the formation of patterns [3]. This reconstitution provides a minimal system that enables precise control of reaction parameters and geometrical constraints, thus making

1

the Min system a paradigmatic model system for protein-based pattern formation [4–7]. A remarkably rich plethora of dynamic membrane-bound patterns is found *in vitro*; predominantly traveling waves and spirals [3], but also "mushrooms", "snakes", "amoebas" and "bursts" [8, 9], chaotic patterns [10, 11], "homogeneous pulsing" [12–14] as well as quasi-stationary labyrinths, spots, and mesh-like patterns [11, 15]. Critically, these patterns differ qualitatively and quantitatively from the pole-to-pole oscillations observed *in vivo*. This dichotomy has remained puzzling so far. It raises the central question whether the *in vitro* and *in vivo* patterns even share the same underlying pattern-forming mechanism, and, more generally, how we can gain insights on *in vivo* self-organization from *in vitro* studies with reconstituted proteins.

In general, protein patterns form by the self-organized interplay of chemical reactions and diffusive transport. The diffusive transport is caused by cytosolic (bulk) concentration gradients that form due to the attachment and detachment of proteins to and from the membrane surface. In turn, local changes in total protein concentrations change the reaction kinetics. Mathematically, this interplay is described in terms of mass-transport modes that can be identified by means of a linear stability analysis [5, 16, 17]. This theory has been recently developed as an extension of the canonical theory for Turing pattern formation in reaction-diffusion systems [18].

In *E. coli* cells, the Min proteins are cyclically transported from one cell pole to the other and back, giving rise to so-called pole-to-pole oscillations. In the underlying lateral mass-transport mode, the cytosol acts as a "transport medium" for transport along the length of the cell [17, 19]. In contrast to the cellular confinement of an *E. coli* cell, typical *in vitro* setups have a much larger bulk volume per membrane area. Therefore, significant concentration gradients form not only laterally along the membrane, but also in the direction orthogonal to the membrane. These vertical gradients have been shown in a recent theoretical study to facilitate oscillations driven by diffusive transport of proteins between the membrane and the bulk further away from the membrane [5]. In these membrane-to-bulk oscillations, the bulk acts not only as a transport medium but also as an effective particle reservoir. In experiments, membrane-to-bulk oscillations manifest as homogeneous "blinking" of vesicles, where the proteins oscillate between the membrane and the bulk without breaking the rotational symmetry of the spherical vesicle [12–14]. The presence of at least two fundamentally different mass-transport modes — lateral and vertical — that may drive pattern formation in the Min system raises two important questions: What are the key control parameters that determine the operation of these modes? Which of these modes govern pattern formation *in vivo*, and which govern pattern formation in the classical *in vitro* setups? Answering these questions will be crucial to identify mechanistic similarities and differences between the well studied Min pattern formation phenomena *in vivo* and *in vitro*, and help unify our understanding of this remarkable dynamical system.

Here, we aim to answer these questions, by combining *in vitro* experiments with numerical simulations and the theoretical analysis of an established mathematical Min-model. Importantly, the experiments are performed in a setup that allows us to unambiguously identify and distinguish the mass-transport modes driving the observed dynamics. The

2

key role of bulk concentration gradients in the different mass-transport modes suggests that the geometric confinement of the bulk volume, quantified by the ratio of bulk volume to surface area (short: bulk-surface ratio) is a key parameter that controls pattern formation. To systematically study the role of this parameter, we use laterally large microchambers with flat surfaces on top and bottom and carefully control the heights of these chambers in the range between 2 to $60\,\mu\text{m}$ (see Fig. 1A). The microchambers' height directly determines the bulk-surface ratio while keeping all other parameters — like the lateral dimensions of the system, total protein concentrations, and kinetic rates — fixed. Specifically, the microchamber height confines only the vertical concentration gradients, while leaving the lateral mode unaffected such that membrane-bound protein patterns can evolve freely in the lateral directions along the membrane surfaces. This eliminates the confounding effects of lateral confinement that is inherent to previous experimental setups using various 3D confinements [8, 12–14, 20–22]. The second advantage of our microchambers is that we can directly study the correlation (synchronization) between the membrane-bound patterns at the two juxtaposed membrane surfaces. This correlation reveals the coupling between the two membranes through the bulk in-between them and provides evidence for the vertical bulk gradients. In particular, we find a vertical mass-transport mode that is specific to the two-membrane setup, where it drives membrane-to-membrane oscillations. This mode becomes unstable only above a critical bulk height and marks the transition to a new dynamical regime. For lower bulk heights, only the lateral mass-transport mode is unstable, corresponding to the situation in cells and representing the mechanistic analogue to the *in vivo* system. Above a critical bulk height, our theory predicts that multiple different mass-transport modes become unstable leading to multistability of patterns, i.e. the emergence of different patterns under the same set of conditions. We confirm this prediction experimentally and compile an experimental phase diagram in the parameter plane of bulk height and MinE to MinD concentration ratio. The topology of this phase diagram agrees with the prediction from linear stability analysis and numerical simulations.

Taken together, systematic variation of the bulk height experimentally confirms our theoretical prediction that the bulk-surface ratio is the key parameter that continuously connects the *in vivo* and *in vitro*. The (qualitative) *in vivo* vs *in vitro* dichotomy is resolved by our finding that they are governed by different pattern-forming mechanisms. The key geometric constraint that gives rise to the *in vivo* phenomenology (pole-to-pole oscillations, stripe oscillations in long cells, absence of homogeneous oscillations / "blinking") is the vertical (radial) confinement of the cytosolic volume, not the lateral confinement.

Results

Finite bulk heights lead to drastically different Min patterns

To study the effect of the bulk-surface ratio on Min pattern formation *in vitro*, we need to control this parameter without imposing lateral spatial constraints that affect pattern
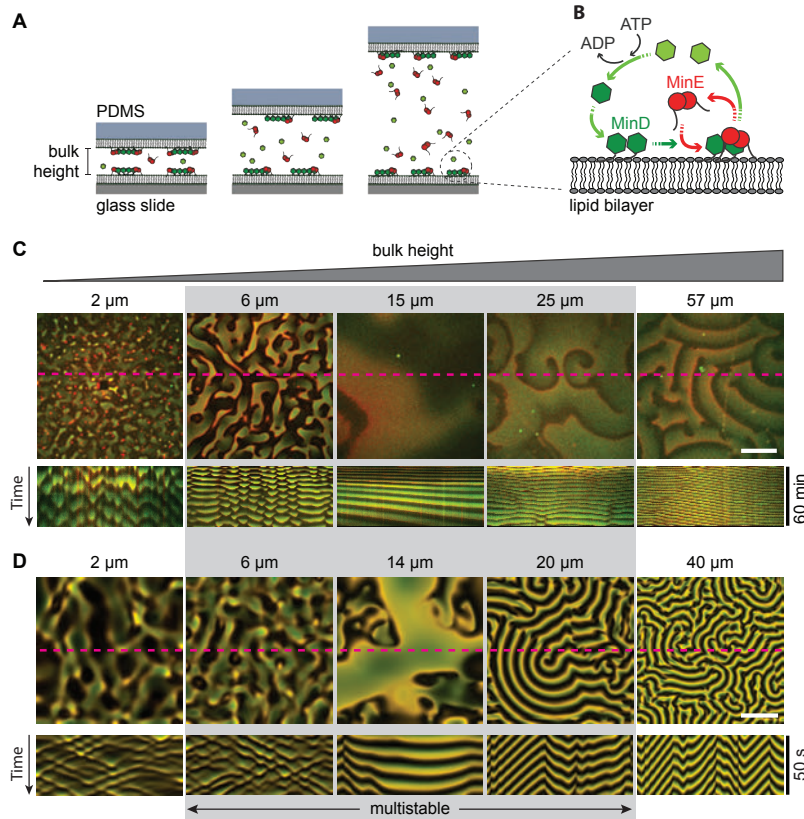
3

Fig. 1. Effect of a change of a bulk height on Min pattern formation. (**A**) General concept of the experimental setup. MinD and MinE proteins were reconstituted in laterally large and flat microchambers of different heights. All inner walls of microchambers were covered with supported lipid bilayers made of DOPC:DOPG:TFCL ($66:32.99:0.01\,\text{mol\%}$) mimicking the *E. coli* membrane composition. Min proteins cycle between bulk and the membrane upon which they self-organize into dynamic spatial protein-density patterns. (**B**) Min-protein interaction scheme. MinD monomers (light-green hexagons) bind ATP resulting in dimerization and cooperative accumulation on membrane (dark-green hexagons). Next, MinE dimers bind to MinD, activating its ATPase activity, detachment from the membrane, and diffusion to the bulk where ADP is exchanged to ATP, and the cycle repeats. (**C**) Influence of the bulk height on Min pattern formation. Snapshots show overlays of MinD channel (green) and MinE channel (red) imaged on the membrane 30 minutes after injection. Kymographs below were generated along the dashed magenta lines. In each microchamber, the concentrations of the reconstituted proteins are $1\,\mu$M MinE and $1\,\mu$M MinD (corresponding to a 1:1 *E:D* ratio). The gray shaded area marks the range of bulk heights where different patterns are observed in repeated experiments (multistability), cf. Fig. 3. (**D**) Snapshots and kymographs from numerical simulations of the reaction–diffusion model describing the skeleton Min-model in a three-dimensional box geometry with a membrane on top and bottom surfaces and reflective boundaries at the sides (see SI Secs. 3 and 5 for details). The colors are an overlay of MinD density (green) and MinE density (red) on the top membrane. Parameters (from left to right): $H = 2\,\mu$m, $E{:}D = 0.8$; $H = 6\,\mu$m, $E{:}D = 0.75$; $H = 14\,\mu$m, $E{:}D = 0.75$; $H = 20\,\mu$m, $E{:}D = 0.725$; $H = 40\,\mu$m, $E{:}D = 0.625$. Lateral system dimensions: $200\,\mu\text{m}\times200\,\mu\text{m}$. The remaining, fixed model-parameters are given in Suppl. Tab. 1. (White scale bars in C and D: $50\,\mu$m.)

4

formation. To achieve this, we created a set of PDMS-based microfluidic chambers of large lateral dimensions ($2\,mm \times 6\,mm$) but with a low height in a range from 2 to 57 µm (Fig. 1A). In these wide chambers, the membrane-bound protein patterns can freely evolve in the lateral direction while we study the effects of vertical bulk-concentration gradients which are constrained by the microchamber height. All inner surfaces of the microchambers were covered with supported lipid bilayers composed of DOPG:DOPC (3:7) which has been shown to mimic the natural *E. coli* membrane composition [23]. Proteins were administered by rapid injection of a solution containing 1 µM of MinE and 1 µM of MinD proteins, together with 5 mM ATP and an ATP-regeneration system [21].

Figure 1C and Movie 1 show snapshots and kymographs of the characteristic patterns observed in microchambers of different heights. We clearly observe distinct Min patterns that can be identified qualitatively by simple visual inspection: standing wave chaos, homogeneous oscillations, and traveling (spiral) waves. Moreover, for intermediate bulk heights (range shaded in gray in Fig. 1) we observe that the system has the capacity to robustly exhibit different pattern types for the same conditions (parameters). This *multistability* is discussed further below.

For low bulk heights (2–6 µm in Fig. 1C) we observe incoherent wave fronts of the protein density propagating from low density towards high density regions, thus continually shifting these regions in a chaotic manner as can be seen in the kymographs. We will refer to these patterns as *standing wave chaos*. The chaos-like character is also evidenced by the irregular shapes and non-uniform propagation velocities of wave fronts within the same pattern (see Supplementary Fig. 1). Still, these patterns clearly have a characteristic wavelength.

For an intermediate bulk height (15 µm in Fig. 1C), we observe patterns with large areas that have fairly homogeneous Min-protein density and temporally oscillate as a whole. We refer to these patterns as *homogeneous oscillations*. (We will use this term whenever there are large patches where the temporal oscillations are in phase, yielding a spatially homogeneous pattern in these patches.) Phenomenologically similar oscillations have been observed as initial transients in some previous experiments [8, 24]. In contrast, however, the oscillations that we observed for intermediate bulk heights persisted throughout the entire duration of the experiment (90 minutes).

In the large bulk height regime (57 µm in Fig. 1C) we find *traveling waves* that are characterized by high spatial coherence of the consecutive wave fronts that propagate together at the same velocity and with a well-controlled wavelength. Finally, the wave patterns found at 25 µm shows phenomena indicative of defect-mediated turbulence: continual creation, annihilation, and movement of spiral defects (Movie 2). This behavior is commonly found in oscillatory media at the transition between spiral waves and homogeneous oscillations / phase waves [25, 26].

Taken together, we find that the bulk height has a profound effect on the phenomenology of Min protein pattern formation. Notably, the bulk-surface ratio at the lowest bulk height (2 µm) is of the same order of magnitude as in *E. coli* cells which have a diameter of about 0.5–1 µm. However, there is no obvious phenomenological correspondence between the *in vivo* system and the laterally unconfined *in vitro* system as the patterns found

5

in these two settings differ qualitatively. Despite this lack of obvious phenomenological correspondence, the theoretical analysis carried out below, based on a minimal model of the Min-protein interactions, allows us to find the connection between the *in vivo* and *in vitro* dynamics by identifying the underlying mesoscopic mechanisms (mass-transport modes).

A minimal model reproduces the salient, qualitative pattern features

To explain the observed diversity of patterns found in experiments, we performed numerical simulations and a theoretical analysis. We used a minimal model of the Min-protein dynamics that is based on the known biochemical interactions between MinD and MinE (Fig. 1B). This model encapsulates the core features of the Min system and has successfully reproduced and predicted experimental findings in a broad range of conditions both *in vivo* [19, 27, 28] and *in vitro* [5, 10]. Finite-element simulations of this model in the same geometry as the microchambers (laterally wide cuboid with membrane on both top and bottom surfaces, see Supplementary Fig. 2) qualitatively reproduce three pattern types found in experiments in the three regimes of bulk heights, as shown in Fig. 1D and Movie 3. (A fourth type of pattern, termed "amoebas" is found in experiments outside the parameter regime accounted for by our minimal model; see Fig. 3.)

For low bulk heights (0.5–5 μm in Fig. 1D), the model exhibits standing wave chaos (incoherent fronts that chaotically shift high- and low-density regions) in close qualitative resemblance of the patterns found experimentally. For intermediate bulk heights (5–15 μm in Fig. 1D), we find nearly homogeneous oscillations, meaning large areas with a nearly homogeneous protein density that oscillate temporally . Gradients in the oscillation phase lead to the impression of propagating fronts, with a velocity inversely proportional to the phase gradient (sometimes called "pseudo waves" or "phase waves" in the theoretical literature [29, 30]). In contrast to genuine traveling waves, phase waves are merely phase-shifted local oscillations. They do not require lateral material transport (lateral mass redistribution) and the visual impression of "propagation" is merely a consequence of the phase gradient. In addition, continual creation and annihilation of topological defects in the phase (like the two spiral defects in Fig. 1C, 25 μm) can give rise to defect-mediated turbulence [25, 31]. We note that the pattern observed for 14 μm possess the visual characteristics of such turbulence. However, a detailed quantification of this phenomenon is beyond the scope of the present work. Finally, for large bulk heights (> 20 μm in Fig. 1D), we find traveling (spiral) waves. This is in agreement with simulations performed for the same reaction kinetics in a setup with a planar membrane on only one side of a large bulk volume [5].

In summary, the model qualitatively reproduces the salient features of our experimental observations across the whole range of bulk heights remarkably well (Fig. 1C,D). However, the characteristic wavelength and oscillation periods of the patterns are not matched quantitatively (although they are of the same order of magnitude). Given the lack of a theoretical understanding of the principles underlying nonlinear wavelength selection, the large number of experimentally unknown kinetic rates, and the potential need to further extend the model [10, 11], fitting parameters is beyond the scope of the present

6

study (please refer to the *Discussion* and SI Sec. 6 for further elaboration on the question of length- and time-scales).

Rather than wavelength selection, our focus here are the fundamental pattern-forming mechanisms, which can be identified by robust, qualitative signatures of these mechanisms: the topology of the phase diagram in the parameter space of bulk height and MinE/MinD concentration ratio, and the synchronization of patterns between the two opposite membrane surfaces.

Distinct mass-transport modes underlie pattern formation at different bulk heights

To identify the pattern-forming mechanisms governing the dynamics for different bulk heights, we performed a linear stability analysis of the homogeneous steady states. This analysis identifies the mass-transport modes that govern pattern formation (see SI Sec. 3 for technical details). For each set of parameters (such as total protein concentrations, bulk height and kinetic rates), only those modes that are *unstable* contribute to the dynamics, while the stable modes are "inactive."

We find three types of mass-transport modes: a lateral mode, transporting mass along membrane, and two types of vertical modes transporting mass orthogonally to the membranes (membrane-to-membrane and membrane-to-bulk). The vertical modes do not require lateral coupling (lateral redistribution of mass) and therefore correspond to *local* instabilities a recently developed theoretical framework for pattern-formation [5, 16]. Here, we use the term *local* regarding the direction along the membrane, as an antonym to lateral. Importantly, the local instabilities still involve spatial gradients in the direction *orthogonal* to the membrane, i.e. in the vertical direction in the microchamber geometry.

The phase diagram in Fig. 2A shows the regimes where the three mass-transport modes are unstable as a function of the bulk height and the ratio of MinE concentration and MinD concentration (*E:D ratio* for brevity). Notably these regimes largely overlap, meaning that multiple distinct mass-transport modes can contribute to the dynamics at the same time.

Low bulk height: only lateral oscillations. At low bulk height, diffusion mixes the bulk in vertical direction quickly, such that no substantial vertical protein gradients can form (see Movie 5). Consequentially, the vertical mass-transport modes are stable. In other words, the up-down symmetry of the system is not spontaneously broken. This corresponds to the azimuthal symmetry of rod-shaped cells, which is not broken by pole-to-pole oscillations. If a compartment were isolated laterally, it would not exhibit any instabilities, because the lateral isolation suppresses the lateral mode (see Fig. 2B, top). In the laterally extended system, there is an instability driven by lateral mass redistribution (illustrated by the green arrows in Fig. 2B, bottom) due to lateral cytosolic gradients [16]. Lateral mass redistribution also underlies the Turing instability and *in vivo* Min patterns [19]. Consistently, simulations performed in a cell geometry with the dimensions of an *E. coli* bacterium, using the same kinetic rates as in the remainder of
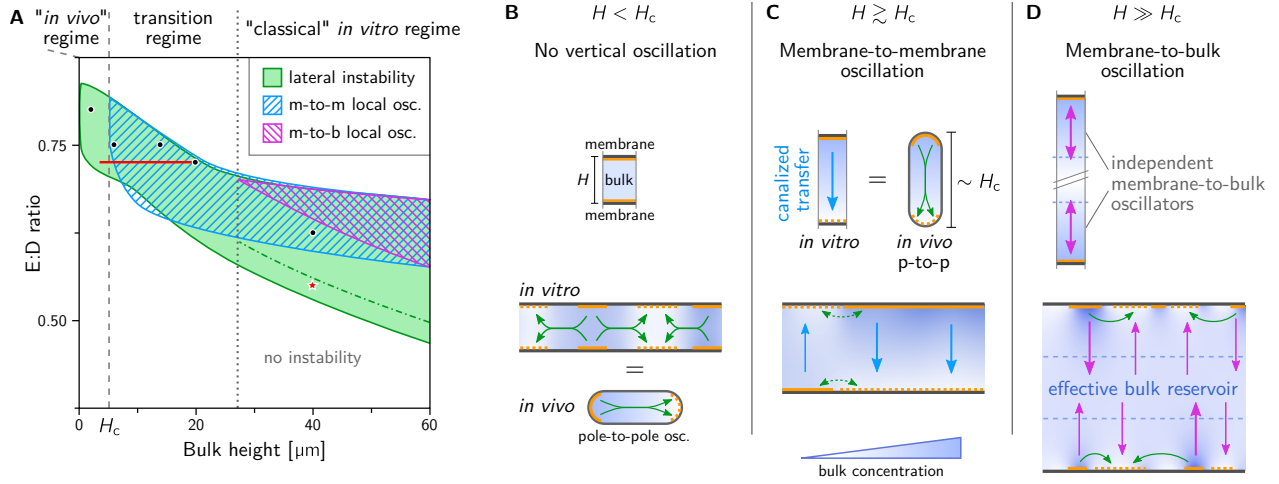
7

Fig. 2. Distinct lateral and vertical mass-transport modes at different bulk heights.
(**A**) Phase diagram for bulk height and $E{:}D$ ratio showing three types of mass-transport modes, identified by linear stability analysis, that exist in overlapping regimes: lateral instability (green), local membrane-to-membrane instability ("m-to-m", blue) and local membrane-to-bulk instability ("m-to-b", magenta). See Supplementary Fig. 3 for representative dispersion relations in the various regimes. Green dot-dashed line marking the transition from chaotic to coherent patterns [5]. A representative example of a chaotic pattern is shown in Movie 4 for the parameter combination marked by the red star. Black dots mark the parameters used for the simulations shown in Fig. 1D. Red line: parameter range for adiabatic sweeps shown in Supplementary Fig. 6 demonstrating hysteresis as a signature of multistability. Panels (**B**–**D**) illustrate the mass-transport modes at different bulk heights. The top row shows laterally isolated compartments to illustrate local vertical oscillations due to *vertical* bulk gradients. The bottom row illustrates the interplay of lateral and vertical mass-transport modes in a laterally extended system. (**B**) For low bulk height, the bulk height is too small for significant vertical concentration gradients to form. Hence, a laterally isolated compartment does not exhibit any instabilities (top). In a laterally extended system (bottom), exchange of mass can drive a lateral instability (green arrows); see Movie 5. The cartoon of an *E. coli* cell illustrates that this instability also underlies pattern formation *in vivo*; see Movies 19 and 20. (**C**) For bulk heights above H_c, vertical concentration gradients become significant enough to enable vertical membrane-to-membrane oscillations (blue arrows); see Movie 6. These oscillations do not require lateral exchange of mass, i.e. they occur in a laterally isolated bulk column (top). The cartoon of an *E. coli* cell illustrates that the membrane-to-membrane oscillations in a laterally isolated compartment can also be pictured as equivalent to *in vivo* pole-to-pole oscillations. The laterally extended *in vitro* system constitutes a continuum of such oscillators (bottom). (**D**) For bulk-heights larger than the penetration depth of vertical gradients, the top and bottom membrane effectively decouple (see Movies 7 and 8). In this regime, which corresponds to the classical *in vitro* regime, the bulk in-between the membranes acts as an effective protein reservoir that facilitates membrane-to-bulk oscillations.

8

this study (see Supplementary Table 1), show pole-to-pole in normal sized cells and stripe oscillations in long (filamentous) cells, in agreement with experimental observations (see Movie 19). For a detailed analysis of the *in vivo* dynamics see Ref. [32]. If, instead of lateral mass transport, *in vivo* Min-protein patterns were driven by vertical oscillation (mass-transport) modes, spherical minicells would blink homogeneously. Homogeneous blinking of cells has not been observed experimentally [33, 34]. We conclude that the patterns observed *in vitro* for low bulk height are governed by the same mechanism as that *in vivo* — a lateral mass-transport mode (corresponding to a "Turing instability"). This finding reveals the underlying cause for the correlation between bulk depletion and the occurrence of standing waves (pole-to-pole/stripe oscillations in cells and "bursts" *in vitro*) reported in Ref. [9]: bulk depletion by attachment of proteins to the membrane generates the lateral gradients that drive the standing wave pattern.

Intermediate bulk height: membrane-to-membrane oscillations. For a sufficiently large bulk height, vertical concentration gradients drive a membrane-to-membrane mass-transport mode as illustrated in Fig. 2C (cf. Movie 6). We define the critical height H_c as the lowest bulk height for which this mode becomes unstable, i.e. starts to contribute to the dynamics. It is determined by the penetration depth of vertical concentration gradients in the bulk that arise as a consequence of the attachment and detachment of proteins at the membranes. The value of H_c depends on the kinetic rates and bulk diffusivities. For the parameters used here, it is approximately $5\,\mu m$ (see Fig. 2A). Characteristically, these membrane-to-membrane oscillations are in *anti-phase* between the top and the bottom membrane. This alternation in protein density will later serve as a signature of the vertical concentration gradients that drive membrane-to-membrane oscillations in the experiment.

Notably, an analogy can be drawn to *in vivo* pole-to-pole oscillations. The two membrane "patches" at the top and bottom of a laterally isolated ("local") compartment in the *in vitro* system can be pictured as analogous to the cell poles *in vivo*. Hence, the vertical membrane-to-membrane oscillations *in vitro* share their mechanism of operation with the *in vivo* pole-to-pole oscillations. Yet there are two key differences. First, the orientation of the gradient is turned by 90 degrees (compare Fig. 2B bottom with Fig. 2C top). Second, the extended membrane surfaces in the *in vitro* system constitute a continuum of laterally coupled oscillators (i.e. an oscillatory medium, see Fig. 2C bottom) while the cellular confinement accommodates only a single oscillator (see Fig. 2B top). Therefore, even though some aspects of the *in vivo* system are present for bulk heights above H_c, we denote only the regime $H < H_c$ as "*in vivo* like" (see Fig. 2A).

Large bulk height: membrane-to-bulk oscillations. When the bulk height is larger than the penetration depth of the bulk gradients, the bulk further away from the membranes acts as a protein reservoir and facilitates oscillations between the membrane and the bulk reservoir — individually and independently for both the top and bottom membrane, as illustrated by magenta arrows in Fig. 2D (see also Movies 7 and 8). Diffusion from the membrane to the bulk reservoir and back provides the delay that underlies these

9

membrane-to-bulk oscillations for a large bulk height. The bulk reservoir in-between the membranes acts as a buffer that decouples the two membranes. Thus, for large chamber heights, the microchamber geometry with two membranes is equivalent to two independent systems with a single membrane, such as "classical" *in vitro* setups with a large bulk volume on top of a supported lipid bilayer.

Fully developed nonlinear patterns and multistability. The different patterns shown in Fig. 1D correspond to the three mass-transport modes discussed above: Lateral mass-transport alone drive standing waves (Movie 5). Dominance of vertical membrane-to-membrane mass-transport leads to laterally homogeneous oscillations (Movie 6). These homogeneous oscillations clearly demarcate the transition from the *in-vivo*-like regime, where only lateral oscillations but no vertical oscillations exist, to the *in vitro* regime where vertical oscillations come into play. Notably, in the "transition regime" lateral instability and vertical membrane-to-membrane instability coexist in largely overlapping regions of parameter space (Fig. 2A). As a result of the competition between these distinct mass-transport modes, we expect multistability, that is, the emergence of different pattern types for the same set of conditions, depending on the initial conditions (see Supplementary Fig. 5). Moreover, in simulations where the bulk height was increased/decreased very slowly compared to the oscillation period of patterns show pronounced hysteresis in the transitions between the different pattern types (Supplementary Fig. 6; simulations details given in SI Sec. 5). Moreover, for intermediate bulk height ($\sim 18\,\mu\mathrm{m}$) we observe spatiotemporal intermittency (Supplementary Fig. 7). This phenomenon can be pictured as the coexistence of homogeneous oscillations, traveling waves, and standing waves in space where they continually transitioned from one to another over time.

For large bulk height, the interplay of lateral oscillations and vertical membrane-to-bulk oscillations drives traveling waves (Movie 7) and standing wave chaos at low $E{:}D$ ratios (see Movies 4 and 8 for simulations the full geometry (2+3D) and in slice geometry (1+2D), respectively). The large bulk-height regime was investigated in detail in a previous theoretical study [5], which focused on the transition from standing wave chaos to traveling waves.

In passing, we note that the patterns we find in numerical simulations have large amplitude. It is no a priori clear whether the linear stability analysis of the homogeneous steady state is informative regarding such large amplitude patterns. In SI Sec. 4, we briefly describe how a recently developed theoretical framework called "local equilibria theory" can be used to characterize large amplitude patterns locally and regionally [5, 16]. Centrally, this framework utilizes the fact that the Min-protein dynamics conserve the total amounts of MinD and MinE. We performed an analysis using local equilibria theory for the patterns found in numerical simulations to confirm the intuition from linear stability analysis. In particular, this analysis shows explicitly how the different mass-transport modes described above drive the pattern of fully developed patterns that have large amplitude (see SI Sec. 4 and Movies 16–18).
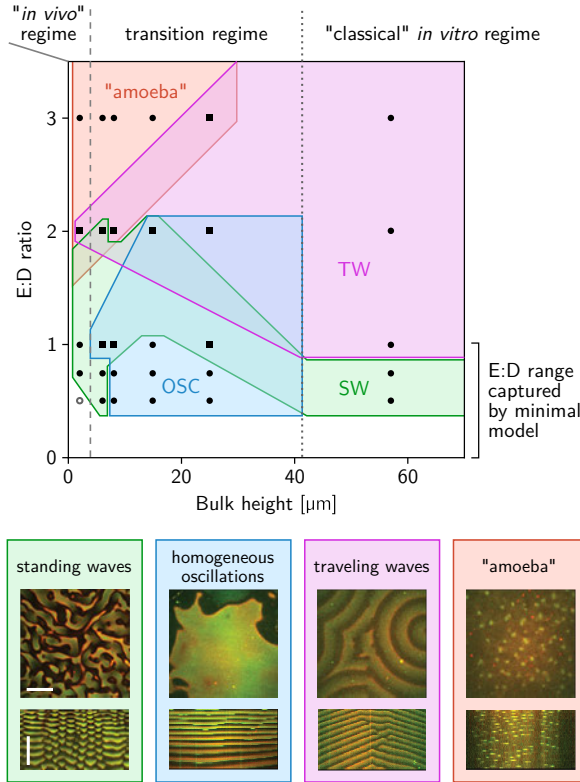
10

Fig. 3. Experimental phase diagram showing multistability. Black symbols mark parameter combinations where experiments were performed. To vary the E:D ratio, the concentration of MinE was varied from 0.5 to 3 µM at a constant MinD concentration of 1 µM. Circles (squares) mark monostable (multisatble) regions, where one (multiple) pattern types were found in repeated experiments. The observed pattern types are indicated by the colored regions; the legend shows representative snapshots and kymographs (see Supplementary Fig. 9 for representative snapshots for each parameter combination and pattern type separately). Note that the topology of the phase diagram agrees with the prediction from linear stability analysis (Fig. 2A) within the regime captured by the minimal model ($E : D < 1$). (Scale bars: 50 µm and 30 min.)

Experimental phase diagram

To experimentally test the predicted multistability, we systematically varied the bulk height (from 2 to 57 µm) and the E:D ratio (from 0.5 to 3), and repeated the experiment several times ($N = 2$ to 5) for each parameter combination. Figure 3 shows the phase diagram obtained from this large assay. Detailed descriptions and quantifications the patterns observed in the different regimes of the phase diagram are provided in Supplementary Information Sec. 1. Critically, within the regime captured by the minimal model (E:$D < 1$), the topology of this experimental phase diagram agrees with the prediction from linear stability analysis (Fig. 2A). In particular, for intermediate bulk height, we observed qualitatively different patterns in repeated experiments with the same parameters, which clearly indicates multistability (see the overlapping regions in Fig. 3, and Movie 15 showing an example of threefold multistability). By contrast, for low bulk height (2 µm) we found only a single instance of (twofold) multistability ($H = 2$ µm, E:$D = 2$), whereas for large bulk height (57 µm) we did not observe any multistability at all. In agreement to these experimental findings, numerical simulations for small and large bulk heights do not show multistability of qualitatively different patterns. Note that for E:$D > 1$, the minimal model does not exhibit pattern formation [19]. An extension to the model, accounting for the switching of MinE between an active and an inactive conformation, is

required to capture pattern formation in this regime [10]. This extension, however, would significantly increase the number of parameters and variables and require a readjustment of parameters to the observed phenomenology at the computational cost of several weeks CPU time. Given that the minimal model captures the phenomenology we are interested in, we refrain from considering the model extension explicitly.

Interplanar pattern synchronization reveals vertical mass-transport modes in experiments

Recall that the vertical synchronization of patterns on the opposite (top and bottom) membranes is a key signature that distinguishes the lateral mass-transport mode for low bulk height, the vertical membrane-to-membrane mass-transport mode for intermediate bulk height, and the vertical membrane-to-bulk mass-transport mode for large bulk height. Respectively, these modes cause strong in-phase coupling, anti-phase coupling, and de-coupling of the dynamics on the two opposites membranes (Fig. ??B).

In the following, we will use these characteristics to infer the underlying mass-transport modes directly from the experimentally observed patterns. To analyze interplanar synchronization of patterns, we imaged the Min patterns on both membranes simultaneously (delay < 0.1 s) in a set of experiments with bulk heights ranging from 10 to 51 µm at 1:1 E:D ratio. Figure ??D and Movie 9 show the patterns found in this set of experiments. We calculated correlation histograms to quantify the observed synchronization between the membrane-bound patterns forming on the two membrane surfaces (Fig. ??E). In agreement with the predictions, we find fully synchronized patterns for low bulk height (10 µm). For intermediate bulk heights (21–30 µm), we find coexisting spatial regions where patterns are clearly synchronized in anti-phase as well as regions of in-phase synchronization. In particular, strong anti-correlation, indicating anti-phase synchronisation, is found for bulk heights 26 µm and 30 µm. This is a strong indication of the membrane-to-membrane oscillations predicted by the theoretical model. Notably, coexistence of in-phase synchronized patterns and anti-phase oscillations in neighboring regions of the membranes is also observed in numerical simulations in three-dimensional geometry (Supplementary Fig. 7 and Movie 10). Finally, and in agreement with the theoretical prediction, patterns become increasingly de-synchronized between the opposite membranes for large bulk heights, with a near-complete dissimilarity for (51 µm).

Figure ??G summarizes the bulk height dependency of the pattern correlation and clearly shows that in-phase correlation is maximal at small bulk heights, anti-correlation peaks for intermediate bulk heights, and that the overall correlation decreases as bulk height increases and both membranes decouple from each other. These findings provide strong experimental evidence for the existence and importance of vertical concentration gradients in the bulk. Critically, our theoretical analysis above has shown that the synchronization across the bulk is a consequence of the different mass-transport modes underlying pattern formation and hence reveals the role of these mass-transport modes in the experimental system.

A

top

bottom

overlay

B

H = 2 μm   *H* = 20 μm   *H* = 40 μm

top

bottom

overlay

time

60 s

25 μm

C correlation

freq. [%]

D

H = 10 μm   21 μm   26 μm   30 μm   43 μm   51 μm

top

bottom

overlay

kymograph

350 s

time

E

10 μm   21 μm   26 μm   30 μm   43 μm   51 μm

frequency [%]

correlation

F

350 s

uncorrelated

in-phase

anti-phase

50 μm

G

○ in-phase
□ anti-phase

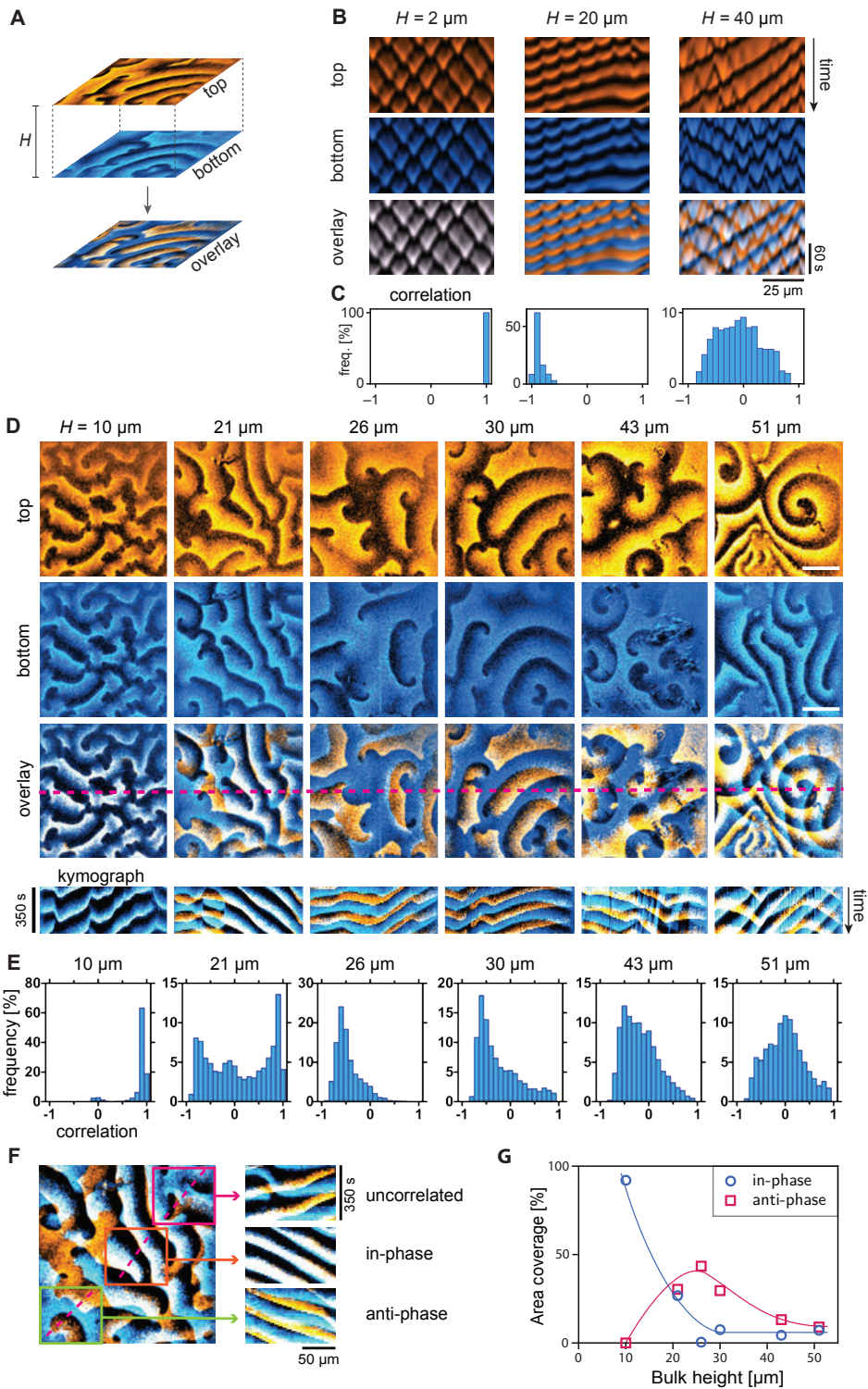Area coverage [%]

Bulk height [μm]

13

Fig. 4. Min cross-talk between opposite membranes. (**A**) Patterns form on the membranes both on the top and bottom surface of the microchambers. Overlaying these patterns in different colors (blue and orange) reveals the synchronization between them. In the overlay, blue and orange additively mix to white such that white areas signify high concentration on both membranes. Black indicates areas of coinciding low protein density. (**B**) Kymographs from simulations in slice geometry (1+2D) showing perfect in-phase synchrony of patterns at low bulk height, anti-phase synchrony driven by membrane-to-membrane mass-transport for intermediate bulk height and de-synchronization for large bulk height, where two membranes effectively decouple. (E:D ratios from left to right: $0.75, 0.725$, and 0.55). (**C**) Histograms of the correlation between top and bottom membrane corresponding to the kymographs in B. The correlation was calculated between concentration time-traces over a $100\,\mathrm{s}$ interval at regularly spaced spatial positions ($\Delta x = 0.25\,\mu\mathrm{m}$). (**D**) Snapshots and kymographs from simultaneous ($< 0.1\,\mathrm{s}$ delay) imaging of MinE on the top (orange) and bottom (blue) membrane in microchambers of different heights ($1\,\mu\mathrm{M}$ MinD, $1\,\mu\mathrm{M}$ MinE). Bars correspond to $50\,\mu\mathrm{m}$. (**E**) Each field of view (FOV) was divided into a grid of cells for which the correlation analysis was performed individually. Histograms show frequency distribution of correlations of individual cells in the grid measured for 30 timepoints in each FOV. Perfect in-phase correlation corresponds to a correlation value of 1 and perfect anti-phase to a value of -1 respectively; lack of correlation corresponds to a correlation measure of 0. (**F**) Example of coexistence of in-phase and anti-phase synchrony within adjacent spatial regions. (**G**) Classification of top-bottom correlation as a function of bulk height, extracted from the histograms in panel D. Correlation values above 0.7 are classified as correlated, values less than -0.3 as anticorrelated. (Source data are provided as a Source Data file.)

Discussion

The starting point for this study was the puzzling qualitative and quantitative differences between the phenomena exhibited by the MinDE-protein system *in vivo* and *in vitro*. We found that different patterns emerge from and are maintained by distinct pattern-forming mechanisms (mass-transport modes) that depend on how far concentration gradients can penetrate into the cytosolic bulk, and thus on the *geometry* of the system, especially the bulk height. Thus, a principled theoretical approach together with a minimal model and direct experimental verification has enabled us to disentangle the Min system's complex phenomenology and identify the pattern-forming mode *in vitro* that is mechanistically equivalent to the mode driving *in vivo* patterns. This implies that no new biochemical insight is necessary to qualitatively resolve the dichotomy between *in vivo* and *in vitro* phenomenology.

Rather, our results show that the bulk height, or more generally the bulk-surface ratio, is a control parameter of equal importance as the protein concentrations and kinetic rates. Importantly, this implies that to faithfully emulate the *in vivo* system in an *in vitro* setup, one needs to confine the bulk volume sufficiently to suppress vertical mass-transport modes. The presence of homogeneous oscillations (sometimes called "blinking" or "pulsing") of Min proteins in vesicles and micro-droplets with diameters as small as $10\,\mu\mathrm{m}$ [12–14] indicates that previous *in vitro* setups have not succeeded in suppressing the vertical mass-transport modes. Conversely, we predict that *E. coli* cells sculpted into spherical shape of sufficient diameters (about $10\,\mu\mathrm{m}$) will exhibit homogeneous oscilla-

14

tions.

A major phenomenological feature of patterns that is typically discussed in the context of the *in vivo* vs *in vitro* dichotomy is the pattern wavelength which is $\sim 50\,\mu m$ *in vitro* compared to $\sim 5\,\mu m$ *in vivo*. Unfortunately, the principles of wavelength selection of highly nonlinear patterns in general, and of the Min-protein patterns in particular, remains an open problem, both theoretically and experimentally. In the Supplementary Information Sec. 6, we provide a more in-depth discussion of the topic of length-scale selection and show that the width of interfaces of the large-amplitude patterns, rather than their wavelength, is characteristic for the underlying pattern-forming mode. Future studies, pursuing a systematic understanding of wavelength selection, might ultimately answer why the Min-pattern wavelengths are so different *in vivo* and *in vitro*. Rather than attempting a quantitative fit, we relied on robust qualitative features to relate our theoretical results to experimental observations. These qualitative features, predicted from the model and confirmed in experiments, are the topology of the phase diagram (critically including a region of multistability) and the synchronization of patterns between the two membrane surfaces. Remarkably, by simply varying the distance between the membrane surfaces (i.e. the bulk height) we found both in-phase and anti-phase synchronization. These interesting phenomena deserve more detailed experimental and theoretical investigations.

From a broader perspective, bulk-surface coupling (cycling of proteins between membrane and cytosol) is a fundamental feature of protein-based pattern formation in cells [7, 32]. Thus our results suggest that geometric properties, like the bulk-surface ratio, will have an impact on the dynamics in many such systems.

Studying parameters that can be varied on a continuous axis—namely the $E{:}D$ ratio and the microchamber height—has been key to our study. It has allowed us to obtain a "phase diagram" which reveals the transitions and relations between the regimes where different pattern-formation modes are operating. This lays the foundation to tailor the Min system for specific applications [35].

Methods

Experiments were performed with purified Min proteins in PDMS microchambers and glass flow-cells coated with lipid bilayers as described below.

The mathematical model accounting for the core set of Min-protein interactions [5, 19, 27], termed skeleton Min model, was analyzed using linear stability analysis and numerical simulations as described in the Supplementary Information (Sections 3–6).

Chemicals. All phospholipids used in this study (1,2-dioleoyl-sn-glycero-3-phosphocholine; 1,2-dioleoyl-sn-glycero-3-phospho-(1'-rac-glycerol) (sodium salt); 1,1',2,2'-tetraoleoyl cardiolipin[4-(dipyrrometheneboron difluoride)butanoyl] (ammonium salt) Top-Fluor® Cardiolipin were purchased from Avanti Polar Lipids. Phosphoenolpyruvic acid was from Alfa Aesar. RTV 615 PDMS and crosslinker were purchased from Momentive. All other chemicals were purchased from Sigma-Aldrich (or otherwise as indicated).

15

Microfabrication. Fabrication of microstructures took place in a class 10000 cleanroom. 4-inch silicon wafers were cleaned with isopropanol and baked for 10 min at 200 °C. A thin layer of a primer hexamethyldisilazane (BASF) was spin-coated on the wafer at 1000 rpm for 1 min and baked at 200 °C for 2 min. Next, a thick layer of NEB22a resist (Sumitomo Chemicals) was deposited by spin-coating at 500 rpm for 15 s and pre-baking at 110 °C for 3 min. Patterns were designed using the Klayout software and written into the NEB22a layer with the use of electron-beam lithography (EBPG-5000+, Raith GmbH) with a dose of $16\,\mu\mathrm{C\,cm^{-2}}$, acceleration voltage of 100 kV, and with aperture 400 μm. Subsequently, the wafer was baked at 105 °C for 3 min. Non-crosslinked resist was removed using a MF322 developer (Dow Chemical Company) bath for 1 min followed by a subsequent 10% MF322 bath for 30 s and cleaning with distilled water for 30 s. Structures were etched with a Bosch deep reactive ion etching process into the silicon wafer using inductive coupled plasma reactive-ion etcher (Adixen AMS 100 I-speeder). The etching step involved 200 sccm SF_6 for 7 s and the passivation step was done with 80 sccm C4F8 for 3 s. The etching time was chosen to achieve the desired height of microstructure. Resist was removed from wafer using oxygen plasma for 15 min. Quality of structures was examined using widefield microscopy and the height of structures was measured using a profilometer (Bruker Dektak XT). Wafers with microstructures were silanized over night using silane vapors in a vacuum chamber.

Preparation of PDMS microchambers and glass flow-cells. A 5 mm layer of degassed PDMS (9:1 PDMS:curing agent ratio) was poured onto the wafer with microstructures and degassed in the vacuum chamber for an additional 1 h to remove any air bubbles. Afterwards, the PDMS was baked for 4 h at 80 °C and individual microchambers were cut out of a PDMS slab. Inlet and outlet holes were punched using a stainless steel 0.75 mm diameter biopsy punch (World Precision Instruments). Cover slips were cleaned in 1 M KOH for 1 h followed by 1 H methanol cleaning, both in a sonicator bath. Right before annealing, the PDMS device and a cover slip were briefly flushed with isopropanol, blown with an N_2 stream and treated with oxygen plasma for 20 s using oxygen plasma PREEN I (Plasmatic System, Inc.) with a flow of 1 SCFH of O_2. The PDMS device was then placed on the cover slip and baked for 10 min at 100 °C to facilitate bonding between PDMS and the glass. Right after that, a solution of small unilamellar vesicles (SUVs) containing 1 mg/ml lipids (including fluorescent lipids) in a buffer containing 25 mM Tris-HCl (pH 7.5), 150 mM KCl and 5 mM $MgCl_2$ was incubated in the device at 37 °C for 30 min to facilitate the formation of supported lipid bilayer (SLB). Subsequently the device was washed for 10 min with the same buffer without lipids. The quality and cleanliness of the formation of membrane were inspected using fluorescence microscopy. The chamber height was confirmed by acquiring z-stacks in multiple places over each device.

For the assay where we probe top-bottom synchronization, we used glass-based flow chambers. For their preparation, we used two rectangular cleaned cover slips (bottom one 22/50 mm, top one 5/30 mm) with thin parafilm stripes on both ends in between them as spacers. The top glass slip had two holes (inlet and outlet) drilled close to the opposite

16

edges, to which tubing was attached. Sides were sealed using scotch tape to allow for elasticity. To form a SLB, the flow cell was filled with SUV solution through the inlet tube and incubated for 30 min. Subsequently, the flow cell was washed thoroughly using buffer to remove excess SUVs. Next, the distance between bottom and the top membrane was set using a custom-built screw-based mini press attached to the microscopic sample holder. The screw was pressing the top cover slip through a large metal pad to achieve a homogenous distance between cover slips over a a large area. The height between top and bottom membrane was monitored using fluorescent microscope by performing z-scan profile of membrane fluorophore emission. Upon reaching the desired height, flow cell was ready for injection of the proteins.

Preparation of SUVs. SUVs were prepared using a thin lipid hydration method. Lipids were dissolved in chloroform and evaporated in a glass vial under vacuum for 3 h. In all experiments the same lipid composition was used (DOPC:DOPG:TopFluorCardiolipin 67:33:0.02 mol%). Next, 25 mM Tris-HCl (pH 7.5), 150 mM KCl buffer was added to achieve a 5 mg/ml final lipid concentration, and a vial was incubated on a shaker for 1 h. Finally, lipid solution was extruded using Avanti Mini Extruder (Avanti Polar Lipids) through 30 nm filter. Aliquots were snap frozen in liquid nitrogen and stored in −80 °C. For preparation of the SLBs, an aliquot was thawed on ice, diluted in a buffer to a final composition 25 mM Tris-HCl (pH 7.5), 150 mM KCL 5 mM $MgCl_2$ and incubated in an ultrasonic bath at 37 °C for 15 min.

Purification and labeling of Min proteins. Min proteins were purified as described in [21]. Briefly, 6xHis-MinE and 6xHis-MinD were expressed in *E. coli* from the pET28a plasmid. Upon collection, cells were resuspended in lysis buffer containing 10 mM imidazole, 5 mM TCEP, complete protease inhibitor cocktail (Roche) and 100 μM ADP (for MinD only), and broken using a French Press. Cell debris free lysate was loaded on a HisTrap column (GE Helthcare). MinE was eluted using lysis buffer containing 250 mM imidazole and MinD 160 mM imidazole. Subsequently proteins were purified using size exclusion Sephacryl S-300 HR 16/60 column using buffer conting 50 mM Hepes pH 7.25 at 4 °C, 150 mM KCl, 10% V/V glycerol, 0.1 mM EDTA pH 7.4 and 80 mM of ADP (for the MinD protein). Protein concentration was measured using a QuantiProTM BCA assay kit (Sigma-Aldrich). MinD was labeled using NHS-Cy3 and MinE using Maleimide-Cy5 accordingly to the manufacturer procedure (GE Healthcare). The degree of labeling was Cy3-MinD 0:88, Cy5-MinE 0:45.

Observation of Min patterns. A solution containing 0.8 M MinD, 0.2 mM MinD-Cy3, 0.8 mM MinE, 0.2 mM MinE-Cy5, 5 mM ATP, 4 mM phosphoenolpyruvate, 0.01 mg/ml pyruvate kinase, 25 mM Tris-HCl (pH 7.5), 150 mM KCl and 5 mM $MgCl_2$ was injected into the microchambers / flow cells using a syringe pump. The volume of protein solution was chosen 50 times larger than the volume of the microdevice to fully replace the buffer solution. To avoid accumulation of proteins on the membranes during filling the device,

17

the solution was rapidly (5 s) flushed through. Observation of the patterns was initiated after a 30 min incubation period.

Image acquisition and data analysis

Fluorescence images were acquired using an Olympus IX-81 inverted microscope equipped with an Andor Revolution XD spinning disk system with FRAPPA, illumination and detection system Andor Revolution and Yokogawa CSU X1, EM-CCD Andor iXon X3 DU897 camera (software version Andor iQ3 v3.1), motorized x-y stage and a z-piezo stage, using a 20× objective (UPlansApo, NA 0.85, oil immersion). For visualization of MinD-Cy3 and MInE-Cy5 we used 561 nm and 640 nm laser lines and 617/73 band-pass and 690 long-pass filters respectively. Images were captured in multiple places at 30–60 s intervals. For the top–bottom correlation assay, images at the two planes were acquired at the same (x, y)-position. A shift of the Z-stage over the largest distance (57 μm) between observation planes was quicker than 0.1 s. Imaging of the membrane for quality control was done using 491 nm laser line and a 525/50 band-pass filter.

Image sequence analysis. Analysis of the image sequences was performed using a ImageJ (v1.52j) and custom Matlab (2016) scripts. Background correction and artefact removal was carried out as follows: First, for movies, frames were corrected for fluorescence bleaching by normalizing each frame on its mean intensity value. This corrected for the max. 20% intensity decay over long movies. Next, two correction images were processed: (1) A 'static background'-image `Imstat` was obtained by averaging out all moving (wave pattern) features of the movie stack and removing any residual background level. Thus, this image only contained static fluorescent features such as specks, holes and scratches. (2) An 'illumination correction' image `Imillum` was made by strongly smoothening out and averaging all movie frames and normalizing the result to its maximum. Finally, each movie frames `Immovie` was corrected as via the following image operation: `Imcorrected = (Immovie - Imstat)/Imillum`. This way, irregularities are suppressed and wave amplitudes on the edge of each image are not underestimated compared to the amplitudes in the center of the image.

Correlation histograms (Fig. 4E): To quantify the synchronization of patterns patterns on the opposite membrane surfaces, we performed a correlation analysis of the fluorescence image time-lapse sequences. Because we found that spatial sub-regions within one field of view (FOV) exhibit different synchronization behavior (Fig. 4F), we divided each FOV into a grid of smaller sub-regions ($\approx 10 \times 10\ \mu m^2$) and determined the temporal correlation between the top and bottom membrane individually for each sub-region. The averaged correlation values from all sub-regions are collected in histograms shown in Fig. 4E. The data for the histograms is provided in the Source Data file.

The quantitative correlation analysis confirms the qualitative finding from visual inspection of the snapshots and kymographs in Fig. 4C. For low bulk height, the two membranes are almost perfectly synchronized in-phase (correlation close to 1). As the height increases, the distribution of correlation becomes bimodal as correlations close to

18

−1 appear, indicating emerging regions of anti-phase synchronization, which coexist with regions of in-phase synchronization. Anti-phase synchronization reaches its maximum at 26 μm. For larger bulk heights, the correlation measure clusters around zero, indicating de-synchronization of the patterns on the two opposite membranes.

Length- and timescale analysis (Figs. 10, S11): Autocorrelation analysis to obtain the typical length- and timescales of the experimentally observed patterns (cf. Fig. **??**) was performed in Matlab. Spatial autocorrelation analysis was performed on 10 individual images per movie. For each autocorrelation output image, a radial average was recorded starting from the main central correlation peak. From the resulting spatial radial correlation curve we determined the first maximum indicating the dominant wavelength of the pattern, irrespective of propagation direction. For temporal correlation, we generated 20 x-t or y-t kymographs per movie (10 in x-direction and 10 in y-direction) evenly distributed over the center 0.7 fraction of an image. For each such kymograph, an autocorrelation analysis was performed. The $x = 0$ and $y = 0$ lines of these x-t autocorrelation maps represent a temporal correlation curve averaged over all the original image points on the respective line. Next, these correlation curves were median averaged between different kymographs. Thus, the final correlation curve represents the average temporal correlation signal sampled from 20×512 surface locations. Analogous to the spatial correlation analysis, the first maximum after $t = 0$ indicates the dominant oscillation period. Experimental repeats of the same conditions (concentrations and height) were median averaged.

Data availability. Figures with associated data provided in the Source Data file: Figs. 3E and 3G and 4 and Supplementary Figs. 10, 11 and 12. The raw data, fluorescence microscopy image sequences and exported simulation data, are available from the corresponding author on reasonable request. A reporting summary for this article is available as a Supplementary Information file.

Code availability. Matlab codes used for experimental data analysis are provided in the repository https://github.com/jacobkers/MinED_patterns. Numerical simulation codes (using COMSOL Multiphysics) and Mathematica codes for linear stability analysis and simulation data analysis are available at https://github.com/f-brauns/Min-bulk-surface-coupling/.

19

Author contributions. F.B., G.P., J.H., E.F., and C.D. designed research; G.P. and C.D. designed and carried out the experiments; F.B., J.H., and E.F. designed the theoretical models and performed the mathematical analyses; F.B., G.P., and J.K. analyzed data; and F.B., G.P., J.H., E.F., and C.D. wrote the paper.

Competing interests. The authors declare no competing interests.

References

1. Adler, H. I., Fisher, W. D., Cohen, A. & Hardigree, A. A. Miniature Escherichia coli cells Deficient in DNA. *Proceedings of the National Academy of Sciences* **57**, 321–326 (1967).

2. de Boer, P. A., Crossley, R. E. & Rothfield, L. I. A division inhibitor and a topological specificity factor coded for by the minicell locus determine proper placement of the division septum in E. coli. *Cell* **56**, 641–649 (1989).

3. Loose, M., Fischer-Friedrich, E., Ries, J., Kruse, K. & Schwille, P. Spatial Regulators for Bacterial Cell Division Self-Organize into Surface Waves in Vitro. *Science* **320**, 789–792 (2008).

4. Frey, E., Halatek, J., Kretschmer, S. & Schwille, P. Protein Pattern Formation. In Bassereau, P. & Sens, P. (eds.) *Physics of Biological Membranes*, 229–260 (Springer International Publishing, Cham, 2018).

5. Halatek, J. & Frey, E. Rethinking pattern formation in reaction–diffusion systems. *Nature Physics* **14**, 507 (2018).

6. Ramm, B., Heermann, T. & Schwille, P. The E. coli MinCDE system in the regulation of protein patterns and gradients. *Cellular and Molecular Life Sciences* **76**, 4245–4273 (2019).

7. Frey, E. & Brauns, F. Self-organisation of Protein Patterns. *arXiv:2012.01797 [nlin, physics:physics]* (2020). `2012.01797`.

8. Ivanov, V. & Mizuuchi, K. Multiple modes of interconverting dynamic pattern formation by bacterial cell division proteins. *Proceedings of the National Academy of Sciences* **107**, 8071–8078 (2010).

9. Vecchiarelli, A. G. *et al.* Membrane-bound MinDE complex acts as a toggle switch that drives Min oscillation coupled to cytoplasmic depletion of MinD. *Proceedings of the National Academy of Sciences* **113**, E1479–E1488 (2016).

10. Denk, J. *et al.* MinE conformational switching confers robustness on self-organized Min protein patterns. *Proceedings of the National Academy of Sciences* **115**, 4553–4558 (2018).

20

11. Glock, P., Brauns, F., Halatek, J., Frey, E. & Schwille, P. Design of biochemical pattern forming systems from minimal motifs. *eLife* **8**, e48646 (2019).

12. Litschel, T., Ramm, B., Maas, R., Heymann, M. & Schwille, P. Beating Vesicles: Encapsulated Protein Oscillations Cause Dynamic Membrane Deformations. *Angewandte Chemie International Edition* **57**, 16286–16290 (2018).

13. Godino, E. *et al.* De novo synthesized Min proteins drive oscillatory liposome deformation and regulate FtsA-FtsZ cytoskeletal patterns. *Nature Communications* **10**, 4969 (2019).

14. Kohyama, S., Yoshinaga, N., Yanagisawa, M., Fujiwara, K. & Doi, N. Cell-sized confinement controls generation and stability of a protein wave for spatiotemporal regulation in cells. *eLife* **8**, e44591 (2019).

15. Glock, P. *et al.* Stationary Patterns in a Two-Protein Reaction-Diffusion System. *ACS Synthetic Biology* **8**, 148–157 (2019).

16. Brauns, F., Halatek, J. & Frey, E. Phase-Space Geometry of Mass-Conserving Reaction-Diffusion Dynamics. *Physical Review X* **10**, 041036 (2020).

17. Brauns, F., Halatek, J. & Frey, E. Diffusive coupling of two well-mixed compartments elucidates elementary principles of protein-based pattern formation. *Physical Review Research* **3**, 013258 (2021).

18. Turing, A. M. The chemical basis of morphogenesis. *Philosophical Transactions of the Royal Society of London. Series B, Biological Sciences* **237**, 37–72 (1952).

19. Halatek, J. & Frey, E. Highly Canalized MinD Transfer and MinE Sequestration Explain the Origin of Robust MinCDE-Protein Dynamics. *Cell Reports* **1**, 741–752 (2012).

20. Zieske, K. & Schwille, P. Reconstitution of self-organizing protein gradients as spatial cues in cell-free systems. *eLife* **3**, e03949 (2014).

21. Caspi, Y. & Dekker, C. Mapping out Min protein patterns in fully confined fluidic chambers. *eLife* **5**, e19271 (2016).

22. Zieske, K., Chwastek, G. & Schwille, P. Protein Patterns and Oscillations on Lipid Monolayers and in Microdroplets. *Angewandte Chemie International Edition* **55**, 13455–13459 (2016).

23. Vecchiarelli, A. G., Li, M., Mizuuchi, M. & Mizuuchi, K. Differential affinities of MinD and MinE to anionic phospholipid influence Min patterning dynamics *in vitro*: Flow and lipid composition effects on Min patterning. *Molecular Microbiology* **93**, 453–463 (2014).

24. Shih, Y.-L. *et al.* Active Transport of Membrane Components by Self-Organization of the Min Proteins. *Biophysical Journal* **116**, 1469–1482 (2019).

21

25. Coullet, P., Gil, L. & Lega, J. Defect-mediated turbulence. *Physical Review Letters* **62**, 1619–1622 (1989).

26. Ouyang, Q. & Flesselles, J.-M. Transition from spirals to defect turbulence driven by a convective instability. *Nature* **379**, 143–146 (1996).

27. Huang, K. C., Meir, Y. & Wingreen, N. S. Dynamic structures in Escherichia coli: Spontaneous formation of MinE rings and MinD polar zones. *Proceedings of the National Academy of Sciences* **100**, 12724–12728 (2003).

28. Wu, F. *et al.* Multistability and dynamic transitions of intracellular Min protein patterns. *Molecular Systems Biology* **12**, 873 (2016).

29. Bordiougov, G. & Engel, H. From trigger to phase waves and back again. *Physica D: Nonlinear Phenomena* **215**, 25–37 (2006).

30. Reusser, E. J. & Field, R. J. The transition from phase waves to trigger waves in a model of the Zhabotinskii reaction. *Journal of the American Chemical Society* **101**, 1063–1071 (1979).

31. Tan, T. H. *et al.* Topological turbulence in the membrane of a living cell. *Nature Physics* **16**, 657–662 (2020).

32. Halatek, J., Brauns, F. & Frey, E. Self-organization principles of intracellular pattern formation. *Philosophical Transactions of the Royal Society B: Biological Sciences* **373**, 20170107 (2018).

33. Corbin, B. D. Exploring intracellular space: Function of the Min system in round-shaped Escherichia coli. *The EMBO Journal* **21**, 1998–2008 (2002).

34. Shih, Y.-L., Kawagishi, I. & Rothfield, L. The MreB and Min cytoskeletal-like systems play independent roles in prokaryotic polar differentiation: Polar differentiation in *Escherichia coli*. *Molecular Microbiology* **58**, 917–928 (2005).

35. Ramm, B. *et al.* ATP driven diffusiophoresis: Active cargo transport without motor proteins. *bioRxiv* doi:10.1101/2020.05.01.072744 (2020).

22

7 Design of biochemical pattern forming systems from minimal motifs

Design of biochemical pattern forming systems from minimal motifs

P. Glock,[1,*] F. Brauns,[2,*] J. Halatek,[2,3,*] E. Frey,[2] and P. Schwille[1]

[1] *Arnold Sommerfeld Center for Theoretical Physics and Center for NanoScience, Department of Physics, Ludwig-Maximilians-Universtiät München, Theresienstraße 37, D-80333 München, Germany*

[2] *Max-Planck-Institute of Biochemistry, D-82152 Martinsried, Germany*

[3] *Biological Computation Group, Microsoft Research, Cambridge CB1 2FB, UK*

[*] PG, FB, and JH contributed equally to this work.

Design of biochemical pattern forming systems from minimal motifs

Philipp Glock[1†], Fridtjof Brauns[2†], Jacob Halatek[2,3†], Erwin Frey[2*], Petra Schwille[1*]

*For correspondence:
frey@lmu.de (EF);
schwille@biochem.mpg.de (PS)

†These authors contributed equally to this work

[1]Max-Planck-Institute of Biochemistry, D-82152 Martinsried; [2]Arnold Sommerfeld Center for Theoretical Physics and Center for NanoScience, Department of Physics, Ludwig-Maximilians-Universität München, Theresienstraße 37, D-80333 München; [3]Biological Computation Group, Microsoft Research, Cambridge CB1 2FB, UK

Abstract

Although molecular self-organization and pattern formation are key features of life, only very few pattern-forming biochemical systems have been identified that can be reconstituted and studied *in vitro* under defined conditions. A systematic understanding of the underlying mechanisms is often hampered by multiple interactions, conformational flexibility and other complex features of the pattern forming proteins. Because of its compositional simplicity of only two proteins and a membrane, the MinDE system from *Escherichia coli* has in the past years been invaluable for deciphering the mechanisms of spatiotemporal self-organization in cells. Here we explored the potential of reducing the complexity of this system even further, by identifying key functional motifs in the effector MinE that could be used to design pattern formation from scratch. In a combined approach of experiment and quantitative modeling, we show that starting from a minimal MinE-MinD interaction motif, pattern formation can be obtained by adding either dimerization or membrane-binding motifs. Moreover, we show that the pathways underlying pattern formation are recruitment-driven cytosolic cycling of MinE and recombination of membrane-bound MinE, and that these differ in their *in vivo* phenomenology.

Introduction

Patterns are a defining characteristic of living beings, and are found throughout all kingdoms of life. In the last years, it has become increasingly clear that protein patterns formed by reaction–diffusion mechanisms are responsible for a large range of spatiotemporal regulation (*Green and Sharpe, 2015*). Such processes allow organisms and cells to achieve robust intracellular patterning rooted in basic physical and chemical principles.

However, there is a lack of mechanistic understanding of the relationship between biomolecular features of proteins, i.e. their interaction domains and conformational states, and the collective properties of protein networks resulting in self-organized pattern formation. In other words, it is often unclear what exactly constitutes a *mechanism* of self-organization *on the biochemical level*. A major question is to what degree system-level biological functions, e.g. geometry sensing or length-scale selection, depend on particular biomolecular features. Some of these features may be essential for function, others may be irrelevant or redundant. The ability to unravel this *feature–function relationship* crucially depends on our ability to reconstitute biochemically distinct minimal systems experimentally and to compare these minimal variants to corresponding quantitative

theoretical models. The key merit of such a combined approach is the ability to dissect different network architectures and also explore a broad range of reaction rates, and thereby uncover biomolecular mechanisms for system-level properties.

Here we address this feature-function relationship in the context of a fairly well-understood biological pattern-forming system: the Min-protein system of *Escherichia coli*. All its components are known – only two proteins are needed to form the pattern (MinD and MinE) – and the system has been successfully reconstituted in an easily malleable *in vitro* system (*Loose et al., 2008*; *Ivanov and Mizuuchi, 2010*; *Vecchiarelli et al., 2014*; *Caspi and Dekker, 2016*; *Kretschmer et al., 2017*). In the bacterial cell, this system contributes to the positioning of FtsZ, a key component of the division ring, at mid-cell. Two proteins, MinD and MinE, oscillate between the cell poles and thereby form a concentration gradient with a minimum at mid-cell. MinC, piggybacking on MinD, consequently inhibits FtsZ polymerization at the poles and thus positions the Z-ring in the middle.

Even though the Min protein system seems simple at first glance, there is much (and biologically relevant) complexity within the protein domain sequences and structures, and hence in the interaction between proteins. MinD is an ATPase which is believed to dimerize upon ATP-binding, raising its membrane affinity via the C-terminal membrane targeting sequence (MTS) (*Lackner et al., 2003*; *Hu et al., 2002*; *Szeto et al., 2003*). Bound to the membrane, MinD recruits further MinD-ATP, as well as its ATPase-activating protein MinE, which together form membrane-bound MinDE complexes (*Hu and Lutkenhaus, 2001*; *Hu et al., 2002*). MinE stimulates MinD's ATPase activity, thereby initiating disintegration of MinDE complexes and subsequent release of MinE and ADP-bound MinD into the cytosol. MinE, although only 88 amino acids in length, is a biochemically complex protein. It is found as a dimer in two distinct conformations (*Pichoff et al., 1995*; *Park et al., 2011*): While diffusing in the cytoplasm, both the N-terminal MTS and the sequence directly interacting with MinD are buried within the protein. Upon sensing membrane-bound MinD, these features are released, which allows interaction with both the membrane and MinD (*Park et al., 2011*).

In summary, MinE exhibits four distinct functional features: activating MinD's ATPase, membrane binding, dimerization, and a switch between an open, active and a closed, inactive conformation. The roles of these distinct functional features of MinE for pattern formation have previously been studied and discussed in the literature (*Vecchiarelli et al., 2016*; *Kretschmer et al., 2017*; *Denk et al., 2018*). It has been shown that MinE's conformational switch is not essential for pattern formation, but conveys robustness to the Min system, as it allows pattern formation over a broad range of ratios between MinE and MinD concentrations (*Denk et al., 2018*). Furthermore, membrane binding of MinE was found to be non-essential for pattern formation (*Kretschmer et al., 2017*). These previous studies essentially retained the structure of MinE, predominantly mutating single residues.

Here, we chose a more radical strategy, in order to attempt a minimal design of fundamental modules towards protein pattern formation from the bottom-up. Specifically, we reduced MinE to its bare minimum function: binding to MinD, and thereby catalyzing MinD's ATPase activity. We then reintroduced additional features—membrane binding and dimerization—one by one in a modular fashion, to study their specific role in pattern formation. This approach allowed us to identify the essential biochemical modules of MinE, and show that these facilitate two biochemically distinct mechanisms of pattern formation. We further analyzed these mechanisms in terms of reaction–diffusion models using theoretical analysis and numerical simulation. In particular, we show that the dimerization-driven mechanism is likely to be the dominant one for in *in vivo* pattern formation.

Results and Discussion

Full flexibility and control over all parameters was achieved by reconstituting purified Min proteins and peptides in an *in vitro* well setup consisting of a glass-supported lipid bilayer with a large, open reservoir chamber (see Methods section for further details). To minimize the complexity of MinE in this reconstituted experimental system, we removed all sequences not in direct contact with MinD, keeping only 19 amino acids (13-31, further referred to as minimal MinE peptide) (*Figure 1*).
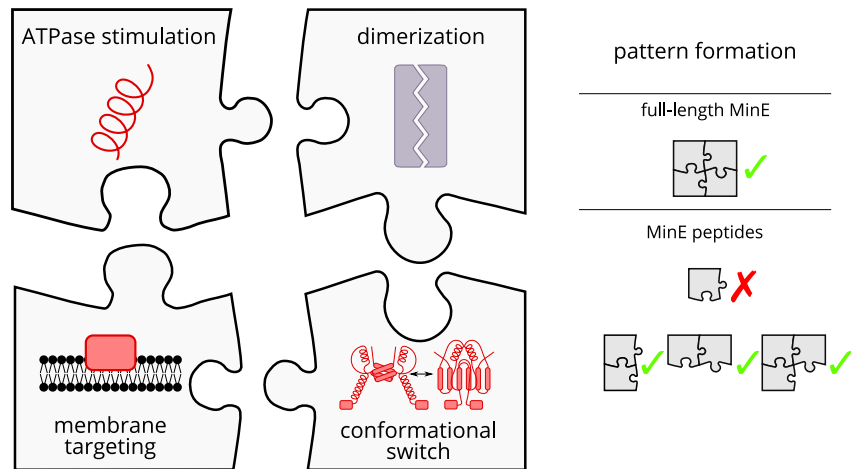
Figure 1. Schematic of the modular approach we took to engineering MinE in the *in vitro* Min system. While MinE has the core function to stimulate MinD's ATPase, three additional properties help MinE to facilitate the emergence of spatiotemporal patterns. We show that two of these properties, dimerization and membrane targeting, can be modularly added to a minimal MinE peptide to facilitate pattern formation.

In agreement with previous studies, we observed (*Loose et al., 2008*; *Glock et al., 2018b*) that the native *in vitro* Min system, consisting of MinD and full-length MinE, forms traveling (spiral) waves (see *Figure 2*a) and (quasi-)stationary patterns. In contrast, we did not observe pattern formation for the reconstituted system containing the minimal MinE peptide in the nanomolar to low micromolar range (see *Figure 2*b), suggesting that it lacks essential molecular features for pattern formation. Instead, membrane binding of MinD was dominant even for high concentrations of up to 20 µM of the minimal MinE peptide. We next tried to rescue pattern formation capability by re-introducing biomolecular features of MinE in a modular fashion.

Previous theoretical research has elucidated the key role of MinE cycling for the Min oscillations (*Halatek and Frey, 2012*). Each cycling step of MinE displaces one MinD from the membrane and thereby drives the oscillations that underlie pattern formation (*Halatek et al., 2018*). Specifically, in this model, MinE is assumed to cycle between a cytosolic state and a MinD-bound state on the membrane. To facilitate pattern formation, this cytosolic-cycling mechanism requires sufficiently strong recruitment of cytosolic MinE by membrane bound MinD (*Halatek and Frey, 2012*) suggesting that the recruitment rate of the minimal MinE peptide is too low. As the native MinE is a dimer, we hypothesized that dimerization might lead to increased recruitment, thus rescuing pattern formation. To test this hypothesis, we introduced dimerization back to the minimal MinE peptide by synthetically fusing it with well-described human and yeast leucine-zippers. Specifically, we cloned and expressed each construct with three different dimerization domains: Fos, Jun and GCN-4 (*Figure 1*) (*Szalóki et al., 2015*; *O'Shea et al., 1989*). Indeed, this modification enabled sustained pattern formation in the system (see *Figure 2*d). Compared to native MinDE patterns, those formed by dimerized peptides have larger wavelengths and are less coherent.

Another feature of native MinE that has been discussed in the context of pattern formation is persistent membrane binding via a membrane targeting sequence (MTS) (*Loose et al., 2011*). The MTS is located at positions 2-12 of the protein and allows MinE to remain membrane-bound after its interaction with MinD, i.e. it decreases the detachment rate of MinE. This persistent MinE-membrane binding facilitates that, after the dissociation of a MinDE complex, the freed-up MinE can bind to another MinD on the membrane, without cycling through the cytoplasm/bulk. Free, membrane-bound MinE is able to form a MinDE complex with membrane-bound MinD. As a shorthand, we will call this process *membrane recombination* of MinE. This process might alleviate the requirement for
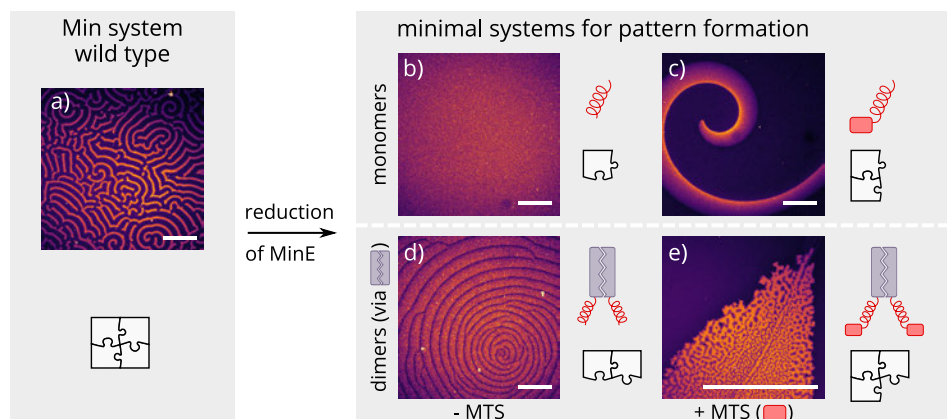
Figure 2. Patterns formed by the wild-type Min system and our minimal biochemical interaction networks. (a) MinD and MinE self-organize to form evenly spaced travelling waves when reconstituted on flat lipid bilayers. (b) The minimal MinE peptide capable of ATPase stimulation is MinE(13-31); it does not facilitate pattern formation. (c) The fragments MinE(1-31) and MinE(2-31)-sfGFP contain the membrane-targeting sequence (MTS) in addition to the ATPase stimulation domain. Substituting MinE with these constructs leads to pattern formation; see supplementary videos 1–3. (d) Fusing the ATPase stimulation domain MinE(13-31) with dimerization domains (we tested Fos, Jun, or GCN-4) facilitates pattern formation in the absence of the MTS. (e) Combining membrane targeting and dimerization in a single construct produces quasi-stationary patterns. (Concentrations and proteins used: (a) 1 μM MinD, 6 μM MinE-His; (b) 1.2 μM MinD, 50 nM MinE(13-31); (c) 1.2 μM MinD, 50 nM MinE(1-31); scalebars = 300 μm; (d) 1 μM MinD, 100 nM MinE(13-31)-Fos; (e) 1.2 μM MinD, 100 nM MinE(1-31)-GCN4. In all assays, MinD is 70 % doped with 30 % Alexa647-KCK-MinD.)

Figure 2–Figure supplement 1. Global view of pattern formation by minimal systems

Figure 2–Figure supplement 2. Titration results for MinE(1-31) and MinE(2-31)-sfGFP

Figure 2–video 1. MinE(1-31) forms chaotic patterns with MinD. Timelapse of a stitched tilescan to visualize the entire assay chamber (5 μM MinD and 100 nM MinE(1-31) form patterns on an SLB formed from DOPC:DOPG (2:1)).

Figure 2–video 2. MinE(2-31)-msfGFP forms chaotic patterns with MinD (1.8 μM MinD and 50 nM MinE(2-31)-msfGFP-His on 2:1 DOPC:DOPG).

Figure 2–video 3. Patterns with vastly different length and timescales coexist and continually transition into one another at certain concentrations of MinD and MinE(2-31)-msfGFP. (0.6 μM MinD and 75 nM MinE(2-31)-msfGFP-His on 2:1 DOPC:DOPG.)

recruitment of MinD from the cytosol by membrane-bound MinD. To test whether the persistent membrane-binding of MinE can facilitate pattern formation, we added back the MTS found in native MinE (residues 2-12) to the N-terminus of the peptide. This construct, contrary to published results (*Vecchiarelli et al., 2016*), forms patterns with MinD. As shown in *Figure 2*c, the observed patterns are traveling waves with wavelengths several orders of magnitude larger than those found for the native *in vitro* Min system. Patterns are sustained over many hours within our assay.

Combining both features, i.e. adding both the MTS and a dimerization sequence to the minimal MinE peptide, resulted in (quasi-)stationary patterns, but the exact outcome depended heavily on the starting conditions of the assay (see *Figure 2*e). In general, patterns formed by MinD and our minimal MinE peptides do not show the same degree of order as patterns formed by the wild-type Min proteins (*Glock et al., 2018b*) or MinD and His-MinE (*Loose et al., 2008*). In particular, there is no well-controlled characteristic length scale (wavelength), and the defined spirals or stationary patterns observed in the wild type Min system are sometimes replaced by chaotic centers as shown in *Figure 2*d. The chaotic behavior is especially pronounced at high MinD concentrations (in this case with a minimal MinE plus MTS and sfGFP or MinE(1-31), respectively) (*video 1* and *video 2*).

Our experimental results suggest that two distinct features of MinE, dimerization and membrane binding, independently facilitate pattern formation of our reconstituted Min system with engineered, minimal MinE peptides. To support these conclusions and gain further insight into the mechanisms underlying pattern formation we performed a theoretical analysis using a reaction–diffusion model that captures all of the above biomolecular features. We extended the Min "skeleton" model introduced in (*Huang et al., 2003*; *Halatek and Frey, 2012*) by MinE membrane binding, similar to the extension considered in (*Denk et al., 2018*). In this model, dimerization of MinE is effectively accounted for by an increased MinE recruitment rate. We performed linear stability analysis of the reaction–diffusion system to find the parameter regimes where patterns form spontaneously from a homogeneous initial state. The two-parameter phase diagram shown in *Figure 3*a shows that increased MinE recruitment as well as slower MinE detachment can rescue pattern formation, via two independent cycling pathways of MinE: cytosolic cycling and membrane recombination. This shows that our hypothesis that dimerization increases recruitment of MinE to MinD is consistent with the experimental findings.

To test whether either or both of these two pattern-forming pathways fulfill the biological function of the Min-protein patterns, we studied pattern formation using the generalized reaction–diffusion model taking into account realistic cell geometry. In *E. coli*, Min oscillations have to take place along the long axis of the rod-shaped cells for correct positioning FtsZ at midcell. Interestingly, linear stability analysis (see *Figure 3–Figure Supplement 4*) shows that the membrane-recombination driven mechanism favors short-axis oscillations which is at odds with the biological function of the Min system. Indeed, our numerical simulations show that pole-to-pole oscillations are only possible for sufficiently strong cytosolic cycling, whereas the recombination-driven mechanism leads to side-to-side oscillations (see *Figure 3*b). A recent theoretical study on axis-selection of the PAR system in *C. elegans* suggests that pattern formation driven by an antagonism of membrane bound proteins generically leads to short-axis selection (*Gessele et al., 2018*). Here, membrane-bound MinE antagonizes membrane-bound MinD via the membrane-recombination pathway. Sufficiently strong MinE-recruitment from the cytosol supersedes the membrane-recombination pathway and leads to long-axis selection (pole-to-pole oscillations) even when MinE-membrane binding is strong.

Taken together, we conclude that Min-pattern formation *in vivo* is driven by cytosolic cycling of MinE, because correct axis selection (pole-to-pole oscillations) is essential for cell-division of *E. coli* and other gram-negative bacteria. In a broader context, our results demonstrate that multiple mechanisms with different characteristics, e.g. in their ability to sense geometry, can coexist in one reaction network. Most importantly, this highlights that a classification of pattern-forming mechanisms in terms of the reaction network topology alone misses important aspects of pattern formation that can be crucial for the biological function.
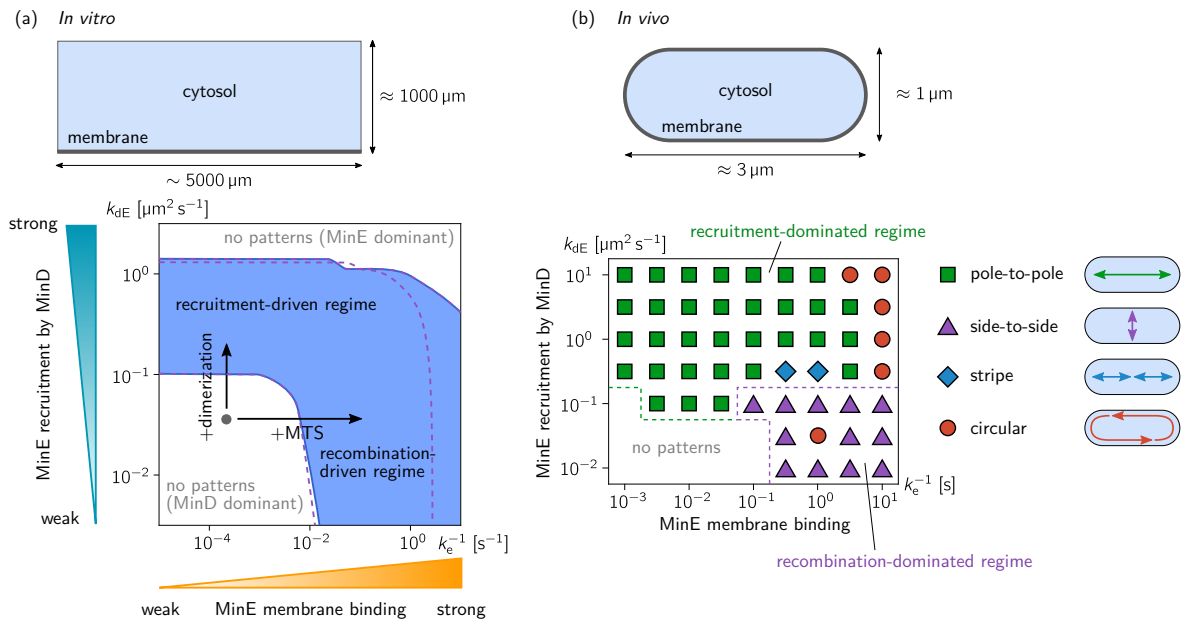
Figure 3. Pattern forming capability of the extended Min model (*Figure Supplement 1*) *in vitro* and *in vivo*. (a) *In vitro* geometry and two-parameter phase diagram obtained by linear stability analysis, showing the pattern formation capabilities of the MinDE-system in dependence of MinE membrane-binding strength (k_e^{-1}) and MinE-recruitment rate k_{dE}. The regime of spontaneous pattern formation (lateral instability) is indicated in blue The gray circle represents minimal MinE(13-31) construct, which does not facilitate self-organized pattern formation. The experimental domain additions are accounted for by respective changes of the kinetic rates, as indicated by the arrows. (Parameters: see *Methods*; blue region: regime of pattern formation for zero MinE attachment, $k_E = 0$; purple dashed lines: boundary of the pattern-formation regime for non-zero MinE attachment rate, $k_E = 5\,\mu m^2\,s^{-1}$.) (b) Two-parameter phase diagram obtained by numerical simulations in *in vivo* geometry. We find regimes of different oscillation pattern types: pole-to-pole oscillations (green squares); side-to-side oscillations (purple triangles); stripe oscillations (blue diamonds); and circular waves (red circles). Videos 1–5 show examples each of these pattern types.

Figure 3–Figure supplement 1. Network cartoon of the MinE "skeleton" model extended by MinE membrane binding.

Figure 3–Figure supplement 2. Phase diagrams in the parameter plane of total concentrations (n_E, n_D).

Figure 3–Figure supplement 3. Phase diagrams showing how the range of MinE concentrations where the system is laterally unstable, depends on the MinE detachment rate and the MinE recruitment rate.

Figure 3–Figure supplement 4. Linear stability analysis in the ellipse geometry.

Figure 3–video 1. Pole-to-pole oscillation for weak MinE binding ($k_{dE} = 3.16\,\mu m^3 s^{-1}$, $k_e = 1000\,s^{-1}$).

Figure 3–video 2. Pole-to-pole oscillation for strong MinE binding ($k_{dE} = 3.16\,\mu m^3 s^{-1}$, $k_e = 0.316\,s^{-1}$).

Figure 3–video 3. Circular wave ($k_{dE} = 3.16\,\mu m^3 s^{-1}$, $k_e = 0.1\,s^{-1}$).

Figure 3–video 4. Stripe oscillation ($k_{dE} = 0.316\,\mu m^3 s^{-1}$, $k_e = 3.16\,s^{-1}$).

Figure 3–video 5. Side-to-side oscillation ($k_{dE} = 0.1\,\mu m^3 s^{-1}$, $k_e = 0.316\,s^{-1}$).

With respect to a potential biochemical origin of the pattern-forming mechanisms, we showed how additional protein domains can move the whole system into a mechanistically distinct regime. Enhancing the strength of MinE recruitment by MinD via dimerization shifts the system into a regime of recruitment-driven pattern formation. Alternatively, adding membrane targeting to the peptide unlocked a new pathway and led to sustained patterns via MinD-MinE recombination on the membrane (see supplementary discussion in *Appendix 1* for further details).

In conclusion, the concept of modular engineering of pattern formation through distinct protein domains adds an entirely new dimension to the Min system, and establishes it further as a paradigmatic model for studying the mechanisms underlying self-organized pattern formation. Now, defined modules can be added, removed and interchanged. Interestingly, our experimental findings provide evidence that the distinct functional modules of MinE need not be provided by native parts of the proteins, but can be substituted with foreign sequences. Moreover, the part of MinE that interacts with MinD can be added as a small peptide tag of 19 amino acids to any host protein (as shown for superfolder-GFP + MTS, *Figure Supplement 2*), leading to a chimera protein that inherits key properties, such as membrane-interactions and protein-protein interactions, from the host protein. The modular domains provide an experimental platform to systematically modify the molecular interactions. Together with systematic theoretical studies, this is a powerful and versatile tool to study the general principles underlying biological pattern formation in multispecies, multicomponent reaction–diffusion systems.

Methods and Materials

Most experimental methods used in this publication were exhaustively described in text and video in a recent publication (*Ramm et al., 2018*). We therefore describe these techniques only in brief.

Membranes

SLBs were prepared from DOPC and DOPG (ratio 2:1) small unilamellar vesicles in Min buffer (25 mM Tris-HCl pH 7.5, 150 mM KCl, 5 mM MgCl$_2$) by adding them (at 0.53 mg/mL) on top of a charged, cleaned glass surface. The solution was diluted after one minute by addition of 150 mL Min buffer. After a total of 3 minutes, membranes in chambers were washed with 2 mL of Min buffer.

Assay chamber

Assay chambers were assembled from piranha-cleaned coverslips and a cut 0.5 ml plastic reaction tube by gluing the tube upside down onto the cleaned and dried surface using UV-curable adhesive.

In vitro self-organization assay

The buffer volume in an assay chamber containing an SLB was adjusted to yield a final volume of 200 μL including protein solutions and ATP. Proteins, peptides and further reactants were added and the solution was mixed by pipetting.

Peptides

Peptides were synthesized using Fmoc chemistry by our in-house Biochemisty Core Facility. MinE(2-31)-KCK-Atto488 was expressed as a SUMO fusion in *E. coli* BL-21 DE3 pLysS cells, the SUMO tag was then cleaved using SenP2 protease and the remaining peptide was labelled using Atto488-maleimide to site-specifically target the cysteine residue. Labelling was done as described below.

Protein design and purifications

Detailed information about cloning procedures and design of proteins can be found in the supplementary information.

234

Protein concentration measurements

Protein concentrations were determined by using a modified, linearized version of the Bradford assay in 96-well format (**Ernst and Zor, 2010**).

Labelling

Atto 488-maleimide in 5–7 μL DMSO (about three molecules of dye per protein) was added dropwise to $\sim$ 0.5 mL of protein solution in storage buffer (50 mM HEPES pH 7.25, 300 mM KCl, 10 % glycerol, 0.1 mM EDTA, 0.4 mM TCEP) in a 1.5 mL reaction tube. The tube was wrapped in aluminium foil and incubated at 4 °C on a rotating shaker for two to three hours. Free dye was separated from proteins first by running the solution on a PD-10 buffer exchange column equilibrated with storage buffer. Then, remaining dye was diluted out by dialysis against storage buffer overnight. The labelling efficiency was measured by recording an excitation spectrum of the labelled protein and measuring the protein concentration as described above. We then calculated the resulting labelling efficiency using the molar absorption provided by the dye supplier (Atto 488: $9.0 \times 10^4 \, \text{M}^{-1} \, \text{cm}^{-1}$).

Imaging

Microscopy was done on commercial Zeiss LSM 780 microscopes with 10x air objectives (Plan-Apochromat 10x/0.45 M27 and EC Plan-Neofluar 10x/0.30 M27). Tile scans with 25 tiles (5x5) at zoom level 0.6 were stitched to obtain overview images of entire assay chambers and resolve the large-scale patterns formed. More detailed images and videos were acquired on the same instruments using EC Plan-Neofluar 20x/0.50 M27 or Plan-Apochromat 40x/1.20 water-immersion objectives.

The Min "skeleton model" extended by MinE membrane binding.

To capture the effect of MinE membrane binding, we extend the "skeleton" model introduced in (**Halatek and Frey, 2012**). **Figure 3–Figure Supplement 1** shows a cartoon of the reaction network. We present the model first for a general geometry with a cytosolic volume coupled to a membrane surface. To perform linear stability analysis, we implemented this model in a "box geometry" representing the *in vitro* setup with a membrane at the bottom, and in an ellipse geometry mimicking the rod-like cell shape of *E. coli*.

On the membrane, proteins diffuse and undergo chemical reactions, including attachment, detachment and interactions between membrane-bound proteins

$$\partial_t m_\text{d} = D_m \nabla_m^2 m_\text{d} + R_\text{d}, \tag{1}$$

$$\partial_t m_\text{de} = D_m \nabla_m^2 m_\text{de} + R_\text{de}, \tag{2}$$

$$\partial_t m_\text{e} = D_m \nabla_m^2 m_\text{e} + R_\text{e}, \tag{3}$$

where ∇_m is the gradient operator along the membrane. In the cytosol, proteins diffuse and MinD undergoes nucleotide exchange with a rate λ

$$\partial_t c_\text{DD} = D_\text{D} \nabla_c^2 c_\text{DD} - \lambda c_\text{DD} \tag{4}$$

$$\partial_t c_\text{DT} = D_\text{D} \nabla_c^2 c_\text{DT} + \lambda c_\text{DD} \tag{5}$$

$$\partial_t c_\text{E} = D_\text{E} \nabla_c^2 c_\text{E} \tag{6}$$

The two domains are coupled via the boundary conditions at the membrane

$$-D_\text{D} \nabla_\mathbf{n} c_\text{DD} = f_\text{DD}, \tag{7}$$

$$-D_\text{D} \nabla_\mathbf{n} c_\text{DT} = f_\text{DT}, \tag{8}$$

$$-D_\text{E} \nabla_\mathbf{n} c_\text{E} = f_\text{E}, \tag{9}$$

where $\nabla_{\mathbf{n}}$ is the gradient along the inward pointing normal to the membrane. The reaction terms are derived from the interaction network *Figure 3–Figure Supplement 1* via the mass-action law and read

$$R_d = (k_D + k_{dD}m_d)c_{DT} - (k_{dE}c_E + k_{ed}m_e)m_d, \tag{10}$$

$$R_{de} = (k_{dE}c_E + k_{ed}m_e)m_d - k_{de}m_{de}, \tag{11}$$

$$R_e = k_E c_E + k_{de}m_{de} - (k_e + k_{ed}m_d)m_e. \tag{12}$$

Correspondingly, the attachment-detachment flows are

$$f_{DT} = -(k_D + k_{dD}m_d)c_{DT}, \tag{13}$$

$$f_{DD} = k_{de}m_{de}, \tag{14}$$

$$f_E = k_{de}m_{de} - (k_E + k_{dE}m_d)c_E, \tag{15}$$

such that the dynamics conserve the global total densities of MinD and MinE

$$N_D = \int_{\text{mem}} dS\,(m_d + m_{de}) + \int_{\text{cyt}} dV\,(c_{DD} + c_{DT}), \tag{16}$$

$$N_E = \int_{\text{mem}} dS\,(m_e + m_{de}) + \int_{\text{cyt}} dV\,c_E. \tag{17}$$

Linear stability analysis

To perform linear stability analysis, we need to find a set of orthogonal basis functions that fulfill the boundary conditions and diagonalize the Laplace operator, ∇^2, on both domains (membrane and cytosol) simultaneously. In general, this is not analytically possible in arbitrary geometry. However, in a box geometry with a flat membrane, a closed form of the basis functions can easily be obtained. Furthermore, in a two dimensional ellipse geometry, a perturbative ansatz can be used to obtain an approximate set of basis functions, as was shown in (*Halatek and Frey, 2012*) and used in (*Wu et al., 2016*; *Gessele et al., 2018*). In the following, we briefly outline how the basis functions can be determined and employed to perform linear stability analysis. For details we refer to the supplementary materials of Refs. (*Halatek and Frey, 2018*; *Denk et al., 2018*; *Halatek and Frey, 2012*; *Gessele et al., 2018*).

In vitro box geometry.

For linear stability analysis of the *in vitro* system, we consider a two-dimensional box with a membrane at the bottom surface, representing a slice through the *in vitro* system. The cytosol domain is a rectangle in the *x–z* plane with height h and length L. The bottom boundary at $z = 0$ is the one-dimensional membrane domain – a line of length L. It is coupled to the bulk via reactive boundary conditions, Eqs. (7) to (9). The other boundaries of the rectangular bulk domain are equipped with reflective boundaries. In this geometry, the gradient operators tangential and normal to the membrane are simply $\nabla_m \equiv \partial_x$ and $\nabla_{\mathbf{n}} \equiv \partial_z$.

The first step of a linear stability analysis is to calculate the steady state whose stability is to be analyzed. Typically this is a homogeneous steady state. In the system considered here, the most simple steady state is homogeneous along the *x*-direction. However, there must be cytosolic gradients in the *z*-direction due to the reactive boundary condition and the nucleotide exchange in the cytosol. Because the cytosol dynamics are linear, they can be solved in closed form.

To analyze the stability of such a steady state, one linearizes the dynamics around it. The ansatz to solve the resulting linear system is to diagonalize the Laplace operator. Importantly, in a system with multiple coupled domains, one needs to find a set of basis functions that diagonalize the Laplace operator on all domains (here membrane and cytosol), and that fulfill the reactive boundary conditions that couple these domains, simultaneously. In the *x*-direction, i.e. the lateral direction along the one-dimensional membrane, the eigenfunctions are simply Fourier modes. The bulk

eigenfunctions in the z-direction, normal to the membrane, are exponential profiles and can be obtained in closed form by solving the linear cytosol dynamics, Eqs. (4) to (6).

These eigenfunctions can then be plugged into the the membrane dynamics and the boundary conditions linearized around the homogeneous steady state. The resulting set of linear algebraic equations can be solved for the growth rates of the Fourier modes. Thus, one obtains a relationship between wavenumber q of a mode and its growth rate $\sigma(q)$. This relationship is called dispersion relation.

For details of the implementation of the linear stability analysis outlined above, we refer the reader to the supplementary materials of (*Halatek and Frey, 2018*) and (*Denk et al., 2018*). Note that the bulk height dependence saturates above around 50 μm, the maximal penetration depth of bulk gradients (*Halatek and Frey, 2018*). The bulk heights in the experiments were well above this saturation threshold at around 1 mm, allowing us to use the limit of large bulk height h.

In vivo ellipse geometry.

Linear stability analysis in an ellipse geometry is technically more involved, because the curved boundary makes it impossible to find a common eigenbasis of the Laplace operator on membrane and cytosol in closed form. For a detailed exposition of linear stability analysis in an elliptical geometry, we refer the reader to the supplementary materials of (*Halatek and Frey, 2012*).

Parameters

In vitro

We used the kinetic rates and diffusion constants from (*Halatek et al., 2018*); see *Table 1*. In this previous study, the Min skeleton model without MinE membrane binding was studied. Including MinE membrane binding leads to three additional kinetic rates in the model: We set the MinE membrane recombination rate to $k_{ed} = 0.1\,\mu\mathrm{m\,s}^{-1}$, and varied the MinE detachment rate, k_e, in the range $10^{-1}\,\mu\mathrm{m\,s}^{-1}$ to $10^5\,\mu\mathrm{m\,s}^{-1}$. To test the effect of spontaneous MinE membrane attachment ($k_E > 0$) we compared the results from LSA for $k_E = 0$ and $k_E = 5\,\mu\mathrm{m}^3\,\mathrm{s}^{-1}$, and found that spontaneous attachment is only relevant for very small MinE detachment rate, k_e, i.e. strong MinE membrane binding, where it suppresses pattern formation due to a dominance of membrane-bound MinE (see purple dashed line in *Figure 3*a).

For the (k_e^{-1}, k_{dE}) phase diagram (*Figure 3*a), the total densities of MinE and MinD were set to $n_E = 120\,\mu\mathrm{m}^{-2}$, $n_D = 1200\,\mu\mathrm{m}^{-2}$, corresponding to 0.1 μM MinE and 1 μM MinD in bulk solution respectively. (Note that the unit for bulk concentrations is $\mu\mathrm{m}^{-2}$ because we consider a two-dimensional slice through the three-dimensional bulk. The membrane concentrations have a unit $\mu\mathrm{m}^{-1}$ respectively.)

In addition, we calculated (n_E, n_D) phase diagrams at four points in (k_e^{-1}, k_{dE}) phase plane (see *Figure 3–Figure Supplement 2*). In these phase diagrams, one can see that mostly the E/D-concentration ratio, n_E/n_D, determines the regime of pattern formation. This is in *qualitative* agreement with the experimentally found phase diagram for the MinE(1-31) mutant (cf. *Figure 2–Figure Supplement 2*).

To exemplify how the critical E/D-ratio depends on the kinetic rates, we fixed the MinD concentration ($n_D = 1000\,\mu\mathrm{m}^{-2}$) and varied n_E and one of the kinetic rates. For the MinE-recombination driven regime, we set $k_{dE} = 0$ (no MinE recruitment to MinD), and varied the MinE-detachment rate k_e (see *Figure 3–Figure Supplement 3*a). The critical E/D-ratio of approximately 1/20 below which pattern formation is observed for the MinE(1-31) mutant in experiments is fitted for $k_e \approx 0.2\,\mathrm{s}^{-1}$ (dashed red line and inset in *Figure 3–Figure Supplement 3*a). Note however, this "fit" is severely underdetermined, because the remaining kinetic rates are not constrained by experiment. Changing, for instance, the MinE membrane recombination rate k_{ed} (or any other kinetic rate) would lead to a different value for k_e that fits the experimentally found concentration dependence. A remaining quantitative difference to the experimental findings is that the regime of pattern formation extends to very low MinE concentrations in the mathematical model, while there is a lower bound at a

Name	Unit	*in vitro*	*in vivo*
D_m	$\mu m^2\,s^{-1}$	0.013	0.013
D_D	$\mu m^2\,s^{-1}$	60	16
D_E	$\mu m^2\,s^{-1}$	60	10
λ	s^{-1}	6	6
n_D	μm^{-2}	1200 ($\approx 1\,\mu M$)	$2000/V_{cell}$
n_E	μm^{-2}	120 ($\approx 0.1\,\mu M$)	$700/V_{cell}$
k_D	$\mu m\,s^{-1}$	0.065	0.1
k_{dD}	$\mu m^2\,s^{-1}$	0.098	0.108
k_{dE}	$\mu m^2\,s^{-1}$	0.126	0.65
k_{de}	s^{-1}	0.34	0.4
k_{ed}	$\mu m\,s^{-1}$	0.1	0.2
k_e	s^{-1}	10^{-1} to 10^5	10^{-1} to 10^3
k_E	$\mu m\,s^{-1}$	0, 5	0, 5

Table 1. Overview over the parameters used in the mathematical model. *In vitro* parameters from *Halatek and Frey* (*2018*), *in vivo* parameters from *Halatek and Frey* (*2012*); *Wu et al.* (*2016*). The diffusion constants, nucleotide exchange rate λ, and total protein densities are known from experiments *Loose et al.* (*2008*); *Meacci et al.* (*2006*). In *Halatek and Frey* (*2012*), the kinetic rates of the Min skeleton model (k_D, k_{dD}, k_{dE}, and k_{de}) to reproduce the *in vivo* phenomenology quantitatively, and to optimize the biological function of the in vivo pole-to-pole oscillation (mid-cell localization). The additional rates (k_{ed}, k_e, and k_E) of the model extended by MinE-membrane binding are not constrained by experiment. We varied k_e over several orders of magnitude (see *Figure 3* to study the role of persistent MinE-membrane binding. Note that, changing the MinE-recombination rate k_{ed} over several orders of magnitude does not change our results qualitatively (topology of the phase diagrams).

E/D-ratio of about 1/100 in the experiments.

Figure 3–*Figure Supplement 3*b shows the (k_{dE}, n_E) phase diagram for the Min-skeleton model without persistent MinE-membrane binding (corresponding to $m_e \to \infty$).

In vivo

We use the parameters from (*Halatek and Frey, 2012*); see *Table 1*. In this previous study, the Min skeleton model was studied *in vivo* and the kinetic rates where fitted to reproduce the *in vivo* phenomenology. The model extended by MinE membrane binding has three additional kinetic rates: We set the MinE membrane recombination rate to k_{ed} = 0.2 $\mu m\,s^{-1}$, and varied the MinE detachment rate, k_e, in the range 10^{-1} $\mu m\,s^{-1}$ to 10^3 $\mu m\,s^{-1}$. As in the *in vitro* case, spontaneous MinE membrane attachment ($k_E > 0$) has no significant effect, so we set k_E = 0. (Linear stability analysis and numerical simulations for a non-zero attachment rate k_E = 5 $\mu m^3\,s^{-1}$ yield a phase diagram with the same qualitative structure as the one presented in *Figure 3*b.)

We mimic the cell geometry by an ellipse with lengths 0.5 μm and 2 μm for the short and long half axis respectively (the corresponding cell "volume" is V_{cell} = 3.14 μm^2).

Numerical simulations

The bulk-boundary coupled reaction–diffusion dynamics Eqs. (1) to (15) were solved using a finite element solver code (COMSOL Multiphysics).

Due to its large size, simulations of the *in vitro* system are very time consuming and beyond the scope of this work. Because most of the kinetic rates are not known, extensive parameter studies would be necessary to gain insight from such simulations.

238

Acknowledgments

References

Caspi Y, Dekker C. Mapping out Min protein patterns in fully confined fluidic chambers. eLife. 2016 nov; 5(iii):1–53, doi:10.7554/eLife.19271.

Denk J, Kretschmer S, Halatek J, Hartl C, Schwille P, Frey E. MinE conformational switching confers robustness on self-organized Min protein patterns. Proceedings of the National Academy of Sciences of the United States of America. 2018 may; 115(18):4553–4558, doi:10.1073/pnas.1719801115.

Downing BPB, Rutenberg AD, Touhami A, Jericho M. Subcellular Min oscillations as a single-cell reporter of the action of polycations, protamine, and gentamicin on Escherichia coli. PloS one. 2009 sep; 4(9):e7285, doi:10.1371/journal.pone.0007285.

Ernst O, Zor T. Linearization of the Bradford Protein Assay. Journal of Visualized Experiments. 2010 apr; (38):1–6, doi:10.3791/1918.

Gessele R, Halatek J, Frey E. PAR protein activation-deactivation cycles stabilize long-axis polarization in C. elegans. bioRxiv. 2018; , doi:10.1101/451880.

Glock P, Broichhagen J, Kretschmer S, Blumhardt P, Mücksch J, Trauner D, Schwille P. Optical Control of a Biological Reaction-Diffusion System. Angewandte Chemie International Edition. 2018 feb; 57(9):2362–2366, doi:10.1002/anie.201712002.

Glock P, Ramm B, Heermann T, Kretschmer S, Schweizer J, Mücksch J, Alagöz G, Schwille P. Stationary patterns in a two-protein reaction-diffusion system. ACS Synthetic Biology. 2018; p. acssynbio.8b00415, doi:10.1021/acssynbio.8b00415.

Green JBA, Sharpe J. Positional information and reaction-diffusion: two big ideas in developmental biology combine. Development. 2015 apr; 142(7):1203–1211, doi:10.1242/dev.114991.

Halatek J, Frey E. Rethinking pattern formation in reaction–diffusion systems. Nature Physics. 2018 may; 14(5):507–514, doi:10.1038/s41567-017-0040-5.

Halatek J, Brauns F, Frey E. Self-organization principles of intracellular pattern formation. Philosophical transactions of the Royal Society of London Series B, Biological sciences. 2018 may; 373(1747), doi:10.1098/rstb.2017.0107.

Halatek J, Frey E. Highly Canalized MinD Transfer and MinE Sequestration Explain the Origin of Robust MinCDE-Protein Dynamics. Cell Reports. 2012; 1(6):741–752, doi:10.1016/j.celrep.2012.04.005.

Hu Z, Gogol EP, Lutkenhaus J. Dynamic assembly of MinD on phospholipid vesicles regulated by ATP and MinE. Proceedings of the National Academy of Sciences of the United States of America. 2002 may; 99(10):6761–6, doi:10.1073/pnas.102059099.

Hu Z, Lutkenhaus J. Topological regulation of cell division in E. coli: Spatiotemporal oscillation of MinD requires stimulation of its ATPase by MinE and phospholipid. Molecular Cell. 2001; 7(6):1337–1343, doi:10.1016/S1097-2765(01)00273-8.

Huang KC, Meir Y, Wingreen NS. Dynamic structures in Escherichia coli: spontaneous formation of MinE rings and MinD polar zones. Proceedings of the National Academy of Sciences of the United States of America. 2003 oct; 100(22):12724–8, doi:10.1073/pnas.2135445100.

Ivanov V, Mizuuchi K. Multiple modes of interconverting dynamic pattern formation by bacterial cell division proteins. Proceedings of the National Academy of Sciences of the United States of America. 2010; 107(18):8071–8078, doi:10.1073/pnas.0911036107.

Kretschmer S, Zieske K, Schwille P. Large-scale modulation of reconstituted Min protein patterns and gradients by defined mutations in MinE's membrane targeting sequence. PLoS ONE. 2017; p. 1–16, doi:10.1371/journal.pone.0179582.

Lackner LL, Raskin DM, De Boer PaJ. ATP-dependent interactions between Escherichia coli Min proteins and the phospholipid membrane in vitro. Journal of Bacteriology. 2003; 185(3):735–749, doi:10.1128/JB.185.3.735-749.2003.

Loose M, Fischer-Friedrich E, Herold C, Kruse K, Schwille P. Min protein patterns emerge from rapid re-binding and membrane interaction of MinE. Nature structural & molecular biology. 2011; 18(5):577–583, doi:10.1038/nsmb.2037.

Loose M, Fischer-Friedrich E, Ries J, Kruse K, Schwille P. Spatial regulators for bacterial cell division self-organize into surface waves in vitro. Science (New York, NY). 2008; 320(5877):789–792, doi:10.1126/science.1154413.

Meacci G, Ries J, Fischer-Friedrich E, Kahya N, Schwille P, Kruse K. Mobility of Min-proteins in *Escherichia coli* measured by fluorescence correlation spectroscopy. Physical Biology. 2006; 3(4):255–263, doi:10.1088/1478-3975/3/4/003.

O'Shea E, Rutkowski R, Stafford W, Kim P. Preferential heterodimer formation by isolated leucine zippers from fos and jun. Science. 1989 aug; 245(4918):646–648, doi:10.1126/science.2503872.

Park KT, Wu W, Battaile KP, Lovell S, Holyoak T, Lutkenhaus J. The min oscillator uses MinD-dependent conformational changes in MinE to spatially regulate cytokinesis. Cell. 2011; 146(3):396–407, doi:10.1016/j.cell.2011.06.042.

Pichoff S, Vollrath B, Touriol C, Bouché JP. Deletion analysis of gene minE which encodes the topological specificity factor of cell division in Escherichia coli. Molecular microbiology. 1995; 18(2):321–329.

Ramm B, Glock P, Schwille P. In Vitro Reconstitution of Self-Organizing Protein Patterns on Supported Lipid Bilayers. Journal of Visualized Experiments. 2018 jul; (137):e58139, doi:10.3791/58139.

Szalóki N, Krieger JW, Komáromi I, Tóth K, Vámosi G. Evidence for Homodimerization of the c-Fos Transcription Factor in Live Cells Revealed by Fluorescence Microscopy and Computer Modeling. Mol Cell Biol. 2015; 35(August):3785–3798, doi:10.1128/MCB.00346-15.

Szeto TH, Rowland SL, Habrukowich CL, King GF. The MinD membrane targeting sequence is a transplantable lipid-binding helix. Journal of Biological Chemistry. 2003; 278(41):40050–40056, doi:10.1074/jbc.M306876200.

Vecchiarelli AG, Li M, Mizuuchi M, Hwang LC, Seol Y, Neuman KC, Mizuuchi K. Membrane-bound MinDE complex acts as a toggle switch that drives Min oscillation coupled to cytoplasmic depletion of MinD. Proceedings of the National Academy of Sciences. 2016 mar; 113(11):E1479–E1488, doi:10.1073/pnas.1600644113.

Vecchiarelli AG, Li M, Mizuuchi M, Mizuuchi K. Differential affinities of MinD and MinE to anionic phospholipid influence Min patterning dynamics in vitro. Molecular Microbiology. 2014; 93(3):453–463, doi:10.1111/mmi.12669.

Wu F, Halatek J, Reiter M, Kingma E, Frey E, Dekker C. Multistability and dynamic transitions of intracellular Min protein patterns. Molecular Systems Biology. 2016; 12(6):873, doi:10.15252/msb.20156724.

Protein design and cloning

Several instances of MinE(2-31)-sfGFP were cloned, expressed and tested. We started with a construct carrying a His-tag on the N-terminus His-(MinE-2-31)-sfGFP. Then, we became concerned about dimerization of the fluorescent protein and introduced a mutation (V206K) to make His-MinE(2-31)-msfGFP. Then, we discovered that N-terminal tagging influences the properties of our minimal constructs and wt MinE and changed the construct to carrying a C-terminal His-tag (MinE(1-31)-msfGFP-His). The methionine residue was re-introduced here as a start codon, and is cleaved in E. coli. Additionally, we prepared MinE(13-31)-sfGFP and confirmed that without MTS, no patterns are formed.

The first construct, His-MinE(2-31)-sfGFP was cloned as follows: A fragment containing the pET28a vector-backbone and the start of His-MinE was amplified from pET28a-His-MinE using primers PG073+PG074. The sfGFP fragment was amplified from pVRB18-XX-sfGFP using primers PG069+PG070. The two fragments were recombined in E. coli to yield pET28a-His-MinE(2-31)-sfGFP. His-MinE(13-31)-sfGFP was assembled from three fragments. The sfGFP fragment was generated as described above. A second fragment containing the vector backbone and compatible overhangs was generated from pET28a-His-MinE using primers PG073+PG077. Finally, the MinE(13-31) fragment was amplified from pET28a-His-MinE using primers PG072+PG016, then a second PCR reaction was run on this fragment with primers PG076+PG074. All three fragments were recombined in E. coli.

His-MinE(2-31)-msfGFP was generated from His-MinE(2-31)-sfGFP by recombining two fragments generated by PCR with primers PG087+PG043 and PG088+PG044, respectively.

MinE(1-31)-msfGFP-His was recombined from two fragments. The MinE(1-31)-msfGFP was amplified from pET28a-His-MinE(2-31)-msfGFP using primers PG090+PG091. The vector fragment was generated from pET28a-BsMTS-mCherry-His using primers PG089+PG007.

Custom DNA sequences were ordered for GCN-4, c-Jun and c-Fos. DNA fragments consisting of a linker sequence, the respective leucine zipper and another linker sequence were amplified via PCR using primers PG103+PG104 (GCN4), PG105+PG106 (Jun) or PG107+PG108 (Fos). Similarly, FKBP and FRB were amplified using primers PG110+PG111 (FKBP) and PG112+PG113 (FRB). A fragment of MinE(13-31) containing compatible overlaps was generated from PCR on pET28a-MinEL-msfGFP-His using primers PG109+PG102. The vector containing MinE(1-31) and compatible overhangs was amplified from pET28a-MinE-His using primers PG007 and PG102. For the three-fragment assemblies, the vector was created via PCR from BsMTS-mCherry-His (Ramm et al.) using primers PG007+PG089. The desired construct vectors were then created via three-fragment homologous recombination in E. coli TOP10, or two-fragment in case of MinE(1-31) constructs. In an additional step, the protein sequence KCK was inserted into the MinE(13-31) constructs by amplifying two halves of the vector. The first half was amplified using primers PG114+PG43, the second half using primers PG115+PG44. After DpnI digest (done for all fragments amplified from functional vectors), the fragments were transformed in to E. coli TOP10 and selected on kanamycin LB plates for homologous recombination. All constructs' integrity was verified via Sanger sequencing.

SUMO-MinE(1-31)-KCK-His and SUMO-MinE(13-31)-KCK-His were generated via homologous recombination of two fragments each. For the construct with MTS, one fragment was amplified from pET28M-SUMO1-GFP using primers PG043+PG116. The second fragment was amplified from pET28M-SUMO1-MinE (*Glock et al., 2018b*) using primers PG044+PG117. Fragments for the construct without MTS were amplified from the recombined vector described above using primers PG043+PG118 and from pET28M-SUMO1-GFP using primers

PG044+PG119.

Purification of proteins

MinD, MinD-KCK-Alexa647, mRuby3-MinD, His-MinE and MinE-His were purified as previously described (*Ramm et al., 2018*; *Glock et al., 2018a*,b). MinE(13-31)-Fos, MinE(13-31)-Jun and MinE(13-31)-GCN4 were purified as described for MinE-His (*Glock et al., 2018b*). MinE(2-31)-Fos, MinE(2-31)-Jun and MinE(2-31)-GCN4 were highly insoluble and therefore entirely found in the pellet fraction after cell lysis and centrifugation. The supernatant was discarded and the pellet re-solubilised in lysis buffer U (8M Urea, 500 mM NaCl, 50 mM Tris-HCl pH 8) by pipetting, vortexing and submerging the vial in a sonicator bath. The residual insoluble fraction was pelleted by centrifugation at 50000 g for 40 minutes. The supernatant was incubated with Ni-NTA agarose beads ($\sim$ 2 mL per 400 mL initial culture) for 1 h at room temperature on a rotating shaker. Agarose beads were pelleted at 400 g, 4 min and the supernatant was discarded. Purification was continued at RT since proteins were unfolded and kept in 8 M Urea. Agarose beads were loaded on a glass column and washed three times with 10 mL of above lysis buffer U. Further washes (3x) were performed with wash buffer U (8 M Urea, 500 mM NaCl, 20 mM imidazole, 50 mM Tris-HCl pH 8). The protein was eluted with elution buffer U (8 M Urea, 500 mM NaCl, 300 mM imidazole, 50 mM Tris-HCl pH8) and fractions with the highest protein content (Bradford, by eye) were pooled. Re-folding of the pooled eluate was done by dialyzing in multiple steps. In a first step, the solution was dialyzed against buffer D1 (6 M Urea, 500 mM NaCl, 50 mM Tris-HCl pH 8, 10% glycerol) over night. In a second step, against buffer D2 (4 M Urea, 500 mM NaCl, 50 mM Tris-HCl pH8, 10% glycerol) for 2 h, then against buffer D3 (2 M Urea, 500 mM NaCl, 50 mM Tris-HCl pH8, 10% glycerol) for further 2 h. The final dialysis was done against storage buffer (300 mM KCl, 50 mM HEPES pH 7.25, 10% glycerol, 1 mM TCEP, 0.1 mM EDTA). To separate the re-folded protein from aggregates, the protein solution was ultracentrifuged for 40 min at 50000 g, 4 °C. Protein concentration was then determined as described in the methods section. MinE(13-31)-KCK-His-Atto 488 and MinE(2-31)-KCK-His-Atto 488 were expressed and purified as described for MinE-His. SUMO-peptide fusions were then added into 1:100 (protease:protein) of SenP2 protease and dialyzed against storage buffer. Labelling was performed as described in the methods section.

Protein concentration for dimerized constructs

For the dimerized constructs, not enough concentrations combinations were titrated to obtain full phase diagrams. We state here which combinations of protein concentrations we tested. All of the following conditions yielded pattern formation: 0.6 µM MinD, 50 nM MinE(13-31)-GCN4; 0.6 µM MinD, 50 nM MinE(13-31)-Jun; 0.6 µM MinD, 25 nM MinE(13-31)-Jun; 0.6 µM MinD, 30 nM MinE(13-31)-Jun; 0.5 µM MinD, 20 nM MinE(13-31)-Jun; 0.5 µM MinD, 50 nM MinE(13-31)-Fos; 1 µM MinD, 100 nM MinE(13-31)-Fos; 1 µM MinD, 150 nM MinE(13-31)-Fos.

Supplementary discussion

Going forward, it will be interesting to explore the Min system further along the avenue of individual protein domains / features and their role for self-organized pattern formation. We suspect that the minimization of MinE peptides could be taken even further by shortening the peptide. Especially at the C-terminus we expect that several residues do not contribute to function, since they are not visible in a crystal structure of MinE(13-31) with MinD (*Park et al., 2011*). Additionally, the peptide still retains residues required for the dual function in the context of the MinE switch. Therefore, an optimized and further reduced peptide could be screened for. Additionally, our experiments with minimal peptides added to a

superfolder–GFP (*Figure Supplement 2*) show that unrelated proteins can be attached. This opens the possibility to couple the spatiotemporal pattern to a different protein system. In principle, any protein can act as a minimal MinE if a peptide can be added internally or at either terminus of the protein.

Although we have not tested this prediction, we expect that the native MTS of MinE could be replaced with another MTS in our minimal peptides to restore pattern formation. It would be interesting to exchange the native MTS for a quantitatively described, diverse set of MTS to determine the required strength of membrane anchors needed for minimal MinE pattern formation. However, no such set or even just quantitative data on binding strength of multiple MTS is available at the moment.

Since we relate the lack of pattern formation to the recruitment rate of MinE(13-31), it may be possible to alter MinE recruitment by changing the buffer conditions such as salt concentration, type of ions (e.g. Sodium instead of Potassium), viscosity or pH. We can only speculate here, however, since screening a vast amount of conditions was not in the scope of the present study. Studies done on the wild type Min system using different buffer conditions showed some impact on pattern formation (*Downing et al., 2009*; *Vecchiarelli et al., 2014*).

Primers used in this study

Name	Sequence
PG007: AC-pET_for	GTCGAGCACCACCACCA
PG016: B-pET-MinE_rev	GTGCGGCCGCAAGCTTTTAGCGACGGCGTTCAGCAA
PG043: mut_KanR_fw	TGAAACATGGCAAAGGTAGCGT
PG044: mut_KanR_rev	GCTACCTTTGCCATGTTTCAGAAA
PG073: sfGFP-pET_fw	CATGGATGAGCTCTACAAATAAAAGCTTGCGGCCGCAC
PG074: sfGFP-li-MinE31_rev	AAAGTTCTTCTCCTTTGCTCACAGAACCAGAAGAACCAGAAGAGCGACGGCGTTCAGCAAC
PG075: sfGFP-MinE_L_fw	CATGGATGAGCTCTACAAAGCATTACTCGATTTCTTTCTCTCGC
PG076: E-pET-MinEs_fw	GGGTCGCGGATCCGAATTCAAAAACACAGCCAACATTGCAA
PG077: lolipET_rv	GAATTCGGATCCGCGACC
PG087: sfGFP_V206K_fw	TACCTGTCGACACAATCTAAGCTTTCGAAAGATCCCAAC
PG088: sfGFP_V206K_rev	GTTGGGATCTTTCGAAAGCTTAGATTGTGTCGACAGGTA
PG089: pET28a-start_rev	CATGGTATATCTCCTTCTTAAAGTTAAACAA
PG090: pET-MinEL_fw	TAAGAAGGAGATATACCATGGCATTACTCGATTTCTTTCTCTCGC
PG091: pET-msfGFP_rev	TGGTGGTGGTGGTGCTCGACTCCAGATCCACCTTTGTAGAGCT
PG103: GCN4_fw	TCTTCTGGTTCTTCTGGTTCTCGTATGAAACAGCTGGAAGACAA
PG104: GCN4_rev	GTGCTCGACTCCAGATCCACCACGTTCACCAACCAGTTTTTTC
PG105: Jun_fw	TCTTCTGGTTCTTCTGGTTCTCGTATCGCTCGTCTGGAAGA
PG106: Jun_rev	GTGCTCGACTCCAGATCCACCGTAGTTCATAACTTTCTGTTTCAGCTG
PG107: Fos_fw	TCTTCTGGTTCTTCTGGTTCTCTGACCGACACCCTGCAG
PG108: Fos_rev	GTGCTCGACTCCAGATCCACCGTAAGCAGCCAGGATGAATTCC
PG109: pET-MinEs_fw	TAAGAAGGAGATATACCATGAAAAACACAGCCAACATTGCAAAG
PG110: FKBP_fw	TCTTCTGGTTCTTCTGGTTCTGGTGTTCAGGTCGAAACTATCTCTC
PG111: FKBP_rev	GTGCTCGACTCCAGATCCACCTTCCAGTTTCAGCAGTTCAACG
PG112: FRB_fw	TCTTCTGGTTCTTCTGGTTCTGAAATGTGGCATGAGGGTCTC
PG113: FRB_rev	GTGCTCGACTCCAGATCCACCCTGTTTAGAGATGCGACGAAAGAC
PG114: li-KCK_fw	GGATCTGGAGTCGAGAAATGCAAACACCACCACCACCAC

243

PG115: li-KCK_rev	GTGGTGGTGGTGGTGTTTGCATTTCTCGACTCCAGATCC
PG116: KCK-pET_fw	GTTCTTCTGGTAAATGCAAATGAAAGCTTGCGGCCG
PG117: EL_li_rev	TTTGCATTTACCAGAAGAACCAGAACCGCGACGGCGTTCAGC
PG118: SUMO-Es-fw	ACCAGGAACAAACCGGTGGATCAAAAAACACAGCCAACATTGCAAA
PG119: SUMO_rev	TCCACCGGTTTGTTCCTGG

244

8 Adaptability and evolution of the cell polarization machinery in budding yeast

This section is a preprint of the following manuscript currently under revision.

Adaptability and evolution of the cell polarization machinery in budding yeast

F. Brauns,[1] L. M. Iñigo de la Cruz,[2] W. K.-G. Daalman,[2] I. de Bruin,[2] J. Halatek,[1,3] L. Laan,[2] E. Frey,[1]

[1] *Arnold Sommerfeld Center for Theoretical Physics and Center for NanoScience, Department of Physics, Ludwig-Maximilians-Universtiät München, Theresienstraße 37, D-80333 München, Germany*

[2] *Department of Bionanoscience, Kavli Institute of Nanoscience Delft, Delft University of Technology, Van der Maasweg 9, 2629 HZ Delft, the Netherlands*

[3] *Biological Computation Group, Microsoft Research, Cambridge CB1 2FB, UK*

Adaptability and evolution of the cell polarization machinery in budding yeast

Fridtjof Brauns[1], Leila M. Iñigo de la Cruz[2], Werner K.-G. Daalman[2], Ilse de Bruin[2], Jacob Halatek[1,3], Liedewij Laan[2,†], and Erwin Frey[1,†]

Affiliations

[1]Arnold Sommerfeld Center for Theoretical Physics and Center for NanoScience, Department of Physics, Ludwig-Maximilians-Universität München, Munich, Germany.

[2]Department of Bionanoscience, Kavli Institute of Nanoscience Delft, Delft University of Technology, Delft, the Netherlands.

[3]Biological Computation Group, Microsoft Research, Cambridge, UK.

[†]Corresponding authors. E-mail: l.laan@tudelft.nl, frey@lmu.de

Abstract

How can a self-organized cellular function evolve, adapt to perturbations, and acquire new sub-functions? To make progress in answering these basic questions of evolutionary cell biology, we analyze, as a concrete example, the cell polarity machinery of *Saccharomyces cerevisiae*. This cellular module exhibits an intriguing resilience: it remains operational under genetic perturbations and recovers quickly and reproducibly from the deletion of one of its key components. Using a combination of modeling, conceptual theory, and experiments, we show that multiple, redundant self-organization mechanisms coexist within the protein network underlying cell polarization and are responsible for the module's resilience and adaptability. Based on our mechanistic understanding of polarity establishment, we hypothesize how scaffold proteins, by introducing new connections in the existing network, can increase the redundancy of mechanisms and thus increase the evolvability of other network components. Moreover, our work suggests how a complex, redundant cellular module could have evolved from a more rudimental ancestral form.

Introduction

Evolution is driven by an interplay of genotype mutations and selection operating on the level of biological function, that is, the phenotype. A mechanistic understanding of evolution therefore requires frameworks that connect the genotype to the phenotype (Rainey et al., 2017). When the phenotype (function) is determined by a self-organized process, the genotype-to-phenotype relation is not a simple one-to-one mapping (or "blueprint"). As a concrete example take intracellular (protein-based) pattern formation, which is essential for many essential cellular functions, like division and motility (Howard et al., 2011; Bi and Park, 2012; Chiou et al., 2017; Halatek et al., 2018; Ramm et al., 2019). The genotype determines the components (proteins), their interaction network and their copy numbers. Cellular function (the phenotype), on the other hand, emerges by the collective interplay of these

components—governed by physical and chemical processes (diffusion, mass-action law) in the spatially extended cellular domain. A mechanistic understanding of the evolution of such collective (self-organized) functions has remained elusive so far (Johnson and Lam, 2010).

Here, we provide a concrete (and, to the best of our knowledge, first) example of how such understanding can be gained, using the cell Cdc42-polarization machinery of *Saccharomyces cerevisiae* (budding yeast) as a model system. Cell polarization directs cell division of budding yeast through the formation of a polar zone with high Cdc42 concentration on the membrane (see Figure 1A-C). It is organized by a complex interaction network (Figure 1D) around the central polarity protein Cdc42, a GTPase that cycles between an active (GTP-bound) and an inactive (GDP-bound) state. The key features of these two states are that active Cdc42 is strongly membrane bound and recruits many downstream factors, while inactive Cdc42-GDP can detach from the membrane to the cytosol where it diffuses freely.

In wild-type (WT) cells, polarization is directed by upstream cues like the former bud-scar (Kang, 2001; Marston et al., 2001; Kozminski et al., 2003; Bi and Park, 2012). Importantly however, Cdc42 can polarize *spontaneously* in a random direction in the absence of such cues (Irazoqui et al., 2003; Wedlich-Soldner, 2003; Goryachev and Pokhilko, 2008). What are the elementary processes underlying spontaneous Cdc42 polarization? On the timescale of polarity establishment, the total copy number of Cdc42 proteins (as well as its interaction partners) is nearly constant. Hence, to establish a spatial pattern in the protein concentration, the so-called polar zone, the proteins need to be spatially redistributed in the cell by *directed transport*. There are two distinct, mostly independent, pathways for directed transport that have been established by experimental and theoretical studies (Wedlich-Soldner, 2003; Goryachev and Pokhilko, 2008; Freisinger et al., 2013; Klünder et al., 2013; Woods et al., 2015): cytosolic diffusion and vesicle-based active transport along polarized actin cables (Figure 1B,C). Once a polar zone has been established, the ensuing concentration gradient on the membrane leads to a diffusive flux of proteins away from the polar zone. To maintain the polar zone, this flux on the membrane must be counteracted continually by (re-)cycling the proteins back to the polar zone via a flux from the cytosol to the membrane (Goryachev and Pokhilko, 2008; Klünder et al., 2013; Chiou et al., 2017). In WT cells, Cdc42-GTP recruits Bem1 from the cytosol which in turn recruits Cdc24 (see Figure 1D) (Bose et al., 2001; Irazoqui et al., 2003). The membrane-bound Bem1-Cdc24 complex then recruits more Cdc42-GDP from the cytosol and activates it (nucleotide exchange) (Butty, 2002). The hallmark and crucial element of this *mutual recruitment mechanism* is the co-localization of Cdc42 and its GEF (Butty, 2002; Goryachev and Pokhilko, 2008; Howell et al., 2009; Kozubowski et al., 2008; Woods et al., 2015).

Deletion of Bem1 severely impedes the cells' ability to polarize and bud (Chenevert et al., 1992; Irazoqui et al., 2003) by disrupting localized Cdc42 activation (Kozubowski et al., 2008; Woods et al., 2015). Intriguingly, in experimental evolution, *bem1Δ* mutants are reproducibly rescued by the subsequent loss of Bem3 (Laan et al., 2015). Bem3 is one of four known Cdc42-GAPs that catalyze the GTP-hydrolysis and hence switch Cdc42 into its inactive, GDP-bound state. The loss of Bem3 clearly does not replace Bem1 as it does not provide a scaffold between Cdc42 and Cdc24. How then does the loss of Bem3 rescue the pattern-forming capability of the *remaining* Cdc42-polarization machinery? Interestingly, it has been reported that *bem1Δ* cells can be rescued by fragments of Bem1 that do not interact with Cdc42-GTP but still bind to the membrane and to Cdc24 (Smith et al., 2013; Grinhagens et al., 2020). These Bem1 fragments therefore cannot mediate mutual recruitment of Cdc42 and its GEF Cdc24, but only confer increased global (homogeneous) GEF activity by relieving Cdc24's autoinhibition (Shimada et al., 2004; Rapali et al., 2017). This suggests that Cdc42 polarization can emerge *independently* of GEF co-localization, but the underlying mechanism remains unclear.

The adaptability of budding yeast's cell polarization module makes it an ideal model system for studying the evolution of self-organized function. Here, we develop a theory that shows that this cellular module comprises multiple redundant reaction–diffusion mechanisms. It reveals that in addition to the Bem1-mediated mutual recruitment mechanism, a distinct and latent mechanism exists in the

Cdc42-polarization machinery. We show that this latent mechanism operates under different constraints on the protein copy numbers than the wild-type mechanism and is activated by the loss of Bem3 which lowers the total copy number of GAPs. This explains how cell polarization is rescued in *bem1Δ bem3Δ* cells (Laan et al., 2015), and also reconciles the puzzling experimental findings outlined above. Moreover, we experimentally confirm the predictions of our theory on how cell polarization in various mutants can be rescued by changing the Cdc42 copy number. On the basis of the mechanistic understanding of the cell polarization module in budding yeast, we then propose a possible evolutionary scenario for the emergence of this self-organized cellular function. We formulate a concrete hypothesis how evolution might leverage scaffold proteins to introduce new connections in an existing network, and thus increase redundancy of mechanisms within a functional module. This redundancy loosens the constraints on the module and thereby enables further evolution of its components, for instance by duplication and sub-functionalization (Magadum et al., 2013).

Results

As basis for our theoretical analysis, we first need to formulate a mathematical model of the cells' Cdc42-polarization machinery that is able to explain Bem1-independent polarization. The interplay of spatial transport processes (Figure 1B,C) and protein-protein interactions (Figure 1D) is described in the framework of reaction–diffusion dynamics. The biochemical interaction network we propose is based on the quantitative model introduced in (Klünder et al., 2013) and extends it in several important ways. It accounts for the Cdc42 GTPase cycle and the interactions between Cdc42, Bem1 and Cdc24 (Goryachev and Pokhilko, 2008). Importantly — extending previous models — we explicitly incorporate the transient formation of a GAP-Cdc42 complex as an intermediate step in the enzymatic interaction between GAPs and Cdc42 (Zhang et al., 1997). In addition, we include effective self-recruitment of Cdc42-GDP to the membrane which is facilitated by membrane-bound Cdc42-GTP. This effective recruitment accounts for vesicle-based Cdc42 transport along actin cables (Slaughter et al., 2009; Layton et al., 2011; Freisinger et al., 2013) and putative recruitment pathways mediated by Cdc42-GTP downstream effectors such as Cla4 and Gic1/2 (Tiedje et al., 2008; Das et al., 2012; Daniels et al., 2018). A detailed description of the model, illustrated in Figure 1D, and an in-depth biological motivation for the underlying assumptions are given in the SI Section 1.

The Cdc42 interaction network facilitates a latent polarization-mechanism

We first ask whether the proposed reaction–diffusion model of the Cdc42 polarization machinery can explain spontaneous polarization in the absence of Bem1, i.e. without GEF co-localization with Cdc42. To this end, we perform a linear stability analysis of the model which identifies the regimes of self-organized pattern formation. A large-scale parameter study (see SI Section 5) reveals that in the absence of Bem1 there is a range of protein numbers of Cdc42 and GAP where polar patterns are possible (Figure 2B), i.e. that there is a latent polarization mechanism. However, in contrast to the Bem1-dependent mutual recruitment mechanism (Figure 2A), we find that the regime of operation for this latent mechanism is more limited and requires a sufficiently low GAP/Cdc42-concentration ratio (Figure 2B).

What is the mechanistic cause for this constraint? To answer this question, we need to understand how the Cdc42-polarization mechanism works in the absence of Bem1. As emphasized above, Cdc42-polarization requires two essential features—directed transport of Cdc42 to the polar zone and localized activation of Cdc42 there. The first feature, directed transport, is accounted for in the model by effective recruitment of Cdc42-GDP to the membrane mediated by active Cdc42 (Figure 1D).

GAP saturation can localize Cdc42 activity to the polar zone

How is the second feature, localization of Cdc42 activity to the polar zone, implemented in the absence of Bem1? Instead of directly increasing the rate of Cdc42 activation in the polar zone (via recruitment of the GEF Cdc24 by Bem1), localization of activity can also be achieved by decreasing the rate of Cdc42 *deactivation* in the polar zone and increasing it away from the polar zone. In fact, if enzyme

saturation limits the net deactivation rate, a simple increase in Cdc42 density *generically* leads to a decrease of the Cdc42 deactivation rate (per Cdc42 molecule). Enzyme saturation of catalytic reactions occurs when the dissociation of the transient enzyme-substrate complex (here the GAP-Cdc42 complex) is the rate limiting step such that the enzymes are transiently sequestered in enzyme-substrate complexes. Indeed, it has been shown that this is the case for GAP-catalyzed hydrolysis of Cdc42 in budding yeast (Zhang et al., 1997). Furthermore, enzyme saturation requires that a large fraction of enzymes is sequestered in enzyme–substrate complexes, i.e. that the total enzyme density is sufficiently low compared to the substrate density, as we found in the linear stability analysis (Figure 2B).

In summary, GAP saturation localizes Cdc42 activity to the polar zone, by decreasing the deactivation rate in the polar zone, where Cdc42 density is high, relative to the remainder of the membrane, where Cdc42 density is low. This, in conjunction with transport of Cdc42 to the polar zone, drives spontaneous cell polarization. Interestingly, enzyme saturation of Cdc42 hydrolysis is one of the six theoretically possible mechanisms for pattern formation that were hypothesized by a generic mathematical analysis of feedback loops in GTPase cycles (Goryachev and Leda, 2017).

The latent polarization-mechanism explains the rescue of Bem1 deletes

The Bem1-independent rescue mechanism requires a sufficiently low GAP/Cdc42-concentration ratio to be functional (Figure 2B). This suggests that *bem1Δ* cells are not able to polarize because their GAP copy number is too high. Our model predicts that the loss of GAPs can rescue cell polarization by bringing their total copy number into a regime where the Bem1-independent mechanism is operational, as indicated by the arrow in Figure 2B. This is in accordance with evolution experiments showing that *bem1Δ* cells are reproducibly rescued by a subsequent loss-of-function mutation of the GAP Bem3 (Laan et al., 2015). Bem3 accounts for approximately 25% of the total copy number of all Cdc42-GAPs (Kulak et al., 2014), indicating that *bem1Δ* mutants are close to the GAP/Cdc42-ratio threshold of the Bem1-independent mechanism. This proximity of the protein copy numbers to the threshold explains why a low fraction (about 1 in 10^5) of mutants are able to polarize and divide, after *BEM1* has been deleted (Laan et al., 2015): Protein expression levels vary stochastically from cell to cell such that a small fraction of cells lies in the concentration regime where the latent polarization mechanism drives spontaneous cell polarization.[1]

Rather than by the loss of a GAP, the GAP/Cdc42-concentration ratio could also be brought down by an increase of the Cdc42 copy number. Yet another option would be an increase of Cdc24's GEF activity which would increase the critical threshold in GAP/Cdc42-concentration ratio (see dashed line in Figure 2B). However, compared to a loss-of-function mutation, such mutations have a much smaller mutational target size and are therefore much less frequent. Moreover, one might wonder why it is specifically Bem3, rather than one of the other GAPs, that is lost to rescue the *bem1Δ* strain. Some hints to answer this outstanding question are provided by a detailed theoretical analysis of the rescue mechanism discussed below (***Functional submodules of cell polarization***).

Experiments confirm theoretical predictions

Based on the GAP/Cdc42-ratio constraint in the rescue mechanism, our theory makes two specific predictions: (i) Increasing the copy number (i.e. overexpression) of Cdc42 will rescue cell polarization of *bem1Δ* cells by invoking the Bem1-independent mechanism. (ii) Polarization of *bem1Δbem3Δ* cells will break down if the expression level of Cdc42 is lowered compared to the WT level (Figure 2B).

To test these model predictions experimentally, we first constructed different yeast strains with Cdc42 under an inducible galactose promoter such that we can tune the Cdc42 copy number by varying the

---

[1] For the four Cdc42 GAPs, a coefficient of variation around 0.14 for cell-to-cell copy-number variability has been reported (Chong et al., 2015). This is on the same order of magnitude as the upper estimate of 25% for the GAP copy number reduction required to activate the Bem1-independent rescue mechanism, suggesting that this mechanism is operational in a fraction of *bem1Δ* cells.

galactose concentration in the growth media (Yocum et al., 1984): a *bem1Δ* strain (yWKD069), a *bem1Δ bem3Δ* (yWKD070), and a modified WT strain (yWKD065) (see ***Materials and Methods***).

As a next step, we inoculated the different strains at varying galactose concentration in 96 well plates, that were placed in a plate reader to measure the cell density over time, and thereby determined the growth rate (see ***Materials and Methods***). For every galactose concentration, the growth rates are normalized to those of WT cells, with Cdc42 under its native promotor (yLL3a), grown at the same galactose concentration. In Figure 3A the normalized growth rates of the different mutants are plotted. As expected, WT cells grow at all galactose concentrations. In contrast, WT cells with Cdc42 under the galactose promotor (yWKD065), do not grow in the absence of Cdc42 (0% galactose concentration), since a failure to polarize severely impairs cell division and eventually leads to cell death and thus zero growth rate (Irazoqui et al., 2003). Our data show that the WT mechanism is rather insensitive to Cdc42 copy number, even for very low expression of Cdc42, in accordance with theory (Figure 2A).

Our model predicts that *bem1Δ* cells need the highest Cdc42 copy number to polarize, WT cells will need the least, and the *bem1Δ bem3Δ* cells should be in between. We indeed find that the *bem1Δ* strain (yWKD069) grows in media with 0.1% or higher galactose concentration. We did inoculate these strains at lower galactose concentration, but never observed any growth ($n \geq 2$ experiments, with 4 technical replicates per condition). The *bem1Δbem3Δ* cells (yWKD070) grow only in a galactose concentration of at least 0.06%. For WT cells with Cdc42 under the galactose promotor growth we observe and reduced growth rate at 0.01% galactose concentration but growth is only fully inhibited at 0% galactose concentration. All of the above experimental observations agree with our specific theoretical predictions. To show that the differences in population growth rates are directly caused by the ability of cells to polarize, rather than for example pleiotropic changes in another cell cycle phase, we performed a second set of experiments, where we measured the cell radius using light microscopy (Figure 3B). It was previously shown that the cell radius correlates linearly with the time it takes for cells to polarize (Allard et al., 2018; Laan et al., 2015): cells that take longer to polarize are on average larger than cells that polarize fast because yeast cells continue to grow during polarity establishment, allowing us to use the cell radius as a proxy for the polarization time. Additionally, we verified that, at low Cdc42 copy numbers, cells cannot polarize at all and thus die. Consistent with the population growth data, we observed that after 24 hours at 0% galactose concentration, for every genetic background where Cdc42 is under the galactose promotor, the vast majority of cells are not able to polarize or polarize very slowly, because they are either dead (Figure 3B,C) or very large (Figure 3B,D). We also confirm that the average cell radius (and thus the polarization time) and death rate of cells with Cdc42 under its native promotor are not affected by the galactose concentration (Figure 3C,D in red). At 0.06% galactose concentration, *bem1Δ bem3Δ* the cells' radii (and thus polarization times) are closer to WT cell radii than those of *bem1Δ* cells. This agrees with the population growth data. And at 0.1% Gal the average cell radius for live cells for all mutants were approximately equal to the average WT cell radius (Figure 3D). Interestingly, after 24 hours at 0% galactose concentration, WT cells with Cdc42 under the galactose promotor are still polarizing faster than the *bem1Δ* and the *bem1Δ bem3Δ* cells, as indicated by their smaller average cell radius (Figure 3D). This observation confirms our above observation that a very small number of Cdc42 molecules is sufficient for WT cells to polarize and thus for the WT mechanism to be operational.

Taken together, the experimental data confirm the theoretical prediction that the Bem1-independent rescue mechanism is operational only below a threshold GAP/Cdc42-concentration ratio. In addition, we find that the Bem1-dependent WT mechanism is surprisingly insensitive to Cdc42 copy number, i.e. operates also at very low Cdc42 concentration. This significant difference in Cdc42 copy number sensitivity between the WT mechanism and the rescue mechanism is in the context of our theory explained by the qualitative difference of their principles of operation, as we discussed above in the section ***The Cdc42 interaction network facilitates a latent polarization mechanism***. While the WT mechanism is based on recruitment of the GEF Cdc24 to the polar zone, mediated by the scaffold protein Bem1, the rescue mechanism crucially involves enzyme saturation of Cdc42 hydrolysis due to

high Cdc42 density in the polar zone. This enzyme saturation requires a sufficiently large Cdc42 copy number relative to the GAP copy number. In the section ***Functional submodules of cell polarization*** below, we will analyze the mathematical model, and the qualitative and conceptual differences between these two mechanisms in more detail.

The latent rescue mechanism explains and reconciles previous experimental findings

In previous experiments, several Bem1 mutants were studied that perturb Bem1's ability to mediate co-localization of Cdc24 to Cdc42-GTP, the key feature that underlies operation of the WT mechanism (Howell et al., 2009; Smith et al., 2013; Bendezú et al., 2015; Woods et al., 2016; Witte et al., 2017; Grinhagens et al., 2020). The observations from these experiments have remained puzzling and apparently conflicting among one another as of yet. As we show in detail in the Supplementary Discussion in SI Section 6, the latent rescue mechanism predicted by our mathematical model explains and reconciles all of these previous experimental findings. The key insight is that the latent rescue mechanism can be activated by a global increase of GEF activity (see dashed line in Figure 2B). Bem1 mutants that lack the Cdc42-interaction domain but still bind to the GEF Cdc24 may provide such a global increase of GEF activity and thus rescue polarization of *bem1Δ* cells. Moreover, in accordance with optogenetics experiments (Witte et al., 2017), our mathematical model predicts that outside the regime of spontaneous polarization, the latent, Bem1-independent mechanism can also be induced by a sufficiently strong local perturbation of the membrane-bound GEF concentration.

Functional submodules of cell polarization

Cell polarization in budding yeast is a functional module based on a complex protein interaction network with Cdc42 as the central polarity protein (cf. Figure 1B-D). As we discuss next, the full network can be dissected into *functional submodules*. Here, the term functional submodule refers to a *part* of the full interaction network with a well-defined function in one or more pattern-forming mechanisms. Our theoretical analysis will reveal that an interplay of two (or more) *functional submodules* each constitutes a fully functional cell polarization mechanism.

As we argued in the ***Introduction***, establishment and maintenance of cell polarity requires that Cdc42-activity is localized to membrane regions with a high density of Cdc42. This can be achieved in two different ways. First, by the recruitment of the scaffold protein Bem1 to Cdc42-GTP, which in turn recruits the GEF (Cdc24) and thus localizes Cdc42 activation to the polar zone, where Cdc42 density is high (Figure 4A, top left). We call this the *polar activation* submodule. Second, GAP saturation in regions of high local Cdc42 densities can localize Cdc42 activity to the polar zone (Figure 4A, top right), as described above in the subsection ***GAP saturation can localize Cdc42 to the polar zone***. The transient sequestration of GAPs in Cdc42-GAP complexes is essential for this *polar GAP saturation* submodule. The third submodule (Figure 4A, bottom) that we term *Cdc42 transport*, comprises various modes of Cdc42 transport towards the polar zone: vesicle transport along polarized actin cables (cf. Figure 1B) and effective (self-)recruitment of Cdc42 from the cytosol. Several experiments indicate that downstream effectors of active Cdc42, such as Cla4, Gic1 and Gic2 may provide such effective recruitment in the absence of Bem1 (Tiedje et al., 2008; Kang et al., 2018; Daniels et al., 2018).

These three functional submodules represent different mechanistic aspects of the Cdc42-interaction network. Each submodule is operational only under specific constraints on the biochemical properties and copy numbers of the involved proteins. In the following, we exploit these constraints to study the roles of the submodules in the mathematical model by disabling them one at a time. This allows us to tease apart the mechanisms that are operational under the corresponding experimental conditions. The first submodule, *polar activation*, is disabled by the knock-out of Bem1. The second submodule, *polar GAP saturation*, is suppressed if the copy number of GAPs is too high. Alternatively, polar GAP saturation is rendered non-operational if the dissociation rate of the GAP-Cdc42 complex is too fast, or if the free GAPs diffuse very fast making additional free GAPs readily available in the polar zone. The third submodule, *Cdc42 transport*, can be switched off by immobilizing Cdc42, i.e. suppressing its spatial redistribution. Experimentally, this has been achieved in fission yeast by fusing Cdc42 to a

transmembrane protein that strongly binds to the membrane and is nearly immobile there (Bendezú et al., 2015).

By performing linear stability analysis for the full mathematical model under each of these perturbations disabling one of the submodules at a time (as described in detail in SI Section 5, SI Table S4), we find that the remaining two submodules operate in concert to constitute a mechanism for spontaneous Cdc42 polarization, as illustrated in Figure 4B. Figures 4C-E shows the regime of operation of the three different mechanisms as a function of the total Cdc42 and GAP concentrations. Figure 4F-H illustrate the concerted interplay of directed protein-transport and regulation of Cdc42 activity (activation/deactivation) that underlie Cdc42-polarization in these three mechanisms.

Before we turn to the detailed descriptions of these mechanisms, we note that if two submodules are disabled simultaneously, the remaining submodule alone cannot facilitate pattern formation. In particular, and perhaps somewhat counterintuitively, self-recruitment of Cdc42 alone is not sufficient to drive spontaneous cell polarization (Altschuler et al., 2008; Goryachev and Leda, 2017).

Wild-type mechanism: Cdc42 transport plus polar activation

The interplay of the Cdc42 transport submodule and the Cdc42-Bem1-Cdc24 recruitment submodule (polar activation), illustrated in Figure 3F, constitutes the WT mechanism that operates via mutual recruitment of Cdc42 and Bem1 (Irazoqui et al., 2003; Klünder et al., 2013; Freisinger et al., 2013). Characteristic for this mechanism is the co-localization of Cdc24 and Cdc42-GTP in the polar zone, as observed in previous experiments (Woods et al., 2016; Witte et al., 2017). Other than the rescue mechanism, the mutual recruitment mechanism does not require polar GAP saturation. Therefore, it is insensitive against high concentration of GAPs, i.e. it is operational for much higher GAP/Cdc42-concentration ratios than the rescue mechanism. Furthermore, it is robust against high diffusivity of free GAPs and high catalytic rates of the GAPs (fast decay of GAP-Cdc42 complexes into free GAP and Cdc42-GDP). This implies that in mathematical models of the WT mechanism the GAPs can be accounted for *implicitly* by a constant and homogeneous hydrolysis rate, as e.g. in (Goryachev and Pokhilko, 2008; Klünder et al., 2013; Kuo et al., 2014; Woods et al., 2016).

Rescue mechanism: Cdc42 transport plus polar GAP saturation

The interplay of Cdc42 transport (including effective self-recruitment via actin and/or other downstream effectors like Cla4) and GAP saturation in the polar zone, illustrated in Figure 3G, constitutes the latent, Bem1-independent rescue mechanism. Characteristic for this mechanism is that it does not require co-localization of Cdc24 to Cdc42-GTP in the polar zone (see Figure 4G). This lack of Cdc24 polarization would serve as a clear indicator of the rescue mechanism in future experiments using fluorescently labelled Cdc24. As explained above, the rescue mechanism relies on GAP saturation in the polar zone to maintain high Cdc42 activity there. This GAP saturation is suppressed by either high abundance, high catalytic activity, or fast transport (by cytosolic diffusion or vesicle recycling) of the GAPs.

The last constraint provides a plausible explanation why it is specifically Bem3 that needs to be deleted to rescue *bem1Δ* cells. In contrast to Rga1 and Rga2, Bem3 has been found to be highly mobile, probably because it cycles through the cytosol (Mukherjee et al., 2013). GAP saturation, i.e. the depletion of free GAPs in the polar zone, entails a gradient of the free GAP density towards the polar zone. A mobile GAP species like Bem3 will quickly diffuse along this gradient to replenish the free GAPs in the polar zone, relieving the GAP saturation there, and thus counteract the activation of Cdc42 in the incipient polar zone. Therefore, the loss of Bem3, rather than one of the other, less mobile GAPs, promotes the formation of a stable polar zone.

Interestingly, the formation of Min-protein patterns in *E. coli* relies on the same type of mechanism as the rescue mechanism for Cdc42-polarization: self-recruitment of an ATPase (MinD) and enzyme saturation of the AAP (MinE) that catalyzes MinD's hydrolysis and subsequent membrane dissociation (Huang et al., 2003; Halatek and Frey, 2012; Halatek et al., 2018). The transient MinDE complexes play

the analogous role to the Cdc42-GAP complexes here: In regions of high MinD density, MinE is sequestered in MinDE complexes, which limits the rate of hydrolysis until the complexes dissociate or additional MinE comes in by diffusion. Because MinE cycles through the cytosol, it rapidly diffuses into the polar zone where the density of free MinE is low, thus relieving the enzyme saturation there and eventually leading to a reversal of the MinD polarity direction. The repeated switching of MinD polarity due to redistribution of MinE is what gives rise to the Min oscillations in *E. coli*. Recently also stationary Min patterns have been observed *in vitro* (Glock et al., 2019). Conversely, oscillatory Cdc42 dynamics are found in the fission yeast *S. Pombe* (Das et al., 2012), and have also been indirectly observed in budding yeast mutants (Kuo et al., 2014; Ozbudak et al., 2005).

Polarization with immobile Cdc42: Bem1-mediated recruitment plus polar GAP saturation

The interplay of Cdc42-Bem1-Cdc24 recruitment (polar activation) and the polar GAP saturation, illustrated in Figure 3H, facilitates polarization of Cdc42 activity without the spatial redistribution Cdc42's total density. Instead, the proteins that are being redistributed are Bem1 and GEF. The polar zone is characterized by a high concentration of membrane-bound Bem1–GEF complexes which locally increase Cdc42 activity. Cdc42-GTP, in turn, recruits further Bem1 and GEF molecules to the polar zone. Characteristic for this mechanism is that Cdc42-GTP is polarized while the total Cdc42 density remains uniform on the membrane. Experimentally, this has been observed in fission yeast using Cdc42 fused to a transmembrane domain (Cdc42-psy1^{TM}) that renders Cdc42 nearly immobile. The polarization machinery of fission yeast is closely related to the one of budding yeast; it operates based on the same mutual recruitment pathway with Scd1 and Scd2 taking the roles of Cdc24 and Bem1 (Chiou et al., 2017). In future experiments, it would be interesting to test whether the Cdc42-psy1^{TM} also facilitates polarization in budding yeast (potentially in a strain with modified GAP or Cdc42 copy number as the regime of operation might not coincide with the WT copy numbers).

Conclusion and discussion

"How do cells work and how did they come to be the way they are?" (Lynch et al., 2014) We have approached this fundamental question of evolutionary cell biology by analyzing in depth a concrete system — the Cdc42 polarization machinery of budding yeast — that plays an essential role in the cell division of this model organism. Previous experiments showed that this machinery exhibits an intriguing resilience. It remains operational under many experimental (genetic) perturbations (Brown et al., 1997; Smith et al., 2013; Woods et al., 2015; Bendezú et al., 2015; Witte et al., 2017; Grinhagens et al., 2020), and recovers quickly and reproducibly from the deletion of one of its key components, the scaffold protein Bem1 (Laan et al., 2015). In the following we will shortly recapitulate the main insights we gained by studying the cell biology of this system and then show how a mechanistic understanding of self-organized cellular function can lead to fundamental insights into the way this function could have evolved from a more rudimental ancestral form.

Mechanistic understanding of the cell polarization module in budding yeast

We have discovered that multiple, redundant self-organization mechanisms coexist within the protein network underlying cell polarization, that are responsible for the resilience and adaptability of the cell polarization module. By dissecting the full cellular polarization module into *functional submodules,* we have identified distinct mechanisms of self-organized pattern formation, including the wild-type mechanism relying on the colocalization of Cdc42 with its GEF and a latent Bem1-independent rescue mechanism. Our theory, confirmed by experimental analysis, reveals that these mechanisms share many components and interaction pathways of this network. This implies that the redundancy of cell polarization is not at the level of individual components or interactions but arises on the level of the emergent function itself: If one submodule is rendered non-functional, the combination of the remaining submodules still constitutes an operational mechanism of cell polarization — if parameters,

in particular protein copy numbers, are tuned to a parameter regime where these remaining submodules are operational. Redundancy hence provides adaptability — the ability to maintain function despite (genetic) perturbations, like the knockout of Bem1.

The physics of self-organization imposes constraints on evolution

Our theoretical and experimental results highlight the importance of protein copy numbers as control parameters that decide whether a mechanism of spontaneous cell polarization is operational. Phrased from a genetic perspective, the genes that code for components of the cell polarization machinery are *dosage sensitive* (Papp et al., 2003). On the one hand, this entails that mutations of cis-regulatory elements (like promoters and enhancers) (Wittkopp and Kalay, 2012) can tune the copy numbers of proteins to the regime of operation of a specific cell-polarization mechanism and optimize the function within that regime. On the other hand, dosage sensitivity constrains evolution of the polarization-machinery's components via duplication and sub-functionalization (Conant and Wolfe, 2008; Papp et al., 2003).

One of our key findings is that the constraints on a single particular mechanism can be circumvented by the coexistence of several redundant mechanisms of self-organization that operate within the same protein-interaction network. The regimes of operation — and, hence the dosage sensitivity of specific genes — can differ vastly between these distinct mechanisms. Therefore, redundancy on the level of mechanisms allows the module's components to overcome constraints like dosage sensitivity and thus promotes "evolvability" — the potential of components to acquire new (sub-)functions while maintaining the module's original function.

A particular example in budding yeast's cell-polarization module where duplication and sub-functionalization might have taken place is the diversification of the different GAPs of Cdc42 in budding yeast: Rga1, Rga2, Bem2, and Bem3: Bem3, Rga1, and Rga2 play individual roles in specific cellular functions, like the pheromone response pathway (Stevenson et al., 1995; Mukherjee et al., 2013), axial budding (Tong et al., 2007), and the timing of polarization (Knaus et al., 2007). This diversity of GAPs is promoted by cell-polarization mechanisms that are insensitive to GAP copy number, such as the Bem1-mediated WT mechanism. As we will argue below, this notion provides a concrete hypothesis about the role of scaffold proteins, like Bem1, for the evolution of functional modules that operate by the interplay of many interacting components.

How evolution might leverage scaffold proteins

In the context of cellular signaling processes, it was suggested previously that evolution might leverage scaffold proteins to evolve new functions for ancestral proteins by regulating selectivity in pathways, shaping output behaviors, and achieving new responses from preexisting signaling components (Good et al., 2011). Our study of the Cdc42 polarization machinery shows how scaffold proteins may also play an important role in the evolution of intracellular self-organization. The scaffold protein Bem1 — by connecting Cdc42-GTP to Cdc42's GEF — generates a functional submodule that contributes to self-organized Cdc42 polarization. Based on this, we propose a hypothetical evolutionary history for Bem1, illustrated in Figure 4: The latent rescue mechanism is generic and rudimentary as it requires only weak self-recruitment of Cdc42. The second requirement — enzyme saturation of Cdc42 hydrolysis — is a generic consequence of the enzymatic interaction between Cdc42 and its GAPs. That the same pattern-forming mechanism underlies MinD polarization in *E. coli* — based on the proteins MinD and MinE that are evolutionarily unrelated to the Cdc42 machinery — further underlines its generality. We therefore hypothesize that the latent rescue mechanism is a rudimentary, ancestral mechanism of Cdc42 polarization in fungi. On the basis of this ancestral mechanism, Bem1 could then have evolved in a step-wise fashion. Given that Bem1 is highly conserved in fungi (Diepeveen et al., 2018), and that fission yeast polarization is based on the same mutual recruitment mechanism (Lamas et al., 2019; Martin and Arkowitz, 2014), this hypothetical evolutionary pathway would likely lie far in the past.

How might step-wise evolution of Bem1 have occurred? A hypothetical Bem1 precursor binding to Cdc24 but not to Cdc42-GTP might have facilitated a globally enhanced catalytic activity of Cdc24 by relieving its auto-inhibition (Rapali et al., 2017; Shimada et al., 2004). Our theory shows that such an increase of GEF activity enlarges the range of GAP/Cdc42-concentration ratios for which the latent rescue mechanism is operational. This would have entailed an evolutionary advantage by increasing the robustness of the (hypothetical) ancestral mechanism against copy number variations. In a subsequent step the Bem1-precursor might then have gained the Cdc42-binding domain (SH3 domain) by domain fusion (Farr et al., 2017), thus forming the full scaffold protein that connects Cdc24 to Cdc42-GTP that mediates the WT polarization mechanism (mutual recruitment of Cdc24 and Cdc42). Along this hypothetical evolutionary trajectory, the constraints on the GAP/Cdc42 copy number ratio and the molecular properties of the GAPs (kinetic rates, membrane affinities) would be relaxed, thereby allowing the duplication and sub-functionalization of the GAPs (Conant and Wolfe, 2008).

There are several possible routes to test our hypotheses. One possibility is the construction of phylogenetic trees for the different proteins (domains) that could inform on the order they appeared during evolution of the polarity network (Hooff et al., 2019). Another possibility is to search for species in the current tree of life which contain intermediate steps of the evolutionary trajectory, for instance species with a more ancient version of Bem1 lacking the SH3 domain, and identify the protein self-organization principles underlying polarization in these species. This is becoming a more and more realistic option, given the very large (and still expanding) number of fungal species that has been sequenced (Diepeveen et al., 2018) and the growing interest of cell and molecular biologists to work with non-model systems (Russell et al., 2017).

Our mechanistic understanding of the polarization machinery provides a genotype–phenotype mapping where the molecular details have been coarse grained. In future work, one could integrate this map into a cell cycle model to address questions about epistasis, and eventually predict evolutionary trajectories in a population dynamics model.

On a broader perspective, we have shown how understanding the mechanistic principles underlying self-organization can provide insight into the evolution of cellular functions, a central theme in evolutionary cell biology. Specifically, we have presented a concrete example that shows how a self-organizing system can mechanistically evolve from more rudimentary, generic mechanisms that are parameter sensitive, to a specific, robust and tightly controlled mechanism by only incremental changes (Johnson and Lam, 2010).
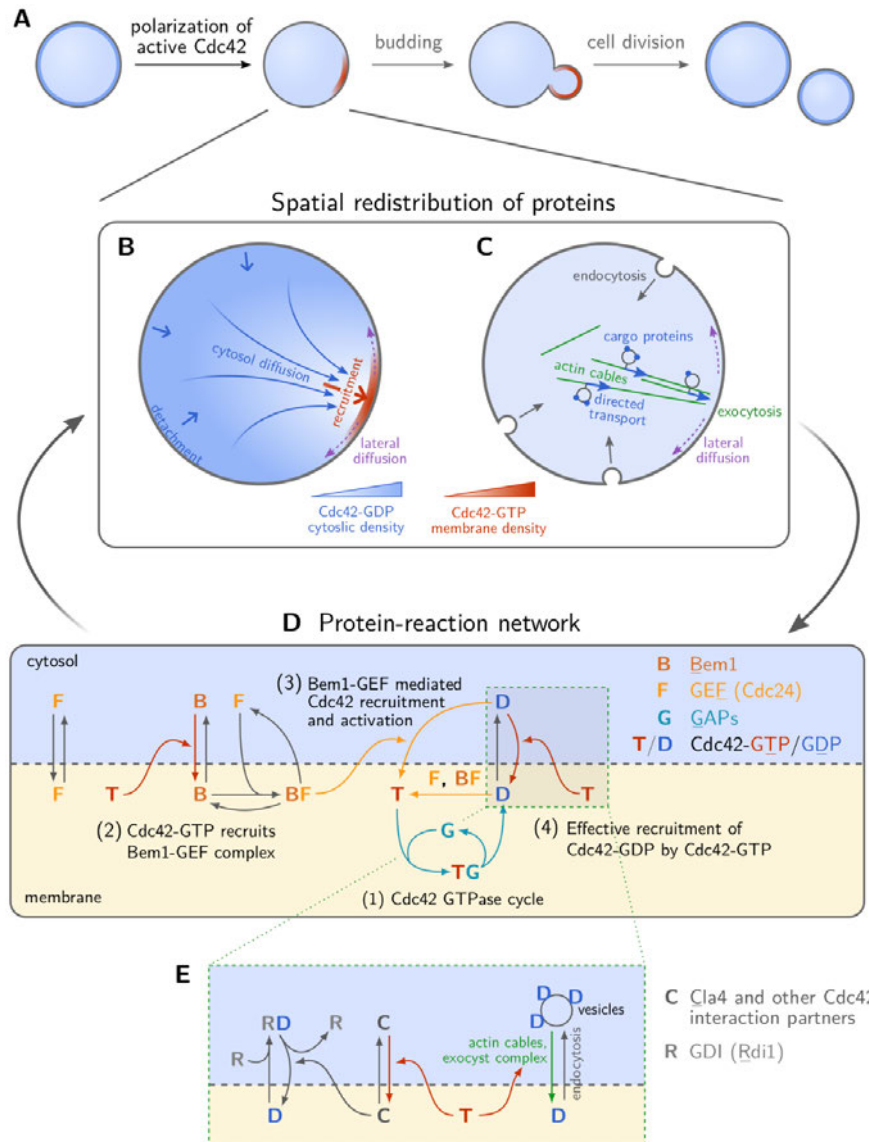
Figures

Figure 1. Cell division of *S. cerevisiae* is spatially controlled by self-organized polarization of Cdc42.
A Starting from an initially homogenous distribution of Cdc42, a polar zone forms, marked by a high concentration of active Cdc42 on the plasma membrane. There are two pathways of directed transport in the cells: **B** Cytosolic diffusion becomes directed by spatially separated attachment (red arrow) and detachment (blue arrow) zones; **C** Vesicle transport (endocytic recycling) is directed along polar-oriented actin cables. Active Cdc42 directs both cytosolic diffusion (by recruiting downstream effectors that in turn recruit Cdc42) as well as vesicle transport (by recruiting Bni1 which initiates actin polymerization). **D** Molecular interaction network around the GTPase Cdc42, involving activity regulators (GEF, GAPs), and the scaffold protein Bem1. An effective recruitment term accounts for Cdc42-recruitment to the membrane directed by Cdc42-GTP facilitated by Cdc42-downstream effectors (**E**). Details of the model and the mathematical implementation are described in the SI Sections 1 and 2.
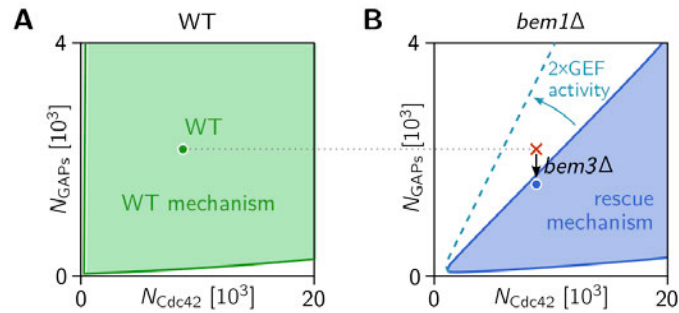
Figure 2. Regimes of operation of the Bem1-mediated wild-type mechanism and the latent mechanism for cell polarity. Stability diagrams as a function of GAP- and Cdc42 concentrations in presence and absence of Bem1 obtained by linear stability analysis (see SI Section 3) of the mathematical model for the Cdc42-polarization machinery (see Figure 1 and SI Section 2). Shaded areas indicate regimes of lateral instability, i.e. where a spontaneous polarization is possible. **A** In WT cells, the scaffold protein Bem1 is present and facilitates spontaneous polarization by a mutual recruitment mechanism that is operational in a large range of Cdc42 and GAP concentrations (Goryachev and Pokhilko, 2008; Klünder et al., 2013). The green point marks the Cdc42 and GAP concentrations of WT cells. **B** In the absence of Bem1, spontaneous polarization is restricted to a much smaller parameter-space region in our model, because the regime of operation of the Bem1-indepenendent mechanism is inherently is delimited by a critical ratio of GAP concentration to Cdc42 concentration. The Cdc42 and GAP concentrations of *bem1Δ* cells and *bem1Δ bem3Δ* are marked by the red cross and blue point, respectively. The experimental observation that *bem1Δ* cells do not polarize, whereas *bem1Δ bem3Δ* polarize can be used to infer a range for the critical GAP/Cdc42-concentration ratio. Increasing the GEF activity of Cdc24 increases this critical ratio (dashed blue line).

(The model parameters were obtained by sampling for parameter sets that are consistent with the experimental findings on various mutants, as described in detail in SI Section 5.)
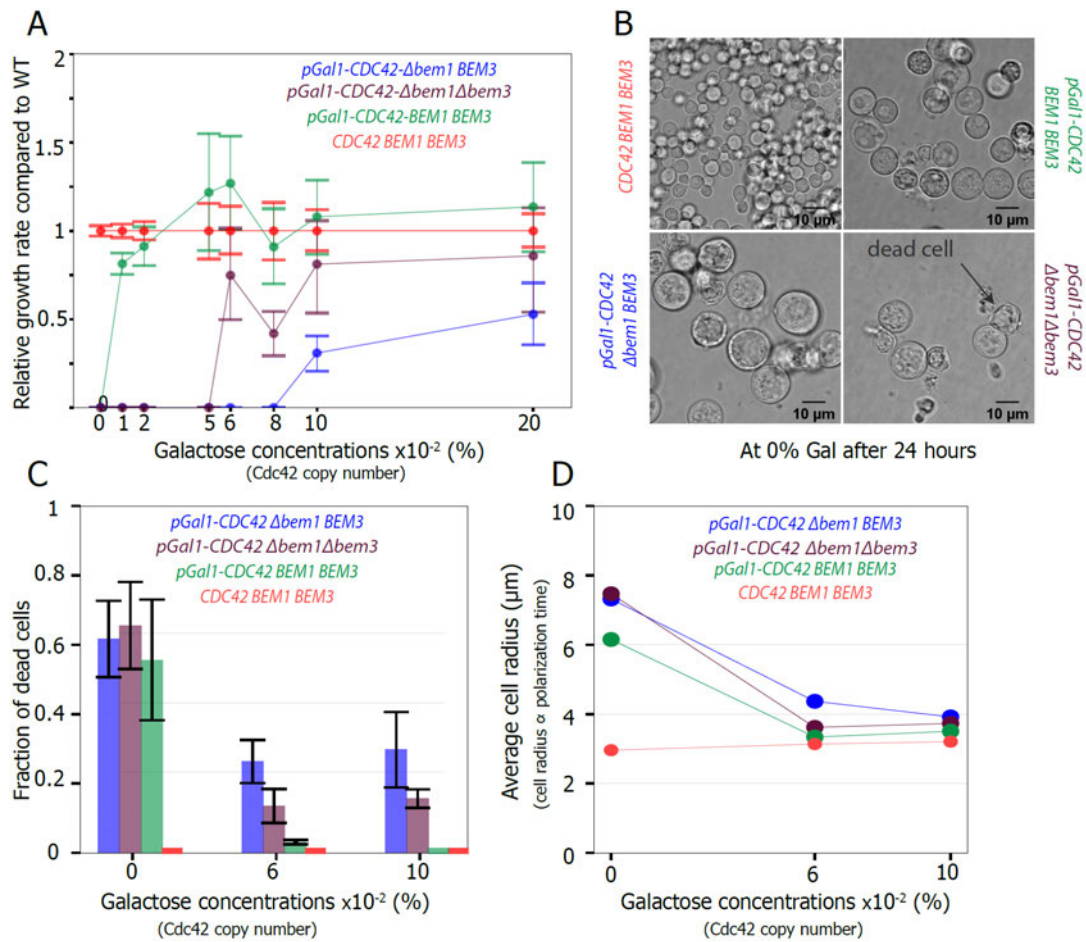
Figure 3. Experiments confirm theoretically predicted effect of Cdc42 copy number on the latent polarity-mechanism. **A** Growth rate of the different mutants (relative to the growth rate of WT cells with Cdc42 under its native promotor at that galactose concentration (red)) against the galactose concentration galactose concentration (proxy for Cdc42 copy number) show that higher expression of Cdc42 rescues *bem1Δ* cells and to a lesser extent *bem1Δ bem3Δ* cells; the error bar indicates the 68% credible interval, see materials and methods). The spread in the data is partially caused by experimental errors, as well by demographic noise, i.e. new fitter mutants arising by random mutations and taking over the population. **B** Microscopy images shows the morphology of dead and alive cells for the different strains after 24 hours at 0% galactose concentration, resulting in a Cdc42 copy number that approximates zero; scale bar indicates 10 μm. **C** The fraction of dead cells for different mutant strains vs galactose concentration shows that increasing Cdc42 copy number reduces cell death in *bem1Δ* and *bem1Δ bem3Δ* cells; the error bar indicates the standard error of the mean. **D** The average cell radius (proxy for polarization time) versus the galactose concentration shows that increasing Cdc42 copy number reduces polarization time; the error bar, which is the standard error of the mean, is smaller than the data symbol.
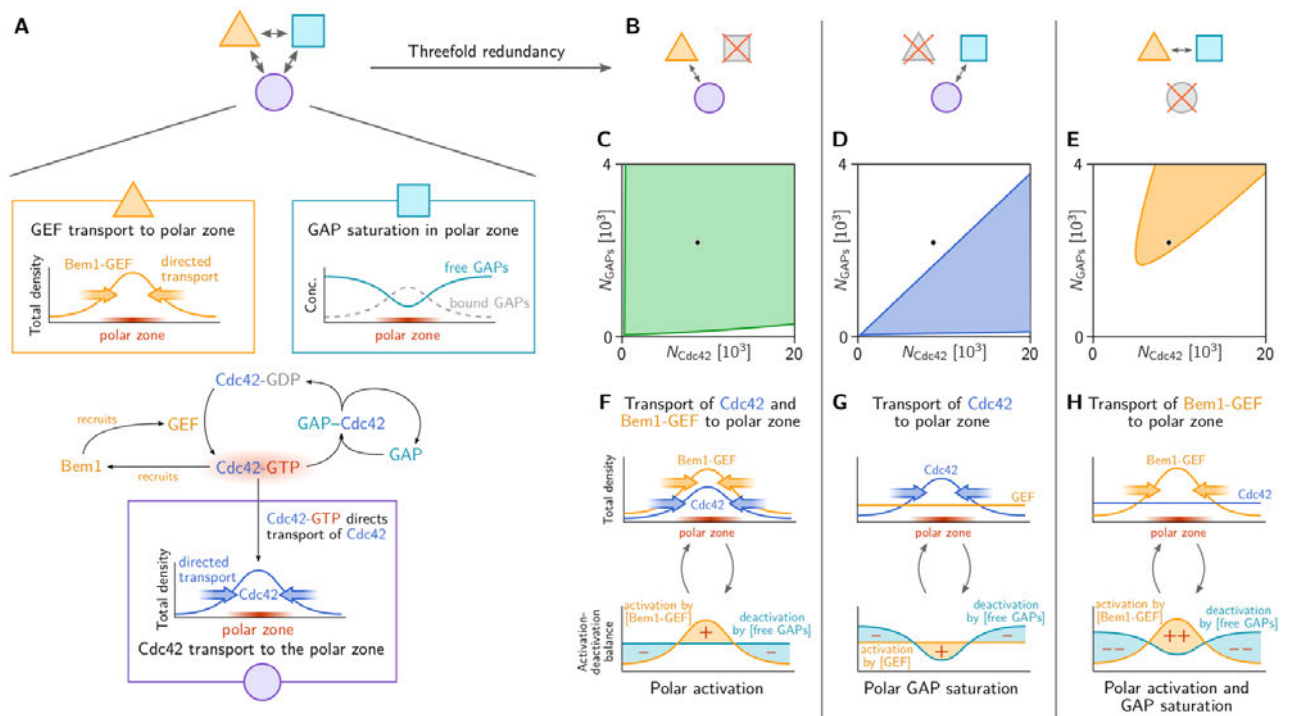
Figure 4: Three functional submodules constitute three distinct mechanisms of Cdc42-GTP polarization. **A** Three functional submodules of the Cdc42 interaction network contribute to the formation and maintenance of a *polar zone* (region of high Cdc42-GTP concentration, highlighted in red): (i) Transport of Cdc42 towards the polar zone. High Cdc42 activity can be maintained due to (ii) GAP saturation in the polar zone and by (iii) transport of the GEF to the polar zone via the scaffold protein Bem1. **B** Combinations of pairs of these functional submodules constitute mechanisms of self-organized pattern formation. **C–E** These mechanisms are operational in different regimes of the total copy number of Cdc42 and GAPs. The WT mechanism (**F**) is largely insensitive to copy number variations (**C**) because it based on mutual recruitment of Cdc42 and Bem1-GEF complexes, and does not depend on saturation of GAPs in the polar zone. In contrast, when the GEF is not transported to the polar zone (e.g. due to a deletion of Bem1), only GAP saturation in the polar zone maintains high Cdc42 activity there, while deactivation dominates away from the polar zone. Therefore, the polarization mechanism (**G**) is sensitive to the GAP copy number (**D**). **H** Remarkably, if transport of Cdc42 is suppressed, e.g. by strongly binding it to the membrane, a combination of Bem1-GEF complex recruitment and polar GAP saturation maintain a localized high Cdc42 activity even though the total density of Cdc42 is homogenously distributed.
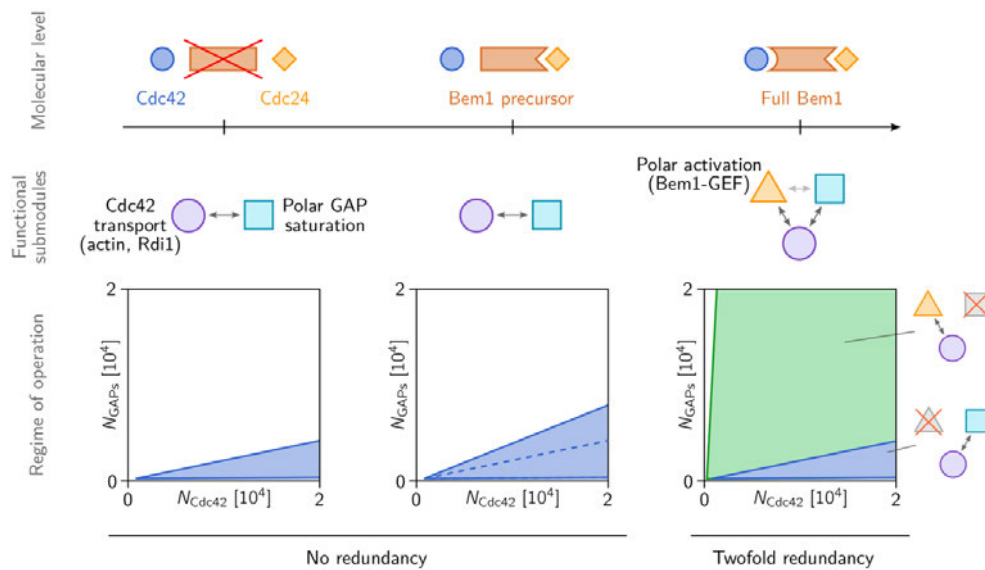
259

Figure 5: Hypothetical evolution of Bem1. (*Left*) The Bem1-independent "rescue" mechanism based on GAP saturation and Cdc42 transport towards membrane bound Cdc42-GTP is operational only in a limited range of the GAP/Cdc42-concentration ratios (cf. Figure 4D). (*Center*) a Bem1 precursor (Bem1-fragment) that binds to Cdc24 and relieves its auto-inhibition increases the range of viable GAP/Cdc42-concentration ratios and thus increases the robustness against copy number variations (cf. Figure 2). It does, however, not change the underlying mechanism qualitatively. (*Right*) Domain fusion of a Cdc42-GTP-binding domain with the Cdc24-binding Bem1-precursor, leads to a new connection in the Cdc42-interaction network that leads to recruitment of Cdc24 to the polar zone. On the level of sub-modules, this new connection constitutes a new functional submodule that we called "polar activation" (yellow triangle). In conjunction with transport of Cdc42 towards the polar zone, polar activation gives rise to the highly robust mutual-recruitment mechanism that is operational in WT yeast (regime of operation shaded in green in the (N_D,N_G)-parameter plane; cf. Figure 4C).

Materials and Methods

Modeling and Theory

For theory materials and methods see the attached "Supplementary Information" file.

Experiments

Media

All used media has the same base with 0.69% w/v Yeast nitrogen base (Sigma) + 0.32% Amino acid mix (4x CSM) (Formedium) + 2% Raffinose (Sigma), shortly, CSM+2% Raff. We used different galactose concentrations, denoted as *x*-Gal, where *x* denotes the Galactose percentage in media (*x* grams per 100 ml).

Name	Genotype	Source
yLL3a	*MATα can1-100, leu2-3, 112, his3-11,15, ura3Δ, BUD4-S288C*	(Laan et al., 2015)
yWKD065a	*MATα , -P$_{gal}$-sfGFP-Cdc42^{SW} (pWKD011 integrated), leu2-3, 112, his3-11,15, ura3Δ, BUD4-S288C*	This work
yWKD069a,b,c	*MATa, bem1:: KanMX6, URA-P$_{gal}$-sfGFP-Cdc42^{SW} (pWKD011 integrated) can1::P$_{mfa}$-HIS3 1, leu2-3, 112, his3-11,15, ura3Δ, BUD4-S288C*	This work
yYWKD070a	*MATa, bem1:: KanMX6, bem3::NATMX4, URA-P$_{gal}$-sfGFP-Cdc42^{SW} (pWKD011 integrated), can1:: P$_{mfa}$-HIS3, leu2-3, 112, his3-11,15, ura3Δ, BUD4-S288C*	This work
yYWKD071a	*MATα, URA3 P$_{gal}$- CDC42 (pWKD010 integrated), can1:: P$_{mfa}$-HIS3, leu2-3, 112, his3-11,15, ura3Δ, BUD4-S288C*	This work
yYWKD073a	*MATa, bem1:: KanMX6, bem3::NATMX4, URA3- P$_{gal}$-CDC42 (pWKD010 integrated), can1:: P$_{mfa}$-HIS3, leu2-3, 112, his3-11,15, ura3Δ, BUD4-S288C*	This work

Table 1. Strains used in this work

The plasmid pWKD010 contains P$_{gal}$-Cdc42, URA3, Pre/Post-Cdc42 homology regions, with Ampicillin as a selectable marker on the pRL368 backbone (Wedlich-Soldner et al., 2004). The pWKD011 was based on pWKD010 but in this case a superfolder GFP (sfGFP) (Pédelacq et al., 2006) is integrated within in the CdC42 protein based on previous work in *S. cerevisiae*, where a mCherry was integrated within Cdc42 (Woods et al., 2015). We eliminated the fitness effects from mcherry-Cdc42^{SW} by using a superfolder GFP protein, as suggested by work in *S. pombe* (Bendezú et al., 2015). We comfirmed that the presence of the sfGFP insertion did not affect the growthrate of our cells in an detectable way in our growth rate assay compared to cells with Cdc42 under the Gal promotor without sfGFP.

Growth rate assays

We used a plate reader (Infinite M-200 pro, Tecan) for growth rate assays, with 96 well plates from Thermo Scientific, Nunc edge 2 96F CL, Nontreated SI lid, CAT.NO.: 267427. Rows A and H and the columns 1 and 12 were not used for measurements. We inoculated a 96-well plate with 100 μl of medium and 5 μl of cells (from glycerol stocks) in each well, and grew the cells in 96-well plate for 48 hours at 30 °C in a warm room. Afterwards the cells were diluted 200x into a new 96 well plate, which were then placed in the plate reader and the OD600 was measured for 48 hours using a combination of linear and orbital shaking. We used a home-written data analysis program in Matlab to determine the log-phase doubling time for every well. The doubling time was approximated by fitting the slope of the linear regime of the log plot of the raw data. We performed at least two different experiments per condition, and per experiments we performed at least 4 technical replicates per strain/plate.

The error in the growth rate plot is the 68 % credible interval of the posterior distribution of these rates. The posteriors of non-WT backgrounds followed from normalization to WT rates by Monte Carlo simulations of the quotient of the original, non-normalized growth rate posteriors in a genetic background and the WT posterior in that medium. The non-normalized posteriors were calculated using the Metropolis-Hastings algorithm (Hastings, 1970), from a rectangular prior and Student-t likelihood functions of doubling time fit estimates of all replicates in that medium. The standard errors of individual estimates come from the standard error of the slope parameter resulting from weighted least squares (WLS) on a moving window per OD curve, using an instrument error proxy for the WLS weights. The standard errors of individual estimates are corrected for overdispersion by the average modified Birge ratio (Bodnar and Elster, 2014) across media for WT.

Microscopy assays

All microscopy images were taken with an Olympus IX81 inverted microscope equipped with Andor revolution and Yokogawa CSU X1 modules. We used a 100x oil objective. The acquisition software installed is Andor iQ3. The CG imaging plates were from Zell-Kontakt. They are black multiwell plates compliant to the SBS (Society for Biomolecular Screening) standard-format with cover glass bottoms made from borosilicate glass.

Cells were grown in an overnight culture in CSM +2% Raffinose +2% Galactose media, without reaching saturation. On the next day, three washing steps with CSM+2% Raffinose were performed and subsequently the cells were re-suspended in the desired media of 0%, 0.06% and 0.1% Galactose. To obtain cell populations at all galactose concentrations, we first incubated all strains in 2% galactose concentration, where Cdc42 is highly overexpressed, such that also *bem1Δ* cells are able to efficiently polarize. After 15 hours of incubation in 2% galactose concentration, we exchanged the medium to the desired galactose concentration. After 24 hours, we observed the cells with light microscopy. After 24 hours leftover Cdc42 from the initial 2% galactose concentration incubation is (very low due to degradation and dilution (Cdc42 half-life is about 8 hours (Christiano et al., 2014)) . From these images, we determined the average cell radius of the cells in the population.

Note that all of them contain the same base media: CSM+2% Raffinose. Afterwards the cells were incubated for 8 hours at 30℃, followed by an imaging session, and subsequently incubated for another 16 hours after which another imaging sessions was performed. We performed three independent experiments for each galactose concentration.

Microscopy data analysis

We performed bright field microscopy assays to monitor the cell size across different levels of Cdc42 in different genetic backgrounds. With ImageJ we manually determined the perimeter of the individual cells by fitting the live cells to a circle with the Measure tool. We performed three independent experiments per condition and per strain. In addition, we visually checked how many of the cells were

alive and how many were dead based on their morphology. The error bar on the fraction of dead cells as well as of the average cell radius, is calculated as the standard error over the total number of analysed cells.

References

Allard, C.A.H., Decker, F., Weiner, O.D., Toettcher, J.E., and Graziano, B.R. (2018). A size-invariant bud-duration timer enables robustness in yeast cell size control. PLOS ONE *13*, e0209301.

Altschuler, S.J., Angenent, S.B., Wang, Y., and Wu, L.F. (2008). On the spontaneous emergence of cell polarity. Nature *454*, 886–889.

Bendezú, F.O., Vincenzetti, V., Vavylonis, D., Wyss, R., Vogel, H., and Martin, S.G. (2015). Spontaneous Cdc42 Polarization Independent of GDI-Mediated Extraction and Actin-Based Trafficking. PLOS Biol. *13*, e1002097.

Bi, E., and Park, H.-O. (2012). Cell Polarization and Cytokinesis in Budding Yeast. Genetics *191*, 347–387.

Bodnar, O., and Elster, C. (2014). On the adjustment of inconsistent data using the Birge ratio. Metrologia *51*, 516–521.

Bose, I., Irazoqui, J.E., Moskow, J.J., Bardes, E.S.G., Zyla, T.R., and Lew, D.J. (2001). Assembly of Scaffold-mediated Complexes Containing Cdc42p, the Exchange Factor Cdc24p, and the Effector Cla4p Required for Cell Cycle-regulated Phosphorylation of Cdc24p. J. Biol. Chem. *276*, 7176–7186.

Brown, J.L., Jaquenoud, M., Gulli, M.-P., Chant, J., and Peter, M. (1997). Novel Cdc42-binding proteins Gic1 and Gic2 control cell polarity in yeast. Genes Dev. *11*, 2972–2982.

Butty, A.-C. (2002). A positive feedback loop stabilizes the guanine-nucleotide exchange factor Cdc24 at sites of polarization. EMBO J. *21*, 1565–1576.

Chenevert, J., Corrado, K., Bender, A., Pringle, J., and Herskowitz, I. (1992). A yeast gene (BEM1) necessary for cell polarization whose product contains two SH3 domains. Nature *356*, 77–79.

Chiou, J., Balasubramanian, M.K., and Lew, D.J. (2017). Cell Polarity in Yeast. Annu. Rev. Cell Dev. Biol. *33*, 77–101.

Chong, Y.T., Koh, J.L.Y., Friesen, H., Kaluarachchi Duffy, S., Cox, M.J., Moses, A., Moffat, J., Boone, C., and Andrews, B.J. (2015). Yeast Proteome Dynamics from Single Cell Imaging and Automated Analysis. Cell *161*, 1413–1424.

Christiano, R., Nagaraj, N., Fröhlich, F., and Walther, T.C. (2014). Global Proteome Turnover Analyses of the Yeasts S. cerevisiae and S. pombe. Cell Rep. *9*, 1959–1965.

Conant, G.C., and Wolfe, K.H. (2008). Turning a hobby into a job: How duplicated genes find new functions. Nat. Rev. Genet. *9*, 938–950.

Daniels, C.N., Zyla, T.R., and Lew, D.J. (2018). A role for Gic1 and Gic2 in Cdc42 polarization at elevated temperature. PLOS ONE *13*, e0200863.

Das, A., Slaughter, B.D., Unruh, J.R., Bradford, W.D., Alexander, R., Rubinstein, B., and Li, R. (2012). Flippase-mediated phospholipid asymmetry promotes fast Cdc42 recycling in dynamic maintenance of cell polarity. Nat. Cell Biol. *14*, 304–310.

Diepeveen, E.T., Gehrmann, T., Pourquié, V., Abeel, T., and Laan, L. (2018). Patterns of Conservation and Diversification in the Fungal Polarization Network. Genome Biol. Evol. *10*, 1765–1782.

Farr, A.D., Remigi, P., and Rainey, P.B. (2017). Adaptive evolution by spontaneous domain fusion and protein relocalization. Nat. Ecol. Evol. *1*, 1562–1568.

Freisinger, T., Klünder, B., Johnson, J., Müller, N., Pichler, G., Beck, G., Costanzo, M., Boone, C., Cerione, R.A., Frey, E., et al. (2013). Establishment of a robust single axis of cell polarity by coupling multiple positive feedback loops. Nat. Commun. *4*, 1807.

Glock, P., Ramm, B., Heermann, T., Kretschmer, S., Schweizer, J., Mücksch, J., Alagöz, G., and Schwille, P. (2019). Stationary Patterns in a Two-Protein Reaction-Diffusion System. ACS Synth. Biol. *8*, 148–157.

Good, M.C., Zalatan, J.G., and Lim, W.A. (2011). Scaffold Proteins: Hubs for Controlling the Flow of Cellular Information. Science *332*, 680–686.

Goryachev, A.B., and Leda, M. (2017). Many roads to symmetry breaking: molecular mechanisms and theoretical models of yeast cell polarity. Mol. Biol. Cell *28*, 370–380.

Goryachev, A.B., and Pokhilko, A.V. (2008). Dynamics of Cdc42 network embodies a Turing-type mechanism of yeast cell polarity. FEBS Lett. *582*, 1437–1443.

Grinhagens, S., Dünkler, A., Wu, Y., Rieger, L., Brenner, P., Gronemeyer, T., Mulaw, M.A., and Johnsson, N. (2020). A time-resolved interaction analysis of Bem1 reconstructs the flow of Cdc42 during polar growth. Life Sci. Alliance *3*, e202000813.

Halatek, J., and Frey, E. (2012). Highly Canalized MinD Transfer and MinE Sequestration Explain the Origin of Robust MinCDE-Protein Dynamics. Cell Rep. *1*, 741–752.

Halatek, J., Brauns, F., and Frey, E. (2018). Self-organization principles of intracellular pattern formation. Philos. Trans. R. Soc. B Biol. Sci. *373*, 20170107.

Hastings, W.K. (1970). Monte Carlo Sampling Methods Using Markov Chains and Their Applications. Biometrika *57*, 97.

Hooff, J.J.E., Tromer, E., Dam, T.J.P., Kops, G.J.P.L., and Snel, B. (2019). Inferring the Evolutionary History of Your Favorite Protein: A Guide for Molecular Biologists. BioEssays *41*, 1900006.

Howard, J., Grill, S.W., and Bois, J.S. (2011). Turing's next steps: the mechanochemical basis of morphogenesis. Nat. Rev. Mol. Cell Biol. *12*, 392–398.

Howell, A.S., Savage, N.S., Johnson, S.A., Bose, I., Wagner, A.W., Zyla, T.R., Nijhout, H.F., Reed, M.C., Goryachev, A.B., and Lew, D.J. (2009). Singularity in Polarization: Rewiring Yeast Cells to Make Two Buds. Cell *139*, 731–743.

Huang, K.C., Meir, Y., and Wingreen, N.S. (2003). Dynamic structures in Escherichia coli: Spontaneous formation of MinE rings and MinD polar zones. Proc. Natl. Acad. Sci. *100*, 12724–12728.

Irazoqui, J.E., Gladfelter, A.S., and Lew, D.J. (2003). Scaffold-mediated symmetry breaking by Cdc42p. Nat. Cell Biol. *5*, 1062–1070.

Johnson, B.R., and Lam, S.K. (2010). Self-organization, Natural Selection, and Evolution: Cellular Hardware and Genetic Software. BioScience *60*, 879–885.

Kang, P.J. (2001). A GDP/GTP Exchange Factor Involved in Linking a Spatial Landmark to Cell Polarity. Science *292*, 1376–1378.

Kang, P.J., Miller, K.E., Guegueniat, J., Beven, L., and Park, H.-O. (2018). The shared role of the Rsr1 GTPase and Gic1/Gic2 in Cdc42 polarization. Mol. Biol. Cell *29*, 2359–2369.

Klünder, B., Freisinger, T., Wedlich-Söldner, R., and Frey, E. (2013). GDI-Mediated Cell Polarization in Yeast Provides Precise Spatial and Temporal Control of Cdc42 Signaling. PLOS Comput. Biol. *9*, e1003396.

Knaus, M., Pelli-Gulli, M.-P., Drogen, F. van, Springer, S., Jaquenoud, M., and Peter, M. (2007). Phosphorylation of Bem2p and Bem3p may contribute to local activation of Cdc42p at bud emergence. EMBO J. *26*, 4501–4513.

Kozminski, K.G., Beven, L., Angerman, E., Tong, A.H.Y., Boone, C., and Park, H.-O. (2003). Interaction between a Ras and a Rho GTPase Couples Selection of a Growth Site to the Development of Cell Polarity in Yeast. Mol. Biol. Cell *14*, 4958–4970.

Kozubowski, L., Saito, K., Johnson, J.M., Howell, A.S., Zyla, T.R., and Lew, D.J. (2008). Symmetry-Breaking Polarization Driven by a Cdc42p GEF-PAK Complex. Curr. Biol. *18*, 1719–1726.

Kulak, N.A., Pichler, G., Paron, I., Nagaraj, N., and Mann, M. (2014). Minimal, encapsulated proteomic-sample processing applied to copy-number estimation in eukaryotic cells. Nat. Methods *11*, 319–324.

Kuo, C.-C., Savage, N.S., Chen, H., Wu, C.-F., Zyla, T.R., and Lew, D.J. (2014). Inhibitory GEF Phosphorylation Provides Negative Feedback in the Yeast Polarity Circuit. Curr. Biol. *24*, 753–759.

Laan, L., Koschwanez, J.H., and Murray, A.W. (2015). Evolutionary adaptation after crippling cell polarization follows reproducible trajectories. ELife *4*, e09638.

Lamas, I., Merlini, L., Vještica, A., Vincenzetti, V., and Martin, S.G. (2019). Optogenetics reveals Cdc42 local activation by scaffold-mediated positive feedback and Ras GTPase. BioRxiv.

Layton, A.T., Savage, N.S., Howell, A.S., Carroll, S.Y., Drubin, D.G., and Lew, D.J. (2011). Modeling Vesicle Traffic Reveals Unexpected Consequences for Cdc42p-Mediated Polarity Establishment. Curr. Biol. *21*, 184–194.

Lynch, M., Field, M.C., Goodson, H.V., Malik, H.S., Pereira-Leal, J.B., Roos, D.S., Turkewitz, A.P., and Sazer, S. (2014). Evolutionary cell biology: Two origins, one objective. Proc. Natl. Acad. Sci. *111*, 16990–16994.

Magadum, S., Banerjee, U., Murugan, P., Gangapur, D., and Ravikesavan, R. (2013). Gene duplication as a major force in evolution. J. Genet. *92*, 155–161.

Marston, A.L., Chen, T., Yang, M.C., Belhumeur, P., and Chant, J. (2001). A localized GTPase exchange factor, Bud5, determines the orientation of division axes in yeast. Curr. Biol. *11*, 803–807.

Martin, S.G., and Arkowitz, R.A. (2014). Cell polarization in budding and fission yeasts. FEMS Microbiol. Rev. *38*, 228–253.

Mukherjee, D., Sen, A., Boettner, D.R., Fairn, G.D., Schlam, D., Bonilla Valentin, F.J., McCaffery, J.M., Hazbun, T., Staiger, C.J., Grinstein, S., et al. (2013). Bem3, a Cdc42 GTPase-activating protein, traffics to an intracellular compartment and recruits the secretory Rab GTPase Sec4 to endomembranes. J. Cell Sci. *126*, 4560–4571.

Ozbudak, E.M., Becskei, A., and van Oudenaarden, A. (2005). A System of Counteracting Feedback Loops Regulates Cdc42p Activity during Spontaneous Cell Polarization. Dev. Cell *9*, 565–571.

Papp, B., Pál, C., and Hurst, L.D. (2003). Dosage sensitivity and the evolution of gene families in yeast. Nature *424*, 194–197.

Pédelacq, J.-D., Cabantous, S., Tran, T., Terwilliger, T.C., and Waldo, G.S. (2006). Engineering and characterization of a superfolder green fluorescent protein. Nat. Biotechnol. *24*, 79–88.

Rainey, P.B., Remigi, P., Farr, A.D., and Lind, P.A. (2017). Darwin was right: where now for experimental evolution? Curr. Opin. Genet. Dev. *47*, 102–109.

Ramm, B., Heermann, T., and Schwille, P. (2019). The E. coli MinCDE system in the regulation of protein patterns and gradients. Cell. Mol. Life Sci. *76*, 4245–4273.

Rapali, P., Mitteau, R., Braun, C., Massoni-Laporte, A., Ünlü, C., Bataille, L., Arramon, F.S., Gygi, S.P., and McCusker, D. (2017). Scaffold-mediated gating of Cdc42 signalling flux. ELife *6*, e25257.

Russell, J.J., Theriot, J.A., Sood, P., Marshall, W.F., Landweber, L.F., Fritz-Laylin, L., Polka, J.K., Oliferenko, S., Gerbich, T., Gladfelter, A., et al. (2017). Non-model model organisms. BMC Biol. *15*.

Shimada, Y., Wiget, P., Gulli, M.-P., Bi, E., and Peter, M. (2004). The nucleotide exchange factor Cdc24p may be regulated by auto-inhibition. EMBO J. *23*, 1051–1062.

Slaughter, B.D., Das, A., Schwartz, J.W., Rubinstein, B., and Li, R. (2009). Dual Modes of Cdc42 Recycling Fine-Tune Polarized Morphogenesis. Dev. Cell *17*, 823–835.

Smith, S.E., Rubinstein, B., Pinto, I.M., Slaughter, B.D., Unruh, J.R., and Li, R. (2013). Independence of symmetry breaking on Bem1-mediated autocatalytic activation of Cdc42. J. Cell Biol. *202*, 1091–1106.

Stevenson, B.J., Ferguson, B., De Virgilio, C., Bi, E., Pringle, J.R., Ammerer, G., and Sprague, G.F. (1995). Mutation of RGA1, which encodes a putative GTPase-activating protein for the polarity-establishment protein Cdc42p, activates the pheromone-response pathway in the yeast Saccharomyces cerevisiae. Genes Dev. *9*, 2949–2963.

Tiedje, C., Sakwa, I., Just, U., and Höfken, T. (2008). The Rho GDI Rdi1 Regulates Rho GTPases by Distinct Mechanisms. Mol. Biol. Cell *19*, 2885–2896.

Tong, Z., Gao, X.-D., Howell, A.S., Bose, I., Lew, D.J., and Bi, E. (2007). Adjacent positioning of cellular structures enabled by a Cdc42 GTPase-activating protein–mediated zone of inhibition. J. Cell Biol. *179*, 1375–1384.

Wedlich-Soldner, R. (2003). Spontaneous Cell Polarization Through Actomyosin-Based Delivery of the Cdc42 GTPase. Science *299*, 1231–1235.

Wedlich-Soldner, R., Wai, S.C., Schmidt, T., and Li, R. (2004). Robust cell polarity is a dynamic state established by coupling transport and GTPase signaling. J. Cell Biol. *166*, 889–900.

Witte, K., Strickland, D., and Glotzer, M. (2017). Cell cycle entry triggers a switch between two modes of Cdc42 activation during yeast polarization. ELife *6*, e26722.

Wittkopp, P.J., and Kalay, G. (2012). Cis-regulatory elements: molecular mechanisms and evolutionary processes underlying divergence. Nat. Rev. Genet. *13*, 59–69.

Woods, B., Kuo, C.-C., Wu, C.-F., Zyla, T.R., and Lew, D.J. (2015). Polarity establishment requires localized activation of Cdc42. J. Cell Biol. *211*, 19–26.

Woods, B., Lai, H., Wu, C.-F., Zyla, T.R., Savage, N.S., and Lew, D.J. (2016). Parallel Actin-Independent Recycling Pathways Polarize Cdc42 in Budding Yeast. Curr. Biol. *26*, 2114–2126.

Yocum, R.R., Hanley, S., West, R., and Ptashne, M. (1984). Use of lacZ fusions to delimit regulatory elements of the inducible divergent GAL1-GAL10 promoter in Saccharomyces cerevisiae. Mol. Cell. Biol. *4*, 1985–1998.

Zhang, B., Wang, Z.-X., and Zheng, Y. (1997). Characterization of the Interactions between the Small GTPase Cdc42 and Its GTPase-activating Proteins and Putative Effectors. J. Biol. Chem. *272*, 21999–22007.